

Metal-Substrate Interactions at Heterometallic Complexes and Clusters

Raphael Philip Bühler

Vollständiger Abdruck der von der TUM School of Natural Sciences der Technischen Universität München zur Erlangung des akademischen Grades eines

Doktors der Naturwissenschaften (Dr. rer. nat.)

genehmigten Dissertation.

Vorsitz: Prof. Dr. Angela Casini

Prüfende der Dissertation:

1. Prof. Dr. Roland A. Fischer
2. Prof. Dr. Ulrich K. Heiz
3. Prof. Dr. Jean-Yves Saillard

Die Dissertation wurde am 09.10.2024 bei der Technischen Universität München eingereicht und durch die TUM School of Natural Sciences am 14.11.2024 angenommen.

Die vorliegende Arbeit wurde im Zeitraum von Januar 2021 bis September 2024 im Fachgebiet Anorganische und Metallorganische Chemie der Technischen Universität München angefertigt.

Danksagung

Zuallererst möchte ich Ihnen, **Prof. Dr. Roland A. Fischer**, als Doktorvater meinen größten Dank dafür aussprechen, dass Sie mich über die Jahre hinweg unterstützt haben und mir die Möglichkeit gaben, in dieser fantastischen Gruppe zu arbeiten. Es ist ein besonderes Umfeld, das Sie hier am AMC geschaffen haben, voll mit diversen Charakteren und Expertisen. Es war ein richtiges Vergnügen, in einer so multidisziplinären Gruppe zu arbeiten. Ich möchte Ihnen auch für das Vertrauen danken, das Sie mir über die Jahre entgegengebracht haben, und für die Freiheit, die Sie mir gegeben haben, verschiedene Ideen zu verfolgen. Das war definitiv eine bereichernde Erfahrung für mich, die ohne Sie nicht möglich gewesen wäre!

Ich muss mich natürlich auch zutiefst bei dir **Dr. Christian Gemel** für die Unterstützung über all die Jahre bedanken. Deine Begeisterung für diese Chemie ist ansteckend und es macht einfach wahnsinnig Spaß mit dir zu arbeiten. Die viele Diskussionen in deinem Büro, ob über konkrete Themen oder über grundlegende Fragen zu philosophieren werde ich sehr vermissen. Ich will mich im speziellen bei dir für deine Unterstützung in den schwierigen Momenten bedanken. Dein offenes Ohr und deine ratsamen Vorschläge haben das worst-case Szenario bei Kupfer-Oxo erträglich gemacht. Vielen Dank und bitte bleib wie du bist!

Merci beaucoup à **Dr. Samia Kahlal** et **Prof. Dr. Jean-Yves Saillard**, pour la fructueuse collaboration sur ces dernières années. Vos calculs enrichissent énormément cette thèse et je vous en suis extrêmement reconnaissant. Au-delà de cela, nos régulières réunions **Prof. Dr. Jean-Yves Saillard** furent toujours un plaisir et je vous remercie pour votre soutien et tout ce que vous m'avez appris.

I am also extremely grateful to **Dr. Karla Andriani** and **Prof. Dr. Juarez L. F. Da Silva** for the collaboration. Your calculations are incredibly enriching to our experimental results, and this leads to a very unique work. Thank you for all the help over the years!

Außerdem möchte ich mich noch bei euch, **Dr. Mirza Cokoja**, **Dr. Gabriele Raudaschl-Sieber**, **Dr. Zahid Hussain**, **Dr. Julien Warnan**, **PD Dr. Alexander Pöthig**, **PD Dr. Gregor Kieslich**, **Dr. Dominik Halter** und **Dr. Romy Ettlinger** bedanken für eure Hilfsbereitschaft und Ratschläge über die Jahre. Diese positive Lehrstuhlatmosphäre ist sehr wertvoll! Darüber hinaus möchte ich mich noch bei dir **Dr. Markus Drees** bedanken für die witzigen Diskussionen über die Jahre und deine Hilfsbereitschaft mit der Graduate School. Auch dir **Dr. Eliza Gemel** möchte ich danken für die schönen Gespräche und deine Unterstützung bei den teilweise haarausreisenden NMR Probleme. Ich wünsche dir das Beste bei deiner neuen Position! Wenn schon NMR angesprochen wird, dann muss ich mich auch bei Ihnen **Dr. Rainer Haessner** für Ihre Unterstützung bedanken, als wir mit unserem Latein am Ende waren.

Auch ein herzliches Dankeschön an **Dr. Dana Weiß**, **Martin Schellerer** und **Rodica Dumitrescu**, eure organisatorische Unterstützung habe ich sehr geschätzt!

Ganz lieben Dank geht an alle meine Studenten **Robert Wolf**, **Sophia Ling**, **Ivan Antsiburov**, **Balasai Bock** und **Fabrizio Napoli**. An der Stelle freue ich mich, dass **Ivan**, **Fabrizio** und **Robert**, die ich in ihrer Masterarbeit betreuen durfte, ihre Promotion weiter in der OM-Gruppe machen. Ich war selbst noch keine drei Monate in der Promotion als ich deine Masterarbeit betreuen durfte **Ivan**. Durch deine Begeisterung war es sehr angenehm mit dir zu arbeiten und

ich wünsche dir viel Erfolg für das Ende deiner Promotion. Auch mit dir **Fabrizio**, war die Arbeit während deiner Masterarbeit und danach weiter als Laborpartner im „OM-West“ extrem spannend und bereichernd. Deine Beharrlichkeit bei diesem schwierigen Thema ist beeindruckend sowie deine Flexibilität auf einmal Kupfer-Oxo auf der ICCC vorzustellen. Es war echt super mit zusammen zu arbeiten und mit dir gemeinsam **Christian** immer wieder voll zulabern. Die Gespräche über die jeweiligen Projekte haben immer sehr viel Spaß gemacht und ich wünsche dir noch ganz viel Erfolg mit dem Rest deiner Promotion. Tja und dann haben wir noch den mehrfachen Wiederholungstäter **Robert**. Nach deiner Bachelorarbeit und deinem Forschungspraktikum, durfte ich, zusammen mit **Fabrizio**, deine Masterarbeit betreuen. Es war einfach top mit euch zu arbeiten und zusammen die Feinheiten der CoCo Chemie zu lernen. Du bist jetzt noch am Anfang deiner Promotion, aber ich bin mir sicher, dass es ein großer Erfolg sein wird. Viel Mut und vergiss nicht im Labor auch Spaß zu haben!

An dieser Stelle will ich mich bei allen aus der OM-Gruppe bedanken: **Max Schütz, Patricia Weishäupl, Maximilian Muhr, Richard Weininger, Ivan Anstiburov, Johannes Stephan, Fabrizio Napoli, Benedikt Kerscher und Robert Wolf**. Es war immer toll mit euch zu arbeiten, zusammen über das LIFDI zu verzweifeln und schön einmal pro Woche auf der Couch mit Kaffee über die letzten Errungenschaften oder, wie so oft, Misserfolge zu reden. Bei dir **Maxi** will ich mich nochmal bedanken für deine Betreuung während meiner Masterarbeit, die schöne Zeit als Laborpartner und für die Freundschaft, die über die Zeit entstanden ist. Mit dir über alles austauschen zu können und die spannenden gemeinsamen Projekte waren echt ein Highlight meiner Promotion.

A big thank goes out to the entire AMC Lab crew for the fantastic time over the years, the fascinating discussion (even though I don't always understand your topics) and for the fun times at the different group activities. Insbesondere möchte ich **Sarah Dummett, Kathrin Kollmansberger, Silva Kronawitter, Philip Stanley, Karina Hemmer, Patrick Mollik, Thomas Pickl und Sebastian Hallweger** hier danken. Es war mit euch immer lustig!

Ich möchte mich bei allen Freundinnen und Freunden bedanken die mich auf dem Weg unterstützt haben. En premier lieu, merci à mes amis du lycée, en particulier **Marija et Boris**. On ne se voit certes pas souvent mais c'est chaque fois un immense plaisir. Merci! Auch an **Laura** möchte ich mich bedanken, du bist eine wahre Freundin. Vielen Dank, dass du mir immer zuhörst und deine Leidenschaft für Photographie mit mir teilst. Ein riesiges Dankeschön geht natürlich an alle Uni Freunde **Micha, Richard, Sarah, Patrick, Theri, Robin und Abi**. Seit neun Jahren kennen wir uns und ich bin euch unendlich dankbar für die witzigen Momente und die gegenseitige Hilfe im Studium. Bei dir **Micha** möchte ich mich noch für diese großartige Freundschaft bedanken. Du warst in meinen schwierigsten Momenten immer für mich da und ich hätte es ohne dich nicht geschafft. Danke, für die Freundschaft, die so fest wie Familie ist und danke, dass ich mich immer auf dich verlassen kann.

Zum Schluss möchte ich mich bei meiner Familie bedanken. Meine Eltern **Hans-Peter und Geneviève** und meine Schwester **Caroline**. Je ne sais pas quels mots sont à la hauteur de ce que je vous dois. Merci beaucoup pour tout le soutien pendant toutes ces années, merci beaucoup de m'avoir poussé à suivre cette voie und danke schön, dass ihr so seid wir ihr seid. Ich wüsste nicht, was ich ohne euch machen würde. Merci beaucoup d'être aussi génial!

“The whole is greater than the sum of the parts.”

— Aristotle

Table of Content

Abstract	1
Zusammenfassung	2
List of Abbreviations.....	4
1 Introduction	5
1.1 Heterometallics as Powerful Tool in Bond Activation	7
1.1.1 Bond Activation at Heterobimetallic Complexes	7
1.1.2 Solid-State Heterometallics: The Cu/ZnO/Al ₂ O ₃ Example	9
1.2 Clusters: From Fundamental Principles to Reactivity Probing.....	12
1.2.1 Mackay Magic Numbers	13
1.2.2 Electronic Models	15
1.2.3 Metal Substrate Interactions with Hume-Rothery Clusters	18
1.2.4 Synthetic Challenges for Ligated <i>Hume-Rothery</i> Clusters	21
1.2.5 Strategies Towards Reactivity Probing	24
2 Objectives and Motivation.....	29
3 Synthetic Challenges Towards the Generation of Reactive Sites	31
3.1 Study I: Homoleptic Hexa- and Penta-Coordinated Gallium(I) Amide Complexes of Ruthenium and Molybdenum.....	31
3.2 Study II: C–H and Si–H Activation Reactions at Ru/Ga Complexes: A Combined Experimental and Theoretical Case Study on the Ru–Ga Bond.....	39
3.3 Study III: Photochemically Generated Reactive Sites at Ruthenium/Gallium Complexes: Catalysis vs. Cluster Growth	46
4 Accessing Chemical Diversity in Solution	53
4.1 Study IV: A living library concept to capture the dynamics and reactivity of mixed-metal clusters for catalysis	53
4.2 Study V: Cuprophilic Interaction in Polymeric [Cu ₁₀ O ₂ (Mes) ₆] _n	74
5 Conclusion and Outlook.....	84
6 References.....	87

7	Supporting Information	90
7.1	Supporting Information for Study I	90
7.2	Supporting Information for Study II	130
7.3	Supporting Information for Study III	154
7.4	Supporting Information for Study IV	185
7.5	Supporting Information for Study V	468
8	Appendix	483
8.1	Complete List of Publications	483
8.1.1	First Author Publications.....	483
8.1.2	Contributions to other Publications	484
8.1.3	Conference Contributions.....	485
8.2	Reprint Permissions	486
9	Eidesstattliche Erklärung.....	518

Abstract

This thesis explores the study of small *Hume-Rothery* inspired ligated heterometallic clusters and complexes of transition metals (TM) and group 12/13 metals (E) to gain insights into metal-substrate interactions relating to complex heterogeneous surfaces. The main challenge lies in balancing the stabilization of low-valent metals with the promotion of reactive sites.

To address this, the first strategy is exploring the organic ligand sphere and its variation influence on promoting reactive sites based on the ruthenium-gallium combination. The properties of amide ligands in stabilizing TM/E complexes are investigated through the exploration of $[\text{Ru}(\text{GaTMP})_5]$ and $[\text{Mo}(\text{GaTMP})_6]$, which reveals a competing π -interaction between the transition metal centers and the amido substituent with the unoccupied p_{π} orbitals of gallium. The reversible stabilization of reactive TM/E complexes through labile ligands is an additional key strategy for promoting reactive sites. The *in-situ* formation of unsaturated $[\text{Ru}(\text{GaCp}^*)_3\text{H}_2]$ allows for the direct exploration of TM/E species' properties in bond activation. Mass spectrometry based investigations confirm this 16 VE compound's capability for C-H activation, forming $[\text{Ru}(\text{GaCp}^*)_3(\text{C}_7\text{H}_7)\text{H}_3]$, and Si-H activation, yielding $[(\text{Ru}(\text{GaCp}^*)_3(\text{SiEt}_3)\text{H}_3]$, characterized by single-crystal X-ray diffraction. The reductive elimination of triethyl silane from $[(\text{Ru}(\text{GaCp}^*)_3(\text{SiEt}_3)\text{H}_3]$ under UV light (350 nm) demonstrates the principle of controlled dissociation of labile ligands, yielding the Ru^0 complex $[(\text{dppe})\text{Ru}(\text{GaCp}^*)_3]$ when irradiated in the presence of 1,2-bis(diphenylphosphino)ethane (dppe). Additionally, irradiation in the presence of 3-hexyne under a hydrogen atmosphere leads to catalytic hydrogenation. The silyl and hydride groups thus serve as selectively removable protective groups for the active transition metal center.

When viewing ligated *Hume-Rothery* inspired TM/E clusters as homogeneous mimics of structural motifs found in heterogeneous catalysts, the lack of chemical diversity poses a significant problem. The last strategy for investigating reactive sites is exploring the “living cluster libraries” concept, which emulates the diversity found on the surface of solid-state catalysts through unselective organometallic reactions. The libraries are characterized *via* LIFDI-MS using a double labeling strategy and varied collision energy experiments, with their evolution monitored by mass spectrometry. This approach provides chemical information without separating the clusters. Structural information is obtained through a framework combining density functional theory (DFT) with data mining analysis techniques to explore the full compositional configuration space. This methodology efficiently characterizes the clusters' structure-reactivity relationships, highlighted by the detection of the formate-containing species $[\text{Cu}_{11}\text{Zn}_6]\text{Cp}^*_8(\text{CO}_2)_2(\text{HCO}_2)$ and the isolation of $[\text{Cu}_4\text{Zn}_{10}]\text{Cp}^*_8$, acting as a pre-catalyst for the catalytic semihydrogenation of alkynes. First insights concerning incorporating an additional complexity parameter – the generation of sub-oxidic heterometallic clusters – are obtained by investigating the sub-oxidic organocopper polymer $[\text{Cu}_{10}\text{O}_2\text{Mes}_6]_n$.

Zusammenfassung

In dieser Arbeit werden kleine, *Hume-Rothery* inspirierte, ligierte heterometallische Cluster und Komplexe von Übergangsmetallen (TM) und Metallen der Gruppe 12/13 (E) untersucht, um Einblicke in Metall-Substrat-Wechselwirkungen zu gewinnen, welche relevant für komplexe heterogene Oberflächen sind. Die größte Herausforderung dabei ist, ein Gleichgewicht zwischen der Stabilisierung Metalle niedriger Oxidationsstufen und der Generierung reaktiver Stellen zu erreichen.

Die erste Strategie besteht darin, den Einfluss der organischen Ligandensphäre und deren Variation auf die Erschaffung reaktiver Stellen zu erforschen, basierend auf der Ruthenium-Gallium-Kombinationen. Die Eigenschaften von Amidliganden bei der Stabilisierung von TM/E Komplexen werden anhand von $[\text{Ru}(\text{GaTMP})_5]$ und $[\text{Mo}(\text{GaTMP})_6]$ untersucht, die eine konkurrierende π -Wechselwirkung zwischen den Übergangsmetallzentren und dem Amidliganden mit den unbesetzten p_{π} Orbitalen von Gallium zeigen. Die reversible Stabilisierung von reaktiven TM/E-Komplexen durch labile Liganden ist eine weitere Schlüsselstrategie zur Erschaffung reaktiver Stellen. Die *in-situ* Bildung von ungesättigtem $[\text{Ru}(\text{GaCp}^*)_3\text{H}_2]$ ermöglicht die direkte Erforschung der Eigenschaften von TM/E-Spezies bei Bindungsaktivierungen. Massenspektrometrische Untersuchungen bestätigen die Befähigung dieser 16 VE-Verbindung zur C-H Aktivierung unter Bildung von $[\text{Ru}(\text{GaCp}^*)_3(\text{C}_7\text{H}_7)\text{H}_3]$ und zur Si-H Aktivierung unter Bildung von $[(\text{Ru}(\text{GaCp}^*)_3(\text{SiEt}_3)\text{H}_3]$, welches durch Einkristall-Röntgenbeugung charakterisiert wurde. Die reduktive Eliminierung von Triethylsilan aus $[(\text{Ru}(\text{GaCp}^*)_3(\text{SiEt}_3)\text{H}_3]$ unter UV-Licht (350 nm) demonstriert das Prinzip der kontrollierten Dissoziation von labilen Liganden und führt zu dem Ru^0 -Komplex $[(\text{dppe})\text{Ru}(\text{GaCp}^*)_3]$, wenn dieser in Gegenwart von 1,2-Bis(diphenylphosphino)ethan (dppe) bestrahlt wird. Bestrahlung in Gegenwart von 3-Hexin unter Wasserstoffatmosphäre führt außerdem zur katalytischen Hydrierung. Die Silyl- und Hydridgruppen fungieren somit als selektiv entfernbare Schutzgruppen für das aktive Übergangsmetallzentrum.

Wenn man ligierte, *Hume-Rothery* inspirierte TM/E Cluster als homogene Imitatoren von Strukturmotiven in heterogenen Katalysatoren betrachtet, so stellt die fehlende chemische Vielfalt ein erhebliches Problem dar. Die letzte Strategie zur Untersuchung reaktiver Stellen ist die Erforschung des Konzepts der „lebenden Clusterbibliotheken“, welche die Diversität, die auf der Oberfläche von Festkörperkatalysatoren zu finden ist, durch unselektive organometallische Reaktionen nachahmt. Die Bibliotheken werden durch LIFDI-MS mit doppelter *Labeling*-Strategie und verschiedenen Kollisionsenergieexperimenten charakterisiert und ihre Entwicklung wird durch Massenspektrometrie überwacht. Dieser Ansatz liefert chemische Informationen, ohne die Cluster voneinander zu separieren. Strukturelle Informationen werden durch eine Kombination aus Dichtefunktionaltheorie (DFT) und *Data-Mining* Analyse gewonnen, um den gesamten Konfigurationsraum der

Zusammensetzung zu analysieren. Mit dieser Methode lassen sich die Struktur-Reaktivitäts-Beziehungen der Cluster effizient charakterisieren, was durch den Nachweis der Formiat-haltigen Spezies $[\text{Cu}_{11}\text{Zn}_6]\text{Cp}^*_8(\text{CO}_2)_2(\text{HCO}_2)$ und die Isolierung von $[\text{Cu}_4\text{Zn}_{10}]\text{Cp}^*_8$, das als Präkatalysator für die katalytische Semihydrierung von Alkinen fungiert, deutlich wird. Erste Erkenntnisse zur Einbeziehung eines zusätzlichen Komplexitätsparameters – die Erzeugung von suboxidischen heterometallischen Clustern – werden durch die Untersuchung des suboxidischen Organokupfer-Polymers $[\text{Cu}_{10}\text{O}_2\text{Mes}_6]_n$ gewonnen.

List of Abbreviations

δ	Chemical shift
ν	Wavenumber
ATR-IR	Attenuated total reflectance infrared spectroscopy
COD	1,5-Cyclooctadiene
COT	1,3,5-Cyclooctatriene
CO ₂	Carbon dioxide
Cp*	1,2,3,4,5-Pentamethylcyclopentadienyl
Cp* ^{Et}	1-Ethyl-2,3,4,5-tetramethylcyclopentadienyl
Cp*H	1,2,3,4,5-Pentamethylcyclopentadiene
DFT	Density functional theory
dppe	1,2-bis(diphenylphosphino)ethane
E	Group 12/13 metal
eq.	Equivalents
FT-IR	Fourier transform infrared spectroscopy
LIFDI-MS	Liquid injection field desorption ionization mass spectrometry
MeAllyl	2-Methylallyl
Mes	Mesityl
NMR	Nuclear magnetic resonance spectroscopy
SC-XRD	Single crystal X-ray diffraction
TM	Transition metal
TMP	2,2,6,6-Tetramethyl piperidinyl
VE	Valence electron

1 Introduction

Given the nature of metal-metal bonds and the plethora of possible combinations, the ensuing properties represent an immense realm of possibilities. Due to their varying atomic scale parameters, *i.e.*, the atomic radius, electronegativity, and valence electron concentration, which are decisive factors for structure formation and alloying in the solid state, drastically different properties can be obtained based on the choice of metals combined.^[1] Polarized bonds with a high covalent character between two metals can be obtained if the atomic radii are of a similar range ($\pm 15\%$) and the difference in electronegativity, while necessarily present, is not so significant as to favor ionic bonding ($\Delta EN \leq 0.5$ as a general rule).^[2] Together with the structure defining electron concentration (e/a), these are the criteria of *Hume-Rothery* phases^[2], of which the different Cu/Zn alloys are the most prominent examples, generally associating late transition metals with group 12/13 metals (Figure 1).

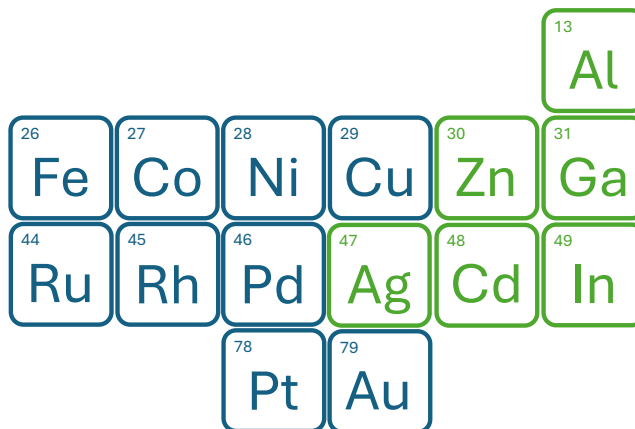


Figure 1: Relevant metals typically associated in Hume-Rothery phases, such as copper and zinc in the different brass phases.

Naturally, such polarized metal-metal bonds affect the chemical properties and behavior of the system. This phenomenon is nicely shown when comparing different Pd, Pd/Ag, Ni, and Ni/Zn phases.^[3] While the fundamental reactivity of the transition metals Pd and Ni in the hydrogenation of unsaturated carbon-carbon bonds does not change upon alloying, the selectivity observed is radically influenced. Whereas the pure Pd and Ni catalysts have a poor selectivity towards the semihydrogenation of alkynes, with increasing dilution in the second

metal, the PdAg_3 and NiZn_3 catalysts show remarkably selective semihydrogenation (Figure 2).^[3] This is not due to the chemical properties of the silver and zinc, as the palladium and nickel remain the active centers of the reaction. Instead, they alter the electronic properties of the catalytically active transition metals, reflected in a lower stability of the adsorbed alkene, leading to an enhanced selectivity towards the semihydrogenation product.

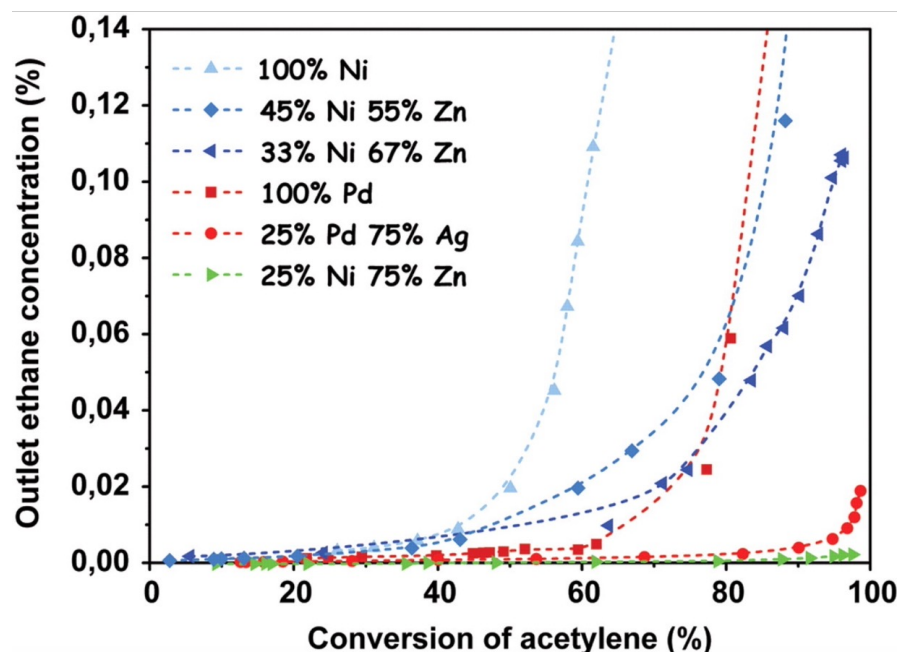


Figure 2: Concentration of ethane in a reactor outlet against acetylene conversion. Zero ethane represents perfect semihydrogenation selectivity. Original material from F. Studt, F. Abild-Pedersen, T. Bligaard, R. Z. Sørensen, C. H. Christensen, J. K. Nørskov, *Science* **2008**, 320, 1320-1322, reprinted with permission from AAAS.

The altering of a catalyst's selectivity upon alloying is a common phenomenon observed for a multitude of systems. Combined with the economic benefit obtained through "diluting" a precious metal, this increases the interest in *Hume-Rothery* phases as alternatives to pure precious metal catalysts.

The peculiarities of the metal-metal interactions observed in *Hume-Rothery* phases can be further expanded to the realms of heterometallic colloids, clusters, and organometallics, with different challenges arising in each size regime. This thesis focuses on studying reactive sites in heterometallic complexes and clusters and probing their reactivities towards small molecules. Before delving into the intricacies of cluster chemistry, let's take a step back and

address the metal-substrate interactions observed in classical organometallic chemistry and solid-state heterogeneous catalysts in the broader sense.

1.1 Heterometallics as Powerful Tool in Bond Activation

1.1.1 Bond Activation at Heterobimetallic Complexes

The activation of small molecules by low valent metal centers has been the cornerstone of organometallic chemistry for decades. Classic examples include the *Wilkinson* catalyst^[4], which is active in the hydrogenation of olefins, or the *Schrock*^[5] and *Grubbs*^[6-7] catalysts used in olefin metathesis. Recently, the behavior of homo- and heterobimetallic compounds towards the bond activation of small molecules has been the subject of intense research.

The first aspect to consider in discussing the properties of such homo- and heterobimetallic complexes is the possibility of metal-metal cooperativity for bond activation, which can be made of use. This is nicely shown by the $[\text{RhCp}^*(\text{GaCp}^*)(\text{CH}_3)_2]$ complex readily rearranging to $[\text{RhCp}^*(\text{C}_5\text{Me}_4\text{Ga}(\text{CH}_3)_3)]$ as reported by *Fischer et al.* (Figure 3).^[8] This exceptional C-C activation is thought to originate from the spatial proximity of a very electrophilic gallium center to a very nucleophilic d⁸ rhodium(I) center.

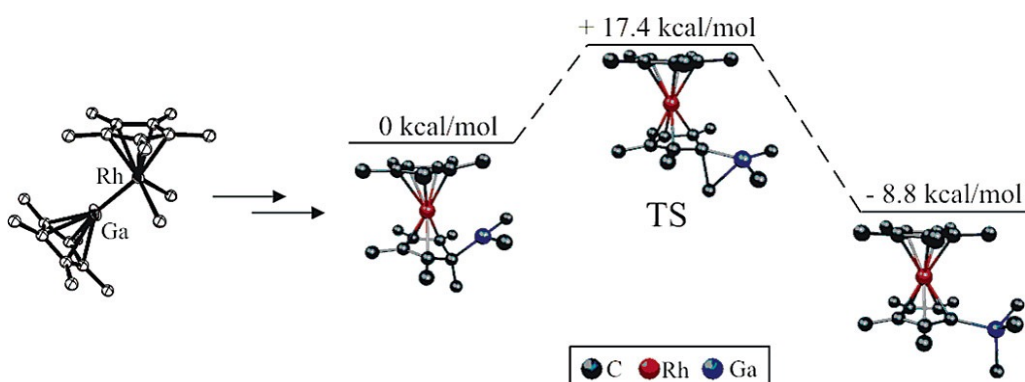


Figure 3: Simplified reaction pathway for the C-C activation forming $[\text{RhCp}^*(\text{C}_5\text{Me}_4\text{Ga}(\text{CH}_3)_3)]$. Reprinted with permission from T. Cadenbach, C. Gemel, R. Schmid, R. A. Fischer, *J. Am. Chem. Soc.* **2005**, 127, 17068-17078. Copyright 2005, Copyright 2005, American Chemical Society.

The effect of the heterometal can be more passive, however, and is nicely shown by the germyl-rhodium complex reported by *Campos et al.*^[9-10] Incorporating the germyl fragment

drastically alters the reactivity of the rhodium center, which, in addition to semi-hydrogenation, permits *cis/trans*-isomerization, favoring the *E*-isomer (Figure 4).

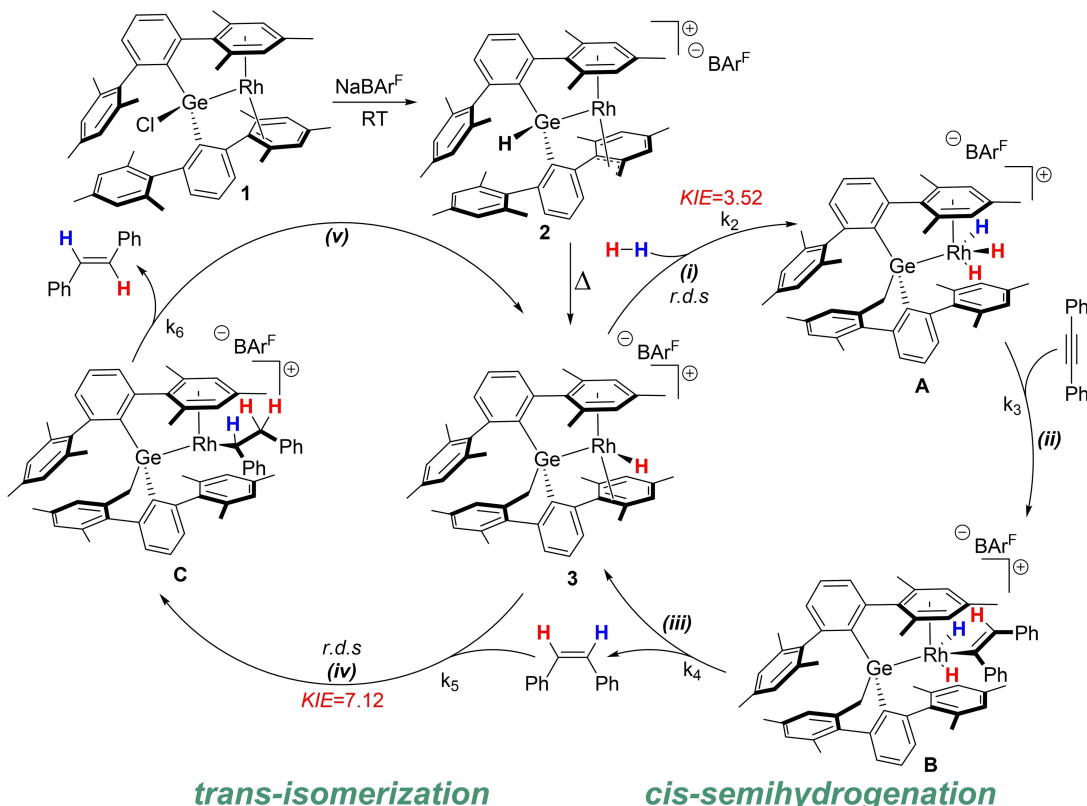


Figure 4: Proposed mechanism for the *cis*-semihydrogenation of alkenes and subsequent isomerization to *trans*-alkenes catalyzed by a germyl-rhodium complex. Reprinted with permission from S. Bajo, C. A. Theulier, J. Campos, *ChemCatChem* **2022**, *14*, e202200157. Copyright 2022, John Wiley and Sons.

Group 13 metals have been reported to be effective reactivity modulators and when incorporated as metalloligands can be used to “tune” the properties of a transition metal. Using a *Lewis* acidic Ga^{III} ligand, Lu *et al.* prepared a Ga^{III}-Ni⁰ complex that catalytically hydrogenates CO₂ to formate^[11-12] (Figure 5) with an impressively high initial turnover frequency (TOF) of 9700 h⁻¹, greatly exceeding prior Ni homogenous catalysts. The Ga^{III} acceptor ligand is crucial for the stabilization of the anionic [HNiGaL]⁻ intermediate.^[12] This is highlighted by the comparison with the gallium-free analog NiLH₃, which is unable to bind and activate H₂ towards deprotonation and is thus catalytically inactive in the hydrogenation of CO₂. This Ga^{III}-Ni⁰ complex is a striking example of how the electronic properties of a TM-E interaction can play a significant role in tailoring the reactivity of the transition metal.

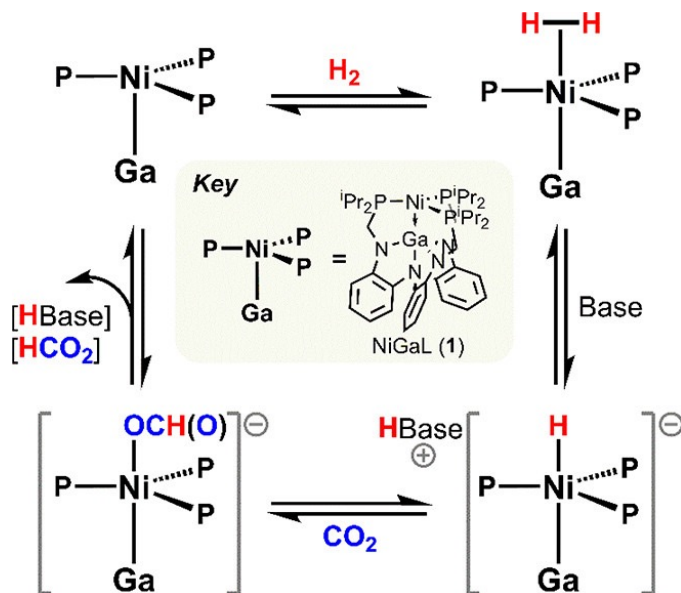


Figure 5: Reaction scheme of the catalytic CO_2 hydrogenation with NiGaL. Reprinted with permission from R. C. Cammarota, M. V. Vollmer, J. Xie, J. Ye, J. C. Linehan, S. A. Burgess, A. M. Appel, L. Gagliardi, C. C. Lu, *J. Am. Chem. Soc.* **2017**, 139, 14244-14250. Copyright 2017, American Chemical Society.

The influence of a heterometal on the reactivity of a transition metal in complex chemistry can be drastic and demonstrates the importance of these TM-E interactions. This is not unlike what has been observed in the solid state, where TM-E bond polarization and cooperativity can be made of use.

1.1.2 Solid-State Heterometallics: The Cu/ZnO/ Al_2O_3 Example

Studying the processes occurring on solid-state catalysts' surfaces during catalytic reactions is challenging, often leading to numerous controversies and intense debates. This is particularly true for catalytic systems involving alloys or metals supported on other metal oxides. The local geometries, such as steps, kinks, edges, or structural defects, are crucial.^[13] However, the local composition and oxidation states may be even more significant. To grasp these complexities, let's examine one of the most well-studied yet complicated systems: the catalytic synthesis of methanol from carbon dioxide.

For the past 50 years, methanol production from syngas has relied on a Cu/ZnO/ Al_2O_3 catalyst.^[14] Today, CO_2 from steel production is utilized for a more environmentally friendly process. Despite producing nearly 30 million tons of methanol annually, the precise

mechanism of this conversion remains unclear.^[15] Notably, oxygen-free Cu/Zn alloys have demonstrated similar catalytic reactivity as ZnO/Cu catalysts. Studies have shown that the Cu/Zn surface oxidizes to Cu/ZnO under catalytic reaction conditions.^[16] Typically, this conversion occurs at temperatures between 200°C and 500°C and pressures of 60 bar, leading to the oxidation of Zn atoms due to their greater affinity for oxygen compared to Cu.^[14] Additionally, it is believed that high-pressure conditions facilitate the coordination of CO/CO₂ conversion intermediates to the surface.^[14] This raises questions about the role of oxidic species in catalytic mechanisms and the structural characteristics of active centers.

Earlier research proposed various models for the surface of Cu/Zn(O) alloys, including a Cu⁰-Zn⁰ surface, a surface with Zn^{δ+} species, a layer of ZnO^x over the Cu⁰ surface, and a Cu⁰ surface interspersed with ZnO species.^[14] However, all models report a strong metal-support interaction (SMSI) between Cu and Zn. Studies on heterogeneous Cu/ZnO catalyst systems for methanol production from syngas have shown that Cu atoms tend to coordinate with H atoms. In contrast, the Zn-O part of the system coordinates with the oxygen atoms of CO₂, CO, or other O* intermediates in the turnover process.^[16-18] The dissociation of dihydrogen on the Cu atoms of the surface is electronically assisted by the oxide sites, which also disperse the Cu sites over the surface layer.^[18] Additionally, sub-oxidic zinc centers appear to enhance catalytic activity further by acting as adsorption sites for oxygen-bearing intermediates.

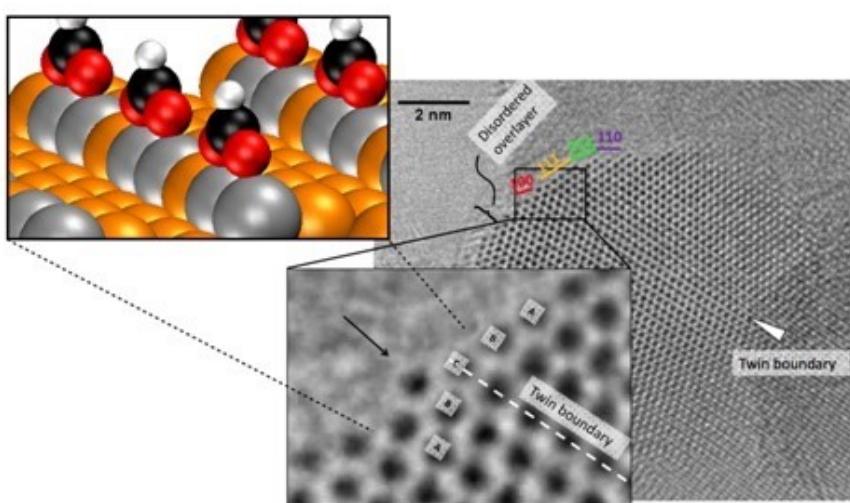
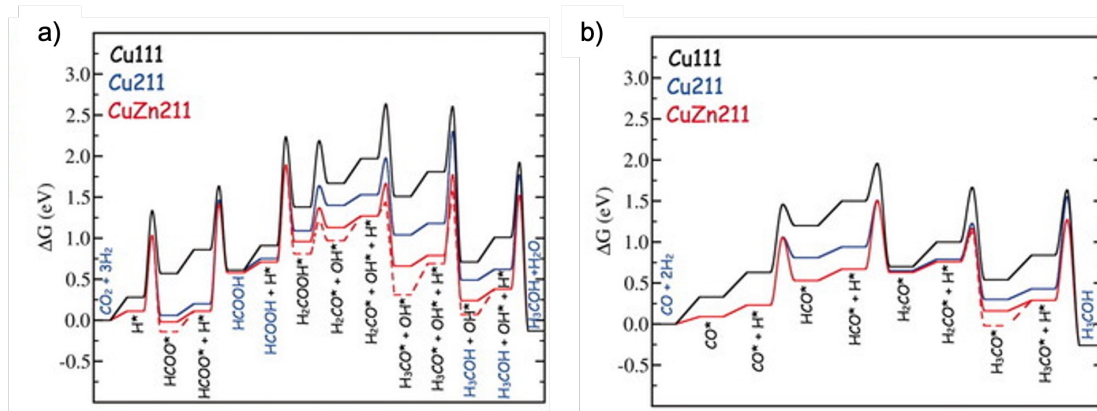


Figure 6: Schematic representation of the active site of Cu/ZnO/Al₂O₃ as suggested by calculations and aberration-corrected HR-TEM images. Copper = orange; zinc = gray; carbon = black; oxygen = red; and hydrogen = white. Reprinted with permission from G. Centi, S. Perathoner, in CO₂: A Valuable Source of Carbon (Eds.: M. D. Falco, G. Iaquaniello, G. Centi), Springer London, London, 2013, pp. 147-169^[19], copyright 2013, Springer Nature, itself based on the findings of Schlägl et al.^[13]

Kinks, edges, steps, and other types of copper atoms stacking faults seem to be the active catalytic centers of the reaction (Figure 6). Regarding the reaction mechanism, two theories are considered most likely. The first one postulates a stepwise reduction of CO_2 to formate (HCOO), dioxomethylene (H_2COO), formaldehyde (H_2CO), and finally to methanol (CH_3OH) (Figure 7). *In-situ* IR studies of the CO_2 hydrogenation to methanol over Cu/SiO_2 and $\text{ZrO}_2/\text{SiO}_2$ suggest a similar mechanism.

Alternatively, a second mechanism suggests that CO primarily forms from CO_2 via a reversed water-gas-shift reaction and is subsequently hydrogenated.^[18] This mechanism aligns with a theoretical study of CO_2 hydrogenation over a Cu/ZrO_2 surface.^[17] The syngas' composition can also influence the mechanism and surface structure. If the proportion of CO_2 in the syngas mixture is very low, the CO-rich atmosphere creates reducing conditions, leading to a $\text{Cu}^0\text{-Zn}^0$ surface and favoring the second mechanism (Figure 7).^[13] Conversely, a higher proportion of CO_2 leads to surface oxidation, resulting in surface species such as ZnO_x or $\text{Zn}^{\delta+}$, which tend to follow the first mechanism described.^[14] Experiments varying CO/ CO_2 ratios have shown that the surface can transition between different models based on these conditions.



*Figure 7: DFT calculated Gibbs free energy diagram for CO_2 (a) and CO (b) hydrogenation on $\text{Cu}(111)$, $\text{Cu}(211)$, and $\text{CuZn}(211)$ surfaces. Original material from M. Behrens, F. Studt, I. Kasatkin, S. Kühl, M. Hävecker, F. Abild-Pedersen, S. Zander, F. Girgsdies, P. Kurr, B.-L. Kniep, M. Tovar, R. W. Fischer, J. K. Nørskov, R. Schlögl, *Science* **2012**, 336, 893-897, reprinted with permission from AAAS.*

The example of the $\text{Cu}/\text{ZnO}/\text{Al}_2\text{O}_3$ system highlights a significant challenge: the dynamic behavior of the catalyst's surface, coupled with the limitations of solid-state analytical methods, makes it enormously difficult, if not impossible, to fully understand the active site(s).

It is crucial to remember the molecular nature of all steps in a catalytic cycle, best summed up by *Helmut Schwarz*^[20]:

"Chemistry is a local event: bond breaking and bond making are confined to the catalytically active center."

This is where metal clusters offer a unique advantage. They can mimic the structural characteristics of heterogeneous catalysts while retaining their molecular nature, thus allowing the full use of the molecular analytics toolbox.

1.2 Clusters: From Fundamental Principles to Reactivity Probing

Before delving into the reactivities of metal clusters and the challenges we face, let us explore the fundamental principles of this diverse class of compounds.

Though situated at the boundary between larger, undefined materials like nanoparticles and bulk phases, metal clusters are fundamentally of a *molecular* nature. As atom-precise compounds: *every atom counts*.^[21-22] Just as the introduction of a simple methyl group to phenylethylamine—a natural regulator of monoamine neurotransmitters in humans^[23]—creates amphetamine, a potent central nervous system stimulant^[24], the properties of metal clusters can also change drastically with even slight variations in their composition.

A clear example of this is the difference observed between Pt₁₂ and Pt₁₃ clusters. The former exhibits more than twofold activity in the catalytic oxygen reduction reaction compared to the latter (Figure 8).^[25] Their structures can explain this: Pt₁₃ adopts a highly stable icosahedron shape due to its magic number composition (which will be explored in the following chapter), whereas Pt₁₂ has a more labile and unsaturated structure.

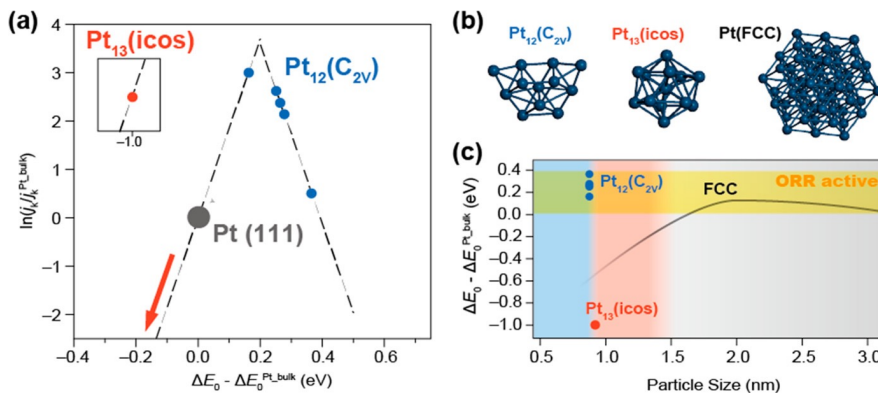


*Figure 8: Volcano plot and free energy diagram for the oxygen reduction reaction by Pt_{12} , Pt_{13} , and bulk Pt with (a) Kinetic current density (j_k) plotted as a function of the calculated oxygen adsorption energy (ΔE_0) (relative to bulk Pt), (b) optimized structures of $\text{Pt}_{12}(\text{C}_{2v})$, $\text{Pt}_{13}(\text{icos})$, and the FCC (face-centered cubic) Pt nanoparticle and (c) diagram of the relation between the particle size and the relative oxygen binding energy (ΔE_0). Reprinted with permission from T. Imaoka, H. Kitazawa, W.-J. Chun, S. Omura, K. Albrecht, K. Yamamoto, *J. Am. Chem. Soc.* **2013**, 135, 13089–13095. Copyright 2013, American Chemical Society.*

1.2.1 Mackay Magic Numbers

Metal clusters' electronic and geometric characteristics are crucial in determining their stability, and various models have been developed to understand them. One such model is the concept of the *atom magic number*. This idea dates back to 1962 when *Mackay* published a thought experiment in which he derived a closed multiple-shell structure of icosahedral geometry (Figure 9) from the dense non-crystallographic packing of equal spheres, predicting its natural occurrence.^[26] Nearly twenty years later, initial experimental evidence supporting the preferred formation of such geometrically closed shell structures emerged from observations of mass abundances of gaseous *magic number* sized xenon clusters in mass spectrometric experiments.^[27]

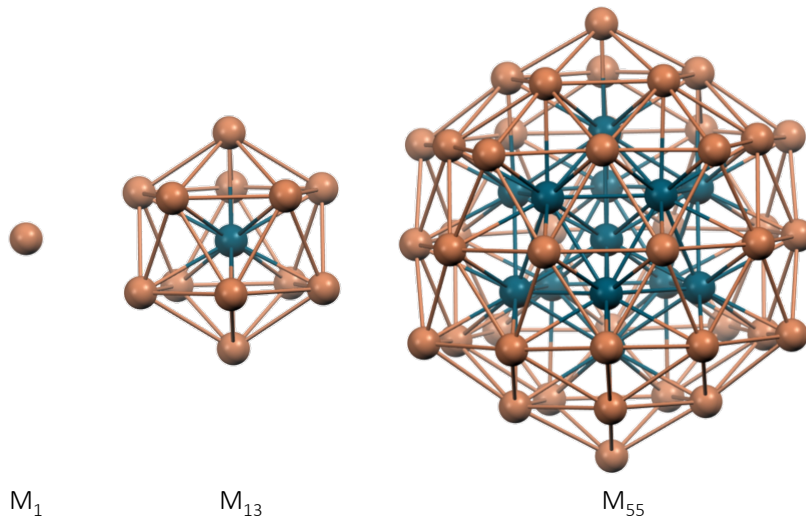
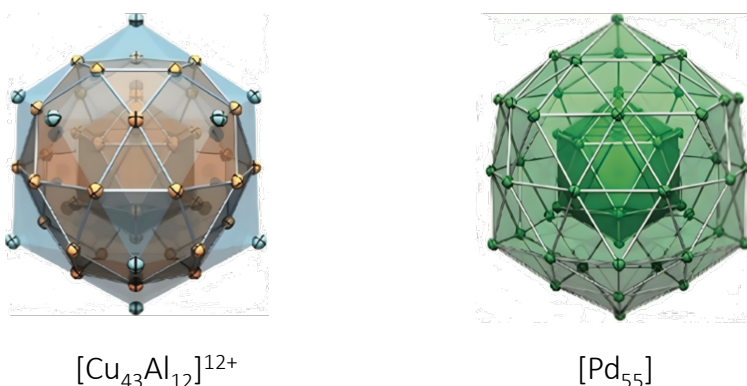


Figure 9: Overview of the icosahedral shell structure of cluster obeying the Mackay magic numbers. M_1 serves as the foundation, with a further 12 atoms forming the first icosahedral shell, resulting in M_{13} , followed by a further 42 atoms for the second icosahedral shell, forming M_{55} , and so on. The atoms of the new shell are marked in orange.

Magic number clusters with 13, 55, 147, 309, 561, ... atoms are recurring motifs in experimental and theoretical studies of naked- and ligand-stabilized metal clusters. Their remarkable stability across the periodic table is attributed to their high sphericity and the inherent minimization of surface energies, following classical *Wulff* construction principles.^[28] In the example above, we discussed how the Pt₁₃ cluster was significantly less catalytically active than the one-atom-lighter Pt₁₂ cluster (Figure 8). This difference is due to the *magic number Mackay* structure of Pt₁₃.^[25]

Similarly, the structures of the two ligated M₅₅ clusters [Pd₅₅(P*i*Pr₃)₁₂(μ₃-CO)₂₀]^[29] and [Cu₄₃Al₁₂Cp*₁₂]^[30] (Figure 10) can be very well rationalized with the *Mackay magic numbers*. In the former, the central Pd₅₅ core forms an icosahedral, two-shell *Mackay* cluster. The latter, best described as Cu@Cu₁₂@(Cu₃₀Al₁₂), exhibits a mixed-metal outer *Mackay* shell and is the first reported example of a ligated heterometallic *Mackay*-type M₅₅ *magic* atom number cluster with a perfect two-shell icosahedral structure.



*Figure 10: Naked metal cores of $[\text{Cu}_{43}\text{Al}_{12}\text{Cp}^*_{12}]$ and $[\text{Pd}_{55}(\text{P}^i\text{Pr}_3)_{12}(\mu_3\text{-CO})_{20}]$ ^[29] with typical $M@M_{12}@M_{42}$ Mackay structure. Reprinted with permission and adapted from J. Weßing, C. Ganesamoorthy, S. Kahlal, R. Marchal, C. Gemel, O. Cador, A. C. H. Da Silva, J. L. F. Da Silva, J.-Y. Saillard, R. A. Fischer, Angew. Chem. Int. Ed. **2018**, *57*, 14630–14634. Copyright 2018, John Wiley and Sons.*

1.2.2 Electronic Models

Besides geometric considerations, electronic models can also help to understand a cluster's stability or instability. One straightforward concept for understanding (inorganic) cluster compounds is based on the 8 valence-electron rule (for main group clusters) or the 18 valence-electron rule (for transition metal clusters).^[31] This concept applies to *Zintl* clusters like NaSi, which forms $[\text{Si}_4]^{4-}$ tetrahedra, where each Si atom obeys the 8-electron rule.^[32] Another example is carbonyl clusters like $[\text{Ir}_4](\text{CO})_{12}$, which forms an Ir₄ tetrahedron, with each Ir atom obeying the 18 valence-electron rule.^[33]

The challenge in assessing the electronic structure of more complex clusters arises because many clusters cannot be adequately described by classical two-center, two-electron bonds, as the connectivity of the vertices often exceeds the number of valence electrons available for bonding.^[31] Several approaches exist to understand these seemingly "electron-deficient" clusters, such as $[\text{B}_6\text{H}_6]^{2-}$. In the *Wade-Mingos* concept, a B-H or M(CO)₃ fragment is associated with three orbitals available for skeletal cluster bonding.^[31] According to this concept, the number of required valence electrons does not change when successively removing vertices from the *closo* cluster, resulting in *nido*, *arachno*, or *hypno* clusters.^[31] The *Wade-Mingos* rules have proven to be a powerful tool for empirical structure prediction based on relatively simple electron counting rules.

The *Jellium* model for spherical clusters and the related *superatom* concept^[34], originally developed as an additional tool for rationalizing magic number clusters, have also proved to be powerful tools for understanding cluster stability. This model allows for a heuristic and empirical estimation of stability and reactivity patterns of ligated metallic clusters by comparing their chemistry with that of single atoms or elements.^[34] The starting premise of this model is that the positive charges of the nuclei are distributed homogeneously, requiring clusters to be spherical or *quasi-spherical*, and the delocalized electrons are subjected to the resulting potential field.^[34] This situation is very similar to that of electrons within an atom, with further similarities found between the occupancy and nature of these resulting *Jellium* orbitals and atomic orbitals^[35] (Figure 11).

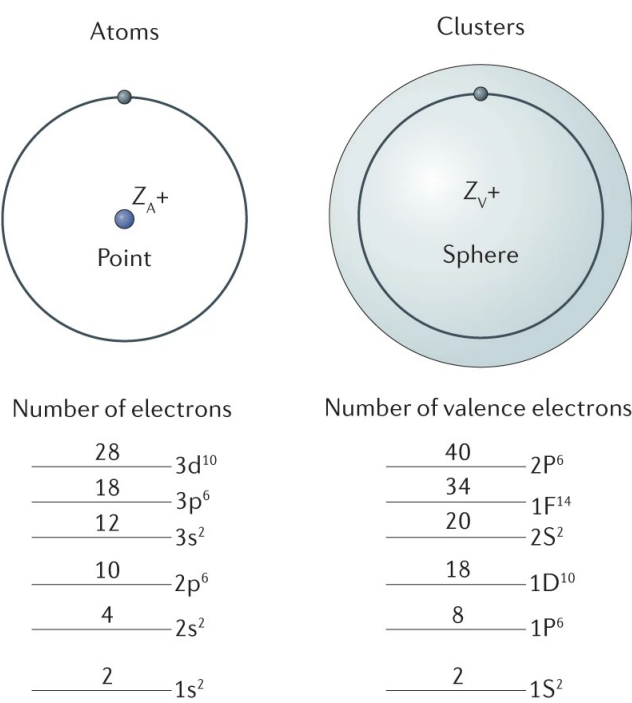


Figure 11: Electron occupancy situation for the orbitals of an atom (left) and a superatom (right). Reprinted with permission from T. Tsukamoto, T. Kambe, T. Imaoka, K. Yamamoto, *Nat. Rev. Chem.* **2021**, 5, 338-347. Copyright 2021, Springer Nature.

As a result, the same degeneracies occur as with an atom and the stabilities of specific cluster sizes can be directly related to the valence electron count. However, the order of the resulting electronic states in the *superatomic* description deviates from that observed for simple atoms (Figure 11). This deviation can be explained by the fact that in the *superatom*, the positive

charge is distributed throughout the cluster sphere, whereas in a single atom, the positive charge is centered at the nucleus.^[36-37]

The heterometallic $[\text{Cu}_{43}\text{Al}_{12}\text{Cp}^*_{12}]$ cluster described earlier, while conforming to the *Mackay magic numbers*, can also be analyzed using the *Jellium* model, yielding a total of 67 electrons, which is close to the closed-shell number 68.^[30] Considering the *superatomic* orbitals led to the prediction of a quadruplet ground state with three unpaired electrons, a hypothesis experimentally verified through magnetic measurements.^[30]

The *Jellium* model has been successfully applied to both small and large clusters, as well as to homometallic and heterometallic compounds. A notable example of a small heterometallic *superatom* is the nanobrass $[\text{Cu}_4\text{Zn}_4]\text{Cp}^*_4(\text{CN}^t\text{Bu})_4$, which exhibits an 8-electron $1\text{S}^21\text{P}^6$ closed-shell configuration for the $[\text{Cu}_4\text{Zn}_4]$ core.^[38] However, the electron count can be much larger, as demonstrated by Schnöke's $[\text{Al}_{50}\text{Cp}^*_{12}]$ ^[39], which has the following configuration: $1\text{S}^21\text{P}^61\text{D}^{10}2\text{S}^21\text{F}^{14}2\text{P}^61\text{G}^{18}2\text{D}^{10}3\text{S}^21\text{H}^{22}2\text{F}^{14}3\text{P}^61\text{I}^{26}$, totaling 138 electrons^[40] (Figure 12).

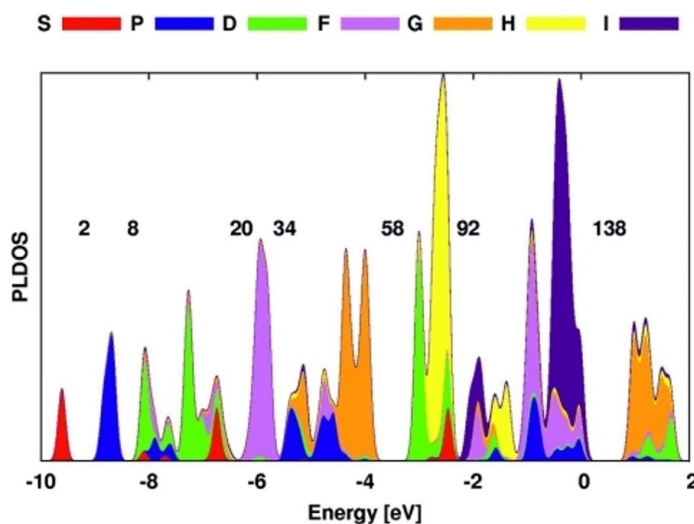


Figure 12: Projected local density of states (PLDOS) for $[\text{Al}_{50}\text{Cp}^*_{12}]$ with significant energy gaps following the closing of the electronic shells for $n = 2, 8, 20, 34, 58, 92$, and 138 . Reprinted with permission from P. A. Clayborne, O. Lopez-Acevedo, R. L. Whetten, H. Grönbeck, H. Häkkinen, Eur. J. Inorg. Chem. **2011**, 2011, 2649-2652. Copyright 2011, John Wiley and Sons.

In the case of "electron-deficient" d^9 transition metals, they can also participate in *superatom* orbitals when combined with "electron-rich" elements such as coinage metals (s^1d^{10} configuration in the M^0 oxidation state). This is well illustrated by the heterometallic

$[\text{RhAg}_{21}\{\text{S}_2\text{P}(\text{O}^n\text{Pr})_2\}_{12}]$ cluster, which contains an icosahedral $[\text{Rh@Ag}_{12}]^{3+}$ 8-electron *superatom* at its core (Figure 13).^[41] The 12 Ag atoms each donate one electron to the *superatom* orbitals, while the Rh atom withdraws one to fill its d shell. Together with the charge of the cluster core, this results in a net reduction of the electron count to 8, yielding the expected $1\text{S}^21\text{P}^6$ configuration.^[41]

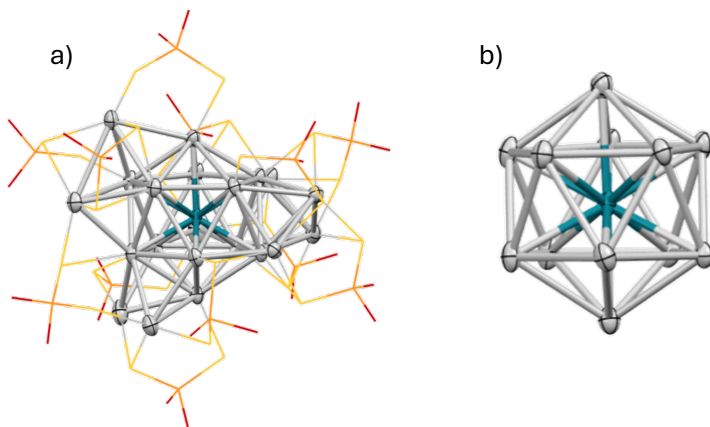


Figure 13: a) Structure of $[\text{RhAg}_{21}\{\text{S}_2\text{P}(\text{O}^n\text{Pr})_2\}_{12}]$ and b) its icosahedral $[\text{Rh@Ag}_{12}]^{3+}$ 8 electron superatom core.

1.2.3 Metal Substrate Interactions with Hume-Rothery Clusters

There is growing interest in experimental and theoretical studies of atom-precise, sub-nanometer *Hume-Rothery* inspired TM/E clusters. For instance, Höltzl *et al.* explored the size- and charge-dependent CO_2 and H_2 activation on small $[\text{Cu}_n\text{Zn}]^{0/+}$ ($n = 3 - 6$) clusters through DFT-based methods.^[42] Exploring notably the interactions of these clusters with CO_2 , they could conclude that CO_2 preferentially binds to the zinc with one of its oxygens and to the adjacent copper with the carbon (Figure 14). This is explained by the partially positive charge of the Zn atom, which results from the polarized Cu-Zn bond.^[42] Such information is precious for further understanding the reactive properties of various Cu/Zn based systems.

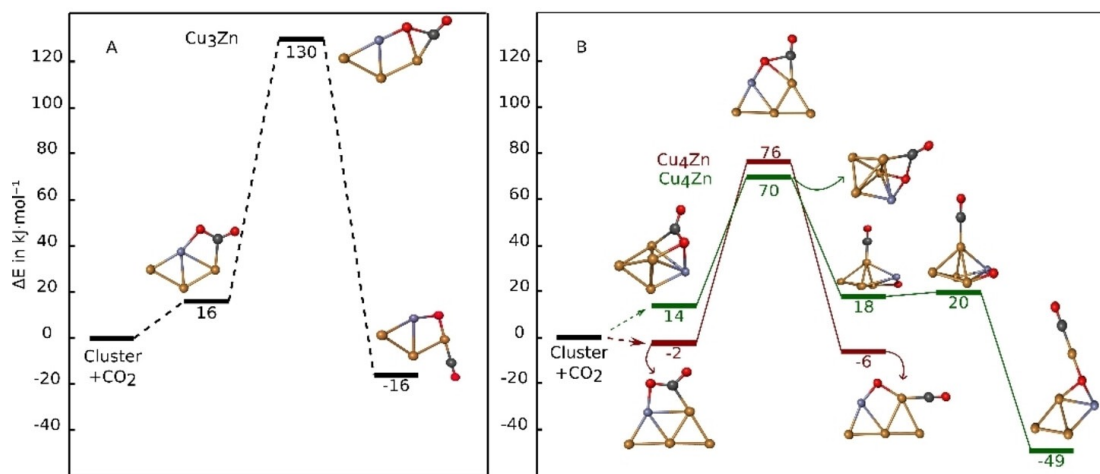


Figure 14: Rate determining steps for the CO_2 dissociation on the neutral clusters Cu_3Zn and Cu_4Zn . Copper = orange; zinc = violet; carbon = grey; oxygen = red. Reprinted with permission from B. Zamora, L. Nyulászi, T. Höltzl, ChemPhysChem 2024, 25, e202300409. Copyright 2024, John Wiley and Sons.

Concerning ligated TM/E clusters, the isolation, characterization, and study of $[\text{H}_4\text{Cu}_6(\text{AlCp}^*)_6]$ ^[43] (Figure 15) was a milestone. The arrangement of copper and aluminum atoms in the M_{12} unit of this compound is in analogy to the polyhedral forms of well-known intermetallic phases such as Cu_9Al_4 , MgCu_2 , and γ -brass. Additionally, Fischer *et al.* discovered that this copper-aluminum species reacts stoichiometrically with benzonitrile to produce the hydrometallated $[\text{H}_3\text{Cu}_6(\text{AlCp}^*)_6(\text{N}=\text{CHPh})]$ (Figure 15).^[43]

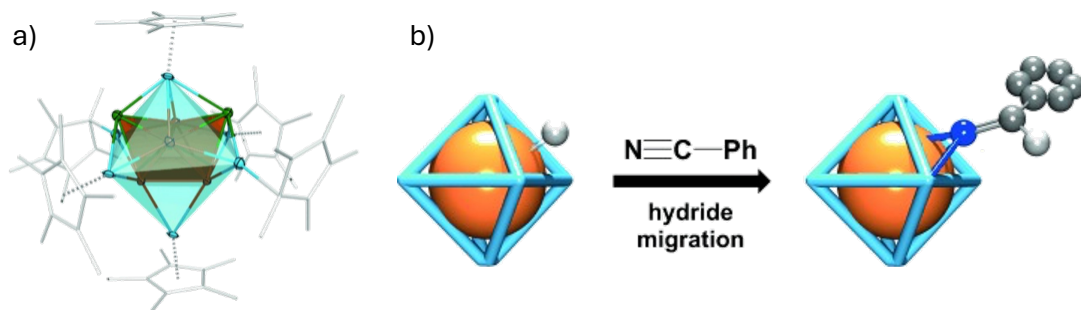
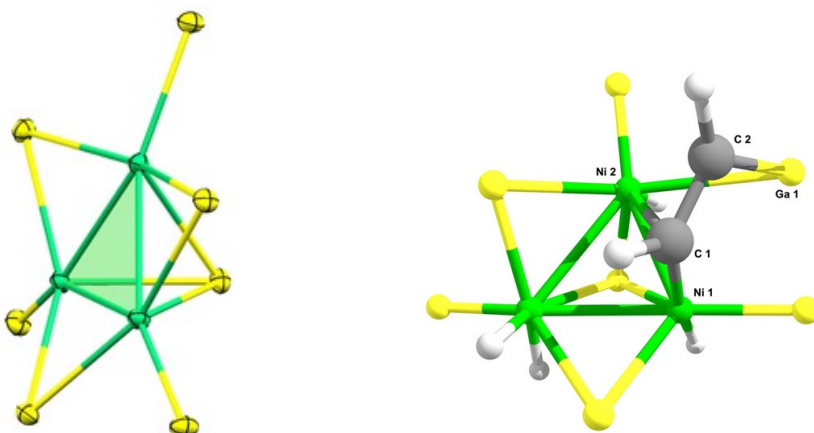


Figure 15: a) Structure of $[\text{H}_4\text{Cu}_6(\text{AlCp}^)_6]$ showing a Cu_6 core embedded in an $(\text{AlCp}^*)_6$ shell. b) schematic reaction of $[\text{H}_4\text{Cu}_6(\text{AlCp}^*)_6]$ with benzonitrile yielding $[\text{H}_3\text{Cu}_6(\text{AlCp}^*)_6(\text{N}=\text{CHPh})]$. Reprinted with permission from C. Ganesamoorthy, J. Weßling, C. Kroll, R. W. Seidel, C. Gemel, R. A. Fischer, Angew. Chem. Int. Ed. 2014, 53, 7943-7947. Copyright 2014, John Wiley and Sons.*

The hydrometallation of the nitrile resembles an insertion, the first fundamental step in the semi-hydrogenation of acetylene. While the reductive elimination of the imine could not be observed, this still marks an apparent success in underlying the chemical similarities of ligated

TM/E clusters to their related solid-state counterparts. Similar reactivity is observed in $[\text{Ni}(\text{ZnCp}^*)_4(\text{ZnCH}_3)_4]$ and $[\text{Pt}(\text{ZnCp}^*)_4(\text{ZnCH}_3)_4]$, where the zinc-coordinated nickel and platinum compounds react with terminal alkynes, releasing methane.^[44] Furthermore, *Fischer et al.* demonstrated through DFT calculations on theoretical complexes of the form $[\text{Ni}(\text{ER})_n(\text{C}_2\text{H}_x)_{4-n}]$ that such compounds can be considered molecular models for semi-hydrogenation catalysts and reaction intermediates.^[45]

Looking at the Ni/Ga system, the reaction of $[\text{Ni}(\text{COD})_2]$ ($\text{COD} = 1, 5\text{-cyclooctadiene}$) with GaTMP (TMP = 2,2,6,6-tetramethylpiperidinyl) forms a $[\text{Ni}_3(\text{GaTMP})_7]$ cluster (Figure 16).^[46] This cluster features a Ni_3 triangle with three terminal GaTMP, three bridging GaTMP, and one face-capping GaTMP, leaving the Ni_3 triangle fully accessible on one side. This accessibility of the transition metal core is, as one can expect, very reactive. Additionally, the gallium-coordinated Ni_3 core is reminiscent of a structural motif of the Ni_5Ga_3 phase proposed to be the active site in semihydrogenation. Under a hydrogen atmosphere, this cluster forms a mixture of di-, tetra-, and hexahydrides. Surprisingly, these hydridic species are only stable under a hydrogen atmosphere, reductively eliminating once the H_2 pressure has been relieved.^[46]



*Figure 16: Molecular structure of $[\text{Ni}_3(\text{GaTMP})_7]$ (left) and DFT optimized geometry of the acetylene coordinated $[\text{H}_4\text{Ni}_3(\text{GaTMP})_7]$ (right). TMP ligands were omitted for clarity. Reprinted with permission from M. Muhr, H. Liang, L. Allmendinger, R. Bühler, F. E. Napoli, D. Uka, M. Cokoja, C. Jandl, S. Kahlal, J.-Y. Saillard, C. Gemel, R. A. Fischer, *Angew. Chem. Int. Ed.* **2023**, *62*, e202308790. Copyright 2023, John Wiley and Sons.*

The polyhydridic $[\text{H}_x\text{Ni}_3(\text{GaTMP})_7]$ ($x = 2, 4, 6$) species are catalytically active in alkyne semihydrogenation.^[46] The selectivity is similar to those observed for other Ni and Ni/Ga based

heterogenous catalysts. DFT calculations of the coordination of acetylene and ethylene of the terahydridic $[H_4Ni_3(GaTMP)_7]$ found an exergonic, *quasi*-perpendicular coordination adduct of acetylene to one of the Ni-Ni bonds ($\Delta G = 4.4$ kcal/mol). In comparison, the coordination of ethene is endergonic ($\Delta G = 25.4$ kcal/mol).^[46] This is in perfect agreement with the observed selectivity towards the semihydrogenation product. The minimum structure of the acetylene adduct shows a noticeably short Ga-C distance, suggesting active participation of the gallium in the stabilization. The selectivity showcased by the $[Ni_3(GaTMP)_7]$ cluster and the analogy to the solid state makes it a very strong candidate for further elucidation of the heterometal's role in tuning the nickel center's properties.

1.2.4 Synthetic Challenges for Ligated *Hume-Rothery* Clusters

As remarkable as the aforementioned ligated TM/E clusters are, several synthetic challenges hinder access to a wide variety of molecular mimics and impede the study of metal-substrate interactions using TM/E complexes and clusters.

The typical synthetic approach towards *Hume-Rothery* inspired TM/E clusters involves the reaction of low-valent organometallic complexes of the two desired metals. Typical starting materials include transition-metal olefins, such as $[M(COD)_2]$ ($M = Ni, Pd, Pt$), $[M_2(dvds)_3]$ ($M = Ni, Pd$; dvds = 1,1,3,3-tetramethyl-1,3-divinyldisiloxane) or $[Mo(1,3-butadiene)_3]$, as well as various transition-metal aryl complexes, $[Fe_2Mes_4]$ or $[CuMes_5]$ for example. These are brought to reaction with low valent group 12/13 compounds, typically of the form E^lR ($E = Al, Ga, In$; $R = C(SiMe_3)_3, Cp^*, TMP$) or Zn_2Cp^{*2} . A complex set of competing reactions – *coordination*^[47-48], *ligand exchange*^[49-50], and *redox reactions*^[30, 51] – are possible between the low valent TM and E complexes and cannot be directly controlled.

The complex nature of these parallel processes makes the synthesis of TM/E clusters impossible to predict and is reflected in the yields – although there are exceptions. Two examples illustrate this problem well: $[Cu_3Zn_4]Cp^{*5}$ ^[52] and the $[Ga_xNi_y](NiCp^*)_6$ ($x = 6 - 7$; $y = 0 - 2$) cluster family^[50]. In both cases, the Cp^* transmetallates to the transition metal,

forming Cu^ICp* and Ni^ICp*. In the case of [Cu₃Zn₄]Cp*₅, the competing reactions occurring during the synthesis lead to a very poor yield, with only a few crystals being obtained.

While this last point is not an issue for the [Ga_xNi_y](NiCp*)₆ ($x = 6 - 7$; $y = 0 - 2$) cluster family, the *quasi-identical* (NiCp*)₆ shell they exhibit makes their separation impossible.^[50] Depending on the choice of the starting nickel-olefin complex and the reaction conditions, the relative quantities of each one of the [Ga_xNi_y](NiCp*)₆ cluster family can be controlled to an extent, it is however not possible to isolate one of them in a pure form (Figure 17). The individual clusters can be seen as *islands of stability* with little energetic difference between them, leading to their parallel formation. The inherent complexity of this cluster family has led to two decades of intense research before they could be fully understood.

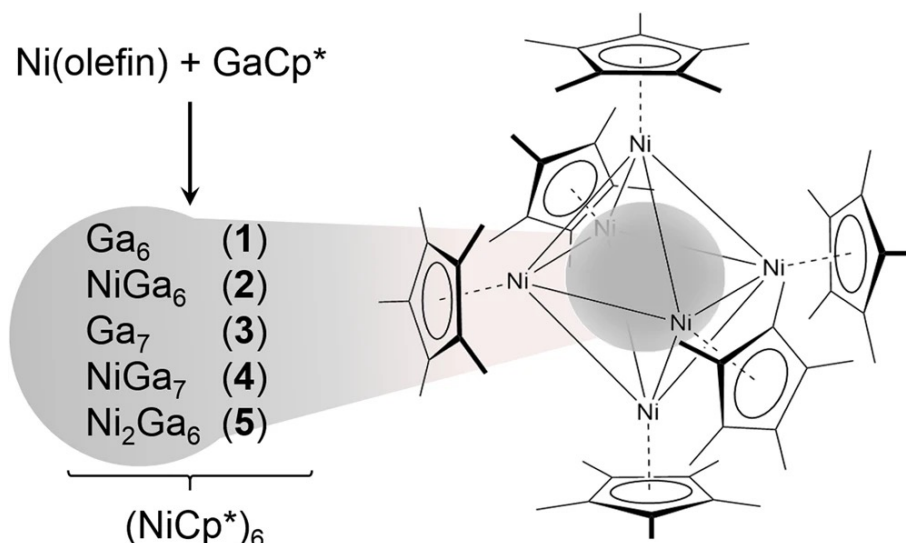


Figure 17: General composition of the $[Ga_xNi_y](NiCp^*)_6$ ($x = 6 - 7$; $y = 0 - 2$) cluster family, sharing a quasi-identical $(NiCp^*)_6$ shell. Reprinted with permission from M. Muhr, J. Stephan, L. Staiger, K. Hemmer, M. Schütz, P. Heiß, C. Jandl, M. Cokoja, T. Kratky, S. Günther, D. Huber, S. Kahlal, J.-Y. Saillard, O. Cador, A. C. H. Da Silva, J. L. F. Da Silva, J. Mink, C. Gemel, R. A. Fischer, *Commun. Chem.* **2024**, *7*, 29. Copyright 2024, Springer Nature.

Finally, the lack of reactivity towards small molecules of most ligated TM/E clusters isolated so far must be addressed. While metal-substrate interactions observed for $[\text{H}_4\text{Cu}_6(\text{AlCp}^*)_6]$, $[\text{Ni}(\text{ZnCp}^*)_4(\text{ZnCH}_3)_4]$ and $[\text{Ni}_3(\text{GaTMP})_7]$ (Chapter 1.2.3) are truly remarkable and offer valuable insights, they remain exceptions rather than the rule. Just as for the $[Ga_xNi_y](NiCp^*)_6$ ($x = 6 - 7$; $y = 0 - 2$) cluster family discussed above, the world of ligated TM/E clusters is full of

species, which, after a painstakingly long process of synthesis optimization and purification, lack any exciting reactivity. In short, they either die or are dead on arrival.

This is illustrated well by the different low-valent ligated Cu/Zn clusters synthesized using organocopper and -zinc complexes. This cluster family exhibits various sizes, Cu:Zn ratios, and electronic configurations (Figure 18). The smallest of this Cu/Zn family, $[\text{CuZn}_2]\text{Cp}^*_3$ ^[53], features a CuZn₂ triangle and can be described as a two-electron σ -aromatic compound, similar to the isostructural $[\text{Cu}_2\text{Al}]\text{Cp}^*_3$ ^[54] and $[\text{Zn}_3\text{Cp}^*_3]^+$ ^[53]. As previously mentioned, $[\text{Cu}_4\text{Zn}_4]\text{Cp}^*_4(\text{CN}^t\text{Bu})_4$ ^[38] has an 8-electron *superatom* core^[38], while the copper-rich $[\text{Cu}_{10}\text{Zn}_2](\text{Mes})_6\text{Cp}^*_2$ ^[55], despite its geometry deviating from a spherical shape, can also be described using the *superatom* model, resulting in a $1S^21P_z^22S^2$ configuration.

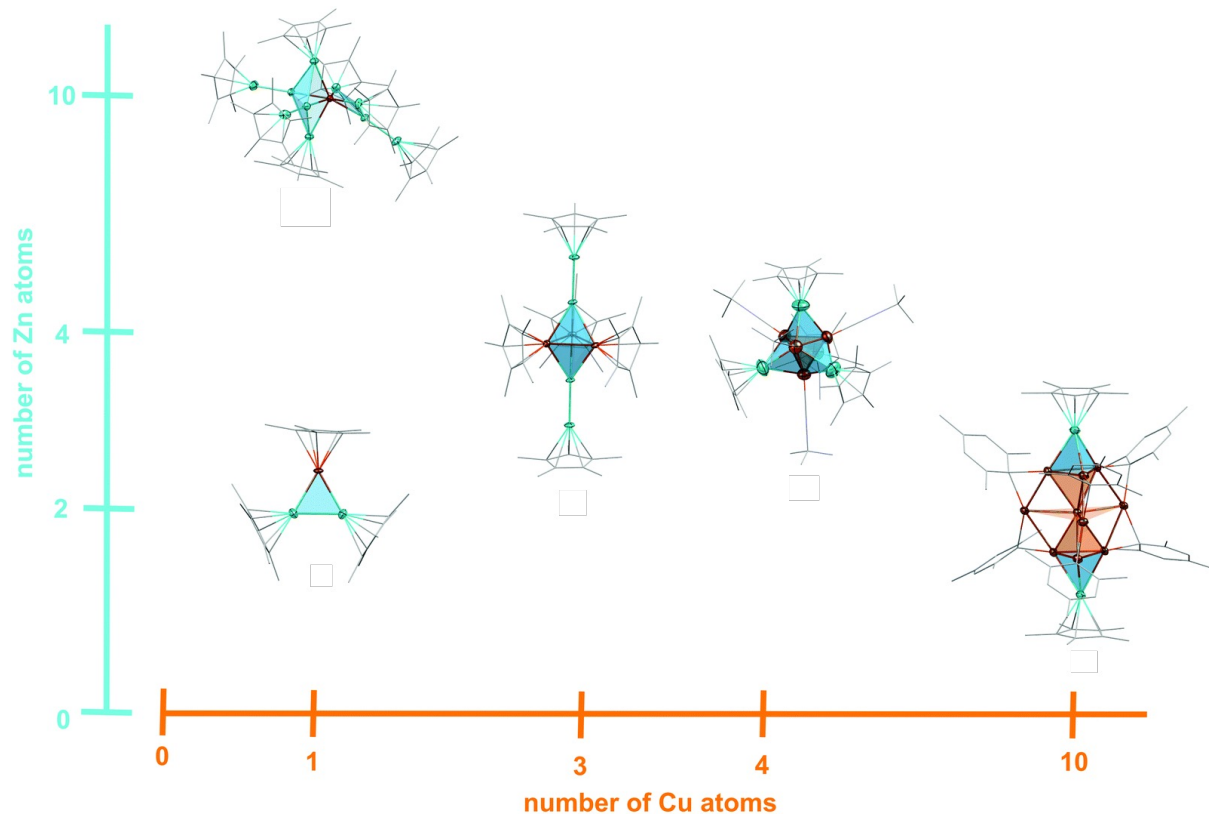


Figure 18: Overview of ligated Cu/Zn clusters with polyhedral faces colored. Hydrogen atoms are omitted for clarity, and organic ligands are shown as wireframes. Color code: Cu = orange, Zn = light blue, C = grey. Reprinted with permission from M. Schütz, C. Gemel, W. Klein, R. A. Fischer, T. F. Fässler, *Chem. Soc. Rev.* **2021**, 50, 8496–8510. Copyright 2021, Royal Society of Chemistry.

While the diversity of geometries, compositions, and electronic structures offered by this family of nanobrass clusters is fascinating, it is essential to note that none of these clusters

exhibit reactivity towards carbon dioxide or any other small molecule. Therefore, contrary to the DFT optimized $[Cu_nZn]^{0/+}$ ($n = 3 - 6$)^[42] clusters discussed earlier, these ligated Cu/Zn compounds are not suitable molecular mimics for the processes occurring during catalytic methanol synthesis.

1.2.5 Strategies Towards Reactivity Probing

1.2.5.1 Placeholder Ligands

This raises the question of how to promote the reactivity of ligated metal clusters, or rather: how can we stabilize the reactive sites of TM/E compounds sufficiently so that they may be isolated while avoiding hindering any metal-substrate interaction?

Introducing labile ligands to the transition metal is a possibility for enabling the reversible and controlled formation of reactive sites. In the field of E(III)-TM heterometallic complexes, several recent examples illustrate this approach: *Nakao et al.* reported an Al(III)-Rh complex that, through the Lewis acidic character of the metalloligand and the dissociation of a placeholder alkene ligand, performs cooperative C-F bond activation.^[57] Similarly, *Ozerov et al.* demonstrated a B(III)-Ir complex capable of activating C-H bonds.^[58]

A particularly elegant strategy utilizing a labile placeholder ligand was reported by *Lu et al.* Using the pincer-type PAIP ligand Al(NPhCH₂PⁱPr₂)₂Mes, they formed the Al(III)-Ni complexes [(PAIP)Ni₂(μ-COD)] and [(PAIP)Ni₂(μ-N₂)] (Figure 19).^[59] These complexes feature labile bridging ligands, COD or N₂, which upon dissociation create reactive sites on the nickel centers, enabling cooperative H-H and C-H bond activation.^[59]

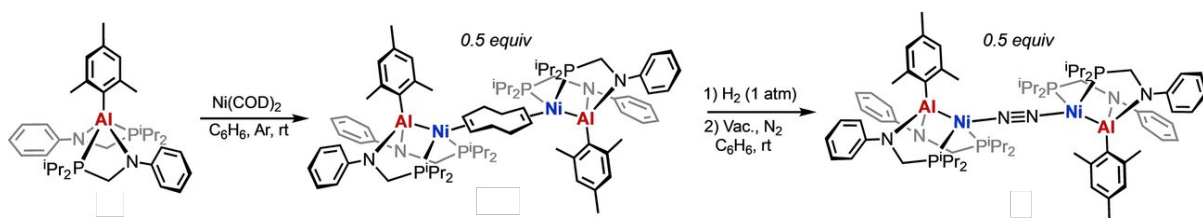


*Figure 19: Synthesis of the complexes $[(\text{PAIP})\text{Ni}_2(\mu\text{-COD})]$ and $[(\text{PAIP})\text{Ni}_2(\mu\text{-N}_2)]$ showcasing labile placeholder ligands. Reprinted with permission from B. J. Graziano, M. V. Vollmer, C. C. Lu, *Angew. Chem. Int. Ed.* **2021**, *60*, 15087–15094. Copyright 2021, John Wiley and Sons.*

In the realm of homoleptic TM/E(I) complexes, the $[\text{Ni}(\text{AlCp}^*)_3\text{H}(\text{SiEt}_3)]$ compound reported by Fischer *et al.* was shown to undergo a thermally induced reductive elimination of triethylsilane, as could be demonstrated by the formation of the homoleptic $[\text{Ni}(\text{AlCp}^*)_4]$ when this reaction is performed in the presence of AlCp^* .^[60] The unsaturated $[\text{Ni}(\text{AlCp}^*)_3]$ intermediate, resulting from the reductive elimination, is highly reactive and was shown to perform C-H activation of benzene, forming $[\text{Ni}(\text{AlCp}^*)_3(\text{H})(\text{AlCp}^*(\text{Ph}))]$ ^[60] (Figure 20).

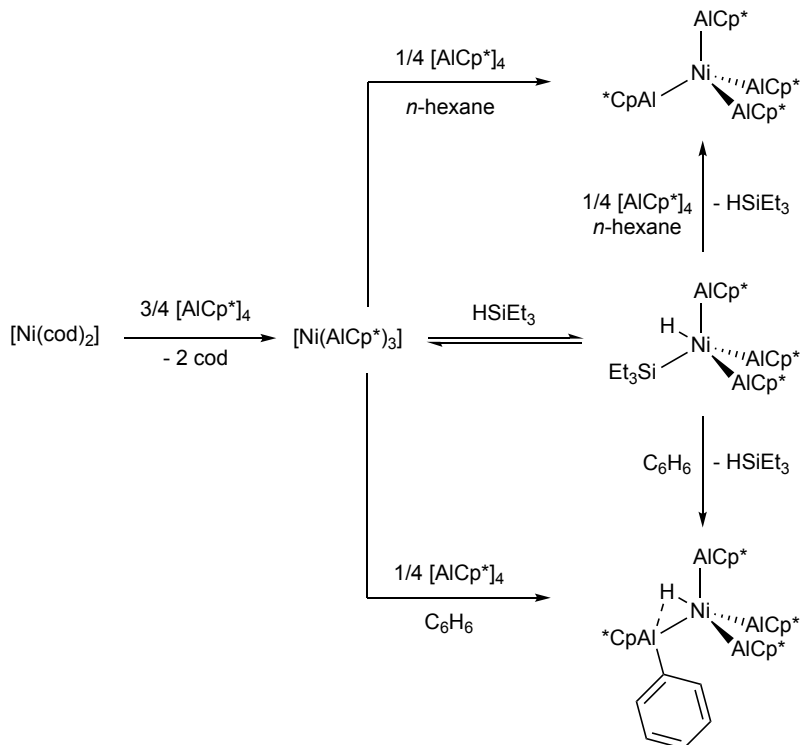


Figure 20: Overview of the reactivity of the in-situ formed unsaturated $[\text{Ni}(\text{AlCp}^)_3]$ able to perform C-H activation of benzene. Reprinted with permission from T. Steinke, C. Gemel, M. Cokoja, M. Winter, R. A. Fischer, *Angew. Chem. Int. Ed.* **2004**, *43*, 2299–2302. Copyright 2004, John Wiley and Sons.*

The analogous reaction with GaCp^* only leads to the formation of the homoleptic complex $[\text{Ni}(\text{GaCp}^*)_4]$, regardless of the presence of triethyl silane, and no C-H activation could be observed. While the C-H activation of benzene is postulated to occur at the Ni^0 center, the phenyl group migrates to the AlCp^* ligand, resulting in a formally Al^{III} center. The C-H activation was not observed when starting from the already formed $[\text{Ni}(\text{AlCp}^*)_4]$ complex (Figure 20), highlighting the labile nature of the oxidatively added H-SiEt_3 .^[60] This can be seen as an example of a protecting group at the nickel center, which, when removed, induces the formation of a reactive site at the transition metal.

1.2.5.2 Living Libraries of Metal Clusters

In biochemistry, working with libraries is a standard method for studying complex systems, which has been used for decades to efficiently investigate, among others, the effects of mutations on a protein's bioactivity.^[61-63] This approach has been crucial in recent biochemical advancements, significantly enhancing our understanding of cellular chemistry and molecular biology.

This concept could also be effectively combined with the strategy of investigating cluster-substrate interactions through the *in-situ* formation of hemi-labile species. Reactive clusters are often too labile to isolate, making their study challenging. Creating "living cluster libraries" would enable the simultaneous study of heterometallic systems with various compositions, fully considering the chemical diversity resulting from organometallic reactions. The term "living" signifies the responsiveness of these species to external parameters, allowing for the direct exploration of chemical complexity and increasing the efficiency of system inquiries (Figure 21).

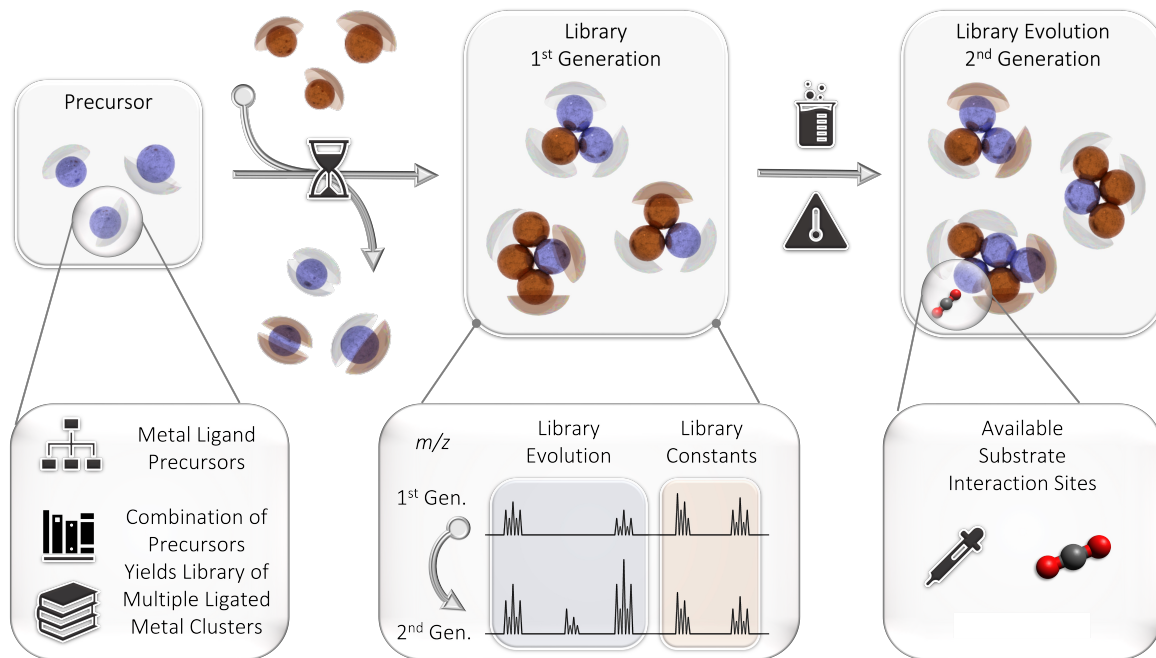


Figure 21: General concept for a library-based strategy for probing metal-substrate interactions of ligated heterometallic clusters.

However, this approach requires the development of new methodologies to analyze and understand complex mixtures of clusters. Similar to how complex mixtures of proteins are analyzed in biochemistry through proteomic analysis, the study of living libraries of metal clusters will rely on *in-situ* mass spectrometry (Figure 21). This necessitates a setup tailored to the challenges of low-valent ligated cluster chemistry.^[64] LIFDI (liquid injection field desorption ionization) is an exceptionally soft ionization technique suitable for organometallic analytes with weakly bound ligands, such as olefins.^[65-66] The principle of LIFDI-MS is related to field desorption (FD), an ionization technique developed for low-polarity, non-ionic analytes. LIFDI-MS has proven very successful in investigating various ligated TM/E clusters.^[67-68]

To accommodate these fragile and highly air- and moisture-sensitive compounds, the LIFDI-MS setup can be coupled with a glovebox, allowing for sample application under completely inert conditions and an orbitrap mass analyzer offering very high *m/z* accuracy. In this system, ions are collected by a C-trap and then injected into the orbitrap in pulses, facilitating the observation of poorly ionizable compounds.^[64]

Nevertheless, transitioning from a crystallographic-based strategy to a mass spectrometric *in-situ* methodology involves the loss of experimental structural information. To address this, a robust combinatorial and theoretical framework must be developed. This framework aims to obtain structural information from sum formula alone. It is part of a collaboration with *Prof. Juarez L. F. Da Silva* at the University of São Paulo, which is integral to developing living libraries of metal clusters.

2 Objectives and Motivation

The synthetic challenge posed by the necessary compromise between stabilizing the low-valent metals and promoting reactive sites is a crucial limitation to the systematic investigation of metal-substrate interactions. The fundamental problem is not the inertness of the low valent metal centers to substrates but rather their inaccessibility. As outlined in chapters 1.2.3 and 1.2.4, the inherent properties of the organic ligand used in the synthesis of TM/E clusters and complexes can play a critical role in the promotion or suppression of reactive sites. This synthetic challenge will be outlined in chapter 3.1 using small TM/E complexes.

In order to expand our synthetic understanding of the influence different organic ligands have on the coordination properties of E|R, the chemistry of the still relatively unexplored gallium amide needs to be examined. This will be studied in chapter 3.1 (*Homoleptic Hexa- and Penta-Coordinated Gallium(I) Amide Complexes of Ruthenium and Molybdenum*). The reversible stabilization of reactive TM/E complexes through labile ligands is an additional key strategy to generate reactive sites *in situ*. The reactive properties of such unsaturated TM/E fragments for various bond activation and their reversible stabilization will be outlined in chapters 3.2 and 3.3 (*C–H and Si–H Activation Reactions at Ru/Ga Complexes: A Combined Experimental and Theoretical Case Study on the Ru–Ga Bond and Photochemically Generated Reactive Sites at Ruthenium/Gallium Complexes: Catalysis vs. Cluster Growth*).

The reactive sites generated at TM/E clusters and complexes can be used to study metal-substrate interactions. When viewing ligated *Hume-Rothery* inspired TM/E clusters as homogeneous mimics of structural motifs found on heterogenous catalysts, a major problem needs to be overcome: the lack of chemical diversity. As discussed in chapter 1.1.2, the surface can have structural defects, local composition variations and is subject to change throughout the catalytic reaction. The isolation of a few TM/E clusters showcasing metal-substrate interactions is a far cry away from the diverse richness found on the surface of their solid-state counterparts. Addressing this requires a paradigm shift in organometallic chemistry. The isolation and investigation of one cluster at a time represents a loss of chemical complexity,

which can be overcome by using unselective organometallic reactions, mimicking *in situ* the diversity found on the surface of a solid-state catalyst. Introduced in chapter 1.2.5.2, evolving from a crystallographic-based approach to a mass spectrometric-based one will enable us to shed light on the chemistry of metastable heterometallic clusters, opening a realm of new possibilities. The development of a new methodology tailored for working with such “libraries” of metal clusters and the novel reactivities discovered for ligated Cu/Zn clusters will be presented in chapter 4.1 (*A living library concept to capture the dynamics and reactivity of mixed-metal clusters for catalysis*).

As discussed in chapter 1.1.2, numerous studies point towards the non-innocent role of oxidic species in catalytic processes in general and in the methanol synthesis from CO₂ in particular. Exploring this will require incorporating an additional complexity parameter: generating sub-oxidic heterometallic clusters. Although incorporating oxygen in low-valent organometallic chemistry may seem counterintuitive, it is a critical issue to address and poses a major synthetic challenge. First results towards the further understanding of sub-oxidic organocopper chemistry are investigated in chapter 4.2 (*Cuprophilic Interaction in Polymeric [Cu₁₀O₂(Mes)₆]_n*).

3 Synthetic Challenges Towards the Generation of Reactive Sites

3.1 Study I: Homoleptic Hexa- and Penta-Coordinated Gallium(I) Amide Complexes of Ruthenium and Molybdenum

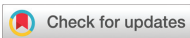
Exploring the chemistry of low valent group-13 metalloligands, E^IR coordinated to d- and f-block metal centers have largely been motivated by the isolobal relationship of E^IR to CO and phosphines. Using GaTMP, it has been possible to isolate the [Ni₃(GaTMP)₇] clusters active in semihydrogenation catalysis.^[46] Yet the chemistry of GaTMP is still limited and needs to be further expanded. In this work, we report the reaction of neutral olefin complexes of ruthenium and molybdenum with GaTMP, leading to the formation of [Ru(GaTMP)₅] and [Mo(GaTMP)₆]. The molybdenum complex shows an octahedral structure, while the ruthenium complex is best described as a highly distorted square pyramid with a τ_5 value indicating a nearly ideal basally distorted square pyramid. The DFT calculations unveiled a competing π interaction between the transition metal centers and the amido substituent with the unoccupied p _{π} orbitals of the gallium, in accordance with earlier models for TM-GaN₂ coordination.

R. Bühler conducted synthesis, characterization, and DFT calculations of both complexes. R. J. J. Weininger contributed to synthesis and characterization. J. Stephan performed SC-XRD measurements. All authors contributed to results discussion and procedure planning, R. A. Fischer providing overarching academic guidance. The manuscript was written by R. Bühler, R. J. J. Weininger, C. Gemel, and R. A. Fischer and subsequently edited by all co-authors.

Reproduced with permission from the Royal Society of Chemistry.

R. Bühler[‡], R. J. J. Weininger[‡], J. Stephan, M. Muhr, B. M.-T. Bock, C. Gemel, R. A. Fischer, *Dalton Trans.* **2024**, 53, 17162-17168.

[‡] Equal contribution



Cite this: DOI: 10.1039/d4dt00823e

Open Access Article. Published on 20 April 2024. Downloaded on 7/9/2024 3:49:10 PM.
 This article is licensed under a Creative Commons Attribution 3.0 Unported Licence.



Received 19th March 2024,
 Accepted 17th April 2024
 DOI: 10.1039/d4dt00823e
rsc.li/dalton

Homoleptic hexa- and penta-coordinated gallium(I) amide complexes of ruthenium and molybdenum[†]

Raphael Bühler, Richard J. J. Weininger, Johannes Stephan, Maximilian Muhr, Balasai M.-T. Bock, Christian Gemel and Roland A. Fischer *

Reaction of neutral olefin complexes of ruthenium and molybdenum with GaTMP (TMP = 2,2,6,6-tetramethylpiperidinyl) by substitution leads to the formation of respective five- and six-coordinated homoleptic products. $[Ru(GaTMP)_5]$ (**1**) and $[Mo(GaTMP)_6]$ (**2**) were isolated and characterized. Core structure geometries were analyzed using continuous shape measure, and the complexes were subjected to DFT calculations unveiling competing π -interactions between the transition metal center and the amido substituent with the unoccupied p_z orbitals of the gallium.

Introduction

Exploring the chemistry of low valent group-13 metallo-ligands ER^* ($E = Al, Ga, In$; R^* = sterically demanding protection group) coordinated to d- and f-block metal centers (transition metals, M) has significantly been motivated by the isolobal relationship between ER^* and CO. The choice or design of R^* has been crucial to allow for preparative access to ER^* compounds and utilize them in organometallic coordination chemistry. The first example of a mononuclear homoleptic complex of the general formula $[M(ER^*)_n]$, namely $[Ni(InC(SiMe_3)_3)_4]$ ($R^* = C(SiMe_3)_3$), was reported by W. Uhl in 1998,¹ followed by P. Jutzi's $[Ni(GaCp^*)_4]$ in 1999 and our $[Ni(AlCp^*)_4]$ in 2005 ($Cp^* = C_5(CH_3)_5$).^{2,3} All these complexes can be viewed as analogues of $[Ni(CO)_4]$. However, there are cases such as the trinuclear, linear $[(Cp^*In)_2Pd(\mu-(InCp^*))_2Pd(\mu-(InCp^*))_2Pd(InCp^*)_2]$,⁴ which has no analogous metal carbonyl $[M_n(CO)_m]$ structure. Other protecting groups, R^* , including amides (e.g. $N(SiMe_3)(2,6\text{-bis-mesityl phenyl})$),⁵ ketoimines (e.g. DDP = 2-((2,6-diisopropylphenyl)amino)-4-((2,6-diisopropylphenyl)imino)-2-pentene) and amidinates (e.g. $[N(Ar)]_2CN Cy_2$; Ar = $C_6H_3^1Pr_2-2,6$; Cy = cyclohexyl), have been introduced with great success, for example, to yield $[Pt(Ga[N(Ar)]_2CN Cy_2)]$, as reported by Jones and co-workers.⁶ Due to the high steric bulk

of these types of metallo-ligands ER^* , the transition metal coordination number of any of their homoleptic complexes has not exceeded three. We and others have reviewed the development of this chemistry in the past.^{7–10} Specifically, an updated comprehensive listing of all structurally elucidated homoleptic complexes $[M_a(ER^*)_b]$, including $[Mo(GaCp^*)_6]$ as the only example of that series with coordination number cn (M) greater than five, is provided in the ESI.^{†11}

The history of heterometallic group-13 metal/transition metal complexes of the more general formula $[(L_aM)_a(ER_{3-a})]$ ($L = CO$, phosphines, etc.; R = any inorganic or organic substituent, i.e. including hydrides or halides) featuring unsupported covalent (donor/acceptor) bonds M–E dates back to the early work of Hieber on $[(CO)_4Co_3In]$ in 1942.^{12,13} The related work since the mid-1990s focused on synthesis, structure and the elucidation of details of the M–E bonding by theoretical approaches applying various computational frameworks.^{14,15} Herein, we are particularly interested in exploring the transition from discrete heterometallic complexes to the related clusters in which an intermetalloid M_aE_b core is protected by an all-hydrocarbon shell of R^* , i.e. matching with the general formula $[M_aE_b](R^*)_c$, with $(a + b) > c$.^{16–18} A recent example of that work is the assignment of individual structures from a preparative inseparable ensemble of Ni/Ga clusters $[Ni_{6+x}Ga_{6+y}]$ ($Cp^*)_6 = $[Ni_xGa_{6+y}](NiCp^*)_6$ ($x + y \leq 2$)). Notably, in this particular case, protection group transfer ($R^* = Cp^*$) occurs from the Ga to the Ni during the synthesis of the clusters from Ni(0) olefin complexes with GaCp* in toluene or mesitylene at elevated temperatures.^{19,20}$

A relationship exists between the molecular coordination and cluster chemistry of the solid-state and the materials chemistry of the respective intermetallic M/E (nano) phases

Chair of Inorganic and Metalorganic Chemistry, Technical University of Munich, School of Natural Sciences, Department of Chemistry, Lichtenbergstraße 4, 85748 Garching, Germany and Catalysis Research Center, Erst-Otto-Fischer-Straße 1, 85748 Garching, Germany. E-mail: roland.fischer@tum.de

[†]Electronic supplementary information (ESI) available. CCDC 2341048 and 2341049. For ESI and crystallographic data in CIF or other electronic format see DOI: <https://doi.org/10.1039/d4dt00823e>

[‡]These authors contributed equally to this work.

[View Article Online](#)

Paper

Dalton Transactions

Open Access Article. Published on 7/9/2024. Downloaded on 7/9/2024 3:49:10 PM.
This article is licensed under a Creative Commons Attribution 3.0 Unported Licence.

and their catalytic properties.^{21–23} For example, the oligonuclear Ni/Ga hydrido clusters $[H_xNi_3(GaR^*)_x]$ ($x = 2,4,6$; $R^* = \text{TMP} = 2,2,6,6\text{-tetramethylpiperidinyl}$) are moderately active in alkyne semi-hydrogenation to alkenes, mimicking the surface chemistry of the respective solid-state Ni/Ga (nano) alloys.²⁰ Compared to the other types of R^* mentioned in this introduction, considerably few studies have been conducted using $R^* = \text{TMP}$ as a protecting group, which was mainly introduced by Linti and co-workers. With respect to GaTMP in particular, only the following few complexes are known in the literature: $[(\text{CO})_5\text{Cr}(\text{GaTMP})]$ and $[(\text{CO})_3\text{Cr}(\mu^2\text{-GaTMP})_3\text{Cr}(\text{CO})_3]$ were prepared simultaneously from $[\text{Cr}(\text{CO})_5(\text{cyclooctene})]$; $[(\text{CO})_3\text{Co}(\mu^2\text{-GaTMP})_2\text{Co}(\text{CO})_3]$ was synthesized from $[\text{Co}_2(\text{CO})_8]$.²⁴ The homoleptic dinuclear $[\text{Ni}_2(\text{GaTMP})_7]$ ²⁴ and trinuclear $[\text{Ni}_3(\text{GaTMP})_3(\mu^2\text{-GaTMP})_3(\mu^3\text{-GaTMP})]$ ²⁰ complexes were accessible from $[\text{Ni}(\text{COD})_2]$ ($\text{COD} = 1,5\text{-cyclooctadiene}$). Searching for any compound with the structural element structure TMP-E-M yielded one more entry to the list. $[(\text{TMP})_2\text{AlFe}(\text{Cp})(\text{CO})_2]$ was reported in 1997 by Nöth *et al.*,²⁵ while Dankert and Hevia published earlier this year the synthesis of $[(\text{TMP})_2\text{AlZn}(\text{Cp}^*)]$.²⁶ However, here, the E center ($E = \text{Al}$) is a tri-coordinate and is formally in a higher oxidation state. Thus, these compounds and any related ones are not of immediate concern to our work. Thus, we further investigate the coordination chemistry of GaTMP against d-block metals M with a focus on homoleptic $[\text{M}_a(\text{GaTMP})_b]$ complexes or clusters $[\text{H}_x\text{M}_a\text{Ga}_b]$ (TMP), and aim for a more expanded library of such compounds. Herein, we now report the first homoleptic GaTMP complexes of second row transition metals, namely $[\text{Ru}(\text{GaTMP})_5]$ (**1**) and $[\text{Mo}(\text{GaTMP})_6]$ (**2**).

Results and discussion

$[\text{Ru}(\text{GaTMP})_5]$ (**1**, Fig. 1) was obtained as a brown, crystalline solid, suitable for SC-XRD, by reacting $[\text{Ru}(\text{COD})(\text{COT})]$ ($\text{COD} = 1,4\text{-cyclooctadiene}; \text{COT} = \eta^6\text{-1,3,5-cyclooctatriene}$) with 1.25 eq. $(\text{GaTMP})_4$ in toluene at 100°C for 19 h (Fig. 2). After workup, compound **1** was isolated at a yield of 20% (based on Ru).

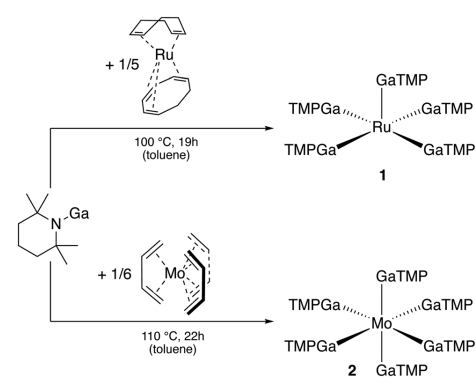


Fig. 2 Reaction scheme for the synthesis of **1** and **2** by ligand substitution.

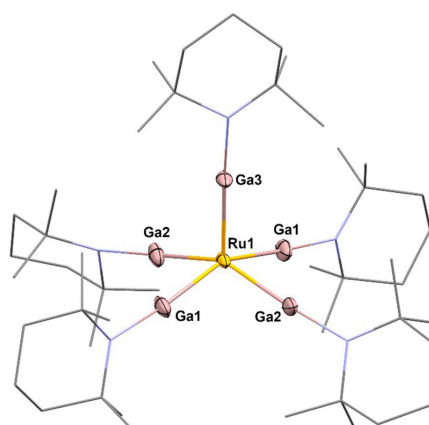


Fig. 1 Left: molecular structure of $[\text{Ru}(\text{GaTMP})_5]$ (**1**) in the solid state determined by single crystal X-ray diffraction. Ru: yellow, Ga: pink, N: blue and C: grey. Hydrogen atoms and disordered molecule fragments are omitted. C and N are displayed as wireframe. Right: square pyramidal coordination polyhedron calculated from crystal structure data. Thermal ellipsoids are shown at the 50% probability level. Selected bond lengths [\AA] and angles [$^\circ$]: Ru1–Ga3: 2.274(10) Ru1–Ga2^{#1}/Ga2: 2.281(7), Ru1–Ga1^{#1}/Ga1: 2.291(6), Ga3–Ru1–Ga2^{#1}/Ga2: 104.6(2), Ga3–Ru1–Ga1^{#1}/Ga1: 103.0(2), Ga2–Ru1–Ga1: 84.2(3), Ga2–Ru1–Ga1^{#1}: 89.3(2). Note: Ga1/Ga1^{#1} and Ga2/Ga2^{#1} are symmetry related.

[View Article Online](#)

Dalton Transactions

Paper

The C, H and N values of **1** obtained by elemental analysis are within the expected range. The ^1H -NMR and ^{13}C -NMR in C_6D_6 (25°C ; see Fig. S1–3†) indicate the presence of five equivalent TMP groups with only minor shifts of all signals with respect to free $(\text{GaTMP})_4$.²⁷ Trace impurities are almost absent. The presence of only one set of signals for all five GaTMP units indicates a fast fluxional process, which is very common for five-coordinate metal complexes.²⁸ The IR spectrum (see Fig. S8†) does not show absorption bands in the region associated with Ru-H vibrations (*ca.* 1900 cm^{-1} – 1700 cm^{-1}) and all features can be assigned to the TMP groups (see Fig. S10†).²⁹ High-resolution LIFDI-MS (Fig. S11–13†) gives a molecular ion $[\text{M}]^+$ signal of 100% rel. intensity at 1151.25 m/z (calcd. m/z 1151.25) and a fragment $[\text{M} - \text{TMP}]^+$ signal at 1011.11 m/z of 1.6% rel. intensity (calcd. m/z 1011.11). Compound **1** crystallizes in the monoclinic space group $C2/c$, and the molecular structure in the solid state is shown in Fig. 1 together with a selection of structural parameters (bond lengths and angles).

The molecular unit of **1** exhibits a square pyramidal coordinated Ru center that is slightly distorted along the z -axis, elevating the Ru above the Ga_4 plane by 0.545 \AA , with Ga_{ax1} –Ru–Ga angles in the range of 103.0 – 104.6° . The Ru–Ga bond lengths show only a slight variance between 2.274 \AA (Ru1–Ga3), 2.291 \AA (Ru1–Ga1) and 2.281 \AA (Ru1–Ga2) but are significantly shortened by 0.10 – 0.15 \AA compared to known Ru–GaCp* complexes.^{29–36} To quantify the distortion of the

$[\text{RuGa}_5]$ core, the so-called continuous shape measures were calculated.²² Using continuous shape measures ($S_Q(P)$), distortions of molecular structures from reference structures (*e.g.* ideal polyhedra) can be quantified (for details and the calculation code see ESI†). In general, $S_Q(P) = 0$ indicates no distortion from the reference, $S_Q(P) < 1.00$ indicates minor distortions and $1.00 < S_Q(P) < 3.00$ indicates major distortions from the reference shape.²² In the case of **1**, $S_Q(P) = 0.99$ was found when compared to an ideal square pyramid with the Ru in the centroid of the polyhedron, while $S_Q(P)$ was distinctly higher for a square pyramidal shape when was placed Ru in the center of the basal square plane ($S_Q(P) = 4.63$) or compared to an ideal trigonal bipyramidal shape with the Ru in the centre of the equatorial plane ($S_Q(P) = 7.63$). With respect to the α and β angles (150.72° and 154.11°), a τ_5 value of 0.0565 is found. This value is close to the ideal value of a basally distorted square pyramid,³⁷ as demonstrated by the Ruthenium center being 0.545 \AA above the square plane.

$[\text{Mo}(\text{GaTMP})_6]$ (**2**, Fig. 3) was obtained in an analogous synthesis to **1** by reaction of $[\text{Mo}(\eta^4\text{-C}_4\text{H}_6)_3]$ with 1.5 eq. of $(\text{GaTMP})_4$ in toluene at 110°C for 22 h. Compound **2** was isolated as a beige, crystalline solid suitable for SC-XRD in a total yield of 42% after workup.

The C, H and N values of **2** obtained by elemental analysis are within the expected range. ^1H -NMR and ^{13}C -NMR spectra in toluene- d_8 exhibit each set of TMP signals, which are only

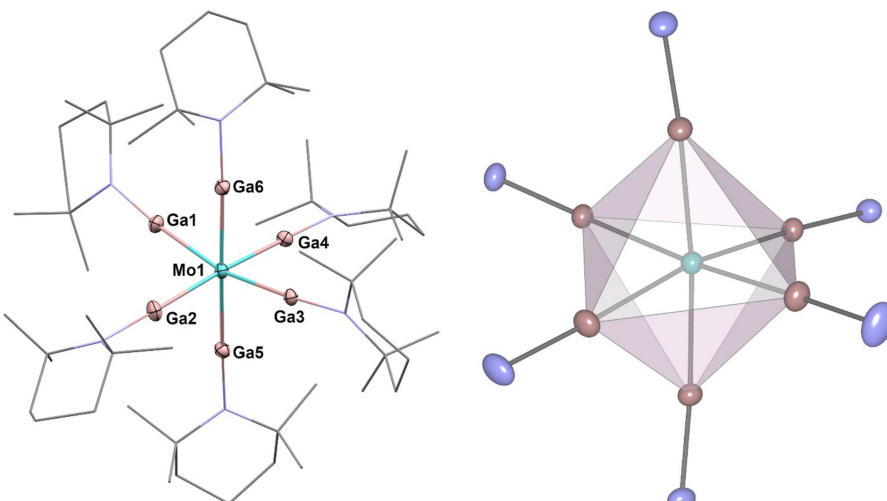


Fig. 3 Left: molecular structure of $[\text{Mo}(\text{GaTMP})_6]$ (**2**) in the solid state determined by single crystal X-ray diffraction. Mo: turquoise, Ga: pink, N: blue and C: grey. Hydrogen atoms and disordered molecule fragments are omitted. C and N are displayed as wireframe. Right: octahedral coordination polyhedron calculated from crystal structure data. The two crystallographically distinct units present in the SC-XRD data are very similar and most likely an effect of packing; the unit with higher deviations in bond lengths is depicted. Thermal ellipsoids are shown at the 50% probability level. Selected bond lengths (\AA) and angles ($^\circ$): Mo1–Ga6: $2.374(2)$, Mo1–Ga3: $2.396(3)$, Ga6–Mo1–Ga1: $81.9(9)$, and Ga5–Mo1–Ga3: $97.7(9)$. (largest/smallest).

[View Article Online](#)

Paper

Dalton Transactions



slightly shifted with respect to the signals of **1** or free $(\text{GaTMP})_4$ (see Fig. S4–6†).²⁷ IR spectroscopy provides data very similar to $[\text{Ru}(\text{GaTMP})_5]$ (**1**) and shows no absorption in the range of typical Mo–H vibrations between 1900 cm^{-1} and 1650 cm^{-1} , indicating the presence of hydrides (see Fig S9†).^{38,39} High-resolution LIFDI-MS (see Fig. S14–16†) gives a molecular ion $[\text{M}]^+$ signal at 1356.32 m/z (calcd. m/z 1356.32) with 100% rel. intensity. The compound crystallizes in the monoclinic space group $P2_1/c$, with two crystallographically distinct units per unit cell, both exhibiting six Ga(TMP)-ligands coordinating in an octahedral fashion around the Mo centers (Fig. 3). In relation to each other, the two independent octahedral units are rotated along all three axes. The average Mo–Ga bond lengths of the independent units are 2.385 \AA and 2.386 \AA with minimal deviation. Ga–Mo–Ga angles in both units point to a slight distortion from the ideal octahedral geometry and range between 81.9° and 97.7° . The analogous $[\text{Mo}(\text{GaCp}^*)_6]$ molecule shows less angular distortion with Ga–Mo–Ga angles between 85.1° and 94.2° with slightly elongated Mo–Ga bonds (average 2.462 \AA ; shortest bond: 2.385 \AA).¹¹ Comparing **2** (both independent molecules in the elementary cell) to the ideal octahedral geometry yielded only minor deviation, giving $S_Q(P) = 0.20$. Both GaCp* and GaTMP are closely related ligands and formally isolobal to CO but are predominantly σ -donor ligands with notably weak π -backbonding.^{7,24,27,40} The slightly shortened M–GaTMP distances with respect to the M–GaCp* distances may be taken as an indication of more significant π -backbonding of GaTMP, compared to GaCp*. This effect is more clearly observed when comparing **2** to its homologue $[\text{Mo}(\text{GaCp}^*)_6]$ although no such direct comparison is available for **1**; however, an indirect comparison to the series of previously reported Ru–GaCp* supports this assignment.^{11,24,27,29–34,36,40} The same trend towards shortened M–Ga bonds when comparing GaTMP to GaCp* can be found across all known M–GaTMP compounds. Seifert *et al.* reported the investigation of a series of heteroleptic M–GaTMP compounds also bearing carbonyl ligands that afford additional insight because they allow for the direct comparison of M–CO vs. M–Ga distances. They observed shorter M–Ga and longer M–CO distances for the TMP stabilized gallium(i) ligand, leading to the suggestion of more pronounced π -backbonding for GaTMP compared to GaCp*.²⁴

Although a square pyramidal ligand sphere around a Ru(0) centre is not uncommon,^{41,42} mononuclear, homoleptic compounds of Ru(0) with this structure are still rare in the literature. The only known examples are $\text{Ru}(\text{CO})_5$, $\text{Ru}(\text{NO})_5$ and bis(2,3,4,5-tetramethylthiophene)ruthenium.^{43,44} These compounds, however, rely on ligands with strong π -backbonding, whereas **1** has primarily only σ -donating ligands. To gain more insights into the structure and bonding situation of **1**, we performed DFT calculations starting with the experimental square pyramidal (**SP**) structure of the molecular crystal structure as the input for modelling **1_{SP}** and from a hypothetical, ideal trigonal bipyramidal (**TB**) structure for modelling **1_{TB}**. The model structures **1_{SP}** and **1_{TB}** were optimized at the BP86/TZVPP level of theory (see computational details), and frequency calcu-

lations were performed to ascertain that the optimized structure is true energy minima. The trigonal bipyramidal structure **1_{TB}** shows a distortion in the equatorial plane with $\text{Ga}_{\text{eq}}\text{–Ru}\text{–}\text{Ga}_{\text{eq}}$ angles of 110° , 118° and 130° , most notable in the outer coordination sphere ($\text{N}_{\text{eq}}\text{–Ru}\text{–}\text{N}_{\text{eq}}$ angles of 104° , 112° and 142°). The axial distortion is also significant with the angles $\text{Ga}_{\text{ax}}\text{–Ru}\text{–}\text{Ga}_{\text{ax}} = 161^\circ$ and $\text{N}_{\text{ax}}\text{–Ru}\text{–}\text{N}_{\text{ax}} = 153^\circ$. Although both computed structure models **1_{SP}** and **1_{TB}** (Fig. S20†) are highly distorted compared to the ideal square pyramidal and trigonal bipyramidal geometries, they are both energy minima structures, as shown by the frequency calculations. On the energetic side, the ΔE and ΔG between **1_{SP}** and **1_{TB}** are very small (0.9 and 2.0 kcal mol⁻¹ respectively, Table 1) and, with respect to the precision of DFT energies, are not significant. Additionally, the HOMO–LUMO gaps are nearly identical (Table 1), indicating similar electronic structures. The NMR data show only one GaTMP signal group. This indicates a rapid exchange between

Table 1 Selected computed data for complexes **1** and **2** and their simplified model structures

Complexes	HOMO–LUMO Gap [eV]	ΔE [kcal mol ⁻¹]	ΔG [kcal mol ⁻¹]
$[\text{Ru}(\text{GaTMP})_5] (\mathbf{1}_{\text{SP}})$	2.56	0.9	2.0
$[\text{Ru}(\text{GaTMP})_5] (\mathbf{1}_{\text{TB}})$	2.51		
$[\text{Ru}(\text{GaNMe}_2)_5] (\mathbf{1}_{\text{NMe2 SP}})$	3.02	0.0	0.2
$[\text{Ru}(\text{GaNMe}_2)_5] (\mathbf{1}_{\text{NMe2 TB}})$	3.08		
$[\text{Mo}(\text{GaTMP})_6] (\mathbf{2})$	3.10		
$[\text{Mo}(\text{GaNMe}_2)_6] (\mathbf{2}_{\text{NMe2}})$	3.15		

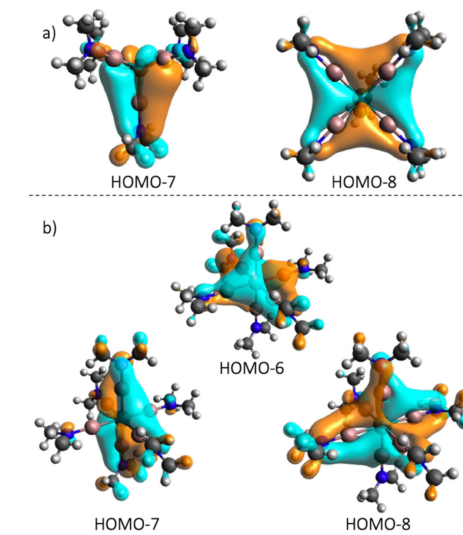


Fig. 4 Occupied molecular orbitals of **1_{NMe2}** (a) and **2_{NMe2}** (b) showing π interactions between the GaNMe₂ ligand and the transition metal.

[View Article Online](#)

Dalton Transactions

Paper

both structures in the solution, while the observed crystal structure might be favored by the packing effects.

To facilitate a straightforward bonding analysis, a simplified model of **1** based on GaNMe_2 model ligands was employed and calculated (**1_{NMe2}**), and the molecular orbitals were analyzed (Fig. S21†). The primary coordination sphere shows a distortion similar to **1_{sp}** and **1_{TB}**. Beyond the expected σ -donating properties of the Ga-amide (Fig. S19†), the orbital analysis shows the occupied π orbital of the Ga–N bond to interact with the d_{yz} and d_{zx} orbitals in the HOMO-7 and HOMO-8 (Fig. 4). This behavior of the gallium(ii) amide ligand is also observed for the **2_{NMe2}** (Fig. S22†) model complex (HOMO-6, -7 and -8, Fig. 4) and is in line with the bonding model for TM–ER, *i.e.* competing TM \rightarrow E π -back-donation and E \leftarrow R π -donation when R has at least one occupied p_π orbital.¹³

Conclusion

$[\text{Ru}(\text{GaTMP})_5]$ (**1**) and $[\text{Mo}(\text{GaTMP})_6]$ (**2**) were prepared by ligand substitution from the olefinic precursor compounds. $[\text{Ru}(\text{GaTMP})_5]$ is a rare example of homoleptic Ru(0) complexes and the first case where the ligand sphere is dominated by σ -donation. $[\text{Mo}(\text{GaTMP})_6]$ was prepared similarly to $[\text{Mo}(\text{GaCp}^*)_6]$ though notably without the need for supporting hydrogenolysis of the butadiene ligands of the Mo(0)-precursor and exhibits the same trends observed in the ruthenium compound. The compounds were characterized using crystallography, ^1H and ^{13}C -NMR, IR spectroscopy, high-resolution mass spectrometry and elemental analysis. Bond lengths between the title compounds and previously reported TM–GaCp* compounds were analyzed, and the results were compared to homologous homoleptic and heteroleptic transition metal-GaCp*/GaTMP compounds that have been reported previously. The findings indicate that the Ru–GaTMP bond, though primarily dominated by the σ -donor property of the gallium amide ligand, exhibits competing π interaction between the π -back-bonding of the ruthenium and the π -donation of the amide to the gallium. The precursor complexes and possible intermediates, such as **1** and **2**, require a thorough theoretical investigation of their bonding situation. The translation of this difference between GaTMP and GaCp* in ligand properties into synthetic access to novel intermetallic clusters $[\text{M}_a\text{Ga}_b](\text{TMP})_c$ is the subject of ongoing research by our group.

Experimental

All manipulations were carried out using standard Schlenk and glovebox techniques under argon atmospheres. Solvents were dried and degassed using an MBraun Solvent Purification System. The final H_2O content of all solvents was checked by Karl Fischer titration and was below 5 ppm. Tris(butadiene)-molybdenum was prepared from MoCl_5 according to the literature-known procedures and characterized by ^1H -NMR (see ESI

Fig. S7†).^{45,46} $(\text{GaTMP})_4$ was prepared from GaCp^* according to the literature.²⁰ NMR spectra were recorded using a Bruker Avance III AV400US (25 °C; ^1H , 400 MHz; ^{13}C , 101 MHz). Chemical shifts are given relative to trimethylsilane and were referenced to the residual solvent peak as internal standards. Chemical shifts are reported in parts per million, downfield shifted from TMS, and are consecutively reported as position (δ_{H} or δ_{C}), relative integral, multiplicity (s = singlet, and m = multiplet) and assignment. FTIR spectra were measured with an ATR setup using a Bruker Alpha FTIR spectrometer under an argon atmosphere inside a glovebox. Liquid Injection Field Desorption Ionization Mass Spectrometry (LIFDI-MS) was measured directly from an inert atmosphere glovebox with a Thermo Fisher Scientific Exactive Plus Orbitrap (mass accuracy 3 ppm; external calibration) equipped with an ion source from Linden CMS.⁴⁷ Reference isotope patterns were calculated using enviPat Web.⁴⁸

Computational details

Computational modelling of the molecular structures was performed using the ORCA5.0⁴⁹ software package with the exchange-correlation functional BP86.⁵⁰ Grimme's Dispersion correction, including Becke-Johnson damping (D3BJ),^{51,52} was used. The structure optimization and analytical calculations of the Hessian were performed using Ahlrich's def2-TZVPP basis set⁵³ with the auxiliary basis def2/J.⁵⁴

Synthesis and analytical data of $[\text{Ru}(\text{GaTMP})_5]$ (**1**)

A 50 mL Schlenk-tube was loaded with a sample of 49.0 mg $[(\text{COD})(\text{COT})\text{Ru}]$ (0.16 mmol, 1.00 eq.), and a sample of 164 mg $(\text{GaTMP})_4$ (0.78 mmol, 1.22 eq.) and the two solids were then dissolved in 5 mL of toluene. The orange-coloured solution was then stirred at 100 °C for 19 h; during this time, a change in colour to dark red occurred. Removing the liquid *in vacuo* yielded a brown solid, which was extracted with 10 mL n-hexane. The resulting solution was reduced *in vacuo* to 1/3 volume and cooled to –80 °C overnight. A brown, crystalline product suitable for SC-XRD was isolated from the reddish-brown supernatant solution *via* filtration at –78 °C and dried *in vacuo*. This yielded 35.0 mg (30 µmol, 20%) of $[\text{Ru}(\text{GaTMP})_5]$ (**1**) as brown crystals. ^1H -NMR (C_6D_6): δ (ppm) = 1.34 [t, $^3J_{\text{HH}} = 6.05$ Hz, 20 H, $(\text{CH}_3)_2\text{CCF}_3$], 1.57 [m, 10 H, $\text{CH}_2\text{CH}_2\text{CH}_2$], 1.71 [s, 60 H, CH_3]. ^{13}C -NMR (C_6D_6): δ (ppm) = 18.9 [$\text{CH}_2\text{CH}_2\text{CH}_2$], 36.3 [CH_3], 41.0 [$\text{CH}_2\text{CH}_2\text{CH}_2$], 55.2 [$\text{C}(\text{CH}_3)_2$]. $\text{C}_{45}\text{H}_{90}\text{Ga}_5\text{N}_5\text{Ru}$ (1150.94): calcd C 46.96, H 7.88, Ga 30.29, N 6.09, Ru 8.78; found C 47.31, H 8.12, N 6.14. LIFDI-MS: m/z 1151.25 [M^+] (calcd. m/z 1151.25).

Synthesis and analytical data of $[\text{Mo}(\text{GaTMP})_5]$ (**2**)

A 100 mL Schlenk-tube was loaded with a sample of 100 mg $[(\eta^4\text{C}_4\text{H}_6)_3\text{Mo}]$ (385.8 µmol, 1.00 eq.), and a sample of 485 mg $(\text{GaTMP})_4$ (2.31 mmol, 6.00 eq.) and both solids were dissolved in 30 mL toluene. The solution was stirred at 110 °C for 22 hours. The liquid was removed *in vacuo*, and the remaining solid was extracted with 5 mL boiling hexane. The resulting solution was set to 0 °C overnight, after which a beige, crystal-

[View Article Online](#)**Paper****Dalton Transactions**

line product was isolated *via* filtration and then dried *in vacuo*, affording 218 mg of [Mo(GaTMP)₆] (2) (160.8 μmol, 42%). ¹H-NMR (Tol-d₆): δ (ppm) = 1.35 [t, ³J_{HH} = 6.11 Hz, 24 H, (CH₃)₂CCH₂], 1.60 [m, 12 H, CH₂CH₂CH₂], 1.73 [s, 72 H, CH₃]. ¹³C-NMR (Tol-d₆): δ (ppm) = 18.9 [CH₂CH₂CH₂], 36.6 [CH₃], 41.2 [CH₂CH₂CH₂], 55.1 [C(CH₃)₂]. C₅₄H₁₀₈Ga₂MoN₆ (1355.79) Calc: C 47.84; H 8.03; N 6.20; Mo 7.08; Ga 40.86. Found: C 47.40; H 8.07; N 5.98. LIFDI-MS: m/z 1356.32 [M]⁺ (calcd. m/z 1356.32).

Author contributions

R. B. and R. J. J. W. contributed equally. R. B.: experimental work, DFT calculations, data analysis and manuscript preparation. R. J. J. W.: experimental work, data analysis, and manuscript preparation. J. S.: SC XRD data acquisition and structure refinement. M. M.: experimental work. B. M. T. B.: experimental work. C. G.: CSHM calculations, research supervision and manuscript preparation. R. A. F.: research conception and manuscript preparation.

Conflicts of interest

There are no conflicts to declare.

Acknowledgements

This work was funded by the German Research Foundation (DFG) within a Reinhart Koselleck Project (FI-502/44-1). The authors thank Fabrizio Napoli M.Sc. (TUM) for providing IR reference data.

References

- W. Uhl, M. Pohlmann and R. Wartchow, *Angew. Chem., Int. Ed.*, 1998, **37**, 961–963.
- P. Jutzi, B. Neumann, L. O. Schebaum, A. Stammmer and H.-G. Stammmer, *Organometallics*, 1999, **18**, 4462–4464.
- B. Buchin, T. Steinke, C. Gemel, T. Cadenbach and R. A. Fischer, *Z. Anorg. Allg. Chem.*, 2005, **631**, 2756–2762.
- T. Steinke, C. Gemel, M. Winter and R. A. Fischer, *Angew. Chem., Int. Ed.*, 2002, **41**, 4761–4763.
- R. J. Wright, M. Brynda, J. C. Fettinger, A. R. Betzer and P. P. Power, *J. Am. Chem. Soc.*, 2006, **128**, 12498–12509.
- S. P. Green, C. Jones and A. Stasch, *Inorg. Chem.*, 2007, **46**, 11–13.
- C. Gemel, T. Steinke, M. Cokoja, A. Kempfer and R. A. Fischer, *Eur. J. Inorg. Chem.*, 2004, **2004**, 4161–4176.
- S. González-Gallardo, T. Bollermann, R. A. Fischer and R. Murugavel, *Chem. Rev.*, 2012, **112**, 3136–3170.
- C. Jones and A. Stasch, in *The Group 13 Metals Aluminium, Gallium, Indium and Thallium: Chemical Patterns and Peculiarities*, vol. 285, John Wiley & Sons, 2011.
- R. A. Fischer and J. Weiß, *Angew. Chem., Int. Ed.*, 1999, **38**, 2830–2850.
- T. Bollermann, T. Cadenbach, C. Gemel, K. Freitag, M. Molon, V. Gwildies and R. A. Fischer, *Inorg. Chem.*, 2011, **50**, 5808–5814.
- W. Hieber and U. Teller, *Z. Anorg. Allg. Chem.*, 1942, **249**, 43–57.
- W. Robinson and D. P. Schussler, *Inorg. Chem.*, 1973, **12**, 848–854.
- J. Uddin and G. Frenking, *J. Am. Chem. Soc.*, 2001, **123**, 1683–1693.
- J. Uddin, C. Boehme and G. Frenking, *Organometallics*, 2000, **19**, 571–582.
- J. Weßing, C. Ganeshamoorthy, S. Kahlal, R. Marchal, C. Gemel, O. Cador, A. C. H. Da Silva, J. L. F. Da Silva, J.-Y. Saillard and R. A. Fischer, *Angew. Chem., Int. Ed.*, 2018, **57**, 14630–14634.
- M. Schütz, C. Gemel, M. Muhr, C. Jandl, S. Kahlal, J.-Y. Saillard and R. A. Fischer, *Chem. Sci.*, 2021, **12**, 6588–6599.
- I. Antsiburov, M. Schütz, R. Bühler, M. Muhr, J. Stephan, C. Gemel, W. Klein, S. Kahlal, J.-Y. Saillard and R. A. Fischer, *Inorg. Chem.*, 2024, **63**, 3749–3756.
- M. Muhr, J. Stephan, L. Staiger, K. Hemmer, M. Schütz, P. Heiß, C. Jandl, M. Cokoja, T. Kratky, S. Günther, D. Huber, S. Kahlal, J.-Y. Saillard, O. Cador, A. C. H. Da Silva, J. L. F. Da Silva, J. Mink, C. Gemel and R. A. Fischer, *Commun. Chem.*, 2024, **7**, 29.
- M. Muhr, H. Liang, L. Allmendinger, R. Bühler, F. E. Napoli, D. Uka, M. Cokoja, C. Jandl, S. Kahlal, J.-Y. Saillard, C. Gemel and R. A. Fischer, *Angew. Chem., Int. Ed.*, 2023, **62**, e202308790.
- C. Ganeshamoorthy, J. Weßing, C. Kroll, R. W. Seidel, C. Gemel and R. A. Fischer, *Angew. Chem., Int. Ed.*, 2014, **53**, 7943–7947.
- M. Molon, C. Gemel, M. von Hopffgarten, G. Frenking and R. A. Fischer, *Inorg. Chem.*, 2011, **50**, 12296–12302.
- T. Cadenbach, T. Bollermann, C. Gemel, M. Tombul, I. Fernandez, M. v. Hopffgarten, G. Frenking and R. A. Fischer, *J. Am. Chem. Soc.*, 2009, **131**, 16063–16077.
- A. Seifert and G. Linti, *Inorg. Chem.*, 2008, **47**, 11398–11404.
- B. N. Anand, I. Krossing and H. Nöth, *Inorg. Chem.*, 1997, **36**, 1979–1981.
- F. Dankert and E. Hevia, *Chem. – Eur. J.*, 2024, **30**, e202304336.
- A. Seifert and G. Linti, *Eur. J. Inorg. Chem.*, 2007, **2007**, 5080–5086.
- W. Zou, Y. Tao and E. Kraka, *J. Chem. Theory Comput.*, 2020, **16**, 3162–3193.
- M. Muhr, R. Bühler, H. Liang, J. Gilch, C. Jandl, S. Kahlal, J.-Y. Saillard, C. Gemel and R. A. Fischer, *Chem. – Eur. J.*, 2022, **28**, e202200887.
- T. Steinke, M. Cokoja, C. Gemel, A. Kempfer, A. Krapp, G. Frenking, U. Zenneck and R. A. Fischer, *Angew. Chem., Int. Ed.*, 2005, **44**, 2943–2946.
- M. Cokoja, C. Gemel, T. Steinke, F. Schröder and R. A. Fischer, *Dalton Trans.*, 2005, 44–54.



[View Article Online](#)

Paper

Dalton Transactions

- | | |
|--|--|
| <p>32 B. Buchin, C. Gemel, A. Kempfer, T. Cadenbach and R. A. Fischer, <i>Inorg. Chim. Acta</i>, 2006, 359, 4833–4839.</p> <p>33 T. Cadenbach, C. Gemel, T. Bollermann and R. A. Fischer, <i>Inorg. Chem.</i>, 2009, 48, 5021–5026.</p> <p>34 T. Cadenbach, C. Gemel, R. Schmid, M. Halbherr, K. Yusenko, M. Cokoja and R. A. Fischer, <i>Angew. Chem., Int. Ed.</i>, 2009, 48, 3872–3876.</p> <p>35 R. Bühlner, M. Muhr, J. Stephan, R. A. Wolf, M. Schütz, C. Gemel and R. A. Fischer, <i>Dalton Trans.</i>, 2023, 52, 10905–10910.</p> <p>36 T. Cadenbach, T. Bollermann, C. Gemel and R. A. Fischer, <i>Dalton Trans.</i>, 2009, 322–329.</p> <p>37 A. G. Blackman, E. B. Schenk, R. E. Jolley, E. H. Krenske and L. R. Gahan, <i>Dalton Trans.</i>, 2020, 49, 14798–14806.</p> <p>38 X. Wang and L. Andrews, <i>J. Phys. Chem. A</i>, 2005, 109, 9021–9027.</p> <p>39 H.-G. Cho and L. Andrews, <i>J. Am. Chem. Soc.</i>, 2005, 127, 8226–8231.</p> <p>40 P. Jutzi, B. Neumann, G. Reumann and H.-G. Stammler, <i>Organometallics</i>, 1998, 17, 1305–1314.</p> <p>41 M. A. Bennett, M. Bown and D. C. R. Hockless, <i>Aust. J. Chem.</i>, 2000, 53, 507–515.</p> <p>42 M. A. Bennett, H. Neumann, A. C. Willis, V. Ballantini, P. Pertici and B. E. Mann, <i>Organometallics</i>, 1997, 16, 2868–2878.</p> | <p>43 S. Luo, T. B. Rauchfuss and S. R. Wilson, <i>Organometallics</i>, 1992, 11, 3497–3499.</p> <p>44 W. Manchot and W. J. Manchot, <i>Z. Anorg. Allg. Chem.</i>, 1936, 226, 385–415.</p> <p>45 J. R. Dilworth, R. L. Richards, G. J. J. Chen and J. W. McDonald, in <i>Inorg. Synth.</i>, 1990, pp. 33–43.</p> <p>46 W. Gausing and G. Wilke, <i>Angew. Chem., Int. Ed. Engl.</i>, 1981, 20, 186–187.</p> <p>47 M. Muhr, P. Heifl, M. Schütz, R. Bühlner, C. Gemel, M. H. Linden, H. B. Linden and R. A. Fischer, <i>Dalton Trans.</i>, 2021, 50, 9031–9036.</p> <p>48 M. Loos, C. Gerber, F. Corona, J. Hollender and H. Singer, <i>Anal. Chem.</i>, 2015, 87, 5738–5744.</p> <p>49 F. Neese, <i>Wiley Interdiscip. Rev.: Comput. Mol. Sci.</i>, 2012, 2, 73–78.</p> <p>50 A. D. Becke, <i>Phys. Rev. A</i>, 1988, 38, 3098–3100.</p> <p>51 S. Grimme, J. Antony, S. Ehrlich and H. Krieg, <i>J. Chem. Phys.</i>, 2010, 132, 154104.</p> <p>52 S. Grimme, S. Ehrlich and L. Goerigk, <i>J. Comput. Chem.</i>, 2011, 32, 1456–1465.</p> <p>53 F. Weigend and R. Ahlrichs, <i>Phys. Chem. Chem. Phys.</i>, 2005, 7, 3297–3305.</p> <p>54 F. Weigend, <i>Phys. Chem. Chem. Phys.</i>, 2006, 8, 1057–1065.</p> |
|--|--|

3.2 Study II: C–H and Si–H Activation Reactions at Ru/Ga Complexes: A Combined Experimental and Theoretical Case Study on the Ru–Ga Bond

Cooperative effects between transition metals and electropositive metals (e.g., group 12 and 13 metals) play an essential role in bond activation reactions of small molecules. Unsaturated TM/E complexes can be highly reactive, as shown by the C–H activation occurring at a $[\text{Ni}(\text{AlCp}^*)_3]$ ^[60] intermediate discussed earlier. In another context, $[\text{Ru}(\text{GaCp}^*)_3\text{H}_2]$, formed by H–H activation, has been identified as an intermediate in forming larger Ru/Ga clusters.

We investigated the reactivity of this unsaturated Ru/Ga fragment in the context of C–H and Si–H activation, leading to the *in situ* study of $[\text{Ru}(\text{GaCp}^*)_3(\text{C}_7\text{H}_7)\text{H}_3]$ and the isolation of $[(\text{Ru}(\text{GaCp}^*)_3(\text{SiEt}_3)\text{H}_3]$. Computational investigation of these species with energy EDA and QTAIM and comparison with hypothetical phosphine analogs showed the strong influence of the gallium on the reactivity of the ruthenium center. The AIM charges indicate a more negatively polarized Ru in the case of Ru–Ga as compared to Ru–P. This points to a bond polarization of the form $\text{TM}(\delta^-)\text{E}(\delta^+)$, which is expected for *Hume-Rothery* inspired TM/E clusters and complexes.

M. Muhr performed experiments, including the synthesis of $[(\text{Ru}(\text{GaCp}^*)_3(\text{SiEt}_3)\text{H}_3]$. R. Bühler performed experiments concerning the C–H activation of toluene. H. Liang performed the calculations, and C. Jandl performed SC-XRD measurements. All authors contributed to results discussion and procedure planning, J.-Y. Saillard and R. A. Fischer providing overarching academic guidance. The manuscript was written by R. Bühler, M. Muhr, and C. Gemel and subsequently edited by all co-authors.

Reproduced with permission, Copyright 2022, John Wiley and Sons.

M. Muhr[‡], R. Bühler[‡], H. Liang, J. Gilch, C. Jandl, S. Kahlal, J.-Y. Saillard, C. Gemel, R. A. Fischer, *Chem. Eur. J.* **2022**, 28, e202200887.

[‡] Equal contribution



C—H and Si—H Activation Reactions at Ru/Ga Complexes: A Combined Experimental and Theoretical Case Study on the Ru—Ga Bond

Maximilian Muhr^a, Raphael Bühler^a, Hao Liang,^b Jonas Gilch,^a Christian Jandl,^a Samia Kahlal,^b Jean-Yves Saillard,^{b*} Christian Gemel,^a and Roland A. Fischer^{*[a]}

Abstract: Treatment of $[\text{Ru}(\text{COD})(\text{MeAllyl})_2]$ and $[\text{Ru}(\text{COD})(\text{COT})]$ with GaCp^* under hydrogenolytic conditions leads to reactive intermediates which activate Si—H or C—H bonds, respectively. The product complexes $[\text{Ru}(\text{GaCp}^*)_3(\text{SiEt}_3)\text{H}_3]$ (1) and $[\text{Ru}(\text{GaCp}^*)_3(\text{C}_6\text{H}_5)\text{H}_3]$ (2) are formed with HSiEt_3 or with toluene as the solvent, respectively. While 1 was isolated and fully characterized by NMR, MS, IR and SC-XRD, 2 was too labile to be isolated and was observed and characterized *in situ* by using mass spectrometry, including

labelling experiments for the unambiguous assignment of the elemental composition. The structural assignment was confirmed by DFT calculations. The relative energies of the four isomers possible upon toluene activation at the *ortho*-, *meta*-, *para*- and CH_3 -positions have been determined and point to aromatic C—H activation. The Ru—Ga bond was analyzed by EDA and QTAIM and compared to the Ru—P bond in the analogue phosphine compound. Bonding analyses indicate that the Ru—GaCp* bond is weaker than the Ru—PR₃ bond.

Introduction

Cooperative effects between transition metals TM and electro-positive metals E (e.g. group 12 and 13 elements) play an important role in bond activation reactions of small molecules^[1–9] both in molecular compounds as well as intermetallic solid-state materials.^[10–12] The cooperative effects are mostly attributed to the electronic properties of intermetallic bonds, featuring electrophilic centers E(δ^+) in direct vicinity to an electron rich TM(δ^-) with pronounced reductive character.^[13–16] Key examples are the Ni/Al complex $[(\text{Cp}^*\text{Al})_2\text{Ni}(\mu\text{-H})\text{Al}(\text{C}_6\text{H}_5)(\eta^1\text{-Cp}^*)]$, which is formed by C—H activation of C_6H_6 (benzene) at the coordinatively unsaturated 16 VE intermediate $[\text{Ni}(\text{AlCp}^*)_3]$,^[17] and the Rh/Ga complex $[\text{Cp}^*\text{Rh}(\eta^1\text{-C}_5\text{Me}_4\text{Ga}(\text{CH}_3)_3)]$, which is formed by C—C

activation of Cp^* .^[18] DFT calculations revealed that the electrophilic character of the gallium center favors the crucial C—C activation reaction step, allowing the reaction to proceed under extremely mild conditions.

Unsaturated Ruthenium phosphine complexes $[\text{Ru}(\text{PR}_3)_n]$ ($n=3, 4$) are well-established and are known to activate H—H,^[19–21] C—H^[22] and C—C^[23] bonds. Berry and co-workers reported on an oxidative-addition/reductive-elimination equilibrium of different substituted silanes in $[\text{Ru}(\text{PMMe}_3)_4(\text{SiR}_3)\text{H}]$.^[24] The same complex is also capable of activating the C—H bond of benzene in a sequence of similar reactions. They also report the formation of the polyhydride $[\text{Ru}((\text{PMMe}_3)_3(\text{SiEt}_3)\text{H}_3)]$ from $[\text{Ru}(\text{PMMe}_3)_4\text{H}_2]$.^[24]

$[\text{Ru}(\text{GaCp}^*)_3\text{H}_2]$, which is formed by H—H activation, has been identified as an intermediate in the formation of the cluster $[(\text{GaCp}^*)_4\text{HRu}(\mu\text{-Ga})\text{RuH}_2(\text{GaCp}^*)_2]$.^[25]

In the light of these results and the fact, that experimental as well as theoretical studies support the isolobal relation between GaCp^* and phosphines^[26–32] we were interested to investigate the reactivity of the unsaturated $[\text{Ru}(\text{GaCp}^*)\text{H}_2]$ in C—H and Si—H bond activation in the context of cluster growth.

The complex $[\text{Ru}(\text{GaCp}^*)_3(\text{SiEt}_3)\text{H}_3]$ (1) is obtained from $[\text{Ru}(\text{COD})(\text{MeAllyl})_2]$ ($\text{COD}=1,5\text{-cyclooctadiene}$; MeAllyl=2-methylallyl) and GaCp^* in HSiEt_3 under hydrogenolytic conditions, whereas in less reactive solvents (*n*-hexane, cyclohexane), uncontrolled cluster growth is observed. Complex 1 is a structural analogue to $[\text{Ru}(\text{PMMe}_3)_3(\text{SiEt}_3)\text{H}_3]$. It was characterized via SC-XRD, NMR, MS, IR, Raman, UV/Vis and elemental analysis. The analogous complex $[\text{Ru}(\text{GaCp}^*)_3(\text{C}_6\text{H}_5)\text{H}_3]$ (2) is formed upon C—H activation of toluene and was identified by high-resolution mass spectrometry, with DFT calculations allowing the assignment of a plausible structure. Finally, we performed a detailed comparison of the Ru—Ga and Ru—P

[a] M. Muhr,* R. Bühler,* J. Gilch, Dr. C. Jandl, Dr. C. Gemel,
Prof. Dr. R. A. Fischer
Chair of Inorganic and Metalorganic Chemistry
Department of Chemistry
Catalysis Research Center (CRC)
Technical University Munich (TUM)
Lichtenbergstraße 4, 85748 Garching (Germany)
E-mail: roland.fischer@tum.de

[b] H. Liang, Dr. S. Kahlal, Prof. Dr. J.-Y. Saillard
UMR-CNRS, 6226 “Institut des Sciences Chimiques de Rennes”
Univ Rennes, CNRS, ISCR-UMR 6226
35000 Rennes (France)
E-mail: jean-yves.saillard@univ-rennes1.fr

[*] These authors contributed equally to this work.

[†] Supporting information for this article is available on the WWW under <https://doi.org/10.1002/chem.202200887>

© 2022 The Authors. Chemistry - A European Journal published by Wiley-VCH GmbH. This is an open access article under the terms of the Creative Commons Attribution Non-Commercial NoDerivs License, which permits use and distribution in any medium, provided the original work is properly cited, the use is non-commercial and no modifications or adaptations are made.

bondings, including energy decomposition analysis (EDA) and quantum theory of atoms in molecules (QTAIM) analysis.

Results and Discussion

Synthesis and characterization $[\text{Ru}(\text{GaCp}^*)_3(\text{SiEt}_3)\text{H}_3]$ (1)

The stoichiometric reaction (based on the Ru/Ga ratio) of $[\text{Ru}(\text{COD})(\text{MeAllyl})_2]$ ($\text{COD}=1,5\text{-cyclooctadiene}$; MeAllyl=2-methylallyl) with three equivalents of GaCp^* in triethylsilane under 3 bar H_2 pressure leads to a dark orange solution after 6 h at 60°C (Figure 1a). After removing all volatiles *in vacuo*, yellow crystals suitable for single crystal x-ray diffraction (SC-XRD) of 1 can be obtained by recrystallization from *n*-hexane at -30°C . SC-XRD reveals a ruthenium centered complex, tetrahedrally surrounded by three GaCp^* ligands and one SiEt_3 unit (Figure 1b). The compound's architecture is isostructural to Berry's complex $[\text{Ru}(\text{PMe}_3)_3(\text{SiEt}_3)\text{H}_3]$. It should be noted that the hydride ligands could not be located with final certainty in the structure refinement. The Ru–Ga bond lengths, which vary only slightly from 2.376(3) Å to 2.385(6) Å, as well as the Ga– Cp^* centroid distances (1.970–1.982 Å), are in good agreement with distances reported in the literature.^[25,33–35] The Ru–Si bond length (2.373(2) Å) also matches Ru–Si bond lengths reported in the literature.^[36,37] Notably, it only differs 0.003 Å from the isostructural $[\text{Ru}(\text{PMe}_3)_3(\text{SiEt}_3)\text{H}_3]$.^[24] The tetrahedral structure is distorted, due to the three sterically demanding GaCp^* , resulting in Ga–Ru–Si angles ranging from 118.1° to 121.0°.

The ^1H NMR gives the expected set of signals for the three Cp^* ($\delta=1.88$ ppm, s, 45 H) and the three ethyl groups of the silyl ($\delta=1.26$ ppm, t, 9 H; $\delta=0.92$ ppm, q, 6 H). This is in good agreement with the ^{13}C signals: The Cp^* ligand (ring carbon at

$\delta=113.5$ ppm and methyl groups at $\delta=10.0$ ppm), as well as the silyl–ethyl signals for CH_3 ($\delta=10.5$ ppm) and CH_2 groups ($\delta=20.2$ ppm). Moreover, the ^1H NMR shows one broad singlet at $\delta=-13.31$ ppm with a relative intensity equivalent to 2.7, strongly indicating the presence of three hydrides similar to $[\text{Ru}(\text{PMe}_3)_3(\text{SiEt}_3)\text{H}_3]$. The presence of hydrides is further supported by vibrational spectroscopy: In the infrared spectrum an intensive broad band at 1898 cm^{-1} , along with a small shoulder at 1771 cm^{-1} is present in the typical Ru–H region. The expected band in the Raman spectrum, is observed at 1913 cm^{-1} (Figure S24). High resolution liquid injection field desorption ionization mass spectrometry (LIFDI-MS) gives rise to signal for $[\text{M}-2\text{H}]^{+*}$ ($m/z=832.131$; calc.=832.134), we attribute the loss of two H atoms to fragmentation. Based on the SC-XRD structural data of 1, its geometry was fully optimized by DFT calculations at the BP86/TZ2P level (see Computational Details). In analogy to the molecular structure of $[\text{Ru}(\text{PMe}_3)_3(\text{SiEt}_3)\text{H}_3]$ ^[24], the structure of lowest energy found for 1 (confirmed as a minimum by frequency calculations) corresponds to a configuration in which the three hydrides are located in an umbrella-like arrangement (Figure 1c). The DFT-simulated spectrum (Figure S22) is in reasonable agreement with the experimental data, showing Ru–H bands at 1985 cm^{-1} (symmetric stretch), 1961 cm^{-1} and 1942 cm^{-1} (both asymmetric stretches). This optimized structure is in very good agreement with the crystal structure. Ru–Ga and Ru–Si bonds only differ by less than 0.005 Å, and bond angles of the ‘metal core’ (Ru/Ga/Si) only by less than 4°. The computed Si...H distances (2.067 Å–2.155 Å) are indicative of no bonding interaction. All calculated Ru–H distance are almost equivalent, ranging from 1.626 to 1.631 Å. The computed H–H distances (2.404 Å–2.493 Å) indicate classical hydride ligands rather than dihydrogen-bonding. This is confirmed in a T_1 relaxation NMR experiment (Figure S5), with $T_1(\text{min})=546$ –1231 ms (193 K–293 K). The computed ^1H hydride chemical shifts (-10.3 ppm) are 3 ppm lower than their experimental counterparts, whereas the other computed ^1H signals differ by less than 1 ppm than their observed homologues. The same situation is found for the hydride signal in the related complex $[\text{Ru}(\text{PMe}_3)_3(\text{SiEt}_3)\text{H}_3]$ (computed: -7.7 ppm; recorded -10.53 ppm^[24]), whereas the average deviation of all other proton signals is also less than 1 ppm. All these results strongly support the trihydride nature of 1.

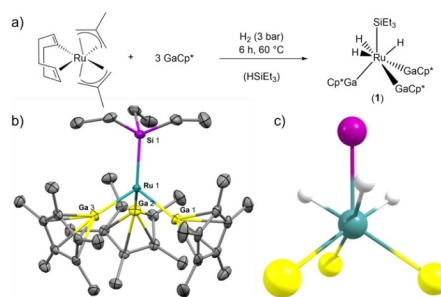


Figure 1. a) Reaction scheme for the synthesis of 1. b) Molecular structure of $[\text{Ru}(\text{GaCp}^*)_3(\text{SiEt}_3)\text{H}_3]$ (1). Ellipsoids at the 50% probability level. H atoms are omitted for clarity. Selected bond lengths (Å) and angles (deg): Ru1–Ga1 = 2.376(3), Ru1–Ga2 = 2.376(4), Ru1–Ga3 = 2.385(6), Ru1–Si1 = 2.373(2), Ga– Cp^* centroid = 1.970–1.982; Ga1–Ru1–Ga2 = 96.43(2), Ga1–Ru1–Ga3 = 99.36(2), Ga2–Ru1–Ga3 = 97.29(2), Ga1–Ru1–Si1 = 120.98(2), Ga2–Ru1–Si1 = 119.73(2), Ga3–Ru1–Si1 = 118.10(3). Space group: P 1 21/c. c) DFT-optimized structure (BP86/TZ2P) showing the hydrides' positions. Ru–H = 1.626–1.631 Å; Si–H = 2.067–2.155 Å Other C and H atoms omitted for clarity.

C–H activation of toluene: $[\text{Ru}(\text{GaCp}^*)_3(\text{C}_6\text{H}_5)_\text{H}_3]$ (2)

After observing that Si–H bonds can be activated, we wanted to investigate whether C–H bonds can also be activated in a similar manner. Thus $[\text{Ru}(\text{COD})(\text{MeAllyl})_2]$ and $[\text{Ru}(\text{COD})(\text{COT})]$ ($\text{COT}=1,3,5\text{-cyclooctatriene}$) were reacted with GaCp^* under analogous reaction conditions to 1 in toluene. Both reactions lead to dark brown solutions even after a short time of 20 minutes. Notably, the formation of 1 seems to be slower as judged by the color change to orange after six hours. LIFDI-MS suggests the formation of a series of toluene containing compounds. As shown by experiments with different Ru precursors, the nature of the Ru source is important for the

product distribution, however, differences become prominent only after prolonged reaction times. After one hour the reaction solutions of $[\text{Ru}(\text{COD})(\text{MeAllyl})_2]/\text{GaCp}^*$ as well as $[\text{Ru}(\text{COD})(\text{COT})]/\text{GaCp}^*$ in toluene contain products producing the same series of ions, which can be assigned to different toluene containing species: $[\text{Ru}_2(\text{GaCp}^*)_4(\text{C}_7\text{H}_8)\text{H}_2]^{+•}$ ($m/z = 1116.056$; $\text{calc} = 1116.058$), $[\text{Ru}_2(\text{Ga})(\text{GaCp}^*)_3(\text{C}_7\text{H}_8)\text{H}]^{+•}$ ($m/z = 980.933$; $\text{calc} = 980.933$), $[\text{Ru}_2(\text{GaCp}^*)_3(\text{C}_7\text{H}_8)\text{H}_2]^{+•}$ ($m/z = 912.015$; $\text{calc} = 912.014$), $[\text{Ru}(\text{GaCp}^*)_3(\text{C}_7\text{H}_8)\text{H}_2]^{+•}$ ($m/z = 810.109$; $\text{calc} = 810.110$), $[\text{Ru}(\text{GaCp}^*)_2(\text{C}_7\text{H}_8)]^{+•}$ ($m/z = 604.051$; $\text{calc} = 604.051$). While the mass spectrum of the reaction solution of $[\text{Ru}(\text{COD})(\text{COT})]/\text{GaCp}^*$ remains largely unchanged over time, the mass spectrum of the reaction solution of $[\text{Ru}(\text{COD})(\text{MeAllyl})_2]/\text{GaCp}^*$ reveals almost exclusively the ion $[\text{Ru}(\text{GaCp}^*)_2(\text{C}_7\text{H}_8)\text{H}]^{+•}$ ($2^{+•}$) after 48 h. We conclude from the measured sum formula that this signal does not represent a fragment but rather the molecular ion $2^{+•}$, since the corresponding neutral complex **2** satisfies the 18 valence electron (VE) rule and is isoelectronic to **1**. A pattern at $m/z = 604.051$ ($[\text{Ru}(\text{GaCp}^*)_2(\text{C}_7\text{H}_8)]^{+•}$) is assigned to the fragment $[\text{M}-\text{GaCp}^*-2\text{H}]^{+•}$ of **2** (Figure 2a). These assignments and the composition of **2** could be confirmed by double labelling experiments with toluene-d₈ (Figure 2b) and with the mono ethyl-substituted derivative $\text{GaCp}^{*\text{Et}}$ ($\text{Cp}^{*\text{Et}} = 1\text{-ethyl-2,3,4,5-tetramethylcyclopentadienyl}$) (Figure 2c), revealing the expected m/z differences of respectively 8 and 42 (three additional CH_2 groups).

In contrast to **1**, compound **2** could not be isolated. It is formed in solution after long reaction times and can be enriched, although some thermal degradation in solution is also observed then, becoming obvious from the formation of metallic precipitate and mirror. We also noticed a stark influence of the concentration, i.e. **2** can be enriched only when working at low concentrations ($c_{\text{total}} < 5 \text{ mg/mL}$). Combined with the unstable nature of **2** under reduced pressure, it was thus impossible to

crystallize the compound or to characterize enriched/pure samples with solution spectroscopic techniques (NMR, IR). Nevertheless ¹H NMR of reaction solutions shows hydride signals (-14.15 , -15.63 , -16.03 and -16.22 ppm , Figure S6), as does the IR spectrum with bands at 1807 and 1861 cm^{-1} (Figure S23). Inspired by the thermal induced reductive elimination of HSiEt_3 from $[(\text{Cp}^*\text{Al})_3\text{Ni}(\mu\text{-H})\text{Al}(\text{C}_6\text{H}_5)(\eta^1\text{-Cp}^*)]$ by subsequent C–H activation of benzene,^[17] we attempted the preparation of a pure sample of **2** from thermal treatment of **1** in toluene. Even under harsh conditions, no reaction was observed. A similar behavior was observed for the treatment of a solution of **2** with an excess of HSiEt_3 .

As no experimental access to structural data was possible, reasonable structures representing energy minima for the postulated trihydride complex **2** were calculated on the DFT level of theory. The energetically most favorable structures correspond to activated toluene in *ortho*, *meta*, *para* and benzylic position, respectively (Figure 3). Their computed relative energies indicate that the products upon C–H activation at an aromatic position are almost equal in energy and are favored with respect to the activation at the benzylic position. The energy difference between the *ortho* and *meta* isomers is insignificant and that of the *para* relative is barely larger. Thus, even if not considering the possibility of topological isomerism for each individual *ortho*, *meta* and *para* system, the possibility of having several isomers in solution should not be excluded. These calculations only reflect thermodynamic stability. In order to investigate differences in regioselectivity between each site's activation, we performed analogous experiments in benzene (all-aromatic) as well as in *tert*-butylbenzene (no benzylic C–H). Indeed, in both cases the respective signals (m/z) of the expected activation products were observed by LIFDI-MS (Figures S12 and S13; benzene: $m/z = 796.094$; $\text{calc} = 796.094$; *tert*-butylbenzene: $m/z = 852.155$; $\text{calc} = 852.157$). The presence of the respective benzene activation is further supported by the corresponding hydride signal (-16.56 ppm ; Figure S7).

Taken together our experimental and computational data it is reasonable to assume that the formation of **2** proceeds via C–H activation of toluene on the electron-deficient intermed-

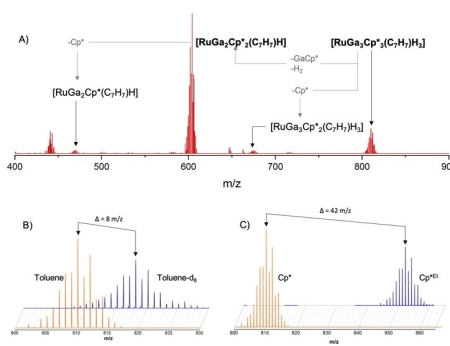


Figure 2. a) Size focused LIFDI-MS spectrum of **2** with the composition of the molecular ion and the main fragments given. b) LIFDI-MS patterns of **2** for the reaction in toluene and the labeling experiment using toluene-d₈ and c) the LIFDI-MS patterns of **2** with Cp^* and $\text{Cp}^{*\text{Et}}$. The m/z difference of 8 and 42 respectively shows the incorporation of one toluene and three Cp^* into the compound.

Chem. Eur. J. 2022, 28, e202200887 (3 of 6)

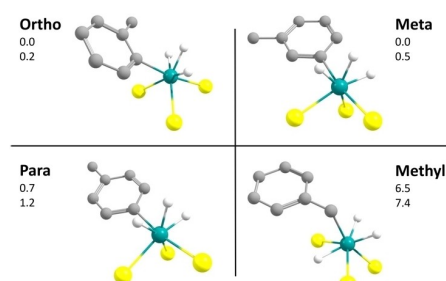


Figure 3. Calculated isomers of **2** with their relative total (ΔE) and free (ΔG) energy differences in kcal/mol (top: ΔE ; bottom: ΔG). Cp^* and hydrogen atoms of toluene omitted for clarity.

© 2022 The Authors. Chemistry - A European Journal published by Wiley-VCH GmbH

ate $[(\text{Cp}^*\text{Ga})_3\text{RuH}_2]$.²⁵ To validate this hypothesis, the hydrogenolysis of ruthenium complexes with GaCp* was performed in *n*-hexane to prevent C–H or Si–H activation. This may lead to the activation of a second H₂ equivalent.^[38] While there is no experimental evidence for a potential $[(\text{Cp}^*\text{Ga})_3\text{RuH}_2]$ cluster growth reactions are observed by LIFDI-MS (Figure S14). This points to reactive intermediates and related competing reactions between bond activation (in aromatic solvents or silane) and cluster growth.

Starting from $[(\text{Cp}^*\text{Ga})_3\text{RuH}_2]$, DFT calculations allow the rationalization of the observed reactivity from a thermodynamic point of view. C–H activation of toluene at $[(\text{Cp}^*\text{Ga})_3\text{RuH}_2]$ is thermodynamically favorable according to free energy calculations ($\Delta G = -11.8 \text{ kcal/mol}$). Note that replacing toluene by benzene barely changes the reaction energy ($\Delta G = -11.3 \text{ kcal/mol}$). Replacing $[(\text{Cp}^*\text{Ga})_3\text{RuH}_2]$ by its hypothetical phosphine-ligated analogue $[(\text{PMe}_3)_3\text{RuH}_2]$ cancels the exergonicity of the toluene C–H activation reaction ($\Delta G = +1.4 \text{ kcal/mol}$). A similar trend and energetic difference are found for the Si–H addition of HSiEt₃ on the same electron-deficient species. In the case of $[(\text{Cp}^*\text{Ga})_3\text{RuH}_2]$, $\Delta G = -43.1 \text{ kcal/mol}$, whereas in the case of $[(\text{PMe}_3)_3\text{RuH}_2]$, $\Delta G = -28.8 \text{ kcal/mol}$.

Theoretical investigations on the Ru–Ga and Ru–P bonding

Both 1 and $[\text{Ru}(\text{PMe}_3)_3(\text{SiEt}_3)\text{H}_3]$ are hepta-coordinated Ru(IV) 18 VE complexes that can be described as made of a pseudo-octahedral $[\text{RuL}_3\text{H}_3]$ ($\text{L} = \text{GaCp}^*$, PMe_3) unit to which an SiEt₃ ligand is added along the C_3 axis. The four Ru(IV) electrons are expected to occupy non-bonding 4d orbitals, i.e., those which do not point towards ligands, namely MOs of dominant xy and x^2-y^2 character (considering the z axis colinear with the Ru–Si bond). As shown by the Kohn-Sham orbital diagrams of 1 and $[\text{Ru}(\text{PMe}_3)_3(\text{SiEt}_3)\text{H}_3]$ (Figure 4), these two orbitals are the HOMO and HOMO-1 of the complexes. Despite their qualitatively related electronic structures, both complexes have some differences, as exemplified by their HOMO-LUMO gaps, that of 1 being much lower than that of its phosphine analogue. The lowest metal-ligand antibonding orbital of 1 is its LUMO, whereas it is the LUMO+1 in the phosphine complex. Selected computed data for both complexes are gathered in Table S1. They show roughly similar bond distances around Ru in both complexes, with similar Wiberg indices, which however indicate that the Ru–Ga bonding is somewhat weaker than the Ru–P one. To gain deeper insights into the Ru–L ($\text{L} = \text{GaCp}^*$, PMe_3) bonding in 1 and $[\text{Ru}(\text{PMe}_3)_3(\text{SiEt}_3)\text{H}_3]$, we performed an energy decomposition analy-

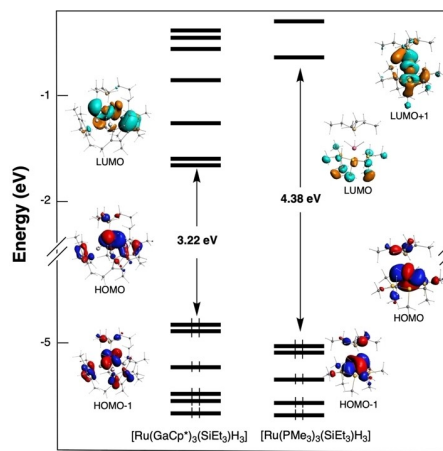


Figure 4. Kohn-Sham MO diagrams of 1 and $[\text{Ru}(\text{PMe}_3)_3(\text{SiEt}_3)\text{H}_3]$.

sis (EDA) of the interaction between two frozen molecular fragments, according to the Morokuma-Ziegler procedure.^[39–41] The decomposition of the total bonding energy (TBE) between the $[\text{RuH}_3(\text{SiEt}_3)]$ fragment and its L_3 shell is provided in Table 1. TBE is expressed as the sum of four components: the Pauli repulsion (E_{Pauli}), the electrostatic interaction energy (E_{elstat}), the orbital interaction energy (E_{orb}) and the component associated with the dispersion forces (E_{disp}). From comparing these TBE values, it is clear that the Ru–L bonding is stronger in the case where $\text{L} = \text{PMe}_3$ than for $\text{L} = \text{GaCp}^*$. Whereas the E_{Pauli} and E_{elstat} components of the two compounds differ significantly, their sum, which is often approximated to the steric part of the interaction energy are about the same ($E_{\text{steric}} = 2.37$ and 2.48 eV for $\text{L} = \text{GaCp}^*$ and PMe_3 , respectively). Since the E_{disp} contributions are also similar, the TBE main difference originates from the E_{orb} components, which reflect difference in covalency. This is also consistent with the difference in the HOMO-LUMO gaps. A similar qualitative trend is found for the hypothetical unsaturated species $[\text{Ru}(\text{GaCp}^*)_3\text{H}_2]$ $[\text{Ru}(\text{PMe}_3)_3\text{H}_2]$.

Another point of view can be provided by the quantum theory of atoms in molecules (QTAIM) approach.^[42–43] Selected QTAIM data associated with the Ru–Ga/P bond critical points in 1 and $[\text{Ru}(\text{PMe}_3)_3(\text{SiEt}_3)\text{H}_3]$ are collated in Table S2. In both

Table 1. Morokuma-Ziegler energy decomposition analysis of 1, $[\text{Ru}(\text{GaCp}^*)_3\text{H}_2]$, and their trimethylphosphine analogues. All values are in eV.

Compound Fragmentation	$[\text{Ru}(\text{GaCp}^*)_3(\text{SiEt}_3)\text{H}_2]$ (1) $[\text{RuH}_3(\text{SiEt}_3)] + [\text{GaCp}^*]_3$	$[\text{Ru}(\text{PMe}_3)_3(\text{SiEt}_3)\text{H}_2]$ $[\text{RuH}_3(\text{SiEt}_3)] + [\text{PMe}_3]_3$	$[\text{Ru}(\text{GaCp}^*)_3\text{H}_2]$ $[\text{RuH}_2] + [\text{GaCp}^*]_3$	$[\text{Ru}(\text{PMe}_3)_3\text{H}_2]$ $[\text{RuH}_2] + [\text{PMe}_3]_3$
E_{Pauli}	11.52	15.19	11.55	16.94
E_{elstat}	-9.15	-12.71	-9.82	-14.35
E_{orb}	-5.99	-8.04	-6.86	-9.67
E_{disp}	-1.45	-1.36	-0.84	-0.94
TBE ^a	-5.08	-6.93	-5.97	-8.02

compounds, the positive value of the Laplacian density, the negative values of the energy and potential energy densities and the larger than 1 $|V|/G$ ratio are not contradicting the typical description of a ligand-to-metal dative bonding in both compounds.^[44–46] The delocalization index is indicative of a weaker Ru–Ga covalent interaction, in agreement with the EDA analysis and Wiberg bond indices. The AIM charges indicate a more negatively polarized Ru in the case of Ru–Ga as compared to Ru–P. This points to a bond polarization of the form $\text{TM}(\delta^-)\text{E}(\delta^+)$, which could already be expected from previous reports.^[19,22–23, 31] As shown in Tables 1, S1 and S2, the Ru–Ga vs. Ru–P bonding features are maintained on the hypothetical 16 VE intermediates $[\text{RuL}_3\text{H}_2]$ ($\text{L} = \text{GaCp}^*, \text{PMMe}_3$).

Conclusion

Ru/Ga complexes have been investigated with respect to their behavior in C–H and Si–H bond activation reactions. $[\text{Ru}(\text{GaCp}^*)_3\text{H}_2]$ has been proposed as the crucial intermediate in the bond activation reactions, DFT calculations confirming the increased reactivity with respect to the phosphine analogue $[\text{Ru}(\text{PMMe}_3)_3\text{H}_2]$.

$[\text{Ru}(\text{GaCp}^*)_3\text{H}_2]$ has also been described in earlier studies as a reactive intermediate on the way to Ru/Ga clusters. Thus, reductive elimination of Cp^*H leads to a ligand stabilized Ru/Ga cluster with a linear Ru–Ga–Ru backbone.^[25] This underlines the crucial role of transient and/or intermediate species in cluster growth reactions. The “proto” cluster species $[\text{Ru}(\text{GaCp}^*)_3\text{H}_2]$ obviously can act as a reactive building block for larger clusters, whereby substrate (e.g. H₂) or solvent molecules actively intervene in the reaction process by stabilizing the intermediate. Controlling the resulting complexity often remains a challenge. One possible approach to control cluster growth, however, which has been recently successfully employed in the synthesis of Ni/Al and Ni/Ga clusters is the use of alkynes as additives.^[47] A propagation of this idea with the aim of investigating larger Ru/Ga clusters is part of an ongoing project and will be presented in future work.

Experimental Section

General remarks: All manipulations were carried out using standard Schlenk techniques under inert atmospheres. Solvents were dried using a MBraun Solvent Purification System. The final H₂O content of all solvents was measured via Karl Fischer titration and was below 5 ppm. Starting materials $[\text{Ru}(\text{COD})(\text{MeAllyl})_2]$, $[\text{Ru}(\text{COD})(\text{COT})]$ and GaCp* were synthesized according to literature procedures. Elemental analysis was conducted at the microanalytical laboratory at the Technical University Munich. NMR spectra were recorded on a Bruker AVIII 400 US spectrometer (¹H, 400 MHz; ¹³C, 101 MHz) in C₆D₆. Chemical shifts (δ) are described in ppm relative to tetramethylsilane (TMS) and referenced to the solvent resonances as internal standards. The signal multiplicity is given as following: s = singlet, d = doublet, t = triplet or q = quartet.

LIFDI-MS: Liquid Injection Field Desorption Ionization Mass Spectrometry (LIFDI-MS) was measured directly from an inert atmosphere glovebox with a Thermo Fisher Scientific Exactive Plus

Orbitrap (mass accuracy 3 ppm; external calibration) equipped with an ion source from Linden CMS.^[48]

For compound 1 X-ray diffraction intensities were collected on a Bruker D8-Venture diffractometer equipped with a CMOS detector (Bruker Photon-100), an IMS microfocus with Mo K_α radiation ($\lambda = 0.71073 \text{ \AA}$) and a Helios optic. Suitable crystals were coated in perfluoropolyether and mounted in the cooled nitrogen stream (100 K) of the diffractometer on a kapton microampler. Diffraction data were processed with APEX III and the implemented SAINT and SADABS programs. Structures were solved using SHELXT and refined with SHELXL-2017 in conjunction with SHELXE. Further crystallographic details are provided in the Supporting Information.

Deposition Number(s) 2158227 (1) contain(s) the supplementary crystallographic data for this paper. These data are provided free of charge by the joint Cambridge Crystallographic Data Centre and Fachinformationszentrum Karlsruhe Access Structures service.

计算细节: Density Functional Theory (DFT) calculations were carried out with the use of the ADF2020 code^[49,50] with the addition of Grimmes's D3 empirical corrections^[51] to take into account dispersion effects. The triple-zeta with two polarization functions (TZ2P) basis set was used, together with the BP86^[52,53] exchange-correlation functional. All the optimized structures were confirmed as true minima on their potential energy surface by analytical vibration frequency calculations. Wiberg bond indices were computed with the NBO 6.0 program^[54] implemented in the ADF2020 package. The QTAIM analysis^[42–43] was performed as implemented in the ADF2019 suite.^[55–56] The ¹H NMR chemical shifts were computed on the BP86/TZ2P-optimized structures, according to the GIAO method,^[57] with the B3LYP functional^[58] and taking into account solvent (benzene) effect via the COSMO model.^[59,60]

Synthetic protocols

$[\text{Ru}(\text{GaCp}^*)_3(\text{SiEt}_3)(\text{H})]$ (1): A solution of 450 mg (1.0 equiv., 1.410 mmol) $[\text{Ru}(\text{COD})(\text{MeAllyl})_2]$ and 867 mg (3.0 equiv., 4.230 mmol) GaCp* in 6 mL HSiEt₃ is freeze-pump-thawed-degassed and pressurized with 3 bar H₂ in a 150 mL Fisher-Porter bottle. The reaction solution turns from yellow to dark orange over 6 h at 60 °C. Residual HSiEt₃ is removed in vacuo and 830 mg (71%, 0.995 mmol) of 1 are obtained by recrystallization from *n*-hexane. ¹H NMR (C₆D₆, 400 MHz): δ [ppm] = 1.88 (s, 45 H, GaCp*), 1.26 (t, 9H, SiCH₂CH₃), 0.92 (q, 6H, Si-H₃C), -13.31 (s, 3H, Ru–H). ¹³C NMR (C₆D₆, 101 MHz): δ [ppm] = 113.5 (s, C₅(CH₃)₅), 20.2 (s, Si-CH₂), 10.5 (s, SiCH₂CH₃), 10.0 (s, C₅(CH₃)₅). ATR-IR [cm⁻¹]: 1898, 1771 (Ru–H). Raman [cm⁻¹]: 1913 (Ru–H). UV-Vis (cyclohexane) λ_{max} = 226 nm, 281 nm, 344 nm. LIFDI-MS m/z = 832.1313 [M-2H]⁺. (calc = 832.1339). Elemental analysis calc. for $\text{RuGa}_3\text{C}_{36}\text{H}_{63}\text{Si}$: C, 51.83; H, 7.61; Ga, 25.07; Ru, 12.12; Si, 3.37. Found: C, 51.74; H, 7.77; Ga, 24.3; Ru, 12.0; Si, 3.79.

$[\text{Ru}(\text{GaCp}^*)_3(\text{C}_7\text{H}_7)\text{H}_3]$ (2): 50.0 mg $[\text{Ru}(\text{cod})(\text{MeAllyl})_2]$ (1.0 equiv., 0.157 mmol) and 65.0 mg GaCp* (2.0, 0.313 mmol) are inserted into a 150 mL Fisher-Porter Bottle, dissolved in 14 mL toluene. The solution is freeze-pump-thawed-degassed and pressurized with 3 bar H₂. The reaction mixture is stirred at 60 °C for 48 h and then canula filtrated. LIFDI-MS m/z = 810.1088 [M]⁺ (calc = 810.1100), m/z = 604.0508 [M-GaCp*₂H]⁺ (calc = 604.0514).

Acknowledgements

This work was funded by the German Research Foundation (DFG) within a Reinhard Koselleck Project (FI-502/44-1), the TUM Graduate School and the GENCI French national computer resource center (grant A0030807367). H.L. thanks the China Scholarship Council for a Ph.D. grant. The authors thank Dardan Ukaj for measuring the Raman spectrum of 1. Open Access funding enabled and organized by Projekt DEAL.

Conflict of Interest

The authors declare no conflict of interest.

Data Availability Statement

The data that support the findings of this study are available from the corresponding author upon reasonable request.

Keywords: bond activation · cluster intermediates · density functional calculations · intermetallic compounds · mass spectrometry

- [1] R. C. Cammarota, M. V. Vollmer, J. Xie, J. Ye, J. C. Linehan, S. A. Burgess, A. M. Appel, L. Gagliardi, C. C. Lu, *J. Am. Chem. Soc.* **2017**, *139*, 14244–14250.
- [2] J. Fajardo, J. C. Peters, *J. Am. Chem. Soc.* **2017**, *139*, 16105–16108.
- [3] I. Fujii, K. Semba, Q.-Z. Li, S. Sakaki, Y. Nakao, *J. Am. Chem. Soc.* **2020**, *142*, 11647–11652.
- [4] H. Kameo, J. Yamamoto, A. Asada, H. Nakazawa, H. Matsuzaka, D. Bourissou, *Angew. Chem. Int. Ed.* **2019**, *131*, 18959–18963.
- [5] R. Seki, N. Hara, T. Saito, Y. Nakao, *J. Am. Chem. Soc.* **2021**, *143*, 6388–6394.
- [6] W.-C. Shih, O. V. Ozerov, *J. Am. Chem. Soc.* **2017**, *139*, 17297–17300.
- [7] J. Takaya, N. Iwasawa, *J. Am. Chem. Soc.* **2017**, *139*, 6074–6077.
- [8] M. V. Vollmer, J. Ye, J. C. Linehan, B. J. Graziano, A. Preston, E. S. Wiedner, C. C. Lu, *ACS Catal.* **2020**, *10*, 2459–2470.
- [9] R. Yamada, N. Iwasawa, J. Takaya, *Angew. Chem. Int. Ed.* **2019**, *58*, 17251–17254; *Angew. Chem.* **2019**, *131*, 17411–17414.
- [10] M. Armbrüster, K. Kovnir, M. Friedrich, D. Teschner, G. Wownick, M. Hahne, P. Gille, L. Szentmiklósi, M. Feuerbacher, M. Heggen, F. Girgsdies, D. Rosenthal, R. Schlogl, Y. Grin, *Nat. Mater.* **2012**, *11*, 690–693.
- [11] J. Prinz, C. A. Pignedoli, O. S. Stöckl, M. Armbrüster, H. Brune, O. Grönig, R. Widmer, D. Passerone, *J. Am. Chem. Soc.* **2014**, *136*, 11792–11798.
- [12] F. Studt, F. Abild-Pedersen, T. Bligaard, Z. Sørensen Rasmus, H. Christensen Claus, K. Nørskov Jens, *Science* **2008**, *320*, 1320–1322.
- [13] M. Armbrüster, *Sci. Technol. Adv. Mater.* **2020**, *21*, 303–322.
- [14] J. Campos, *Nat. Chem. Rev.* **2020**, *4*, 696–702.
- [15] S. Furukawa, T. Komatsu, *ACS Catal.* **2017**, *7*, 735–765.
- [16] K. Mayer, J. Weißing, T. Fässler, R. A. Fischer, *Angew. Chem. Int. Ed.* **2018**, *57*, 14372–14393; *Angew. Chem.* **2018**, *130*, 14570–14593.
- [17] T. Steinke, C. Gemel, M. Cokoja, M. Winter, R. A. Fischer, *Angew. Chem. Int. Ed.* **2004**, *116*, 2349–2352.
- [18] T. Cadenbach, C. Gemel, R. Schmid, R. A. Fischer, *J. Am. Chem. Soc.* **2005**, *127*, 17068–17078.
- [19] R. H. Crabtree, D. G. Hamilton, *J. Am. Chem. Soc.* **1986**, *108*, 3124–3125.
- [20] R. O. Harris, N. K. Hota, L. Sadavoy, J. M. C. Yuen, *J. Organomet. Chem.* **1973**, *54*, 259–264.
- [21] S. Wesselbaum, T. vom Stein, J. Klankermayer, W. Leitner, *Angew. Chem. Int. Ed.* **2012**, *51*, 7499–7502; *Angew. Chem.* **2012**, *124*, 7617–7620.
- [22] Z. Ruan, S.-K. Zhang, C. Zhu, P. N. Ruth, D. Stalke, L. Ackermann, *Angew. Chem. Int. Ed.* **2017**, *56*, 2045–2049; *Angew. Chem.* **2017**, *129*, 2077–2081.
- [23] E. L. Dias, S. T. Nguyen, R. H. Grubbs, *J. Am. Chem. Soc.* **1997**, *119*, 3887–3897.
- [24] V. K. Dioumaev, L. J. Procopio, P. J. Carroll, D. H. Berry, *J. Am. Chem. Soc.* **2003**, *125*, 8043–8058.
- [25] T. Cadenbach, C. Gemel, R. Schmid, M. Halbherr, K. Yusenko, M. Cokoja, R. A. Fischer, *Angew. Chem. Int. Ed.* **2009**, *48*, 3872–3876; *Angew. Chem.* **2009**, *121*, 3930–3934.
- [26] R. A. Fischer, J. Weiß, *Angew. Chem. Int. Ed.* **1999**, *38*, 2830–2850; *Angew. Chem.* **1999**, *111*, 3002–3022.
- [27] J. Hornung, J. Weißing, P. Jerabek, C. Gemel, A. Pöthig, G. Frenking, R. A. Fischer, *Inorg. Chem.* **2018**, *57*, 12657–12664.
- [28] M. Muhr, J. Hornung, J. Weißing, C. Jandl, C. Gemel, R. A. Fischer, *Inorg. Chem.* **2020**, *59*, 5086–5093.
- [29] T. Steinke, C. Gemel, M. Winter, R. A. Fischer, *Chem. Eur. J.* **2005**, *11*, 1636–1646.
- [30] J. Uddin, C. Boehme, G. Frenking, *Organometallics* **2000**, *19*, 571–582.
- [31] J. Uddin, G. Frenking, *J. Am. Chem. Soc.* **2001**, *123*, 1683–1693.
- [32] W. Uhl, M. Bentler, S. Melle, W. Saak, G. Frenking, J. Uddin, *Organometallics* **1999**, *18*, 3778–3780.
- [33] B. Buchin, C. Gemel, A. Kempter, T. Cadenbach, R. A. Fischer, *Inorg. Chim. Acta* **2006**, *359*, 4833–4839.
- [34] T. Cadenbach, T. Böllermann, C. Gemel, R. A. Fischer, *Dalton Trans.* **2009**, 322–329.
- [35] T. Cadenbach, C. Gemel, T. Böllermann, I. Fernandez, G. Frenking, R. A. Fischer, *Chem. Eur. J.* **2008**, *14*, 10789–10796.
- [36] B. Chatterjee, C. Gunanathan, *Chem. Commun.* **2014**, *50*, 888–890.
- [37] T. Komuro, H. Tobita, *Chem. Commun.* **2010**, *46*, 1136–1137.
- [38] B. Chaudret, R. Poilblanc, *Organometallics* **1985**, *4*, 1722–1726.
- [39] F. M. Bickelhaupt, E. J. Baerends, in *Rev. Comput. Chem.*, Vol. 15 (Eds.: K. B. Lipkowitz, D. B. Boyd), Wiley, New-York, **2000**, pp. 1–86.
- [40] K. Morokuma, *J. Chem. Phys.* **1971**, *55*, 1236–1244.
- [41] T. Ziegler, R. Arvi, *Inorg. Chem.* **1979**, *18*, 1558–1565.
- [42] R. F. W. Bader, *Atoms in Molecules - A Quantum Theory*, Oxford University Press, **1990**.
- [43] P. L. A. Popelier, in *The Chemical Bond*, Vol. 1, Wiley-VCH, **2014**, pp. 271–308.
- [44] A. A. Adeniyi, P. A. Ajibade, *J. Biomol. Struct. Dyn.* **2014**, *32*, 1351–1365.
- [45] R. Gericke, J. Wagler, *Inorg. Chem.* **2020**, *59*, 6359–6375.
- [46] C. Lepietti, P. Fau, K. Fajerberg, M. L. Kahn, B. Silvi, *Coord. Chem. Rev.* **2017**, *345*, 150–181.
- [47] P. Heiß, J. Hornung, C. Gemel, R. A. Fischer, *Chem. Commun.* **2022**, *58*, 4332–4335.
- [48] M. Muhr, P. Heiß, M. Schütz, R. Bühler, C. Gemel, M. H. Linden, H. B. Linden, R. A. Fischer, *Dalton Trans.* **2021**, *50*, 9031–9036.
- [49] G. te Velde, F. M. Bickelhaupt, E. J. Baerends, C. Fonseca Guerra, S. J. A. van Gisbergen, J. G. Snijders, T. Ziegler, *J. Comput. Chem.* **2001**, *22*, 931–967.
- [50] E. J. Baerends, T. Ziegler, A. J. Atkins, J. Autschbach, D. Bashford, O. Baseggio, A. Bérçés, F. M. Bickelhaupt, C. Bo, P. M. Boerriger, L. Cavallo, C. Daul, D. P. Chong, D. V. Chulhai, L. Deng, R. M. Dickson, J. M. Dieterich, D. E. Ellis, M. van Faassen, A. Ghysels, A. Giannonna, S. J. A. van Gisbergen, A. Goetz, A. W. Götz, S. Gusarov, F. E. Harris, P. van den Hoek, Z. Hu, C. R. Jacob, H. Jacobsen, et al., *SCM*, **2020**.
- [51] S. Grimme, *J. Comput. Chem.* **2006**, *27*, 1787–1799.
- [52] A. D. Becke, *Phys. Rev. A* **1988**, *38*, 3098–3100.
- [53] J. P. Perdew, *Phys. Rev. B* **1982**, *33*, 8822–8824.
- [54] E. D. Glendening, C. R. Landis, F. Weinhold, *J. Comput. Chem.* **2013**, *34*, 1429–1437.
- [55] J. I. Rodriguez, *J. Comput. Chem.* **2012**, *34*, 681–686.
- [56] J. I. Rodriguez, R. F. W. Bader, P. W. Ayers, C. Michel, A. W. Götz, C. Bo, *Chem. Phys. Lett.* **2009**, *472*, 149–152.
- [57] G. Schreckenbach, T. Ziegler, *J. Phys. Chem.* **1995**, *99*, 606–611.
- [58] P. J. Stephens, F. J. Devlin, C. F. Chabalowski, M. J. Frisch, *J. Phys. Chem.* **1994**, *98*, 11623–11627.
- [59] A. Klamt, G. Schüürmann, *J. Chem. Soc. Perkin Trans. 2* **1993**, 799–805.
- [60] A. Klamt, *J. Phys. Chem.* **1995**, *99*, 2224–2235.

Manuscript received: March 21, 2022

Accepted manuscript online: June 24, 2022

Version of record online: August 3, 2022

3.3 Study III: Photochemically Generated Reactive Sites at Ruthenium/Gallium Complexes: Catalysis vs. Cluster Growth

The controlled dissociation of labile ligands is a key factor for promoting the formation of reactive sites at TM/E clusters and complexes. Using the $[(\text{Ru}(\text{GaCp}^*)_3(\text{SiEt}_3)\text{H}_3]$ compound reported in the previous study, the reductive elimination of triethyl silane, in analogy to the $[\text{Ni}(\text{AlCp}^*)_3\text{H}(\text{SiEt}_3)]$ is investigated.

Through irradiation under UV light (350 nm), it is possible to induce both the reductive elimination of triethyl silane as well as of dihydrogen. This was proven by performing the reaction in the presence of 1,2-bis(diphenylphosphino)ethane (dppe), which yielded the Ru⁰ complex $[(\text{dppe})\text{Ru}(\text{GaCp}^*)_3]$. Furthermore, when irradiating $[(\text{Ru}(\text{GaCp}^*)_3(\text{SiEt}_3)\text{H}_3]$ in the presence of 3-hexyne under a hydrogen atmosphere, the *in situ* formed unsaturated $[(\text{Ru}(\text{GaCp}^*)_3\text{H}_2]$ performed catalytic hydrogenation. A mechanism could be proposed based on *in situ* mass spectrometric analysis of the reaction mixture, and a “poisoning” side reaction, namely the formation of $[\text{Ru}(\text{GaCp}^*)_3(\text{hexyne})(\text{hexene})]$, was identified. The silyl and hydrides can thus be interpreted as selectively removable protecting groups for the active transition metal center.

R. Bühler performed experiments concerning the hydrogenation catalysis, the elucidation of the catalytic cycle, and the characterization of $[(\text{dppe})\text{Ru}(\text{GaCp}^*)_3]$. M. Muhr performed the synthesis and the characterization of $[(\text{dppe})\text{Ru}(\text{GaCp}^*)_3]$. J. Stephan performed SC-XRD measurements. All authors contributed to results discussion and procedure planning, R. A. Fischer providing overarching academic guidance. The manuscript was written by R. Bühler, M. Muhr, and C. Gemel and subsequently edited by all co-authors.

Reproduced with permission from the Royal Society of Chemistry.

R. Bühler[‡], M. Muhr[‡], J. Stephan, R. M. Wolf, M. Schütz, C. Gemel, R. A. Fischer, *Dalton Trans.* **2023**, 52, 10905-10910.

[‡] Equal contribution



Cite this: Dalton Trans., 2023, 52,
10905

Photochemically generated reactive sites at ruthenium/gallium complexes: catalysis vs. cluster growth†

Raphael Bühler, ID ‡ Maximilian Muhr, ID ‡ Johannes Stephan, ID Robert A. Wolf, Max Schütz, Christian Gemel and Roland A. Fischer ID *

Irradiation of $[\text{Ru}(\text{GaCp}^*)_3(\text{SiEt}_3)\text{H}_3]$ (**1**) at 350 nm induces reductive elimination of dihydrogen and triethylsilane and generates unsaturated Ru/Ga species. This photochemically induced cascading reductive elimination processes generate the reactive intermediate $[\text{Ru}(\text{GaCp}^*)_3]$, which can be trapped by diphosphine coordination to yield the stable complex $[(\text{dppe})\text{Ru}(\text{GaCp}^*)_3]$ (**4**). The photochemically generated RuGa_3 species is catalytically active in the hydrogenation of alkynes, which is further investigated by ^1H NMR and mass spectrometry. Formation of intermetallic Ru/Ga clusters is observed as a competing and for the catalytic activity of the species limiting side reaction.

Received 14th June 2023.
Accepted 7th July 2023
DOI: 10.1039/d3dt01847d
rsc.li/dalton

Introduction

The study of ligand-free (naked) metal clusters in the gas phase shows an extensive spectrum of unique species and structure-dependent reactivities towards small molecules as substrates.¹ Heterobimetallic compounds show fascinating and novel reactivities,² however, such gas phase cluster analogues are difficult to access.³ The corresponding wet chemical approach employing ligated clusters offers a complementary range of synthetic and analytical methods to study structure and bonding of metal clusters and cluster–substrate interactions.⁴ We have been interested in developing the coordination and cluster chemistry of ligated transition-metal (M) and main group-12/13 metal (M' = Zn, Al, Ga) bimetallic species of formula $[\text{M}_a\text{M}'_b\text{R}_c]$ (R = hydrocarbon ligand).⁵ Prime examples include $[\text{Mo}(\text{ZnCH}_3)_9(\text{ZnCp}^*)_3]$ ⁶ and $[\text{Cu}_{43}(\text{AlCp}^*)_{12}]$.⁷ Irrespective of the structural appeal, the protective ligand shell, which stabilizes compositions and structures in solution, intrinsically inhibits cluster–substrate interactions. The radical, open shell superatomic $\text{Cu}_4\text{Al}_{12}$ core of $[\text{Cu}_{43}(\text{AlCp}^*)_{12}]$, for instance, is surprisingly inert against small molecules due to the shielding by the twelve Cp* ligands.⁷ In contrast, the related sterically less crowded hydrido-cluster

$[\text{Cu}_6(\text{AlCp}^*)_6\text{H}_4]$ reacts with nitriles via insertion into the cluster metal hydride bonds.⁸ To provoke cluster–substrate interactions, we were thus led to investigate concepts of partial removal of the ligand sphere at $[\text{M}_a\text{M}'_b\text{R}_c]$ in order to generate reactive sites at the $\text{M}_a\text{M}'_b$ cores.⁹

Recently, we reported on the ruthenium–gallium trihydride complex $[\text{Ru}(\text{GaCp}^*)_3(\text{SiEt}_3)\text{H}_3]$ (**1**) in the context of C–H and Si–H bond activations.¹⁰ It can be conveniently prepared from $[\text{Ru}(\text{cod})(2\text{-methylallyl})_2]$ in the presence of GaCp^* in HSiEt_3 as the solvent under hydrogenolytic conditions. Complex **1** is thermally surprisingly stable, quite in contrast to the related Ni/Al complex $[\text{Ni}(\text{AlCp}^*)_3(\text{SiEt}_3)\text{H}]$: a reductive elimination of HSiEt_3 can be induced thermally and yields the 16 VE intermediate $[\text{Ni}(\text{AlCp}^*)_3]$ which is capable of aromatic C–H bond activation.¹¹ Photolysis of related phosphine-ligated ruthenium hydrides yields reductive elimination of hydrogen and transient reactive Ru species.¹² Thus, we studied the photolysis of $[\text{Ru}(\text{GaCp}^*)_3(\text{SiEt}_3)\text{H}_3]$ (**1**).

Results and discussion

Irradiation of **1** at 350 nm

Irradiating the Ru(IV) complex **1** in its local absorption maximum (Fig. S46†) for 30 minutes at 350 nm, leads to the formation of free triethyl silane and dihydrogen as indicated by *in situ* ^1H NMR spectroscopy (sealed tube). The reductive elimination process is not quantitative at these conditions, even at prolonged irradiation times. An equilibrium (photostationary state) of reductive elimination and oxidative addition of hydrogen at the Ru centre is established. Analysis *via* inert atmosphere liquid injection field desorption ionization mass

Chair of Inorganic and Metalorganic Chemistry, Department of Chemistry and Catalysis Research Center, TUM School of Natural Sciences, Technical University of Munich, Lichtenbergstraße 4, 85748 Garching, Germany.

E-mail: roland.fischer@tum.de

†Electronic supplementary information (ESI) available. CCDC 2218507 and 2218508. For ESI and crystallographic data in CIF or other electronic format see DOI: <https://doi.org/10.1039/d3dt01847d>

‡These authors contributed equally to this work.

spectrometry (LIFDI-MS)¹³ shows only negligible cluster growth after eight hours of irradiation (Fig. S29 and 30†). Possible products of reductive elimination include the two 16 VE (valence electron) Ru(ii) species $[\text{Ru}(\text{GaCp}^*)_3(\text{SiEt}_3)\text{H}]$ ($[\text{H}_2\text{HSi}]$), $[\text{Ru}(\text{GaCp}^*)_2\text{H}_2]$ ($[\text{H}_2\text{H}$) as well as the low coordinated, 14 VE Ru(0) fragment $[\text{Ru}(\text{GaCp}^*)_3]$ (3). *In situ* ^1H NMR spectroscopy of the reaction solution reveals the presence of two new hydride signals at -11.46 and -14.58 ppm (Fig. S3-6†). The equilibrium state can be overcome by irradiating 1 in the presence of excess H_2 . This leads to gradual degradation of 1 and the formation of a mixture of larger Ru/Ga cluster species. Free HSiEt_3 can be identified in quantitative amounts after complete conversion of 1 together with considerable amounts of Cp^*H (Fig. S21 and 22†). It can be postulated that photolysis under hydrogen rich conditions lead to the formation of a transient $[\text{Ru}(\text{GaCp}^*)_3\text{H}_2]$ species, in analogy to the $[\text{Ru}(\text{PR}_3)_3\text{H}_2]$,¹⁴ and the lower coordinated species resulting from Cp^*H elimination inducing cluster growth reactions. Analysis of the *in situ* LIFDI-MS data suggest that the major signal at higher mass patterns ($m/z > 1000$) can be attributed to species with the sum formulas $\text{Ru}_2\text{Ga}_4\text{Cp}^*\text{H}_5$, $\text{Ru}_3\text{Ga}_5\text{Cp}^*\text{H}_5$, $\text{Ru}_2\text{Ga}_8\text{Cp}^*\text{H}_3$ and $\text{Ru}_3\text{Ga}_9\text{Cp}^*\text{H}_3$ – all species bearing several hydride ligands (Fig. S43 and 44†). So far, however, our attempts of isolation and structural elucidation of any cluster species failed.

Synthesis of [(dppe)Ru(GaCp*)₃] (4)

The photolysis of **1** was then performed in the presence of phosphines aiming for stabilizing one of the reductive elimination products ($2_{\text{H}2}$, 2_{HSI} and **3**). The use of 1,2-bis(diphenylphosphino)ethane (dppe) under similar conditions (r.t., 24 h, 350 nm) allowed the isolation of $[(\text{dppe})\text{Ru}(\text{GaCp}^*)_3]$ (**4**) as the trapping product in the form of red-orange needles. The composition is supported by a peak at $m/z = 1114.1656$ (calc. 1114.1671) in the LIFDI mass spectrum (Fig. S29 and 30†). Complex **4** is formed by reductive eliminations of H_2 and HSiEt_3 from **1**, indicating that formation of a transient $\text{Ru}(0)$ species $[\text{Ru}(\text{GaCp}^*)_3]$ is possible under photolytic conditions. The compound **4** crystallizes in the space group $P2_1/n$ as a trigonal bipyramidal structure with one co-crystallized *n*-hexane molecule (Fig. 1). The Ru–Ga bond lengths (2.353–2.393 Å) are in the expected range,^{9,10,15} and the Ru–P bond lengths (2.239–2.257) compare well with $[(\text{Cp}^*\text{Ga})_3\text{Ru}(\text{PPh}_3)_2]^{15a}$ and $[(\text{dmpe})_2\text{Ru}(\text{L})]$ ($\text{L} = \text{CO}, \text{PMe}_3$; dmpe = 1,2-bis(dimethylphosphino)ethane),¹⁶ however, they are slightly shorter than in related Ru(0) compounds.¹⁷ The ^1H NMR in C_6D_{12} (Fig. S7–9†) matches the crystal structure: one singlet for the three Cp^* groups ($\delta = 1.65$ ppm, 45 H) of the GaCp^* ligands, due to coalescence, and a multiplet of the ethylene bridge ($\delta = 1.80$ ppm, 4 H) of the dppe ligand as well as the respective two multiplets of the phenyl groups ($\delta = 7.11$ ppm, 12 H; $\delta = 7.73$ ppm, 8 H). The co-crystallised *n*-hexane is also observed ($\delta = 0.89$ ppm, 6 H; $\delta = 1.29$ ppm, 8 H). Low temperature ^1H -NMR spectra recorded in *n*-hexane- d_{14} show a decoalescence of the Cp^* signals below -40 °C, resulting in two singlets ($\delta = 1.64$ ppm, 30 H and $\delta = 1.61$ ppm, 15 H) at -80 °C (Fig. S19†). This is in agreement with the asymmetry of the GaCp^* in **4**.

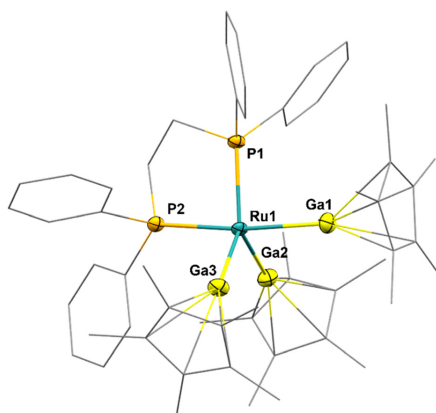


Fig. 1 Molecular structure of the trigonal bipyramidal Ru(0) complex $\left[\text{dppe}\text{Ru}(\text{GaCp}^*)_3\right]$ (4). Thermal ellipsoids are given at 50% probability level. C atoms in wireframes, H atoms and co-crystallized n-hexane unit omitted for clarity. Selected bond lengths (\AA) and angles ($^\circ$): Ru1–Ga1: 2.393; Ru1–Ga2: 2.353; Ru1–Ga3: 2.371; Ru1–P1: 2.239; Ru1–P2: 2.257; Ga–Cp^{*} centroid: 2.049–2.060; Ga1–Ru–P2: 173.16; Ga2–Ru–P1: 117.82; P1–Ru–Ga3: 133.51; Ga2–Ru–Ga3: 108.65

suggesting a trigonal bipyramidal coordination of the ruthenium centre, closely related to the single crystal structure. The expected ^{13}C peaks are observed as well and match the 2D NMR data (Fig. S10–17†). The ^{31}P spectrum shows one singlet at 94.6 ppm along with a very small signal of free dippe at –12.9 ppm (Fig. S18†). Low temperature ^{31}P -NMR spectra recorded in *n*-hexane-d₁₄ do not show a decoalescence, even at –80 °C (Fig. S20†). Neither the ^1H , nor the IR spectrum (Fig. S47†) of **4** shows any peaks that can be attributed to ruthenium hydrides. Compound **4** is not stable in solution over prolonged time, however, no decomposition products could be identified, so far. It can be viewed as the trapping product of the transient, reactive species $[\text{Ru}(\text{GaCp}^*)_3]$. Analogues of **4** were observed *via* LIFDI-MS when using other phosphines such as 1,2-bis(diphenylphosphino)benzene and triethyl phosphine or trimethyl phosphine, respectively (Fig. S33–38†). The trapping products were observed *via* LIFDI mass spectrometry but could not be isolated as pure compounds in preparative yields. Nevertheless, a single crystal of $[(\text{PEt}_3)_2\text{Ru}(\text{GaCp}^*)_3]$, was obtained (Fig. S2‡), though no further analytics could be performed due to lack of quantity.

Catalytic conversion of 3-hexyne under photolytic conditions

The unsaturated nature of the photolytically generated reactive intermediates, supposedly transient $[\text{Ru}(\text{GaCp}^*)_3]$ and $[\text{Ru}(\text{GaCp}^*)_3\text{H}_2]$, suggests the activity of **1** as hydrogenation catalyst for olefins under photolytic conditions. Indeed, photolysis of a solution of **1** in C_6D_{12} in the presence of 3-hexyne (20.0 eq.) under dihydrogen pressure (2 bar) at r.t. leads to the for-

mation of *n*-hexane as the main product together with *cis*- and *trans*-3-hexene in minor amounts (Fig. 2a; Fig. S23 and 24[†]). Stoichiometric amounts (based on 1, 5%) of hydrosilylation products are also detected (Fig. S23[†]). A steep onset of the catalytic conversion of 3-hexyne is observed (1 h, 40%). The conversion rate, however, declines notably: after 6 h only a total of 59% is hydrogenated and only 70% after 18 h. A full conversation is never reached. This observation can be reasoned by competing catalysis vs. cluster growth at lower alkyne concentrations. LIFDI mass spectra (Fig. S45 and 46[†]) after the catalysis confirm the formation of numerous larger Ru/Ga oligohydride clusters. We attribute the gradual cluster growth to a stabilizing effect of alkyne and alkene ligands over the course of the catalysis experiment preventing the active species from fast agglomeration and deactivation and rather undergoing slower and coordination modulated cluster growth reactions.¹⁸ A plausible intermediate, is observed by LIFDI-MS peak at *m/z* = 882.1997. It can be assigned to the 18 VE species [Ru(GaCp*)₃(hexyne)(hexene)] (*m/z* = 882.2044, calc. 882.2039; Fig. 2b and Fig. S39–42[†]). Performing a catalytic 3-hexyne hydrosilylation at analogous conditions to hydrogenation (r.t., 350 nm, 20. eq. 3-hexyne, 100 eq. HSiEt₃) failed, however, as only stoichiometric quantities of hydrosilylation products were observed (Fig. S25 and 26[†]).

Published on 20 July 2023. Downloaded by Technical University of Munich on 7/9/2024 3:48:47 PM.

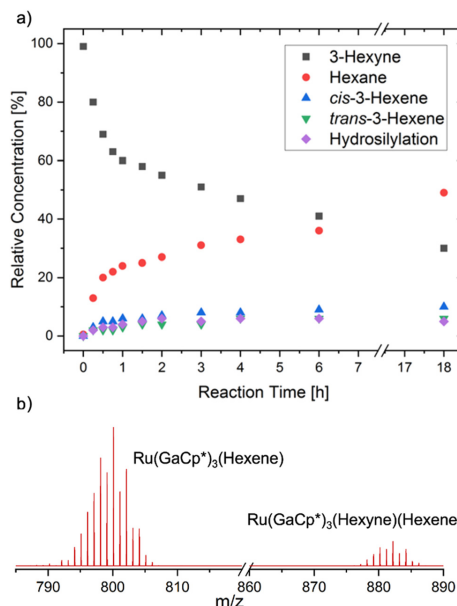


Fig. 2 (a) Relative concentration of the catalysis of 3-hexyne (5 mol% cat.) and the reaction products *n*-hexane, *cis*- and *trans*-hexene and hydrosilylation products. (b) excerpt of *in situ* LIFDI mass spectrum during catalysis, showing peaks attributed to catalytic intermediates.

It is interesting to note, that continuous irradiation is required for the catalysis to proceed. 1 is still observed after 6 hours of irradiation under catalytic conditions (Fig. S24[†]), pointing to a slow conversion of 1 to the catalytically active species. A continuous support of active catalyst is required due to competing cluster formation, which leads to a fast and irreversible deactivation of the catalyst. Thus a solution containing Ru/Ga clusters formed by irradiation of 1 (in the absence of alkynes) is catalytically inactive (Fig S22 and S44[†]).

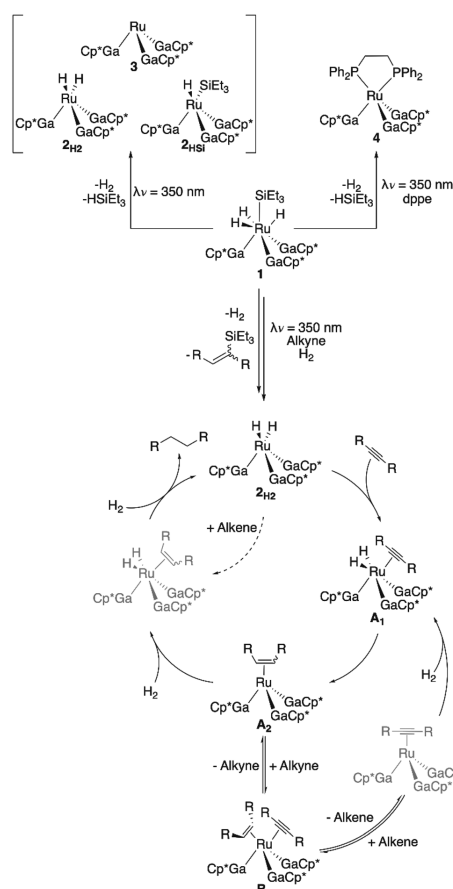


Fig. 3 Overview of the reactions possible from 1 with the presumed photochemically generated species 2_{H2}, 2_{HSi} and 3 as well as the reaction to 4. Additionally, a proposed catalytic cycle for the hydrogenation of 3-hexyne with 1 as catalyst under photochemical conditions is given. Intermediates 2_{H2}, A₁, A₂ and B (depicted in black) are supported by experimental evidence (¹H NMR, LIFDI-MS). Intermediates depicted in grey are logical necessary intermediates for which no experimental evidence could be obtained.

[View Article Online](#)

Paper

Dalton Transactions

Taking together all presented analytical data and spectroscopic observations, we propose the mechanistic reaction scheme and catalytic cycle of Fig. 3. Under photolytic conditions, the activation of the pre-catalyst **1** is achieved through the alkyne hydrosilylation and subsequent dihydrogen activation forming the 16 VE species $[\text{Ru}(\text{GaCp}^*)_3\text{H}_2]$ ($\mathbf{2}_{\text{H}_2}$). This key intermediate then coordinates and activates 3-hexyne forming the 18 VE species $[\text{Ru}(\text{GaCp}^*)_3(\text{hexyne})\text{H}_2]$ (\mathbf{A}_1) and subsequently, through hydride insertion the 16 VE species $[\text{Ru}(\text{GaCp}^*)_3(\text{hexene})]$ (\mathbf{A}_2) is formed. An indication of the presence of the two species is given by LIFDI-MS ($m/z = 800.1251$; calc. 800.1257 ; Fig. S39–42†), even though they cannot be distinguished from one another by MS. Through activation of a further equivalent of H_2 and subsequent insertion, n -hexane is formed and $\mathbf{2}_{\text{H}_2}$ is regenerated. However, a competing cycle occurs where \mathbf{A}_2 is coordinated by a further 3-hexyne yielding the 18 VE species **B**, which is also observed in LIFDI-MS. The observation of free 3-hexene by ^1H NMR can be explained through dissociation of the alkene from **B**. The competing nature of both cycles is supported by *in situ* LIFDI-MS monitoring the hydrogenation catalysis experiment in the presence of 100 eq. 3-hexyne where only **B** is observed (Fig. S39–42†). This results in a much slower alkyne conversion. As such, the competing reactions, H_2 oxidative addition or alkyne coordination both possible at \mathbf{A}_2 are the limiting factor of the catalytic hydrogenation of the alkyne.

Conclusion

In summary, we have presented a novel approach towards the controlled generation of reactive free coordination sites at small bimetallic Ru/Ga cluster species utilizing photochemistry. In this example, we could specifically induce the reductive elimination of dihydrogen and/or triethyl silane from a defined Ru/Ga precursor compound under mild conditions. The silyl and hydride groups can thus be interpreted as selectively removable protecting groups for the active transition metal centre, solely stabilized by group-13 metal-ligands. The generated, reactive species, *i.e.* $[\text{Ru}(\text{GaCp}^*)_3]$ (**3**), could be trapped by phosphines, *i.e.* in the form of **4**. The reactive RuGa_3 species themselves are active in catalytic alkyne and alkene hydrogenation and mass spectrometric investigations provide evidence for key intermediates of a possible catalytic cycle. The deprotected, low coordinated RuGa_3 species act as seeds for cluster growth under certain conditions. Building on this work, we aim to achieve control over the competing catalysis and cluster growth reactions towards libraries of defined bimetallic clusters. Doing so will help us identify either catalytically active clusters or clusters as deactivation products of the catalytically active species. We are therefore currently studying the role of different substrates and additives in similar reactions based on $[\text{Ru}(\text{GaCp}^*)_3(\text{SiEt}_3)\text{H}_3]$ (**1**) and aiming for transfer to other transition-metal group-13 metal complexes and clusters.

Experimental

General procedures

All manipulations were carried out using standard Schlenk techniques under inert atmospheres. Solvents were dried using a MBraun Solvent Purification System. The final H_2O content of all solvents was measured *via* Karl Fischer titration and was below 5 ppm. Starting material $[\text{Ru}(\text{GaCp}^*)_3(\text{SiEt}_3)\text{H}_3]$ ¹⁰ was synthesized according to literature procedures. Chemicals were purchased from Sigma Aldrich and used without further purification. Hydrogen 5.0 was purchased from Westfalen.

NMR spectra were recorded on a Bruker AVIII 400 US spectrometer (^1H , 400 MHz; ^{13}C , 101 MHz; ^{31}P , 162 MHz) in C_6D_{12} . Low temperature NMR experiments were recorded on a Bruker Avance 400 spectrometer (^1H , 400 MHz; ^{31}P , 162 MHz) in n -hexane-d₁₄. Chemical shifts (δ) are described in ppm relative to tetramethylsilane (TMS) and referenced to the solvent resonances as internal standards. The signal multiplicity is given as following: s = singlet, d = doublet, t = triplet or q = quartet.

Elemental analysis was conducted at the microanalytical laboratory at the Technical University Munich.

LIFDI-MS. Liquid Injection Field Desorption Ionization Mass Spectrometry (LIFDI-MS) was measured directly from an inert atmosphere glovebox with a Thermo Fisher Scientific Exactive Plus Orbitrap (mass accuracy 3 ppm; external calibration) equipped with an ion source from Linden CMS.¹³

Single-crystal X-ray diffractometry

Data were collected on a single crystal X-ray diffractometer equipped with a CMOS detector (Bruker APEX IV, κ-CMOS), a TXS rotating anode with MoK_α radiation ($\lambda = 0.71073 \text{ \AA}$) and a Helios optic using the APEX3 software package.¹⁹ Measurements were performed on single crystals coated with perfluorinated ether. The crystals were fixed on top of a kapton micro sampler and frozen under a stream of cold nitrogen. A matrix scan was used to determine the initial lattice parameters. Reflections were corrected for Lorentz and polarisation effects, scan speed, and background using SAINT.²⁰ Absorption correction, including odd and even ordered spherical harmonics was performed using SADABS.²⁰ Space group assignments were based upon systematic absences, E statistics, and successful refinement of the structures. The structures were solved using SHELXT with the aid of successive difference Fourier maps, and were refined against all data using SHELXL-2014/2017 in conjunction with SHELXLE.²¹ $[(\text{Et}_3\text{P})_2\text{Ru}(\text{GaCp}^*)_3]$ was twinned, the integration was performed for both domains and the structure was refined against $hkl f\bar{s}$ data. Hydrogen atoms were calculated in ideal positions as follows: methyl hydrogen atoms were refined as part of rigid rotating groups, with a C–H distance of 0.98 \AA and $U_{\text{iso}(\text{H})} = 1.5 \times U_{\text{eq}(\text{C})}$. Other H atoms were placed in calculated positions and refined using a riding model, with methylene and aromatic C–H distances of 0.99 \AA and 0.95 \AA , respectively, other C–H distances of 1.00 \AA , all with $U_{\text{iso}(\text{H})} = 1.2 \times U_{\text{eq}(\text{C})}$. Non-hydrogen atoms were refined with anisotropic displacement parameters. Full-

[View Article Online](#)

Paper

matrix least-squares refinements were carried out by minimizing $\sum w(F_o^2 - F_c^2)^2$ with the SHELXL weighting scheme.^{21b} Neutral atom scattering factors for all atoms and anomalous dispersion corrections for the non-hydrogen atoms were taken from *International Tables for Crystallography*.²² A split layer refinement was used for disordered groups and additional restraints on distances, angles and anisotropic displacement parameters were employed to ensure convergence within chemically reasonable limits, if necessary. Images of the crystal structures were generated with PLATON (SI) and Mercury (main article).²³ CCDC 2218507 (4) and CCDC 2218508† $[(Et_3P)_2Ru(GaCp^*)_3]$.

Synthesis of $[(dppe)Ru(GaCp^*)_3]$ (4)

A cyclohexane (7 mL) solution of 75.0 mg **1** (1.0 eq.; 89.9 μmol) and 40.0 mg dppe (1.1 eq.; 100 μmol) are irradiated in a photoreactor (350 nm) for 24 h. The reddish solution is filtered through a syringe filter and the solvent is removed *in vacuo*. The residue is dissolved in 3 mL *n*-hexane. The solution is cannula filtered and concentrated to about 1.5 mL. After storing the solution over night at -30°C , 26.0 mg (23.0 μmol ; 26%) of **4** is obtained in the form of orange-red needles. ¹H NMR (C_6D_{12} , 400 MHz): δ [ppm] = 7.33 (m, 8 H, Ph-P), 7.11 (m, 12 H, Ph-P), 1.80 (m, 4 H, $H_2C-\text{CH}_2$), 1.65 (s, 45 H, GaCp *), 1.29 (m, 8 H, CH_2 in *n*-hexane), 0.89 (t, 6 H, CH_3 in *n*-hexane). ¹³C NMR (C_6D_{12} , 101 MHz): δ [ppm] = 128.4 (s, phenyl), 127.4 (m, phenyl), 114.5 (s, Cp * ring), 32.5 (s, *n*-hexane), 23.5 (s, *n*-hexane), 14.4 (s, *n*-hexane), 10.7 (s, Cp * methyl). ³¹P NMR (C_6D_{12} , 101 MHz): δ [ppm] = 94.6 (s, dppe). LIFDI-MS [M] $^+$: m/z = 1114.1656 (calc., 1114.1671). Elemental analysis calc. for $RuGa_3P_2C_{56}H_{69}$: C, 60.36; H, 6.24; Ga, 18.77; Ru, 9.07; P, 5.56. Found: C, 59.43; H, 6.37.

General procedure for catalytic reactions

5.00 mg of **1** (1.0 eq., 5.99 μmol) were dissolved in 0.4 mL cyclohexane-*d*₁₂ in a J-Young NMR tube and 20–100 eq. 3-hexyne were added. The reaction solution was degassed by freeze–pump–thaw and was pressurized with 2.0 bar at 25°C . The NMR tube was irradiated for 24 h in a photoreactor at 350 nm. Conversion and selectivity was determined by ¹H NMR spectroscopy.

General procedure for photochemistry

Photochemical reactions ($\lambda = 350$ nm) were carried out in Duran phototubes (1 cm diameter, 10 mL) or J-Young NMR tube under argon atmosphere in a photoreactor with a cylindrical array of 16 light tubes of the type Luzchem LZC-UVA with 8 W nominal power. Supplier states a spectral range from 300 to 400 nm.

Conflicts of interest

There are no conflicts to declare.

Acknowledgements

The authors are grateful to Daniel P. Schwinger (Research group of Prof. Thorsten Bach, Technical University of Munich) for the experimental introduction to the photochemical setup. In addition, we would like to thank Thomas Pickl for initial refinement of the crystallographic data of **4**. This work was funded by the German Research Foundation (DFG) within a Reinhard Koselleck Project (FI 502/44-1). Support by the TUM Graduate School is acknowledged.

References

- (a) Y. Ren, Y. Yang, Y.-X. Zhao and S.-G. He, *JACS Au*, 2022, **2**, 197–203; (b) J. F. Eckhard, T. Masubuchi, M. Tschurl, R. N. Barnett, U. Landman and U. Heiz, *J. Phys. Chem. A*, 2021, **125**, 5289–5302; (c) E. C. Tyo and S. Vajda, *Nat. Nanotechnol.*, 2015, **10**, 577–588.
- (a) J. Takaya, *Chem. Sci.*, 2021, **12**, 1964–1981; (b) F. Studt, F. Abild-Pedersen, T. Bligaard, R. Z. Sørensen, C. H. Christensen and J. K. Nørskov, *Science*, 2008, **320**, 1320–1322.
- (a) K. Koszinowski, D. Schröder and H. Schwarz, *J. Am. Chem. Soc.*, 2003, **125**, 3676–3677; (b) T. Momin and A. Bhowmick, *J. Alloys Compd.*, 2013, **559**, 24–33.
- (a) M. Schütz, C. Gemel, W. Klein, R. A. Fischer and T. F. Fässler, *Chem. Soc. Rev.*, 2021, **50**, 8496–8510; (b) K. Mayer, J. Weßing, T. F. Fässler and R. A. Fischer, *Angew. Chem., Int. Ed.*, 2018, **57**, 14372–14393; (c) B. E. Petel, W. W. Brennassel and E. M. Matson, *J. Am. Chem. Soc.*, 2018, **140**, 8424–8428.
- (a) S. Gonzalez-Gallardo, T. Bollermann, R. A. Fischer and R. Murugavel, *Chem. Rev.*, 2012, **112**, 3136–3170; (b) T. Steinke, C. Gemel, M. Winter and R. A. Fischer, *Chem. – Eur. J.*, 2005, **11**, 1636–1646; (c) M. Schütz, C. Gemel, M. Muhr, C. Jandl, S. Kahlal, J.-Y. Saillard and R. A. Fischer, *Chem. Sci.*, 2021, **12**, 6588–6599; (d) M. Muhr, J. Hornung, J. Weßing, C. Jandl, C. Gemel and R. A. Fischer, *Inorg. Chem.*, 2020, **59**, 5086–5092.
- T. Cadenbach, T. Bollermann, C. Gemel, I. Fernandez, M. von Hopffgarten, G. Frenking and R. A. Fischer, *Angew. Chem., Int. Ed.*, 2008, **47**, 9150–9154.
- J. Weßing, C. Ganeshamoorthy, S. Kahlal, R. Marchal, C. Gemel, O. Cador, A. C. H. Da Silva, J. L. F. Da Silva, J.-Y. Saillard and R. A. Fischer, *Angew. Chem., Int. Ed.*, 2018, **57**, 14630–14634.
- C. Ganeshamoorthy, J. Wessing, C. Kroll, R. W. Seidel, C. Gemel and R. A. Fischer, *Angew. Chem., Int. Ed.*, 2014, **53**, 7943–7947.
- (a) T. Cadenbach, C. Gemel, R. Schmid, M. Halbherr, K. Yusenko, M. Cokoja and R. A. Fischer, *Angew. Chem., Int. Ed.*, 2009, **48**, 3872–3876; (b) B. Buchin, C. Gemel, T. Cadenbach, I. Fernández, G. Frenking and R. A. Fischer, *Angew. Chem., Int. Ed.*, 2006, **45**, 5207–5210; (c) M. Halbherr, T. Bollermann, C. Gemel and R. A. Fischer,

[View Article Online](#)

Dalton Transactions

Paper

- Angew. Chem., Int. Ed.*, 2010, **49**, 1878–1881; (d) J. Hornung, J. Weßing, M. Molon, K. Dilchert, C. Gemel and R. A. Fischer, *J. Organomet. Chem.*, 2018, **860**, 78–84; (e) J. Hornung, J. Weßing, P. Jerabek, C. Gemel, A. Pöthig, G. Frenking and R. A. Fischer, *Inorg. Chem.*, 2018, **57**, 12657–12664; (f) P. Heiß, J. Hornung, X. Zhou, C. Jandl, A. Pöthig, C. Gemel and R. A. Fischer, *Inorg. Chem.*, 2020, **59**, 514–522.
- 10 M. Muhr, R. Bühler, H. Liang, J. Gilch, C. Jandl, S. Kahlai, J.-Y. Saillard, C. Gemel and R. A. Fischer, *Chem. – Eur. J.*, 2022, **28**, e202200887.
- 11 T. Steinke, C. Gemel, M. Cokoja, M. Winter and R. A. Fischer, *Angew. Chem., Int. Ed.*, 2004, **43**, 2299–2302.
- 12 (a) R. N. Perutz and B. Proacci, *Chem. Rev.*, 2016, **116**, 8506–8544; (b) P. L. Callaghan, R. Fernández-Pacheco, N. Jasim, S. Lachaize, T. B. Marder, R. N. Perutz, E. Rivalta and S. Sabo-Etienne, *Chem. Commun.*, 2004, 242–243; (c) C. Hall, W. D. Jones, R. J. Mawby, R. Osman, R. N. Perutz and M. K. Whittlesey, *J. Am. Chem. Soc.*, 1992, **114**, 7425–7435; (d) P. Bergamini, S. Sostero and O. Traverso, *J. Organomet. Chem.*, 1986, **299**, C11–C14.
- 13 M. Muhr, P. Heiß, M. Schütz, R. Bühler, C. Gemel, M. H. Linden, H. B. Linden and R. A. Fischer, *Dalton Trans.*, 2021, **50**, 9031–9036.
- 14 B. Chaudret and R. Poilblanc, *Organometallics*, 1985, **4**, 1722–1726.
- 15 (a) T. Cadenbach, C. Gemel, T. Bollermann and R. A. Fischer, *Inorg. Chem.*, 2009, **48**, 5021–5026; (b) T. Cadenbach, T. Bollermann, C. Gemel and R. A. Fischer, *Dalton Trans.*, 2009, 322–329; (c) T. Cadenbach, C. Gemel, T. Bollermann, I. Fernandez, G. Frenking and R. A. Fischer, *Chem. – Eur. J.*, 2008, **14**, 10789–10796.
- 16 W. D. Jones and M. Libertini, *Inorg. Chem.*, 1986, **25**, 1794–1800.
- 17 (a) D. J. Tindall, M. Menche, M. Schelwies, R. A. Paciello, A. Schäfer, P. Comba, F. Rominger, A. S. K. Hashmi and T. Schaub, *Inorg. Chem.*, 2020, **59**, 5099–5115; (b) H. Braunschweig, C. Brunecker, R. D. Dewhurst, C. Schneider and B. Wennemann, *Chem. – Eur. J.*, 2015, **21**, 19195–19201; (c) M. Grellier, L. Vendier and S. Sabo-Etienne, *Angew. Chem., Int. Ed.*, 2007, **46**, 2613–2615; (d) S. Sentets, M. D. C. Rodriguez Martinez, L. Vendier, B. Donnadieu, V. Huc, N. Lugan and G. Lavigne, *J. Am. Chem. Soc.*, 2005, **127**, 14554–14555.
- 18 (a) P. Heiß, J. Hornung, C. Gemel and R. A. Fischer, *Chem. Commun.*, 2022, **58**, 4332–4335; (b) J. Hornung, M. Muhr, C. Gemel and R. A. Fischer, *Dalton Trans.*, 2019, **48**, 11743–11748.
- 19 APEX suite of crystallographic software, APEX 3, Version 2015-5.2, Bruker AXS Inc., Madison, Wisconsin, USA, 2015.
- 20 SAINT, Version 8.34A and SADABS, Version 2014/5, Bruker AXS Inc., Madison, Wisconsin, USA, 2014.
- 21 (a) C. B. Hubschle, G. M. Sheldrick and B. Dittrich, *J. Appl. Crystallogr.*, 2011, **44**, 1281–1284; (b) G. Sheldrick, *Acta Crystallogr., Sect. A: Found. Adv.*, 2015, **71**, 3–8.
- 22 International Tables for Crystallography, ed. A. J. Wilson, Kluwer Academic Publishers, Dordrecht, The Netherlands, 1992, vol. C, Tables 6.1.1.4 (pp. pp. 500–502), 4.2.6.8 (pp. 219–222), and 4.2.4.2 (pp. 193–199).
- 23 (a) C. F. Macrae, I. J. Bruno, J. A. Chisholm, P. R. Edgington, P. McCabe, E. Pidcock, L. Rodriguez-Monge, R. Taylor, J. van de Streek and P. A. Wood, *J. Appl. Crystallogr.*, 2008, **41**, 466–470; (b) A. Spek, *Acta Crystallogr., Sect. D: Biol. Crystallogr.*, 2009, **65**, 148–155.

4 Accessing Chemical Diversity in Solution

4.1 Study IV: A living library concept to capture the dynamics and reactivity of mixed-metal clusters for catalysis

The creation of "living cluster libraries" can be achieved by making use of unselective organometallic reactions, mimicking *in situ* the diversity found on the surface of a solid-state catalyst. Herein, we present a novel concept and a methodology for generating and efficiently exploring living libraries of ligated *heterometallic* clusters. We selected the Cu/Zn system for the growing interest in experimental and theoretical studies of atom-precise Cu_xZn_y clusters in relation to industrial methanol synthesis using Cu/ZnO/Al₂O₃ catalysts.

The libraries are characterized *via* LIFDI-MS using double labeling and varied collision energy experiments. Their evolutions are monitored by mass spectrometry so that chemical information is gained without separating the clusters. Structural information is obtained by a framework combining density functional theory (DFT) with data mining analysis techniques to explore the full compositional configuration space. Through this methodology, it is possible to efficiently characterize the clusters' structure reactivity relationships, highlighted by the detection of the formate-containing species [Cu₁₁Zn₆]Cp*₈(CO₂)₂(HCO₂). In addition, a novel cluster, [Cu₄Zn₁₀]Cp*₈, acting as a pre-catalyst for the catalytic semihydrogenation of alkynes, could be isolated by carefully tweaking the library conditions.

R. Bühler performed labeling and fragmentation analysis of libraries **{2}**, **{3}**, and **{4}**, characterized the reaction with CO₂, H₂, and 3-hexyne/H₂, and performed the synthesis and characterization of [Cu₄Zn₁₀]Cp*₈. M. Schütz performed labeling and fragmentation analysis of library **{1}** and characterized the reaction with CO₂ and H₂. K. F. Andriani wrote the algorithm and performed the calculations. S. Kahlal and J.-Y. Saillard performed the bonding analysis of [Cu₄Zn₁₀]Cp*₈. J. L. F. Da Silva and R. A. Fischer provided overarching academic guidance. The manuscript was written by R. Bühler, K. F. Andriani, C. Gemel, J. L. F. Da Silva, and R. A. Fischer.

R. Bühler[‡], M. Schütz[‡], K. F. Andriani, Marcos G. Quiles, J.-P. A. de Mendonça, V. K. Ocampo-Restrepo, Johannes Stephan, Sophia Ling, Samia Kahlal, Jean-Yves Saillard, C. Gemel, J. L. F. Da Silva, R. A. Fischer, *Nat. Chem.*, accepted.

[‡] Equal contribution

A living library concept to capture the dynamics and reactivity of mixed-metal clusters for catalysis

Raphael Bühler,⁺¹ Max Schütz,⁺¹ Karla F. Andriani,^{2,3} Marcos G. Quiles,⁴ João Paulo A. de Mendonça,² Vivianne K. Ocampo-Restrepo,² Johannes Stephan,¹ Sophia Ling,¹ Samia Kahlal,⁵ Jean-Yves Saillard,⁵ Christian Gemel,¹ Juarez L. F. Da Silva,^{2,*} Roland A. Fischer^{1*}

1) Technical University of Munich, School of Natural Sciences Department of Chemistry, Chair of Inorganic and Metal-Organic Chemistry, and Catalysis Research Center, Ernst-Otto-Fischer Straße 1, 85748 Garching, Germany.

2) São Carlos Institute of Chemistry, University of São Paulo, P.O. Box 780, 13560-970 São Carlos, São Paulo, Brazil.

3) Department of Exact Sciences, State University of Santa Cruz, P.O. Box 45662-900, Ilhéus, BA, Brazil.

4) Department of Science and Technology, Federal University of São Paulo, P.O. Box 12247-014, São José dos Campos, SP, Brazil.

5) Univ Rennes CNRS, ISCR-UMR 6226, F-35000, Rennes, France

[+] These authors contributed equally to this work

Abstract

The exploration of ligated metal clusters' chemical space is challenging, partly due to a less targeted access to reactive clusters. Now, dynamic mixtures of clusters, defined as living libraries, are obtained through organometallic precursor chemistry. The libraries are populated with interrelated clusters, including transient and highly reactive ones, as well as more accessible but less reactive species. Their evolutions upon perturbation with substrate molecules are monitored and chemical information is gained without separation of the clusters. We prepared a library of all-hydrocarbon ligated Cu/Zn clusters and developed a bias-free computational framework suited to analyze the full compositional space that yields a reliable structural model for each cluster. This methodology enables efficient searches for structure-reactivity relationships relevant for catalysis with mixed metal clusters: When treating the library with CO₂ or 3-hexyne and H₂, we discovered [Cu₁₁Zn₆](Cp*)₈(CO₂)₂(HCO₂) bearing a formate species related to CO₂ reduction, and [Cu₉Zn₇](Cp*)₆(Hex)₃(H)₃ bearing C₆-species related to alkyne semi-hydrogenation.

Introduction

Access to sub-nanometer metal clusters is largely based on metal evaporation, ionization and atom-precise size-selection by electromagnetic mass filters. This gas-phase synthesis and spectrometry, together with size-conservative deposition to substrates, enable microscopic characterization and reactivity studies of individual, *non-ligated* clusters.¹⁻⁵ Atom-by-atom assembly of clusters in the liquid phase has been demonstrated as well. Dendrimer nano-reactors were designed to coordinatively bind and cage a predefined number of metal ions, which then aggregate to the targeted cluster by a chemical reduction step. Removing the dendrimer yields samples of substrate-supported atom-precise clusters similar to the gas-phase approach.⁶⁻⁸ Neither concept, selection from polydisperse mixtures nor programmed assembly, can be translated to the synthesis of *ligated* metal clusters. Here, the obstacle of selective synthesis design is rooted in the specific chemistries of the molecular metal precursors and reagents that must be chosen. It relates to entangled phenomena of nucleation and growth modulated by ligation, the intricate kinetics of which are not known with sufficient precision. Nevertheless, the outcome of the synthesis may be rationalized *a posteriori* in terms of structure and bonding analysis of the obtained clusters.⁹⁻¹³ Nevertheless, much information is lost as the aforementioned approach is limited to just those few clusters that were stable enough and could be isolated from the reaction solution, eventually in very low yields with uncertain reproducibility.¹³⁻¹⁵ These challenges were discussed within a wider context in our recent review article entitled “*Organometallic Superatom Complexes*”, from which this introduction is derived.¹⁶

Now, we report a novel concept and a methodology for generating and efficiently exploring ligated mixed metal (*heterometallic*) clusters in the form of “living libraries”. Information is gained by directly dealing with chemical complexity without the separation of clusters. A living library is defined as a dynamic mixture of clusters, including growth species and additives such as ligands and reactants. Portfolios of cluster libraries can be generated for a given metal combination by settings of initial components and library evolution conditions. The libraries are populated with interrelated clusters, including transient and highly reactive ones, as well as more accessible but less reactive ones. Its distribution of clusters is sensitive to perturbation, e.g., the interaction with reactants to be trapped or converted at the cluster surface that may also influence cluster structure rearrangement, growth, or degradation reactions.

We demonstrate our methodology by employing non-aqueous *organometallic* precursor chemistry under inert gas, tailored for living libraries of *all-hydrocarbon ligated* Cu/Zn clusters of the formula $[Cu_aZn_b](R)_k$ (metal atomicity $n = a+b$, coordination k with ligands R = H, 2,4,6-

$C_6H_2(CH_3)_3 = \text{Mes}$ or $C_5(CH_3)_5 = \text{Cp}^*$). Organometallic chemistry offers a unique toolbox for generating living libraries of clusters such as highly reactive metal precursors, prone to releasing metal atoms by reversible and irreversible fundamental reactions, including ligand exchange and transfer^{17, 18}, protolysis¹⁹⁻²¹, transmetallation^{22, 23}, oxidative addition/reductive elimination²⁴⁻²⁶, hydrogenolysis^{27, 28}, etc.

We selected the Cu/Zn system for two reasons: First, we have previously explored Cu/Zn clusters.²⁹⁻³² Our “embryonic brass” chemistry proved very suitable for library generation due to the variety of species formed and its high sensitivity to the reaction parameters. Second, there is interest in experimental and theoretical studies of atom-precise, sub-nanometer Cu_n clusters³³⁻³⁶, including hetero metal doped species³⁷ in relation to the industrial methanol synthesis using Cu/ZnO/Al₂O₃ catalysts³⁸⁻⁴¹. Liu et al. have evaluated the catalytic properties of the superatomic clusters Cu_aZn_b ($a+b = 14$) by a density functional theory study.⁴² Höltzl et al. explored the size- and charge-dependent CO₂ and H₂ activation on small clusters $[\text{Cu}_n\text{Zn}]^{0/+}$ ($n = 3 - 6$).⁴³ Similarly, Li et al. reported on the electronic structure of a Cu-Zn dual atom catalyst site⁴⁴, being highly selective in Cu-based alkyne semi-hydrogenation.^{45, 46} Our studies on a wide range of ligand-stabilized Cu/Zn clusters will thus broaden the understanding of Cu/Zn intermetallics at the molecular scale (Figure 1).

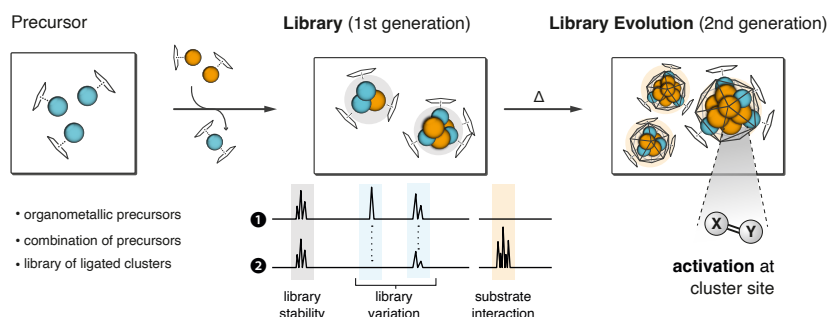


Figure 1: The living library concept. Mixed metal cluster libraries are generated by combining highly reactive organometallic precursors at a defined set of conditions. Library perturbation is initiated by changing the conditions, e.g., by the addition of substrates, and the evolution over time is monitored via mass spectrometry (Cu = orange, Zn = blue, carbon = grey, oxygen = red).

Results and Discussion

Living Library Generation

On combining Cu₅Mes₅ with decamethyldizincocene, Zn₂Cp^{*2}, as precursors, Zn(I) is oxidized to yield Zn(II) species while Cu(I) is reduced to Cu(0). Cp^{*} and Mes ligated Cu/Zn clusters are formed by choosing initial excess or specific quantities of either Cu₅Mes₅ or Zn₂Cp^{*2} added after a particular incubation time (Figure 1). For example, the library {[Cu_aZn_b](R)_k}, denoted as {1}, is reproducibly prepared from Cu₅Mes₅ (12.0 μmol) with 3.75 eq. of Zn₂Cp^{*2} (45.6 μmol) in dry toluene (0.50 mL) at 25 °C under argon as a dark-red solution within 120 min. Characterization of {1} by *in situ* liquid-injection field desorption ionization mass spectrometry (LIFDI-MS) with a setup coupled to a glovebox⁴⁷ gives more than 100 peak patterns up to the detection limit of our instrument (*m/z* = 6000 a.m.u.), each pattern representing a unique species which is either present in solution or is formed upon ionization and fragmentation. We were able to selectively synthesize, isolate, and characterize a few clusters of {1}, *e.g.*, [CuZn₂](Cp^{*})₃ (**A**), [Cu₃Zn₄](Cp^{*})₅ (**B**) and [Cu₁₀Zn₂](Cp^{*})₂(Mes)₆ (**C**).^{29, 31, 32} The vast majority of clusters present, however, exhibit previously unknown structures with a diversity of *n* and *k*. This highlights both a rich chemical space to be explored and the challenge of isolation and characterization of individual clusters facing their very labile, air-, moisture-, and temperature-sensitive nature. A methodology needs to be developed to efficiently exploit this chemical space towards the identification of those clusters, which hold promise for exciting properties and would justify the effort for in-depth investigations, including iterative size focusing, separation, and isolation of specific clusters.

Mass Spectrometric Library Characterization

Each cluster library is characterized by its LIFDI mass spectrum, which allows for the identification of all ionizable molecular species in the reaction mixture at a given parameter set of library generation and evolution conditions. Two problems must be addressed. First, an exact and unique sum formula [Cu_aZn_b](R)_k (R = Cp^{*c}, Mes_d, H_h; *c* + *d* + *h* = *k*) has to be assigned to each pattern in the spectrum. This problem is solved by introducing a double labeling strategy with isotopically enriched ⁶⁸Zn₂Cp^{*2} ($\Delta m/z$ = 2.62) and Cp^{*Et} ($\Delta m/z$ = 14) for library preparation. This labeling strategy can certainly be done with ²H, ¹³C, and with other markers for R or reactants with other isotopically enriched metals M, thus matching the organometallic precursor chemistry employed with the available MS instrument resolution. Second, a differentiation between molecular and fragment ions must be established to define a unique set of clusters that characterizes the library. This problem is solved by introducing varied collision energy experiments. The approach is akin to *energy-dependent* electron-spray mass

spectrometry (ESI-MS) and *stepped collision energy*, known from peptide fragmentation analysis. Thus, we were able to reliably assign sum formulas $[Cu_aZn_b](R)_k$ to an extensive list of molecular ions for clusters present in the solution (Methods section and Supplementary Table 2).

It is extremely difficult, ineffective, or even impossible to separate all or at least the majority of clusters from a library and collect specific analytical data, including experimental structure determination of individual clusters. Furthermore, it is *a priori* unknown which of the clusters may be particularly interesting, could and should possibly be isolated, rigorously characterized, and justify the effort of scaled-up synthesis for more investigations. Therefore, a novel bias-free computational framework was developed to efficiently obtain well-founded suggestions of structures for any given candidate based on the sum formula derived from the libraries' MS data analysis. The whole workflow for identification and structure assessment of clusters is depicted in Figure 2. It guides the experiments with the 1st generation library {1}, and it can particularly be applied to reactivity investigations with substrates leading to the 2nd generation libraries {2}-{4}.

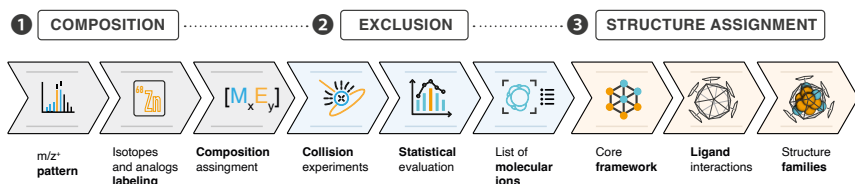


Figure 2: Workflow for the identification (1, 2) and structure assignment (3) of clusters in a library based on mass spectrometry involving labeling and varied collision energy experiments combined with a calculation framework using the obtained composition of the molecular ions of the clusters as the only input.

Calculation Framework for Structural Assignment

The calculation framework is based on the combination of Density Functional Theory (DFT) with Data Mining analysis techniques. This multi-step method is developed to obtain a reliable family of cluster structures without or with little additional information other than the sum formula deduced by the mass spectrometric library characterization (*vide supra*). The first step involves determining plausible metal core structure configurations without considering ligands, i.e., the core's frame. To obtain the initial structures, we employed an internal subroutine, where each atom is iteratively added to the frame with the constraint that each atom must be placed inside defined cube and sphere boxes. Therefore, the input parameters are the total number of

metal atoms ($n = a + b$) from a given Cu_aZn_b composition. Additionally, the core frames can also be imported from the literature and included in the binary cores design. Then, the binary cores are generated by taking all possible permutations obtained by replacing the original atoms of the frames with a atoms of Cu and b atoms of Zn.

In order to attain feasible calculation times, the number of binary cores needs to be reduced using an appropriate filter. To exclude quasi-identical configurations, we encode the structures using the eigenvalues of their Coulomb matrices and apply the *k-means* clustering algorithm to automatically select several representative structures (one from each group). Then, those trial structures are optimized (e.g., FHI-aims⁴⁸) through DFT with low-computational self-consistency and geometry optimization parameters. After a set of Cu_aZn_b optimized cores are obtained, the ligands ($R = \text{Cp}^*, \text{Mes}, \text{Hex}, \text{CO}_2, \text{H}, \dots$) are distributed around the binary core to yield the desired $[\text{Cu}_a\text{Zn}_b](R)_k$ clusters under two steps: First, n sites are generated and distributed (using a Fibonacci lattice) over a sphere that circumscribes the binary core, followed by a fine adjustment based on a coarse force-field process. Then, the ligands are added randomly or oriented by a predetermined distance to the given sites.

However, due to the intrinsically unbiased and random nature of ligand distributions, certain structures may exhibit undesired configurations with overlapping atoms, particularly in the case of large metal cores and large numbers of ligands. Therefore, a covalent-radii-based filter was used as a cutoff to remove those configurations from the set. The resulting configurations are grouped into sets of quasi-identical structures. Then, the representative structures obtained through *k-means* are submitted to low-cost DFT calculations. Finally, as an optional step, the remaining representative structures can be submitted using tighter convergence parameters in the DFT calculations, particularly for properties. This leads to a family of local minimum structures for each Cu/Zn and other miscellaneous clusters.

We chose the two experimentally resolved and previously fully characterized $[\text{CuZn}_2](\text{Cp}^*)_3$ (**A**) and $[\text{Cu}_3\text{Zn}_4](\text{Cp}^*)_5$ (**B**) to assess the validity of the calculation framework.^{29, 31} Starting with the sum formula only, families of 10 and 15 structures were generated for **A** and **B**, respectively. For both tests, the lowest energy configurations agreed with the experimental structures and DFT calculations, showcasing the great accuracy of the calculation framework with only ligand conformation distinguishing the lowest energy conformers. Nonetheless, clusters with a large number of core atoms and unusual structures become a challenge. However, this can be overcome by repeating the entire framework to guarantee a good sampling of structures. Additionally, design-based structures from the computational living library can be incorporated into the final family of clusters to reinforce structures that exhibit specific

physical-chemical experimental characteristics. In this way, reliable computational structures can be assigned to all clusters of interest (see Supporting Information).

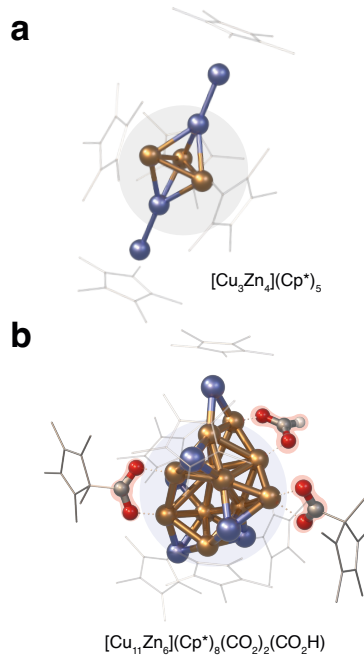


Figure 3. Results of the computational framework “cluster assembler”. a) Lowest energy structure of $[\text{Cu}_3\text{Zn}_4](\text{Cp}^*)_5$ (**B**) present in $\{\mathbf{1}\}$ showing a perfect match with the previously reported crystal structure²⁹ and b) lowest energy structure of $[\text{Cu}_{11}\text{Zn}_6](\text{Cp}^*)_8(\text{CO}_2)_2(\text{HCO}_2)$ (**Z**) present in $\{\mathbf{3}\}$. Color code: Cu = orange, Zn = blue, C = grey, O = red, H = white; Cp* and ligands are depicted as wireframes for the sake of clarity.

Probing Cluster Reactivity in Libraries

To demonstrate the potential of our approach, we probed the perturbation of $\{\mathbf{1}\}$ by small molecules such as carbon dioxide, hydrogen, and 3-hexyne (Figure 4). An overview of our experiments is also provided in Supplementary Figure 1.

Reactivity towards CO_2 and hydrogen. Treating $\{\mathbf{1}\}$ with CO_2 reveals two new clusters, $[\text{Cu}_5\text{Zn}_5](\text{Cp}^*)_6(\text{CO}_2)_2$ (**X**, $m/z = 1543$) and $[\text{Cu}_8\text{Zn}_3](\text{Cp}^*)_5(\text{Mes})_4(\text{CO}_2)$ (**Y**, $m/z = 1630$) (Figure 4). The unambiguous assignment was achieved by labeling with $^{68}\text{Zn}_2\text{Cp}^*_2$ and $^{13}\text{CO}_2$. The sum formulas for **X** and **Y** would also be in line with a CO_2 splitting into M-CO and M-O (M= Cu, Zn), which was excluded by the absence of $\nu(\text{CO})$ vibrations in the FT-IR spectra of $\{\mathbf{2}\}$ (Supplementary Figure 135). Monitoring this weak perturbation of $\{\mathbf{1}\}$ to yield $\{\mathbf{2}\}$ via *in situ* $^1\text{H-NMR}$ (Supplementary Figure 131) suggests $[\text{H}_3\text{Cu}_6\text{Zn}_5](\text{Cp}^*)_5(\text{Mes})$ (**D**) and

$[\text{HCu}_8\text{Zn}_3](\text{Cp}^*)_4(\text{Mes})_3$ (**E**) as precursors for **X** and **Y** (Supplementary Figures 12 and 13). Clusters **D** and **E** are the only species of $\{1\}$ to disappear in $\{2\}$. The release of H_2 and a formula unit CuMes (via NMR and LIFDI-MS) is assigned to the conversion **D** \rightarrow **X** (Supplementary Figure 12). The formation of HCp^* and tetramethylfulvene, together with H_2 evolution, is assigned to the conversion **E** \rightarrow **Y** (Supplementary Figure 13). The calculation framework proposes structures for **X** and **Y**. In **X**, both CO_2 units feature a bent geometry (O-C-O angle of 129°) with monodentate coordination of O to Cu, while C coordinates to Zn and Cu sites in one case and solely to Zn in the other (Supplementary Figure 14). This is reminiscent of the structures adopted by adsorbed CO_2 on Fe_{13} , Co_{13} , and Ni_{13} clusters.⁴⁹ In contrast, **Y** shows an insertion of the activated CO_2 into the hydrocarbon ligand sphere, forming a mesityl-carboxylate bridge to Cu sites (Supplementary Figure 14).

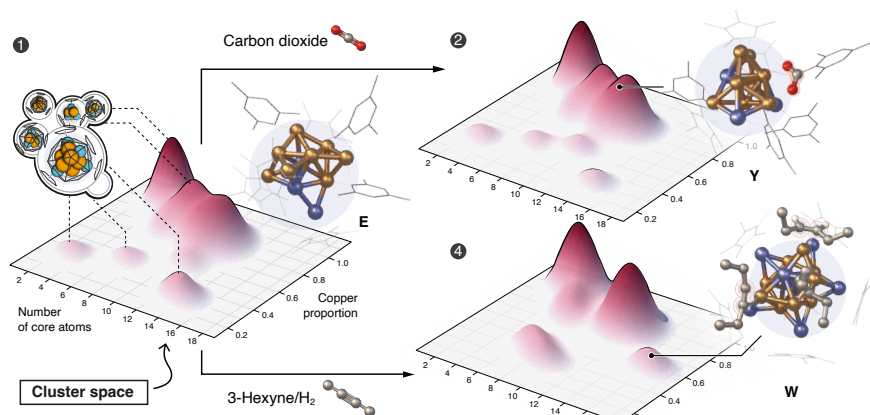


Figure 4. A selection of clusters $[\text{Cu}_a\text{Zn}_b](\text{R})_k$ identified in the libraries $\{1\}$, $\{2\}$, and $\{4\}$ are presented as heat maps based on the number of core metal atoms $n = a+b$ and the Cu proportion. The relative abundance of different clusters with similar number n of core atoms and proportion of Cu are qualitatively shown by the intensity of the domes. The computed structures of examples of clusters that have not been isolated in pure form, but identified by our methodology as important species during weak or strong perturbation of $\{1\}$ and the derived libraries $\{2\}$ and $\{4\}$ are depicted: $[\text{HCu}_8\text{Zn}_3](\text{Cp}^*)_4(\text{Mes})_3$ (**E**) and the mesityl-carboxylate insertion product upon CO_2 activation $[\text{Cu}_8\text{Zn}_3](\text{Cp}^*)_3(\text{Mes})_4(\text{CO}_2)$ (**Y**) occurring in $\{2\}$; computed structure of $[\text{Cu}_8\text{Zn}_7](\text{Cp}^*)_6(\text{Hex})_3\text{H}_3$ (**W**) that occurs in $\{4\}$ after treatment of $\{1\}$ with 3-hexyne and H_2 . The notations $(\text{Hex})_3$ and $(\text{H})_3$ refer to $3 \times \text{C}_6\text{H}_{10}$ and $3 \times \text{H}$ as part of the cluster's composition deduced from the MS data. Color code for the displayed structures: Cu = orange; Zn = blue, C = grey, O = red, H = white; Cp^* and Mesityl ligands are depicted as wireframes for the sake of clarity.

Subsequent admission of H₂ to this CO₂-treated library {2} leads to a third library {3} revealing a strong perturbation with 14 species of {2} reacting off (Supplementary Table 5). However, both CO₂ containing species X and Y of {2} remained, while a new formate containing species [Cu₁₁Zn₆](Cp*)₈(CO₂)₂(HCO₂) (Z, *m/z* = 2305) was identified in {3} (Supplementary Figures 6 and 15). The origin of Z could not be unambiguously traced back to any cluster of the original library {1}. Notably, the presence of clusters, so far not identified by our methodology but possibly involved in the formation of Z cannot be excluded. The computed structure of Z (Figure 3b, Supplementary Figure 16) suggests an HCO₂ moiety bridging two Cu atoms and flanked by a Zn atom, as well as two mesityl carboxylate moieties linked to Cu sites, quite similar to Y. The formate species was confirmed *via* monitoring {3} by ¹H-NMR (peak at 8.32 ppm;^{50,51} Supplementary Figures 132 and 133) and FT-IR spectroscopy (bands at 1380 cm⁻¹ and 1327 cm⁻¹;^{52,53} Supplementary Figures 136 and 137). The occurrence of formate in our organometallic Cu/Zn library {3} is well in line with *in situ* FT-IR studies on Cu/ZnO, Cu/SiO₂, and Cu/Al₂O₃ solid state systems exposed to CO₂/H₂ mixtures.^{54,55} It also reflects the mechanism for methanol formation on size-selected Cu₄ clusters supported on Al₂O₃.³⁸

Reactivity towards 3-hexyne and hydrogen. Treating {1} with an excess of 3-hexyne and H₂ yields the strongly perturbated {4}. *In situ* ¹H-NMR reveals free 3-hexene (*cis:trans* = 9:1) without *n*-hexane. At least one of the species of {4} appears *catalytically* active in alkyne semi-hydrogenation. The cluster [Cu₉Zn₇](Cp*)₆(Hex)₃(H)₃ (W, *m/z* = 2091) is the dominant C₆-containing species (Hex = C₆H₁₀) of {4}, also including three additional H atoms (Supplementary Table 6). The computed structure of W (Figure 5 and Supplementary Figure 148) shows a distorted Cu₉Zn pentagonal antiprismatic core with five ZnCp* moieties capping every second of the ten triangular faces and one ZnCp* capping the Cu₅ pentagonal face. The other Cu₄Zn pentagonal face contains the one Zn atom that is not ligated to Cp* as to interact with the other four Cu atoms, which bear the Cu-bound species $\mu_1\eta^2$ -3-hexyne (Hex+0H), $\mu_1\eta^2$ -*cis*-3-hexene (Hex+2H) and $\mu_2\eta^1$ -*cis*-3-hexenyl (Hex +1H). These species and their coordination modes are beautifully in line with the alkyne semi-hydrogenation mechanism. Thus, we suggest W as a molecular model surface. All Cp* ligands are grouped to form a protective half-sphere around a Cu₅Zn₆ sub-surface structure and expose the non-ligated Cu₄Zn plane for “adsorption” of substrates. Evidently, selective synthesis and full experimental characterization of W is a target of our future efforts.

The composition of W deviates much from the 10 clusters of {1} that are reacting off to yield {4}. Identifying a particular cluster or a set of clusters related to the formation of W requires narrowing down the chemical space of {1}. Careful tweaking the preparation

parameters of **{1}** allowed us to isolate and fully characterize the new cluster $[\text{Cu}_4\text{Zn}_{10}](\text{Cp}^*)_8$ (**F**) as one of the clusters reacting off when treating **{1}** with 3-hexyne and H_2 . Details on the X-ray single crystal diffraction analysis and the corresponding DFT calculations used to rationalize the structure and bonding of **F** are given in the SE.

Treatment of 3-hexyne with H_2 in the presence of 5 mol% of isolated **F** leads to catalytic alkyne semi-hydrogenation with near-perfect selectivity (Figure 5 and Supplementary Figures 151–153). The highest activity was observed at 100 °C with a quantitative conversion and a *cis:trans* ratio of 9:1 after 21 h. Monitoring the catalytic test reaction by LIFDI-MS reveals the quantitative consumption of **F** and the formation of **W** (Supplementary Figure 145) without significant abundance of other clusters. Thus, we assign **F** as a pre-catalyst and regard **W** as likely to be involved in the catalytic cycle. After four hours, 48% of the 3-hexyne was converted with $\text{TOF} = 0.60 \text{ h}^{-1}\text{Cu}^{-1}$ as compared to $\text{TOF} = 0.15 \text{ h}^{-1}\text{Cu}^{-1}$ for library **{4}** that is derived from **{1}** at the same conditions. Notably, **{1}** contains a relatively small amount of **F** besides inactive clusters. The transformation **F** → **W** occurs under the elimination of $\text{Zn}_2\text{Cp}^{*}_2$ and traces of $[\text{Cu}_3\text{Zn}_4](\text{Cp}^*)_5$ (**B**) and by restructuring towards a Cu-enriched core. The by-product $\text{Zn}_2\text{Cp}^{*}_2$ decomposes rapidly to elemental zinc under the conditions (Supplementary Figure 146).

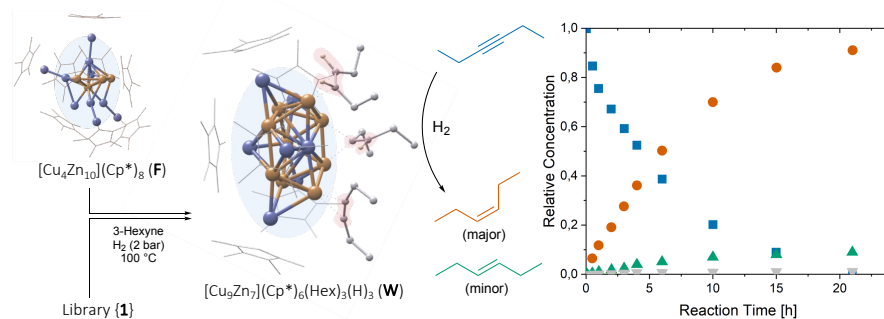


Figure 5: Catalytic semi-hydrogenation of 3-hexyne using either the whole library **{4}** or the pre-catalyst $[\text{Cu}_4\text{Zn}_{10}](\text{Cp}^*)_8$ (**F**) that was isolated from library **{1}**. Cluster **F** disappears in both cases and $[\text{Cu}_9\text{Zn}_7](\text{Cp}^*)_6(\text{Hex})_3(\text{H})_3$ (**W**) emerges while *cis*-3-hexene is formed with high selectivity (*cis:trans* = 9:1). The computed structure of **W** features various coordination modes of C_6 -species ($\text{Hex} + 0, 1$ or 2 H) such as $\mu_1\eta^2$ -3-hexyne, $\mu_1\eta^2$ -*cis*-3-hexene and $\mu_2\eta^1$ -*cis*-3-hexenyl. The relative concentrations as a function of the reaction time of 3-hexyne, *cis*- and *trans*-3-hexene, as well as *n*-hexane, are given for the catalytic conversion of 3-hexyne with 5 mol% **F** under a dihydrogen atmosphere at 100 °C.

Conclusions and Perspectives

We introduced the concept of living libraries using Cu/Zn clusters as an example and reported a methodology for probing their chemical space directly without separating and isolating individual clusters. Conclusions regarding the reactive properties of the clusters can be obtained by monitoring the library evolution upon weak and strong perturbations. A weak perturbation is caused by CO₂ to yield CO₂-activated species bound at specific clusters while many remain inert. A strong perturbation is caused by 3-hexyne and H₂, with many clusters reacting off during alkyne semi-hydrogenation. Here, we demonstrated the targeted synthesis, isolation, and full characterization of [Cu₄Zn₁₀](Cp^{*})₈ (**F**), establishing it as a pre-catalyst. In turn, we discovered [Cu₉Zn₇](Cp^{*})₆(Hex)₃H₃ (**W**) as a molecular surface model likely to be involved in the catalytic cycle. Altogether, the examples showcase the usefulness of the living library approach for efficiently exploring a diverse (hetero)metallic cluster landscape. The concept is ready to be transferred to related metal combinations such as Cu/Al¹³ and Ni/Ga⁵⁶. Our approach holds much promise for cluster science in general as it may enable exploiting organometallic precursor chemistry to systematically identify novel, highly reactive, even catalytically active, all-hydrocarbon ligated mixed metal clusters across the periodic table.

Acknowledgments

This work was funded by the German Research Foundation (DFG) within a Reinhard Koselleck Project (grant number FI 502/44-1; R.A.F.). Support by the TUM Graduate School is acknowledged (R.B., M.S., J. S.). The authors gratefully acknowledge support from FAPESP (São Paulo Research Foundation, Grant Numbers 2017/11631-2 and 2018/21401-7; J.L.F.D.S.), Shell, and the strategic importance of the support given by ANP (Brazil's National Oil, Natural Gas and Biofuels Agency; J.L.F.D.S.) through the R&D levy regulation.

Author Contributions Statement

R.B. and M.S. performed all the experimental work with the cluster libraries as well as the mass spectrometry data analysis. K.F.A., M.G.Q., J.P.A.M. and V.K.O.R. wrote the algorithm and performed the initial calculations. K.F.A. and M.G.Q. conducted the new calculations and refined the code, respectively. J.S. collected the SC-X-ray data, solved and refined the structure of **E**. S.L. investigated the catalytic test reaction. S.K. and J.-Y. S. performed the bonding analysis. C.G. co-supervised the project. R.A.F and J.L.F.D.S. developed the idea and supervised the project. All the authors discussed the results. R.B., K.F.A., C.G., J.L.F.D.S., and R.A.F. wrote the manuscript with input from all authors.

Corresponding Authors

Correspondence to Juarez L. F. Da Silva and Roland A. Fischer.

Competing Interests Statement

The authors declare no competing interests.

References

1. Beniya, A., Higashi, S., Ohba, N., Jinnouchi, R., Hirata, H. & Watanabe, Y. CO oxidation activity of non-reducible oxide-supported mass-selected few-atom Pt single-clusters. *Nat. Commun.* **11**, 1888 (2020)
2. Crampton, A. S., *et al.* Structure sensitivity in the nonscalable regime explored via catalysed ethylene hydrogenation on supported platinum nanoclusters. *Nat. Commun.* **7**, 10389 (2016)
3. Tyo, E. C. & Vajda, S. Catalysis by clusters with precise numbers of atoms. *Nat. Nanotechnol.* **10**, 577-588 (2015)
4. Watanabe, Y. & Isomura, N. A new experimental setup for high-pressure catalytic activity measurements on surface deposited mass-selected Pt clusters. *J. Vac. Sci. Technol. A* **27**, 1153-1158 (2009)
5. Zheng, Y.-R., *et al.* Monitoring oxygen production on mass-selected iridium–tantalum oxide electrocatalysts. *Nat. Energy* **7**, 55-64 (2022)
6. Bronstein, L. M. & Shifrina, Z. B. Dendrimers as Encapsulating, Stabilizing, or Directing Agents for Inorganic Nanoparticles. *Chem. Rev.* **111**, 5301-5344 (2011)
7. Imaoka, T., Kitazawa, H., Chun, W.-J., Omura, S., Albrecht, K. & Yamamoto, K. Magic Number Pt₁₃ and Misshapen Pt₁₂ Clusters: Which One is the Better Catalyst? *J. Am. Chem. Soc.* **135**, 13089-13095 (2013)
8. Imaoka, T., Kitazawa, H., Chun, W.-J. & Yamamoto, K. Finding the Most Catalytically Active Platinum Clusters With Low Atomicity. *Angew. Chem. Int. Ed.* **54**, 9810-9815 (2015)
9. Eulensteiner, A. R., *et al.* Substantial π -aromaticity in the anionic heavy-metal cluster [Th@Bi₁₂]⁴⁻. *Nat. Chem.* **13**, 149-155 (2021)
10. Lichtenberger, N., *et al.* Main Group Metal–Actinide Magnetic Coupling and Structural Response Upon U⁴⁺ Inclusion Into Bi, Tl/Bi, or Pb/Bi Cages. *J. Am. Chem. Soc.* **138**, 9033-9036 (2016)
11. Min, X., *et al.* All-Metal Antiaromaticity in Sb₄-Type Lanthanocene Anions. *Angew. Chem. Int. Ed.* **55**, 5531-5535 (2016)
12. Schütz, M., *et al.* Exploring Cu/Al cluster growth and reactivity: from embryonic building blocks to intermetalloid, open-shell superatoms. *Chem. Sci.* **12**, 6588-6599 (2021)
13. Weßing, J., *et al.* The Mackay-Type Cluster [Cu₄₃Al₁₂](Cp*)₁₂: Open-Shell 67-Electron Superatom with Emerging Metal-Like Electronic Structure. *Angew. Chem. Int. Ed.* **57**, 14630-14634 (2018)
14. Nguyen, T.-A. D., *et al.* A Cu₂₅ Nanocluster with Partial Cu(0) Character. *J. Am. Chem. Soc.* **137**, 13319-13324 (2015)
15. Schütz, M., Gemel, C., Klein, W., Fischer, R. A. & Fässler, T. F. Intermetallic phases meet intermetalloid clusters. *Chem. Soc. Rev.* **50**, 8496-8510 (2021)

16. Fischer, R. A. Organometallic Superatom Complexes. *Bulletin of Japan Society of Coordination Chemistry* **81**, 20-38 (2023)
17. Butovskii, M. V., Döring, C., Bezugly, V., Wagner, F. R., Grin, Y. & Kempe, R. Molecules containing rare-earth atoms solely bonded by transition metals. *Nat. Chem.* **2**, 741-744 (2010)
18. Dabringhaus, P. & Krossing, I. From mixed group 13 cations $[M(AlCp^*)_3]^+$ ($M = Ga/In/Tl$) to an Al_4^{+} cluster. *Chem. Sci.* **13**, 12078-12086 (2022)
19. Buchin, B., Gemel, C., Cadenbach, T., Fernández, I., Frenking, G. & Fischer, R. A. “Naked” Ga^+ and In^+ as Pure Acceptor Ligands: Structure and Bonding of $[GaPt(GaCp^*)_4][BAr^F]$. *Angew. Chem. Int. Ed.* **45**, 5207-5210 (2006)
20. Halbherr, M., Bollermann, T., Gemel, C. & Fischer, R. A. Selective Oxidative Cleavage of Cp^* from Coordinated $GaCp^*$: Naked Ga^+ in $[GaNi(GaCp^*)_4]^+$ and $[(\mu^2-Ga)_nM_3(GaCp^*)_6]^{n+}$ *Angew. Chem. Int. Ed.* **49**, 1878-1881 (2010)
21. Sánchez, R. H., Willis, A. M., Zheng, S.-L. & Betley, T. A. Synthesis of Well-Defined Bicapped Octahedral Iron Clusters $[({}^{tren}L)_2Fe_8(PMe_2Ph)_2]_n$ ($n=0, -1$). *Angew. Chem. Int. Ed.* **54**, 12009-12013 (2015)
22. Cadenbach, T., et al. Twelve One-Electron Ligands Coordinating One Metal Center: Structure and Bonding of $[Mo(ZnCH_3)_9(ZnCp^*)_3]$. *Angew. Chem. Int. Ed.* **47**, 9150-9154 (2008)
23. Muhr, M., Hornung, J., Weßing, J., Jandl, C., Gemel, C. & Fischer, R. A. Formation of a Propeller-Shaped Ni_4Ga_3 Cluster Supported by Transmetalation of Cp^* from Ga to Ni. *Inorg. Chem.* **59**, 5086-5093 (2020)
24. Bühler, R., et al. Photochemically generated reactive sites at ruthenium/gallium complexes: catalysis vs. cluster growth. *Dalton Trans.* **52**, 10905-10910 (2023)
25. Muhr, M., et al. C–H and Si–H Activation Reactions at Ru/Ga Complexes: A Combined Experimental and Theoretical Case Study on the Ru–Ga Bond. *Chem. Eur. J.* **28**, e202200887 (2022)
26. Steinke, T., Gemel, C., Cokoja, M., Winter, M. & Fischer, R. A. $AlCp^*$ as a Directing Ligand: C–H and Si–H Bond Activation at the Reactive Intermediate $[Ni(AlCp^*)_3]^\ddagger$. *Angew. Chem. Int. Ed.* **43**, 2299-2302 (2004)
27. Cadenbach, T., et al. Substituent-Free Gallium by Hydrogenolysis of Coordinated $GaCp^*$: Synthesis and Structure of Highly Fluxional $[Ru_2(Ga)(GaCp^*)_7(H)_3]$. *Angew. Chem. Int. Ed.* **48**, 3872-3876 (2009)
28. Martínez-Prieto, L. M. & Chaudret, B. Organometallic Ruthenium Nanoparticles: Synthesis, Surface Chemistry, and Insights into Ligand Coordination. *Acc. Chem. Res.* **51**, 376-384 (2018)
29. Banh, H., et al. Embryonic brass: pseudo two electron Cu/Zn clusters. *Chem. Sci.* **9**, 8906-8913 (2018)
30. Freitag, K., et al. Molecular brass: Cu_4Zn_4 , a ligand protected superatom cluster. *Chem. Commun.* **50**, 8681-8684 (2014)
31. Freitag, K., et al. The σ -Aromatic Clusters $[Zn_3]^+$ and $[Zn_2Cu]$: Embryonic Brass. *Angew. Chem. Int. Ed.* **54**, 4370-4374 (2015)
32. Schütz, M., et al. Contrasting Structure and Bonding of a Copper-Rich and a Zinc-Rich Intermetalloid Cu/Zn Cluster. *Inorganic Chemistry* **59**, 9077-9085 (2020)
33. Halder, A., et al. CO₂ Methanation on Cu-Cluster Decorated Zirconia Supports with Different Morphology: A Combined Experimental In Situ GIXANES/GISAXS, Ex Situ XPS and Theoretical DFT Study. *ACS Catal.* **11**, 6210-6224 (2021)
34. Iyemperumal, S. K. & Deskins, N. A. Activation of CO₂ by supported Cu clusters. *Phys. Chem. Chem. Phys.* **19**, 28788-28807 (2017)

35. Liu, C., He, H., Zapol, P. & Curtiss, L. A. Computational studies of electrochemical CO₂ reduction on subnanometer transition metal clusters. *Phys. Chem. Chem. Phys.* **16**, 26584-26599 (2014)
36. López-Caballero, P., Hauser, A. W. & Pilar de Lara-Castells, M. Exploring the Catalytic Properties of Unsupported and TiO₂-Supported Cu₅ Clusters: CO₂ Decomposition to CO and CO₂ Photoactivation. *J. Phys. Chem. C* **123**, 23064-23074 (2019)
37. Szalay, M., *et al.* Screening of transition metal doped copper clusters for CO₂ activation. *Phys. Chem. Chem. Phys.* **23**, 21738-21747 (2021)
38. Liu, C., *et al.* Carbon Dioxide Conversion to Methanol over Size-Selected Cu₄ Clusters at Low Pressures. *J. Am. Chem. Soc.* **137**, 8676-8679 (2015)
39. Yang, B., *et al.* Copper Cluster Size Effect in Methanol Synthesis from CO₂. *J. Phys. Chem. C* **121**, 10406-10412 (2017)
40. Yang, B., *et al.* Dynamic Interplay between Copper Tetramers and Iron Oxide Boosting CO₂ Conversion to Methanol and Hydrocarbons under Mild Conditions. *ACS Sustain. Chem. Eng.* **7**, 14435-14442 (2019)
41. Yang, Y., Evans, J., Rodriguez, J. A., White, M. G. & Liu, P. Fundamental studies of methanol synthesis from CO₂ hydrogenation on Cu(111), Cu clusters, and Cu/ZnO(000). *Phys. Chem. Chem. Phys.* **12**, 9909-9917 (2010)
42. Liu, Q., Hu, Y. & Cheng, L. Catalytic properties of nano-brass clusters: A density functional theory study. *Comput. Theor. Chem.* **1200**, 113237 (2021)
43. Zamora, B., Nyulászi, L. & Höltzl, T. CO₂ and H₂ Activation on Zinc-Doped Copper Clusters. *ChemPhysChem* **25**, e202300409 (2024)
44. Shi, X., *et al.* Copper Catalysts in Semihydrogenation of Acetylene: From Single Atoms to Nanoparticles. *ACS Catal.* **10**, 3495-3504 (2020)
45. Huang, F., *et al.* Anchoring Cu₁ species over nanodiamond-graphene for semi-hydrogenation of acetylene. *Nat. Commun.* **10**, 4431 (2019)
46. Yue, Y., *et al.* Tailoring Cu-Zn Dual-Atom Sites with Reordering d-Orbital Splitting Manner for Highly Efficient Acetylene Semihydrogenation. *ACS Catal.* **14**, 3900-3911 (2024)
47. Muhr, M., *et al.* Enabling LIFDI-MS measurements of highly air sensitive organometallic compounds: a combined MS/glovebox technique. *Dalton Trans.* **50**, 9031-9036 (2021)
48. Blum, V., *et al.* Ab initio molecular simulations with numeric atom-centered orbitals. *Comput. Phys. Commun.* **180**, 2175-2196 (2009)
49. Ocampo-Restrepo, V. K., Verga, L. G. & Da Silva, J. L. F. Ab Initio Study of the C–O Bond Dissociation in CO₂ Reduction by Redox and Carboxyl Routes on ³d Transition Metal Systems. *J. Phys. Chem. C* **125**, 26296-26306 (2021)
50. Kang, U., *et al.* Photosynthesis of formate from CO₂ and water at 1% energy efficiency via copper iron oxide catalysis. *Energy Environ. Sci.* **8**, 2638-2643 (2015)
51. Motokura, K., Kashiwame, D., Takahashi, N., Miyaji, A. & Baba, T. Highly Active and Selective Catalysis of Copper Diphosphine Complexes for the Transformation of Carbon Dioxide into Silyl Formate. *Chem. Eur. J.* **19**, 10030-10037 (2013)
52. Carter, R. O., Poindexter, B. D. & Weber, W. H. Vibrational spectra of copper formate tetrahydrate, copper formate dihydrate and three anhydrous forms of copper formate. *Vib. Spectrosc.* **2**, 125-134 (1991)
53. Edwards, J. F. & Schrader, G. L. Methanol, Formaldehyde, and Formic Acid Adsorption on Methanol Synthesis Catalysts. *J. Phys. Chem.* **89**, 782-788 (1985)
54. Lam, E., *et al.* CO₂ Hydrogenation on Cu/Al₂O₃: Role of the Metal/Support Interface in Driving Activity and Selectivity of a Bifunctional Catalyst. *Angew. Chem. Int. Ed.* **58**, 13989-13996 (2019)

-
55. Millar, G. J., Rochester, C. H. & Waugh, K. C. An in situ high pressure FT-IR study of CO₂/H₂ interactions with model ZnO/SiO₂, Cu/SiO₂ and Cu/ZnO/SiO₂ methanol synthesis catalysts. *Catal. Lett.* **14**, 289-295 (1992)
56. Muhr, M., *et al.* Catalytic Alkyne Semihydrogenation with Polyhydride Ni/Ga Clusters. *Angew. Chem. Int. Ed.* **62**, e202308790 (2023)

Methods

General. All manipulations were carried out using standard *Schlenk* techniques under inert atmospheres. Solvents were dried using an *MBraun Solvent Purification System*. The final H₂O content of all solvents was measured *via Karl-Fischer* titration and was below 5 ppm. The organometallic precursors Cu₅Mes₅⁵⁷ and Zn₂Cp*₂⁵⁸ were synthesized and characterized according to literature procedures.

¹H-NMR spectra were recorded on a *Bruker AVIII 400 US* spectrometer (400 MHz) in benzene-d₆ or toluene-d₈. Chemical shifts (δ , ppm) and referenced to the solvent resonances as internal standards and corrected tetramethylsilane (TMS) as the standard. Liquid Injection Field Desorption Ionization Mass Spectrometry (LIFDI-MS) was measured via sample transfer under an argon atmosphere (glove box) using a *Thermo Fisher Scientific Exactive Plus Orbitrap* (mass range up to 6000 a.m.u; mass accuracy 3 ppm; external calibration) that was equipped with an LIFDI source from *Linden CMS*. The FT-IR spectra were taken on an *ALPHA-T TFT-IR* spectrometer from *Bruker* with a transmission cell unit under an argon atmosphere (glove box) with 512 scans per measurement and a resolution of 4 cm⁻¹. The spectra were evaluated using the software *OPUS*.

The computational framework for structure generation is compiled in an iterative Python code, namely *cluster assembler*, which is available at <https://doi.org/10.5281/zenodo.8136872>.

Library Generations and Evolutions. The Cu/Zn library {1} was prepared by reacting 1.0 eq. Cu₅Mes₅ (e.g., 24.0 mol, 22.0 mg) with 3.75 eq. Zn₂Cp*₂ (e.g., 90.0 μ mol, 36.6 mg) in 1.0 mL dry toluene for two hours before analysis *via* LIFDI-MS either using a flame-dried Schlenk Tube or in a flame-dried J-Young NMR tube. Labeling was carried out with ⁶⁸Zn₂Cp*₂ and Zn₂Cp*^{Et₂} accordingly, with quantities of 37.0 mg and 39.6 mg, respectively. The library generation can be scaled when keeping the overall concentration and molar ratio of the reactants constant.

The evolution of library {1} to library {2}, i.e., perturbation with CO₂, was conducted by pressurizing a sample of 0.5 mL {1} with 1 bar of CO₂ in a flame-dried J-Young NMR tube after freeze-pump-thaw degassing. After 18 h reaction time, the CO₂ adducts [Cu₅Zn₅](Cp*)₆(CO₂)₂ (X) and [Cu₈Zn₃](Cp*)₃(Mes)₄(CO₂) (Y) were observed by LIFDI-MS analysis. Reactions with ¹³CO₂ are performed accordingly

The evolution of library **{2}** to library **{3}**, i.e., the subsequent perturbation of **{1}** with CO₂ and then with H₂, was conducted by pressurizing 0.5 mL **{1}** in a flame-dried J-Young NMR tube with 1 bar of CO₂ to obtain **{2}** as described earlier. After a reaction time of 18 h at room temperature, CO₂ was released from the tube (glovebox). The tube was then pressurized with 2 bar H₂ after freeze-pump-thaw degassing. Formate is detected by ¹H-NMR after 4 hours reaction time and [Cu₁₁Zn₆](Cp^{*})₈(CO₂)₂(HCO₂) (**Z**) is detected via LIFDI-MS.

The evolution of library **{1}** to library **{4}**, i.e., the simultaneous treatment with 3-hexyne and H₂, was conducted by placing 0.5 mL of **{1}** in a flame-dried J-Young NMR tube together with 5.0 μL 3-hexyne (44.0 μmol, 3.66 eq. based on Cu) and pressurizing with 2 bar H₂ after freeze-pump-thaw degassing. After 4 hours at 100 °C, 3-hexene is detected by ¹H-NMR and [Cu₉Zn₇](Cp^{*})₆(Hex)₃(H)₃ (**W**) in detected via LIFDI-MS.

Mass Spectrometric Library Characterization. The assignment of sum formulas for clusters is based on the *m/z* value and the isotopic pattern of the observed molecular ions in the LIFDI MS experiment. Differences of one H atom are well recognized by a shift of Δ*m/z* = 1. However, the difference in atomic masses of Cu and Zn is also only 1. When including the possibility of cluster hydrides, it leads to a very large number of possible compositions for each *m/z* value. The mass accuracy of 3 ppm and the instrumental resolution at optimum sensitivity of 35000 prevents us from using the isotopic pattern alone for unambiguous identification, even for medium-sized clusters (Supplementary Figure 18). A double labeling strategy was applied to solve this problem by introducing Cp^{*Et} (Δ*m/z* = 14) and isotopically enriched ⁶⁸Zn₂Cp^{*2} (Δ*m/z* = 2.62). The clusters [Cu_aZn_b](R)_k (R = Cp^{*}_c, Mes_d, H_h; *c* + *d* + *h* = *k*) are generally ligated by Cp^{*} and Mes, while H may occur as well. The number of Cp^{*} ligands *c* of a species can thereafter be determined by scanning the Cp^{*Et} labeled spectrum for peaks with a Δ*m/z* shift of *c* × 14. The number of matches for each peak is thus reduced to species carrying the same number *c* of Cp^{*}. For multiple computed compositions with the same *c*, matching the experimental patterns and unambiguous peak identification was achieved by the second labeling experiment with ⁶⁸Zn₂Cp^{*2}. Thus, definite sum formulas [Cu_aZn_b](R)_k (R_k = Cp^{*}_c, Mes_d, H_h; *c* + *d* + *h* = *k*) were assigned to nearly every observed peak pattern, including the unique deconvolution of overlapping patterns. The results are given in Supplementary Table 1.

Collision experiments enable discrimination between molecular ions and fragments. The collision energy (CE) in the higher-energy collisional dissociation cell (HCD) of the ORBITRAP mass spectrometer was increased stepwise, and a spectrum of the original cluster library was recorded for each collision energy. The intensities (*I*) of the peaks of interest were determined for the different collision energies by integrating them relative to the overall integral

of the respective spectrum. Molecular ion peaks are associated with a continuous *decrease* in peak intensity for increasing collision energies. This is due to the enhanced fragmentation of parent ions at higher collision energies. For fragment ions, an *increase* in peak intensity is expected for increasing collision energies due to their enhanced formation at higher collision energies. The approach is akin to *energy-dependent* electron-spray mass spectrometry (ESI-MS) and *stepped collision energy* known from peptide fragmentation.^{59, 60} The resulting *I* vs. *CE* plots for every ion pattern of {1} are shown in the Supporting Information (Supplementary Figures 73-129). For some species, no significant variation in peak intensity was detected. Hence, discrimination between a fragment and a molecular ion failed in these few cases. However, the method is reliable for the great majority of the peaks and reliably yields the assignment of sum formulas to an extensive list of molecular ions for clusters present in the solution (Supplementary Table 2). This methodology can also be applied to reactivity investigations of cluster libraries (*vide supra*).

Synthesis and Characterization of the new cluster [Cu₄Zn₁₀](Cp^{*})₈ (F). Samples of Cu₅Mess (420 mg, 0.46 mmol, 1.00 eq.) and Zn₂Cp^{*}₂ (876 mg, 2.18 mmol, 4.7 eq.) were dissolved in toluene (75 mL) and stirred at room temperature for 2 h. After concentrating the solution under reduced pressure to 8 mL, the mixture was filtered and left to crystallize at –30 °C for six days. Then, the mother liquor was filtered off at –30 °C, and the deposited crystals were washed thoroughly with *n*-hexane (4 x 10 mL) and filtered off with cooling. The volume of the combined filtrates was further reduced *in vacuo* and left to crystallize again at –30 °C for a few days to give another batch of crystals. The combined crude product still contains significant quantities of [CuZn₂]Cp^{*}₃ (A). It was then further purified by careful decantation by suspending the collected crystals in *n*-hexane (3 x 10 mL) and stirring it strongly before letting the yellow-orange [CuZn₂]Cp^{*}₃ (A) settle for a few seconds and decanting off the black suspension using a narrow Teflon cannula. The resulting black suspension was allowed to settle and decanted, and the remaining crystals were dried *in vacuo* at room temperature. The remaining impurities of [CuZn₂]Cp^{*}₃ (A) were removed by crystal picking from that sample under the microscope in the glove box to yield a homogeneous black crystalline sample of [Cu₄Zn₁₀](Cp^{*})₈ (F, 80 mg, 40.2 μmol, 7 % based on Cu). Analytical data of F: ¹H-NMR (400 MHz, Toluene-d₈): δ [ppm] = 2.27 (s, 45H), 2.21 (s, 75H); ¹H-NMR (400 MHz, C₆D₆): δ [ppm] = 2.30 (s, 45H), 2.24 (s, 75H). ¹³C-NMR (101 MHz, Tol-d₈): δ [ppm] = 110.4 (s, C₅Me₅), 107.6 (s, C₅Me₅), 12.6 (s, C₅Me₅), 10.6 (s, C₅Me₅). LIFDI-MS [m/z]: found [M]⁺ 1989.9273 (calculated 1989.9327). Elemental analysis (C, H, Cu, Zn) yielded non-satisfactory results due to still not fully removed impurities of A (traces detected by ¹H-NMR).

Single crystal X-ray crystallography. A black, plate-shaped crystal of **F**, $C_{80}H_{120}Cu_4Zn_{10}$, coated with perfluorinated ether and fixed on top of a Kapton micro sampler was used for X-ray crystallographic analysis. The X-ray intensity data were collected at 100(2) K on a Bruker D8 VENTURE three-angle diffractometer with a TXS rotating anode with $MoK\alpha$ radiation ($\lambda=0.71073 \text{ \AA}$) using APEX4.⁶¹ The diffractometer was equipped with a Helios optic monochromator, a Bruker PHOTON-100 CMOS detector, and a low temperature device. The results of the structure solution and refinement are given in the SE.

Bonding Analysis. DFT calculations at the BP86/TZ2P/ D3(BJ) level were carried out specifically on $[Cu_4Zn_{10}](Cp^*)_8$ (**F**) in order to guide and ascertain the Cu vs. Zn nature of the M positions in the experimental structure obtained via single crystal X-ray diffraction and to provide a rationalization of its electronic structure. The DFT calculations were carried out with the use of the Amsterdam Density Functional code (ADF2020.101)⁶², incorporating scalar relativistic corrections *via* the ZORA Hamiltonian^{63,64}. The BP86 functional^{65,66} was used, with the addition of Grimme's D3(BJ) empirical corrections^{67,68} to account for dispersion effects. All the geometry optimizations were performed with the all-electron triple- ξ Slater basis set plus two polarization functions (STO-TZ2P).⁶⁹ Natural atomic charges and Wiberg bond indices were computed with the natural bond orbital NBO6.0 program⁷⁰ implemented in the ADF2020.101 package.

From the electron counting point of view, the number of cluster metal valence electrons (discarding 3d electrons) of $[Cu_4Zn_{10}](Cp^*)_8$ (**F**) is $4 + (10 \times 2) - 8 = 16$. Assuming that the Zn-Zn bonds in the four Zn-ZnCp* units are localized 2-electron/2-center bonds, the number of electrons associated with metal-metal bonding within the coordination sphere of the central Cu atom is $16 - (4 \times 2) = 8$. Together with the 10 non-bonding 3d(Cu) electrons, this results in a central Cu atom following the 18-electron rule, analogous to a regular ML_n organometallic complex (Supplementary Figure 144). A full discussion of the results is given in the SE.

Catalytic test reaction. A sample of $[Cu_4Zn_{10}](Cp^*)_8$ (**F**) (2.50 mg, 1.26 μmol , 1.00 eq.) obtained as described earlier, and a sample of 3-hexyne (2.90 μL , 25.1 μmol , 20 eq.) were dissolved in toluene-d₈ (0.50 mL) and placed in a flame dried J-Young NMR tube. After degassing the solution, the mixture was pressurized with H₂ (2 bar) and heated to 100 °C for 21 hours to obtain quantitative conversion of the 3-hexyne to *cis*-3-hexene and *trans*-3-hexene in a molar ratio of 9:1 obtained by ¹H-NMR signal integration: ¹H-NMR (400 MHz, Tol-d₈): δ [ppm] = 5.41 (tt, 2H, H_{trans}), 5.35 (ddd, 2H, H_{cis}). Treating 0.5 mL of library {1} with 3-hexyne and H₂ under the same conditions yields the same result. Note: Using Cu₅Mes₅ or Zn₂Cp*₂ or the cluster $[CuZn_2]Cp^*_3$ (**A**) as pre-catalysts instead of a sample of **F** did not show any

conversion of 3-hexyne. Also, in order to exclude catalysis induced by any metal nanoparticles (Zn, Cu, Cu/Zn), test reactions were performed in the presence of elemental mercury, known to amalgamate with metals and thus passivate nanoparticles⁵⁶, and no change in the catalytic performance of our system was observed.

Data Availability

Crystallographic data for the structures of **A**, **B**, and **F** are available at the Cambridge Crystallographic Data Centre under deposition numbers 1013577, 1854852, and 2390361 respectively. Copies of the data can be obtained free of charge via <https://www.ccdc.cam.ac.uk/structures/>. Full experimental (LIFDI-MS, IR, NMR) and computational datasets are available at the Research Data Service MediaTUM under the DOI [10.14459/2023mp1715745](https://doi.org/10.14459/2023mp1715745).

Code Availability

We provided the procedure for structure generation compiled in an automated Python code, namely *Cluster Assembler* (*v.1.2.0*), available at <https://doi.org/10.5281/zenodo.12819855>.

Methods-only References

57. Meyer, E. M., Gambarotta, S., Floriani, C., Chiesi-Villa, A. & Guastini, C. Polynuclear aryl derivatives of Group 11 metals. Synthesis, solid state-solution structural relationship, and reactivity with phosphines. *Organometallics* **8**, 1067-1079 (1989)
58. Grirrane, A., et al. Zinc– Zinc Bonded Zincocene Structures. Synthesis and Characterization of Zn₂(η⁵-C₅Me₅)₂ and Zn₂(η⁵-C₅Me₄Et)₂. *J. Am. Chem. Soc.* **129**, 693-703 (2007)
59. Diedrich, J. K., Pinto, A. F. & Yates III, J. R. Energy dependence of HCD on peptide fragmentation: stepped collisional energy finds the sweet spot. *J. Am. Chem. Soc. Mass Spectrom.* **24**, 1690-1699 (2013)
60. Dyson, P. J., Johnson, B. F., McIndoe, J. S. & Langridge-Smith, P. R. Energy-dependent electrospray ionisation mass spectrometry: applications in transition metal carbonyl chemistry. *Rapid Commun. Mass Spectrom.* **14**, 311-313 (2000)
61. APEX4 Suite of Crystallographic Software. Version 2021-10.0 ed: Bruker AXS Inc., Madison, Wisconsin, USA; 2021.
62. te Velde, G., et al. Chemistry with ADF. *J. Comput. Chem.* **22**, 931-967 (2001)
63. van Lenthe, E., Baerends, E. J. & Snijders, J. G. Relativistic regular two-component Hamiltonians. *J. Chem. Phys.* **99**, 4597-4610 (1993)
64. van Lenthe, E., Baerends, E. J. & Snijders, J. G. Relativistic total energy using regular approximations. *J. Chem. Phys.* **101**, 9783-9792 (1994)
65. Becke, A. D. Density-functional exchange-energy approximation with correct asymptotic behavior. *Phys. Rev. A* **38**, 3098-3100 (1988)
66. Perdew, J. P. Density-functional approximation for the correlation energy of the inhomogeneous electron gas. *Phys. Rev. B* **33**, 8822-8824 (1986)

67. Grimme, S. Semiempirical GGA-type density functional constructed with a long-range dispersion correction. *J. Comput. Chem.* **27**, 1787-1799 (2006)
68. Grimme, S. Density functional theory with London dispersion corrections. *WIREs Comp. Mol. Sci.* **1**, 211-228 (2011)
69. van Lenthe, E. & Baerends, E. J. Optimized Slater-type basis sets for the elements 1–118. *J. Comput. Chem.* **24**, 1142-1156 (2003)
70. Glendening, E. D., *et al.* NBO 6.0, University of Wisconsin (Madison, WI, 2001, <http://nbo6.chem.wisc.edu>).

4.2 Study V: Cuprophilic Interaction in Polymeric $[Cu_{10}O_2(Mes)_6]_n$

The reaction of $[CuMes]_5$ with dioxygen, as initially reported by *Håkansson et al.*, leads to the formation of a vivid red crystalline product identified as $[Cu_{10}O_2Mes_6]$.^[69] We performed a new study of this compound using state-of-the-art experimental and theoretical analysis techniques, unveiling the polymeric nature of the species best written as $[Cu_{10}O_2Mes_6]_n$ with unsupported Cu(I)…Cu(I) contacts linking the monomers.

The monomeric unit exhibits an O-Cu-O central axis with three $Cu_3(\mu_2\text{-Mes})_2$ units assembled as pedal wheels around it. Additionally, various cuprophilic contacts bridged by mesityl or oxo ligands are observed *via* SC-XRD and confirmed using DFT calculations. The compound was analyzed in its solid state, revealing luminescent properties resulting from two distinct fluorescent emissions, typically observed in compounds showcasing cuprophilic interactions, as well as in solution, in which its polymeric structure reversibly decomposes.

QTAIM analysis allows us to characterize the different Cu^I…Cu^I contacts, of which only a few and not the shortest, are associated with a bond critical point. The strength of these cuprophilic interactions is quite significant, with the energy decomposition analysis of the interactions between two monomers revealing a total bond energy of 53.8 kcal/mol. The considerable computed inter-monomer bond energy is mainly the result of stabilizing ligand…ligand and metal…ligand dispersion forces, with some weak covalent contributions, underlying the importance of ligand-ligand attraction in the stabilization of metallophilic architectures.

R. Bühler conducted experiments, including synthesis, characterization, and luminescence studies, with contributions from J. Stephan and S. N. Deger. S. Kahlal and J.-Y. Saillard performed the calculations. R. A. Fischer and J.-Y. Saillard provided overarching academic guidance. The manuscript was written by R. Bühler and J.-Y. Saillard.

Reproduced with permission, Copyright 2024, American Chemical Society.

R. Bühler, R. M. Wolf, C. Gemel, J. Stephan, S. N. Deger, S. Kahlal, R. A. Fischer, J.-Y. Saillard, *Inorg. Chem.* **2024**, 63, 17617-17625.

Inorganic Chemistry

pubs.acs.org/IC

Article

Cuprophilic Interactions in Polymeric $[Cu_{10}O_2(Mes)_6]_n$

Raphael Bühler, Robert M. Wolf, Christian Gemel, Johannes Stephan, Simon N. Deger, Samia Kahla, Roland A. Fischer,* and Jean-Yves Saillard*



Cite This: *Inorg. Chem.* 2024, 63, 17617–17625



Read Online

ACCESS |

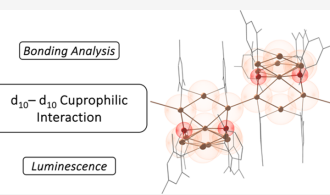
Metrics & More

Article Recommendations

Supporting Information

Downloaded via TU MÜNCHEN on September 23, 2024 at 11:34:45 (UTC).
See https://pubs.acs.org/sharingguidelines for options on how to legitimately share published articles.

ABSTRACT: The properties of cuprophilic compounds and the underlying fundamental principles responsible for the Cu(I)…Cu(I) interactions have been the subject of intense research as their diverse structural and physical attributes are being explored. In this light, we performed a new study of the compound $[Cu_{10}O_2(Mes)_6]$ reported by Haakansson et al. using state of the art experimental and theoretical analysis techniques. Doing this, we found the compound to be a polymer in the solid state, best written as $[Cu_{10}O_2(Mes)_6]_n$, with unsupported Cu(I)…Cu(I) contacts linking the monomers (2.776 Å). The monomeric unit also exhibits various cuprophilic contacts bridged by mesityl and/or oxo ligands. The compound was analyzed in its solid state, revealing luminescent properties resulting from two distinct fluorescent emissions, as well as in solution, in which its polymeric structure reversibly decomposes. A quantum theory of atoms in molecules (QTAIM) analysis based on density functional theory (DFT) calculations allows to characterize the various Cu(I)…Cu(I) contacts, in which only a few, and not necessarily the shortest, are associated with a bond critical point. Additionally, an energy decomposition analysis of the bonding between monomers indicates that it is dominated by dispersion forces in which the ligands play a dominant role, resulting in bonding energies significantly larger than found in previous DFT investigations based on less bulky models.



INTRODUCTION

In the intricate landscape of Group 11 metal complexes and clusters, the significance of closed-shell metallophilic interactions is increasingly recognized for shaping their diverse structural and physical attributes.^{1–6} While extensive investigations have delved into the well-established aurophilic and argentophilic interactions,^{3,4,7} cuprophilic interactions have remained relatively less explored experimentally, although a significant number of computational investigations has been devoted to them over the years.^{1,8–23}

They have recently received renewed attention, as they have been shown to be implicated in unexpected properties of Cu(I) compounds such as photoluminescence.^{24–27} Various types of Cu(I)…Cu(I) contact have been characterized by crystallographic analyses.^{1,2,28,29} The precision offered by these analyses provides valuable insights into the character of these interactions and their potential implications for the overall properties of copper complexes. As for other metallophilic interactions,³⁰ short Cu(I)…Cu(I) contacts are believed to stem from a combination of sd or spd orbital hybridization (covalency), London dispersion forces (van der Waals) and other electron correlation effects, relativistic effect, ligand pincer effect or, in the case of unsupported contacts, ligand…ligand attracting dispersion forces. Closed shell…closed shell Pauli repulsion also participates in the game.³⁰ The relative importance of each of these components in the overall bonding (if any) is still a matter of discussion.^{8–10,20}

Adding complexity to this exploration is the incorporation of O²⁻ ions into copper clusters. Such species have attracted attention as the importance of suboxidic copper species in CO₂ activation has been reported.^{31–33} O²⁻ ions pose challenges in merging with coinage-metal clusters due to their affinity for binding with hard Lewis acid transition metals, resulting in the formation of polyoxometalates (POMs).³⁴ This challenge arises from the highly reactive nature of O²⁻ ions and the inherent mismatch between their hard Lewis base character and the soft Lewis acid nature of copper(I) ions, deviating from the classical HSAB (hard and soft acids and bases) rule.³⁵

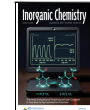
The reaction product of mesityl copper(I) and dioxygen, as reported by Haakansson et al.,³⁶ provides opportunities for a thorough investigation into cuprophilic interactions and the attributes of suboxidic copper clusters. With contemporary methodologies providing enhanced capabilities, we present new insights into the nature of this compound. Our study enriches the understanding of the unique properties of cuprophilic interactions by employing a combination of experimental and theoretical methods.

Received: June 10, 2024

Revised: August 29, 2024

Accepted: August 30, 2024

Published: September 10, 2024



<https://doi.org/10.1021/acs.inorgchem.4cd2377>
Inorg. Chem. 2024, 63, 17617–17625

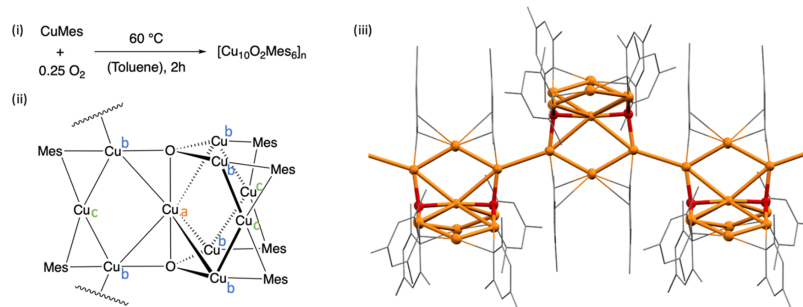


Figure 1. (i) Reaction scheme of I and (ii) simplified representation of the $[Cu_{10}O_2Mes_6]$ monomer. (iii) Crystal structure of I with ellipsoids drawn at 50% probability (Mesityl ligands as wireframe for the sake of simplicity). Orange = copper; red = oxygen.

RESULTS AND DISCUSSION

The interaction between $[CuMes]$ ($Mes = mesityl$) and 0.5 equiv of dioxygen results in the formation of a vivid red crystalline product, as reported by Haakansson et al., identified as $[Cu_{10}O_2Mes_6]$ (I).³⁶ Contrary to being a singular molecule, our characterization using single-crystal X-ray diffraction (SC-XRD) reveals that this species exhibits a polymeric nature in the solid state, with $[Cu_{10}O_2Mes_6]$ serving as the monomeric unit (Figure 1), a feature that was not noticed in the original work of Haakansson et al.³⁶

In the crystal ($C2/c$ space group), the $[Cu_{10}O_2Mes_6]$ monomer has exact C_2 symmetry. It consists of a $O-Cu_a-O$ central axis with three $Cu_3(\mu_3\text{-}Mes)_2$ units assembled as pedal wheels around it. As already noticed by Haakansson et al.,³⁶ the oxygen atoms are bonded to four copper atoms in a particularly unusual trigonal pyramidal coordination mode. The axial Cu_a-O distances are of 1.883(2) Å each, while the equatorial Cu_b-O distances range between 1.852(2) and 1.861(2) Å. Two distinct groups of copper–copper contacts can be found within the monomer: The mesityl bridged $Cu_b\cdots Cu_c$ and the oxygen bridged $Cu_a\cdots Cu_b$ contacts. The $Cu_b\cdots Cu_c$ distances range from 2.380(1) to 2.424(1) Å while the $Cu_a\cdots Cu_b$ distances range from 2.687(1) to 2.738(1) Å. All Cu–Cu distances are shorter than the sum of the van der Waals radii of two copper atoms (2.80 Å)³⁷ and lie in the range of reported cuprophilic compounds.² Additionally, the link between two $[Cu_{10}O_2Mes_6]$ monomers is made by an unsupported $Cu_b\cdots Cu_b'$ contact (i.e., no bridging ligands) with a distance of 2.790(1) Å. This is shorter than the $Cu\cdots Cu$ distances reported for a number of bis- and tris-diphosphine supported cuprophilic interactions (up to 2.9 and 3.0 Å respectively).^{38,39} It should be noted here that the $\mu_2\text{-}Mes$ ligands that are bonded to the Cu_b atoms involved in the unsupported $Cu\cdots Cu$ contacts exhibit some η^2 character (i.e. some π -type interaction) within each monomer, with Cu_b-C_{ortho} long contacts of 2.53(3) Å. Not considering this weakly bonding feature and other minor structural differences, the overall symmetry of the $[Cu_{10}O_2Mes_6]$ monomer can be in first approximation considered close to D_{3h} . Selected averaged distances are reported in Table 1.

While ¹H MAS NMR spectroscopy gives signals too broad for evaluation, the ¹³C MAS NMR spectra shows broad mesitylene signals at 30.41 and 154.16 ppm as well as cocrystallized toluene at 22.12, 126.81, and 140.15 ppm (Figure S1). FT-IR spectroscopy shows the characteristic C–H vibrations of the

Table 1. Selected Experimental (SC-XRD) and Density Functional Theory (DFT)-Computed Distances (in Å) for I, Averaged Assuming Ideal D_{3h} Symmetry for the $[Cu_{10}O_2(Mes)_6]$ Motif (WBI = Wiberg Bond Index)

	experimental distances	DFT-optimized distances and WBI in brackets $[Cu_{10}O_2(Mes)_6]$ monomer	DFT-optimized distances, Central unit in the $[Cu_{10}O_2(Mes)_6]_3$ trimer
$Cu_b\cdots Cu_b'$	2.790		2.554
$Cu_a\cdots Cu_b$	2.705	2.669 [0.051]	2.674
$Cu_b\cdots Cu_c$	2.409	2.403 [0.100]	2.402
$Cu_a\cdots Cu_c$	3.205	3.224 [0.031]	3.249
Cu_a-O	1.883	1.910 [0.143]	1.850
Cu_b-O	1.856	1.835 [0.174]	1.849
Cu_b-C	1.950	1.915 [0.392]	1.940
Cu_c-C	2.032	2.011 [0.239]	2.011

mesitylene ligands from 2700 to 3100 cm⁻¹ (Figure S3). Furthermore, the intensive bands at 608 and 844 cm⁻¹ are assigned to Cu–O stretching vibrations (621 and 798 cm⁻¹ for Cu₂O).⁴⁰ The solid-state UV-vis spectrum gives two absorption maxima at 290 and 510 nm as well as strong absorption between 350 and 430 nm (Figure 3).

Upon heating at 60 °C, I completely dissolves in toluene and benzene giving a near colorless solution, with a UV-vis spectrum displaying only absorption below 400 nm (Figure S4) as opposed to the intense absorption bands in the visible region when measured in the solid state. This drastically different behavior in solution suggests a decomposition of the species in solution as was described in the original publication.³⁶ Analysis of the solution via ¹H NMR shows the formation of different mesityl bearing species (Figure S2) and Liquid Injection Field Desorption Ionization (LIFDI) mass spectrometry under inert conditions⁴¹ reveals a complex set of ions adhering to the general formula $Cu_xMes_{x-(2n+1)}O_n$, with $x = 5-9$ for $n = 0$; $x = 8-11$ for $n = 1$; $x = 11-16$ for $n = 2$; and $x = 15-20$ for $n = 3$ (Figures S7–S13 and Table S1). However, none of these ions are molecular ions (Figure S14) and this strongly indicates the presence of larger molecules in solution, outside of the range of the mass spectrometer (6000 m/z). We observe, however, that the red crystalline product forms again after a few hours at room temperature and the powder X-ray diffractogram shows the title compound to be reformed (Figures S5 and S6).

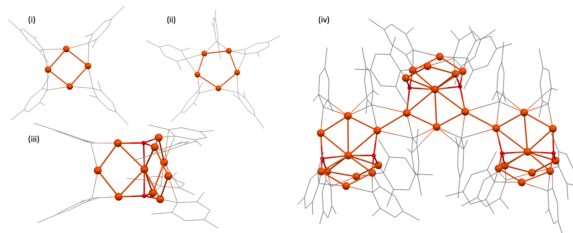


Figure 2. DFT optimized structures for (i) Cu_4Mes_4 , (ii) Cu_5Mes_5 , (iii) $[\text{Cu}_{10}\text{O}_2(\text{Mes})_6]$ monomer and (iv) $[\text{Cu}_{10}\text{O}_2(\text{Mes})_6]_n$ trimer.

Table 2. NAO and Quantum Theory of Atoms in Molecules (QTAIM) Averaged Charge Distribution in the $[\text{Cu}_{10}\text{O}_2(\text{Mes})_6]$ Motif

atom	NAO charge (monomer)	NAO configuration ($[\text{Cu}_{10}\text{O}_2(\text{Mes})_6]$ monomer)	QTAIM charge ($[\text{Cu}_{10}\text{O}_2(\text{Mes})_6]$ monomer)	QTAIM charge (central unit in the $[\text{Cu}_{10}\text{O}_2(\text{Mes})_6]_3$ trimer)
Cu _a	0.66	4s ^{0.52} 3d ^{9.78} 4p ^{0.02}	0.51	
Cu _b	0.72	4s ^{0.51} 3d ^{9.74} 4p ^{0.01}	0.46	0.50
Cu _c	0.65	4s ^{0.48} 3d ^{9.85} 4p ^{0.01}	0.40	0.37
O	-1.58	2s ^{1.84} 2p ^{5.72}	-1.18	-1.16

Table 3. Topological Cu···Cu BCP Descriptors in $\text{Cu}_2(\mu\text{-H})_2$, Linear HCuCuH (SP with $\text{Cu} \cdots \text{Cu} = 2.800 \text{ \AA}$) and $[\text{Cu}_{10}\text{O}_2(\text{Mes})_6]_3$ Trimer^a

	$\text{Cu}_2(\mu\text{-H})$ (D_{2h})	$\text{HCu} \cdots \text{CuH}$ (D_{coh} , SP)	$[\text{Cu}_{10}\text{O}_2(\text{Mes})_6]_3$ trimer (optimized geometry)		$[\text{Cu}_{10}\text{O}_2(\text{Mes})_6]_3$ trimer (SP from SC-XRD structure)	
			$1 \times \text{Cu}_a \cdots \text{Cu}_b^b$ (central unit)	$2 \times \text{Cu}_a \cdots \text{Cu}_b$ (intermonomers)	$3 \times \text{Cu}_a \cdots \text{Cu}_c^c$ (av.)	$2 \times \text{Cu}_b \cdots \text{Cu}_b$ (intermonomers)
bcp indicators ^b	ρ	0.071	0.012	0.027	0.034	0.021
	$\nabla^2 \rho$	0.256	0.034	0.048	0.080	0.033
	H	-0.013	0.001	-0.003	-0.004	-0.002
	V	-0.091	-0.006	-0.018	-0.027	-0.012
	$ \mathcal{W} / G$	1.17	0.842	1.19	1.15	1.17

^a ρ , $\nabla^2 \rho$, H , V , and G are the electron density, Laplacian of ρ density, energy density, potential energy density and kinetic energy density values at the bcp, respectively. All values in a.u. ^bOnly one among the three $\text{Cu}_a \cdots \text{Cu}_c$ contacts in the central unit. ^cOnly one $\text{Cu}_a \cdots \text{Cu}_c$ contact per monomeric unit.

The solution of **1** has a remarkable complexity which we are not able to fully comprehend. It however reverts back to the highly ordered structure upon recrystallization. This suggests that weak interactions are responsible for the thermodynamic minimum in the solid state which are reversibly broken in solution.

Compound **1** being a polymer in the solid state, DFT calculations were first performed on the $[\text{Cu}_{10}\text{O}_2(\text{Mes})_6]$ monomer, which was fully optimized at the PBE0/TZ2P-D3(BJ) level (see Computational Details). Note that the dispersion (London) forces were considered in the calculations, as Grimme's empirical corrections,⁴² for such long-range noncovalent attractions of electron correlation origin are known to play a decisive role in metallophilic interactions.⁴³ The monomer geometry (Figure 2), which was optimized without any symmetry constraint, is in good agreement with its experimental SC-XRD counterpart. It also exhibits some η^2 character of two *trans* $\mu_2\text{-Mes}$ ligands, with two $\text{Cu} - \text{C}_{\text{ortho}}$ long contacts of 2.614 Å. Neglecting these very weak interactions, the monomer optimized geometry can be approximated to D_{3h} . Selected averaged computed data are given in Tables 1 and 2.

The small $\text{Cu} \cdots \text{Cu}$ Wiberg bond indices (WBIs), as well as the natural atomic charges are consistent with metallophilic Cu(I)···Cu(I) interactions.⁴⁴ Yet, the WBI value (0.100) of the shortest

$\text{Cu}_b \cdots \text{Cu}_c$ (2.403 Å) contacts reflects the existence of some weak covalent character. The natural orbital populations (Table 2) indicate that the Cu(I) atoms receive significant ligand donation into their formally empty 4s AO. The trend within the metal natural charges is somewhat counterintuitive, owing to the fact that one would expect the charge of Cu to increase with the number of hard base oxygen atoms it is connected to. However, the trend is reordered when considering the quantum theory of atoms in molecules (QTAIM)⁴⁵ charges which are expected to have better physical meaning. Surprisingly, the QTAIM analysis of the electron density does not reveal any $\text{Cu} \cdots \text{Cu}$ bond critical point (BCP), even for the shortest $\text{Cu}_b \cdots \text{Cu}_c$ separations. Only ring critical points (RCPs) can be found in the middle of the $\text{Cu}_a\text{Cu}_b\text{Cu}_c\text{Cu}_b$ "squares". This is at variance with a former detailed QTAIM investigation on a series of cuprophilic dimers by Dinda et al.,¹⁰ which concluded that only in a few cases BCPs cannot be found. Since our level of calculation is not that different from the one considered in the DFT calculations of Dinda et al.,¹⁰ we presumed that the cause for the absence of BCPs in our $[\text{Cu}_{10}\text{O}_2(\text{Mes})_6]$ monomer could be due to the peculiar nature of the bridging ligands (mesityls). Consistently, our calculations on the mesityl-bridged cyclic oligomers $\text{Cu}_4(\mu\text{-Mes})_4$ and $\text{Cu}_5(\mu\text{-Mes})_5$ ⁴⁶ did not yield Cu···Cu BCPs, but similar electronic features as found in the $[\text{Cu}_{10}\text{O}_2(\text{Mes})_6]$

monomer (see selected computed data in **Tables S3 and S4**). Switching from mesityl to the simpler hydride ligand, we also calculated the $\text{Cu}_n(\mu\text{-H})_n$ ($n = 2\text{--}5$) model series (**Tables S3 and S4**), which is known for having planar structures in their global energy minima.²³ Again, no BCP was found for these oligomers, except for the $\text{Cu}_2(\mu\text{-H})_2$ dimer (see its descriptors in **Table 3**). In this homogeneous series, this feature appears to be related to the Cu···Cu distance. Indeed, applying the dimer optimized Cu···Cu short distance (2.157 Å) to the trimer results in the appearance of Cu···Cu BCPs with similar characteristics as that of the dimer. On the other hand, applying the longer trimer optimized Cu···Cu distance (2.357 Å) to the dimer results in the BCP disappearance. It is, however, to be noticed that copper connectivity is also playing a role, as exemplified by a single-point (SP) calculation on the linear (D_{coh}) H–Cu···Cu–H model with a substantially longer Cu···Cu distance of 2.800 Å, which in fact exhibits a BCP (**Table 3**). This last result is consistent with the work of Dinda et al.,¹⁰ who found Cu···Cu BCPs for $(\text{LCuX})_2$ dimers at distances larger than 3 Å. Therefore, at this stage one could conclude that, at least at the DFT level, a Cu(I)···Cu(I) metallophilic interaction may or may not be associated with the presence of a BCP, independently of the nature of the ligands and with a flexible dependence on the Cu···Cu distance.

As expected for a stable Cu(I) species, the computed highest occupied molecular orbital–lowest unoccupied molecular orbital (HOMO–LUMO) gap of the monomer is large (4.28 eV). The highest occupied Kohn–Sham orbitals have a large 3d(Cu) character with some minor mesityl and still less oxygen admixtures. The lowest vacant orbitals have mixed 4s/4p(Cu) and mesityl character. As a whole, the level ordering and localization is not much different from that found earlier at the EHT level by Haakansson et al.³⁶

In order to investigate the unsupported Cu···Cu interaction linking the $[\text{Cu}_{10}\text{O}_2(\text{Mes})_6]$ repeat units in the solid state structure of **1**, we optimized the geometry of a $[\text{Cu}_{10}\text{O}_2(\text{Mes})_6]_3$ trimer in C_2 symmetry, for having its central monomer mimicking as much as possible the repeat unit in the infinite polymer (**Figure 2**). Its metrical data (**Table 1**) are very similar to those of the isolated monomer and close to their SC-XRD counterparts. Interestingly, the Cu···Cu contacts which link the monomers together (2.554 Å) are shorter than the experimental ones (2.776 Å). This difference may originate in part from the fact that, in the optimized trimer, this “unsupported” contact is in fact (weakly) bridged by mesityl ligands with two long C_{ipso}···Cu contacts of 2.613 and 2.629 Å. Another peculiarity of this optimized geometry is the appearance of three long Cu_a···Cu_c intramonomer contacts (2.869 Å in each of the external monomers and 2.730 Å in the central unit, **Figure 2**). The corresponding distance in the SC-XRD structure of **1** is a bit longer (2.902 Å). Overall, the above-discussed structural differences between the SC-XRD structure of **1** and the optimized geometry of the trimer remain rather small in terms of relative variations, considering the lengths of the contacts in question. Whereas natural orbital analysis was not possible owing to the large size of this computed model, a QTAIM analysis could be performed. The QTAIM charges of the central unit are very close to those in the isolated monomer (**Table 2**). Surprisingly, three (and only three) Cu···Cu BCPs are now present in the trimer. Two of them are associated with the intermonomer “unsupported” Cu_b···Cu_{b'} contacts (2.554 Å) and the other one is the short Cu_a···Cu_c contact within the central monomer (2.730 Å). It is of note that these contacts are

not the shortest Cu···Cu ones in the trimer (**Table 1**). The corresponding topological parameters characterizing these BCPs are given in **Table 3**. They are of the same order of magnitude as those found by Dinda et al.¹⁰ in their investigation of various Cu(I) dimeric systems. The low values of ρ , $\nabla^2\rho$, and H at the BCP's, as well as the $|V|/G$ ratio somewhat larger than 1, are indicative of a weak bonding with some covalent character, reminding hydrogen bonds.¹⁰

In order to get an energetic point of view on the bonding between monomers in the $[\text{Cu}_{10}\text{O}_2(\text{Mes})_6]_3$ trimer, the intermonomer bond dissociation energy (BDE) was calculated as half of the difference between the energy of the relaxed trimer and three times the energy of the relaxed monomer. Whereas a value lower than 10 kcal/mol is expected for the corresponding BSSE-corrected BDE,¹¹ a surprisingly large value is found, 43.4 kcal/mol, *i.e.* reaching that of a Br–Br bond. Deeper insight into this energetics can be achieved through an energy decomposition analysis (EDA) of the interaction between two frozen molecular fragments, according to the Morokuma–Ziegler procedure.^{47–49} The two fragments considered are the central monomer on one side and the two terminal monomers (as a single entity) on the other side. The total bonding energy (TBE) between the two fragments is expressed as the sum of four components, the Pauli repulsion (E_{Pauli}), the electrostatic interaction energy (E_{elstat}), the orbital interaction energy (E_{orb}) and the component associated with the dispersion forces (E_{disp}). Their values are given in **Table 4**, divided by 2 to express them with respect to only one intermonomer bond.

Table 4. Morokuma–Ziegler Energy Decomposition Analysis in the Trimer $[\text{Cu}_{10}\text{O}_2(\text{Mes})_6]_3$, Based on the Interaction between the Central $[\text{Cu}_{10}\text{O}_2(\text{Mes})_6]$ Unit and the Fragment Composed of the Two Other (External) Units^a

	DFT-optimized geometry	SC-XRD frozen geometry
$E_{\text{Pauli}}/2$	119.4	66.9
$E_{\text{elstat}}/2$	-88.4	-51.2
$E_{\text{orb}}/2$	-37.7	-23.4
$E_{\text{disp}}/2$	-53.0	-44.7
TBE/2 ^b	-59.8	-52.5

^aAll values in kcal/mol. ^bTotal bonding energy (TBE) = $E_{\text{Pauli}} + E_{\text{elstat}} + E_{\text{orb}} + E_{\text{disp}}$.

As expected, the TBE/2 value is larger than that of BDE, mainly because the considered fragments geometries are not relaxed. When BSSE corrections are applied, it is lowered to 53.8 kcal/mol, thus leaving the contribution of the fragment geometry relaxation to the reasonable value of ~10 kcal/mol. The various TBE components in **Table 4** are significantly larger in absolute value than those reported by Brands et al. in their DFT investigation of a series of Cu(I) dimers.⁸ The E_{orb} component (which represents the covalent contribution) and the E_{disp} component are of the same order of magnitude, but the latter dominates. Neglecting E_{disp} in the TBE sum, would end up with TBE = 6.8 kcal/mol, a value of the expected order of magnitude for an unsupported Cu(I)···Cu(I) metallophilic interaction.^{8,11} The large E_{disp} value originates mainly from the ligand···ligand interactions, the Cu···Cu contribution being evaluated to ~2 kcal/mol from linear RCU(I)···Cu(I)R models. Metal···mesityl contributions may also contribute through the two long bridging C_{ipso}···Cu contacts of 2.613 and 2.629 Å (see above).

Thus, one may be tempted to explain the much larger than expected BDE or TBE/2 values by the fact that the optimized trimer is somehow “artificially” more compact than the SC-XRD structure, with in particular the existence of these (although long) C_{ipso}···Cu contacts bridging the intermonomer Cu···Cu contacts, which are missing in the solid-state structure. This is why we also carried out both QTAIM and EDA calculations on a nonoptimized trimer geometry extracted from the SC-XRD structure of the polymer. This time, five Cu···Cu BCPs are found. Two of them are associated with the intermonomer unsupported Cu_b···Cu_{b'} contacts (2.766 Å). The other three correspond to one Cu_a···Cu_c contact in each monomeric unit (2.902 Å). Thus, the only difference with the optimized monomer is the presence of two supplementary Cu_a···Cu_c BCPs in the terminal monomers, which is consistent with the fact that in this structure the three monomers are identical. The corresponding BCP descriptors (Table 3) are also identical and quite similar to those obtained for the optimized trimer (Table 3).

The TBE components obtained for this experimental geometry (Table 4) are all lower in absolute values than their counterparts in the optimized trimer. This is particularly noticeable for $E_{\text{Pauli}}/2$ and $E_{\text{elstat}}/2$, whose sum can be assimilated to the steric repulsion energy. Nevertheless, the $E_{\text{orb}}/2$ and $E_{\text{disp}}/2$ values are of the same order of magnitude as in the optimized trimer and the resulting TBE/2 value (~52.5 kcal/mol) remains close to that of the optimized structure. Yet, the intermonomer BSSE-corrected BDE computed from frozen SC-XRD geometries (43.2 kcal/mol) is almost equal to that found for our optimized models (43.4 kcal/mol). One can thus conclude that the rather large computed intermonomer bond energy is mainly the result of stabilizing ligand···ligand and metal···ligand dispersion forces, with some weak covalent contributions. The importance of ligand···ligand attraction in the stabilization of metallophilic architectures has already been demonstrated by Wan *et. al.* for some d⁸ and d¹⁰ organometallic systems,³⁰ as well as in a modeling investigation of cuprophilic systems under high pressure.¹³

The combination in the trimer of the monomer orbitals, results in its highest occupied orbitals being antibonding between the monomers, whereas a bonding character is observed for its lowest vacant orbitals. As a result, the HOMO–LUMO gap of the trimer is substantially reduced to 3.14 eV. This difference between the monomer and the trimer in their HOMO–LUMO gaps, is reflected in their TD-DFT-simulated UV/vis spectra, which are shown in Figure 3 together with that of Cu₅(Mes)₅ as a reference. Whereas the latter compound exhibits a single MLCT absorption band peaking at 275 nm (experimentally 290 nm in toluene), the [Cu₁₀O₂(Mes)₆] monomer absorbs in a large range below 400 nm, due to a series of MLCT transitions. When going from the monomer to the trimer, a new band appears at lower energy around 500 nm. This band is principally due to a HOMO–LUMO transition, thus associated with the intermonomer bonding and of major Cu(3d) → Cu(4s/4p) nature. It is likely that this band will grow up in intensity with the degree of [Cu₁₀O₂(Mes)₆] oligomerization, thus reaching its maximum in the infinite polymer. Accordingly, this band can be associated with the strong absorption massif around 500 nm observed in the experimental solid-state spectrum of 1 (Figure 3).

As is the case with many compounds showcasing cuprophilic interactions, compound 1 exhibits notable fluorescent properties in the solid state when irradiated at 360 nm, featuring a

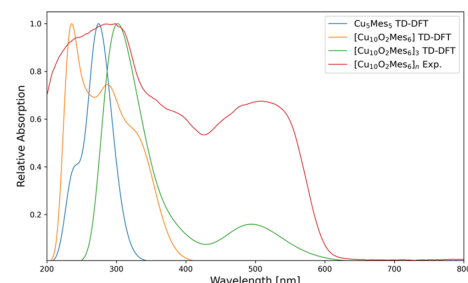


Figure 3. TD-DFT-simulated spectra of Cu₅Mes₅, the [Cu₁₀O₂(Mes)₆] monomer and the [Cu₁₀O₂(Mes)₆]₃ trimer, all considered in their optimized geometries as well as the experimental solid-state UV-vis of [Cu₁₀O₂(Mes)₆]_n (1).

broad emission band peaking at 590 nm and gradually diminishing intensity until 800 nm (Figure 4). To discern its

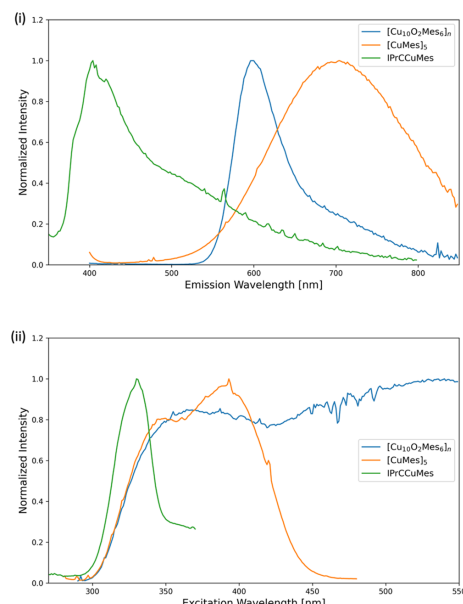


Figure 4. Emission (i) and Excitation (ii) spectra of I, [CuMes]₅, and IPrCuMes.

luminescent characteristics, we compared it with [CuMes]₅, known to display luminescence,⁵⁰ and the NHC stabilized IPrCuMes, analyzing emission and excitation spectra, quantum yield, and lifetime measurements. While IPrCuMes, devoid of cuprophilic interactions, only demonstrates an emission peak at 400 nm, both I and [CuMes]₅ manifest broad emission bands at longer wavelengths, typical for Cu···Cu based luminescence.^{24–26} NHC coordinated copper complexes are known to be phosphorescent and emit at lower wavelengths through

LMCT.⁵¹ The solution of **1** also displays a broad emission band peaking at 710 nm, indicating the presence of Cu···Cu metallophilic interactions in the complex set of species present in solution (Figure S15).

Lifetime measurements reveal both $[\text{CuMes}]_5$ and IMes-CuMes to be phosphorescent (Table 5), whereas the polymeric

Table 5. Luminescent Properties of **1, $[\text{CuMes}]_5$ and IPrCuMes**

compound	λ_{ex} [nm]	λ_{em} [nm]	Φ [%]	τ_1 [ns]	τ_2 [ns]
$[\text{Cu}_{10}\text{O}_2(\text{Mes})_6]_n$ (1)	350–550	590	4.8	7.4	30.9
$[\text{CuMes}]_5$	345; 390	710	1.5	>20000	
IPrCuMes	330	400	2.5	>20000	

compound **1** exhibits two distinct fluorescent emissions ($\tau_1 = 7.4$ ns and $\tau_2 = 30.9$ ns). Furthermore, excitation spectra illustrate IMesCuMes with a narrow range (maximizing at 330 nm). This contrasts with the cuprophilic compounds which display luminescent properties across a broad spectrum of excitation, especially **1** exhibiting emissions at 600 nm for excitations ranging quasi-continuously between 350 and 550 nm (Figure 4).

CONCLUSIONS

The exploration of **1** originally reported by Haakansson et al.³⁶ allowed us to delve into the complex properties of cuprophilic interactions. We found **1** to, in fact, be a polymer with $[\text{Cu}_{10}\text{O}_2(\text{Mes})_6]_n$ repeating unit showcasing both supported as well as unsupported cuprophilic interactions. The bonding analysis of **1** and related cuprophilic models underlines the complexity of these Cu(I)···Cu(I) interactions, which, at least at the DFT level, may or may not be associated with bond critical points, regardless of the fact they are ligand-supported or not, but depending mainly on the nature and configuration of the metal coordination spheres and only loosely on the Cu(I)···Cu(I) distance. On the other hand, the Morokuma–Ziegler energy decomposition analysis underpins the importance of ligand···ligand and metal···ligand dispersion forces in the bonding between monomers, resulting in bonding energies significantly larger than found in previous reports based on simpler dimeric models where Cu(I)···Cu(I) interaction predominates. As can be expected for cuprophilic compounds, **1** showcases strong luminescent properties, which come from two distinct fluorescent emissions. Through the new information generated in this study, we believe that we can provide better understanding of Cu(I)···Cu(I) interactions, as well as of their fascinating properties.

EXPERIMENTAL SECTION

All manipulations were carried out using standard Schlenk techniques under inert atmospheres. Schlenk tubes were rinsed with 1,1,1,3,3-hexamethyldisilazane (HMDS), evacuated, heated with a heat gun at 650 °C and filled with argon after cooling. Solvents were dried using an MBraun Solvent Purification System. The final H₂O content of all solvents was measured via Karl Fischer titration and was below 5 ppm. Starting materials Cu_xMes₅⁴⁶ and IPrCuMes⁵² were synthesized according to literature procedures.

Synthesis of $[\text{Cu}_{10}\text{O}_2(\text{Mes})_6]_n$ (1**)**. 153 mg of CuMes (840 μmol, 1.00 equiv) was dissolved in 2.50 mL of toluene in a Schlenk tube with total volume of 13.0 mL. The yellow solution was degassed, the tube was filled with argon again and the argon atmosphere inside of the tube was pressurized with 0.50 bar of dioxygen (0.25 equiv, caution: the gas volume is of utmost importance) The solution was stirred at 60 °C for 2 h and the reaction tube then stored over 30 min at room temperature.

During this time, the solutions discolored from yellow to a darker brown-yellow tone. A Whatman filtration was carried out in order to get rid of some dark particles. The solvent was then removed *in vacuo* and the residue was solved in 3.00 mL of hexane. The cloudy whitish solution was stored at -32 °C overnight to give a bright red powder which was filtered by a Whatman filtration and then washed with 3.00 mL of hexane and dried *in vacuo* affording 25.8 mg of **1** (18.7 mmol, 22.2%).

¹³C MAS NMR (r.t., neat, 75 MHz): δ (ppm) = 30.41 (mesityl, CH₃), 154.16 (mesityl, CH).

Computational Details. Density Functional Theory (DFT) calculations were carried out with the use of the Amsterdam Density Functional code (ADF2020.101)⁵³ incorporating scalar relativistic corrections via the ZORA Hamiltonian.^{54,55} The PBE0 hybrid functional^{56–58} was used, with the addition of Grimme's D3(BJ) empirical corrections⁴² in order to take into account dispersion effects. All the geometry optimizations were performed with the all-electron triple- ξ Slater basis set plus two polarization functions (STO-TZP).⁵⁹ Natural atomic orbital (NAO) populations and Wiberg bond indices were computed with the natural bond orbital NBO6.0 program⁶⁰ implemented in the ADF2020.101 package. Energy decomposition analysis (EDA) calculations were carried out according to the Morokuma–Ziegler formalism.^{47–49} Because of the size of the computed trimer, the reported quantum theory of atoms in molecules (QTAIM)^{45,61,62} data were obtained with the smaller STO-TZP basis set,⁵⁹ after having checked on the smaller $\text{Cu}_2(\mu\text{-H})_4$, $\text{Cu}_4(\mu\text{-Mes})_4$, $\text{Cu}_5(\mu\text{-Mes})_5$ models, as well as the $[\text{Cu}_{10}\text{O}_2(\text{Mes})_6]$ monomer that the results obtained with the larger STO-TZP basis set are similar. For the sake of computational time, time-dependent-DFT (TD-DFT) calculations were performed by using the Gaussian16 package,⁶³ with the PBE0 functional^{56–58} and the Def2SVP basis set.^{64,65} The UV-visible spectra were simulated from the computed TD-DFT singlet–singlet transitions and their oscillator strengths, each transition being associated with a Gaussian function of half-height width equal to 2000 cm⁻¹. Since compound **1** is not phosphorescent, the (forbidden) singlet–triplet transitions were not computed when performing TD-DFT calculations.

ASSOCIATED CONTENT

Supporting Information

The Supporting Information is available free of charge at <https://pubs.acs.org/doi/10.1021/acs.inorgchem.4c02377>.

Additional information containing analytical methods details, supplementary NMR, IR, UV-vis, powder XRD, LIFDI-MS spectra and diffractograms, SC-XRD details and additional DFT values (PDF)

Cartesian coordinates of the DFT optimized structures (XYZ)

Accession Codes

CCDC 2360768 contains the supplementary crystallographic data for this paper. These data can be obtained free of charge via www.ccdc.cam.ac.uk/data_request/cif, by emailing data-request@ccdc.cam.ac.uk, or by contacting The Cambridge Crystallographic Data Centre, 12 Union Road, Cambridge CB2 1EZ, UK; fax: +44 1223 336033.

AUTHOR INFORMATION

Corresponding Authors

Roland A. Fischer – Technical University of Munich, TUM
School of Natural Sciences, Department of Chemistry, Chair of Inorganic and Metal–Organic Chemistry, 85748 Garching, Germany; Catalysis Research Centre, Technical University of Munich, 85748 Garching, Germany; orcid.org/0000-0002-7532-5286; Email: roland.fischer@tum.de

Jean-Yves Saillard — Univ Rennes, CNRS, ISCR-UMR 6226, 35000 Rennes, France; [ORCID iD](https://orcid.org/0000-0003-4469-7922)
Email: jean-yves.saillard@univ-rennes1.fr

Authors

Raphael Bühler — Technical University of Munich, TUM School of Natural Sciences, Department of Chemistry, Chair of Inorganic and Metal–Organic Chemistry, 85748 Garching, Germany; Catalysis Research Centre, Technical University of Munich, 85748 Garching, Germany; [ORCID iD](https://orcid.org/0009-0005-9277-8809)

Robert M. Wolf — Technical University of Munich, TUM School of Natural Sciences, Department of Chemistry, Chair of Inorganic and Metal–Organic Chemistry, 85748 Garching, Germany; Catalysis Research Centre, Technical University of Munich, 85748 Garching, Germany

Christian Gemel — Technical University of Munich, TUM School of Natural Sciences, Department of Chemistry, Chair of Inorganic and Metal–Organic Chemistry, 85748 Garching, Germany; Catalysis Research Centre, Technical University of Munich, 85748 Garching, Germany

Johannes Stephan — Technical University of Munich, TUM School of Natural Sciences, Department of Chemistry, Chair of Inorganic and Metal–Organic Chemistry, 85748 Garching, Germany; Catalysis Research Centre, Technical University of Munich, 85748 Garching, Germany; [ORCID iD](https://orcid.org/0000-0003-4087-0070)

Simon N. Deger — Technical University of Munich, TUM School of Natural Sciences, Department of Chemistry, Chair of Inorganic and Metal–Organic Chemistry, 85748 Garching, Germany; Catalysis Research Centre, Technical University of Munich, 85748 Garching, Germany

Samia Kahhal — Univ Rennes, CNRS, ISCR-UMR 6226, 35000 Rennes, France; [ORCID iD](https://orcid.org/0000-0001-5719-553X)

Complete contact information is available at:
<https://pubs.acs.org/10.1021/acs.inorgchem.4c02377>

Author Contributions

The manuscript was written through contributions of all authors. All authors have given approval to the final version of the manuscript.

Funding

This work was funded by the German Research Foundation (DFG) within a Reinhart Koselleck Project (FI-502/44-1) and the TUM Graduate School.

Notes

The authors declare no competing financial interest.

ACKNOWLEDGMENTS

The authors thank Dr. Gabriele Raudaschl-Sieber for the MAS NMR measurements and Silva M. Kronawitter for the powder XRD measurements.

REFERENCES

- (1) Carvajal, M. A.; Alvarez, S.; Novoa, J. J. The Nature of Intermolecular Cu¹⁺–Cu¹⁺ Interactions: A Combined Theoretical and Structural Database Analysis. *Chem.—Eur. J.* **2004**, *10* (9), 2117–2132.
- (2) Harisomayajula, N. V. S.; Makovetsky, S.; Tsai, Y.-C. Cuprophilic Interactions in and between Molecular Entities. *Chem.—Eur. J.* **2019**, *25* (38), 8936–8954.
- (3) Schmidbaur, H.; Schier, A. Auophilic interactions as a subject of current research: an up-date. *Chem. Soc. Rev.* **2012**, *41* (1), 370–412.
- (4) Sculfert, S.; Braunstein, P. Intramolecular d₁₀–d₁₀ interactions in heterometallic clusters of the transition metals. *Chem. Soc. Rev.* **2011**, *40* (5), 2741–2760.
- (5) Zhang, L.; Li, X.-X.; Lang, Z.-L.; Liu, Y.; Liu, J.; Yuan, L.; Lu, W.-Y.; Xia, Y.-S.; Dong, L.-Z.; Yuan, D.-Q.; Lan, Y.-Q. Enhanced Cuprophilic Interactions in Crystalline Catalysts Facilitate the Highly Selective Electroreduction of CO₂ to CH₄. *J. Am. Chem. Soc.* **2021**, *143* (10), 3808–3818.
- (6) Zheng, J.; Lu, Z.; Wu, K.; Ning, G.-H.; Li, D. Coinage-Metal-Based Cyclic Trinuclear Complexes with Metal–Metal Interactions: Theories to Experiments and Structures to Functions. *Chem. Rev.* **2020**, *120* (17), 9675–9742.
- (7) Schmidbaur, H.; Schier, A. Argentophilic Interactions. *Angew. Chem., Int. Ed.* **2015**, *54* (3), 746–784.
- (8) Brands, M. B.; Nitsch, J.; Guerra, C. F. Relevance of Orbital Interactions and Pauli Repulsion in the Metal–Metal Bond of Coinage Metals. *Inorg. Chem.* **2018**, *57* (5), 2603–2608.
- (9) Claveria-Cadiz, F.; Arriatá-Perez, R.; Guajardo-Maturana, R.; Muñoz-Castro, A. Survey of short and long cuprophilic d₁₀–d₁₀ contacts for tetrานuclear copper clusters. Understanding of bonding and ligand role from a planar superatom perspective. *New J. Chem.* **2018**, *42* (11), 8874–8881.
- (10) Dinda, S.; Samuelson, A. G. The Nature of Bond Critical Points in Dinuclear Copper(I) Complexes. *Chem.—Eur. J.* **2012**, *18* (10), 3032–3042.
- (11) Hermann, H. L.; Boche, G.; Schwerdtfeger, P. Metallophilic Interactions in Closed-Shell Copper(I) Compounds—A Theoretical Study. *Chem.—Eur. J.* **2001**, *7* (24), 5333–5342.
- (12) Kölmel, C.; Ahlrichs, R. An ab Initio Investigation of Copper Complexes with Supershort Copper–Copper Distances. *J. Phys. Chem. A* **1990**, *94*, 5536–5542.
- (13) Lu, Z.; Archambault, C. M.; Li, S.; Syed, U.; Wang, S.; Kumar, A.; Shen, G.; Liu, Z.; Omary, M. A.; Yan, H. Modulating the Extent of Anisotropic Cuprophilicity via High Pressure with Piezochromic Luminescence Sensitization. *J. Phys. Chem. Lett.* **2023**, *14* (2), 508–S15.
- (14) Mehrotra, P. K.; Hoffmann, R. Copper(I)–copper(I) interactions. Bonding relationships in d₁₀–d₁₀ systems. *Inorg. Chem.* **1978**, *17* (8), 2187–2189.
- (15) Merz, K. M.; Hoffmann, R. d₁₀–d₁₀ Interactions: Multinuclear Copper(I) Complexes. *Inorg. Chem.* **1988**, *27*, 2120–2127.
- (16) Muñoz-Castro, A. Magnetic Response Properties of Coinage Metal Macrocycles. Insights into the Induced Magnetic Field through the Analysis of [Cu₄(Mes)₅]⁺, [Ag₄(Mes)₅]⁺, and [Au₅(Mes)₅]⁺ (Mes = 2,4,6-Me₃C₆H₂). *J. Phys. Chem. C* **2012**, *116* (32), 17197–17203.
- (17) Poblet, J.-M.; Bénard, M. Cuprophilicity, a still elusive concept: a theoretical analysis of the ligand-unsupported Cu¹⁺–Cu¹⁺ interaction in two recently reported complexes. *Chem. Commun.* **1998**, No. 11, 1179–1180.
- (18) Pyykö, P. Strong Closed-Shell Interactions in Inorganic Chemistry. *Chem. Rev.* **1997**, *97* (3), 597–636.
- (19) Pyykö, P.; Runeberg, N.; Mendizabal, F. Theory of the d₁₀–d₁₀ Closed-Shell Attraction: I. Dimers Near Equilibrium. *Chem.—Eur. J.* **1997**, *3* (9), 1451–1457.
- (20) Rabåå, H.; Sundholm, D.; Omary, M. A. A theoretical study of M–M' polar-covalent bonding in heterobimetallic multinuclear organometallic complexes of monovalent group 11 metal centres. *Phys. Chem. Chem. Phys.* **2023**, *25* (11), 7642–7647.
- (21) Rabilloud, F. Structure and Bonding in Coinage Metal Halide Clusters M_nX_n, M = Cu, Ag, Au; X = Br, I; n = 1–6. *J. Phys. Chem. A* **2012**, *116* (13), 3474–3480.
- (22) Stewart, K. R.; Lever, J. R.; Whangbo, M.-H. Molecular Orbital Study of the Bonding and Structure of Organocuprates. *J. Org. Chem.* **1982**, *47*, 1472–1474.
- (23) Tsipis, A. C.; Tsipis, C. A. Hydrometal Analogues of Aromatic Hydrocarbons: A New Class of Cyclic Hydrocoppers(I). *J. Am. Chem. Soc.* **2003**, *125* (5), 1136–1137.

- (24) Biswas, S.; Negishi, Y. A Comprehensive Analysis of Luminescent Crystallized Cu Nanoclusters. *J. Phys. Chem. Lett.* **2024**, *15* (4), 947–958.
- (25) Huitorel, B.; Utrera-Melero, R.; Massuyeau, F.; Mevelec, J.-Y.; Baptiste, B.; Polian, A.; Gacoin, T.; Martineau-Corcos, C.; Perruchas, S. Luminescence mechanochromism of copper iodide clusters: a rational investigation. *Dalton Trans.* **2019**, *48* (22), 7899–7909.
- (26) Li, B.; Fan, H.-T.; Zang, S.-Q.; Li, H.-Y.; Wang, L.-Y. Metal-containing crystalline luminescent thermochromic materials. *Coord. Chem. Rev.* **2018**, *377*, 307–329.
- (27) Liu, G.-N.; Xu, R.-D.; Guo, J.-S.; Miao, J.-L.; Zhang, M.-J.; Li, C. Regulating the near-infrared region to visible-light emission by adjusting cuprophilic interactions for blue light-excited phosphors. *J. Mater. Chem. C* **2021**, *9* (27), 8589–8595.
- (28) Harisomayajula, N. V. S.; Wu, B.-H.; Lu, D.-Y.; Kuo, T.-S.; Chen, I. C.; Tsai, Y.-C. Ligand-Unsupported Cuprophilicity in the Preparation of Dodecacopper(I) Complexes and Raman Studies. *Angew. Chem., Int. Ed.* **2018**, *57* (31), 9925–9929.
- (29) Zhang, J.-P.; Wang, Y.-B.; Huang, X.-C.; Lin, Y.-Y.; Chen, X.-M. Metallophilicity versus π - π Interactions: Ligand-Unsupported Argentophilicity/Cuprophilicity in Oligomers-of-Dimers $[M_2L_n]_n$ ($M = \text{CuI}$ or AgI , $L =$ tridentate ligand). *Chem.—Eur. J.* **2005**, *11* (2), 552–561.
- (30) Wan, Q.; Yang, J.; To, W.-P.; Che, C.-M. Strong metal–metal Pauli repulsion leads to repulsive metallophilicity in closed-shell d_8 and d_{10} organometallic complexes. *Proc. Natl. Acad. Sci. U.S.A.* **2021**, *118* (1), No. e2019265118.
- (31) Favaro, M.; Xiao, H.; Cheng, T.; Goddard, W. A.; Yano, J.; Crumlin, E. J. Subsurface oxide plays a critical role in CO_2 activation by $\text{Cu}(111)$ surfaces to form chemisorbed CO_2 , the first step in reduction of CO_2 . *Proc. Natl. Acad. Sci. U.S.A.* **2017**, *114* (26), 6706–6711.
- (32) Laudenschleger, D.; Ruland, H.; Muhrer, M. Identifying the nature of the active sites in methanol synthesis over $\text{Cu}/\text{ZnO}/\text{Al}_2\text{O}_3$ catalysts. *Nat. Commun.* **2020**, *11* (1), No. 3898.
- (33) Li, C. W.; Kanan, M. W. CO_2 Reduction at Low Overpotential on Cu Electrodes Resulting from the Reduction of Thick Cu_2O Films. *J. Am. Chem. Soc.* **2012**, *134* (17), 7231–7234.
- (34) Yang, Y.; Jia, T.; Han, Y.-Z.; Nan, Z.-A.; Yuan, S.-F.; Yang, F.-L.; Sun, D. An All-Alkynyl Protected 74-Nuclei Silver(I)–Copper(I)–Oxo Nanocluster: Oxo-Induced Hierarchical Bimetal Aggregation and Anisotropic Surface Ligand Orientation. *Angew. Chem., Int. Ed.* **2019**, *58* (35), 12280–12285.
- (35) Pearson, R. G. Hard and soft acids and bases, HSAB, part II: Underlying theories. *J. Chem. Educ.* **1968**, *45* (10), 643.
- (36) Haakansson, M.; Ortsdahl, M.; Jagner, S.; Sigala, M. P.; Eisenstein, O. Splitting Dioxygen with Mesitylcopper(I). An Arylcopper(I) Intermediate, Formed in a Coupling Reaction, Containing Two Trapped Trigonal Pyramidal Coordinated Oxides. *Inorg. Chem.* **1993**, *32*, 2018–2024.
- (37) Bondi, A. van der Waals Volumes and Radii. *J. Phys. Chem. A* **1964**, *68*, 441–451.
- (38) Che, C.-M.; Mao, Z.; Miskowski, V. M.; Tse, M.-C.; Chan, C.-K.; Cheung, K.-K.; Phillips, D. L.; Leung, K.-H. Cuprophilicity: Spectroscopic and Structural Evidence for Cu–Cu Bonding Interactions in Luminescent Dinuclear Copper(I) Complexes with Bridging Diposphane Ligands. *Angew. Chem., Int. Ed.* **2000**, *39* (22), 4084–4088.
- (39) Mao, Z.; Chao, H.-Y.; Hui, Z.; Che, C.-M.; Fu, W.-F.; Cheung, K.-K.; Zhu, N. $^3[(d_{x^2-y^2}, d_y)(p_z)]$ Excited States of Binuclear Copper(I) Phosphine Complexes: Effect of Copper–Ligand and Copper–Copper Interactions on Excited State Properties and Photocatalytic Reductions of the 4,4'-Dimethyl-2,2'-bipyridinium Ion in Alcohols. *Chem.—Eur. J.* **2003**, *9* (12), 2885–2894.
- (40) Ho, W. C.; Tay, Q.; Qi, H.; Huang, Z.; Li, J.; Chen, Z. Photocatalytic and Adsorption Performances of Faceted Cuprous Oxide (Cu_2O) Particles for the Removal of Methyl Orange (MO) from Aqueous Media. *Molecules* **2017**, *22* (4), 677 DOI: 10.3390/molecules22040677.
- (41) Muhr, M.; Heiß, P.; Schütz, M.; Bühler, R.; Gemel, C.; Linden, M. H.; Linden, H. B.; Fischer, R. A. Enabling LIFDI-MS measurements of highly air sensitive organometallic compounds: a combined MS/glovebox technique. *Dalton Trans.* **2021**, *50* (26), 9031–9036.
- (42) Grimme, S. Semiempirical GGA-type density functional constructed with a long-range dispersion correction. *J. Comput. Chem.* **2006**, *27* (15), 1787–1799.
- (43) Grimme, S.; Djukic, J.-P. Cation–Cation “Attraction”: When London Dispersion Attraction Wins over Coulomb Repulsion. *Inorg. Chem.* **2011**, *50* (6), 2619–2628.
- (44) Silalahi, R. P. B.; Chiu, T.-H.; Liang, H.; Kahlah, S.; Saillard, J.-Y.; Liu, C. W. A heteroleptic fused bi-cubooctahedral Cu_{21}S_2 cluster. *Chem. Commun.* **2023**, *59* (63), 9638–9641.
- (45) Bader, R. F. W. *Atoms in Molecules: A Quantum Theory*; Oxford University Press: Oxford, England, 1990.
- (46) Meyer, E. M.; Gambarotta, S.; Floriani, C.; Chiesi-Villa, A.; Guastini, C. Polyunary aryl derivatives of Group 11 metals. Synthesis, solid-state-solution structural relationship, and reactivity with phosphines. *Organometallics* **1989**, *8* (4), 1067–1079.
- (47) Bickelhaupt, F. M.; Baerends, E. J. *Reviews in Computational Chemistry*; Wiley: New York, 2000; pp 1–86.
- (48) Morokuma, K. Molecular Orbital Studies of Hydrogen Bonds. III. C = O–H–O Hydrogen Bond in $\text{H}_3\text{CO} \cdots \text{H}_2\text{O}$ and $\text{H}_2\text{CO} \cdots 2\text{H}_2\text{O}$. *J. Chem. Phys.* **1971**, *55* (3), 1236–1244.
- (49) Ziegler, T.; Rauk, A. A theoretical study of the ethylene–metal bond in complexes between copper(1+), silver(1+), gold(1+), platinum(0) or platinum(2+) and ethylene, based on the Hartree–Fock–Slater transition-state method. *Inorg. Chem.* **1979**, *18* (6), 1558–1565.
- (50) Yam, V. W.-W.; Lee, W.-K.; Cheung, K. K.; Lee, H.-K.; Leung, W.-P. Photophysics and photochemical reactivities of organocupper(I) complexes. Crystal structure of $[\text{Cu}_2(\text{PPh}_3)_2]_2(\mu,\mu)^1\text{C}\equiv\text{CPh}_2$. *J. Chem. Soc., Dalton Trans.* **1996**, No. 13, 2889–2891.
- (51) Li, Q.; Zhao, F.; Xu, S.; Xia, H.; Wang, J.; Wang, Y. Accesses to electronic structures and the excited states of blue luminescent copper(I) complexes containing N-heterocyclic carbene ligands: a DFT/TDDFT exploitation. *J. Mol. Model.* **2014**, *20* (9), No. 2416.
- (52) Kuehn, L.; Eichhorn, A. F.; Schmidt, D.; Marder, T. B.; Radius, U. NHC-stabilized copper(I) aryl complexes and their transmetalation reaction with aryl halides. *J. Organomet. Chem.* **2020**, *919*, No. 121249.
- (53) te Veld, G.; Bickelhaupt, F. M.; Baerends, E. J.; Fonseca Guerra, C.; van Gisbergen, S. J. A.; Snijders, J. G.; Ziegler, T. Chemistry with ADF. *J. Comput. Chem.* **2001**, *22* (9), 931–967.
- (54) Lenthe, E. v.; Baerends, E. J.; Snijders, J. G. Relativistic regular two-component Hamiltonians. *J. Chem. Phys.* **1993**, *99* (6), 4597–4610.
- (55) van Lenthe, E.; Baerends, E. J.; Snijders, J. G. Relativistic total energy using regular approximations. *J. Chem. Phys.* **1994**, *101* (11), 9783–9792.
- (56) Adamo, C.; Barone, V. Toward reliable density functional methods without adjustable parameters: The PBE0 model. *J. Chem. Phys.* **1999**, *110* (13), 6158–6170.
- (57) Perdew, J. P.; Burke, K.; Ernzerhof, M. Generalized Gradient Approximation Made Simple. *Phys. Rev. Lett.* **1996**, *77* (18), 3865–3868.
- (58) Perdew, J. P.; Burke, K.; Ernzerhof, M. Generalized Gradient Approximation Made Simple [Phys. Rev. Lett. 77, 3865 (1996)]. *Phys. Rev. Lett.* **1997**, *78*, 1396.
- (59) van Lenthe, E.; Baerends, E. J. Optimized Slater-type basis sets for the elements 1–118. *J. Comput. Chem.* **2003**, *24* (9), 1142–1156.
- (60) Glendening, E. D.; Badenhorst, J. K.; Reed, A. E.; Carpenter, J. E.; Bohmann, J. A.; Morales, C. M.; Weinhold, F. NBO 6.0, University of Wisconsin (Madison, WI, 2001, <http://nbo6.chem.wisc.edu>).
- (61) Rodriguez, J. I. An efficient method for computing the QTAIM topology of a scalar field: The electron density case. *J. Comput. Chem.* **2013**, *34* (8), 681–686.
- (62) Rodriguez, J. I.; Bader, R. F. W.; Ayers, P. W.; Michel, C.; Götz, A. W.; Bo, C. A high performance grid-based algorithm for computing QTAIM properties. *Chem. Phys. Lett.* **2009**, *472* (1), 149–152.
- (63) Frisch, M. J.; Trucks, G. W.; Schlegel, H. B.; Scuseria, G. E.; Robb, M. A.; Cheeseman, J. R.; Scalmani, G.; Barone, V.; Petersson, G.

A.; Nakatsuji, H.; Li, X.; Caricato, M.; Marenich, A. V.; Bloino, J.; Janesko, B. G.; Gomperts, R.; Mennucci, B.; Hratchian, H. P.; Ortiz, J. V.; Izmaylov, A. F.; Sonnenberg, J. L.; Williams-Young, D.; Ding, F.; Lipparini, F.; Egidi, F.; Goings, J.; Peng, B.; Petrone, A.; Henderson, T.; Ranasinghe, D.; Zakrzewski, V. G.; Gao, J.; Rega, N.; Zheng, G.; Liang, W.; Hada, M.; Ehara, M.; Toyota, K.; Fukuda, R.; Hasegawa, J.; Ishida, M.; Nakajima, T.; Honda, Y.; Kitao, O.; Nakai, H.; Vreven, T.; Throssell, K.; Montgomery Jr., J. A.; Peralta, J. E.; Ogliaro, F.; Bearpark, M. J.; Heyd, J. J.; Brothers, E. N.; Kudin, K. N.; Staroverov, V. N.; Keith, T. A.; Kobayashi, R.; Normand, J.; Raghavachari, K.; Rendell, A. P.; Burant, J. C.; Iyengar, S. S.; Tomasi, J.; Cossi, M.; Millam, J. M.; Klene, M.; Adamo, C.; Cammi, R.; Ochterski, J. W.; Martin, R. L.; Morokuma, K.; Farkas, O.; Foresman, J. B.; Fox, D. J. *Gaussian 16 Rev. A.03*; Wallingford, CT, 2016.

(64) Weigend, F. Accurate Coulomb-fitting basis sets for H to Rn. *Phys. Chem. Chem. Phys.* **2006**, *8* (9), 1057–1065.

(65) Weigend, F.; Ahlrichs, R. Balanced basis sets of split valence, triple zeta valence and quadruple zeta valence quality for H to Rn: Design and assessment of accuracy. *Phys. Chem. Chem. Phys.* **2005**, *7* (18), 3297–3305.

5 Conclusion and Outlook

The study of metal-substrate interactions using ligated heterometallic TM/E clusters and complexes contains numerous synthetic and conceptual difficulties that need to be overcome. Expanding the toolbox of available E'R ligands is a necessity in order to broaden our horizon of synthetically available TM/E clusters and complexes, as showcased by the first isolation of an all gallylene coordinated homoleptic ruthenium complex, namely $[\text{Ru}(\text{GaTMP})_5]$. The saturated ruthenium center, however, is detrimental to the study of metal substrate interactions.

The labile $[(\text{Ru}(\text{GaCp}^*)_3\text{H}_2]$ species formed through hydrogenolysis enables the study of the role played by the GaCp^* ligand in bond activations at the Ru center. The synthesis of $[(\text{Ru}(\text{GaCp}^*)_3(\text{SiEt}_3)\text{H}_3]$ and the *in situ* study of $[\text{Ru}(\text{GaCp}^*)_3(\text{C}_7\text{H}_7)\text{H}_3]$ show that the properties of the Ga^{l} ligand play a significant role in the formation of these Si-H and C-H activated species as compared to “classic” ruthenium phosphine complexes. This underlines the high potential offered by tuning the properties of the transition metal using TM-E bonds.

Remains the question of controlling the reactivity of the isolated species. In the case of $[(\text{Ru}(\text{GaCp}^*)_3(\text{SiEt}_3)\text{H}_3]$, this could be achieved through a photoinduced reductive elimination of dihydrogen and triethyl silane, leading to the transient 14 valence electron $[(\text{Ru}(\text{GaCp}^*)_3]$ intermediate. The ensuing catalytic hydrogenation of alkynes underlines the potential of incorporating such “protecting groups” for the controlled promotion of reactive sites. The isolation of the homoleptic $[\text{Ru}(\text{GaTMP})_5]$, the investigations into the C-H activation leading to $[\text{Ru}(\text{GaCp}^*)_3(\text{C}_7\text{H}_7)\text{H}_3]$, and the “deprotection” of $[(\text{Ru}(\text{GaCp}^*)_3(\text{SiEt}_3)\text{H}_3]$ (Figure 22) show the possibilities for reactivity directing by tuning the ligand shell of the heterometallic system. Nevertheless, when attempting to mimic the reactions occurring at heterogeneous catalysts and the structural diversity they showcase, the issue remains of how representative a single isolated cluster or complex is.

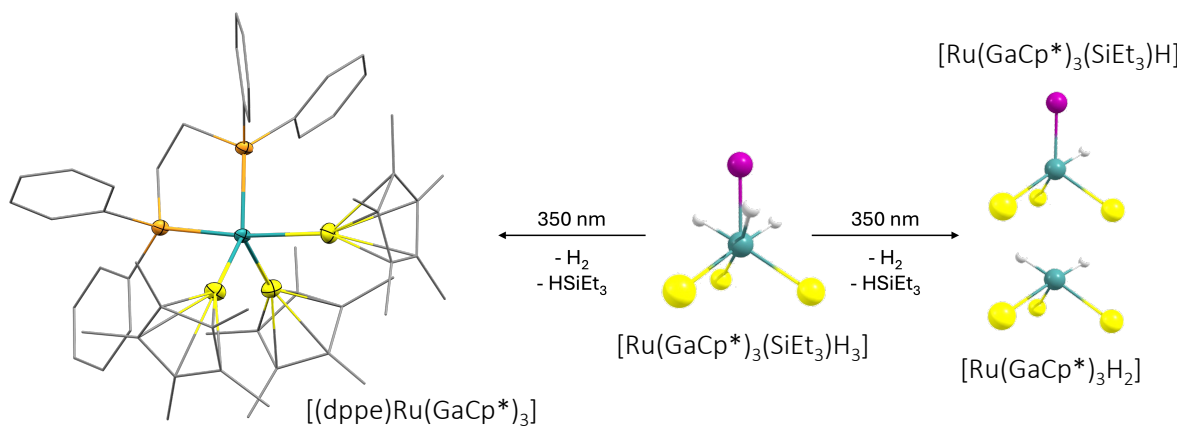
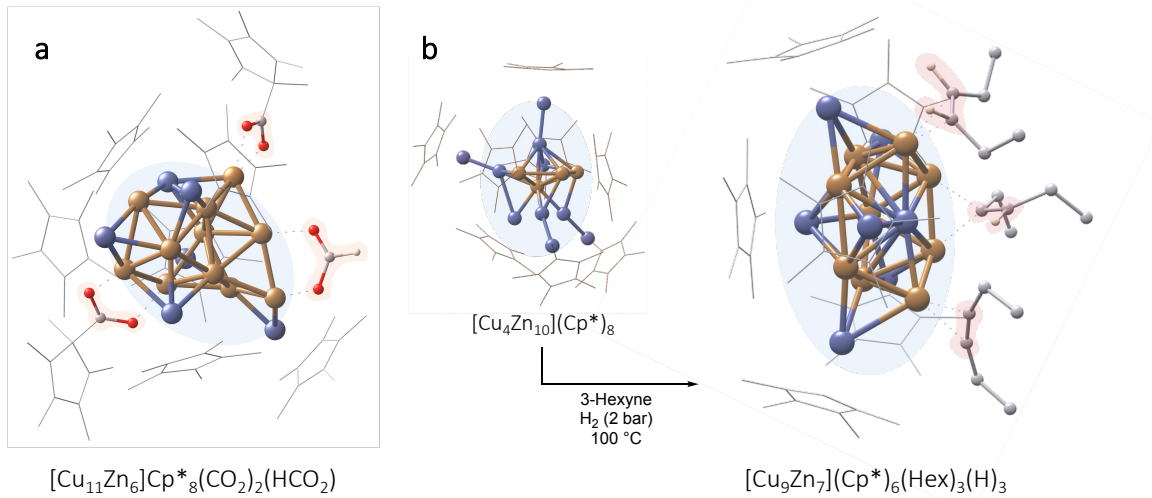


Figure 22: Overview of the photochemically induced reactivity of $[(\text{Ru}(\text{GaCp}^)_3(\text{SiEt}_3)\text{H}_3]$. The photoinduced reductive elimination dihydrogen and triethyl silane leads to reactive species showing catalytic activity in the hydrogenation of alkynes. (ruthenium = green, gallium = yellow, silicon = violet, carbon = grey, hydrogen = white).*

Studying metal substrate interactions using ligated heterometallic TM/E clusters and complexes faces a major challenge: structural diversity, or lack thereof. The concept of “living libraries” of heterometallic clusters makes the exploration of metal substrate interactions possible with the full chemical complexity offered by the unselective nature of the organometallic reactions occurring during cluster formation.

Conclusions regarding reactive properties of the all-hydrocarbon ligated Cu/Zn clusters can be obtained by monitoring the library evolution after both weak and strong perturbations. The formation of the formate-containing cluster $[\text{Cu}_{11}\text{Zn}_6]\text{Cp}^*_8(\text{CO}_2)_2(\text{HCO}_2)$ (Figure 23a) after subsequent conversion of the original Cu/Zn library with CO_2 and H_2 is the illustration of the possibilities offered by this approach. Additionally, the pre-catalyst $[\text{Cu}_4\text{Zn}_{10}](\text{Cp}^*)_8$ (Figure 23b) for the observed semihydrogenation catalysis of 3-hexyne could be isolated and fully characterized, showcasing the usefulness of the library approach for reactivity screening of a complex heterometallic cluster landscape.



*Figure 23: a) Computed structure of $[Cu_{11}Zn_6]Cp^*_8(CO_2)_2(HCO_2)$ formed through the treatment of the Cu/Zn library with CO_2 and H_2 ; b) Crystal structure of the isolated $[Cu_4Zn_{10}](Cp^*)_8$ which upon conversion with 3-hexyne and H_2 forms $[Cu_9Zn_7](Cp^*)_6(Hex)_3H_3$, acting as catalyst in the semihydrogenation of 3-hexyne (copper = orange, zinc = blue carbon = grey, hydrogen = white),*

The next step for a comprehensive simulation of chemical complexity mimicking heterogeneous surfaces is the incorporation of oxygen. First results towards this goal have been obtained by synthesizing the polymeric $[Cu_{10}O_2Mes_6]_n$. Though the preparation of this sub-oxidic organocopper compound can be achieved, its undefined nature in solution makes it a poor candidate for preparing sub-oxidic heterometallic clusters. Moving away from dioxygen, the use of oxidizing reagents such as amine oxides or aminoxy radicals could make way for an exciting new cluster landscape.

6 References

- [1] R. Ferro, A. Saccone, *Intermetallic Chemistry*, Pergamon Materials Science, Elsevier, Amsterdam, **2008**.
- [2] M. Ellner, B. Predel, in *Intermetallic compounds - principles and practice*, Vol. 1, J. H. Westbrook, R. L. Fleischer, Ed.; John Wiley & Sons Ltd, Chichester, **1994**, pp. 91-125.
- [3] F. Studt, F. Abild-Pedersen, T. Bligaard, R. Z. Sørensen, C. H. Christensen, J. K. Nørskov, *Science* **2008**, *320*, 1320-1322.
- [4] in *Beyer/Walter: Lehrbuch der Organischen Chemie*, Hirzel Verlag, 23 ed., **1998**, p. 406.
- [5] R. R. Schrock, *Acc. Chem. Res.* **1986**, *19*, 342-348.
- [6] M. Scholl, S. Ding, C. W. Lee, R. H. Grubbs, *Org. Lett.* **1999**, *1*, 953-956.
- [7] P. Schwab, M. B. France, J. W. Ziller, R. H. Grubbs, *Angew. Chem. Int. Ed.* **1995**, *34*, 2039-2041.
- [8] T. Cadenbach, C. Gemel, R. Schmid, R. A. Fischer, *J. Am. Chem. Soc.* **2005**, *127*, 17068-17078.
- [9] S. Bajo, M. M. Alcaide, J. López-Serrano, J. Campos, *Chem. Eur. J.* **2021**, *27*, 16422-16428.
- [10] S. Bajo, C. A. Theulier, J. Campos, *ChemCatChem* **2022**, *14*, e202200157.
- [11] R. C. Cammarota, C. C. Lu, *J. Am. Chem. Soc.* **2015**, *137*, 12486-12489.
- [12] R. C. Cammarota, M. V. Vollmer, J. Xie, J. Ye, J. C. Linehan, S. A. Burgess, A. M. Appel, L. Gagliardi, C. C. Lu, *J. Am. Chem. Soc.* **2017**, *139*, 14244-14250.
- [13] M. Behrens, F. Studt, I. Kasatkin, S. Kühl, M. Hävecker, F. Abild-Pedersen, S. Zander, F. Girgsdies, P. Kurr, B.-L. Kniep, M. Tovar, R. W. Fischer, J. K. Nørskov, R. Schlögl, *Science* **2012**, *336*, 893-897.
- [14] D. Laudenschleger, H. Ruland, M. Muhler, *Nat. Commun.* **2020**, *11*, 3898.
- [15] S. P. Bhaskar, B. R. Jagirdar, *J. Alloys Compd.* **2017**, *694*, 581-595.
- [16] S. Kattel, P. J. Ramírez, J. G. Chen, J. A. Rodriguez, P. Liu, *Science* **2017**, *355*, 1296-1299.
- [17] Q.-L. Tang, Q.-J. Hong, Z.-P. Liu, *J. Catal.* **2009**, *263*, 114-122.
- [18] Y. Yang, J. Evans, J. A. Rodriguez, M. G. White, P. Liu, *Phys. Chem. Chem. Phys.* **2010**, *12*, 9909-9917.
- [19] G. Centi, S. Perathoner, in *CO₂: A Valuable Source of Carbon* (Eds.: M. D. Falco, G. Iaquaniello, G. Centi), Springer London, London, **2013**, pp. 147-169.
- [20] H. Schwarz, *Catal. Sci. Technol.* **2017**, *7*, 4302-4314.
- [21] U. Heiz, F. Vanolli, A. Sanchez, W. D. Schneider, *J. Am. Chem. Soc.* **1998**, *120*, 9668-9671.
- [22] T. Tsukamoto, T. Kambe, A. Nakao, T. Imaoka, K. Yamamoto, *Nat. Commun.* **2018**, *9*, 3873.
- [23] K. Wimalasena, *Med. Res. Rev.* **2011**, *31*, 483-519.
- [24] G. M. Miller, *J. Neurochem.* **2011**, *116*, 164-176.
- [25] T. Imaoka, H. Kitazawa, W.-J. Chun, S. Omura, K. Albrecht, K. Yamamoto, *J. Am. Chem. Soc.* **2013**, *135*, 13089-13095.
- [26] A. L. Mackay, *Acta Crystallogr.* **1962**, *15*, 916-918.
- [27] O. Echt, K. Sattler, E. Recknagel, *Phys. Rev. Lett.* **1981**, *47*, 1121-1124.
- [28] M. v. Laue, *Z. Kristallogr.* **1943**, *105*, 124-133.

- [29] J. D. Erickson, E. G. Mednikov, S. A. Ivanov, L. F. Dahl, *J. Am. Chem. Soc.* **2016**, *138*, 1502-1505.
- [30] J. Weßing, C. Ganesamoorthy, S. Kahlal, R. Marchal, C. Gemel, O. Cador, A. C. H. Da Silva, J. L. F. Da Silva, J.-Y. Saillard, R. A. Fischer, *Angew. Chem. Int. Ed.* **2018**, *57*, 14630-14634.
- [31] D. J. Wales, R. B. King, in *Encyclopedia of Inorganic Chemistry*, 2nd Ed., King RB, Editor-in-Chief, John-Wiley and Sons, Ltd, **2005**.
- [32] S. Scharfe, F. Kraus, S. Stegmaier, A. Schier, T. F. Fässler, *Angew. Chem. Int. Ed.* **2011**, *50*, 3630-3670.
- [33] M. R. Churchill, J. P. Hutchinson, *Inorg. Chem.* **1978**, *17*, 3528-3535.
- [34] P. Jena, Q. Sun, *Chem. Rev.* **2018**, *118*, 5755-5870.
- [35] T. Tsukamoto, T. Kambe, T. Imaoka, K. Yamamoto, *Nat. Rev. Chem.* **2021**, *5*, 338-347.
- [36] W. Ekardt, *Z. Phys. B - Condensed Matter* **1996**, *103*, 305-312.
- [37] S. N. Khanna, P. Jena, *Phys. Rev. B* **1995**, *51*, 13705-13716.
- [38] K. Freitag, H. Banh, C. Gemel, R. W. Seidel, S. Kahlal, J.-Y. Saillard, R. A. Fischer, *Chem. Commun.* **2014**, *50*, 8681-8684.
- [39] J. Vollet, J. R. Hartig, H. Schnöckel, *Angew. Chem. Int. Ed.* **2004**, *43*, 3186-3189.
- [40] P. A. Clayborne, O. Lopez-Acevedo, R. L. Whetten, H. Grönbeck, H. Häkkinen, *Eur. J. Inorg. Chem.* **2011**, *2011*, 2649-2652.
- [41] T.-H. Chiu, J.-H. Liao, Y.-Y. Wu, J.-Y. Chen, Y. J. Chen, X. Wang, S. Kahlal, J.-Y. Saillard, C. W. Liu, *J. Am. Chem. Soc.* **2023**, *145*, 16739-16747.
- [42] B. Zamora, L. Nyulászi, T. Höltzl, *ChemPhysChem* **2024**, *25*, e202300409.
- [43] C. Ganesamoorthy, J. Weßing, C. Kroll, R. W. Seidel, C. Gemel, R. A. Fischer, *Angew. Chem. Int. Ed.* **2014**, *53*, 7943-7947.
- [44] J. Hornung, J. Weßing, M. Molon, K. Dilchert, C. Gemel, R. A. Fischer, *J. Organomet. Chem.* **2018**, *860*, 78-84.
- [45] J. Hornung, M. Muhr, C. Gemel, R. A. Fischer, *Dalton Trans.* **2019**, *48*, 11743-11748.
- [46] M. Muhr, H. Liang, L. Allmendinger, R. Bühler, F. E. Napoli, D. Ukaj, M. Cokoja, C. Jandl, S. Kahlal, J.-Y. Saillard, C. Gemel, R. A. Fischer, *Angew. Chem. Int. Ed.* **2023**, *62*, e202308790.
- [47] T. Bollermann, T. Cadenbach, C. Gemel, K. Freitag, M. Molon, V. Gwildies, R. A. Fischer, *Inorg. Chem.* **2011**, *50*, 5808-5814.
- [48] P. Jutzi, B. Neumann, L. O. Schebaum, A. Stammler, H.-G. Stammler, *Organometallics* **1999**, *18*, 4462-4464.
- [49] B. Buchin, C. Gemel, A. Kempter, T. Cadenbach, R. A. Fischer, *Inorg. Chim. Acta* **2006**, *359*, 4833-4839.
- [50] M. Muhr, J. Stephan, L. Staiger, K. Hemmer, M. Schütz, P. Heiß, C. Jandl, M. Cokoja, T. Kratky, S. Günther, D. Huber, S. Kahlal, J.-Y. Saillard, O. Cador, A. C. H. Da Silva, J. L. F. Da Silva, J. Mink, C. Gemel, R. A. Fischer, *Commun. Chem.* **2024**, *7*, 29.
- [51] I. Antsiburov, M. Schütz, R. Bühler, M. Muhr, J. Stephan, C. Gemel, W. Klein, S. Kahlal, J.-Y. Saillard, R. A. Fischer, *Inorg. Chem.* **2024**.
- [52] H. Banh, J. Hornung, T. Kratz, C. Gemel, A. Pöthig, F. Gam, S. Kahlal, J.-Y. Saillard, R. A. Fischer, *Chem. Sci.* **2018**, *9*, 8906-8913.
- [53] K. Freitag, C. Gemel, P. Jerabek, I. M. Oppel, R. W. Seidel, G. Frenking, H. Banh, K. Dilchert, R. A. Fischer, *Angew. Chem. Int. Ed.* **2015**, *54*, 4370-4374.
- [54] M. Schütz, C. Gemel, M. Muhr, C. Jandl, S. Kahlal, J.-Y. Saillard, R. A. Fischer, *Chem. Sci.* **2021**, *12*, 6588-6599.

-
- [55] M. Schütz, M. Muhr, K. Freitag, C. Gemel, S. Kahlal, J.-Y. Saillard, A. C. H. Da Silva, J. L. F. Da Silva, T. F. Fässler, R. A. Fischer, *Inorg. Chem.* **2020**, *59*, 9077-9085.
 - [56] M. Schütz, C. Gemel, W. Klein, R. A. Fischer, T. F. Fässler, *Chem. Soc. Rev.* **2021**, *50*, 8496-8510.
 - [57] I. Fujii, K. Semba, Q.-Z. Li, S. Sakaki, Y. Nakao, *J. Am. Chem. Soc.* **2020**, *142*, 11647-11652.
 - [58] W.-C. Shih, O. V. Ozerov, *J. Am. Chem. Soc.* **2017**, *139*, 17297-17300.
 - [59] B. J. Graziano, M. V. Vollmer, C. C. Lu, *Angew. Chem. Int. Ed.* **2021**, *60*, 15087-15094.
 - [60] T. Steinke, C. Gemel, M. Cokoja, M. Winter, R. A. Fischer, *Angew. Chem. Int. Ed.* **2004**, *43*, 2299-2302.
 - [61] R. Dramanac, I. Labat, I. Brukner, R. Crkvenjakov, *Genomics* **1989**, *4*, 114-128.
 - [62] M. J. Rosok, D. E. Yelton, L. J. Harris, J. Bajorath, K.-E. Hellström, I. Hellström, G. A. Cruz, K. Kristensson, H. Lin, W. D. Huse, S. M. Glaser, *J. Biol. Chem.* **1996**, *271*, 22611-22618.
 - [63] I. Yofe, U. Weill, M. Meurer, S. Chuartzman, E. Zalckvar, O. Goldman, S. Ben-Dor, C. Schütze, N. Wiedemann, M. Knop, A. Khmelinskii, M. Schuldiner, *Nat. Methods* **2016**, *13*, 371-378.
 - [64] M. Muhr, P. Heiß, M. Schütz, R. Bühler, C. Gemel, M. H. Linden, H. B. Linden, R. A. Fischer, *Dalton Trans.* **2021**, *50*, 9031-9036.
 - [65] J. H. Gross, N. Nieth, H. B. Linden, U. Blumbach, F. J. Richter, M. E. Tauchert, R. Tompers, P. Hofmann, *Anal. Bioanal. Chem.* **2006**, *386*, 52-58.
 - [66] H. B. Linden, *Eur. J. Mass Spectrom.* **2004**, *10*, 459-468.
 - [67] P. Heiß, J. Hornung, C. Gemel, R. A. Fischer, *Chem. Commun.* **2022**, *58*, 4332-4335.
 - [68] M. Muhr, J. Hornung, J. Weßing, C. Jandl, C. Gemel, R. A. Fischer, *Inorg. Chem.* **2020**, *59*, 5086-5093.
 - [69] M. Hakansson, M. Ortendahl, S. Jagner, M. P. Sigalas, O. Eisenstein, *Inorg. Chem.* **1993**, *32*, 2018-2024.

7 Supporting Information

7.1 Supporting Information for Study I

Electronic Supplementary Material (ESI) for Dalton Transactions.
This journal is © The Royal Society of Chemistry 2024

SUPPORTING INFORMATION

Homoleptic Hexa and Penta Coordinated Gallium(I) Amide Complexes of Ruthenium and Molybdenum

Raphael Bühler^{#a}, Richard J. J. Weininger^{#a}, Johannes Stephan^a, Maximilian Muhr^a, Balasai M.-T. Bock^a, Christian Gemel^a, Roland A. Fischer^{a*}

#These authors contributed equally to this work

*Email: roland.fischer@tum.de

Chair of Inorganic and Metal-Organic Chemistry, Technical University of Munich, School of Natural Sciences, Department of Chemistry Lichtenbergstr. 4, 85748 Garching and Catalysis Research Center, Ernst-Otto-Fischer-Straße 1, 85748 Garching.

Table of Content

General Remarks.....	3
Analytical Methods	3
Computerized Analysis of Mass Spectra	3
Continuous Shape Measure ²	4
Comprehensive listing of homoleptic and closely related [M(ER*) _n] complexes known	5
NMR Data.....	9
IR Data.....	12
LIFDI-Mass Spectra.....	14
Crystallography	17
SC-XRD structure report for compound 1.....	17
SC-XRD structure report for compound 2.....	22
Calculated XYZ Coordinates	33
[Ru(GaTMP) ₅]	33
[Mo(GaTMP) ₆]	37

General Remarks

Unless stated otherwise, all synthetic manipulations were carried out using standard Schlenk techniques under an atmosphere of argon 4.6 purified by BTC-catalyst and dried over 3 Å molecular sieves or in a glovebox under an atmosphere of purified argon. All reactions were carried out in standardized Schlenk flasks and tubes which were rinsed with 1,1,1,3,3-hexamethyldisilyzane (HMDS), heated with a heat gun to 650 °C and cooled under vacuum argon. All synthesis of light sensitive compounds were performed under the red light. All solvents were carefully dried over molecular sieves and deuterated solvents were degassed prior to their use. All non-dried solvents used were distilled prior to their use. All the reagents were purchased from commercial sources and used as such without further purification.

Analytical Methods

NMR spectra were recorded on a Bruker Avance III 400US (1H, 400 MHz; 13C 101MHz). Chemical shifts are given relative to TMS and were referenced to the residual solvent peak as internal standards. Chemical shifts are reported in parts per million, downfield shifted from TMS, and are consecutively reported as position (δ H or δ C), relative integral, multiplicity (s = singlet, t = triplet, and m = multiplet) and assignment. FT-IR spectra were measured on an ATR setup with a Bruker Alpha FTIR spectrometer under an inert gas atmosphere in a glove-box. The mass spectra were taken using a Linden CMS LIFDI as ionization source and a ThermoFisher Scientific Exactive Plus Orbitrap as detector. The sample application was performed via a fumed silica capillary from a glovebox under an argon atmosphere to enable the measurement of highly air-sensitive compounds. The recorded mass spectra were evaluated using the FreeStyle 1.3 program from ThermoFisher Scientific and a fitting program developed by *Dr. Christian Gemel* details of which are outlined below. Reference isotope patterns were simulated using the enviPat Web application.¹

Computerized Analysis of Mass Spectra

The general procedure for computerized peak identification in LIFDI-MS involves utilizing a Java computer program (Java 11, openjdk-1.11.0). The program's fundamental principles and workflow are outlined below.

To begin spectrum analysis, the program employs automated pattern recognition, identifying local maxima above a specified threshold value (which users can adjust, defaulting to 1% of the highest peak in the spectrum) as peaks. These peaks are then grouped automatically into peak groups and subsequently into isotopic patterns through a recursive process. The algorithm initiates at the highest remaining peak in the peak list and searches both left and right for peaks with an exact m/z shift of $1/z$ from each other, within a user-defined error range (ϵ). Users input the charge z of the ions (defaulting to 1) and the recursive process terminates when no peaks remain in the peak list.

The resulting list comprises peak groups, which are considered isotopic patterns if they contain a minimum number of peaks (defaulting to 5, user-adjustable).

For pattern analysis, users provide a list of potential fragments by loading a file containing all conceivable fragments the observed ions may consist of (such as metal atoms, ligands, solvents, etc.). The program generates weight matches for each pattern by recursively combining these fragments into ions. All possible fragment combinations up to the m/z value of the respective pattern are calculated, using the pattern centroid (intensity-weighted average, (m/z)centroid) as the experimental average weight. Acceptable fragment combinations have a molar weight (Mw) falling within the range: (m/z)centroid – 2.1 < Mw < (m/z)centroid + 4.1. The subtraction of 2.1 accounts for a possible loss of 2 hydrogen atoms and the addition of 4.1 accounts for the possibility of up to four additional hydrogens, which are not part of the input fragments (accounting for dehydrogenation or hydrogenation/protonation during ionization).

As the list of fragment formulas is often extensive, a "sieving" step is conducted. Isotopic patterns for each fragment are calculated, and an "offset" value is determined by comparing exact m/z values of calculated and experimental patterns. Only patterns with an average offset value below a specified threshold (defaulting to 0.2, user-adjustable) are further considered. The program then computes the goodness of fit (GoF) value between experimental and calculated patterns, and vice versa, using least squares fitting resulting in a total GoF, ranging between 0 (no common peaks) and 1 (identical patterns).

In the output file, each pattern is listed with possible pattern matches and their corresponding final GoF values. Additionally, users can visually compare patterns to their calculated counterparts.

Continuous Shape Measure²

The method of continuous shape measure uses the N vertices of an experimentally determined coordination polyhedron normalized and centered in the origin of a three-dimensional cartesian coordinate system as their position vectors Q_i ($i = 1, 2, 3, \dots, N$). These are compared to the position vectors P_i ($i = 1, 2, 3, \dots, N$) of the N vertices of an ideal reference polyhedron that is equally centered and normalized. This is expressed as

$$S_Q(P) = \frac{1}{N} \min \sum_{i=1}^N |\vec{Q}_i - \vec{P}_i|^2 \times 100$$

A value of $S_Q(P) = 0$ thus represents the exact ideal shape, with increasing values indicating increasing distortions. This value was calculated from most ideal superimposition, determined by minimizing the distance between the superimposed polyhedral vertices by a numerical rotation algorithm. $S_Q(P)$ thus is the global minimum of these permutations.

In order to identify the cartesian coordinates of two polyhedra with minimized average distances of their vertices, a Java program has been used (Java 15, openjdk-15). The program takes as input the cartesian coordinates of two polyhedra, both centered at the origin. The program then freely rotates (and also stretches/shrinks on demand) one of the two polyhedra, finally locating the coordinates with minimized distances between the vertices of the two polyhedra in a recursive process.

The code for both programs can be obtained from the authors on request.

Comprehensive listing of homoleptic and closely related [M(ER^{*})_n] complexes known

In an endeavor to explore the then arising topic of isolobality between CO and E-R ligands (E = Al, Ga, In)(R = C(SiMe₃)₃, 1,2,3,4,5-pentamethylcyclopentadienyl (Cp^{*})) to gain access to a new class of mononuclear intermetallic complexes, *W. Uhl et. al.* in 1998 published the first mononuclear homoleptic transition metal (TM)-ER_x compound Ni(InC(SiMe₃)₃)₄.³ The homologous Ni(GaC(SiMe₃)₃)₄ followed shortly after further proving the concept beyond Indium.⁴ Pt(InC(SiMe₃)₃)₄ provided the first example of a homoleptic 3rd row TM-ER_(x) compound.⁵ During this time *P. Jutzi et. al.* presented Ni(GaCp^{*})₄, thus providing a vital broadening of the field.⁶ With Pd(GaCp^{*})₄, Pd(InC(SiMe₃)₃)₄ and Pt(GaCp^{*})₄ the homologous Ni-Pd-Pt row was completed by *R. A. Fischer et. al.* in 2003.⁷ The homologous homoleptic, mononuclear compounds of AlCp^{*}, Ni(AlCp^{*})₄ and Pd(AlCp^{*})₄ established Al within the row of E-R ligands.^{8, 9} The more electron rich metals yielded the respective cationic, homoleptic compounds Zn(GaCp)₄[BArF]₂ ([BArF] = Tetrakis[3,5-bis(trifluoromethyl)phenyl]borate), Cu(GaCp)₄[BArF] and Ag(GaCp)₄[BPh₄].^{10, 11} Fe(AlCp^{*})₅ and Ru(AlCp^{*})₅ are the first examples of homoleptic C-H activated isomers of TM-E-R complexes outside the d¹⁰ group with more than four group 13 metals coordinated.¹² Though not strictly homoleptic (GaCp)₄Rh(MeGa(η^1 -Cp^{*})) and (GaCp)₄Rh((OTf)Ga(η^1 -Cp^{*})) (OTf = trifluoromethanesulfonate) continue a trend of higher coordination numbers.^{13, 14} The haptotropically shifted, halogen bridged (GaCp)₃Ru(GaCl(η^1 -Cp^{*}))(Ga₂(μ -Cl)(η^1 -Cp^{*}))₂ provided the first hexa group 13 coordinated compound within the family.¹⁵ The highest unhalogenated coordination number within the group stands at six provided by the only haptoropically shifted Mo(GaCp)₆.^{14, 16}

Another group of mononuclear homoleptic intermetallic TM-E-R compounds is based on Ga(DDP) (DDP = 2-((2,6-diisopropylphenyl)amino-4-((2,6-diisopropylphenyl)imino)-2-pentene). The first one Au(Ga-(THF)(DDP))₂[BArF] was also presented by *R. A. Fischer et. al.* in 2006.¹⁷ This was followed up by Zn(Ga(Me)(DDP))₂.¹⁰ With Hg(Ga(SC₆F₅)(DDP))₂ the first homoleptic TM-E-R compound of Mercury was obtained.¹⁸ Cu(Ga(DDP))₂[OTf] then was the first and as of now only homoleptic complex of the series where the Ga(DDP) was only bound to the central TM atom.¹⁹ Interest in this

class of compounds has not abated, just in 2022, *J. Okuda et. al.* published their work around $Zn(GaH(DDP))_2$.²⁰ This group of compounds generally does not exceed a coordination number of two E-R. However *C. Jones et. al.* reported a coordination number of three with their NHC-analogous $Ga[N(Ar)]_2CNCy_2$ ($Ar = C_6H_3^iPr_2-2,6$) ($Cy = cyclohexyl$) in the homoleptic $Pt(Ga[N(Ar)]_2CNCy_2)_3$.²¹

Table S 1: List of homoleptic and closely related $[M(ER^*)_n]$ compounds known and sorted by coordination number of central atom M and element E

Compounds with central atom coordination number = 2	
$Au(Ga\cdot(THF)(DDP))_2[BArF]$	A. Kempfer, C. Gemel, N. J. Hardman, R. A. Fischer, <i>Inorg. Chem.</i> , 2006, 45 , 3133
$Hg(Ga(SC_6F_5)(DDP))_2$	G. Prabusankar, C. Gemel, M. Winter, R. W. Seidel, R. A. Fischer, <i>Chem. Eur. J.</i> , 2010, 16 , 6041
$Zn(GaH(DDP))_2$	L. J. Morris, T. Rajeshkumar, L. Maron, J. Okuda, <i>Chem. Eur. J.</i> , 2022, 28 , e202201480,
$Cu(Ga(DDP))_2[OTf]$	G. Prabusankar, S. Gonzalez-Gallardo, A. Doddi, C. Gemel, M. Winter, R. A. Fischer, <i>Eur. J. Inorg. Chem.</i> , 2010, 4415
$Zn(Ga(Me)(DDP))_2$	A. Kempfer, C. Gemel, T. Cadenbach, R. A. Fischer, <i>Inorg. Chem.</i> , 2007, 46 , 9481
Compounds with central atom coordination number = 3	
$Pt(Ga[N(Ar)]_2CNCy_2)_3$	S. P. Green, C. Jones, A. Stasch, <i>Inorg. Chem.</i> , 2007, 46 , 11
Compounds with central atom coordination number = 4	
$Pt(GaCp^*)_4$	C. Gemel, T. Steinke, D. Weiss, M. Cokoja, M. Winter, R. A. Fischer, <i>Organometallics</i> , 2003, 22 , 2705
$Pd(GaCp^*)_4$	C. Gemel, T. Steinke, D. Weiss, M. Cokoja, M. Winter, R. A. Fischer, <i>Organometallics</i> , 2003, 22 , 2705
$Ni(GaCp^*)_4$	P. Jutzi, B. Neumann, L. O. Schebaum, A. Stammmer, H.-G. Stammmer, <i>Organometallics</i> , 1999, 18 , 4462
$Ag(GaCp^*)_4[BPh_4]$	T. Bollermann, A. Puls, C. Gemel, T. Cadenbach, R. A. Fischer, <i>Dalton Trans.</i> , 2009, 1372
$Zn(GaCp^*)_4[BAr^F_2]$	A. Kempfer, C. Gemel, T. Cadenbach, R. A. Fischer, <i>Inorg. Chem.</i> , 2007, 46 , 9481

Cu(GaCp*) ₄ [BAr ^F]	T. Bollermann, A. Puls, C. Gemel, T. Cadenbach, R. A. Fischer, <i>Dalton Trans.</i> , 2009, 1372
Ni(GaC(TMS) ₃) ₄	W. Uhl, M. Benter, S. Melle, W. Saak, G. Frenking, J. Uddin, <i>Organometallics</i> , 1999, 18 , 3778
Pd(AlCp*) ₄	B. Buchin, T. Steinke, C. Gemel, T. Cadenbach, R. A. Fischer, <i>Z. anorg. allg. Chem.</i> , 2005, 631 , 2756
Ni(AlCp*) ₄	B. Buchin, T. Steinke, C. Gemel, T. Cadenbach, R. A. Fischer, <i>Z. anorg. allg. Chem.</i> , 2005, 631 , 2756
Ni(InC(TMS) ₃) ₄	W. Uhl, M. Pohlmann, R. Wartchow, <i>Angew. Chem. Int. Ed.</i> , 1998, 37 , 961 W. Uhl, M. Benter, S. Melle, W. Saak, G. Frenking, J. Uddin, <i>Organometallics</i> , 1999, 18 , 3778
Pt(InC(TMS) ₃) ₄	W. Uhl, S. Melle, <i>Z. anorg. allg. Chem.</i> , 2000, 626 , 2043
Pd(InC(TMS) ₃) ₄	C. Gemel, T. Steinke, D. Weiss, M. Cokoja, M. Winter, R. A. Fischer, <i>Organometallics</i> , 2003, 22 , 2705

Compounds with central atom coordination number = 5

(GaCp*) ₄ Rh(Ga(O ₃ SCF ₃)Cp*)	T. Bollermann, T. Cadenbach, C. Gemel, K. Freitag, M. Molon, V. Gwildies, R. A. Fischer, <i>Inorg. Chem.</i> , 2011, 50 , 5808
(GaCp*) ₄ Rh(MeGa(η^1 -Cp*)	T. Cadenbach, C. Gemel, D. Zacher, R. A. Fischer, <i>Angew. Chem. Int. Ed.</i> , 2008, 47 , 3438
Fe(AlCp*) ₅ (C-H activated)	T. Steinke, M. Cokoja, C. Gemel, A. Kempter, A. Krapp, G. Frenking, U. Zennek, R. A. Fischer, <i>Angew. Chem. Int. Ed.</i> , 2005, 44 , 2943
Ru(AlCp*) ₅ (C-H activated)	T. Steinke, M. Cokoja, C. Gemel, A. Kempter, A. Krapp, G. Frenking, U. Zennek, R. A. Fischer, <i>Angew. Chem. Int. Ed.</i> , 2005, 44 , 2943

Compounds with central atom coordination number = 6

Ru(GaCp*) ₄ (ClGaCp*) ₂	B. Buchin, C. Gemel, A. Kempter, T. Cadenbach, R. A. Fischer, <i>Inorg. Chim. Acta</i> , 2006, 359 , 4833
Mo(GaCp*) ₆ (Haptotropic Shifted)	T. Cadenbach, T. Bollermann, C. Gemel, I. Fernandez, M. von Hopffgarten, G. Frenking, R. A. Fischer, <i>Angew. Chem. Int. Ed.</i> , 2008, 47 , 9150, T. Bollermann, T. Cadenbach, C. Gemel, K. Freitag, M. Molon, V. Gwildies, R. A. Fischer, <i>Inorg. Chem.</i> , 2011, 50 , 5808

References

1. M. Loos, C. Gerber, F. Corona, J. Hollender and H. Singer, *Anal. Chem.*, 2015, **87**, 5738-5744.
2. M. Molon, C. Gemel, M. von Hopffgarten, G. Frenking and R. A. Fischer, *Inorg. Chem.*, 2011, **50**, 12296-12302.
3. W. Uhl, M. Pohlmann and R. Wartchow, *Angew. Chem. Int. Ed.*, 1998, **37**, 961-963.
4. W. Uhl, M. Benter, S. Melle, W. Saak, G. Frenking and J. Uddin, *Organometallics*, 1999, **18**, 3778-3780.
5. W. Uhl and S. Melle, *Z. anorg. allg. Chem.*, 2000, **626**, 2043-2045.
6. P. Jutzi, B. Neumann, L. O. Schebaum, A. Stammler and H.-G. Stammler, *Organometallics*, 1999, **18**, 4462-4464.
7. C. Gemel, T. Steinke, D. Weiss, M. Cokoja, M. Winter and R. A. Fischer, *Organometallics*, 2003, **22**, 2705-2710.
8. T. Steinke, C. Gemel, M. Cokoja, M. Winter and R. A. Fischer, *Angew. Chem. Int. Ed.*, 2004, **43**, 2299-2302.
9. B. Buchin, T. Steinke, C. Gemel, T. Cadenbach and R. A. Fischer, *Z. anorg. allg. Chem.*, 2005, **631**, 2756-2762.
10. A. Kempfer, C. Gemel, T. Cadenbach and R. A. Fischer, *Inorg. Chem.*, 2007, **46**, 9481-9487.
11. T. Bollermann, A. Puls, C. Gemel, T. Cadenbach and R. A. Fischer, *Dalton Trans.*, 2009, DOI: 10.1039/B815319A, 1372-1377.
12. T. Steinke, M. Cokoja, C. Gemel, A. Kempfer, A. Krapp, G. Frenking, U. Zenneck and R. A. Fischer, *Angew. Chem. Int. Ed.*, 2005, **44**, 2943-2946.
13. T. Cadenbach, C. Gemel, D. Zacher and R. A. Fischer, *Angew. Chem. Int. Ed.*, 2008, **47**, 3438-3441.
14. T. Bollermann, T. Cadenbach, C. Gemel, K. Freitag, M. Molon, V. Gwildies and R. A. Fischer, *Inorg. Chem.*, 2011, **50**, 5808-5814.
15. B. Buchin, C. Gemel, A. Kempfer, T. Cadenbach and R. A. Fischer, *Inorg. Chim. Acta.*, 2006, **359**, 4833-4839.
16. T. Cadenbach, T. Bollermann, C. Gemel, I. Fernandez, M. von Hopffgarten, G. Frenking and R. A. Fischer, *Angew. Chem. Int. Ed.*, 2008, **47**, 9150-9154.
17. A. Kempfer, C. Gemel, N. J. Hardman and R. A. Fischer, *Inorg. Chem.*, 2006, **45**, 3133-3138.
18. G. Prabusankar, C. Gemel, M. Winter, R. W. Seidel and R. A. Fischer, *Chem. Eur. J.*, 2010, **16**, 6041-6047.
19. G. Prabusankar, S. Gonzalez-Gallardo, A. Doddi, C. Gemel, M. Winter and R. A. Fischer, *Eur. J. Inorg. Chem.*, 2010, **2010**, 4415-4418.
20. L. J. Morris, T. Rajeshkumar, L. Maron and J. Okuda, *Chem. Eur. J.*, 2022, **28**, e202201480.
21. S. P. Green, C. Jones and A. Stasch, *Inorg. Chem.*, 2007, **46**, 11-13.

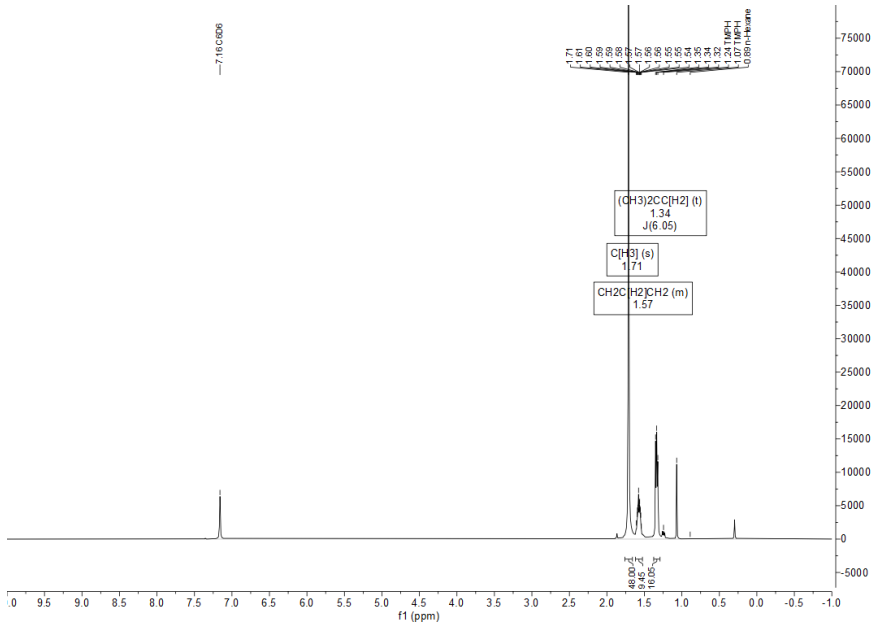
NMR Data

Figure S 1: ¹H-NMR Spectrum of **1** in benzene-*d*₆.

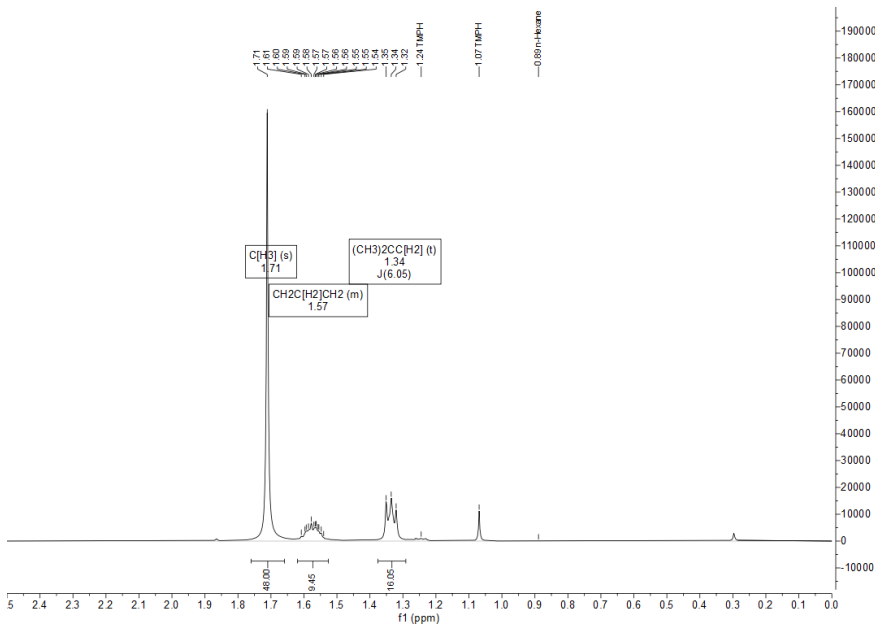


Figure S 2: ¹H-NMR Spectrum of **1** in benzene-*d*₆ from 2.50 ppm to 0.00 ppm.

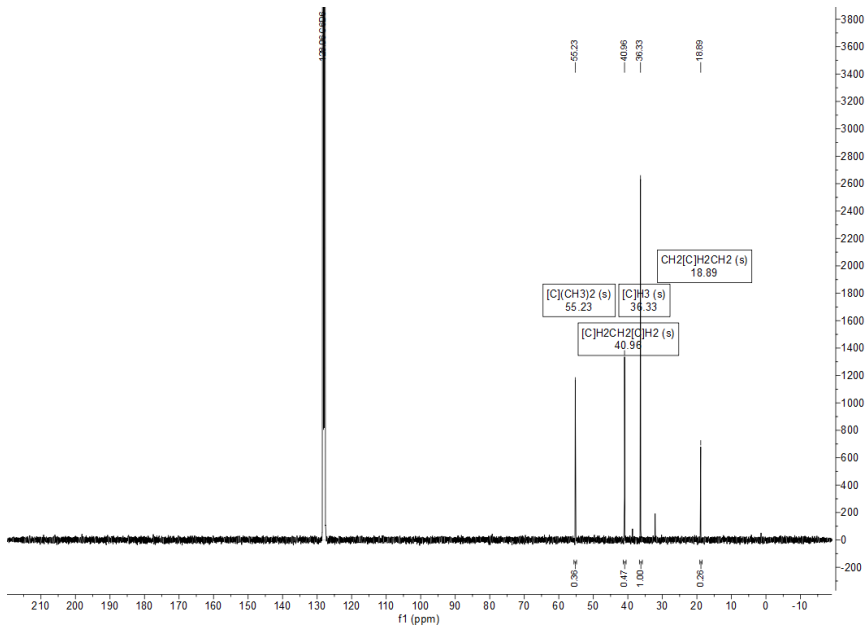


Figure S 3: ^{13}C -NMR Spectrum of **1** in benzene- d_6 .

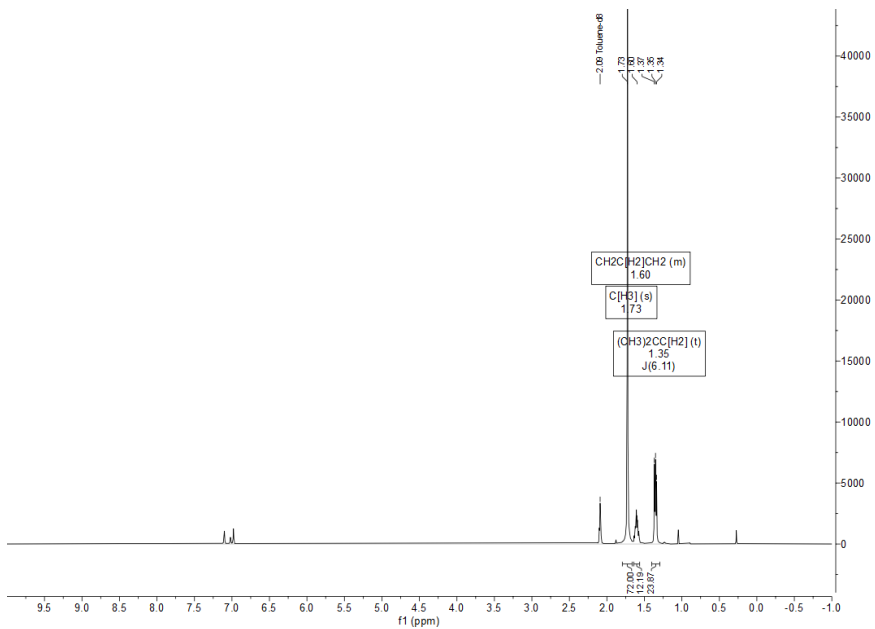


Figure S 4: ^1H -NMR Spectrum of **2** in toluene- d_6 from 2.50 ppm to 0.00 ppm.

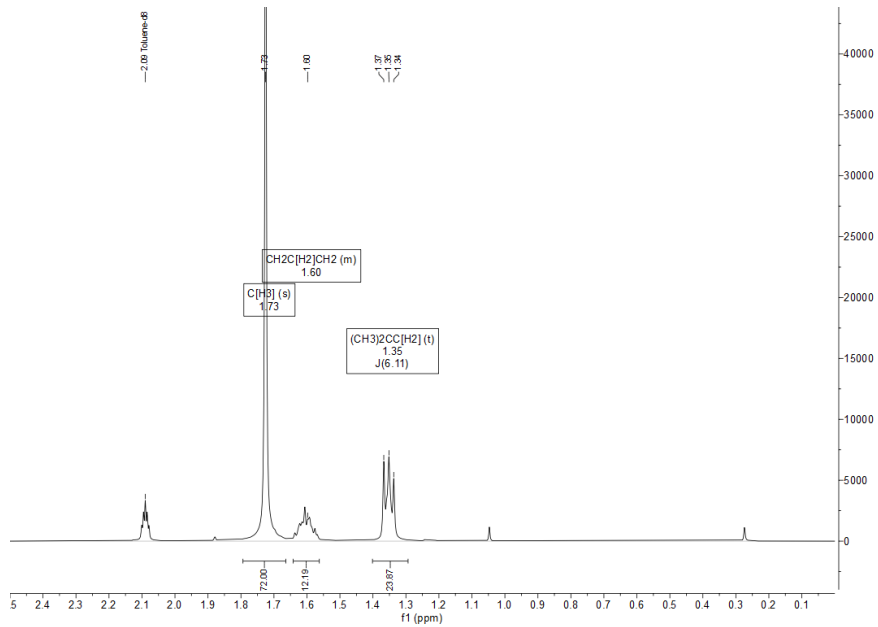


Figure S 5: ^1H -NMR Spectrum of **2** in toluene- d_8 .

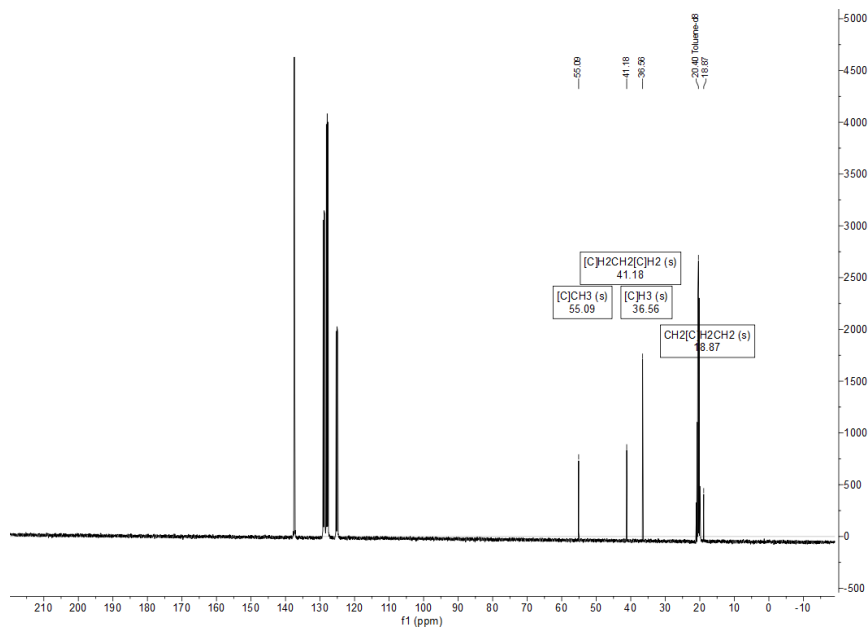


Figure S 6: ^{13}C -NMR Spectrum of **2** in toluene- d_8 .

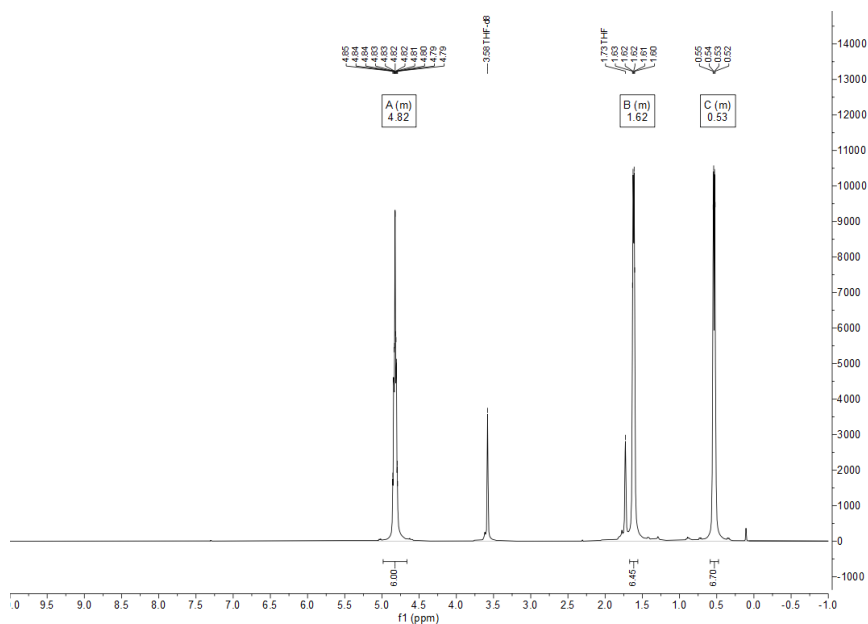


Figure S 7: ^1H -NMR Spectrum of $[\text{Mo}(\eta^4\text{-C}_4\text{H}_6)_3]$ in thf-d_6 .

IR Data

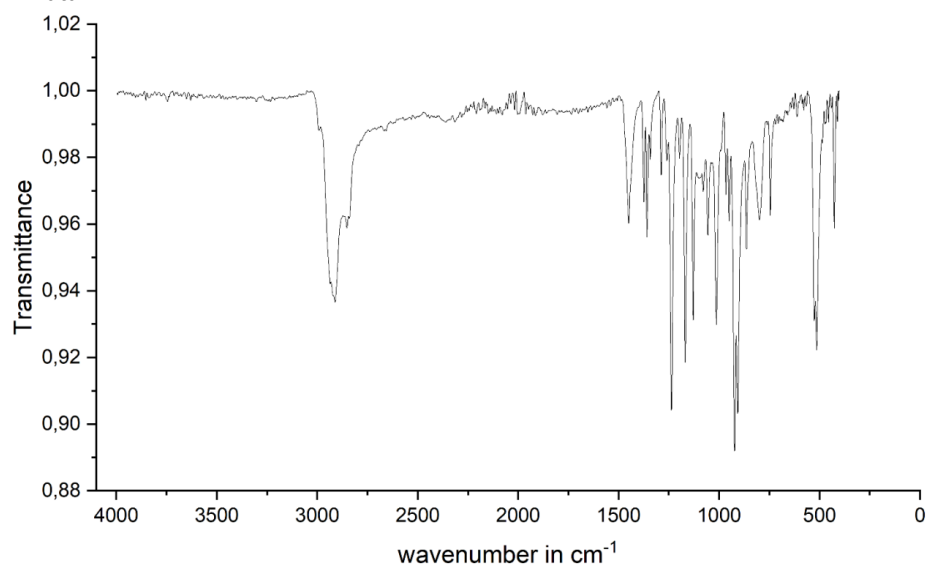


Figure S 8: IR Spectrum of 1.

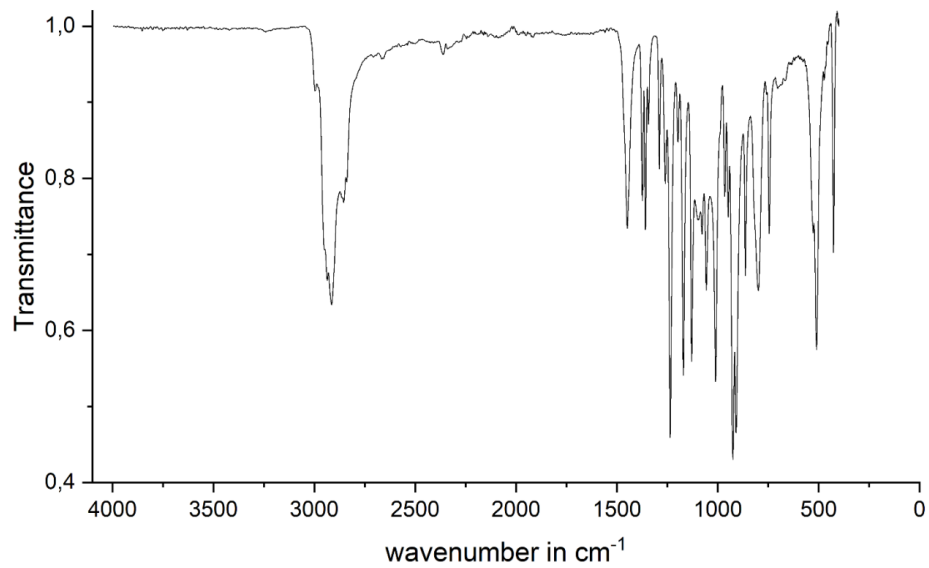


Figure S 9: IR-Spectrum of **2**.

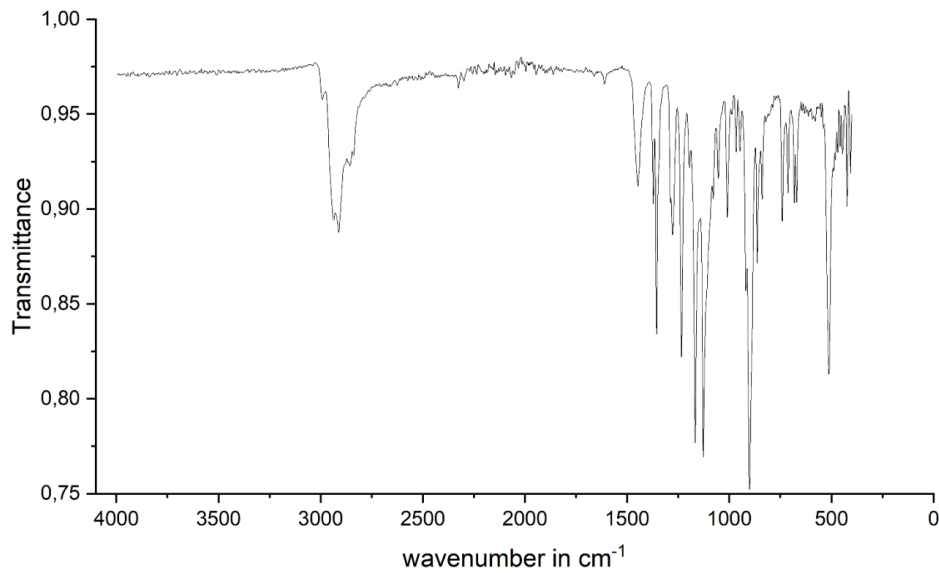


Figure S 10: IR-Spectrum of [GaTMP]₄.

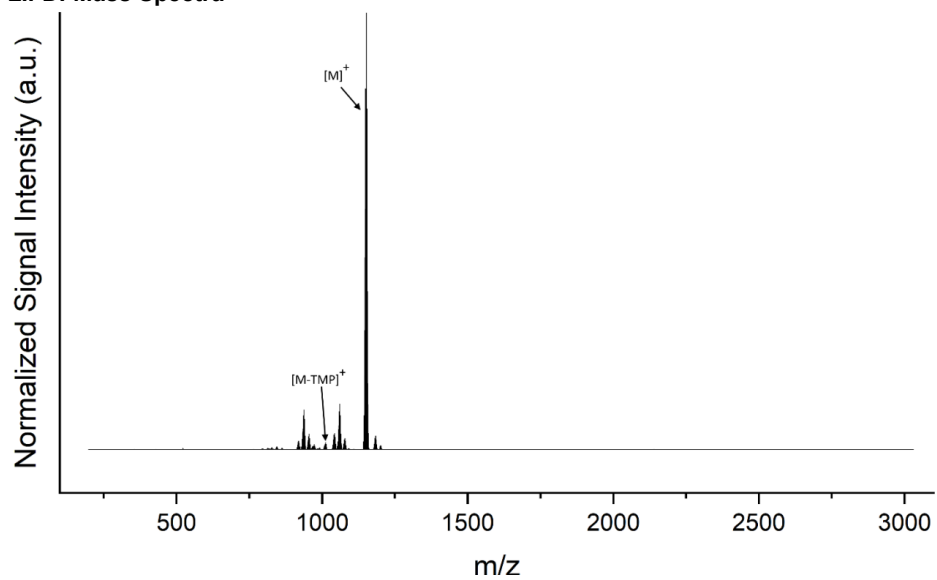
LIFDI-Mass Spectra

Figure S 11: Mass Spectrum of **1** from 200 – 3000 m/z.

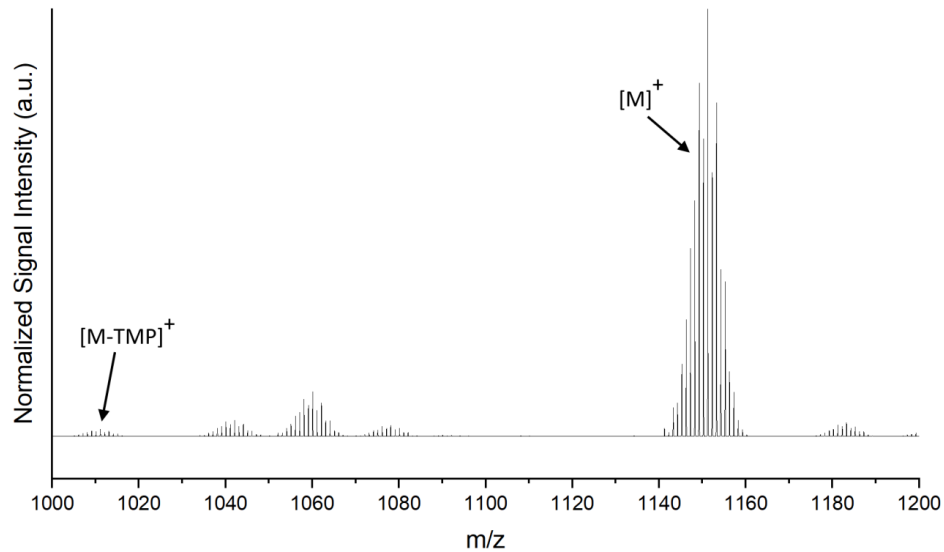


Figure S 12: Mass Spectrum of **1** from 1000 – 1200 m/z.

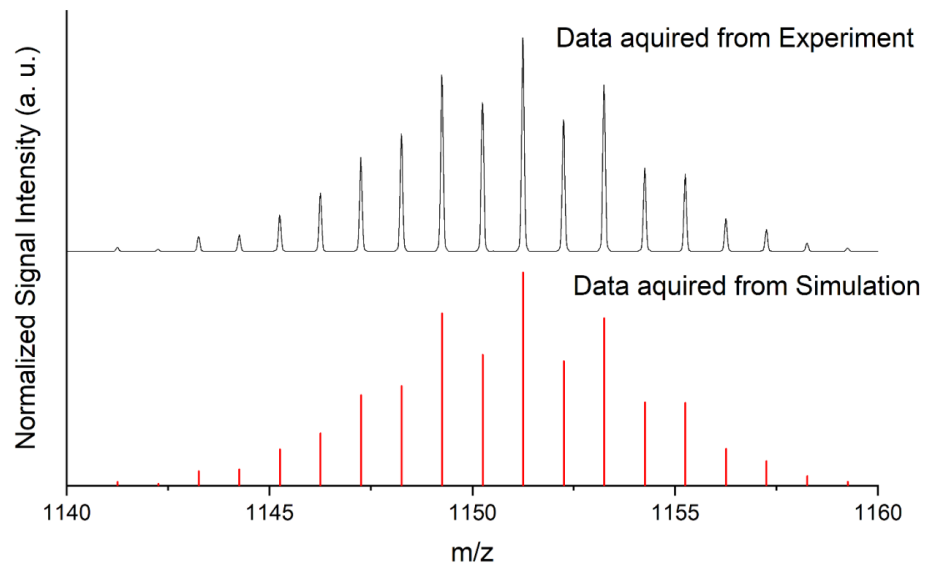


Figure S 13: Isotopic pattern of **1** and simulated isotopic pattern for $\text{RuGa}_5\text{N}_5\text{C}_{45}\text{H}_{90}$ (red).

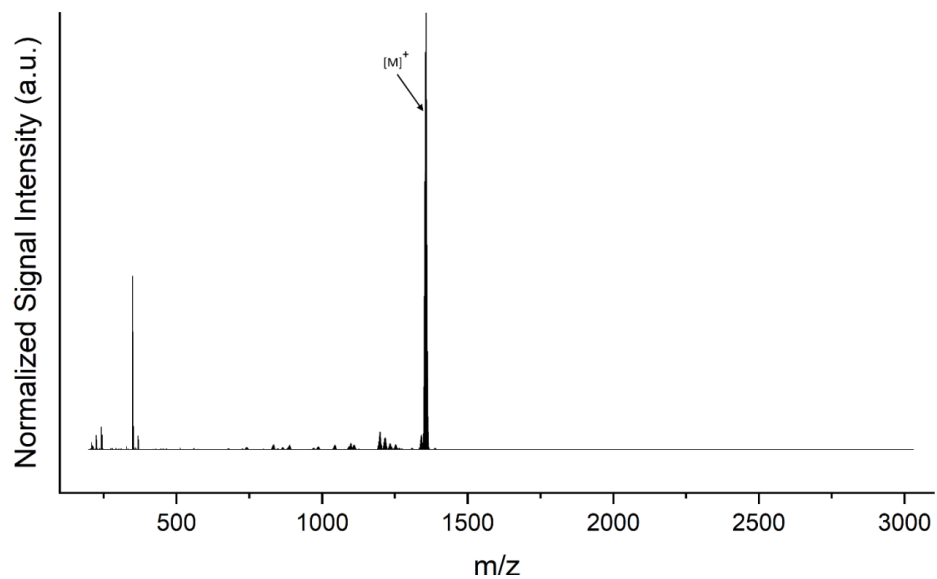


Figure S 14: Mass Spectrum of **2** from 200 – 3000 m/z

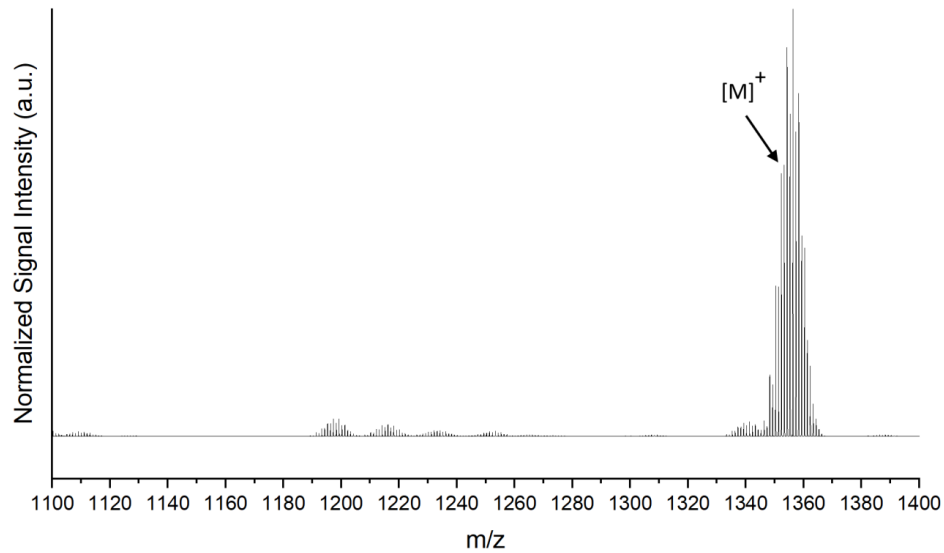


Figure S 15: Mass Spectrum of **2** from 1100 – 1400 m/z

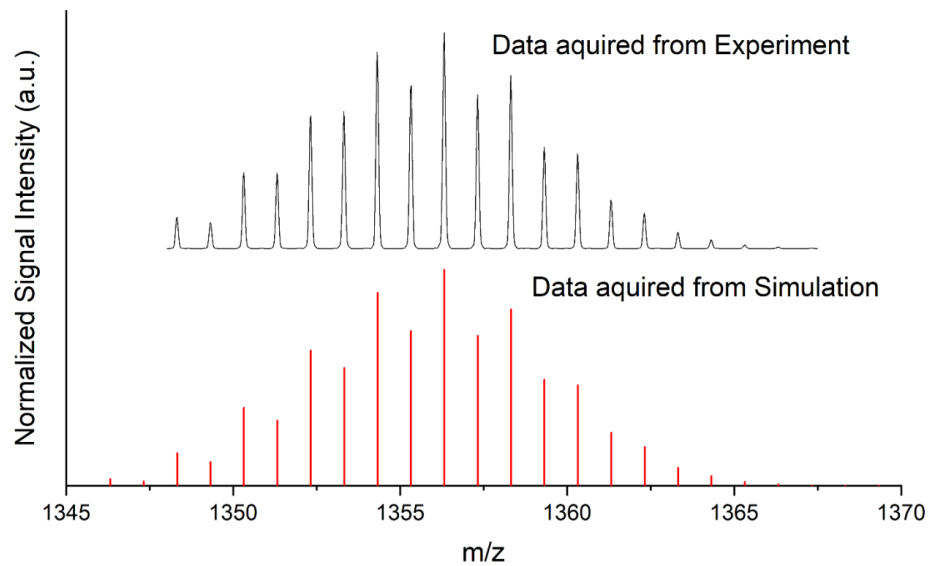


Figure S 16: Isotopic pattern of **2** and simulated isotopic pattern for $\text{MoGa}_6\text{N}_6\text{C}_{54}\text{H}_{108}$ (red).

Crystallography

SC-XRD structure report for compound **1**.

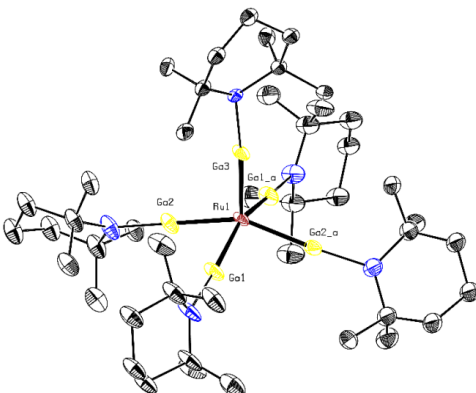


Figure S 17: Molecular structure of $[\text{Ru}(\text{GaTMP})_5]$ (**1**) in the solid state determined by single crystal X-ray diffraction. Ru: orange, Ga: yellow, N: blue and C: black. Hydrogen atoms and disordered molecule fragments are omitted. Thermal ellipsoids are shown at the 50% probability level.

A yellow, block-shaped crystal of $\text{C}_{45}\text{H}_{90}\text{Ga}_5\text{N}_5\text{Ru}$ coated with perfluorinated ether and fixed on top of a Kapton micro sampler was used for X-ray crystallographic analysis. The X-ray intensity data were collected at 100(2) K on a Bruker D8 VENTURE Duo three-angle diffractometer with an IMS microsource with MoK_α radiation ($\lambda=0.71073 \text{ \AA}$) using APEX4.^[1C1] The diffractometer was equipped with a Helios optic monochromator, a Bruker PHOTON II detector, and a low temperature device.

A matrix scan was used to determine the initial lattice parameters. All data were integrated with the Bruker SAINT V8.40B software package using a narrow-frame algorithm and the reflections were corrected for Lorentz and polarisation effects, scan speed, and background.^[2C1] The integration of the data using a monoclinic unit cell yielded a total of 5479 reflections within a 2θ range [$^\circ$] of 3.82 to 52.83 (0.80 \AA), of which 5479 were independent. Data were corrected for absorption effects including odd and even ordered spherical harmonics by the multi-scan method (TWINABS 2012/1).^[3C1] Space group assignment was based upon systematic absences, E statistics, and successful refinement of the structure.

The structure was solved by direct methods using SHELXT and refined by full-matrix least-squares methods against F^2 by minimizing $\Sigma w(F_o^2 - F_c^2)^2$ using SHELXL in conjunction with SHELXLE.^[4C1-6C1] All non-hydrogen atoms were refined with anisotropic displacement parameters. Hydrogen atoms were refined isotropically on calculated positions using a riding model with their U_{iso} values constrained to 1.5 times the U_{eq} of their pivot atoms for terminal sp^3 carbon atoms and a C–H

distance of 0.98 Å. Non-methyl hydrogen atoms were refined using a riding model with methylene, aromatic, and other C–H distances of 0.99 Å, 0.95 Å, and 1.00 Å, respectively, and U_{iso} values constrained to 1.2 times the U_{eq} of their pivot atoms. Severe whole molecule and rotational disorder of the TMP moieties was modelled using the DSR tool plugin within SHELXLE.^[7C1]

Neutral atom scattering factors for all atoms and anomalous dispersion corrections for the non-hydrogen atoms were taken from International Tables for Crystallography.^[8C1] Crystallographic data for the structures reported in this paper have been deposited with the Cambridge Crystallographic Data Centre.^[9C1] Supplementary crystallographic data reported in this paper have been deposited with the Cambridge Crystallographic Data Centre (CCDC 2341048) and can be obtained free of charge from The Cambridge Crystallographic Data Centre via www.ccdc.cam.ac.uk/structures.^[9C1] This report and the CIF file were generated using FinalCif.^[10C1] Figures showing the coordination polyhedra around the ruthenium centre were created using VESTA 3.^[11C1]

Refinement details for compound 1.

1 was refined as a two-component twin.

Table S 2: Crystal data and structure refinement for compound **1**.

CCDC number	2341048
Empirical formula	C ₄₅ H ₉₀ Ga ₅ N ₅ Ru
Formula weight	1150.88
Temperature [K]	100(2)
Crystal system	monoclinic
Space group (number)	$\frac{C_2}{c}$ (15)
<i>a</i> [Å]	23.4724(19)
<i>b</i> [Å]	11.9908(9)
<i>c</i> [Å]	18.9429(14)
α [°]	90
β [°]	93.343(3)
γ [°]	90
Volume [Å ³]	5322.5(7)
<i>Z</i>	4
ρ_{calc} [gcm ⁻³]	1.436
μ [mm ⁻¹]	2.804
<i>F</i> (000)	2376
Crystal size [mm ³]	0.113×0.120×0.312
Crystal colour	yellow
Crystal shape	fragment
Radiation	MoK α ($\lambda=0.71073$ Å)
2θ range [°]	3.82 to 52.83 (0.80 Å)
Index ranges	-29 ≤ <i>h</i> ≤ 29 0 ≤ <i>k</i> ≤ 14

	$0 \leq l \leq 23$
Reflections collected (HKLF4)	9221
Reflections collected (HKLF5)	5479
Independent reflections	5479 $R_{\text{int}} = 0.0617$ $R_{\text{sigma}} = 0.0456$
Completeness to $\theta = 25.242^\circ$ (HKLF4)	99.6 %
Data / Restraints / Parameters	5479 / 1051 / 493
Goodness-of-fit on F^2	1.154
Final R indexes $[l \geq 2\sigma(l)]$	$R_1 = 0.0562$ $wR_2 = 0.0928$
Final R indexes [all data]	$R_1 = 0.0745$ $wR_2 = 0.0989$
Largest peak/hole [$e\text{\AA}^{-3}$]	0.56/-0.85

Table S 3: Atomic coordinates and U_{eq} [\AA^2] for compound 1.

Atom	x	y	z	U_{eq}
Ru1	0.500000	0.62210(5)	0.250000	0.02208(15)
Ga1	0.54972(3)	0.66491(5)	0.35415(4)	0.03276(17)
Ga2	0.58257(3)	0.67017(5)	0.19995(4)	0.02960(16)
Ga3	0.500000	0.43247(7)	0.250000	0.0291(2)
N1	0.5932(9)	0.6901(17)	0.4384(8)	0.041(2)
C1	0.5972(7)	0.8026(13)	0.4684(9)	0.041(2)
C2	0.6580(9)	0.8257(16)	0.5006(10)	0.040(2)
H2A	0.658150	0.897449	0.526483	0.048
H2B	0.684447	0.832707	0.462032	0.048
C3	0.6794(8)	0.7323(13)	0.5517(10)	0.038(2)
H3A	0.719147	0.748050	0.569220	0.045
H3B	0.655297	0.729391	0.592794	0.045
C4	0.6769(10)	0.6216(15)	0.5133(12)	0.039(2)
H4A	0.688781	0.561740	0.546980	0.047
H4B	0.704345	0.622822	0.475570	0.047
C5	0.6179(9)	0.5942(15)	0.4804(13)	0.042(2)
C6	0.5850(8)	0.8876(12)	0.4073(9)	0.047(3)
H6A	0.587460	0.963650	0.426192	0.070
H6B	0.546673	0.874656	0.385587	0.070
H6C	0.613242	0.878024	0.371643	0.070
C7	0.5519(6)	0.8297(14)	0.5222(9)	0.051(3)
H7A	0.556279	0.907314	0.537795	0.077
H7B	0.557187	0.779979	0.563142	0.077
H7C	0.513654	0.818878	0.499738	0.077
C8	0.6266(10)	0.5004(19)	0.4318(11)	0.048(4)
H8A	0.643388	0.437233	0.458478	0.071
H8B	0.652374	0.523534	0.395649	0.071
H8C	0.589818	0.478035	0.409011	0.071
C9	0.5779(7)	0.5612(15)	0.5421(9)	0.047(3)
H9A	0.592847	0.493955	0.566039	0.071
H9B	0.539162	0.546769	0.522041	0.071
H9C	0.576997	0.622536	0.576220	0.071

N1A	0.5983(12)	0.706(2)	0.4301(11)	0.040(2)
C1A	0.6047(9)	0.8248(18)	0.4473(11)	0.041(2)
C2A	0.6620(12)	0.847(2)	0.4865(13)	0.040(3)
H2AA	0.692444	0.840795	0.452648	0.048
H2AB	0.662358	0.923890	0.504984	0.048
C3A	0.6753(10)	0.7674(17)	0.5471(13)	0.038(3)
H3AA	0.647526	0.777662	0.583928	0.046
H3AB	0.714029	0.782508	0.568585	0.046
C4A	0.6720(13)	0.648(2)	0.5188(16)	0.039(3)
H4AA	0.681585	0.595472	0.558038	0.047
H4AB	0.700717	0.638341	0.482984	0.047
C5A	0.6110(12)	0.619(2)	0.4844(17)	0.042(2)
C6A	0.6022(9)	0.8935(17)	0.3796(11)	0.041(4)
H6AA	0.614037	0.970279	0.390516	0.062
H6AB	0.563118	0.893498	0.358416	0.062
H6AC	0.627930	0.860971	0.346195	0.062
C7A	0.5581(9)	0.8675(19)	0.4945(12)	0.053(4)
H7AA	0.559700	0.949103	0.497036	0.079
H7AB	0.564387	0.836327	0.542181	0.079
H7AC	0.520534	0.844317	0.474445	0.079
C8A	0.6113(12)	0.502(2)	0.4464(15)	0.044(4)
H8AA	0.628414	0.445931	0.478954	0.066
H8AB	0.633723	0.506809	0.404444	0.066
H8AC	0.572102	0.479980	0.432218	0.066
C9A	0.5672(10)	0.605(2)	0.5387(13)	0.051(4)
H9AA	0.579426	0.545748	0.571978	0.077
H9AB	0.530420	0.584703	0.515012	0.077
H9AC	0.563269	0.675034	0.564466	0.077
N2	0.6524(2)	0.7043(4)	0.1650(3)	0.0368(11)
C10	0.6515(9)	0.819(2)	0.1320(12)	0.039(2)
C11	0.7010(8)	0.822(2)	0.0799(11)	0.041(2)
H11A	0.690824	0.772220	0.039188	0.049
H11B	0.705054	0.898292	0.061478	0.049
C12	0.7575(8)	0.7846(19)	0.1140(11)	0.041(3)
H12A	0.769394	0.835346	0.153365	0.049
H12B	0.787205	0.785707	0.079012	0.049
C13	0.7497(9)	0.6647(19)	0.1422(12)	0.038(2)
H13A	0.738295	0.614730	0.102204	0.046
H13B	0.786530	0.637535	0.163816	0.046
C14	0.7055(14)	0.660(2)	0.1958(17)	0.035(2)
C15	0.5967(9)	0.840(2)	0.0897(12)	0.039(4)
H15A	0.566325	0.854872	0.121778	0.059
H15B	0.586802	0.773750	0.061138	0.059
H15C	0.601091	0.904138	0.058599	0.059
C16	0.6573(11)	0.917(2)	0.1829(14)	0.043(4)
H16A	0.652021	0.986753	0.156741	0.065
H16B	0.695416	0.915590	0.207063	0.065
H16C	0.628359	0.910564	0.217918	0.065
C17	0.6923(14)	0.537(3)	0.211(2)	0.033(4)
H17A	0.724477	0.504077	0.238777	0.049
H17B	0.686007	0.496921	0.166340	0.049
H17C	0.657858	0.532817	0.237848	0.049

C18	0.7298(13)	0.715(2)	0.2626(13)	0.035(4)
H18A	0.759930	0.667459	0.284472	0.053
H18B	0.699438	0.724452	0.295472	0.053
H18C	0.745692	0.787679	0.251256	0.053
N2A	0.6524(2)	0.7043(4)	0.1650(3)	0.0368(11)
C10A	0.6627(8)	0.8017(16)	0.1190(10)	0.037(2)
C11A	0.7135(7)	0.7851(17)	0.0738(9)	0.040(2)
H11C	0.703185	0.730181	0.036226	0.048
H11D	0.722167	0.856634	0.050614	0.048
C12A	0.7663(7)	0.7451(18)	0.1155(10)	0.042(2)
H12C	0.778136	0.801217	0.151791	0.050
H12D	0.797864	0.735985	0.083473	0.050
C13A	0.7546(8)	0.6351(17)	0.1508(10)	0.038(2)
H13C	0.789297	0.611213	0.178975	0.046
H13D	0.746098	0.577999	0.113925	0.046
C14A	0.7029(12)	0.642(2)	0.2008(15)	0.035(2)
C15A	0.6075(7)	0.8121(16)	0.0697(10)	0.034(3)
H15D	0.611861	0.873574	0.036323	0.050
H15E	0.574862	0.826961	0.098240	0.050
H15F	0.601131	0.742361	0.043450	0.050
C16A	0.6699(10)	0.9092(19)	0.1643(11)	0.044(4)
H16D	0.668057	0.974615	0.133188	0.066
H16E	0.706996	0.907597	0.190933	0.066
H16F	0.639368	0.913355	0.197251	0.066
C17A	0.6845(13)	0.523(2)	0.2160(18)	0.036(4)
H17D	0.718084	0.478067	0.230889	0.054
H17E	0.665952	0.490178	0.173086	0.054
H17F	0.657678	0.523166	0.253707	0.054
C18A	0.7211(11)	0.694(2)	0.2740(11)	0.038(4)
H18D	0.753080	0.651506	0.296018	0.056
H18E	0.688822	0.691660	0.304519	0.056
H18F	0.732788	0.771492	0.267376	0.056
N3	0.4948(6)	0.2783(6)	0.2606(6)	0.0199(17)
C19	0.552(3)	0.222(4)	0.277(3)	0.0236(18)
C20	0.5625(5)	0.1045(9)	0.2457(6)	0.0275(18)
H20A	0.577562	0.112768	0.198186	0.033
H20B	0.591748	0.065380	0.276252	0.033
C21	0.5094(6)	0.0360(8)	0.2399(7)	0.0296(19)
H21A	0.496829	0.019344	0.287794	0.036
H21B	0.517101	-0.035641	0.216300	0.036
C22	0.4620(5)	0.0988(9)	0.1974(6)	0.0271(18)
H22A	0.472904	0.105249	0.147835	0.033
H22B	0.426635	0.053724	0.197066	0.033
C23	0.449(3)	0.215(4)	0.225(3)	0.0233(18)
C24	0.6073(5)	0.2904(9)	0.2642(7)	0.030(2)
H24A	0.640895	0.246930	0.280671	0.045
H24B	0.606635	0.360761	0.290410	0.045
H24C	0.609144	0.306023	0.213605	0.045
C25	0.5491(5)	0.2139(9)	0.3582(6)	0.028(2)
H25A	0.587368	0.199039	0.379577	0.042
H25B	0.523386	0.153058	0.369864	0.042
H25C	0.534832	0.284307	0.376554	0.042

C26	0.4176(5)	0.2794(9)	0.1664(6)	0.027(2)
H26A	0.382069	0.240506	0.151958	0.041
H26B	0.441553	0.285107	0.125830	0.041
H26C	0.408741	0.354294	0.183223	0.041
C27	0.4136(5)	0.2104(9)	0.2887(6)	0.026(2)
H27A	0.377318	0.172859	0.276234	0.039
H27B	0.406147	0.286245	0.305040	0.039
H27C	0.434520	0.168760	0.326450	0.039

U_{eq} is defined as 1/3 of the trace of the orthogonalized U_{ij} tensor

References

- [1C1] APEX4 Suite of Crystallographic Software, Version 2021-10.0, Bruker AXS Inc., Madison, Wisconsin, USA, **2021**.
- [2C1] Bruker, SAINT, V8.40B, Bruker AXS Inc., Madison, Wisconsin, USA.
- [3C1] L. Krause, R. Herbst-Irmer, G. M. Sheldrick, D. Stalke, *J. Appl. Cryst.* **2015**, *48*, 3–10, doi:10.1107/S1600576714022985.
- [4C1] G. M. Sheldrick, *Acta Cryst.* **2015**, *A71*, 3–8, doi:10.1107/S2053273314026370.
- [5C1] G. M. Sheldrick, *Acta Cryst.* **2015**, *C71*, 3–8, doi:10.1107/S2053229614024218.
- [6C1] C. B. Huebschle, G. M. Sheldrick, B. Dittrich, *J. Appl. Cryst.* **2011**, *44*, 1281–1284, doi:10.1107/S0021889811043202.
- [7C1] D. Kratzert, J. J. Holstein, I. Krossing, *J. Appl. Cryst.*, **2015**, *48*, 933–938.
- [8C1] Ed. E. Prince, *International Tables for Crystallography Volume C, Mathematical, Physical and Chemical Tables*, International Union of Crystallography, Chester, England, **2006**, 500–502; 219–222; 193–199.
- [9C1] C. R. Groom, I. J. Bruno, M. P. Lightfoot, S. C. Ward, *Acta Cryst.* **2016**, *B72*, 171–179, doi:10.1107/S2052520616003954.
- [10C1] D. Kratzert, FinalCif, V106, <https://dkratzert.de/finalcif.html>.
- [11C1] K. Momma, F. Izumi, *J. Appl. Crystallogr.* **2011**, *44*, 1272–1276.

SC-XRD structure report for compound **2**.

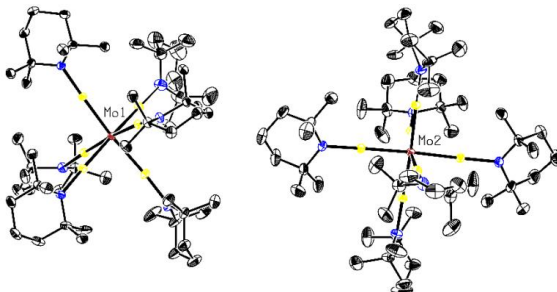


Figure S 18: Molecular structure of $[\text{Mo}(\text{GaTMP})_6]$ (**2**) in the solid state determined by single crystal X-ray diffraction. Mo: red, Ga: yellow, N: blue and C: black. Hydrogen atoms and disordered molecule fragments are omitted. Thermal ellipsoids are shown at the 50% probability level.

A colourless, block-shaped crystal of $\text{C}_{54}\text{H}_{108}\text{Ga}_6\text{MoN}_6$ coated with perfluorinated ether and fixed on top of a Kapton micro sampler was used for X-ray crystallographic analysis. The X-ray intensity data were collected at 100(2) K on a Bruker D8 VENTURE Duo three-angle diffractometer with an IMS microsource with $\text{MoK}\alpha$ radiation ($\lambda=0.71073 \text{ \AA}$) using APEX4.^[1C2] The diffractometer was

equipped with a Helios optic monochromator, a Bruker PHOTON II detector, and a low temperature device.

A matrix scan was used to determine the initial lattice parameters. All data were integrated with the Bruker SAINT V8.40B software package using a narrow-frame algorithm and the reflections were corrected for Lorentz and polarisation effects, scan speed, and background.^[2C2] The integration of the data using a monoclinic unit cell yielded a total of 776202 reflections within a 2θ range [$^\circ$] of 4.08 to 52.83 (0.80 Å), of which 26306 were independent. Data were corrected for absorption effects including odd and even ordered spherical harmonics by the multi-scan method (SADABS 2016/2).^[3C2] Space group assignment was based upon systematic absences, E statistics, and successful refinement of the structure.

The structure was solved by direct methods using SHELXT and refined by full-matrix least-squares methods against F^2 by minimizing $\Sigma w(F_o^2 - F_c^2)^2$ using SHELXL in conjunction with SHELXLE.^[4C2-6C2] All non-hydrogen atoms were refined with anisotropic displacement parameters. Hydrogen atoms were refined isotropically on calculated positions using a riding model with their U_{iso} values constrained to 1.5 times the U_{eq} of their pivot atoms for terminal sp³ carbon atoms and a C–H distance of 0.98 Å. Non-methyl hydrogen atoms were refined using a riding model with methylene, aromatic, and other C–H distances of 0.99 Å, 0.95 Å, and 1.00 Å, respectively, and U_{iso} values constrained to 1.2 times the U_{eq} of their pivot atoms. Whole molecule disorder and rotational disorder, e.g. of TMP moieties, was modelled using the DSR tool plugin within SHELXLE.^[7C2]

Neutral atom scattering factors for all atoms and anomalous dispersion corrections for the non-hydrogen atoms were taken from International Tables for Crystallography.^[8C2] Crystallographic data for the structures reported in this paper have been deposited with the Cambridge Crystallographic Data Centre.^[9C2] Supplementary crystallographic data reported in this paper have been deposited with the Cambridge Crystallographic Data Centre (CCDC 2341049) and can be obtained free of charge from The Cambridge Crystallographic Data Centre via www.ccdc.cam.ac.uk/structures.^[9C2] This report and the CIF file were generated using FinalCif.^[10C2] Figures showing the coordination polyhedra around the molybdenum centre were created using VESTA 3.^[11C2]

Table S 4: Crystal data and structure refinement for compound 2.

CCDC number	2341049
Empirical formula	C ₅₄ H ₁₀₈ Mo ₆ N ₆
Formula weight	1355.72
Temperature [K]	100(2)
Crystal system	monoclinic
Space group (number)	$P\bar{2}_1$ (14) c
<i>a</i> [Å]	26.9295(18)
<i>b</i> [Å]	21.9030(15)

c [Å]	24.2260(15)
α [°]	90
β [°]	116.221(2)
γ [°]	90
Volume [Å ³]	12819.0(15)
Z	8
ρ_{calc} [gcm ⁻³]	1.405
μ [mm ⁻¹]	2.709
F(000)	5616
Crystal size [mm ³]	0.278×0.339×0.428
Crystal colour	colourless
Crystal shape	block
Radiation	MoK α ($\lambda=0.71073$ Å)
2θ range [°]	4.08 to 52.83 (0.80 Å)
Index ranges	-33 ≤ h ≤ 33 -27 ≤ k ≤ 27 -30 ≤ l ≤ 30
Reflections collected	776202
Independent reflections	26306 $R_{\text{int}} = 0.0429$ $R_{\text{sigma}} = 0.0122$
Completeness to $\theta = 25.242^\circ$	99.9 %
Data / Restraints / Parameters	26306 / 739 / 1436
Goodness-of-fit on F^2	1.028
Final R indexes [$I \geq 2\sigma(I)$]	$R_1 = 0.0198$ $wR_2 = 0.0441$
Final R indexes [all data]	$R_1 = 0.0255$ $wR_2 = 0.0466$
Largest peak/hole [eÅ ⁻³]	0.55/-0.46

Table S 5: Atomic coordinates and Ueq [Å²] for compound 2.

Atom	x	y	z	U_{eq}
Mo1	0.38238(2)	0.74227(2)	0.23060(2)	0.01366(3)
Mo2	0.11461(2)	0.23662(2)	0.34993(2)	0.01461(3)
Ga1	0.32971(2)	0.72828(2)	0.28718(2)	0.01931(4)
Ga2	0.32465(2)	0.67490(2)	0.15029(2)	0.02012(4)
Ga3	0.45061(2)	0.74184(2)	0.19234(2)	0.01487(4)
Ga4	0.43058(2)	0.81839(2)	0.30507(2)	0.01559(4)
Ga5	0.32948(2)	0.82742(2)	0.17237(2)	0.01659(4)
Ga6	0.43626(2)	0.66305(2)	0.29688(2)	0.01627(4)
Ga7	0.17039(2)	0.31657(2)	0.33955(2)	0.01780(4)
Ga8	0.05019(2)	0.23283(2)	0.24396(2)	0.01641(4)
Ga9	0.06052(2)	0.15865(2)	0.36589(2)	0.01725(4)
Ga10	0.17637(2)	0.22566(2)	0.45628(2)	0.02001(4)
Ga11	0.16747(2)	0.16462(2)	0.32425(2)	0.01861(4)
Ga12	0.06146(2)	0.31313(2)	0.36953(2)	0.01758(4)
N1	0.29434(6)	0.72121(8)	0.33751(7)	0.0263(3)
N3	0.50659(6)	0.73802(6)	0.16701(7)	0.0174(3)

N4	0.46444(6)	0.87955(7)	0.36181(7)	0.0194(3)
N5	0.28979(6)	0.89690(7)	0.13216(7)	0.0201(3)
N6	0.47526(6)	0.60219(6)	0.35206(7)	0.0192(3)
N7	0.21475(6)	0.37883(7)	0.33388(7)	0.0249(3)
N8	0.00095(6)	0.22435(7)	0.16147(7)	0.0215(3)
N9	0.01804(6)	0.09709(7)	0.37621(7)	0.0237(3)
N10	0.22489(7)	0.21346(8)	0.53826(7)	0.0297(4)
N12	0.01959(6)	0.37220(7)	0.38440(7)	0.0237(3)
C1	0.23537(9)	0.73903(12)	0.31267(10)	0.0377(5)
C2	0.22532(10)	0.77367(12)	0.36204(11)	0.0444(6)
H2A	0.243627	0.814038	0.368915	0.053
H2B	0.185091	0.780681	0.346790	0.053
C3	0.24697(10)	0.73964(12)	0.42285(11)	0.0421(6)
H3A	0.226736	0.700635	0.417299	0.051
H3B	0.241021	0.764449	0.453562	0.051
C4	0.30852(9)	0.72711(10)	0.44553(9)	0.0339(5)
H4A	0.322256	0.703565	0.484364	0.041
H4B	0.328707	0.766428	0.454504	0.041
C5	0.32101(8)	0.69143(9)	0.39859(8)	0.0256(4)
C6	0.22264(10)	0.78276(14)	0.25888(11)	0.0521(7)
H6A	0.184035	0.796219	0.242405	0.078
H6B	0.228561	0.761795	0.226543	0.078
H6C	0.247180	0.818304	0.273221	0.078
C7	0.19534(9)	0.68477(14)	0.28765(12)	0.0545(7)
H7A	0.157326	0.699981	0.265770	0.082
H7B	0.198428	0.658743	0.321925	0.082
H7C	0.204756	0.661015	0.259309	0.082
C8	0.38354(8)	0.69198(10)	0.42046(9)	0.0307(4)
H8A	0.402001	0.675794	0.462440	0.046
H8B	0.395957	0.733939	0.419926	0.046
H8C	0.392833	0.666552	0.393050	0.046
C9	0.30443(10)	0.62397(10)	0.39771(11)	0.0401(5)
H9A	0.328994	0.604630	0.436808	0.060
H9B	0.307645	0.602779	0.363811	0.060
H9C	0.266099	0.621596	0.391963	0.060
N2	0.27960(7)	0.62157(8)	0.08901(8)	0.0349(4)
C10	0.3029(11)	0.5847(11)	0.0551(11)	0.0364(10)
C11	0.2653(2)	0.5913(3)	-0.0148(2)	0.0575(11)
H11A	0.266396	0.634142	-0.027383	0.069
H11B	0.279534	0.564952	-0.037783	0.069
C12	0.20507(18)	0.5736(3)	-0.0316(2)	0.0659(12)
H12A	0.181951	0.576998	-0.076578	0.079
H12B	0.203153	0.531120	-0.018832	0.079
C13	0.18584(19)	0.6161(2)	0.0011(3)	0.0626(12)
H13A	0.146786	0.606624	-0.009114	0.075
H13B	0.187099	0.658064	-0.013345	0.075
C14	0.2206(2)	0.6138(3)	0.0722(3)	0.0454(10)
C15	0.3611(2)	0.6059(3)	0.0684(3)	0.0413(12)
H15A	0.375016	0.581172	0.044519	0.062
H15B	0.385568	0.601152	0.112365	0.062
H15C	0.359954	0.648909	0.056808	0.062
C16	0.3103(3)	0.5173(3)	0.0706(3)	0.0547(13)

H16A	0.334648	0.499190	0.054657	0.082
H16B	0.274211	0.496940	0.051942	0.082
H16C	0.326916	0.512129	0.115415	0.082
C17	0.2010(2)	0.6722(3)	0.0926(3)	0.0661(16)
H17A	0.161698	0.668300	0.082728	0.099
H17B	0.206200	0.707611	0.070952	0.099
H17C	0.222638	0.677838	0.137081	0.099
C18	0.2073(2)	0.5550(3)	0.0960(3)	0.0683(14)
H18A	0.167733	0.554073	0.085610	0.102
H18B	0.229035	0.552911	0.140731	0.102
H18C	0.216390	0.520096	0.076862	0.102
N2A	0.27960(7)	0.62157(8)	0.08901(8)	0.0349(4)
C10A	0.302(2)	0.584(2)	0.055(2)	0.0370(18)
C11A	0.2620(5)	0.5657(5)	-0.0058(5)	0.064(2)
H11C	0.278599	0.534945	-0.022701	0.077
H11D	0.251095	0.601578	-0.033557	0.077
C12A	0.2077(4)	0.5369(6)	-0.0018(5)	0.073(2)
H12C	0.218161	0.501218	0.026113	0.088
H12D	0.179698	0.523969	-0.043000	0.088
C13A	0.1823(4)	0.5951(6)	0.0266(5)	0.062(2)
H13C	0.176649	0.632577	0.001704	0.074
H13D	0.146523	0.583148	0.025772	0.074
C14A	0.2248(5)	0.6056(6)	0.0911(4)	0.0411(16)
C15A	0.3473(5)	0.6245(6)	0.0523(5)	0.044(2)
H15D	0.363682	0.603996	0.028385	0.067
H15E	0.376072	0.632194	0.094145	0.067
H15F	0.331011	0.663437	0.032686	0.067
C16A	0.3266(5)	0.5244(5)	0.0967(5)	0.053(2)
H16D	0.343453	0.497756	0.077192	0.080
H16E	0.296690	0.502485	0.100818	0.080
H16F	0.354670	0.536638	0.137499	0.080
C17A	0.2094(4)	0.6519(5)	0.1238(5)	0.055(2)
H17D	0.169384	0.650146	0.110636	0.082
H17E	0.219370	0.692309	0.114551	0.082
H17F	0.229049	0.644285	0.168144	0.082
C18A	0.2292(4)	0.5579(6)	0.1343(6)	0.070(3)
H18D	0.193717	0.553577	0.136138	0.105
H18E	0.258137	0.568533	0.175132	0.105
H18F	0.238611	0.519306	0.120779	0.105
C19	0.51820(7)	0.79215(8)	0.13789(8)	0.0196(4)
C20	0.52709(8)	0.77282(9)	0.08185(9)	0.0272(4)
H20A	0.491310	0.759234	0.048595	0.033
H20B	0.539732	0.808635	0.066550	0.033
C21	0.56921(9)	0.72171(9)	0.09642(9)	0.0298(4)
H21A	0.606124	0.736057	0.126670	0.036
H21B	0.571854	0.709207	0.058538	0.036
C22	0.55100(8)	0.66763(9)	0.12271(9)	0.0251(4)
H22A	0.579100	0.634881	0.133592	0.030
H22B	0.515711	0.651432	0.090653	0.030
C23	0.54311(7)	0.68420(8)	0.17998(8)	0.0185(3)
C24	0.46758(8)	0.83436(9)	0.11477(9)	0.0269(4)
H24A	0.472927	0.868209	0.091493	0.040

H24B	0.463018	0.850562	0.149964	0.040
H24C	0.434433	0.811269	0.088080	0.040
C25	0.56786(8)	0.82959(8)	0.18306(9)	0.0255(4)
H25A	0.570468	0.867667	0.163256	0.038
H25B	0.601931	0.805910	0.194889	0.038
H25C	0.562843	0.839046	0.219814	0.038
C26	0.51522(8)	0.62998(8)	0.19461(9)	0.0241(4)
H26A	0.537459	0.593127	0.199685	0.036
H26B	0.478207	0.623952	0.160796	0.036
H26C	0.512097	0.638092	0.232742	0.036
C27	0.59985(8)	0.69257(9)	0.23643(9)	0.0273(4)
H27A	0.618156	0.652832	0.248911	0.041
H27B	0.594346	0.710234	0.270483	0.041
H27C	0.623001	0.719955	0.225650	0.041
C28	0.43591(8)	0.90769(9)	0.39572(8)	0.0245(4)
C29	0.44225(9)	0.97736(9)	0.39691(9)	0.0314(5)
H29A	0.419117	0.993657	0.355205	0.038
H29B	0.428324	0.994850	0.425096	0.038
C30	0.50149(9)	0.99782(9)	0.41740(9)	0.0325(5)
H30A	0.524339	0.985431	0.460640	0.039
H30B	0.502906	1.042868	0.415028	0.039
C31	0.52428(9)	0.96906(9)	0.37626(9)	0.0309(4)
H31A	0.563313	0.981763	0.390591	0.037
H31B	0.503015	0.984301	0.333717	0.037
C32	0.52130(7)	0.89904(8)	0.37603(8)	0.0220(4)
C33	0.37425(9)	0.89261(11)	0.36199(10)	0.0384(5)
H33A	0.354416	0.914032	0.381744	0.058
H33B	0.369018	0.848488	0.363617	0.058
H33C	0.359781	0.905646	0.318976	0.058
C34	0.45670(9)	0.88248(9)	0.46152(9)	0.0316(5)
H34A	0.431697	0.895581	0.478814	0.047
H34B	0.494022	0.898037	0.487153	0.047
H34C	0.457609	0.837781	0.460473	0.047
C35	0.53536(8)	0.87578(9)	0.32518(9)	0.0271(4)
H35A	0.571621	0.891587	0.331841	0.041
H35B	0.507131	0.889766	0.285160	0.041
H35C	0.536338	0.831047	0.325908	0.041
C36	0.56549(8)	0.87318(10)	0.43711(9)	0.0313(4)
H36A	0.602412	0.881481	0.440257	0.047
H36B	0.560344	0.828995	0.438363	0.047
H36C	0.561840	0.892599	0.471574	0.047
C37	0.32059(8)	0.95043(8)	0.12662(8)	0.0233(4)
C38	0.28620(9)	1.00868(9)	0.11634(10)	0.0340(5)
H38A	0.283365	1.018844	0.154670	0.041
H38B	0.305480	1.042827	0.107175	0.041
C39	0.22840(9)	1.00251(10)	0.06410(11)	0.0381(5)
H39A	0.207251	1.040562	0.060184	0.046
H39B	0.230616	0.995555	0.024873	0.046
C40	0.19938(8)	0.94928(10)	0.07730(10)	0.0324(5)
H40A	0.162238	0.944405	0.042362	0.039
H40B	0.194205	0.958731	0.114382	0.039
C41	0.23088(7)	0.88885(9)	0.08755(8)	0.0228(4)

C42	0.37251(8)	0.95758(9)	0.18803(10)	0.0330(5)
H42A	0.391383	0.995742	0.187732	0.050
H42B	0.397487	0.923066	0.193777	0.050
H42C	0.361818	0.958485	0.221790	0.050
C43	0.33947(9)	0.94339(10)	0.07555(10)	0.0332(5)
H43A	0.363154	0.977943	0.077061	0.050
H43B	0.306980	0.942492	0.035380	0.050
H43C	0.360280	0.905253	0.081688	0.050
C44	0.20537(8)	0.84438(10)	0.11618(10)	0.0325(5)
H44A	0.165907	0.839311	0.088610	0.049
H44B	0.209743	0.860448	0.155830	0.049
H44C	0.224042	0.804787	0.122505	0.049
C45	0.22342(9)	0.86214(11)	0.02565(9)	0.0344(5)
H45A	0.184506	0.851125	0.000928	0.052
H45B	0.246580	0.825678	0.033047	0.052
H45C	0.234412	0.892614	0.003530	0.052
C46	0.45656(8)	0.53804(8)	0.33662(8)	0.0211(4)
C47	0.46760(8)	0.50261(8)	0.39547(9)	0.0254(4)
H47A	0.442399	0.517678	0.412301	0.030
H47B	0.459346	0.458862	0.385256	0.030
C48	0.52708(8)	0.50908(9)	0.44423(9)	0.0290(4)
H48A	0.552644	0.492463	0.428601	0.035
H48B	0.532468	0.485894	0.481539	0.035
C49	0.53934(8)	0.57630(9)	0.45991(8)	0.0277(4)
H49A	0.578235	0.580732	0.491234	0.033
H49B	0.515223	0.591588	0.478071	0.033
C50	0.53019(7)	0.61551(8)	0.40361(8)	0.0209(4)
C51	0.39382(8)	0.53840(9)	0.29622(9)	0.0300(4)
H51A	0.380113	0.496303	0.288420	0.045
H51B	0.385646	0.558575	0.257027	0.045
H51C	0.375617	0.560536	0.317375	0.045
C52	0.48286(9)	0.50489(9)	0.30007(9)	0.0305(4)
H52A	0.464100	0.465740	0.285073	0.046
H52B	0.522192	0.497658	0.326839	0.046
H52C	0.479052	0.530154	0.265033	0.046
C53	0.53139(8)	0.68243(9)	0.42189(9)	0.0279(4)
H53A	0.566188	0.690969	0.458282	0.042
H53B	0.500169	0.690659	0.431280	0.042
H53C	0.528591	0.708597	0.387816	0.042
C54	0.57812(8)	0.60617(9)	0.38612(9)	0.0285(4)
H54A	0.613135	0.617490	0.420997	0.043
H54B	0.572168	0.631855	0.350616	0.043
H54C	0.579569	0.563204	0.375624	0.043
C55	0.20120(10)	0.44307(10)	0.33975(12)	0.0382(5)
C56	0.21250(10)	0.48399(11)	0.29543(13)	0.0478(6)
H56A	0.184122	0.475959	0.252920	0.057
H56B	0.208950	0.527216	0.305088	0.057
C57	0.26963(10)	0.47416(11)	0.29850(12)	0.0458(6)
H57A	0.274039	0.499946	0.267393	0.055
H57B	0.298541	0.485831	0.339675	0.055
C58	0.27583(10)	0.40737(11)	0.28625(11)	0.0412(6)
H58A	0.313236	0.400660	0.289085	0.049

H58B	0.248479	0.397122	0.243826	0.049
C59	0.26748(8)	0.36473(9)	0.33125(10)	0.0293(4)
C60	0.13849(11)	0.44646(11)	0.32025(16)	0.0621(9)
H60A	0.126919	0.489314	0.316121	0.093
H60B	0.130244	0.426619	0.351514	0.093
H60C	0.118425	0.425616	0.280717	0.093
C61	0.23238(16)	0.46717(13)	0.40545(14)	0.0703(10)
H61A	0.217585	0.507239	0.408504	0.105
H61B	0.271799	0.471018	0.415935	0.105
H61C	0.227738	0.438709	0.434042	0.105
C62	0.26371(11)	0.29959(11)	0.30717(15)	0.0532(7)
H62A	0.296285	0.290825	0.300398	0.080
H62B	0.230169	0.295339	0.268269	0.080
H62C	0.262256	0.270805	0.337394	0.080
C63	0.31807(10)	0.36727(13)	0.39407(12)	0.0523(7)
H63A	0.350446	0.351223	0.390397	0.078
H63B	0.311113	0.342551	0.423651	0.078
H63C	0.325028	0.409673	0.408386	0.078
C64	-0.04103(8)	0.17506(9)	0.14135(8)	0.0253(4)
C65	-0.05258(9)	0.15229(10)	0.07698(9)	0.0346(5)
H65A	-0.019939	0.129433	0.079452	0.042
H65B	-0.084390	0.123810	0.062184	0.042
C66	-0.06525(10)	0.20423(11)	0.03088(10)	0.0429(6)
H66A	-0.071277	0.187825	-0.009676	0.051
H66B	-0.099291	0.225811	0.025879	0.051
C67	-0.01646(11)	0.24819(12)	0.05473(10)	0.0457(6)
H67A	-0.024368	0.282160	0.025065	0.055
H67B	0.016837	0.226565	0.057488	0.055
C68	-0.00438(9)	0.27456(9)	0.11835(9)	0.0315(5)
C69	-0.01728(10)	0.12078(10)	0.18522(10)	0.0396(5)
H69A	-0.042134	0.085655	0.169339	0.059
H69B	-0.013769	0.131764	0.226000	0.059
H69C	0.019238	0.110243	0.188343	0.059
C70	-0.09531(9)	0.19318(12)	0.14289(12)	0.0460(6)
H70A	-0.119252	0.157237	0.134398	0.069
H70B	-0.114040	0.224473	0.111630	0.069
H70C	-0.087386	0.209414	0.183644	0.069
C71	0.05074(10)	0.30848(12)	0.14301(11)	0.0521(7)
H71A	0.049637	0.338697	0.112655	0.078
H71B	0.080688	0.279303	0.150738	0.078
H71C	0.057296	0.329221	0.181471	0.078
C72	-0.04880(11)	0.32117(11)	0.11205(12)	0.0518(7)
H72A	-0.047036	0.355901	0.087471	0.078
H72B	-0.042452	0.335460	0.152978	0.078
H72C	-0.085396	0.302057	0.091665	0.078
C73	0.03434(8)	0.03234(9)	0.37763(9)	0.0276(4)
C74	-0.01559(9)	-0.00660(10)	0.33765(11)	0.0377(5)
H74A	-0.027495	0.003895	0.293866	0.045
H74B	-0.004723	-0.050182	0.343247	0.045
C75	-0.06394(10)	0.00268(11)	0.35331(13)	0.0469(6)
H75A	-0.053215	-0.009888	0.396342	0.056
H75B	-0.095825	-0.022540	0.325862	0.056

C76	-0.07983(9)	0.06997(11)	0.34505(13)	0.0459(6)
H76A	-0.111037	0.076500	0.355534	0.055
H76B	-0.092557	0.081286	0.301324	0.055
C77	-0.03136(9)	0.11180(10)	0.38551(10)	0.0328(5)
C78	0.07655(9)	0.02801(10)	0.35152(11)	0.0369(5)
H78A	0.085477	-0.014962	0.348991	0.055
H78B	0.110292	0.050015	0.378507	0.055
H78C	0.060945	0.046195	0.310336	0.055
C79	0.06286(10)	0.00571(10)	0.44324(10)	0.0424(6)
H79A	0.079146	-0.034022	0.442160	0.064
H79B	0.035513	0.000618	0.459327	0.064
H79C	0.092058	0.033608	0.469933	0.064
C80	-0.04799(10)	0.17755(11)	0.36528(13)	0.0461(6)
H80A	-0.083448	0.186440	0.365806	0.069
H80B	-0.051683	0.183222	0.323511	0.069
H80C	-0.019551	0.205282	0.393507	0.069
C81	-0.02065(12)	0.10718(12)	0.45312(12)	0.0519(7)
H81A	-0.051952	0.124893	0.457878	0.078
H81B	0.013255	0.129510	0.479042	0.078
H81C	-0.016405	0.064190	0.465583	0.078
C82	0.27721(8)	0.24819(10)	0.56663(9)	0.0335(5)
C83	0.32433(9)	0.20704(13)	0.61050(10)	0.0481(6)
H83A	0.333748	0.177170	0.585932	0.058
H83B	0.357511	0.232469	0.633617	0.058
C84	0.31003(10)	0.17306(14)	0.65551(11)	0.0532(7)
H84A	0.303248	0.202327	0.682580	0.064
H84B	0.341140	0.146171	0.681570	0.064
C85	0.25867(12)	0.13531(12)	0.61999(11)	0.0521(7)
H85A	0.248817	0.113077	0.649348	0.063
H85B	0.266629	0.104681	0.594911	0.063
C86	0.20942(10)	0.17456(11)	0.57773(9)	0.0403(5)
C87	0.29190(10)	0.26886(14)	0.51538(11)	0.0549(7)
H87A	0.328594	0.287940	0.533534	0.082
H87B	0.264352	0.298445	0.488960	0.082
H87C	0.292180	0.233444	0.490799	0.082
C88	0.27367(11)	0.30556(12)	0.60092(13)	0.0533(7)
H88A	0.307613	0.329588	0.613296	0.080
H88B	0.269366	0.293649	0.637560	0.080
H88C	0.241759	0.330126	0.573820	0.080
C89	0.16355(14)	0.13091(15)	0.53620(12)	0.0787(12)
H89A	0.157577	0.099570	0.561520	0.118
H89B	0.174546	0.111389	0.506901	0.118
H89C	0.129211	0.153900	0.513666	0.118
C90	0.18668(11)	0.21071(16)	0.61543(13)	0.0627(8)
H90A	0.170047	0.182561	0.633979	0.094
H90B	0.158519	0.239503	0.588553	0.094
H90C	0.216869	0.233279	0.647974	0.094
N11	0.2084(8)	0.1077(9)	0.3077(6)	0.0258(17)
C91	0.2496(4)	0.0715(5)	0.3456(4)	0.0376(15)
C92	0.3036(2)	0.0753(3)	0.3378(2)	0.0501(12)
H92A	0.319553	0.116681	0.349433	0.060
H92B	0.330736	0.045705	0.365995	0.060

C93	0.29378(19)	0.0618(2)	0.2721(2)	0.0419(11)
H93A	0.278950	0.019941	0.260268	0.050
H93B	0.329048	0.064718	0.268763	0.050
C94	0.2521(2)	0.1087(3)	0.2293(3)	0.0348(11)
H94A	0.267735	0.150293	0.240560	0.042
H94B	0.245203	0.100797	0.186262	0.042
C95	0.1977(4)	0.1050(4)	0.2342(4)	0.0256(13)
C96	0.2629(5)	0.0979(5)	0.4108(5)	0.063(3)
H96A	0.294784	0.076186	0.442104	0.094
H96B	0.230766	0.092445	0.419155	0.094
H96C	0.271631	0.141428	0.411990	0.094
C97	0.2307(3)	0.0043(3)	0.3390(3)	0.0609(15)
H97A	0.257565	-0.019488	0.373519	0.091
H97B	0.228033	-0.012251	0.300247	0.091
H97C	0.194354	0.002047	0.339101	0.091
C98	0.16093(18)	0.1583(2)	0.19836(18)	0.0353(10)
H98A	0.155274	0.156765	0.155554	0.053
H98B	0.178847	0.196935	0.217052	0.053
H98C	0.125083	0.155392	0.199512	0.053
C99	0.1642(2)	0.0476(2)	0.2019(3)	0.0539(14)
H99A	0.152643	0.050489	0.157573	0.081
H99B	0.131350	0.044651	0.209445	0.081
H99C	0.187216	0.011200	0.218295	0.081
N11A	0.2087(8)	0.1106(9)	0.2992(7)	0.0246(16)
C91A	0.1959(5)	0.0934(5)	0.2440(5)	0.0337(16)
C92A	0.2018(2)	0.0249(2)	0.2357(3)	0.0462(12)
H92C	0.170366	0.003483	0.237987	0.055
H92D	0.198754	0.018029	0.193901	0.055
C93A	0.2535(3)	-0.0032(3)	0.2805(3)	0.0575(14)
H93C	0.284811	0.012128	0.273421	0.069
H93D	0.251395	-0.047978	0.274627	0.069
C94A	0.2640(3)	0.0120(3)	0.3478(3)	0.0558(15)
H94C	0.236587	-0.010114	0.357113	0.067
H94D	0.301295	-0.002853	0.376523	0.067
C95A	0.2602(4)	0.0804(5)	0.3585(4)	0.0351(16)
C96A	0.1358(3)	0.1090(4)	0.2040(2)	0.069(2)
H96D	0.123972	0.090708	0.163198	0.104
H96E	0.131562	0.153468	0.199892	0.104
H96F	0.113026	0.093004	0.222939	0.104
C97A	0.2322(4)	0.1274(4)	0.2202(4)	0.0614(19)
H97D	0.216525	0.122865	0.175442	0.092
H97E	0.269681	0.110281	0.239291	0.092
H97F	0.233674	0.170776	0.230714	0.092
C98A	0.2521(5)	0.0829(5)	0.4161(6)	0.0430(19)
H98D	0.281904	0.060239	0.449010	0.064
H98E	0.216353	0.064610	0.408146	0.064
H98F	0.252809	0.125543	0.428721	0.064
C99A	0.3135(2)	0.1112(4)	0.3676(3)	0.0657(17)
H99D	0.344635	0.092460	0.402499	0.099
H99E	0.311642	0.154746	0.375807	0.099
H99F	0.318819	0.106419	0.330307	0.099
C100	0.04312(8)	0.40672(9)	0.44309(9)	0.0289(4)

C101	-0.00032(10)	0.41389(13)	0.46661(11)	0.0489(6)
H10A	-0.006929	0.373665	0.480786	0.059
H10B	0.014111	0.441745	0.502484	0.059
C102	-0.05435(10)	0.43851(16)	0.41900(14)	0.0667(9)
H10C	-0.048952	0.480501	0.407513	0.080
H10D	-0.081571	0.440162	0.436140	0.080
C103	-0.07628(9)	0.39785(12)	0.36227(12)	0.0446(6)
H10E	-0.110975	0.415635	0.330596	0.054
H10F	-0.085153	0.357150	0.373325	0.054
C104	-0.03495(8)	0.39025(9)	0.33516(9)	0.0239(4)
C105	0.09140(12)	0.36994(13)	0.49063(11)	0.0603(8)
H10G	0.106259	0.391035	0.530376	0.090
H10H	0.120514	0.365952	0.476983	0.090
H10I	0.078354	0.329273	0.494961	0.090
C106	0.06694(11)	0.46889(12)	0.43887(12)	0.0500(6)
H10J	0.086543	0.486406	0.480176	0.075
H10K	0.036787	0.496224	0.413041	0.075
H10L	0.092768	0.463911	0.420690	0.075
C107	-0.05646(9)	0.33879(11)	0.28784(10)	0.0370(5)
H10M	-0.093896	0.348740	0.256731	0.055
H10N	-0.057352	0.300617	0.308484	0.055
H10O	-0.031938	0.334007	0.267956	0.055
C108	-0.03275(12)	0.44783(12)	0.30095(13)	0.0570(7)
H10P	-0.068921	0.454604	0.265935	0.085
H10Q	-0.004543	0.442992	0.286059	0.085
H10R	-0.023362	0.482902	0.328871	0.085

U_{eq} is defined as 1/3 of the trace of the orthogonalized U_{ij} tensor.

References

- [1C2] APEX4 Suite of Crystallographic Software, Version 2021-10.0, Bruker AXS Inc., Madison, Wisconsin, USA, **2021**.
- [2C2] Bruker, SAINT, V8.40B, Bruker AXS Inc., Madison, Wisconsin, USA.
- [3C2] L. Krause, R. Herbst-Irmer, G. M. Sheldrick, D. Stalke, *J. Appl. Cryst.* **2015**, *48*, 3–10, doi:10.1107/S1600576714022985.
- [4C2] G. M. Sheldrick, *Acta Cryst.* **2015**, *A71*, 3–8, doi:10.1107/S2053273314026370.
- [5C2] G. M. Sheldrick, *Acta Cryst.* **2015**, *C71*, 3–8, doi:10.1107/S2053229614024218.
- [6C2] C. B. Huebschle, G. M. Sheldrick, B. Dittrich, *J. Appl. Cryst.* **2011**, *44*, 1281–1284, doi:10.1107/S0021889811043202.
- [7C2] D. Kratzert, J. J. Holstein, I. Krossing, *J. Appl. Cryst.* **2015**, *48*, 933–938.
- [8C2] Ed. E. Prince, *International Tables for Crystallography Volume C, Mathematical, Physical and Chemical Tables*, International Union of Crystallography, Chester, England, **2006**, 500–502; 219–222; 193–199.
- [9C2] C. R. Groom, I. J. Bruno, M. P. Lightfoot, S. C. Ward, *Acta Cryst.* **2016**, *B72*, 171–179, doi:10.1107/S2052520616003954.
- [10C2] D. Kratzert, FinalCif, V106, <https://dkratzert.de/finalcif.html>.
- [11C2] K. Momma, F. Izumi, *J. Appl. Crystallogr.* **2011**, *44*, 1272–1276.

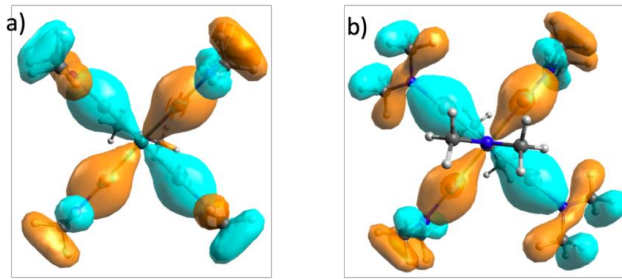
Computational Data

Figure S 19: Excerpt of the occupied molecular orbitals of $\mathbf{1}_{\text{NMe}_2}$ (a) and $\mathbf{2}_{\text{NMe}_2}$ (b) showing σ bonding between the GaNMe_2 ligand and the transition metal (HOMO-14 and HOMO-15 respectively).

[Ru(GaTMP)₅]:

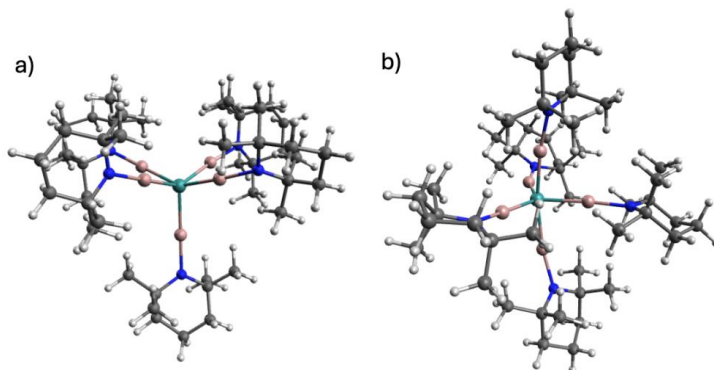


Figure S 20: Optimized structure of a) $\mathbf{1}_{\text{sp}}$ and b) $\mathbf{1}_{\text{tb}}$.

$\mathbf{1}_{\text{sp}}$ xyz Coordinates:

Ru 10.9625336746	4.8135270062	14.0514953028	C 6.3877457719	5.6884313486	14.5450005207
Ga 8.9579178587	4.2189633336	15.0126425439	C 7.2395033664	1.1420891350	15.4789396073
Ga 9.8770435308	4.0789227423	12.1584183817	C 8.3745323128	2.3658680583	17.3308440194
Ga 10.9386770320	7.1139679443	14.0382222113	C 6.7269503017	4.0169690516	9.4723890665
N 7.2652546234	3.6652428843	15.5932863857	C 7.3005757982	1.6429504311	10.0095849464
N 8.7726702528	3.4898159543	10.7665230187	C 8.9966597734	4.7891277876	8.6109386698
N 10.9056697601	9.0005334848	14.1097230863	C 8.0069629197	5.8108922599	10.6579394186
C 4.8301064920	4.1317936911	15.7352420791	C 9.7579611560	1.6503612586	9.3411495329
C 5.8713449542	2.4080402624	17.2133004052	C 9.0920813914	1.2570767085	11.7104041606
C 5.8600405684	3.4841309639	13.4978390880	C 11.9601551507	9.7222856711	14.8645940913
			C 10.7970217487	11.9725808586	14.3461227313
			C 12.1092358699	11.1619727122	14.3254773931

C 10.1311397123	10.0411664024	11.9715884888	H 12.6058876085	2.3088206831	11.3547338405
C 8.5193821530	8.9054217694	13.5098876655	H 13.6142125650	1.3204281703	10.2631422014
Ga 12.9762646072	4.1807476768	13.1316079506	H 14.4599169910	0.1044601896	12.2651970356
Ga 12.0165675792	4.1605201435	15.9903427778	H 13.5753082257	1.1779014626	13.4038452141
N 14.6709382700	3.5625324678	12.6160072475	H 15.3394394035	0.9406602090	13.5785306276
N 13.0698825507	3.6214094338	17.4389295818	C 8.7348143902	2.0457210229	10.4363213734
C 17.1316882719	3.8901040023	12.5946050529	H 9.5011654688	2.0649644059	8.3488279705
C 16.0883749377	2.1383904310	11.1544129397	H 9.8146578089	0.5470682437	9.2345802765
C 15.9511821866	3.4066585609	14.7944389532	H 10.7649644444	2.0266333716	9.6114890625
C 15.5976966386	5.5841805791	13.6232781188	H 9.0315899020	0.1655973182	11.5258582574
C 14.5230240929	1.0518010290	12.8404208859	H 8.3999773155	1.5111052469	12.5380954158
C 13.6018440528	2.2551398413	10.8595580861	H 10.1276615138	1.4745593987	12.0543903201
C 15.0999086614	4.1835746563	18.7428303443	C 6.7107988034	2.5782805391	8.9526750966
C 14.5138788787	1.7937841044	18.2906799962	H 6.6526392401	1.6711949847	10.9130108018
C 12.8229177704	5.0056346964	19.5388150788	H 7.3097442468	0.5910068499	9.6524838899
C 13.8515563602	5.9394818413	17.4703982589	H 7.2845180220	2.5034415782	8.0036217266
C 12.0494266427	1.8525301282	18.9262226615	H 5.6726237765	2.2712010332	8.7064420788
C 12.7399213860	1.3523272157	16.5841297374	C 8.1459092619	4.4922232884	9.8723919935
C 11.6380958506	9.7373499476	16.3815887469	H 8.5748679093	5.6447833626	8.0438447365
C 13.3038039387	8.9884343959	14.6686072505	H 9.0460058057	3.9264057566	7.9213211485
H 12.4300502316	10.2532915148	16.9654349045	H 10.0343651809	5.0433539331	8.9074574252
H 11.5543556388	8.6957918508	16.7559121577	H 6.0786134259	4.0785616995	10.3738254227
H 10.6734755076	10.2384957270	16.5905802071	H 6.3050135874	4.7188472701	8.7216925023
H 13.5838976976	8.9660529347	13.5964457460	H 7.4994804331	6.5820891271	10.0445257631
H 13.2414946906	7.9356340195	15.0244277242	H 9.0000928560	6.2204588690	10.9462372057
H 14.1177305163	9.4785974290	15.2415144565	H 7.4180086216	5.6572469113	11.5843126381
H 12.8999806927	11.6855973466	14.9030753030	C 15.0976106490	2.7660237891	19.3173278346
H 12.4888106437	11.0840429407	13.2857526905	H 16.1301407296	2.4610086016	19.5886659319
C 9.5483152860	11.0751641443	14.2234093006	H 14.5119182645	2.7322690053	20.2615507201
H 10.8197263768	12.7146616193	13.5213152336	C 13.0892759659	2.1916470810	17.8279355138
H 10.7241165747	12.5657065981	15.2812711033	H 13.4493325536	1.5530227378	15.7567695425
C 9.8063427032	9.7558640850	13.4611196930	H 11.7145073692	1.5709495357	16.2121286877
H 10.3004206797	9.0839321851	11.4366468426	H 12.7775355711	0.2699622442	16.8207142529
H 11.0492705293	10.6489235430	11.8592948055	H 14.4897969869	0.7575342001	18.6905259826
H 9.2999060960	10.5794418249	11.4680106245	H 15.1740782325	1.7786092373	17.3960550208
H 8.6603166301	7.9342194048	12.9847899662	H 11.0522481618	2.2377069524	18.6343330424
H 7.6756085754	9.4246478261	13.0107952100	H 12.3059629675	2.2953378266	19.9062390313
H 8.2328982865	8.6850979071	14.5578911945	H 11.9717746298	0.7547539454	19.0698071699
H 8.7209825772	11.6249473703	13.7269729730	C 13.6904872823	4.6532011592	18.3034158203
H 9.1749928126	10.8035079140	15.2327060104	H 14.4584597926	5.7485683281	16.5626023563
C 17.2880334583	2.4717766675	12.0428883480	H 14.3505187000	6.7316444833	18.0636088932
H 18.2316312596	2.3845600414	11.4644275089	H 12.8667976376	6.3430000918	17.1469589081
H 17.3702136381	1.7398736750	12.8758689428	H 15.7618068028	4.2060123680	17.8495353792
C 15.8224164312	4.0749305659	13.3984401742	H 15.5162192107	4.9104199521	19.4726692791
H 17.1187640365	4.6042916644	11.7420232113	H 11.7906249033	5.2511517468	19.2171370630
H 17.9938768686	4.1687949135	13.2372986592	H 13.2405272916	5.8833907058	20.0743543180
H 15.4866436501	6.1115975671	12.6549751853	H 12.7601429384	4.1740615413	20.2646272421
H 16.4447606700	6.0320247059	14.1812643287	C 7.1695252767	2.4092795883	16.3706773971
H 14.6770073613	5.7741481764	14.2195026956	H 8.1517343560	1.1774217052	14.8483934635
H 16.1972883397	2.3301673774	14.7256890104	H 6.3688255403	1.0543924199	14.8027716134
H 15.0000578503	3.4958111234	15.3598752063	H 7.2797848787	0.2194927509	16.0948921089
H 16.7489714372	3.8917284257	15.3953985252	H 9.3334428318	2.3276392945	16.7664032801
C 14.7386554933	2.2673285545	11.9010305197	H 8.3436300528	1.4624021544	17.9727530077
H 16.1730063927	1.1147802623	10.7310032812	H 8.3917554505	3.2639472719	17.9805714251
H 16.0771542632	2.8434716075	10.2942680053	C 4.6344678147	2.7608148572	16.3852663877
H 13.6897826785	3.1199813023	10.1719471083	H 5.9873592813	3.1636498207	18.0209980554

H 5.7569823827 1.4197367098 17.7076900948
H 4.4507420771 1.9838199734 15.6112198202
H 3.7302389031 2.7682711278 17.0295394034
C 6.0996881490 4.2045964684 14.8515562383
H 6.7871206285 3.4832395403 12.8864424201
H 5.0665702807 3.9946085272 12.9123537424
H 5.5461806609 2.4311078163 13.6284945410
H 7.2848026099 5.8057866747 13.8969637041
H 6.5737994021 6.2522166990 15.480962390
H 5.5364488709 6.1548198075 14.0093739252
H 4.9265679624 4.8946442230 16.5386492661
H 3.9465777167 4.4164654239 15.1249325111
C 10.7507496573 11.1377428379 16.2750577105
C 12.7696116213 9.8530963573 15.5517095094
H 11.3841295131 11.9260693751 16.7348068968
H 10.5424103412 10.3651416475 17.0430587147
H 9.7824801525 11.5946790383 15.9965154446
H 13.3259180311 9.3930438738 14.7095011509
H 12.5764799579 9.0589038658 16.3080599075
H 13.4205457068 10.6094277021 16.0363142251
H 12.4439692758 12.3223044554 14.4345919233
H 12.4140373561 11.0327336122 13.2141715956
C 9.331793168 11.2447041974 13.3478774781
H 10.8085415656 12.4603061172 12.2798933606
H 10.2945785083 13.1293671715 13.8341293128
C 9.6877233741 9.7419995389 13.3417536544
H 10.5665105901 8.2572144275 11.9953164414
H 11.2674658780 9.8854807218 11.7954993800
H 9.6351160632 9.5317774944 11.1329170473
H 8.5923035530 7.8437733342 13.5432653542
H 7.6780088085 9.1208774704 12.6832605946
H 7.8864735059 9.2052827692 14.4732017857
H 8.6629391314 11.4557018676 12.4871041596
H 8.7270448185 11.4378713793 14.2577168973
C 16.7205309251 4.8221619432 10.7239988158
H 17.7528720449 4.9686789073 10.3427719990
H 16.2077135842 4.1764048129 9.9782710931
C 15.3433309184 3.9272083057 12.6952252477
H 17.3327623650 4.7794131328 12.7932066930
H 17.2774542535 3.1606304250 12.0416817216
H 15.9906217380 4.4010456355 14.7337758064
H 16.1263120577 2.6551225737 14.3069013649
H 14.5309566007 3.3546076040 14.6754276486
H 14.5527335723 2.8748639798 10.9035307992
H 13.5986750379 2.6289898005 12.3936682309
H 15.1694796338 1.7846522848 12.1792668285
C 14.5635142759 6.0236491141 11.3928374822
H 15.9719039803 6.6974157503 9.8709577751
H 16.5756530117 6.8138170579 11.5483111758
H 14.6797230175 7.8530922443 12.5923966297
H 12.9995294479 7.3837646595 12.1611355813
H 14.0546854739 8.1102176638 10.9200824266
H 13.5290791137 6.1797738076 9.4437513819
H 12.6095118495 5.2956545006 10.7076176021
H 13.9785506017 4.5055628898 9.8783908317
C 9.798963703 2.4598469027 10.8121650439
H 10.8778267892 2.7618239266 8.8937117021
H 11.3595940273 1.2906741629 9.7841461247
H 11.8938845774 2.9088055186 10.3561524762
H 10.3277823720 0.6379886099 11.9140454441
H 9.2603780399 1.7623358808 12.8263932884
H 11.0053560732 2.1280440258 12.6284240878
C 7.9858771809 2.6242912197 9.0077593427
H 7.7988989251 1.6264886435 10.9158425331
H 8.8770544519 0.7760462134 9.7745331455
H 8.7167721208 2.7268878652 8.1764496576
H 7.1000768302 2.1143586688 8.5742179831
C 8.7838991409 4.7503147293 10.1953220927

H 9.2158561476 6.0563718628 8.4756462481
H 10.1227763796 4.5183938901 8.4341152239
H 10.6087458308 5.7994343903 9.5804806745
H 6.8036716714 3.8736126375 10.3156649064
H 7.1601617187 4.6365488132 8.7411232643
H 7.6921200756 6.6521931371 10.3045680746
H 9.0457630950 6.5345670342 11.4606246392
H 7.5275724257 5.6223100890 11.7688446495
C 14.7065210277 0.2524813756 17.8421555624
H 15.6596026380 -0.3146071961 17.7895894589
H 14.1279733995 -0.1985231607 18.6772188148
C 12.6119387336 0.9219522549 16.5242149113
H 12.8130801656 1.4708464245 14.4070641930
H 11.1274345538 1.5331948980 15.0135162182
H 11.8967891568 -0.0489646220 14.6918445707
H 13.7167029769 -0.9473918082 16.2985747966
H 14.5725268959 0.5017776524 15.7001686811
H 10.6259705781 0.8242588150 17.4442046623
H 11.8817377786 -0.0009292530 18.4111485851
H 11.2640183396 -0.7737517900 16.9249761327
C 13.6911212631 2.5826239655 18.1707017401
H 14.6322254441 4.3207787821 17.2084715406
H 14.7498999937 4.3153418868 19.0027472074
H 13.2017230284 4.7336969801 18.2157082664
H 15.6295059991 2.1322945849 17.3113971310
H 15.5421975472 1.8600253215 19.0754141252
H 11.9610750723 2.8822821544 19.4809530939
H 13.5155820684 2.6900563897 20.3650517246
H 12.6998882382 1.2649670121 19.6643042287
C 7.2942702837 2.5118711738 16.6442372817
H 8.7267359026 1.5024076726 15.3270724392
H 7.0351018865 1.0137143975 15.0234422250
H 7.8898763486 0.3893188894 16.4638607983
H 9.3306348836 2.8364761868 17.4261192464
H 8.3060908427 1.8087909481 18.4640479796
H 8.0279708998 3.5892948213 18.4076921193
C 4.7678056944 2.3883848877 16.2230566480
H 5.7277348484 3.0170588652 18.0517237507
H 5.8798319810 1.2646373437 17.7411865349
H 4.8542648155 1.5931878793 15.4507080999
H 3.7829587303 2.2315067744 16.7111516890
C 6.1866553523 4.0662533487 14.9056625843
H 7.3005041390 3.4540042624 13.1045100221
H 5.5353451825 3.6378095784 12.8403129479
H 6.1681265599 2.2029084508 13.6923938951
H 7.2160617724 5.8389202112 14.0893884776
H 6.1726849821 6.1753664694 15.5108384400
H 5.4427927731 5.8688094089 13.8911148259
H 4.6537387927 4.5408317658 16.3630055590
H 4.0130957740 3.8973167117 14.8247327269

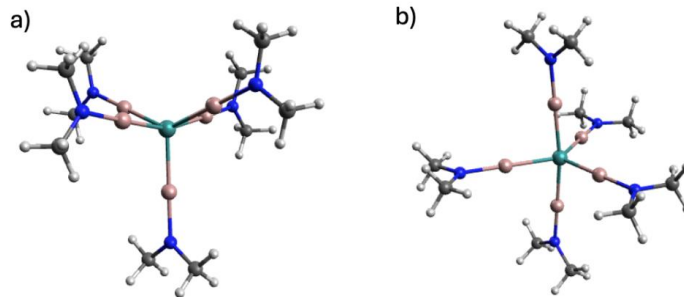


Figure S 21: Optimized structure of a) **1NMe₂ SP** and b) **1NMe₂ TB**.

1NMe₂ SP xyz Coordinates:

Ru 10.9097358574 4.6220579939 14.1831367948
Ga 8.9098995421 3.8123330315 15.0168153896
Ga 10.0241848266 4.2400610219 12.0795669431
Ga 10.9083481843 6.9284299560 14.1880693506
N 7.3113955296 3.1623922225 15.6814441479
N 9.3120987181 3.8914865989 10.4135840070
N 10.9079192730 8.7889013009 14.1935084266
C 11.9931034639 9.5839961292 13.6503876482
Ga 12.9113134578 3.8185830582 13.3474117086
Ga 11.7941575450 4.2340036287 16.2860280201
N 14.5118322691 3.1730056029 12.6832350906
N 12.5040472232 3.8819937845 17.9521852793
C 9.8220277624 9.5802973578 14.7406120450
C 15.5931862892 4.0340911333 12.2448096291
C 14.7932701938 1.7564164804 12.5510796505
C 9.0377645151 2.5467663862 9.9448285943
C 8.9783485467 4.9329889811 9.4613869823
C 12.7808112046 2.5365883681 18.4175038119
C 12.8344258341 4.9215923528 18.9076396581
C 7.0305103406 1.7449560055 15.8053277799
C 6.2302336046 4.0205645186 16.1259793733
H 7.9023119141 4.9207716420 9.1999845041
H 9.5472229307 4.8239854287 8.5175937143
H 9.2083922870 5.9252107611 9.8758519142

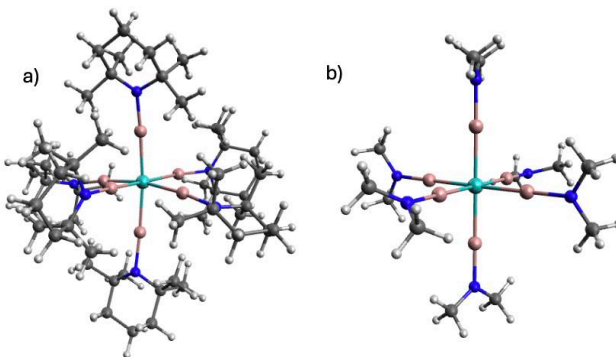
H 7.9644534048 2.4037895406 9.7124382771
H 9.3134566020 1.8063238141 10.7098341566
H 9.6079961288 2.3073770468 9.0261731177
H 9.0308034741 8.9285745015 15.1403758710
H 9.3609281267 10.2349237707 13.9747400724
H 10.1640142708 10.2358070815 15.5658559343
H 11.6507686577 10.2432099378 12.8282360946
H 12.7850712185 8.9349749650 13.2477136055
H 12.4533643967 10.2353113315 14.4195749340
H 14.9945656890 1.4732342378 11.4994272331
H 13.9383400716 1.1580997878 12.8986927868
H 15.6771474026 1.4553569618 13.1467040550
H 15.8396767761 3.8732628622 11.1771052355
H 16.5196376864 3.8583317362 12.8255947393
H 15.3193367940 5.0920872683 12.3674610326
H 12.6026483052 5.9144491691 18.4956642235
H 13.9101782372 4.9110447955 19.1702847237
H 12.2646690002 4.8086650527 19.8504308146
H 12.5074971677 1.7976703013 17.6501789959
H 12.2101091770 2.2934776592 19.3348867449
H 13.8541762520 2.3952418618 18.6506504304
H 6.5035562732 5.0793347961 16.0089739656
H 5.9851444690 3.8536157911 17.1930612220
H 5.3031255699 3.8477345721 15.5453579742
H 7.8852183537 1.1490215412 15.4531049560
H 6.1460030236 1.4471748947 15.2089883757
H 6.8306301584 1.4553496971 16.8554988393

1_{NMe₂}T_B xyz Coordinates:

Ru 10.7952760000 4.6513340000 13.9973720000
Ga 8.7759520000 3.7144370000 14.6245350000
Ga 9.9357500000 4.8118980000 11.8541710000
Ga 10.9358010000 6.9293790000 14.3357000000
N 7.1590560000 2.9699020000 15.1337100000
N 9.2390990000 4.9373470000 10.1512300000
N 11.0575650000 8.7659000000 14.6010700000
C 12.1934920000 9.5554420000 14.1624060000
Ga 12.7199180000 3.7437210000 13.0887050000
Ga 11.5964710000 4.0750480000 16.0908770000
N 14.2699700000 3.0303340000 12.3672030000

N 12.2210470000 3.5976490000 17.7591020000
C 10.0273060000 9.5434980000 15.2641730000
C 15.4492080000 3.8264590000 12.0848440000
C 14.4068160000 1.6298140000 12.0154750000
C 8.8782730000 3.7781230000 9.3579490000
C 9.0217610000 6.2068150000 9.4843620000
C 12.4546680000 2.2201630000 18.1479790000
C 12.5381200000 4.5691000000 18.7881960000
C 6.8869370000 1.5472830000 15.0588350000
C 6.0497220000 3.7575420000 15.6362370000
H 7.9576660000 6.3514290000 9.2143650000
H 9.6124470000 6.2870540000 8.5511900000
H 9.3152480000 7.0422960000 10.1364910000
H 7.8061270000 3.7885170000 9.0813020000
H 9.0679190000 2.8510500000 9.9181590000
H 9.4606340000 3.7262450000 8.4175020000
H 9.1948750000 8.8962840000 15.5777380000
H 9.6106500000 10.3267820000 14.6008070000
H 10.4142340000 10.0525900000 16.1687030000
H 11.8953100000 10.3401780000 13.4396490000
H 12.9414570000 8.9170650000 13.6691710000
H 12.6940480000 10.0634510000 15.0099670000
H 14.6130280000 1.4946980000 10.9356470000
H 13.4830960000 1.0802550000 12.2489040000
H 15.2341480000 1.1457770000 12.5703710000
H 15.7080310000 3.8121240000 11.0079950000
H 16.3346140000 3.4596170000 12.6398900000
H 15.2865020000 4.8750310000 12.3741260000
H 12.3392870000 5.5902650000 18.4317370000
H 13.6036050000 4.5202280000 19.0858560000
H 11.9332360000 4.4098880000 19.7018750000
H 12.1949870000 1.5363500000 17.3268470000
H 11.8456300000 1.9337130000 19.0273080000
H 13.5156520000 2.0411320000 18.4098470000
H 6.3157050000 4.8242340000 15.6677200000
H 5.7608050000 3.4538430000 16.6614030000
H 5.1503540000 3.6550950000 14.9980490000
H 7.7628880000 1.0056510000 14.6726700000
H 6.0337200000 1.3260460000 14.3881390000
H 6.6420710000 1.1227620000 16.0520630000

[Mo(GaTMP)₆]:

Figure S 22: Optimized structure of a) 2 and b) 2NMe₂·2:**2 xyz Coordinates:**

Mo -1.0040099031 5.1244944252 7.9708433404
 H 3.2576609760 6.9094131019 8.8112118534
 C 3.9299112208 8.5560392616 8.6493898859
 Ga 0.6236938715 6.7744001920 7.4118087707
 C -2.8596625703 4.0392921656 3.3271380984
 Ga -1.4923485639 5.0588761973 5.6451842655
 C -2.6201122999 3.6360647305 1.8520753482
 Ga -2.7117857684 3.4500624679 8.1140789332
 H -1.7475751588 2.9467855159 1.8234667931
 Ga -0.3220855460 4.7320644589 10.2425172511
 H -3.4977553379 3.0622263995 1.4852696075
 Ga 0.7355943818 3.5871958641 7.4304219203
 C -2.3242648856 4.8349557826 0.9504860262
 Ga -2.4977513878 6.9781768936 8.3005511007
 H -2.1414509894 4.4973518587 -0.0913614617
 N 1.8560925146 8.0335399915 6.7436935581
 H -3.2039715235 5.5133391596 0.9018154790
 N -1.7708883801 4.9305361204 3.7942314582
 C -1.1016040848 5.5776129854 1.4889586828
 N -3.9920513729 2.0897476135 7.9009992579
 H -0.85053312485 6.4545462985 0.8551713075
 N 0.5080917860 4.1878215122 11.8450945436
 H -0.2265107912 4.8920206373 1.4528652356
 N -3.5528770584 8.5329823580 8.3569198368
 C -1.2675781618 6.0485397887 2.9538409585
 C 1.4543788624 9.4575732199 6.8566246713
 C -2.8254422211 2.7568576490 4.1828762726
 C 2.3571472315 10.3452228445 5.9665042697
 H -3.5688479206 2.0202699946 3.8157991352
 H 2.0966632626 10.1423046603 4.9044477906
 H -3.0790234715 2.9564150950 5.2467486106
 H 2.1164598097 11.4122814283 6.1596370400
 H -1.8197500957 2.2912248199 4.1485230818
 C 3.8464111515 10.0635981143 6.1632499318
 C -4.2675557554 4.6708009834 3.4913994067
 H 4.4531339361 10.7137923205 5.4985062959
 H -5.0670134426 3.9341123322 3.2665948996
 H 4.1582527585 10.3100644062 7.2016075582
 H -4.4197941523 5.5418119584 2.8269652802
 C 4.1167029706 8.5908522728 5.8573436452
 H -4.4041856459 5.0215762188 4.5352026233
 H 5.1933779425 8.3434241291 5.9734773519
 C 0.1110106971 6.4641480269 3.4815494273
 H 3.8549747957 8.3963778729 4.7940647947
 C 0.5519880257 7.2587992686 2.8465411833
 C 3.2836748015 7.6298927027 6.7404694406
 H 0.7986131548 5.5956093375 3.4920239123
 C 0.0096111850 9.5753585545 6.3311576949
 H 0.0663799454 6.8708691885 4.5147513809
 H -0.3370827234 10.6281917720 6.3508188056
 C -2.1983124339 7.2940152780 3.0148182393
 H -0.7035264212 8.9896706578 6.9516724422
 H -0.0563279330 9.1970858702 5.2918688137
 C -1.7613851666 8.1471148798 2.4547856072
 C 1.4723165074 9.9692868129 8.3210033854
 H -2.3368238928 7.6116239420 4.0692308775
 H 1.0675143392 11.0002040339 8.3965481850
 H -3.2009021313 7.0939114971 2.5929436140
 H 2.4917023915 9.9753179708 8.7520221180
 C -3.5604726363 0.6736998776 7.9286818575
 H -4.3749626220 -0.1416194760 6.8923137796
 H 0.8477103868 9.3076014793 8.9575748332
 H -4.0435516918 0.1698968075 5.8774796258
 C 3.3704396756 6.2235483600 6.1151224361
 H -4.1254863508 -1.2193706595 6.9962352816
 C 2.9249281763 6.2296601245 5.1006299419
 C -5.8828666164 0.0882126980 7.0085380471
 H 2.8316610180 5.4577193906 6.7145362676
 H -6.4198532407 -0.4874763305 6.2255105185
 C 3.8854944809 7.5605997694 8.1682972678
 C -6.1886578933 1.5805148405 6.8717978042
 H 4.9149497472 7.1452759555 8.1553850741
 H -7.2790757895 1.7756934388 6.9583308556

H -5.8785137332 1.9184721371 5.8584068931
C -5.4302063845 2.4411646595 7.9130584130
C -2.0754162485 0.6141727283 7.5204316200
H -1.7297390677 -0.4367789087 7.4550038652
H -1.4241200879 1.1268283618 8.2613044061
H -1.9154912177 1.0963430289 6.5347950144
C -3.6731240900 0.0329635493 9.3359555422
H -3.2061072984 -0.9739082100 9.3487145146
H -4.7202026729 -0.0831621165 9.6715999043
H -3.1506645188 0.6680662153 10.0793515310
C -5.5624160805 3.9198398182 7.5012250608
H -6.6281919409 4.2197162373 7.4466071919
H -5.0988444120 4.1012771798 6.5104138454
H -5.0704121549 4.5917291815 8.2385197463
C -6.0780256401 2.2955823759 9.3139652065
H -7.1062313221 2.7135143616 9.3186385265
H -5.4739321772 2.8435448301 10.0649977955
H -6.1476157875 1.2423796953 9.6434361805
C 1.4182521295 5.1289326772 12.5369422783
C 2.6236973343 4.3556936930 13.1303059422
H 3.2596400700 4.0159920454 12.2836539833
H 3.2402545890 5.0514191969 13.7387938158
C 2.2014603481 3.1334935775 13.9475780941
H 1.6380576098 3.4482817766 14.8528759911
H 3.0969636170 2.5919760766 14.3187935731
C 1.3448303432 2.2083379859 13.0815686081
H 1.0196441945 1.3119138773 13.6518574291
H 1.9612167495 1.8448717806 12.2299419296
C 0.0992467757 2.9219052010 12.4968755933
C 1.9635761896 6.1246992390 11.4935138927
H 2.6923741272 6.8189395310 11.9579580977
H 1.1528082623 6.7469443748 11.0549293028
H 2.4686969147 5.5909587287 10.6636343442
C 0.7106516669 5.9599330625 13.6383349111
H 1.3792061767 6.7594243961 14.0209241507
H 0.4010674132 5.3472463761 14.5053696288
H -0.199957628 6.4361089384 13.2219709978
C -0.5158949168 2.0025480595 11.4242789628
H -0.7815813886 1.0175670221 11.8574826287
H 0.1955262031 1.8372410437 10.5907645732
H -1.4459569533 2.4385077016 10.9990755592
C -0.9751555929 3.1244213202 13.5964961054
H -1.3682729746 2.1480060755 13.9488377089
H -1.8204627420 3.7159334842 13.1907690058
H -0.5824154183 3.6607407735 14.4796099945
C -3.4055521167 9.4683853650 9.4956314155
C -4.8021682753 9.9128293797 9.9978056487
H -5.2840856332 9.0362720794 10.4846505828
H -4.6839552056 10.6936795118 10.7797942784
C -5.7043371021 10.4040373060 8.8635662042
H -5.2879674789 11.3315262535 8.4131603061
H -6.7036576964 10.6812507757 9.2603250532
C -5.8418908312 9.3137678233 7.7987662079
H -6.4854885614 9.6563012640 6.9600098702
H -6.3442919742 8.4309253707 8.2523333600
C -4.4738785006 8.8466897538 7.2399860601

C -2.5371644311 10.7060757375 9.1507504399
H -2.3069296734 11.2901884019 10.06586555030
H -3.0353822348 11.3908956084 8.4403079877
H -1.5822058478 10.3823533271 8.6934516457
C -4.7015060983 7.5613280056 6.4221350936
H -5.4280731856 7.7382031941 5.6043103035
H -5.0894090971 6.7433887150 7.0626066983
H -3.7588234207 7.2088962718 5.9508840774
C -3.8967269601 9.9047900867 6.2640906264
H -4.5395128535 9.9988614768 5.3643257732
H -2.8822444443 9.6027495037 5.9366585285
H -3.8176334675 10.9088188352 6.7196644270
C -2.6937036902 8.7219890356 10.6407498195
H -1.6644754374 8.4151634776 10.3504135195
H -3.2553870829 7.8095612919 10.9300173811
H -2.6027577945 9.3712685441 11.5347236511
H 3.8769870714 2.7593594293 9.9304676861
C 3.1799104212 3.0869444923 9.1324998484
H 3.5570942370 4.0369995289 8.7033460749
H 2.2071770383 3.2943822984 9.6292722692
H 5.0684929398 1.1992101145 8.3171364758
H 3.0262975238 0.4430464611 9.6025024586
H 4.9901105143 2.6721030350 7.3099331406
C 4.4869158621 1.7017732913 7.5150539177
C 3.0617505442 2.0045468320 8.0398941738
C 2.4529952533 0.7401398818 8.6995374727
H 1.4074920359 0.9457833835 9.0074495582
C 4.4800899059 0.8727661890 6.2309488496
H 2.4321370865 -0.1280497456 8.0143993563
H 5.5186087935 0.6928022846 5.8818555222
N 2.2209567804 2.5443229126 6.9446908498
H 4.0414348690 -0.1313214610 6.4190829388
C 3.6810905182 1.6149700629 5.1601093771
H 4.1873732974 2.5819743335 4.9466049774
C 2.2280472160 1.9242392556 5.5976824112
H 1.7556093549 -0.1802954451 6.1390589621
H 2.2084036144 3.8962417206 4.6426131656
C 1.3554262072 0.6448328460 5.5205161815
H 3.6584946635 1.0460123525 4.2062430814
C 1.6450662381 2.9435784715 4.5994053614
H 0.3316505108 0.8674244598 5.8835460034
H 0.5768179920 3.1707897918 4.8056107865
H 1.279387312 0.2743387733 4.4768148906
H 1.6900711083 2.5515809257 3.5633356391

Z_{NMe2}xyz Coordinates:

Mo -0.7424650016 5.0773824570 7.6018918863
Ga 0.9337347424 6.7982788000 7.3014933744
Ga -1.3131041590 5.2232999193 5.2539878080
Ga -2.4280831163 3.3683485955 7.9044233666
Ga -0.1789219872 4.9175233866 9.9499529581
Ga 0.8917827461 3.3760556775 7.064283623
Ga -2.3800745038 6.7796580258 8.1307987220
N 2.2169808259 8.1272303391 7.0773056192
N -1.7514482205 5.3180932974 3.4481599896
N -3.7289192271 2.0600468618 8.1460069301

N 0.2507364902 4.7896704796 11.7560910797
N -3.6215513840 8.1055355254 8.5341432869
C 1.8812261540 9.5334023328 6.9796045703
C 3.6339450746 7.8402182440 6.9802074573
C -1.5847106025 6.5243426625 2.6627483761
C -3.4134109632 0.6490206262 8.2409868371
C -5.1412020028 2.3678759808 8.2458590302
C 1.4788498068 5.3227150576 12.3109287651
C -0.6210373494 4.1559116581 12.7248356060
C -3.4686584504 8.9953992227 9.6678274361
C -4.8263050257 8.3208151209 7.7589595000
C 2.7330891545 1.1822852726 7.6081750130
N 2.1249753890 2.0543551757 6.6237709163
C 2.5712564379 1.8283545197 5.2635805435
H 2.3479223638 1.4063947160 8.6257589074
H 3.8461987383 1.2922247222 7.6432259445
H 2.5222140243 0.1025771851 7.4038675665
H 2.0649191457 2.5242304222 4.5611026126
H 2.3521940398 0.7882269511 4.9143058855
H 3.6734512262 1.9829242053 5.1467816949
H -4.3095297385 8.8985666247 10.3997176167
H -3.4296907703 10.0706614189 9.3605049721
H -2.5282152254 8.7759791436 10.2171029908
H -4.8796055890 7.6101735983 6.9065912642
H -4.8749030372 9.3540110764 7.3322042316
H -5.7545819167 8.1794361187 8.3678991989
H 3.8219951025 6.7482568192 7.0596866680
H 4.2237030555 8.3380189080 7.7904613870
H 4.0699161316 8.1816279594 6.0079259095
H 2.2062814786 9.9800782216 6.0064279468
H 2.3596910500 10.1402800400 7.7885447395
H 0.7835015745 9.6837875677 7.0605370973
H -2.3181104776 0.4829205173 8.1578696068
H -3.9018031118 0.0495770483 7.4320810643
H -3.7431012384 0.2061838109 9.2143093160
H -5.3129536331 3.4627113025 8.1681766263
H -5.5798372487 2.0320037140 9.2189367471
H -5.7403477008 1.8799290292 7.4364030221
H -1.5406123053 3.7697875535 12.2352677826
H -0.9457440425 4.8624212411 13.5297735108
H -0.1286606914 3.2900350113 13.2349471879
H 2.0974669107 5.7953958507 11.5183633163
H 2.1053872190 4.5304745657 12.7927648175
H 1.2876141206 6.1020632144 13.0909722809
H -0.8959133158 6.3718101947 1.7945034027
H -1.1575474907 7.3423513832 3.2817330961
H -2.5537801221 6.8966775803 2.2449580626
C -2.3125558872 4.1989486848 2.7191098031
H -1.6771794747 3.8985987946 1.8483010581
H -3.3302872001 4.4252107959 2.3122257069
H -2.4113375220 3.3090752287 3.37691854

7.2 Supporting Information for Study II

Chemistry—A European Journal

Supporting Information

C—H and Si—H Activation Reactions at Ru/Ga Complexes: A Combined Experimental and Theoretical Case Study on the Ru—Ga Bond

Maximilian Muhr, Raphael Bühler, Hao Liang, Jonas Gilch, Christian Jandl, Samia Kahlal,
Jean-Yves Saillard,* Christian Gemel, and Roland A. Fischer*

Table of Contents

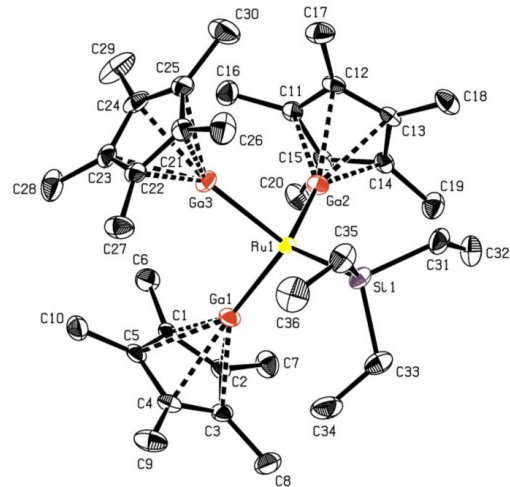
Experimental Section	2
Crystallographic Data.....	2
NMR spectra	6
LIFDI-MS spectra.....	10
Vibrational spectra	18
UV-Vis spectra.....	22
Computational Results	23
Bonding details.....	23
XYZ coordinates	24

Experimental Section

Crystallographic Data

X-ray Crystallographic Details

Data were collected on a single crystal x-ray diffractometer equipped with a CMOS detector (Bruker Photon-100), a TXS rotating anode with MoK α radiation ($\lambda = 0.71073 \text{ \AA}$) and a Helios optic using the APEX3 software package.¹ The measurements were performed on single crystals coated with perfluorinated ether. The crystals were fixed on top of a kapton micro sampler and frozen under a stream of cold nitrogen. A matrix scan was used to determine the initial lattice parameters. Reflections were corrected for Lorentz and polarisation effects, scan speed, and background using SAINT.² Absorption correction, including odd and even ordered spherical harmonics was performed using SADABS.² Space group assignment was based upon systematic absences, E statistics, and successful refinement of the structure. The structures were solved using SHELXT with the aid of successive difference Fourier maps, and were refined against all data using SHELXL in conjunction with SHELXLE.^{3,4,5} Hydrogen atoms were calculated in ideal positions as follows: Methyl hydrogen atoms were refined as part of rigid rotating groups, with a C–H distance of 0.98 \AA and $U_{\text{iso}}(\text{H}) = 1.5 \cdot U_{\text{eq}}(\text{C})$. Non-methyl H atoms were placed in calculated positions and refined using a riding model with methylene, aromatic, and other C–H distances of 0.99 \AA , 0.95 \AA , and 1.00 \AA , respectively, and $U_{\text{iso}}(\text{H}) = 1.2 \cdot U_{\text{eq}}(\text{C})$. Non-hydrogen atoms were refined with anisotropic displacement parameters. Full-matrix least-squares refinements were carried out by minimizing $\Sigma w(F_o^2 - F_c^2)^2$ with the SHELXL weighting scheme.³ Neutral atom scattering factors for all atoms and anomalous dispersion corrections for the non-hydrogen atoms were taken from *International Tables for Crystallography*.⁶ Images of the crystal structure were generated with Mercury and PLATON.^{7,8} Deposition Number 2158227 contains the supplementary crystallographic data for this paper. These data are provided free of charge by the joint Cambridge Crystallographic Data Centre and Fachinformationszentrum Karlsruhe Access Structures service www.ccdc.cam.ac.uk/structures.

Compound 1 (CCDC 2158227)

Diffractometer operator C. Jandl
 scanspeed 1-10 s per frame
 dx 70 mm
 3051 frames measured in 10 data sets
 phi-scans with delta_phi = 0.5
 omega-scans with delta_omega = 0.5
 shutterless mode

Crystal data

$M_r = 831.16$

$D_x = 1.399 \text{ Mg m}^{-3}$

Monoclinic, P2₁/c

Melting point: ? K

Hall symbol: -P 2ybc

Mo K α radiation, $\lambda = 0.71073 \text{ \AA}$

$a = 19.487 (2) \text{ \AA}$

Cell parameters from 9377 reflections

$b = 11.1759 (13) \text{ \AA}$

$\theta = 2.5\text{--}25.7^\circ$

$c = 19.650 (2) \text{ \AA}$

$\mu = 2.45 \text{ mm}^{-1}$

$\beta = 112.779 (3)^\circ$

$T = 100 \text{ K}$

$V = 3945.7 (7) \text{ \AA}^3$

Fragment, yellow

$Z = 4$

$0.20 \times 0.14 \times 0.11 \text{ mm}$

$F(000) = 1708$

Data collection

Bruker D8 Venture diffractometer 7224 independent reflections
 Radiation source: TXS rotating anode 6728 reflections with $I > 2\sigma(I)$
Helios optic monochromator $R_{\text{int}} = 0.048$
 Detector resolution: 16 pixels mm⁻¹ $\theta_{\text{max}} = 25.4^\circ$, $\theta_{\text{min}} = 2.3^\circ$
phi- and omega-rotation scans $h = -23 \text{--} 23$
 Absorption correction: multi-scan $k = -13 \text{--} 11$
SADABS 2016/2, Bruker
 $T_{\text{min}} = 0.681$, $T_{\text{max}} = 0.745$ $l = -23 \text{--} 23$
82487 measured reflections

Refinement

Refinement on F^2 Secondary atom site location: difference Fourier map
 Least-squares matrix: full Hydrogen site location: inferred from neighbouring sites
 $R[F^2 > 2\sigma(F^2)] = 0.025$ H-atom parameters constrained
 $wR(F^2) = 0.065$ $W = 1/[\Sigma^2(FO^2) + (0.0237P)^2 + 7.0356P]$
 $S = 1.04$ WHERE $P = (FO^2 + 2FC^2)/3$
7224 reflections $(\Delta/\sigma)_{\text{max}} = 0.022$
388 parameters $\Delta\rho_{\text{max}} = 1.12 \text{ e \AA}^{-3}$
0 restraints $\Delta\rho_{\text{min}} = -0.85 \text{ e \AA}^{-3}$
0 constraints Extinction correction: none
 Primary atom site location: iterative Extinction coefficient: \pm

References

- 1) *APEX suite of crystallographic software*, APEX 3, Version 2019-1.0, Bruker AXS Inc., Madison, Wisconsin, USA, 2019.
- 2) *SAINT*, Version 8.40A and *SADABS*, Version 2016/2, Bruker AXS Inc., Madison, Wisconsin, USA, 2016/2019.
- 3) G. M. Sheldrick, *Acta Crystallogr. Sect. A* **2015**, *71*, 3–8.

- 4) G. M. Sheldrick, *Acta Crystallogr. Sect. C* **2015**, *71*, 3–8.
- 5) C. B. Hübschle, G. M. Sheldrick, B. Dittrich, *J. Appl. Cryst.* **2011**, *44*, 1281–1284
- 6) *International Tables for Crystallography, Vol. C* (Ed.: A. J. Wilson), Kluwer Academic Publishers, Dordrecht, The Netherlands, **1992**, Tables 6.1.1.4 (pp. 500–502), 4.2.6.8 (pp. 219–222), and 4.2.4.2 (pp. 193–199).
- 7) C. F. Macrae, I. J. Bruno, J. A. Chisholm, P. R. Edgington, P. McCabe, E. Pidcock, L. Rodriguez-Monge, R. Taylor, J. van de Streek, P. A. Wood, *J. Appl. Cryst.* **2008**, *41*, 466–470.
- 8) A. L. Spek, *Acta Crystallogr. Sect. D* **2009**, *65*, 148–155.

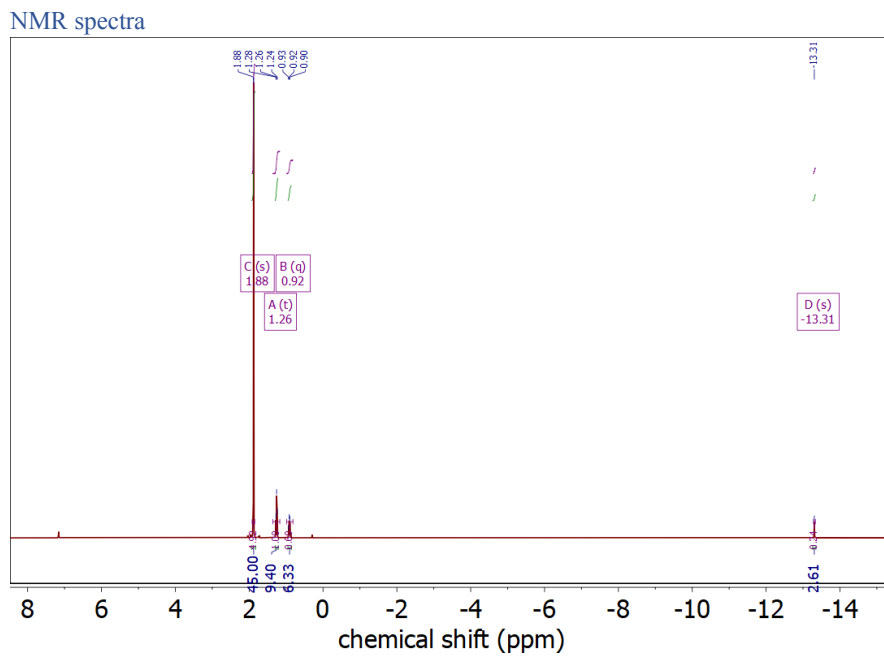


Figure S1: Proton NMR spectrum of **1** in C_6D_6 .

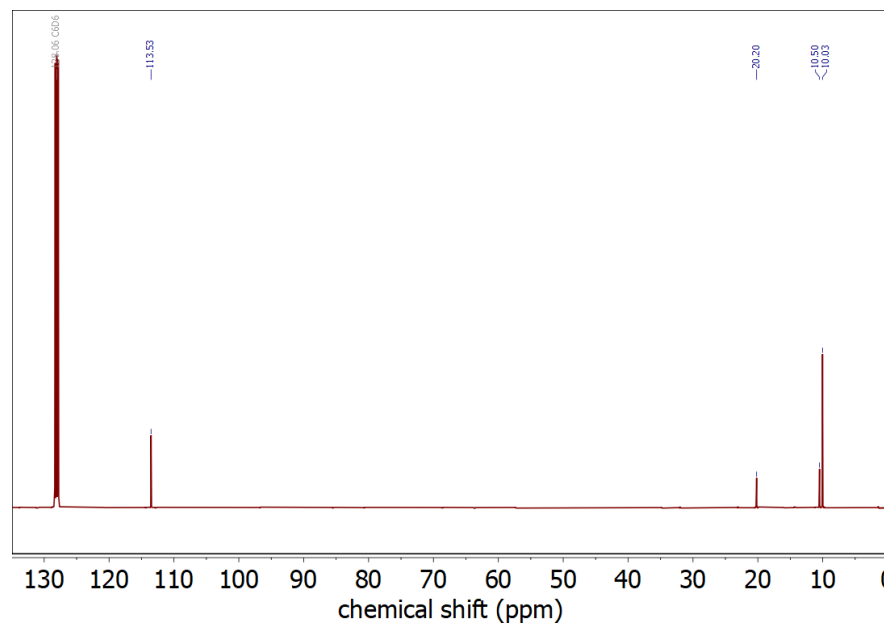


Figure S2: ^{13}C NMR spectrum of **1** in C_6D_6 .

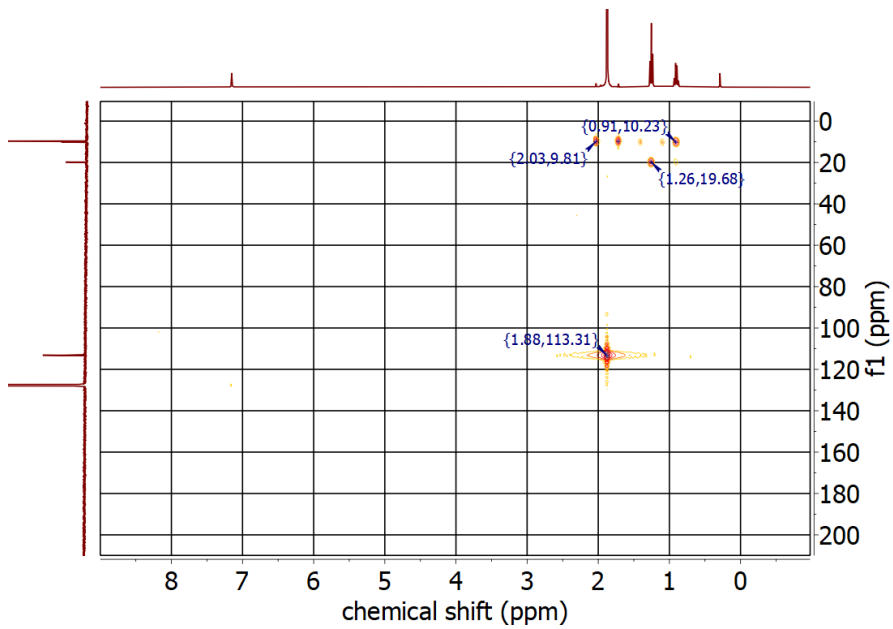
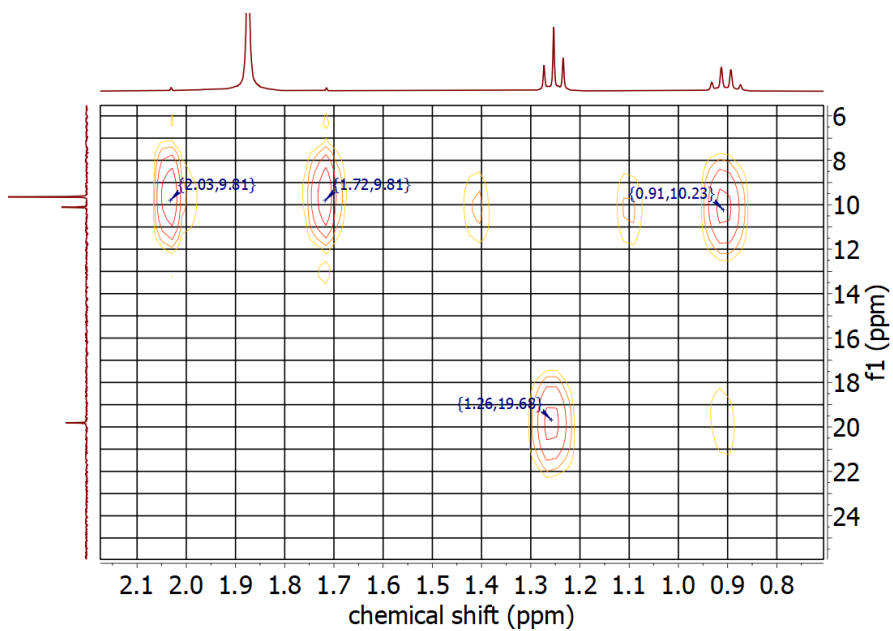
Figure S3: Heteronuclear Multiple Bond Correlation (HMBC) NMR spectrum of **1**.

Figure S4: HMBC zoomed-in.

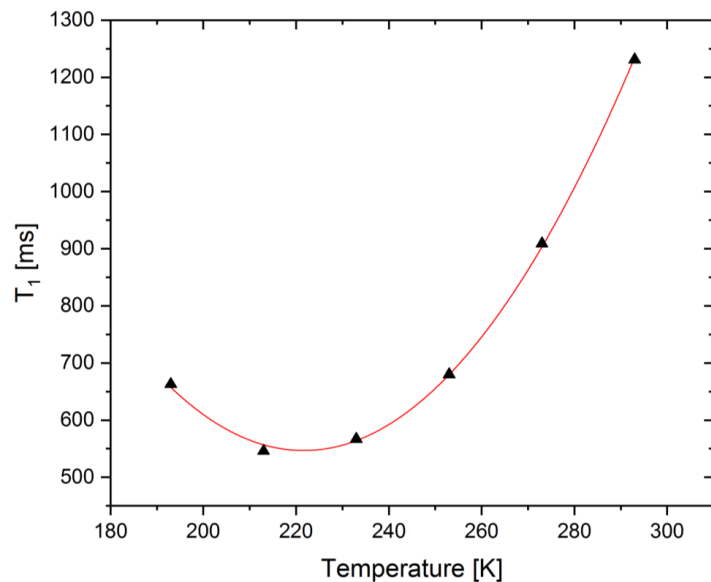


Figure S5: T_1 values of the hydrides of **1** determined via NMR as a function of temperature.

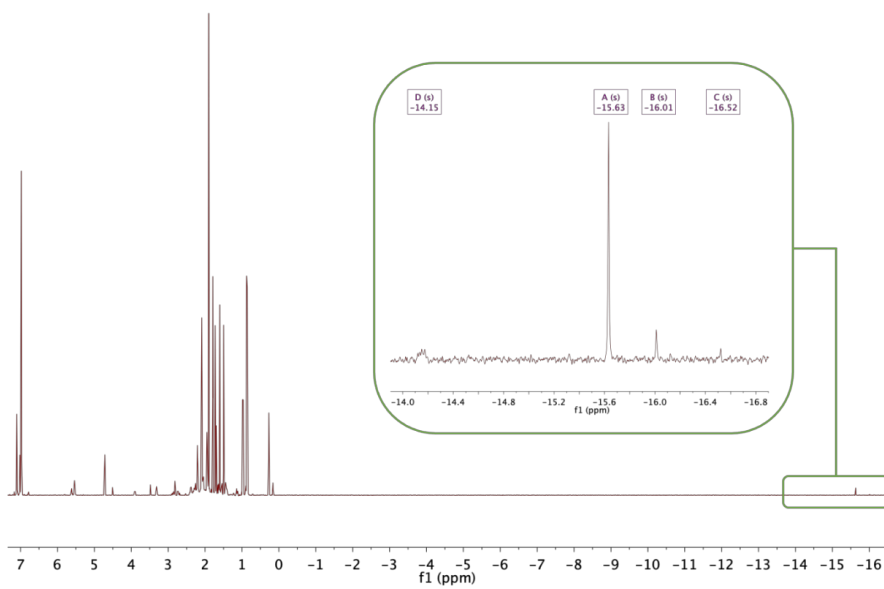


Figure S6: ^1H NMR spectrum of the reaction solution of **2** in toluene- d_8 .

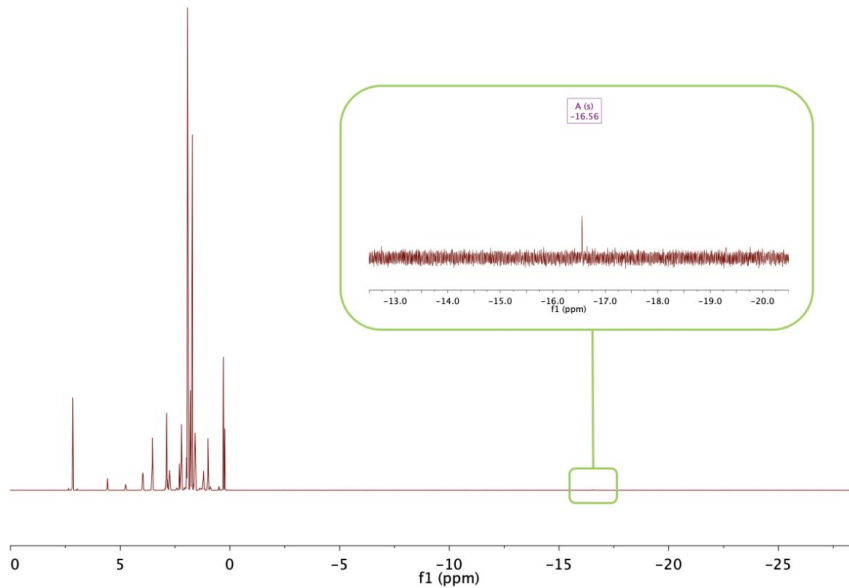
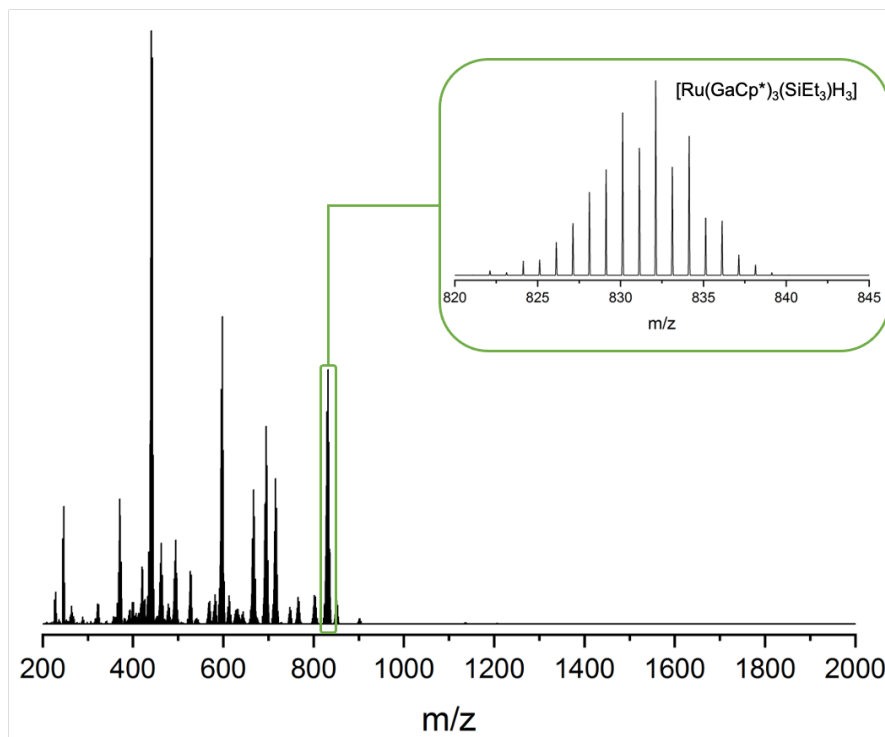


Figure S7: ¹H NMR spectrum of the reaction solution of the benzene analogue of **2** in *C*₆*D*₆.

LIFDI-MS spectra

Figure S8: LIFDI-MS of **1**.

10

140

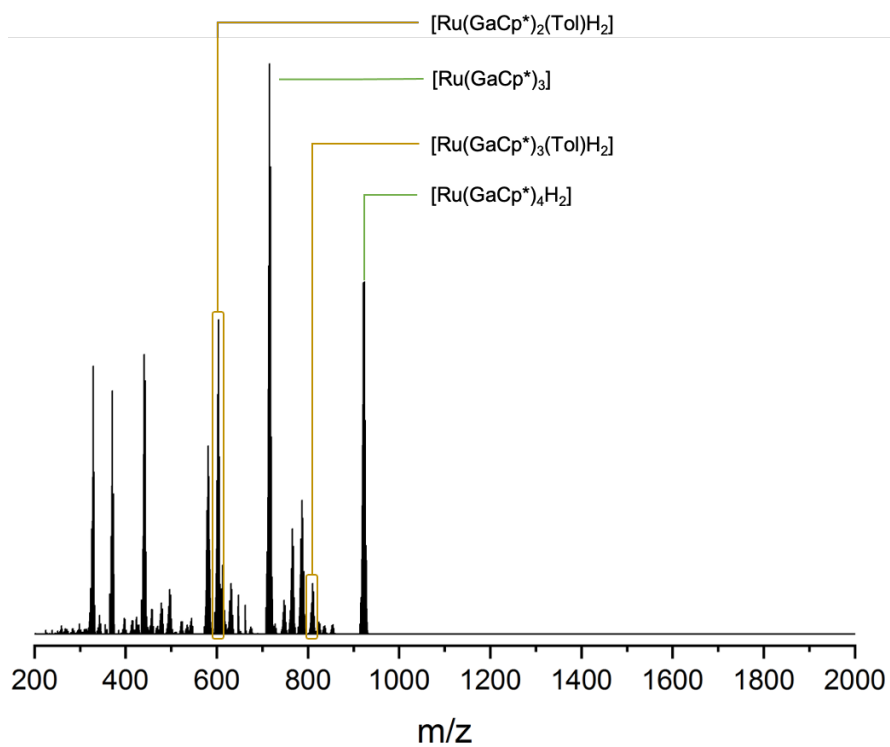


Figure S9: LIFDI-MS of the reaction solution of $[\text{Ru}(\text{COD})(\text{COT})]$ with GaCp^* under H_2 after 1 hour.

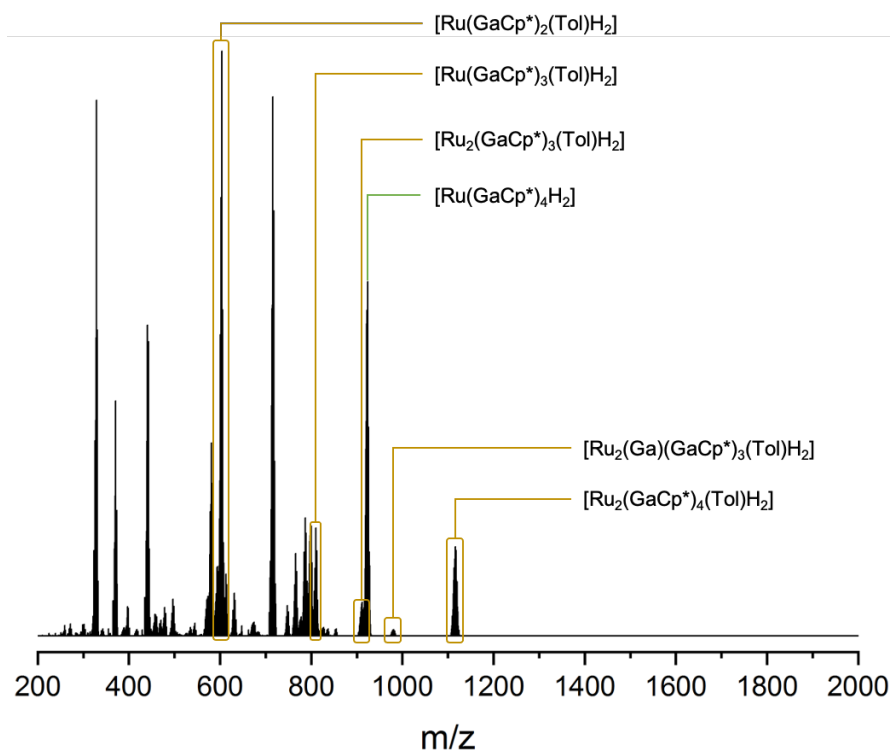


Figure S10: LIFDI-MS of the reaction solution of $[\text{Ru}(\text{COD})(\text{MeAllyl})_2]$ with GaCp^* under H_2 after 1 hour

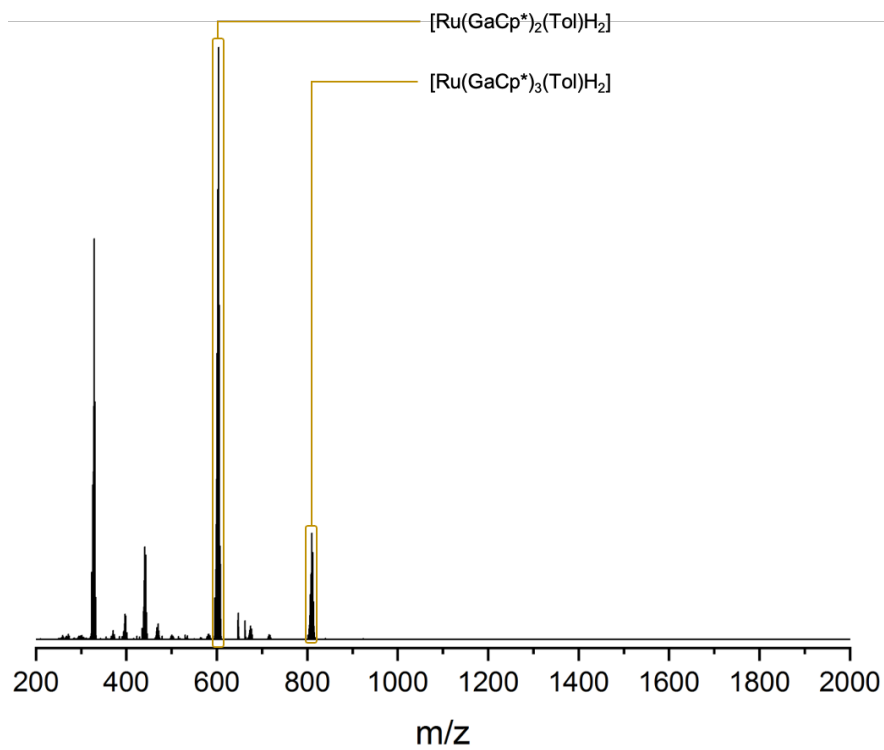


Figure S11: LIFDI-MS of the size-focused reaction solution of **2**.

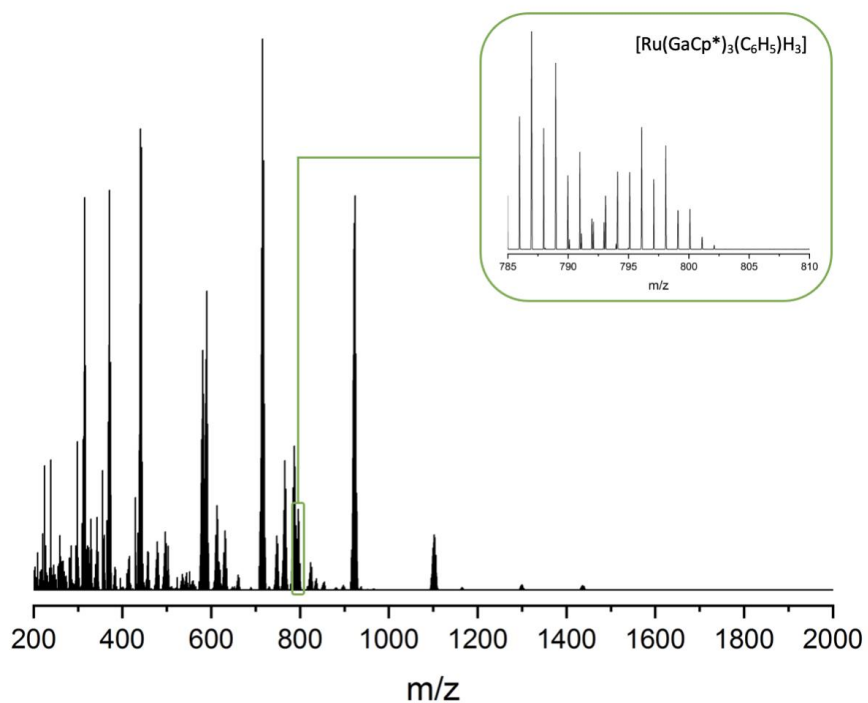


Figure S12: LIFDI-MS of the reaction solution of the analog of **2** in benzene.

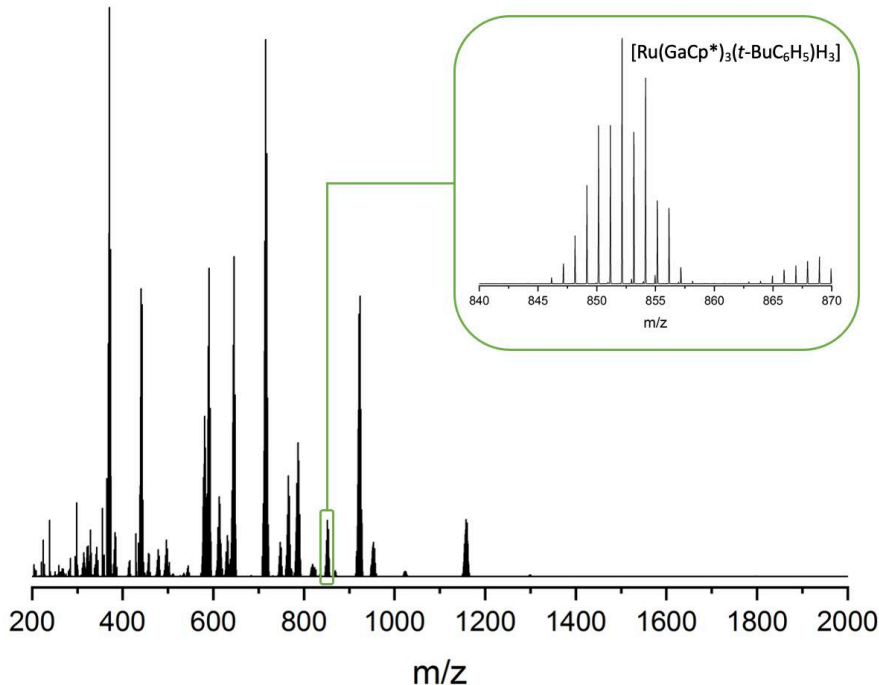


Figure S13: LIFDI-MS of the reaction solution of the analog of **2** in tert-butyl benzene.

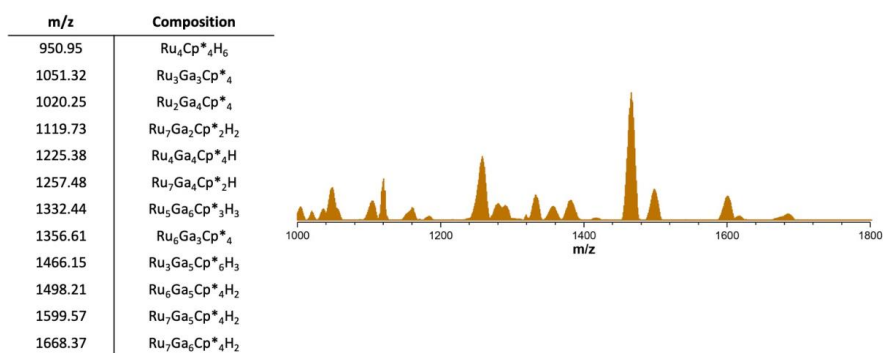


Figure S14: LIFDI-MS of the reaction solution of $[\text{Ru}(\text{COD})(\text{MeAllyl})_2]$ with GaCp^* under dihydrogen in cyclohexane with the sum formula of the RuGa polyhydride clusters obtained via $\text{Cp}^{*\text{et}}$ labelling experiments.

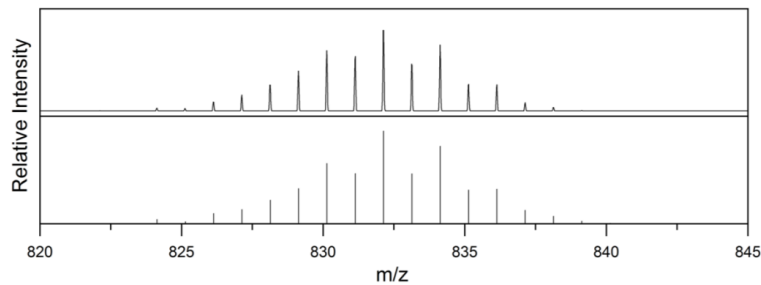


Figure S15: Experimental (top) and theoretical (bottom) pattern of $[M-2H]^{+}$ fragment of $[Ru(GaCp^*)_3(SiEt_3)H_3]$ (**1**).

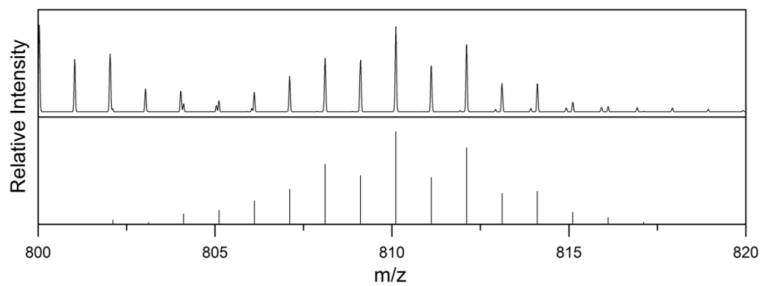


Figure S16: Experimental (top) and theoretical (bottom) pattern of $[Ru(GaCp^*)_3(C_7H_7)H_3]$ (**2**).

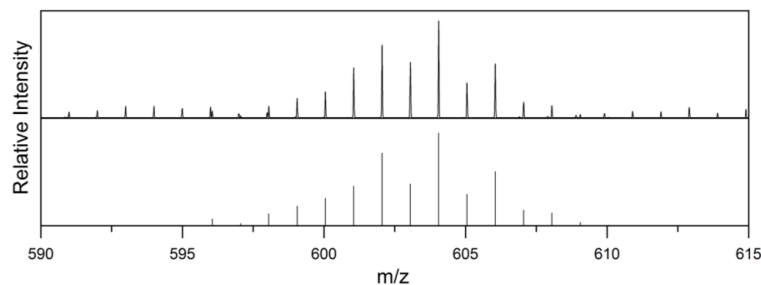


Figure S17: Experimental (top) and theoretical (bottom) pattern of $[M-GaCp^*-2H]^{+}$ fragment of $[Ru(GaCp^*)_3(C_7H_7)H_3]$ (**2**).

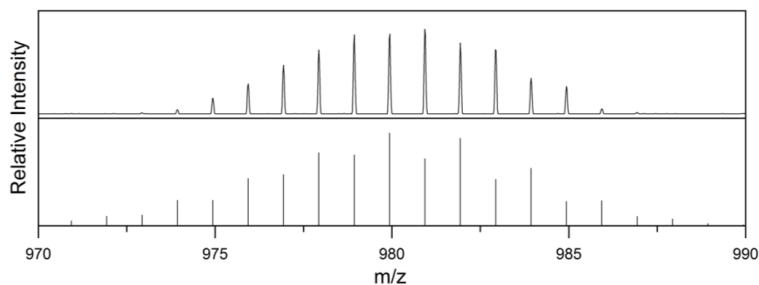


Figure S18: Experimental (top) and theoretical (bottom) pattern of $[Ru_2(GaCp^*)_4(Tol)H_2]^+$.

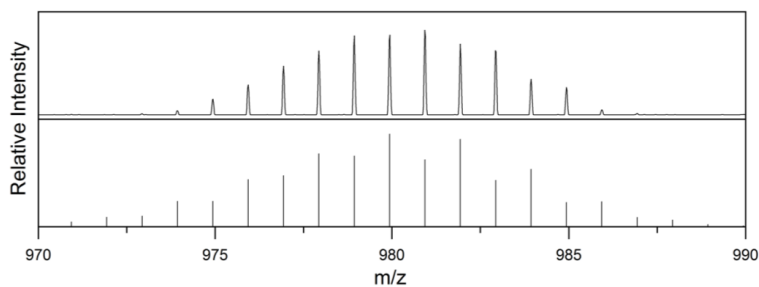


Figure S19: Experimental (top) and theoretical (bottom) pattern of $[Ru_2(Ga)(GaCp^*)_3(Tol)H]^+$.

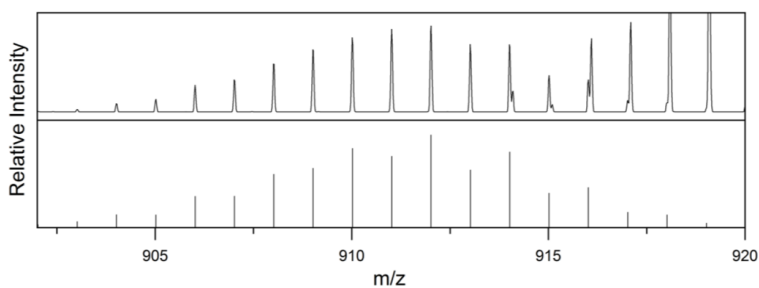


Figure S20: Experimental (top) and theoretical (bottom) pattern of $[Ru_2(GaCp^*)_3(Tol)H_2]^+$.

Vibrational spectra

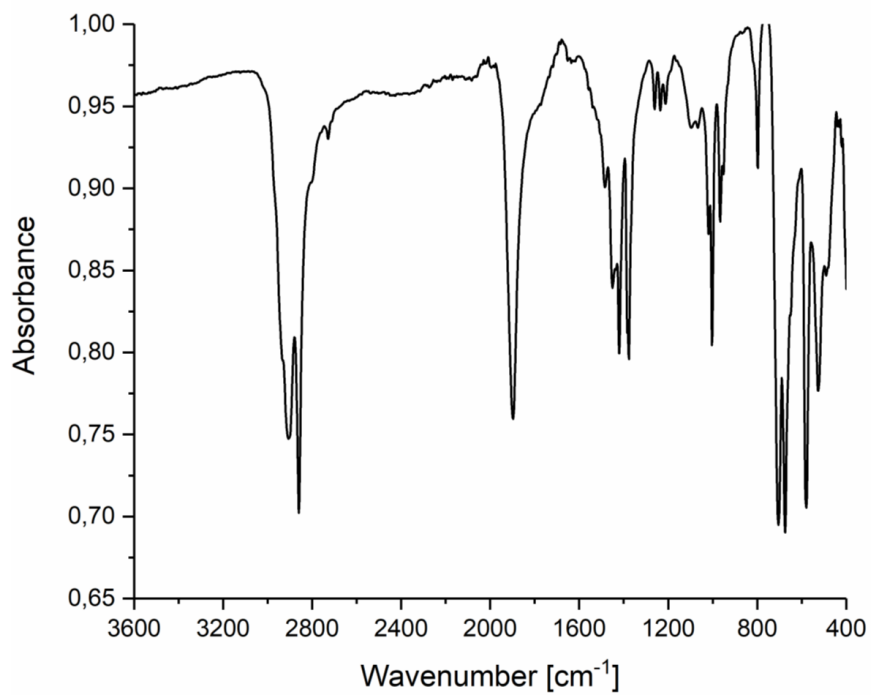


Figure S21: ATR-IR spectrum of 1.

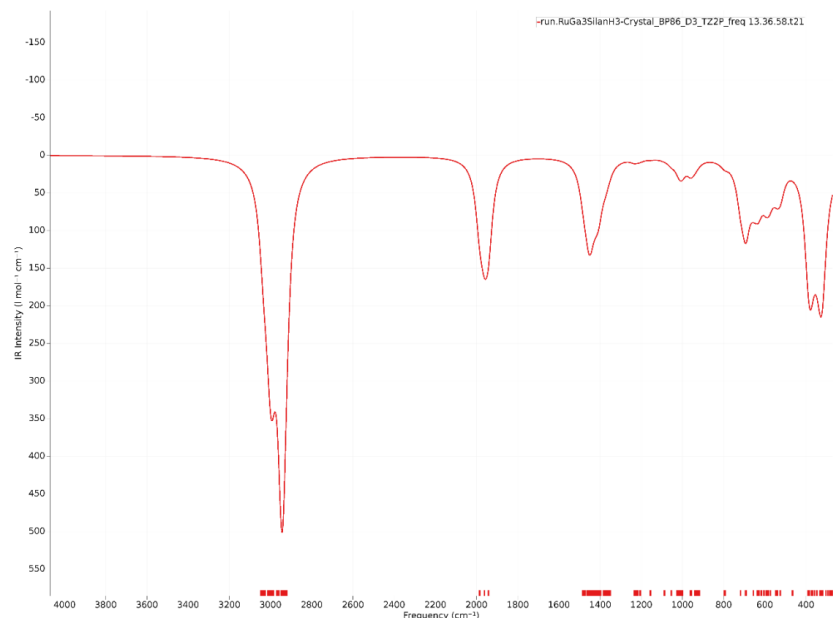


Figure S22: Calculated IR spectra of 1.

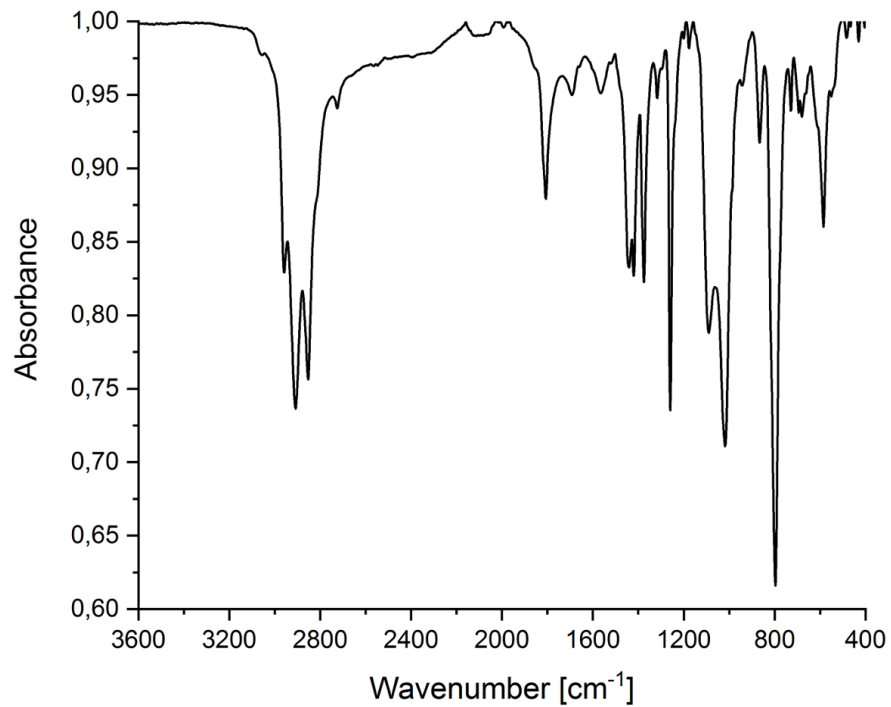


Figure S23: ATR-IR spectrum of the reaction solution of **2** (solvent evaporated of the window).

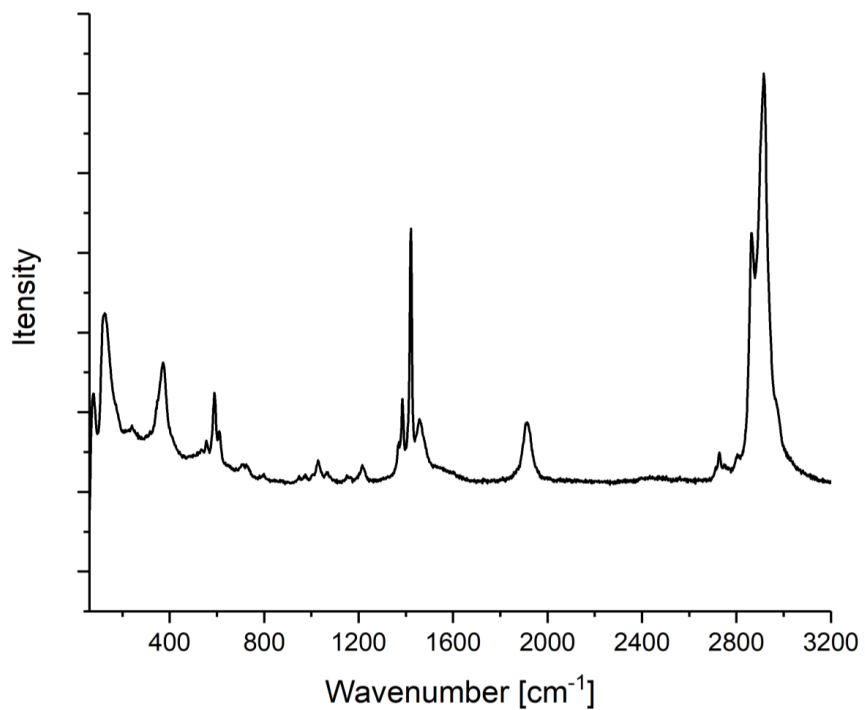
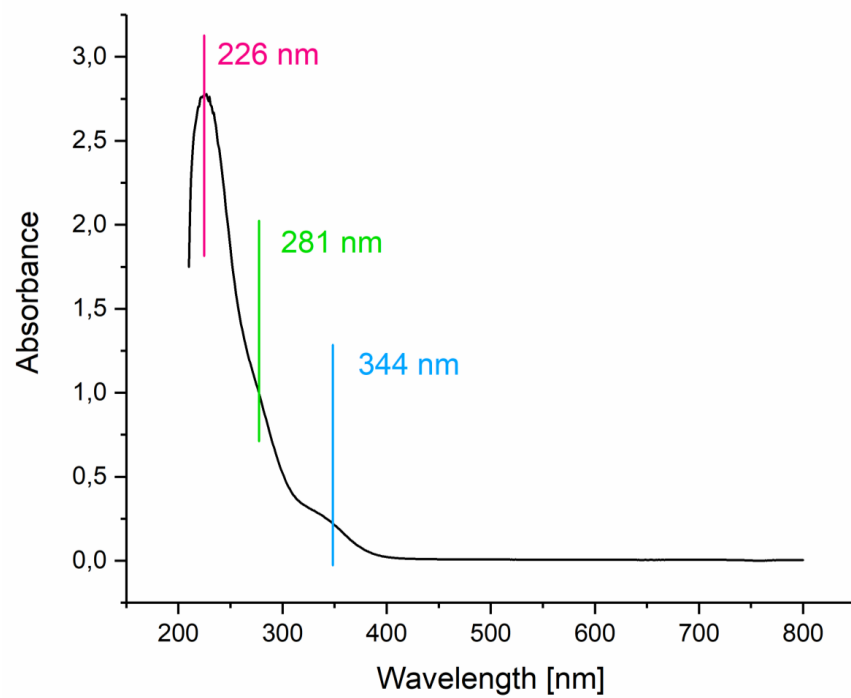


Figure S24: Solid-state Raman spectrum of **1**.

UV-Vis spectra

Figure S25: UV-Vis of **1** in cyclohexane.

Computational Results

Bonding details

Table S1. Selected computed data for complexes **1**, $[\text{Ru}(\text{GaCp}^*)_3\text{H}_2]$, and their triphenylphosphine analogues.

Compound	Distances (Å) and WBI's into brackets		
	Ru-H (av.)	Ru-Ga/P (av.)	Ru-Si
$[\text{Ru}(\text{GaCp}^*)_3(\text{SiEt}_3)\text{H}_3]$ (1)	1.628 [0.343]	2.381 [0.361]	2.370 [0.283]
$\text{Ru}(\text{PMe}_3)_3(\text{SiEt}_3)\text{H}_3]$	1.656 [0.374]	2.317 [0.419]	2.404 [0.277]
$[\text{Ru}(\text{GaCp}^*)_3\text{H}_2]$	1.624 [0.476]	2.350 [0.517]	-
$[\text{Ru}(\text{PMe}_3)_3\text{H}_2]$	1.658 [0.509]	2.256 [0.600]	-

Table S2. QTAIM descriptors of the Ru-E ($E = \text{Ga}, \text{P}$) bonds in **1**, $[\text{Ru}(\text{PMe}_3)_3(\text{SiEt}_3)\text{H}_3]$, $[\text{Ru}(\text{GaCp}^*)_3\text{H}_2]$ and their triphenylphosphine analogues.^{a,b}

Compound		$[\text{Ru}(\text{GaCp}^*)_3(\text{SiEt}_3)\text{H}_3]$ (1)	$[\text{Ru}(\text{PMe}_3)_3(\text{SiEt}_3)\text{H}_3]$	$[\text{Ru}(\text{GaCp}^*)_3\text{H}_2]$	$[\text{Ru}(\text{PMe}_3)_3\text{H}_2]$
Atom charge ^a	Ru	-0.35	0.02	-0.17	0.07
	E	0.63	1.32	0.60	1.27
Delocalisation index ^a	δ	0.87	0.94	1.06	1.00
bcp indicators ^{a,b}	ρ	0.069	0.095	0.075	0.098
	$\nabla^2\rho$	0.122	0.166	0.133	0.179
	H	-0.023	-0.043	-0.028	-0.045
	V	-0.077	-0.127	-0.088	-0.135
	$ V /G$	1.426	1.512	1.467	1.500

^aAveraged values. ^b ρ , $\nabla^2\rho$, H, V and G are the electron density, Laplacian of ρ density, energy density, potential energy density and kinetic energy density values at the bcp, respectively. All values in a.u.

7.3 Supporting Information for Study III

This journal is © The Royal Society of Chemistry 2023

Supporting Information

Photochemically Generated Reactive Sites at Ruthenium/Gallium Complexes: Catalysis vs. Cluster Growth.

Raphael Bühler^{# a}, Maximilian Muhr^{# a}, Johannes Stephan^a, Robert Wolf^a, Max Schütz^a,
Christian Gemel^a, Roland A. Fischer *a

a) Chair of Inorganic and Metalorganic Chemistry, Department of Chemistry, TUM School of Natural Sciences, Technical University Munich, Lichtenbergstraße 4, D-85748 Garching, Germany and Catalysis Research Center, Ernst-Otto-Fischer-Straße 1, D-85748 Garching, Germany.

Email: roland.fischer@tum.de

[#]M.M. and R.B. equally contributed to this work

Table of Contents

Crystallographic Data	3
NMR spectra	7
LIFDI mass spectra	21
IR spectra	30
UV-Vis spectra	31

Crystallographic Data

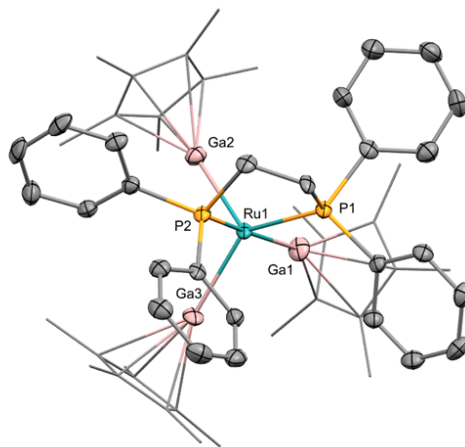


Figure S1: Crystal structure of $[(dppe)Ru(GaCp^*)_3]$. Co-crystallized molecule *n*-hexane and hydrogen atoms omitted for clarity. Ellipsoids drawn at 50% probability. Cp^* in wireframes.

Table S1: Crystallographic data table for compound 4.

Chemical formula	$C_{62}H_{83}Ga_3P_2Ru$		
Formula weight	1200.45		
Temperature	100(2) K		
Wavelength	0.71073 Å		
Crystal size	0.059 x 0.066 x 0.225 mm		
Crystal habit	red-orange fragment		
Crystal system	monoclinic		
Space group	P 1 21/n 1		
Unit cell dimensions	$a = 19.841(3)$ Å	$\alpha = 90^\circ$	
	$b = 12.724(2)$ Å	$\beta = 99.625(7)^\circ$	
	$c = 22.940(4)$ Å	$\gamma = 90^\circ$	
Volume	$5709.8(16)$ Å ³		
Z	4		
Density (calculated)	1.397 g/cm ³		
Absorption coefficient	1.753 mm ⁻¹		
F(000)	2488		
Diffractometer	Bruker D8 Venture		

Radiation source	TXS rotating anode, Mo
Theta range for data collection	2.41 to 25.68°
Index ranges	-24<=h<=24, -15<=k<=15, -27<=l<=27
Reflections collected	226471
Independent reflections	10838 [R(int) = 0.1954]
Coverage of independent reflections	99.9%
Absorption correction	Multi-Scan
Structure solution technique	direct methods
Structure solution program	SHELXT 2014/5 (Sheldrick, 2014)
Refinement method	Full-matrix least-squares on F ²
Refinement program	SHELXL-2018/3 (Sheldrick, 2018)
Function minimized	$\Sigma w(F_o^2 - F_c^2)^2$
Data / restraints / parameters	10838 / 0 / 630
Goodness-of-fit on F ²	1.021
Δ/σ_{\max}	0.001
Final R indices	6979 data; $I > 2\sigma(I)$ R1 = 0.0496, all data wR2 = 0.0861 R1 = 0.1073, wR2 = 0.1037
Weighting scheme	$w = 1/[\sigma^2(F_o^2) + (0.0318P)^2 + 16.8706P]$ where $P = (F_o^2 + 2F_c^2)/3$
Largest diff. peak and hole	0.982 and -0.774 eÅ ⁻³
R.M.S. deviation from mean	0.114 eÅ ⁻³

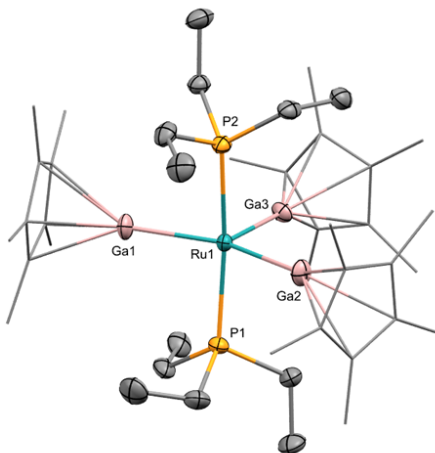


Figure S2: Crystal structure of $[(Et_3P)_2Ru(GaCp^*)_3]$. Co-crystallized molecule n-hexane and hydrogen atoms omitted for clarity. Ellipsoids drawn at 50% probability. Cp^* in wireframes.

Table S2: Crystallographic data table for compound $[Ru(GaCp^*)_3(PEt_3)_2]$.

Chemical formula	$C_{48}H_{88.07}Ga_3P_2Ru$		
Formula weight	1037.42		
Temperature	123(2) K		
Wavelength	0.71073 Å		
Crystal size	0.238 x 0.321 x 0.374 mm		
Crystal habit	orange block		
Crystal system	orthorhombic		
Space group	P 21 21 21		
Unit cell dimensions	$a = 12.268(4)$ Å	$\alpha = 90^\circ$	
	$b = 19.291(7)$ Å	$\beta = 90^\circ$	
	$c = 21.580(6)$ Å	$\gamma = 90^\circ$	
Volume	$5107.(3)$ Å ³		
Z	4		
Density (calculated)	1.349 g/cm ³		
Absorption coefficient	1.948 mm ⁻¹		
F(000)	2172		
Diffractometer	Bruker D8 Venture		
Radiation source	TXS rotating anode, Mo		

Theta range for data collection	2.51 to 25.90°
Index ranges	-14≤h≤15, -23≤k≤23, -26≤l≤26
Reflections collected	137547
Independent reflections	9855 [R(int) = 0.0279]
Coverage of independent reflections	99.3%
Absorption correction	Multi-Scan
Structure solution technique	direct methods
Structure solution program	SHELXT 2014/5 (Sheldrick, 2014)
Refinement method	Full-matrix least-squares on F^2
Refinement program	SHELXL-2019/1 (Sheldrick, 2019)
Function minimized	$\sum w(F_o^2 - F_c^2)^2$
Data / restraints / parameters	9855 / 101 / 531
Goodness-of-fit on F^2	1.051
Δ/σ_{\max}	0.003
Final R indices	9563 data; $ I > 2\sigma(I)$ R1 = 0.0172, all data wR2 = 0.0451 R1 = 0.0183, wR2 = 0.0455
Weighting scheme	$w=1/[\sigma^2(F_o^2)+(0.0257P)^2+1.6529P]$ where $P=(F_o^2+2F_c^2)/3$
Largest diff. peak and hole	0.485 and -0.396 eÅ ⁻³
R.M.S. deviation from mean	0.049 eÅ ⁻³

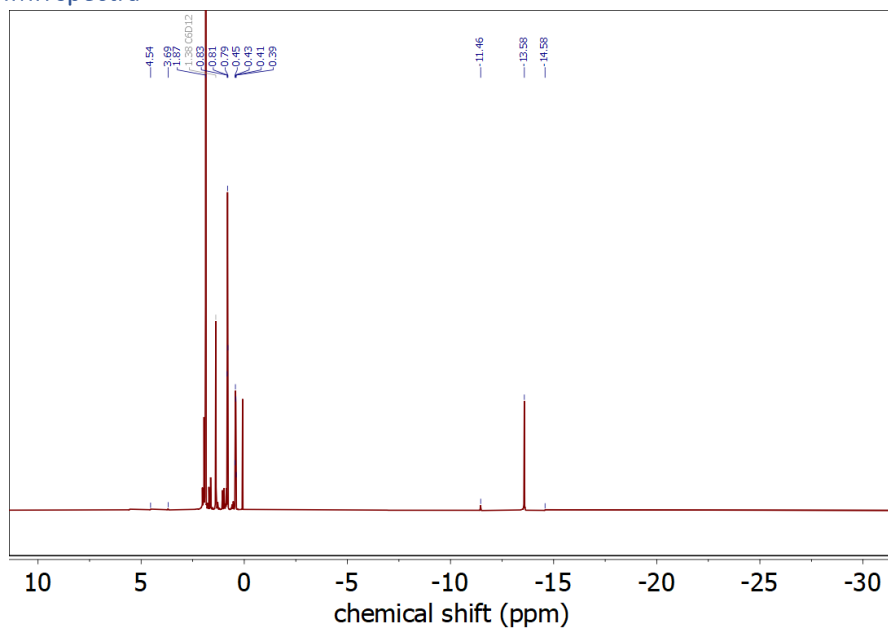
NMR spectra

Figure S3: ¹H NMR spectrum of **1** after 30 min irradiation at 350 nm in *C₆D₁₂*.

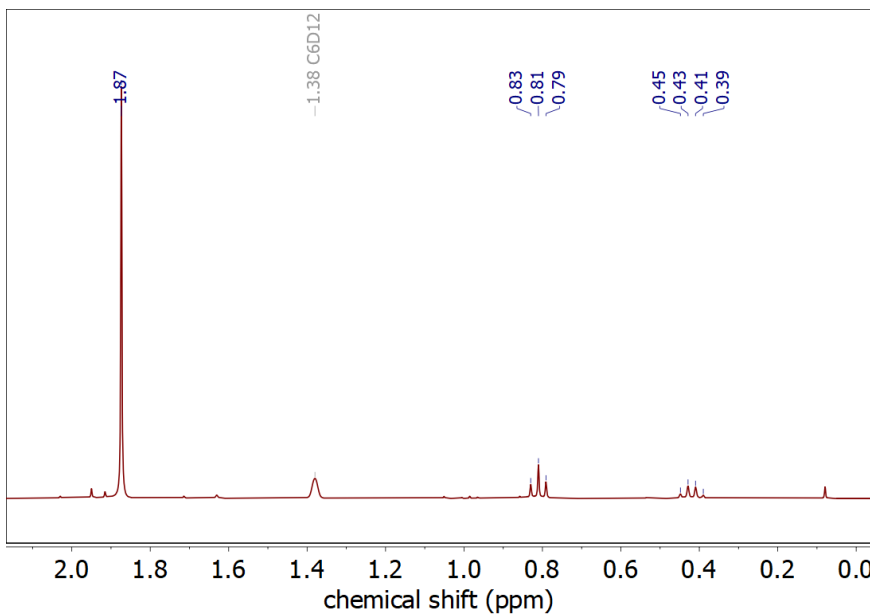


Figure S4: ¹H NMR spectrum of **1** after 30 min irradiation at 350 nm in *C₆D₁₂*. Excerpt of the aliphatic range.

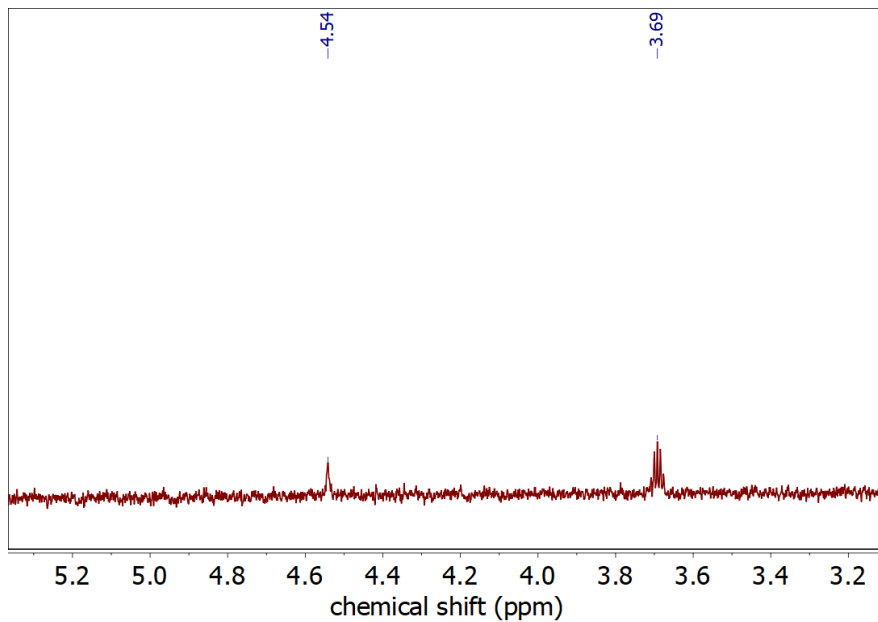


Figure S5: ¹H NMR spectrum of **1** after 30 min irradiation at 350 nm in C₆D₁₂. Excerpt showing free hydrogen (4.54 ppm) and free triethylsilane (3.69 ppm, H-Si).

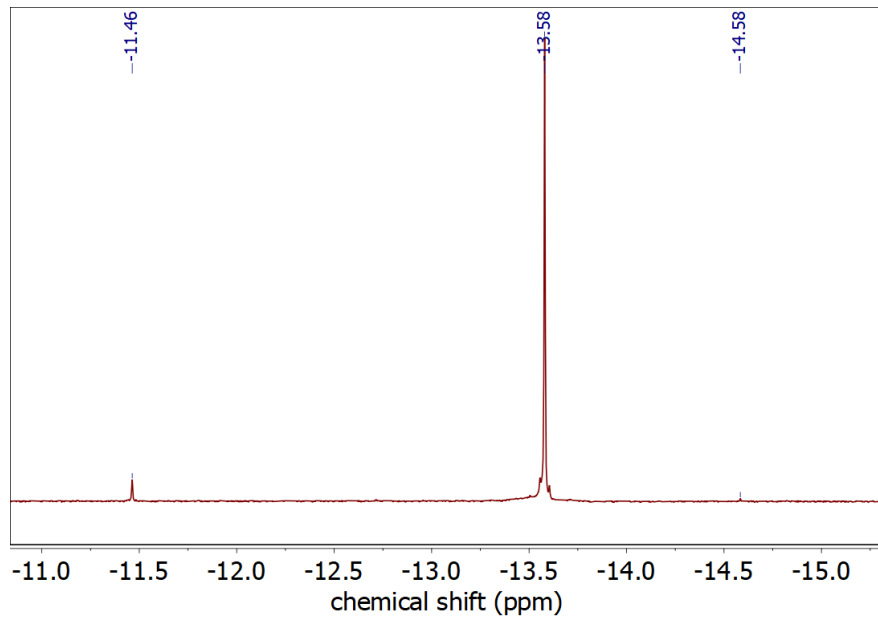


Figure S6: ¹H NMR spectrum of **1** after 30 min irradiation at 350 nm in C₆D₁₂. Excerpt of the hydridic range, showing two new signals at -11.46 and -14.58 ppm.

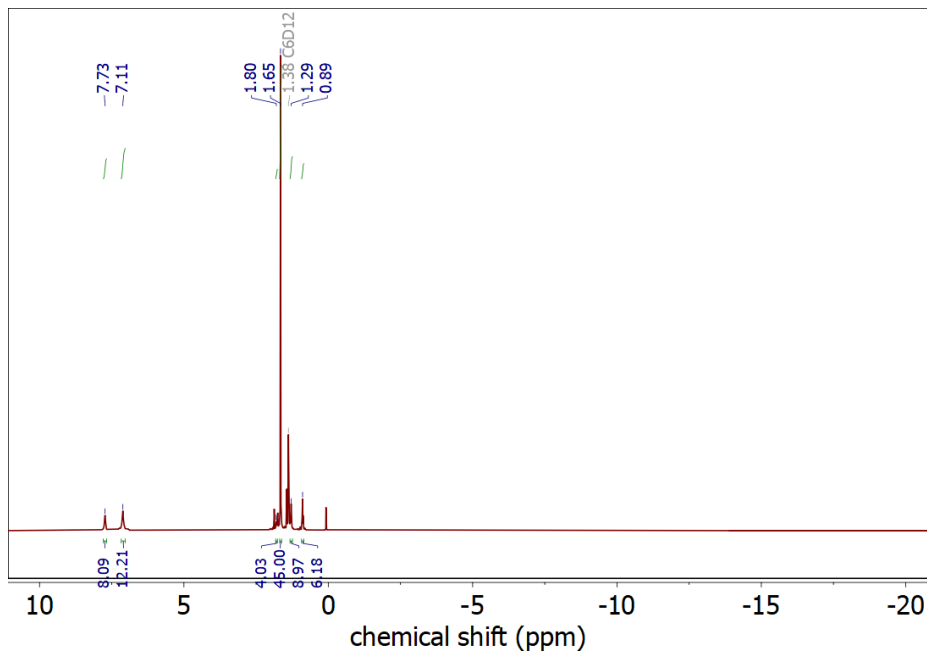


Figure S7: Full range ¹H NMR of **4** in ¹²C₆D₁₂. No new hydride signals.

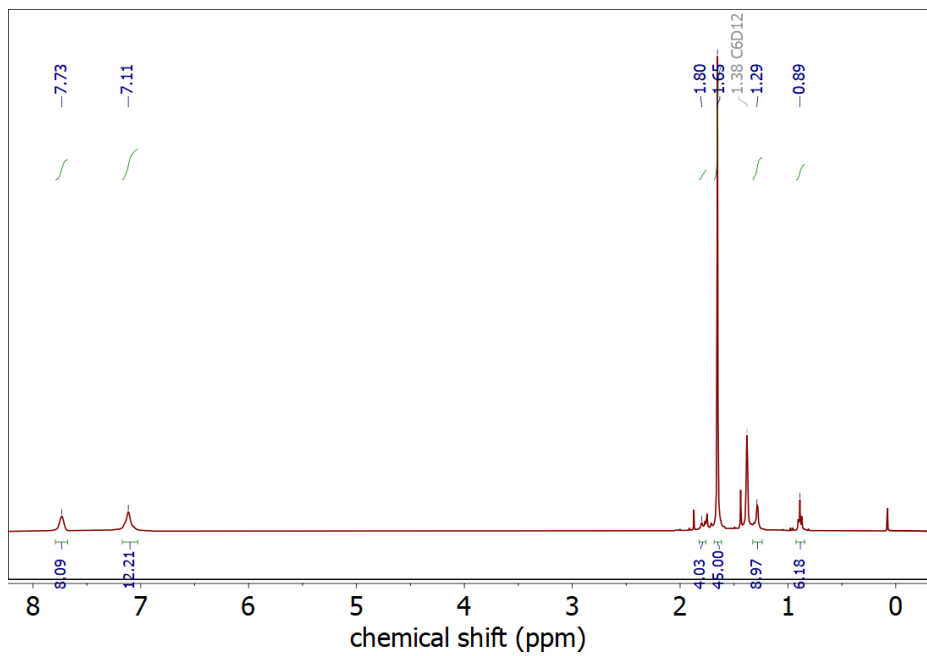
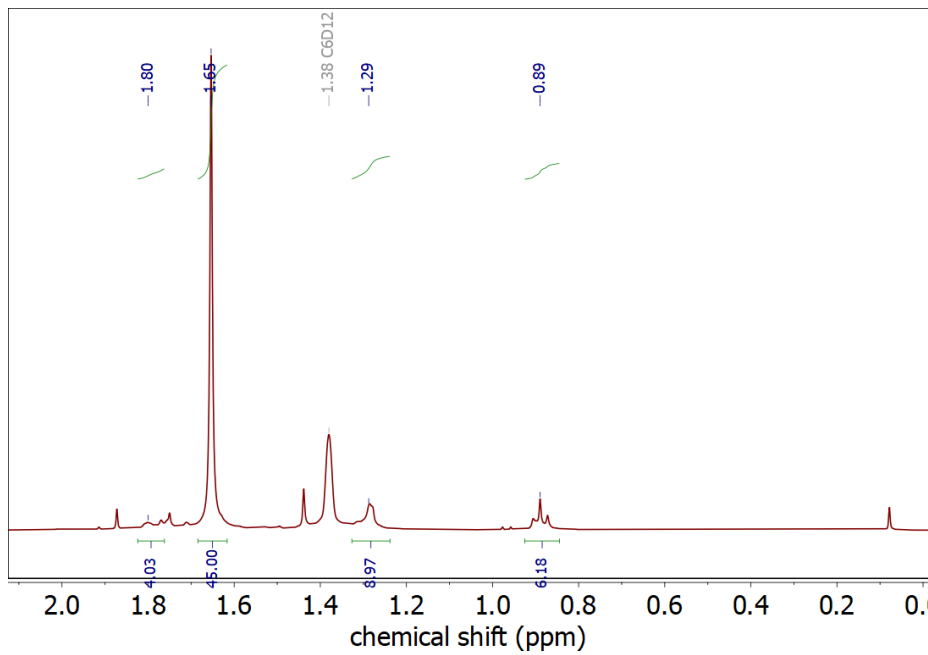
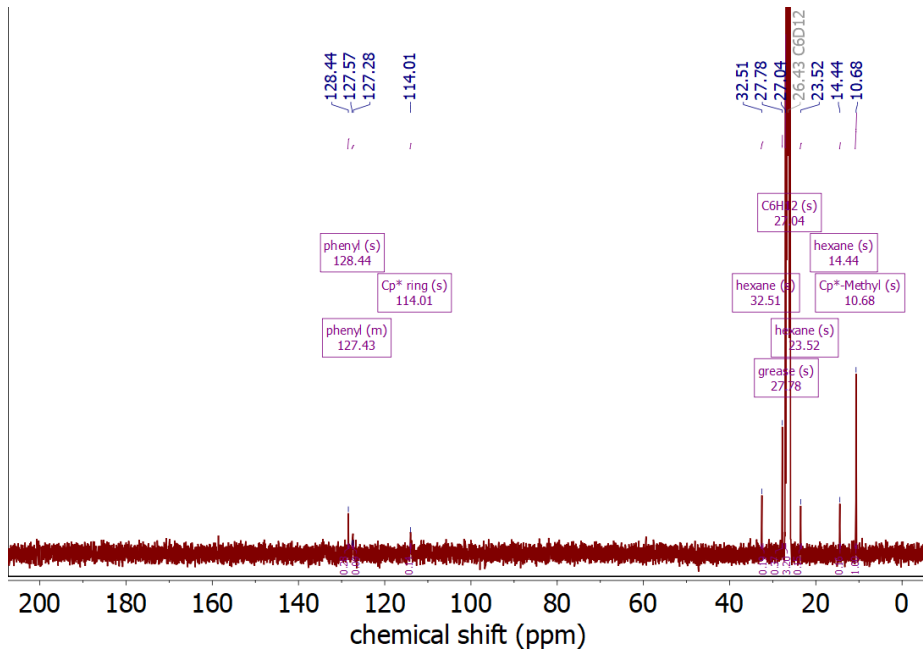


Figure S8: Zoomed into ¹H NMR of **4** in ¹²C₆D₁₂.

Figure S9: Zoomed into 1H NMR of **4** in C_6D_{12} – aliphatic range.Figure 10: SFULL range ^{13}C NMR of **4** in C_6D_{12} .

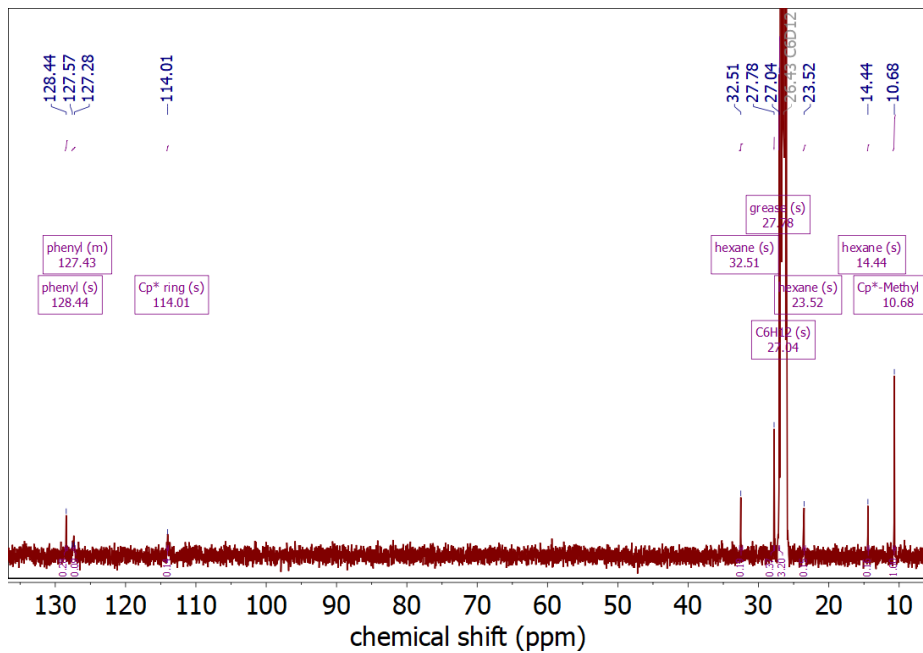


Figure S11: Zoomed into ^{13}C NMR of **4** in C_6D_{12} .

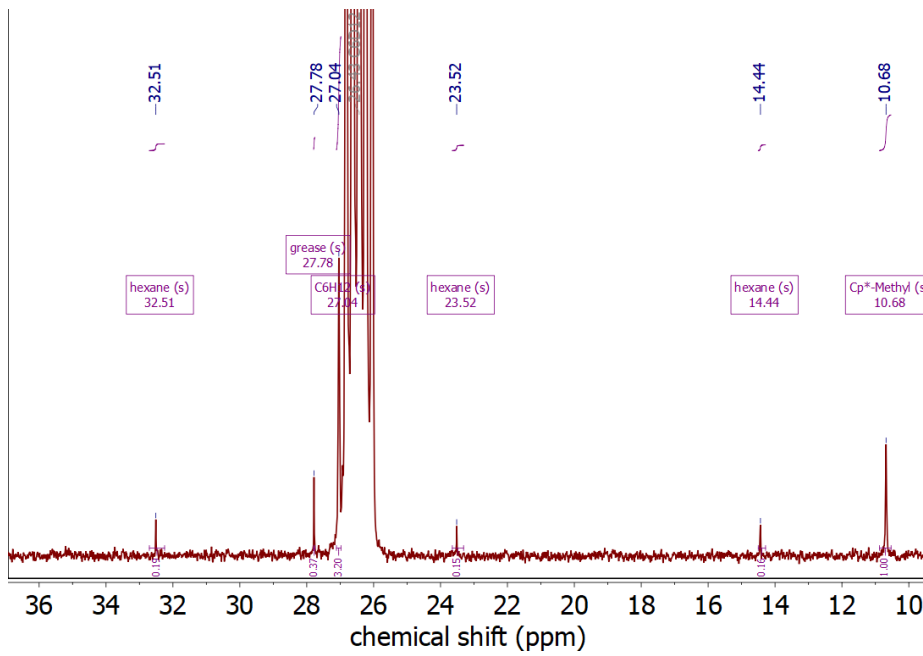


Figure S12: ^{13}C NMR of **4** in C_6D_{12} – aliphatic range.

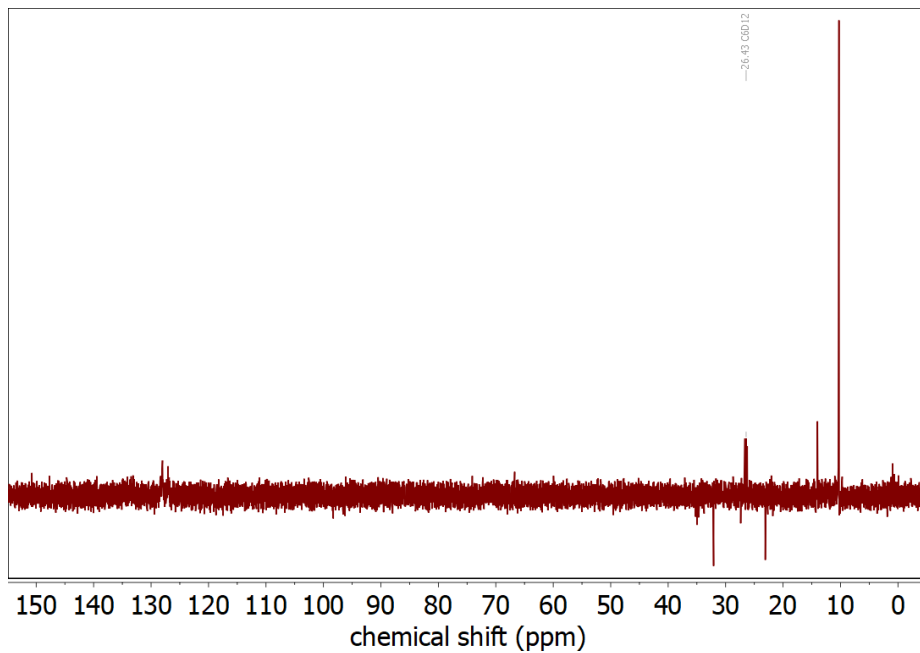


Figure S13: Full range DEPT 135 of **4** in C_6D_{12} .

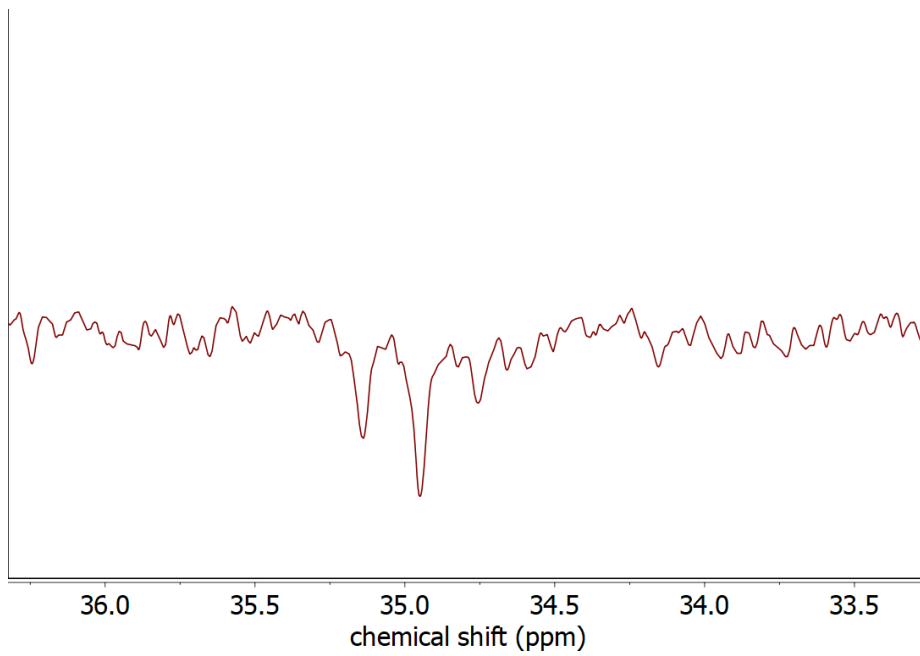
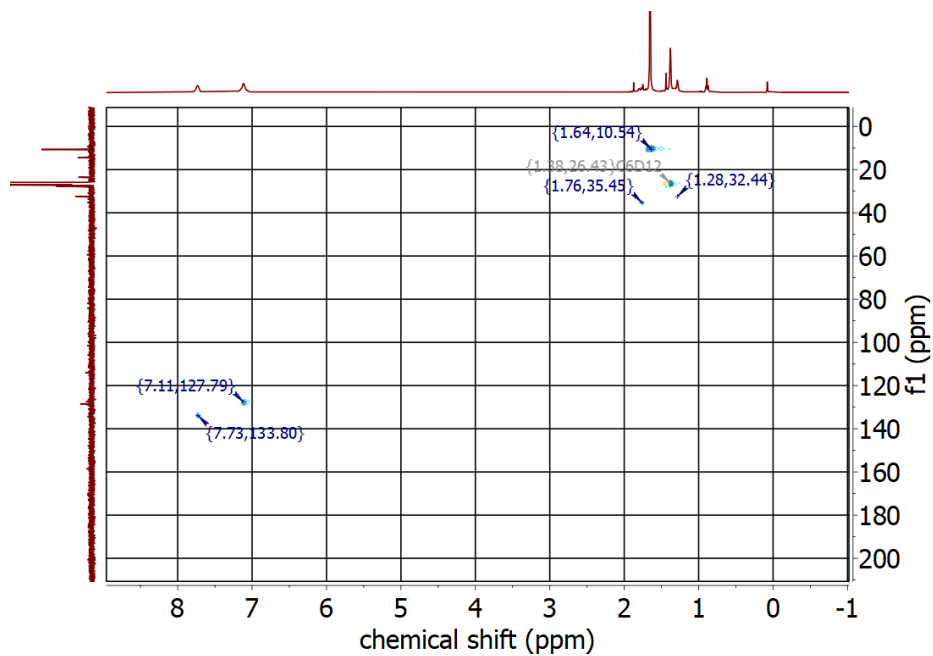
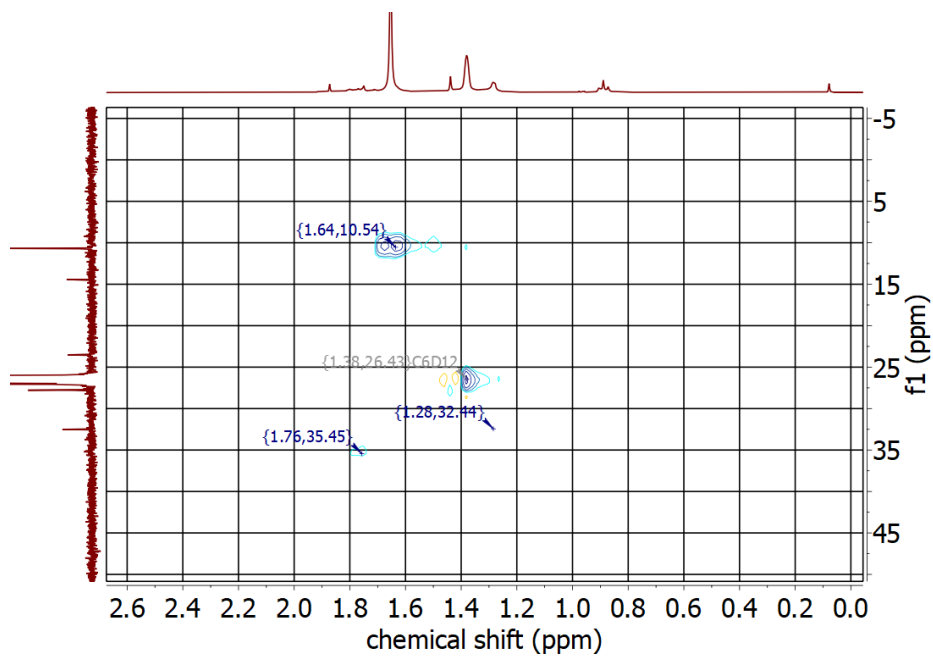


Figure S14: Zoomed into DEPT 135 of **4** in C_6D_{12} . Negative ¹³C triplet (due to ³¹P coupling) of dppe H_2C-CH_2 bridge.

12

Figure S15: Full range HSQC spectrum of **4** in C_6D_{12} .Figure S16: HSQC spectrum of **4** in C_6D_{12} – aliphatic range.

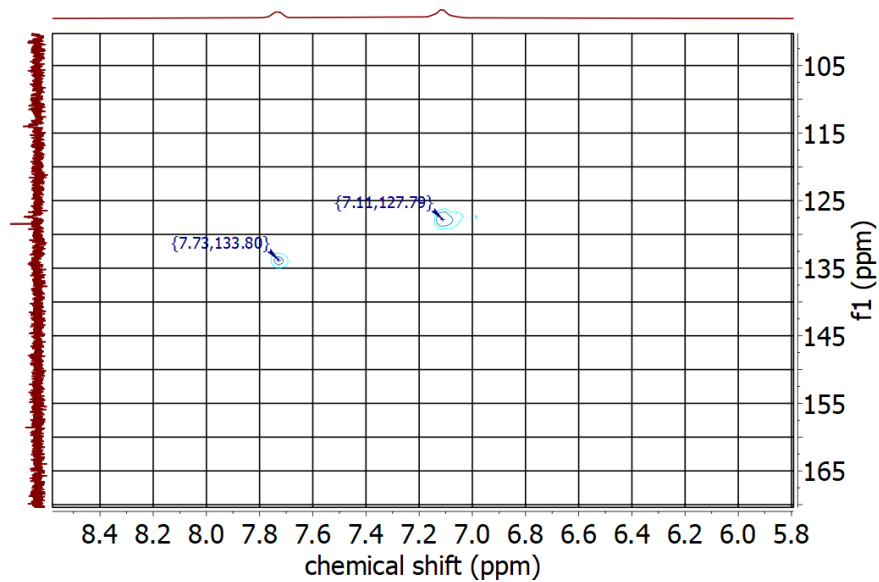


Figure S17: HSQC spectrum of **4** in C_6D_{12} – aromatic range.

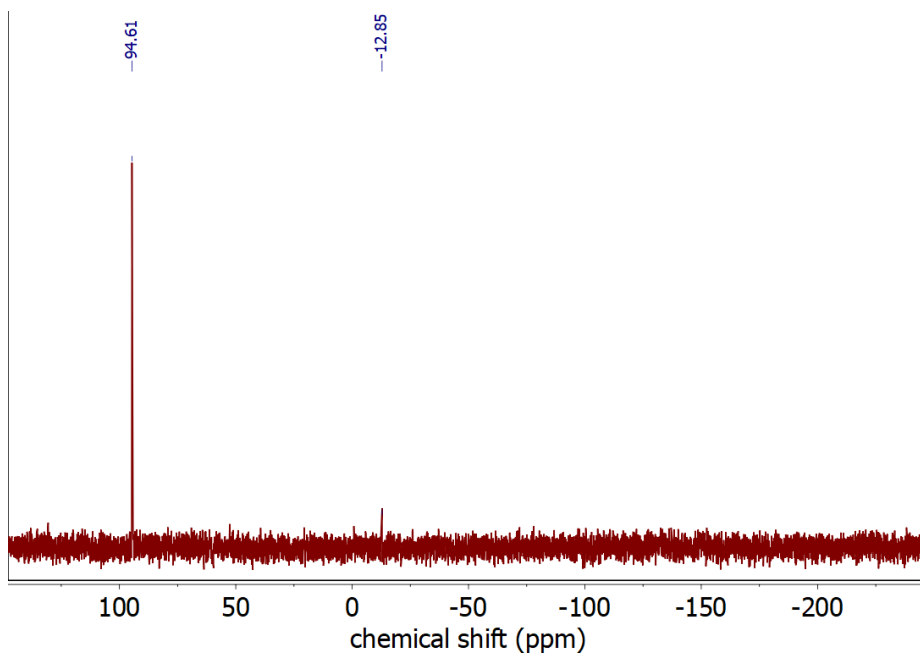
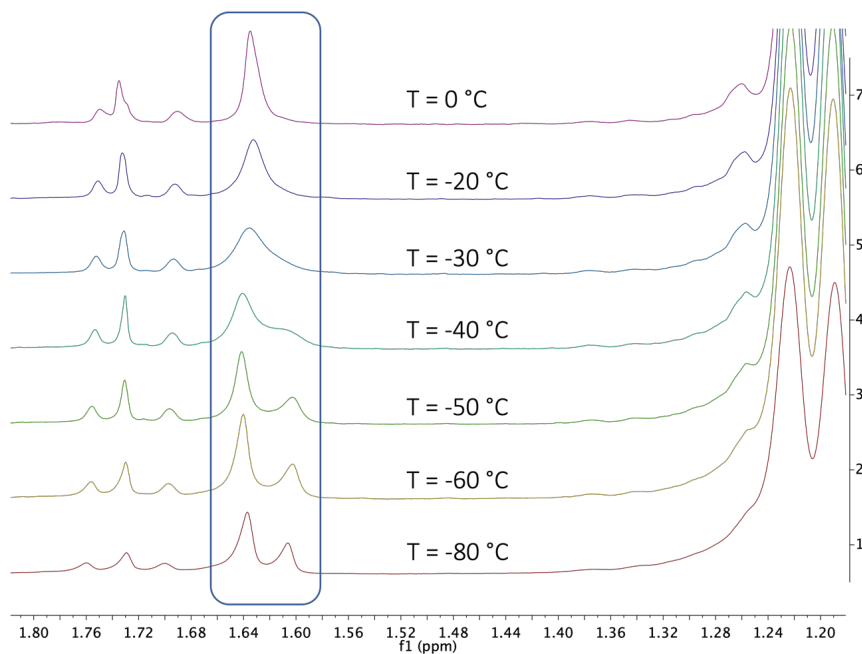
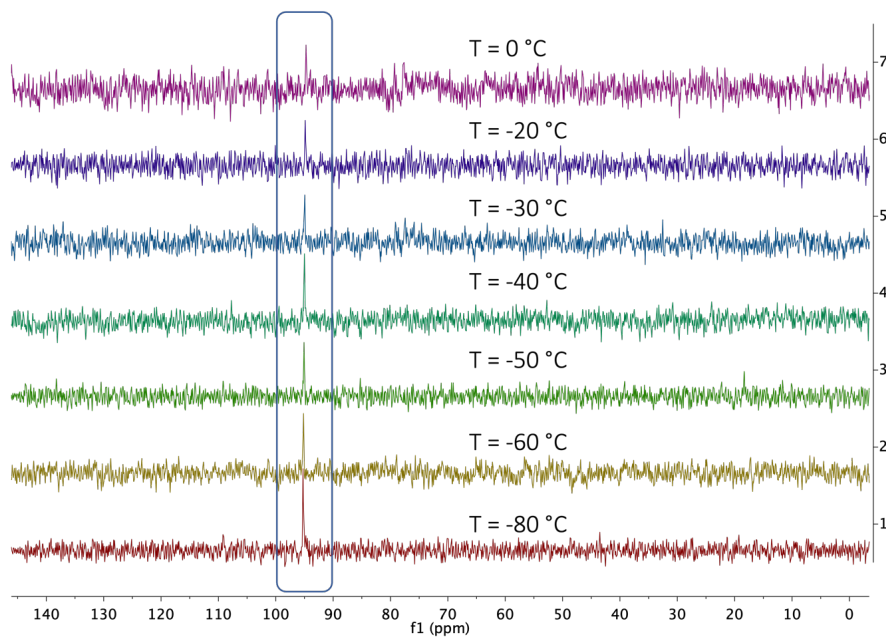


Figure S18: Full range ^{31}P spectrum of **4** in C_6D_{12} .

Figure S19: Variable Temperature ^1H -NMR spectra of **4** between -80 and 0 $^\circ\text{C}$ in $\text{n-hexane-}d_{14}$.Figure S20: Variable Temperature ^{31}P -NMR spectra of **4** between -80 and 0 $^\circ\text{C}$ in $\text{n-hexane-}d_{14}$.

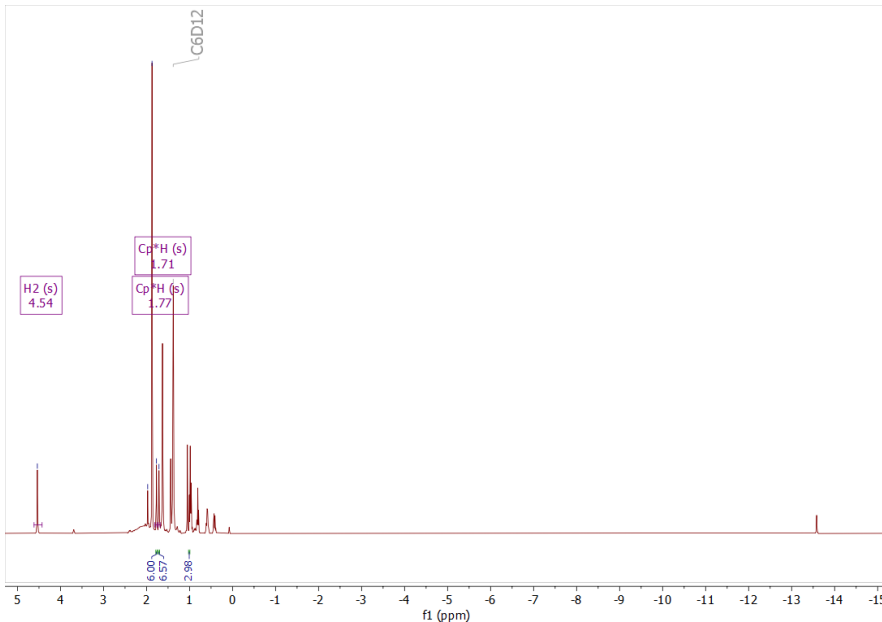


Figure S21: ¹H NMR spectrum of the reaction of **1** with H₂ under 1 h irradiation (350 nm).

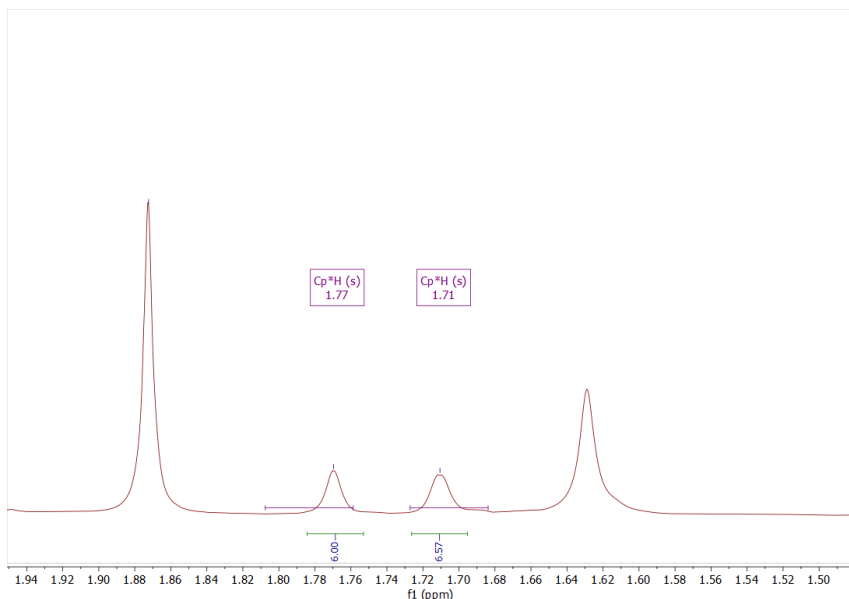


Figure S22: Excerpt of ¹H NMR spectrum of the reaction of **1** with H₂ under 1 h irradiation (350 nm). Showing peaks of free Cp*H at 1.71 and 1.77 ppm.

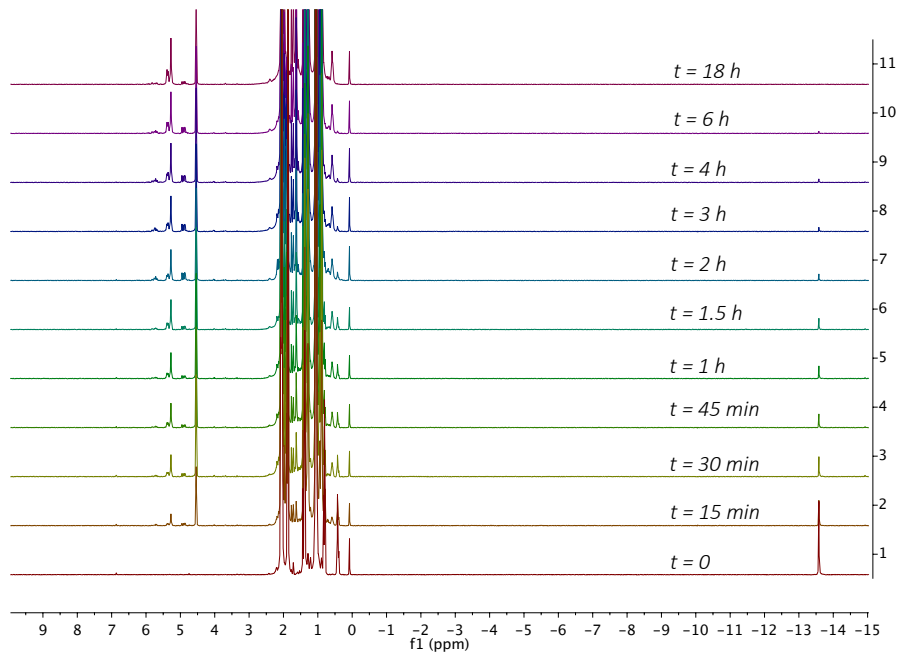


Figure S23: Full range stacked ^1H NMR spectra of the conversion of 3-hexyne with **1** (5 mol%) under a dihydrogen atmosphere (2 bar) at 350 nm. Hydride shift of **1** at -13.6 ppm; alkenes and hydrosilylation products between 4.75 and 6.0 ppm.

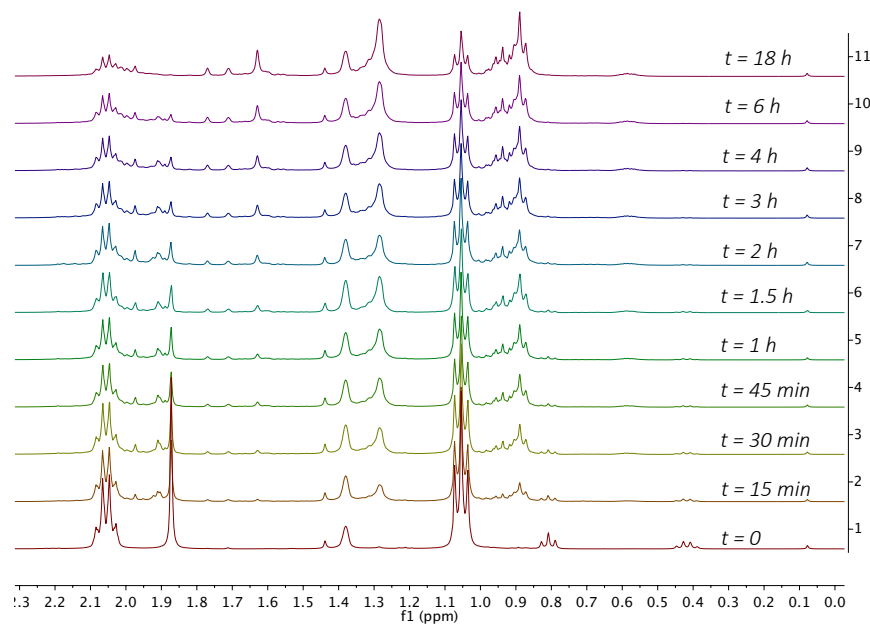


Figure S24: Zoomed in stacked ¹H NMR spectra of the conversion of 3-hexyne with **1** (5 mol%) under a dihydrogen atmosphere (2 bar) at 350 nm. 3-Hexyne at 2.06 and 1.05 ppm; *n*-hexane (CH₂) between 1.20 and 1.36 ppm; CH₃ of *n*-hexane and hexenes between 0.85 and 1.01 ppm.

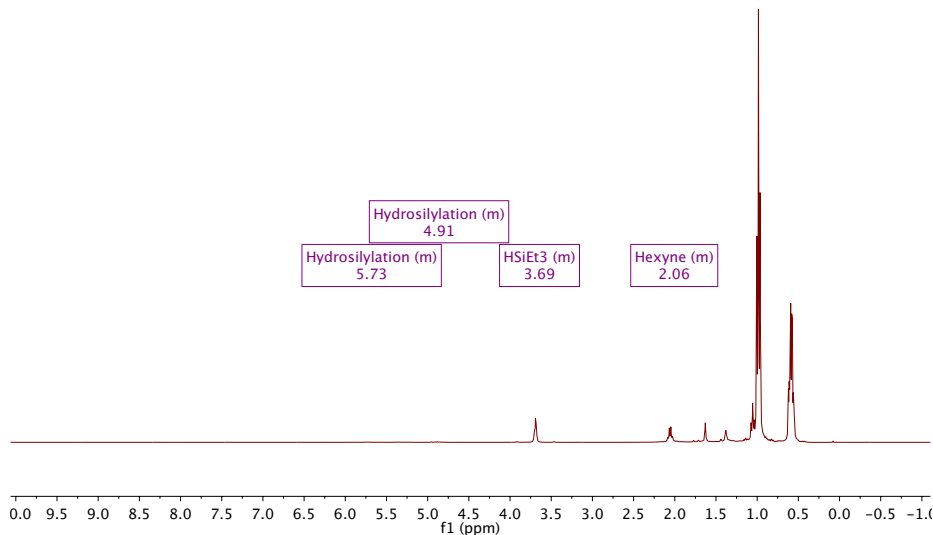


Figure S25: Full range ^1H NMR spectrum of the conversion of 3-hexyne (1.0 eq.) and HSiEt₃ (5.0 eq.) with **1** (5 mol% against 3-hexyne) at 350 nm.

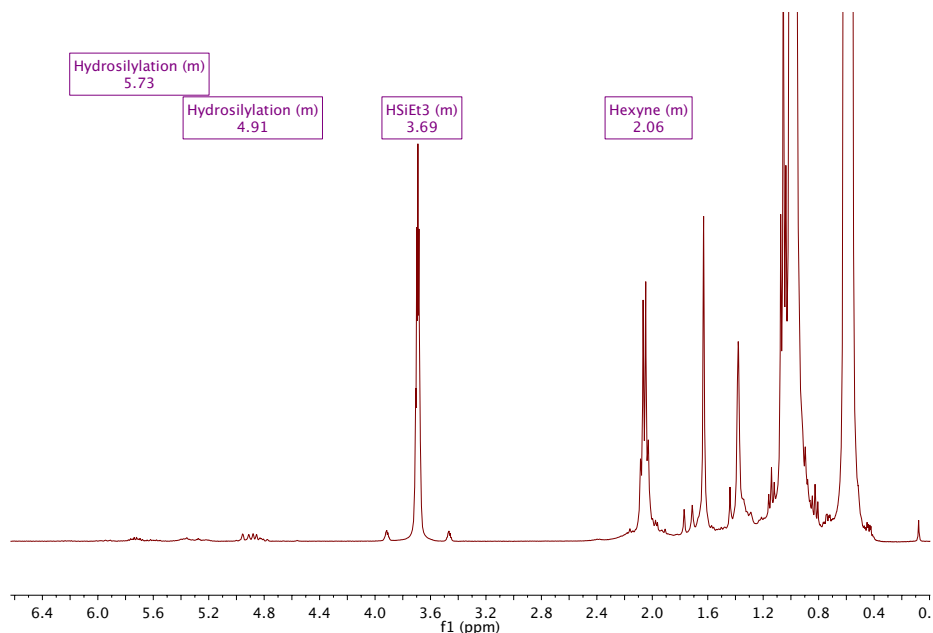


Figure S26: Zoomed in ^1H NMR spectrum of the conversion of 3-hexyne (1.0 eq.) and HSiEt₃ (5.0 eq.) with **1** (5 mol% against 3-hexyne) at 350 nm.

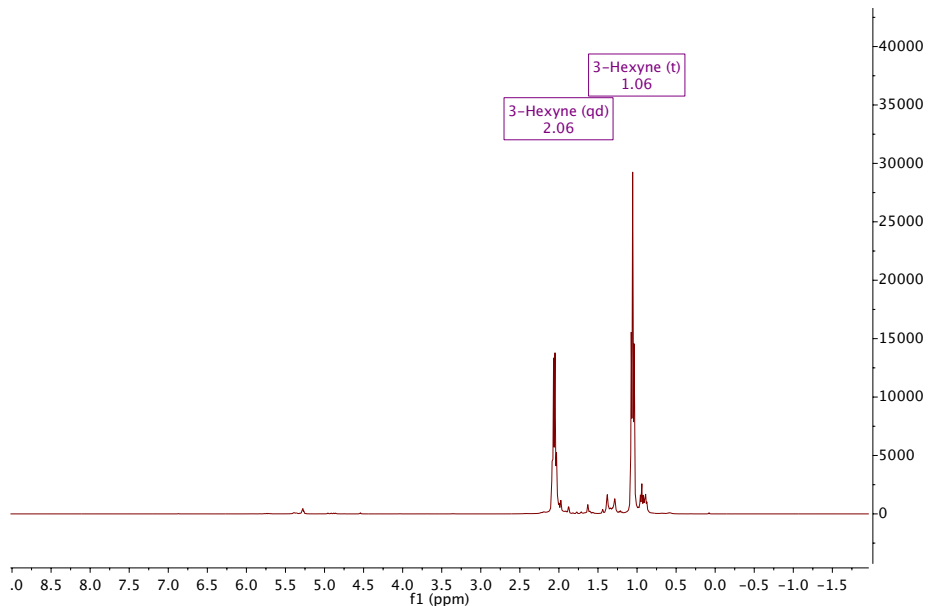


Figure S27: Full range ^1H NMR spectra of the conversion of 3-hexyne with **1** (1 mol%) under a dihydrogen atmosphere (2 bar) after 24h at 350 nm.

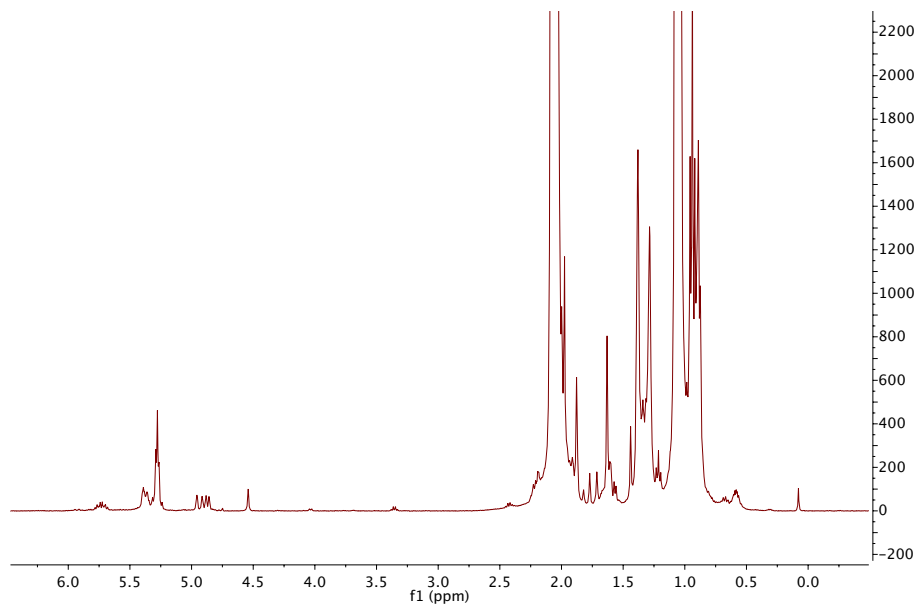


Figure S28: Zoomed in ^1H NMR spectra of the conversion of 3-hexyne with **1** (1 mol%) under a dihydrogen atmosphere (2 bar) after 24h at 350 nm. Hexenes and hydrosilylation products between 4.75 and 6.0 ppm; n-hexane (CH_3) between 1.20 and 1.36 ppm; CH_3 of n-hexane and hexenes between 0.85 and 1.01 ppm.

LIFDI mass spectra

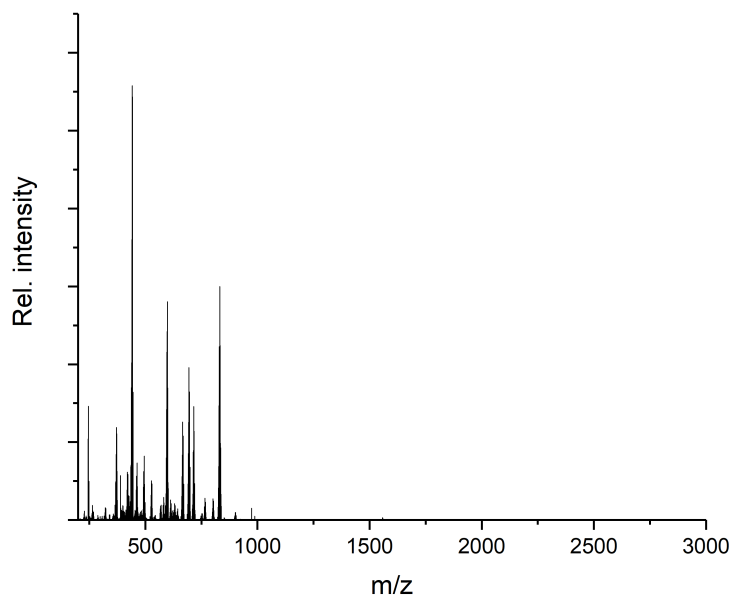


Figure S29: LIFDI mass spectrum of **1** after 8 h irradiation in cyclohexane. Main pattern corresponds to **1** ($m/z = 832.13$) [$M-2H]^+$.

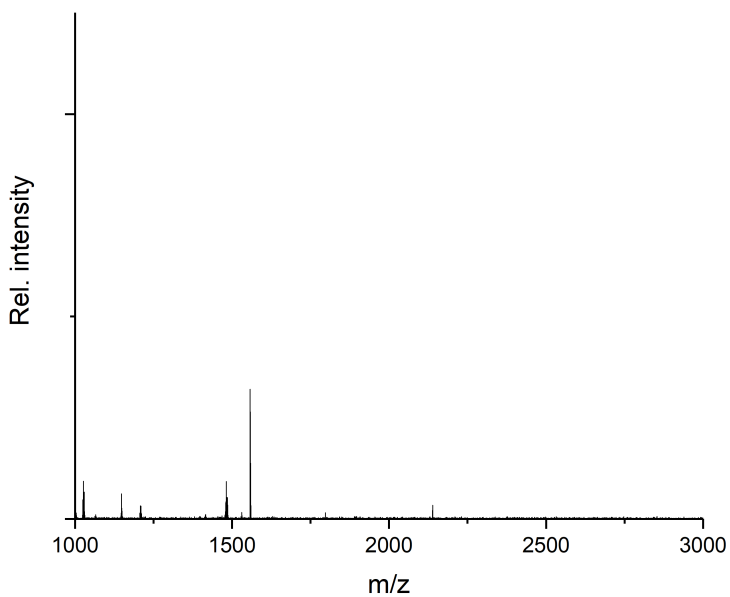


Figure S30: Excerpt of LIFDI mass spectrum of **1** after 8 h irradiation in cyclohexane. No peaks at higher masses – barely any cluster growth visible.

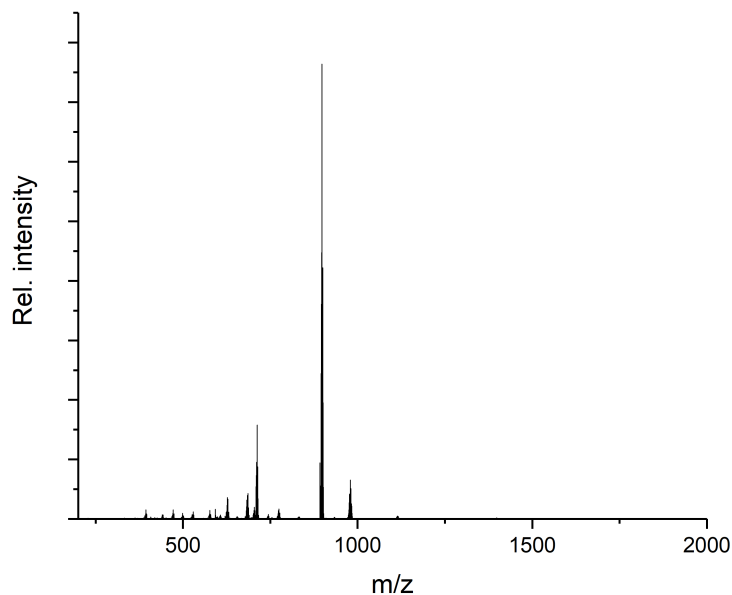


Figure S31: LIFDI mass spectrum of $[(dppe)Ru(GaCp^*)_3] \textbf{4}$. $[M]^+$ ($m/z = 1114.1656$; calc. 1114.1671); $[M\text{-}Cp^*]^+$ ($m/z = 979.0478$; calc. 979.0497); $[M\text{-}2Cp^*\text{-}Ga]^+$ ($m/z = 775.0068$; calc. 775.0080). Main peak at $m/z = 898.1727$ attributed to $[Ru(dppe)_2]$ (calc. 775.0080), formation assumed upon ionization.

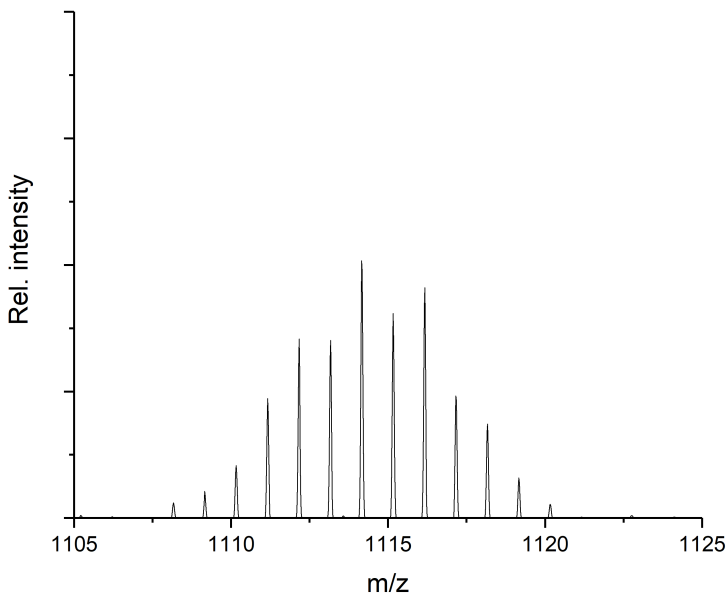


Figure S32: LIFDI mass spectrum of **4**. Excerpt of isotopic pattern of **4**. $[M]^+$ ($m/z = 1114.1656$; calc. 1114.1671).

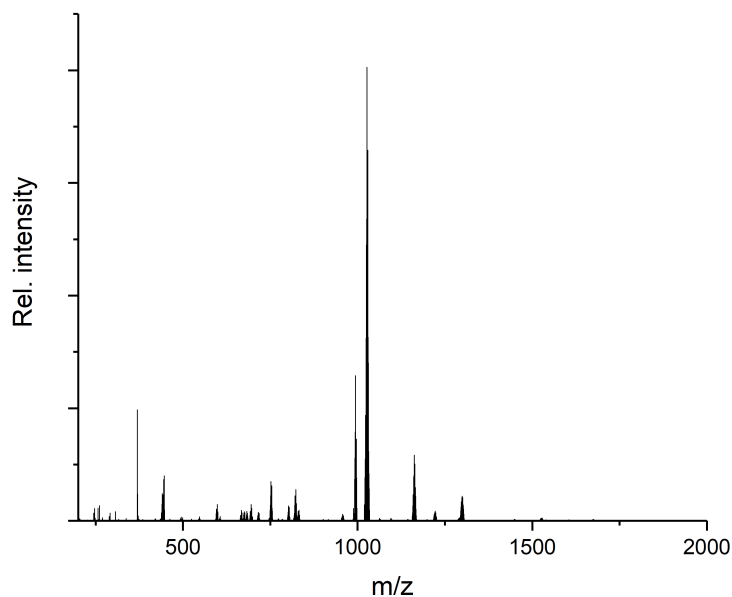


Figure S33: *In situ* LIFDI mass spectrum of the reaction **1** with 1 eq 1,2-bis(diphenylphosphino)benzene after 24 h irradiation (350 nm).

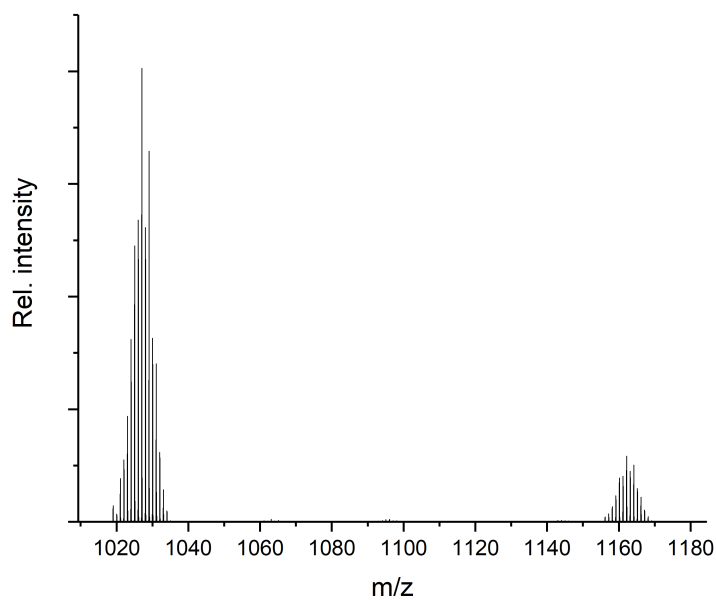


Figure S34: Excerpt of LIFDI mass spectrum of the reaction **1** with 1 eq 1,2-bis(diphenylphosphino)benzene (dppbz) after 24 h irradiation (350 nm). Peaks assigned to: $m/z = 1162.18 [(dppbz)Ru(GaCp^*)_3]^+$ (calc. 1162.17); $m/z = 1027.05 [M-Cp^*]^+$ (calc. 1027.05).

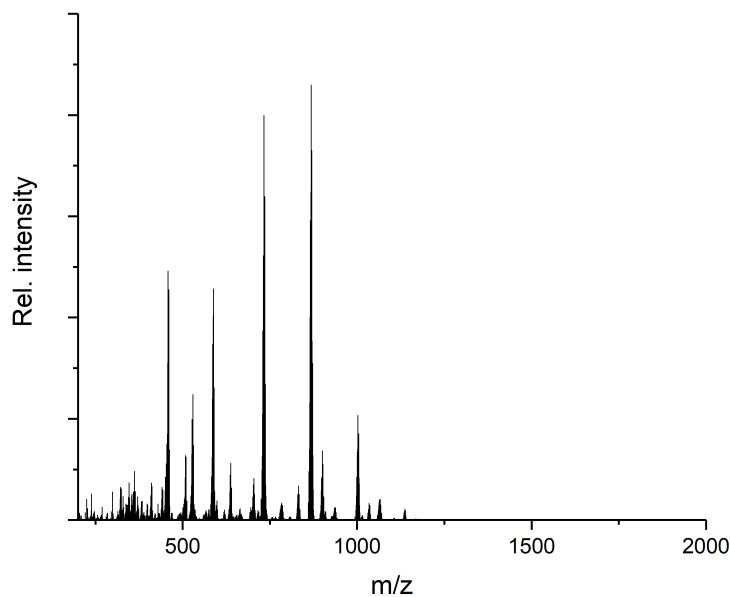


Figure S35: *In situ* LIFDI mass spectrum of the reaction **1** with 2 eq trimethyl phosphine after 24 h irradiation (350 nm).

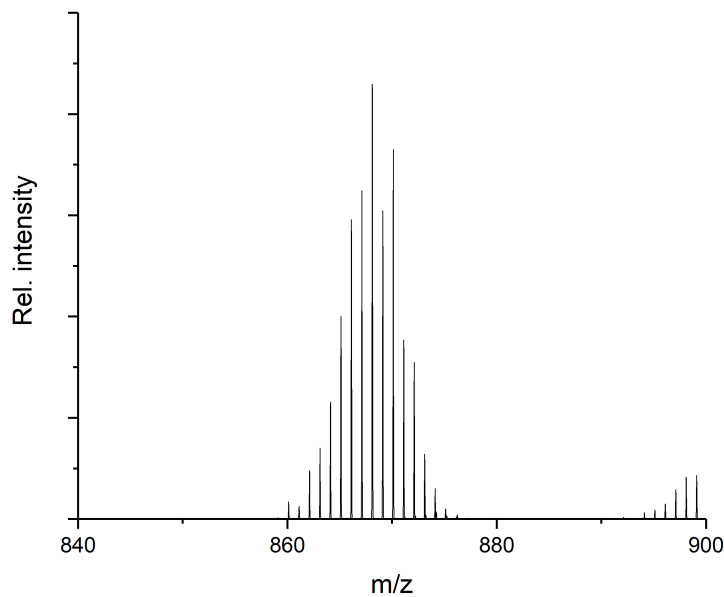


Figure S36: Excerpt of LIFDI mass spectrum of the reaction **1** with 2 eq trimethyl phosphine (PMe_3) after 24 h irradiation (350 nm). Peak assigned to: $m/z = 868.1195 [(\text{Me}_3\text{P})_2\text{Ru}(\text{GaCp}^*)_3]^+$ (calc. 868.1202).

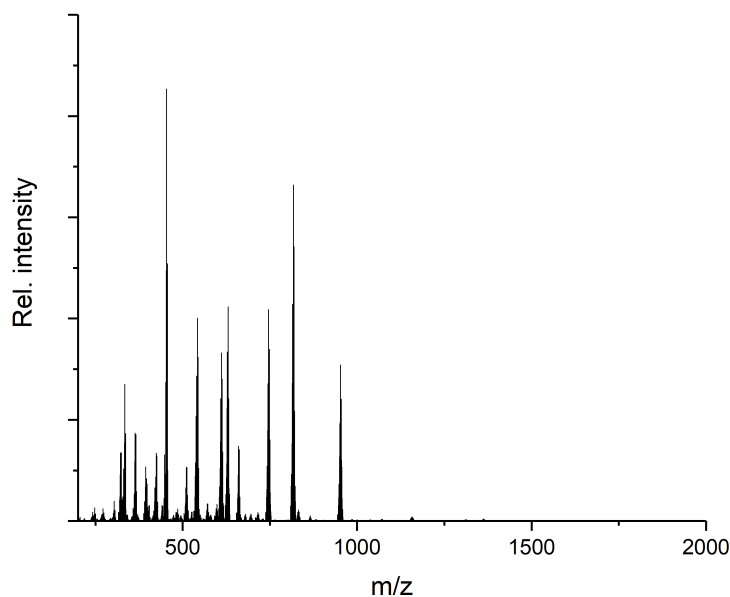


Figure S37: *In situ* LIFDI mass spectrum of the reaction **1** with 2 eq triethyl phosphine after 24 h irradiation (350 nm).

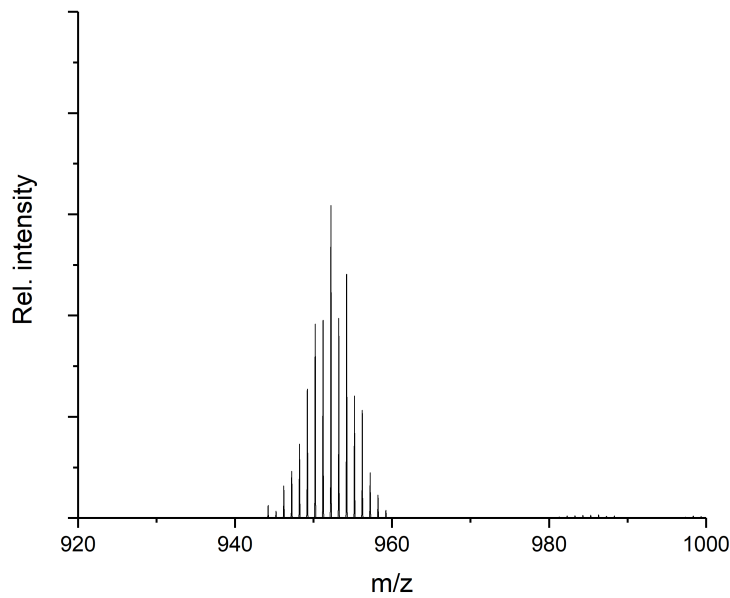


Figure S38: Excerpt of LIFDI mass spectrum of the reaction **1** with 2 eq triethyl phosphine (PEt_3) after 24 h irradiation (350 nm). Peak assigned to: $m/z = 952.2143$ $[(\text{Et}_3\text{P})_2\text{Ru}(\text{GaCp}^*)_3]^+$ (calc. 952.2141).

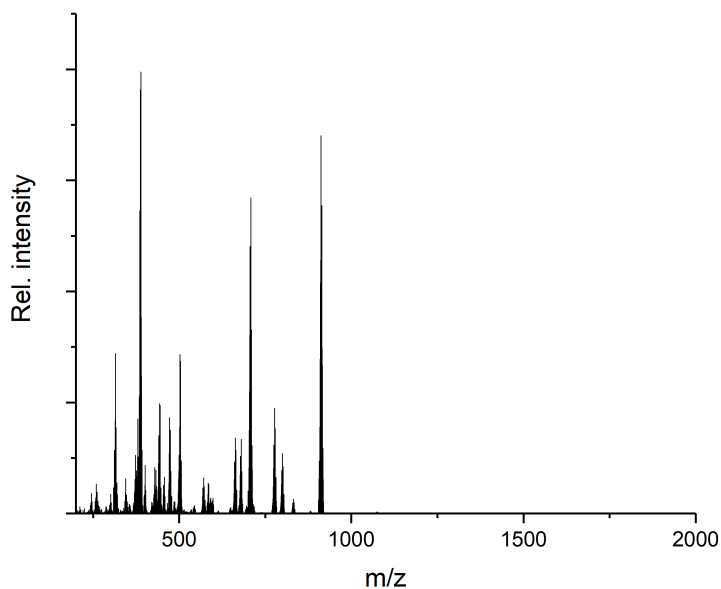


Figure S39: In-situ LIFDI mass spectrum of catalytic hydrogenation of 20 eq 3-hexyne under irradiation.

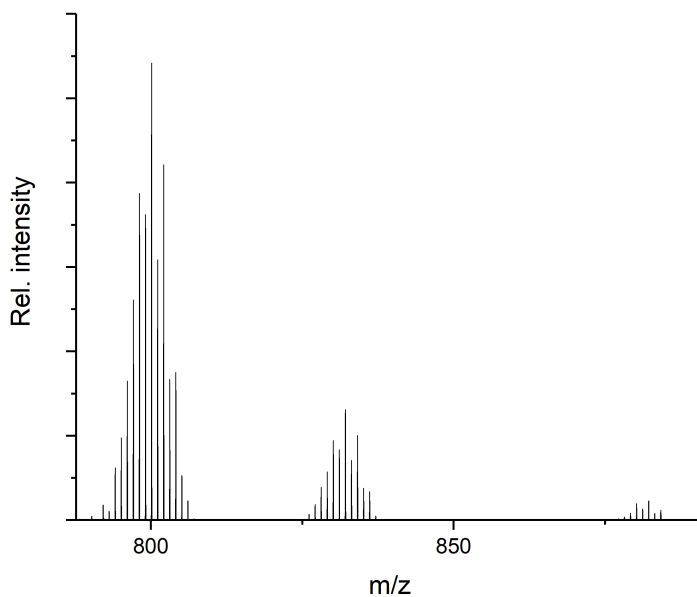


Figure S40: Excerpt of in-situ LIFDI mass spectrum of catalytic hydrogenation of 20 eq 3-hexyne under irradiation. Peak attributed to $[Ru(GaCp^*)_3(\text{hexene})]$ (A; $m/z = 800.1251$; calc. 800.1257) significantly more intense than peak attributed to $[Ru(GaCp^*)_3(\text{hexyne})(\text{hexene})]$ (B; $m/z = 882.2044$; calc. 882.2039). Inverse to reaction with higher 3-hexyne concentration. Peak at $m/z = 832$ results from unconverted 1.

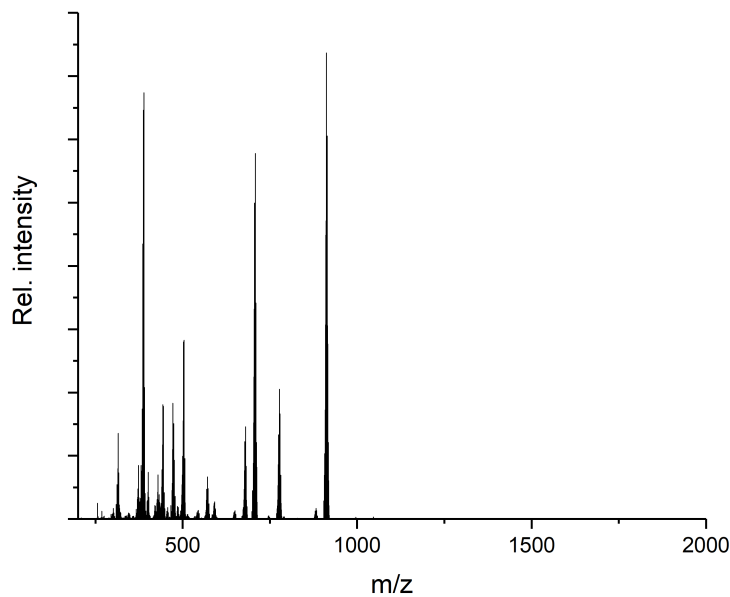


Figure S41: In-situ LiFDI mass spectrum of catalytic hydrogenation of 100 eq 3-hexyne under irradiation.

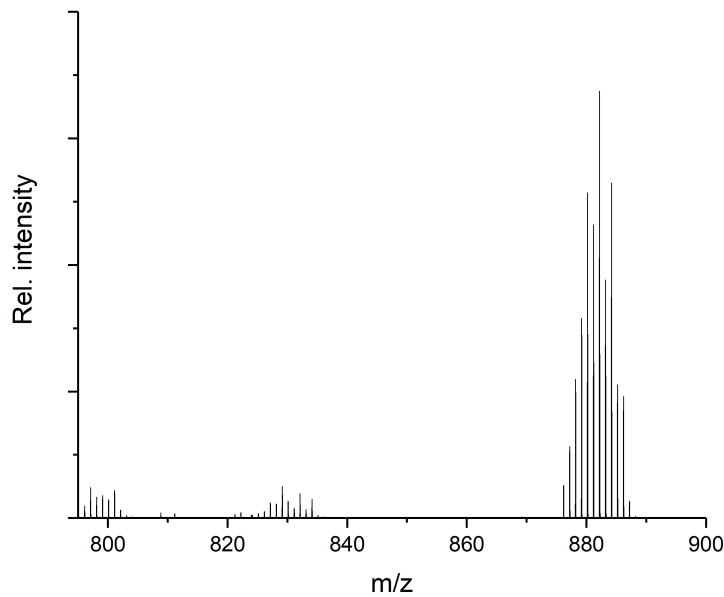


Figure S42: Excerpt of in-situ LiFDI mass spectrum of catalytic hydrogenation of 100 eq 3-hexyne under irradiation. Peak attributed to $[\text{Ru}(\text{GaCp}^*)_3(\text{hexyne})(\text{hexene})]$ (B; $m/z = 882.1997$; calc. 882.2039) significantly more intense than peak attributed to $[\text{Ru}(\text{GaCp}^*)_3(\text{hexene})]$ (A₂; $m/z = 800.1180$; calc. 800.1257). Inverse to reaction with lower 3-hexyne concentration. Peak at $m/z = 832$ results from unconverted 1.

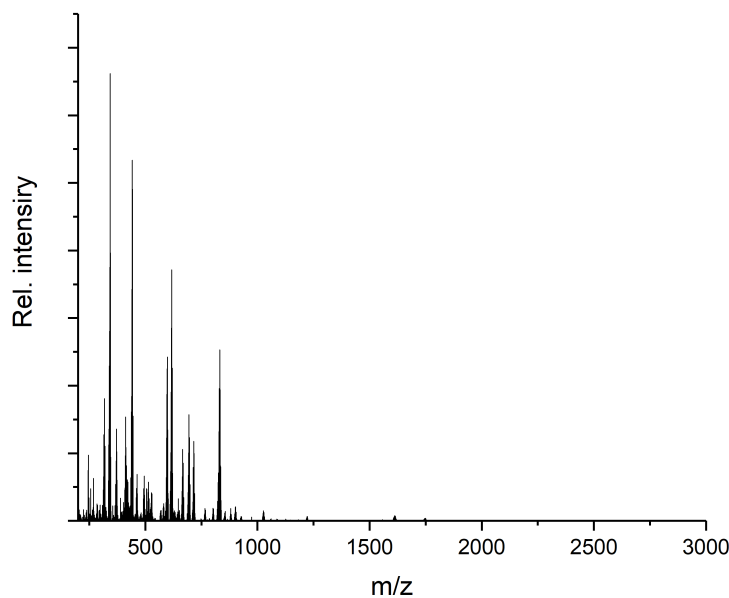


Figure S43: LIFDI mass spectrum of the reaction of **1** with H_2 under 3 h irradiation (350 nm).

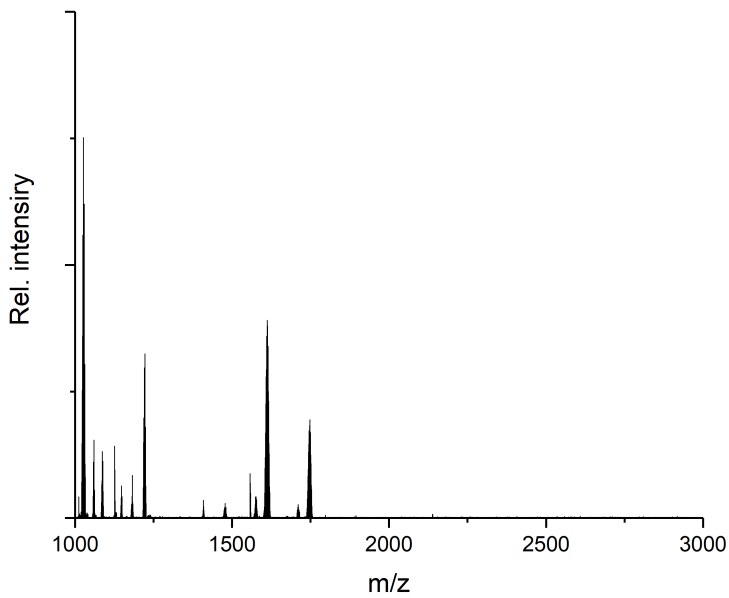


Figure S44: Excerpt of LIFDI mass spectrum of the reaction of **1** with H_2 under 3 h irradiation (350 nm). Peaks assigned to composition as following: $m/z = 1026.96$ ($Ru_2Ga_4Cp^{*}_4H_5$), $m/z = 1612.60$ ($Ru_3Ga_9Cp^{*}_5H_5$), $m/z = 1710.07$ ($Ru_2Ga_8Cp^{*}_7H_3$) and $m/z = 1747.73$ ($Ru_3Ga_9Cp^{*}_6H_5$).

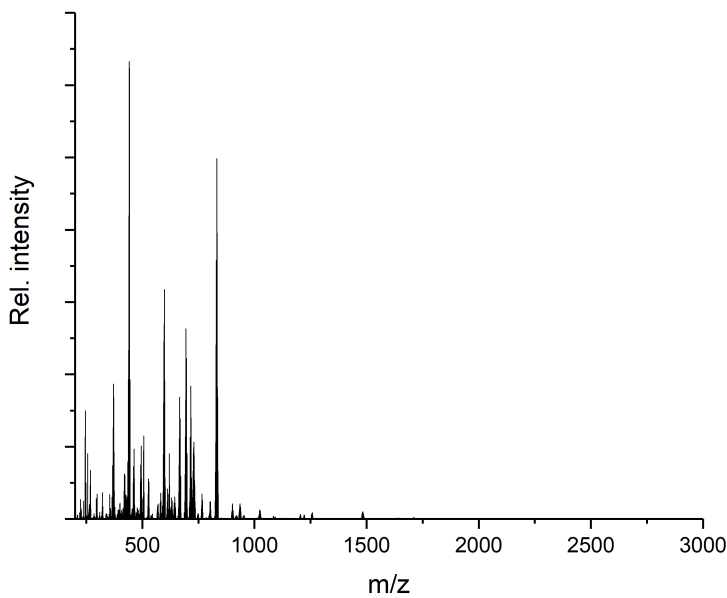


Figure S45: LIFDI mass spectrum after the catalytic conversion 3-hexyne with **1** and H₂ (2 bar) under 24 h irradiation (350 nm) in cyclohexane-d₁₂.

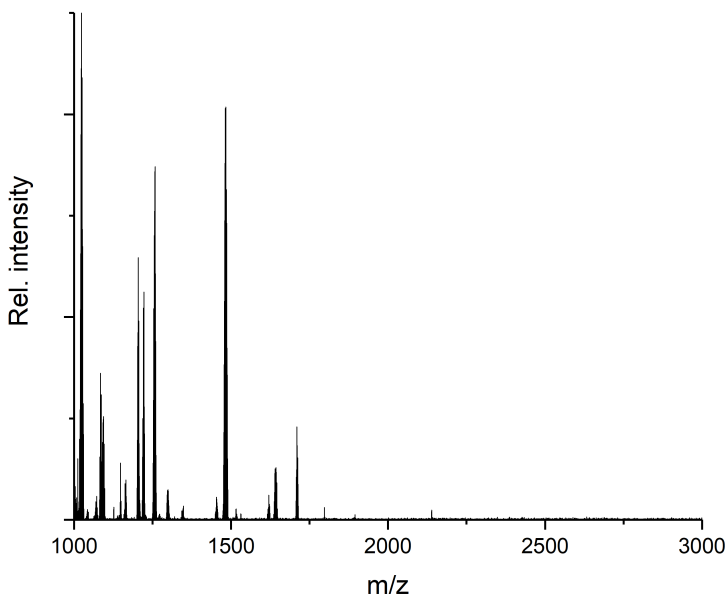


Figure S46: Excerpt of LIFDI mass spectrum after the catalysis. Several new clusters are formed: m/z = 1024.00 ($\text{Ru}_2\text{Ga}_4\text{Cp}^*\text{H}_2$); m/z = 1093.92 ($\text{Ru}_2\text{Ga}_5\text{Cp}^*\text{H}$); 1481.96 ($\text{Ru}_2\text{Ga}_7\text{Cp}^*\text{SiEt}_3\text{H}$); m/z = 1710.07 ($\text{Ru}_2\text{Ga}_8\text{Cp}^*\text{H}_3$).

IR spectra

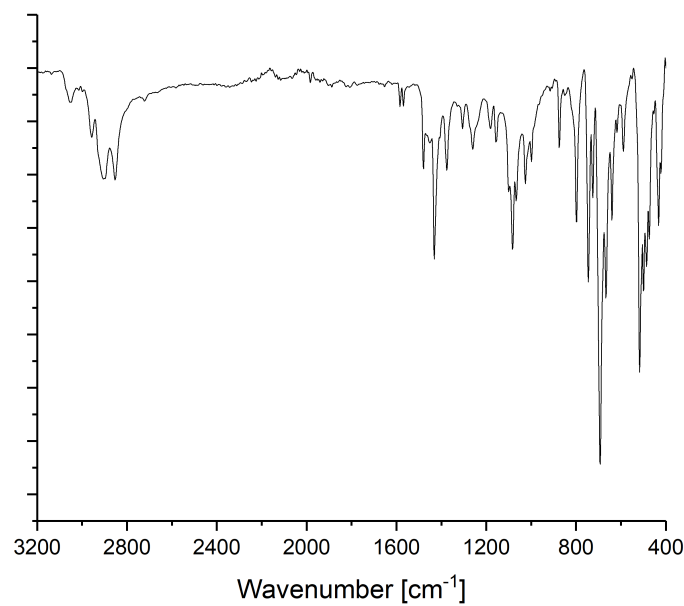


Figure S47: ATR-IR spectrum of $[Ru(GaCp^*)_3(dppe)]$ (4). No typical Ru-H bands (range between 1600 and 2000 cm⁻¹).

UV-Vis spectra

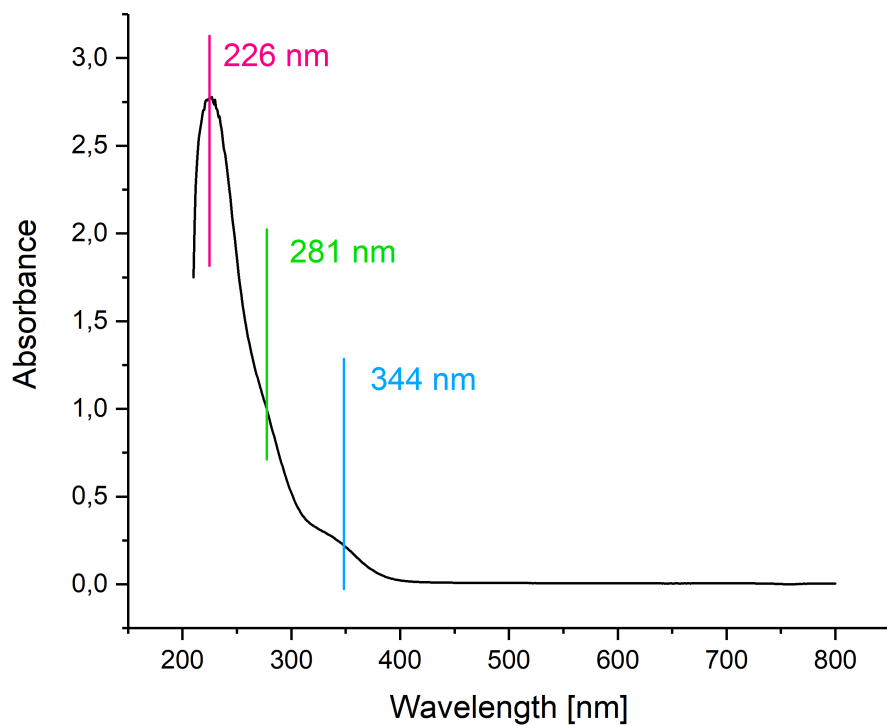


Figure S48: UV-Vis of **1** in cyclohexane. Reprinted with permission.^[S1]

7.4 Supporting Information for Study IV

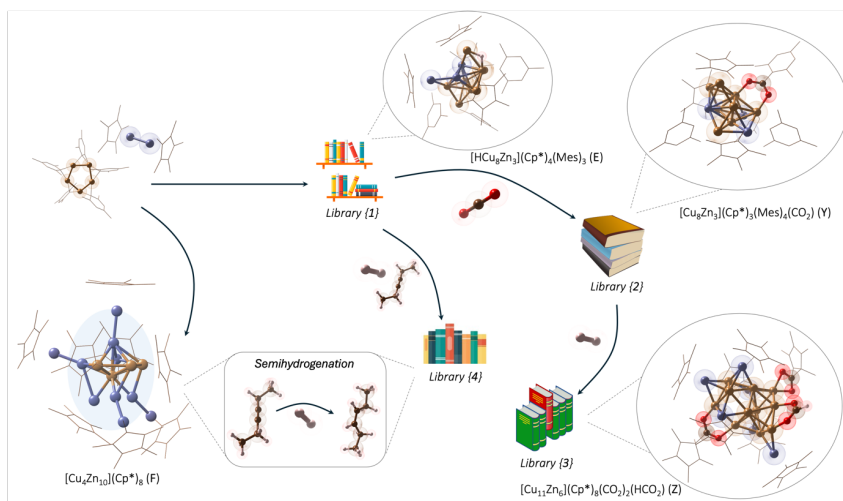
Table of Contents

1. Experimental Section.....	3
1.1. Cu/Zn Libraries.....	3
1.1.1. Mass Spectrometric Characterization.....	4
1.1.1.1. LIFDI Mass Spectra	4
1.1.1.2. Composition Tables.....	9
1.1.1.3. Peak Identification	17
Molecular Ions	18
Fragments.....	28
1.1.1.4. Fragmentation Analysis.....	37
1.1.2. NMR Spectra	68
1.1.3. FT-IR Spectra	71
1.2. [Cu ₄ Zn ₁₀]Cp* ₈ (F).....	73
1.2.1. Experimental Characterization.....	73
1.2.1.1. Single-Crystal Crystallography.....	74
1.2.1.2. DFT Bonding Analysis	77
1.3. Catalytic Semi-Hydrogenation	81
1.4. References	86
2. Computational Framework.....	87
2.1. Introduction to the Generation of Metal Complexes	87
2.2. Additional Computational Details on the Framework for the Generation of Metal Complexes	89
2.2.1. Generation of Molecular Unary Frames	89
2.2.2. Clustering of Molecular Structures via Coulomb Matrix Representation	90
2.2.3. Generation of the Binary Core Structures.....	92
2.2.4. Low-cost Geometric Optimizations for the Core	92
2.2.5. Generation of Sites on the Core Surface.....	93
2.2.6. Addition of Ligands on the Core Surface.....	93
2.2.7. Complexes Filtering.....	94
2.2.8. Representative Complexes via Clustering Algorithm.....	94
2.2.9. Low-cost Geometric Optimization of Metal Complexes	94
2.2.10. Optimization with Tight Criteria.....	95
2.3. Additional Details on the Theoretical Approach and Computational Details for the Optimization Calculations.....	95
2.4. Cluster_Assembler-Documentation.....	96
2.5. Computational Parameters to Generate the Family of Metal Complexes.....	99
2.6. Additional Results for the A _a B _b Cores	100
2.6.1. [CuZn ₂]	100

2.6.2.	[Cu ₃ Zn ₄]	102
2.6.3.	[Cu ₅ Zn ₅]	111
2.6.4.	[Cu ₆ Zn ₅]	119
2.6.5.	[Cu ₈ Zn ₃]	125
2.6.6.	[Cu ₄ Zn ₁₀]	137
2.6.7.	[Cu ₁₁ Zn ₆]	148
2.6.8.	[Cu ₈ Al ₆]	162
2.6.9.	[Ni ₇ Ga ₆]	171
2.7.	Additional Results for Metal Complexes	180
2.7.1.	[CuZn ₂](Cp [*]) ₃ Complexes	181
2.7.2.	[Cu ₃ Zn ₄](Cp [*]) ₅ Complexes	182
2.7.3.	[Cu ₅ Zn ₅](Cp [*]) ₆ (CO ₂) ₂ Complexes	198
2.7.4.	[Cu ₆ Zn ₅](Cp [*]) ₅ (Mes)H ₃ Complexes	211
2.7.5.	[Cu ₈ Zn ₃](Cp [*]) ₃ (Mes) ₄ CO ₂ Complexes	223
2.7.6.	[Cu ₈ Zn ₃](Cp [*]) ₄ (Mes) ₃ H Complexes	237
2.7.7.	[Cu ₉ Zn ₇](Cp [*]) ₆ (Hex) ₃ H ₃ Complexes	247
2.7.8.	[Cu ₁₁ Zn ₆](Cp [*]) ₈ (CO ₂) ₂ (HCO ₂) Complexes	252
2.7.9.	[Cu ₈ Al ₆](Cp [*]) ₆ Complexes	258
2.7.10.	[Ni ₇ Ga ₆](Cp [*]) ₆ Complexes	270
2.8.	References	280

1. Experimental Section

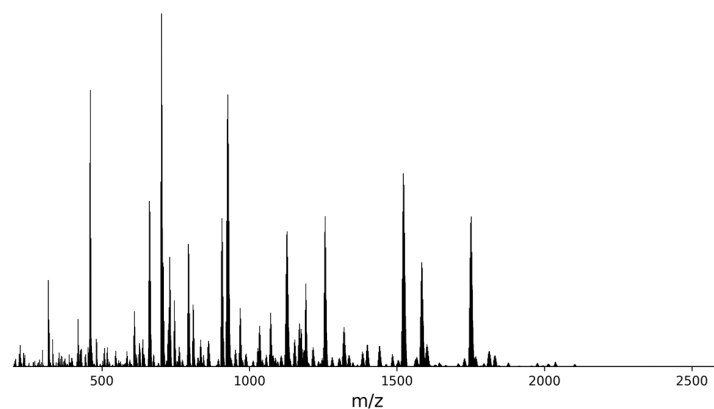
1.1. Cu/Zn Libraries



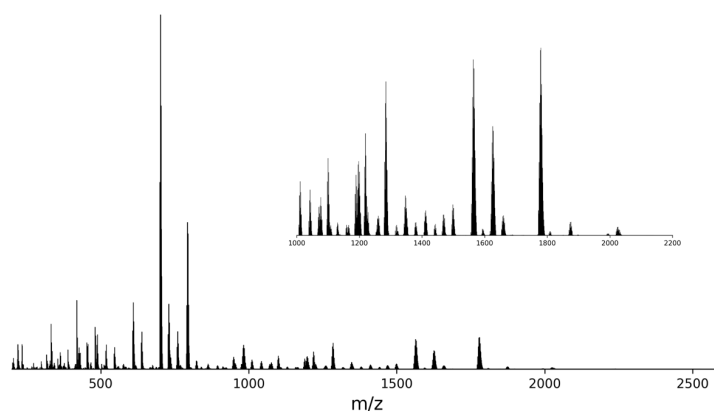
Supplementary Figure 1: Schematic overview of the different reactions investigated. The reaction of copper mesityl with $Zn_2Cp^{*}_2$ leads to the formation of library {1}, that contains, among others, the clusters $[H_3Cu_6Zn_5](Cp^*)_5(Mes)$ (D) and $[HCu_8Zn_3](Cp^*)_4(Mes)_5$ (E) and $[Cu_4Zn_{10}](Cp^*)_8$ (F). Cluster F can be enriched, isolated and obtained in acceptable purity form by targeted optimization of the synthesis parameters of {1}. The treatment of {1} with CO_2 leads to the formation of library {2}, containing the clusters $[Cu_5Zn_5](Cp^*)_6(CO_2)_2$ (X) and $[Cu_5Zn_3](Cp^*)_3(Mes)(CO_2)$ (Y). The treatment of {2} with H_2 leads to the formation of library {3}, in particular containing the formate bearing cluster $[Cu_{11}Zn_6](Cp^*)_8(CO_2)_2(HCO_2)$ (Z). Library {4}, obtained from {1} under treatment with 3-hexyne and H_2 , is catalytically active towards the semi-hydrogenation of 3-hexyne. The isolated $[Cu_4Zn_{10}](Cp^*)_8$ (F) acts as a pre-catalyst for the semi-hydrogenation of 3-hexyne to cis-3-hexene.

1.1.1. Mass Spectrometric Characterization

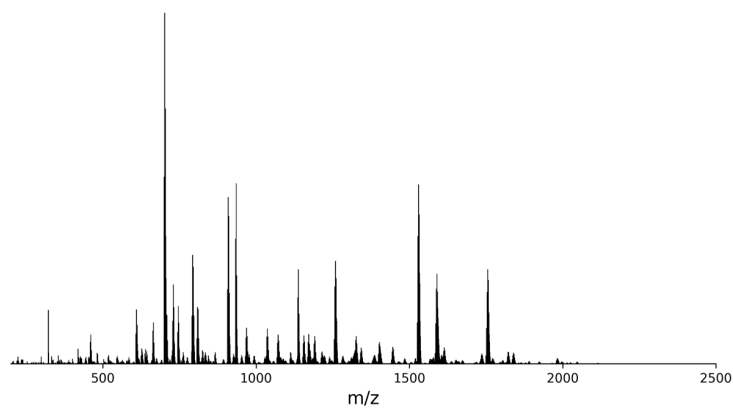
1.1.1.1. LIFDI Mass Spectra



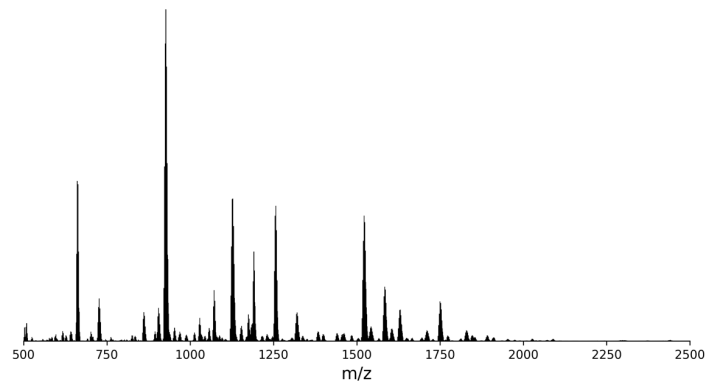
Supplementary Figure 2: Full range LIFDI mass spectrum of the Cu/Zn library {1}.



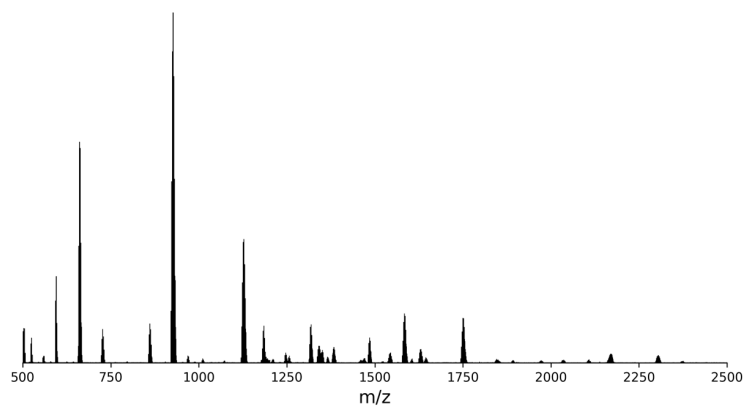
Supplementary Figure 3: Full range LIFDI mass spectrum of the Cu/Zn library {1} with Cp*^{Et} labelling.



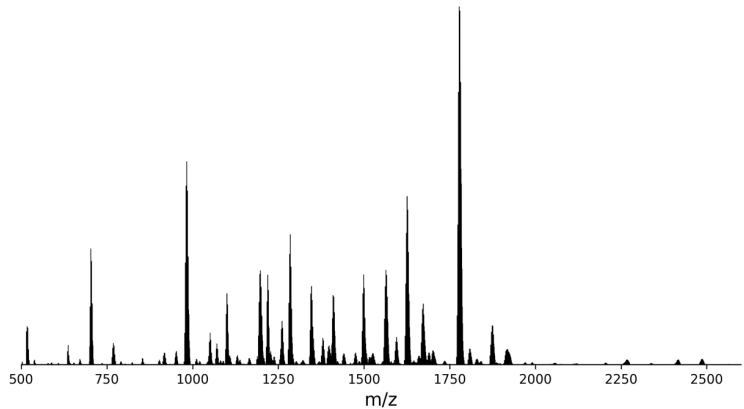
Supplementary Figure 4: Full range LIFDI mass spectrum of the Cu/Zn library {1} with ^{68}Zn labelling.



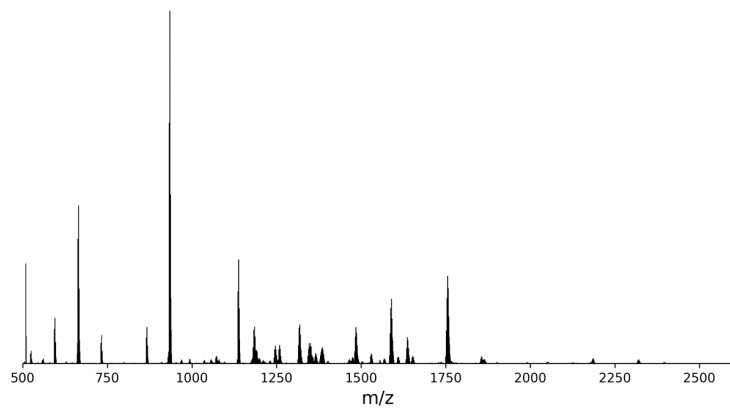
Supplementary Figure 5: Full range LIFDI mass spectrum of the reaction of the Cu/Zn library {1} with CO_2 yielding {2}.



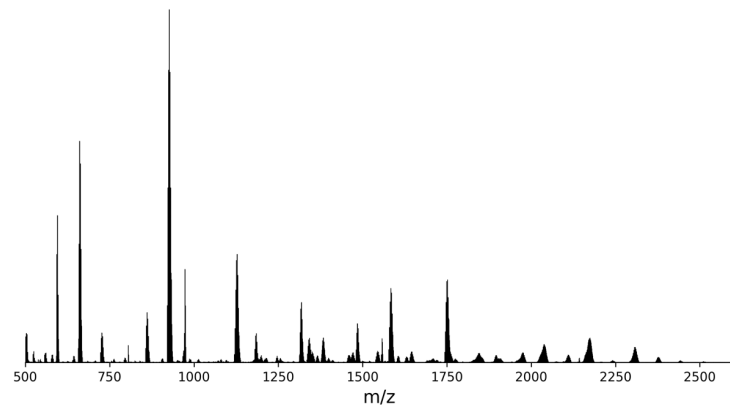
Supplementary Figure 6: Full range LIFDI mass spectrum of the reaction of the Cu/Zn library **{1}** with CO₂ and H₂ yielding library **{3}**.



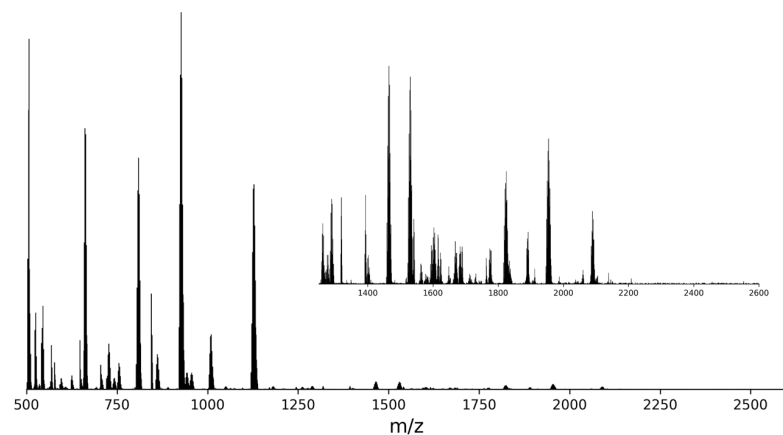
Supplementary Figure 7: Full range LIFDI mass spectrum of the reaction of the Cu/Zn library **{1}** with CO₂ and H₂ with Cp*Et labelling yielding **{3}**.



Supplementary Figure 8: Full range LIFDI mass spectrum of the reaction of the Cu/Zn library **{1}** with CO₂ and H₂ with ⁶⁸Zn labelling yielding **{3}**.



Supplementary Figure 9: Full range LIFDI mass spectrum of the reaction of the Cu/Zn library **{1}** with ¹³CO₂ and H₂ yielding library **{3}**.



Supplementary Figure 10: Full range LIFDI mass spectrum of the reaction of the Cu/Zn library {1} with 3-hexyne and H₂ yielding {4}.

1.1.1.2. Composition Tables

Supplementary Table 1: List of all identified patterns in the LIFDI mass spectrum of the Cu/Zn library {1} with composition and m/z, as well as indications if a species has been identified by Cp*^{EI} labelling, ⁶⁸Zn labelling or both.

Composition	m/z	Cp* ^{EI} Label	⁶⁸ Zn Label
ZnCp*Mes	318,1289	✓	✓
[CuZn](Cp*) ₂	399,0865	✓	✓
[Cu ₂](Cp*) ₂	461,0168	✓	✓
[HCu ₄](Cp*) ₂	524,9531	✓	✓
[H ₂ Cu ₃](Cp*) ₃	598,1309	✓	✓
[CuZn ₂](Cp*) ₃ (A)	600,1593	✓	✓
[H ₂ Cu ₂ Zn](Cp*) ₃	600,1593	✓	✓
[Cu ₄](Cp*)(Mes) ₂	627,0009	✓	✓
[Cu ₄](Cp*) ₂ (Mes)	643,0310	✗	✓
[HCu ₃ Zn](Cp*) ₃	661,0653	✓	✓
[Cu ₂ Zn ₃](Mes) ₃	678,9015	✓	✓
[HCu ₅](Cp*) ₂ (Mes)	706,9671	✓	✓
[HCu ₇](Cp*) ₂	715,7538	✓	✓
[HCu ₄ Zn ₂](Cp*) ₃ {-2H}	724,9912	✓	✓
[Cu ₃ Zn](Mes) ₄	731,0599	✓	✓
[Cu ₄](Cp*)(Mes) ₃	746,0845	✓	✓
[HCu ₅ Zn](Cp*) ₃	788,924	✓	✓
[Cu ₄ Zn ₂](Cp*) ₃	788,924	✓	✓
[Cu ₄](Mes) ₄	792,9827	✓	✓
[Cu ₅](Cp*)(Mes) ₃	809,0139	✗	✓
[Cu ₅](Cp*) ₂ (Mes) ₂	825,0443	✓	✓
[HCu ₇](Cp*) ₂ (Mes)	834,8236	✓	✓
[HCu ₇](Cp*) ₃	850,8526	✗	✓
[Cu ₄ Zn ₂](Cp*) ₄	861,1030	✓	✓
[Cu ₄ Zn](Cp*) ₃ (Mes)	907,0021	✓	✓
[Cu ₄ Zn ₂](Cp*) ₄	927,0291	✓	✓
[Cu ₇](Cp*) ₂ (Mes) ₂	952,9009	✓	✓
[Cu ₇](Cp*) ₃ (Mes)	968,9302	✗	✓
[Cu ₂ Zn ₂](Cp*) ₄	988,9597	✓	✓
[H ₂ Cu ₂ Zn](Cp*) ₄	1050,8907	✓	✓
[Cu ₇](Cp*) ₂ (Mes) ₃	1071,9873	✓	✓
[Cu ₉](Cp*) ₂ (Mes) ₂	1080,7580	✓	✓
[Cu ₇](Cp*) ₃ (Mes) ₂	1088,0089	✓	✓
[Cu ₉](Cp*) ₃ (Mes)	1096,7881	✓	✓
[HCu ₅ Zn ₂](Cp*) ₄ (Mes)	1108,0456	✓	✓
[HCu ₈ Zn](Cp*) ₄	1114,8248	✓	✓
[Cu ₇ Zn ₂](Cp*) ₅ (B)	1128,0719	✓	✓
[Cu ₇ Zn](Cp*) ₃ (Mes) ₂	1153,9412	✓	✓
[Cu ₇ Zn](Cp*) ₄ (Mes)	1169,9734	✗	✓
[HCu ₉]Cp*(Mes) ₄	1184,8193	✓	✓
[Cu ₇](Cp*) ₂ (Mes) ₄	1191,0795	✓	✓
[Cu ₉](Cp*) ₃ (Mes) ₂	1215,8734	✓	✓

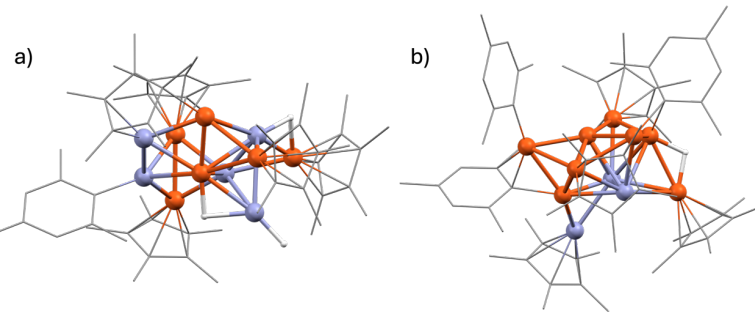
[Cu ₉ Zn ₂](Cp [*]) ₃ (Mes)	1226,6638	✓	✓
[Cu ₇ Zn ₂](Cp [*]) ₄ (Mes)	1233,9060	✗	✓
[Cu ₇ Zn](Cp [*]) ₂ (Mes) ₄	1257,0006	✓	✓
[Cu ₇ Zn ₂](Cp [*]) ₃ (Mes) ₃	1336,9574	✓	✓
[Cu ₉ Zn](Cp [*]) ₃ (Mes) ₃	1400,8855	✓	✓
[Cu ₇ Zn ₂](Cp [*]) ₂ (Mes) ₅	1442,0074	✓	✓
[Cu ₁₀ Zn](Cp [*]) ₃ (Mes) ₃	1461,8229	✗	✓
[H ₃ Cu ₆ Zn ₃](Cp [*]) ₃ (Mes) (D)	1504,8750	✓	✓
[Cu ₇ Zn ₃](Cp [*]) ₃ (Mes) ₄	1521,9694	✓	✓
[Cu ₉ Zn ₂](Cp [*]) ₃ (Mes) ₄	1583,9421	✓	✓
[HCu ₈ Zn ₃](Cp [*]) ₄ (Mes) ₃ (E)	1603,9283	✓	✓
[Cu ₉ Zn ₃](Cp [*]) ₄ (Mes) ₃	1665,8539	✓	✓
[Cu ₁₀ Zn ₂](Cp [*]) ₂ (Mes) ₆	1751,8787	✓	✓
[Cu ₄ Zn ₉](Cp [*]) ₇	1789,4314	✓	✓
[Cu ₁₀ Zn ₃](Cp [*]) ₃ (Mes) ₅	1831,8334	✓	✓
[Cu ₄ Zn ₁₀](Cp [*]) ₇	1852,8166	✗	✓
{[Cu ₃ Zn ₄](Cp [*]) ₆ (Mes) ₆ {-H}}	1975,6995	✓	✓
[Cu ₄ Zn ₁₀](Cp [*]) ₈ (F)	1989,9273	✓	✓

Supplementary Table 2: List of all identified molecular ions in the Cu/Zn library {1} with composition and m/z, as well as indications if a species has been identified by Cp^{*Ei} labelling, ⁶⁸Zn labelling or both.

Composition	m/z	Cp ^{*Ei} Label	⁶⁸ Zn Label
[CuZn ₂](Cp [*]) ₃ (A)	600,1593	✓	✓
[Cu ₄](Cp [*])(Mes) ₂	627,0009	✓	✓
[Cu ₄](Cp [*]) ₂ (Mes)	643,0310	✗	✓
[HCu ₄](Cp [*]) ₂ (Mes)	706,9671	✓	✓
[Cu ₄](Cp [*])(Mes) ₃	746,0845	✓	✓
[Cu ₅](Cp [*])(Mes) ₃	809,0139	✗	✓
[Cu ₅](Cp [*]) ₂ (Mes) ₂	825,0443	✓	✓
[Cu ₅ Zn](Cp [*]) ₃ (Mes)	907,0021	✓	✓
[HCu ₅ Zn ₂](Cp [*]) ₃ (Mes)	1108,0456	✓	✓
[Cu ₆ Zn ₄](Cp [*]) ₅ (B)	1128,0719	✓	✓
[Cu ₇ Zn](Cp [*]) ₃ (Mes) ₂	1153,9412	✓	✓
[Cu ₇ Zn](Cp [*]) ₄ (Mes)	1169,9734	✗	✓
[Cu ₇ Zn ₂](Cp [*]) ₄ (Mes)	1233,9060	✗	✓
[Cu ₇ Zn](Cp [*]) ₂ (Mes) ₄	1257,0006	✓	✓
[Cu ₉ Zn](Cp [*]) ₃ (Mes) ₃	1400,8855	✓	✓
[Cu ₁₀ Zn](Cp [*]) ₃ (Mes) ₃	1461,8229	✗	✓
[H ₃ Cu ₆ Zn ₃](Cp [*]) ₃ (Mes) (D)	1504,8750	✓	✓
[Cu ₇ Zn ₃](Cp [*]) ₃ (Mes) ₄	1521,9694	✓	✓
[Cu ₉ Zn ₂](Cp [*]) ₃ (Mes) ₄	1583,9421	✓	✓
[HCu ₈ Zn ₃](Cp [*]) ₄ (Mes) ₃ (E)	1603,9283	✓	✓
[Cu ₉ Zn ₃](Cp [*]) ₄ (Mes) ₃	1665,8539	✓	✓
[Cu ₁₀ Zn ₂](Cp [*]) ₂ (Mes) ₆ (C)	1751,8787	✓	✓
[Cu ₄ Zn ₁₀](Cp [*]) ₈ (F)	1989,9273	✓	✓

Supplementary Table 3: List of all identified fragments in the Cu/Zn library {1} with composition and m/z, as well as indications if a species has been identified by $\text{Cp}^{*\text{Et}}$ labelling, ^{68}Zn labelling or both.

Composition	m/z	$\text{Cp}^{*\text{Et}}$ Label	^{68}Zn Label
$[\text{CuZn}](\text{Cp}^*)_2$	399,0865	✓	✓
$[\text{Cu}_3](\text{Cp}^*)_2$	461,0168	✓	✓
$[\text{HCu}_4](\text{Cp}^*)_2$	524,9531	✓	✓
$[\text{HCu}_3\text{Zn}_2](\text{Cp}^*)_3 \{-2\text{H}\}$	724,9912	✓	✓
$[\text{HCu}_2\text{Zn}](\text{Cp}^*)_3$	788,924	✓	✓
$[\text{Cu}_2\text{Zn}_2](\text{Cp}^*)_3$	788,924	✓	✓
$[\text{HCu}_7](\text{Cp}^*)_3$	850,8526	✗	✓
$[\text{Cu}_2\text{Zn}_3](\text{Cp}^*)_4$	927,0291	✓	✓
$[\text{Cu}_2\text{Zn}_2](\text{Cp}^*)_4$	988,9597	✓	✓
$[\text{H}_2\text{Cu}_2\text{Zn}](\text{Cp}^*)_4$	1050,8907	✓	✓
$[\text{HCu}_8\text{Zn}](\text{Cp}^*)_4$	1114,8248	✓	✓
$[\text{Cu}_4\text{Zn}_9](\text{Cp}^*)_7$	1789,4314	✓	✓

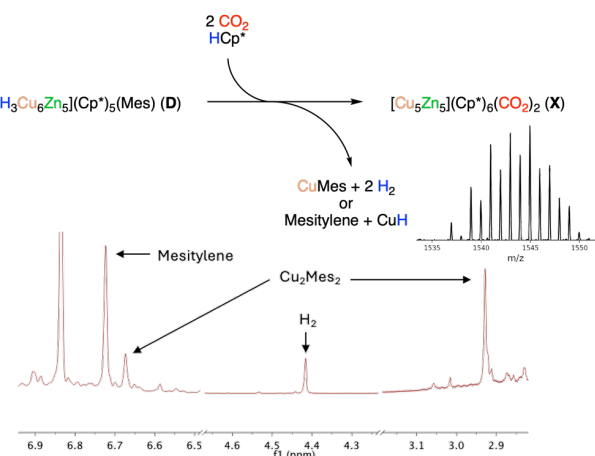


Supplementary Figure 11: Calculated structures of a) $[\text{H}_3\text{Cu}_6\text{Zn}_5](\text{Cp}^*)_5(\text{Mes})$ (**D**) and b) $[\text{HCu}_8\text{Zn}_3](\text{Cp}^*)_4(\text{Mes})_3$ (**E**). Color code: orange = copper, blue = zinc, grey = carbon and white = hydrogen.

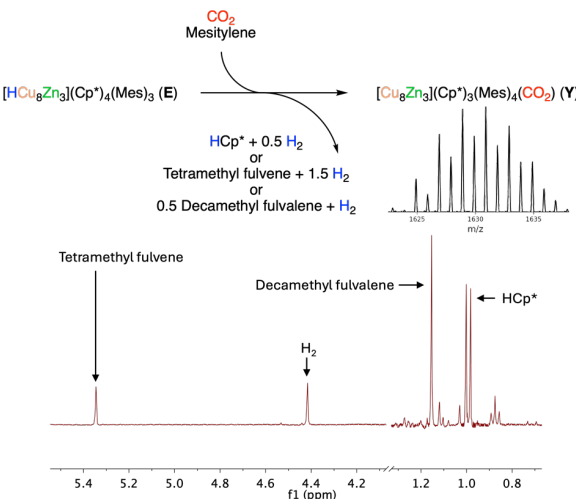
Supplementary Table 4: List of all identified molecular ions in the Cu/Zn library {2} with composition and m/z, species of the substrate library {1} reacting off, as well as indications if a new species (marked in bold) has been identified by ^{68}Zn labelling, $^{13}\text{CO}_2$ labelling or both.

Composition	m/z	Presence in {I}	^{68}Zn Label	$^{13}\text{CO}_2$ Label
$[\text{CuZn}_2](\text{Cp}^*)_3$ (A)	600,1593	✓		
$[\text{Cu}_4](\text{Cp}^*)(\text{Mes})_2$	627,0009	✓		
$[\text{Cu}_4](\text{Cp}^*)_2(\text{Mes})$	643,0310	✓		
$[\text{HCu}_5](\text{Cp}^*)_2(\text{Mes})$	706,9671	✓		
$[\text{Cu}_4](\text{Cp}^*)(\text{Mes})_3$	746,0845	✓		
$[\text{Cu}_5](\text{Cp}^*)(\text{Mes})_3$	809,0139	✓		
$[\text{Cu}_5](\text{Cp}^*)_2(\text{Mes})_2$	825,0443	✓		
$[\text{Cu}_5\text{Zn}](\text{Cp}^*)_3(\text{Mes})$	907,0021	✓		

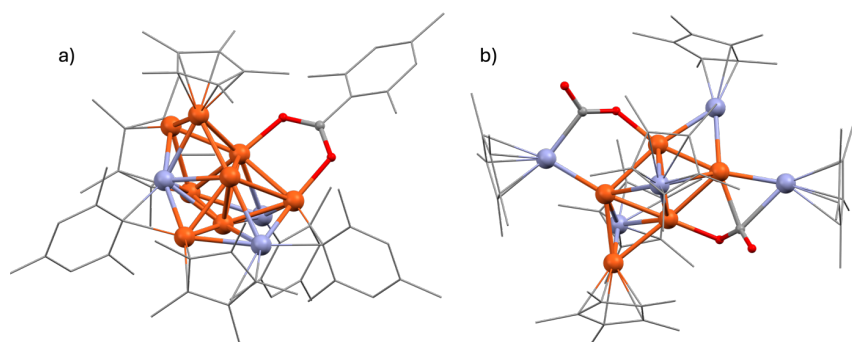
[HCu ₅ Zn ₂](Cp [*]) ₄ (Mes)	1108,0456	✓		
[Cu ₃ Zn ₄](Cp [*]) ₅ (B)	1128,0719	✓		
[Cu ₂ Zn](Cp [*]) ₃ (Mes) ₂	1153,9412	✓		
[Cu ₂ Zn](Cp [*]) ₄ (Mes)	1169,9734	✓		
[Cu ₂ Zn ₂](Cp [*]) ₃ (Mes)	1233,9060	✓		
[Cu ₂ Zn](Cp [*]) ₂ (Mes) ₄	1257,0006	✓		
[Cu ₂ Zn](Cp [*]) ₃ (Mes) ₃	1400,8855	✓		
[Cu ₁₀ Zn](Cp [*]) ₃ (Mes) ₃	1461,8229	✓		
[H ₃ Cu ₆ Zn ₅](Cp [*]) ₅ (Mes) (D)	1504,8750	✓		
[Cu ₇ Zn ₃](Cp [*]) ₃ (Mes) ₄	1521,9694	✓		
[Cu₅Zn₃](Cp[*])₆(CO₂)₂ (X)	1542,9686		✓	✓
[Cu ₉ Zn ₂](Cp [*]) ₃ (Mes) ₄	1583,9421	✓		
[HCu ₈ Zn ₃](Cp [*]) ₄ (Mes) ₃ (E)	1603,9283	✓		
[Cu₅Zn₃](Cp[*])₃(Mes)₄(CO₂) (Y)	1630,9030		✓	✓
[Cu ₆ Zn ₃](Cp [*]) ₄ (Mes) ₃	1665,8539	✓		
[Cu ₁₀ Zn ₂](Cp [*]) ₃ (Mes) ₆ (C)	1751,8787	✓		
[Cu ₄ Zn ₁₀](Cp [*]) ₈ (F)	1989,9273	✓		



Supplementary Figure 12: Reaction scheme for the formation of species **X** from **D** in the conversion of {1} to {2} upon addition of CO_2 . The side products are identified by ^1H -NMR spectroscopy and the pattern of the molecular ion of **X** is shown ($m/z = 1542,9686$; see also Supplementary Table 4).



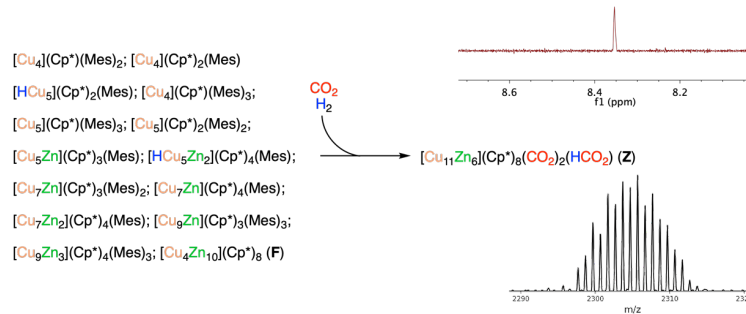
Supplementary Figure 13: Reaction scheme for the formation of species **Y** from **E** in the conversion of **{1}** to **{2}** upon addition of CO_2 . The side products are identified by ^1H -NMR spectroscopy and the pattern of the molecular ion of **Y** is shown ($m/z = 1630, 9030$; see also Supplementary Table 4).



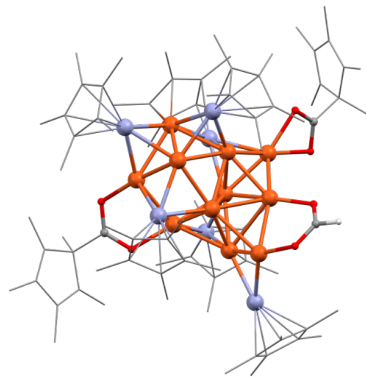
Supplementary Figure 14: Calculated structures of a) $[\text{Cu}_8\text{Zn}_3](\text{Cp}^*)_3(\text{Mes})_4(\text{CO}_2)$ (**Y**) and b) $[\text{Cu}_8\text{Zn}_3](\text{Cp}^*)_6(\text{CO}_2)_2$ (**X**). Color code: orange = copper, blue = zinc, grey = carbon, red = oxygen and white = hydrogen.

Supplementary Table 5: List of all identified molecular ions in the Cu/Zn library {3} with composition and m/z, species of the substrate library {2} reacting off, as well as indications if a new species (marked in bold) has been identified by ^{68}Zn labelling, $^{13}\text{CO}_2$ labelling or both.

Composition	m/z	Presence in {1} or {2}	^{68}Zn Label	$^{13}\text{CO}_2$ Label
[CuZn₂](Cp[*])₃ (A)	600,1593	✓		
[Cu ₄](Cp [*])(Mes) ₂	627,0009	✓		
[Cu ₄](Cp [*]) ₂ (Mes)	643,0310	✓		
[HCu ₅](Cp [*]) ₂ (Mes)	706,9671	✓		
[Cu ₄](Cp [*])(Mes) ₃	746,0845	✓		
[Cu ₃](Cp [*])(Mes) ₃	809,0139	✓		
[Cu ₅](Cp [*]) ₂ (Mes) ₂	825,0443	✓		
[Cu ₅ Zn](Cp [*]) ₃ (Mes)	907,0021	✓		
[HCu ₅ Zn ₂](Cp [*]) ₄ (Mes)	1108,0456	✓		
[Cu₅Zn₄](Cp[*])₅ (B)	1128,0719	✓		
[Cu ₇ Zn](Cp [*]) ₃ (Mes) ₂	1153,9412	✓		
[Cu ₇ Zn](Cp [*]) ₄ (Mes)	1169,9734	✓		
[Cu ₇ Zn ₂](Cp [*]) ₄ (Mes)	1233,9060	✓		
[Cu ₇ Zn](Cp [*]) ₂ (Mes) ₄	1257,0006	✓		
[Cu ₉ Zn](Cp [*]) ₃ (Mes) ₃	1400,8855	✓		
[Cu ₁₀ Zn](Cp [*]) ₃ (Mes) ₃	1461,8229	✓		
[Cu ₅ Zn ₃](Cp [*]) ₃ (Mes) ₄	1521,9694	✓		
[Cu ₈ Zn ₅](Cp [*]) ₆ (CO ₂) ₂ (X)	1542,9686	✓		
[Cu ₈ Zn ₂](Cp [*]) ₃ (Mes) ₄	1583,9421	✓		
[Cu ₈ Zn ₃](Cp [*]) ₃ (Mes) ₄ (CO ₂) (Y)	1630,9030	✓		
[Cu ₆ Zn ₄](Cp [*]) ₄ (Mes) ₃	1665,8539	✓		
[Cu ₁₀ Zn ₂](Cp [*]) ₂ (Mes) ₆ (C)	1751,8787	✓		
[Cu ₄ Zn ₁₀](Cp [*]) ₈ (F)	1989,9173	✓		
[Cu₁₁Zn₆](Cp[*])₈(CO₂)₂(HCO₂) (Z)	2305,7034		✓	✓



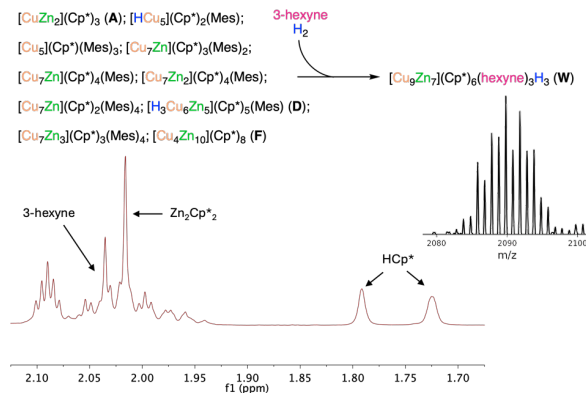
Supplementary Figure 15: Reaction scheme for the formation of species Z in the conversion of {2} to {3} upon addition of H₂. Formate is identified by ¹H-NMR spectroscopy and the pattern of the molecular ion of Z is shown (m/z = 2305,7034; see Supplementary Table 5).



Supplementary Figure 16: Calculated structures of $[\text{Cu}_{11}\text{Zn}_6](\text{Cp}^*)_8(\text{CO}_2)_2(\text{HCO}_2)$ (**Z**). Color code: orange = copper, blue = zinc, grey = carbon, red = oxygen and white = hydrogen.

Supplementary Table 6: List of all identified molecular ions in the Cu/Zn library **{4}** with composition and m/z, species of the substrate library **{1}** reacting off, as well as indications if a new species (marked in bold) has been identified by $\text{Cp}^{*\text{Et}}$ labelling, ^{68}Zn labelling or both.

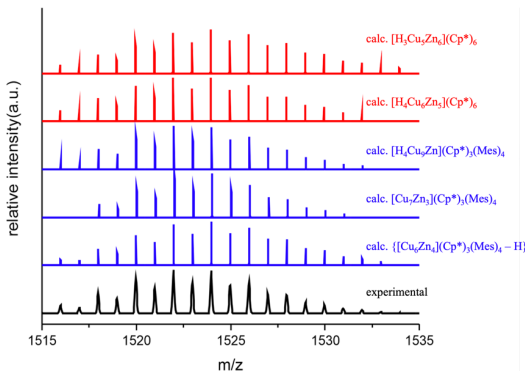
Composition	m/z	Presence in {1}	$\text{Cp}^{*\text{Et}}$ Label	^{68}Zn Label
$[\text{CuZn}_2](\text{Cp}^*)_3$ (A)	600,1593	✓		
$[\text{Cu}_4](\text{Cp}^*)(\text{Mes})_2$	627,0009	✓		
$[\text{HCu}_5](\text{Cp}^*)_2(\text{Mes})$	706,9671	✓		
$[\text{HCu}_5](\text{Cp}^*)_2(\text{Mes})$	706,9671	✓		
$[\text{Cu}_4](\text{Cp}^*)(\text{Mes})_3$	746,0845	✓		
$[\text{Cu}_5](\text{Cp}^*)(\text{Mes})_3$	809,0139	✓		
$[\text{Cu}_5](\text{Cp}^*)_2(\text{Mes})_2$	825,0443	✓		
$[\text{Cu}_5\text{Zn}](\text{Cp}^*)_3(\text{Mes})$	907,0021	✓		
$[\text{HCu}_5\text{Zn}_2](\text{Cp}^*)_4(\text{Mes})$	1108,0456	✓		
$[\text{Cu}_3\text{Zn}_4](\text{Cp}^*)_5$ (B)	1128,0719	✓		
$[\text{Cu}_5\text{Zn}](\text{Cp}^*)_3(\text{Mes})_2$	1153,9412	✓		
$[\text{Cu}_7\text{Zn}](\text{Cp}^*)_4(\text{Mes})$	1169,9734	✓		
$[\text{Cu}_7\text{Zn}_2](\text{Cp}^*)_4(\text{Mes})$	1233,9060	✓		
$[\text{Cu}_7\text{Zn}](\text{Cp}^*)_4(\text{Mes})_4$	1257,0006	✓		
$[\text{Cu}_3\text{Zn}_6](\text{Cp}^*)_4(3\text{-Hex})_2\text{H}_2$	1288,9970		✓	✓
$[\text{Cu}_6\text{Zn}](\text{Cp}^*)_3(\text{Mes})_3$	1400,8855	✓		
$[\text{Cu}_{10}\text{Zn}](\text{Cp}^*)_3(\text{Mes})_3$	1461,8229	✓		
$[\text{H}_3\text{Cu}_6\text{Zn}_5](\text{Cp}^*)_5(\text{Mes})$ (D)	1504,8750	✓		
$[\text{Cu}_7\text{Zn}_3](\text{Cp}^*)_3(\text{Mes})_4$	1521,9694	✓		
$[\text{Cu}_9\text{Zn}_2](\text{Cp}^*)_3(\text{Mes})_4$	1583,9421	✓		
$[\text{HCu}_8\text{Zn}_3](\text{Cp}^*)_4(\text{Mes})_3$ (E)	1603,9283	✓		
$[\text{Cu}_9\text{Zn}_3](\text{Cp}^*)_4(\text{Mes})_3$	1665,8539	✓		
$[\text{Cu}_{10}\text{Zn}_2](\text{Cp}^*)_2(\text{Mes})_6$ (C)	1751,8787	✓		
$[\text{Cu}_4\text{Zn}_{10}](\text{Cp}^*)_8$ (F)	1989,9173	✓		
$[\text{Cu}_9\text{Zn}_7](\text{Cp}^*)_6(3\text{-Hex})_2\text{H}_3$ (W)	2089,8176		✓	✓



Supplementary Figure 17: Reaction scheme for the formation of species **W** in the conversion of **{1}** to **{4}** upon addition of 3-hexyne and H₂. Zn₂Cp*₂ and HCp* are identified by ¹H-NMR spectroscopy and the pattern of the molecular ion of **W** is shown (m/z = 2089,8176; see Supplementary Table 6).

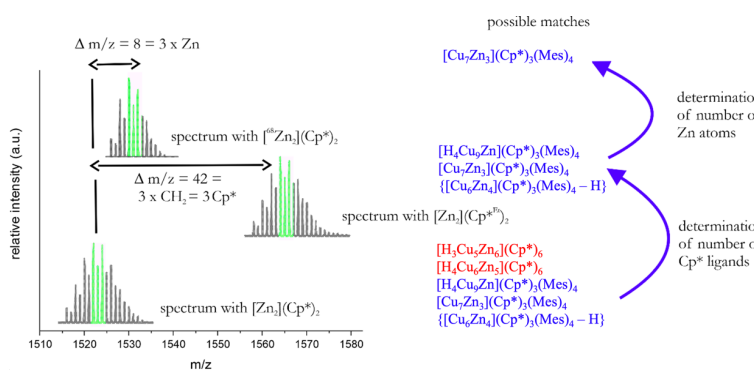
1.1.1.3. Peak Identification

Through the analysis of the m/z value and the isotopic pattern of each peak, one or multiple theoretical compositions could be assigned to each peak in the LIFDI mass spectrum. Below the double labelling work flow for peak pattern assignment is explained.



Supplementary Figure 18: For illustration, selected series of several matching isotopic patterns with similar GooF for an experimental mass spectrometric peak pattern of the Cu/Zn cluster library {1}. Blue = Matches with 3 Cp^* ligands, red = Matches with 6 Cp^* ligands.

In order to discriminate between the different possible compositions, labelling experiments with $\text{Cp}^{*\text{Et}}$ and ^{68}Zn were performed. The procedure is illustrated in Supplementary Figure 19 and must be repeated for every peak in the spectrum. The number of matches for each peak is thereby reduced to species carrying the same number of Cp^* ligands. Notably, the procedure did work for most of the peaks and corresponding, mass-shifted envelopes were identified in the $\text{Cp}^{*\text{Et}}$ labeled spectrum.



Supplementary Figure 19: Determination of the composition via $\text{Cp}^{*\text{Et}}$ and ^{68}Zn labeling.

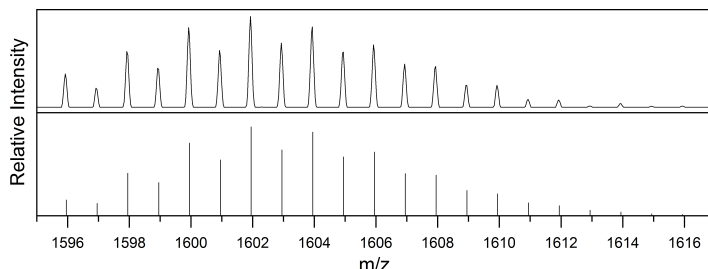
Using the same procedure as for the Cp^*Et labeling experiments, the number of Zn atoms and thereby the cluster core composition can be identified. The labeling with ^{68}Zn additionally changes (simplifies!) the isotopic patterns, leading to an easy and straightforward interpretation of most of the peaks. For many peaks, labeling with ^{68}Zn was sufficient to achieve unambiguous identification. Consequently, many of the cases, for which Cp^*Et labeling did not yield clear results, could eventually be resolved by using the ^{68}Zn label.

The procedure was repeated for all peaks of the spectrum. A list of more than 50 species is produced, which is shown in Supplementary Table 1. It is also denoted in the table, whether a species was identified solely by its ^{68}Zn pattern or by combination of Cp^*Et and ^{68}Zn labeling experiments.

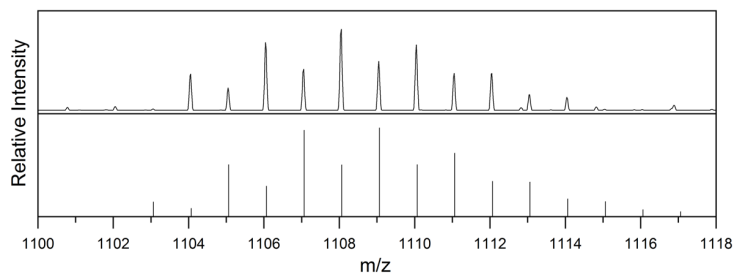
This procedure is described exemplarily for the peak at $m/z = 1521.986$ (Supplementary Figures 18 and 19). The consideration of Cu, Zn, Cp^* , mestiyl and hydrides leads to 5 possible combinations with simulated patterns corresponding well to the experimental one. Through the synthesis of {1} using $\text{Zn}_2\text{Cp}^*\text{Et}_2$, a $\Delta m/z$ of 42 is observed for this pattern. As the m/z difference between Cp^* and Cp^*Et is 14 (additional CH_2 group in Cp^*Et), it is thus determined, that this species bears 3 Cp^* ligands. This reduces the number of possible compositions to those only containing 3 Cp^* ligands: $[\text{Cu}_6\text{Zn}_4]\text{Cp}^*_3\text{Mes}_4\{-\text{H}\}$, $[\text{H}_4\text{Cu}_9\text{Zn}]\text{Cp}^*_3\text{Mes}_4$ and $[\text{Cu}_7\text{Zn}_3]\text{Cp}^*_3\text{Mes}_4$. All remaining possible combinations exhibit an identical hydrocarbon ligand shell. As such, isotopic labeling of the metal atoms is required in order to obtain a definite composition for this peak. This is done using $^{68}\text{Zn}_2\text{Cp}^*\text{Et}_2$ for the synthesis of {1}, yielding a library with peaks shifted by $\Delta m/z = n_{\text{Zn}} \times 2.62$. In this example, the observed peak shift corresponds to 3 zinc atoms. As only one composition matches the information of both the Cp^*Et and ^{68}Zn labeling experiments, namely $[\text{Cu}_7\text{Zn}_3]\text{Cp}^*_3\text{Mes}_4$, this is then determined to be the definite sum formula for the peak at $m/z = 1521.986$.

Molecular Ions

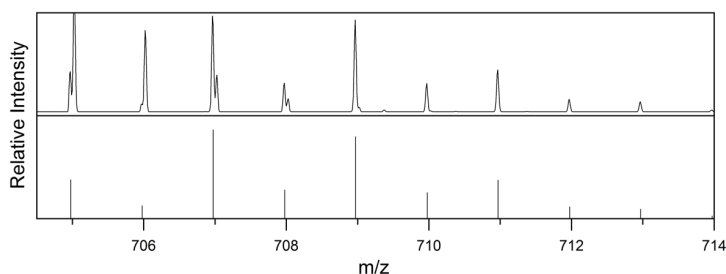
Below we list the data of the identified cluster molecular ions present in the libraries {1}-{4}: comparison of experimental and calculated peak patterns.



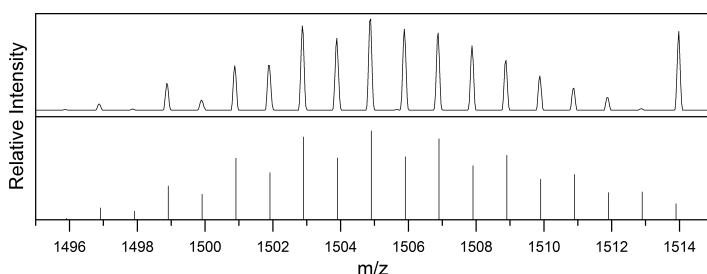
Supplementary Figure 20: Experimental pattern (top) and calculated pattern (bottom) for $[\text{HCu}_8\text{Zn}_3](\text{Cp}^*)_4(\text{Mes})_3$ (**E**).



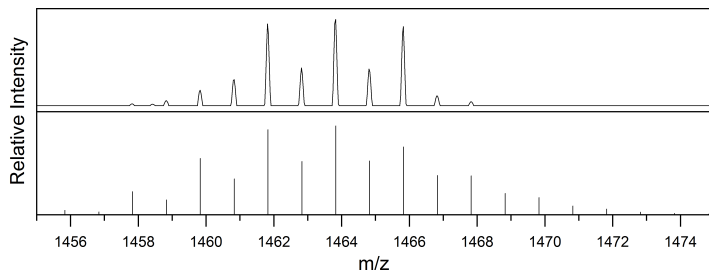
Supplementary Figure 21: Experimental pattern (top) and calculated pattern (bottom) for $[\text{HCu}_5\text{Zn}_2](\text{Cp}^*)_4(\text{Mes})$.



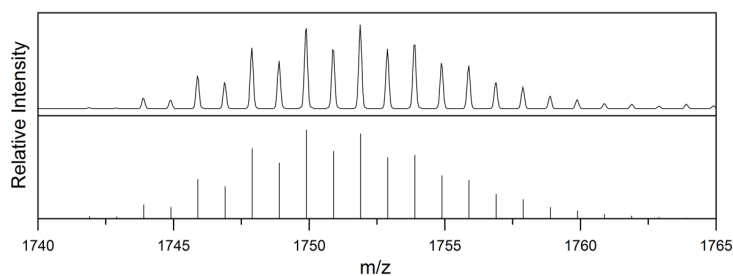
Supplementary Figure 22: Experimental pattern (top) and calculated pattern (bottom) for $[\text{HCu}_5](\text{Cp}^*)_2(\text{Mes})$.



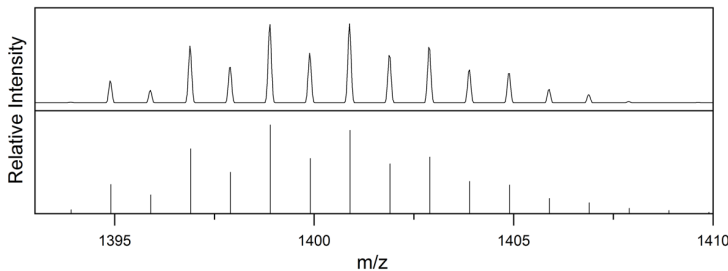
Supplementary Figure 23: Experimental pattern (top) and calculated pattern (bottom) for $[\text{H}_3\text{Cu}_6\text{Zn}_5](\text{Cp}^*)_5(\text{Mes})_3$ (**D**).



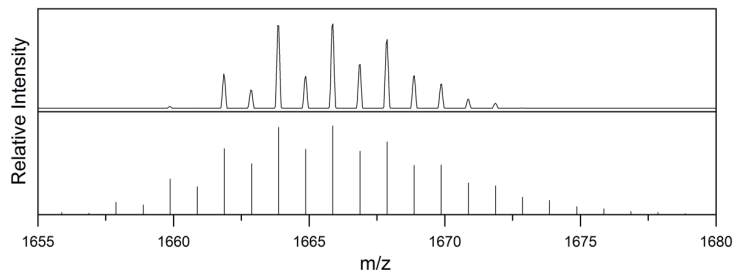
Supplementary Figure 24: Experimental pattern (top) and calculated pattern (bottom) for $[\text{Cu}_{10}\text{Zn}](\text{Cp}^*)_3(\text{Mes})_3$. Low intensity of the pattern gives this “truncated” aspect with peaks at the extremities of the pattern missing.



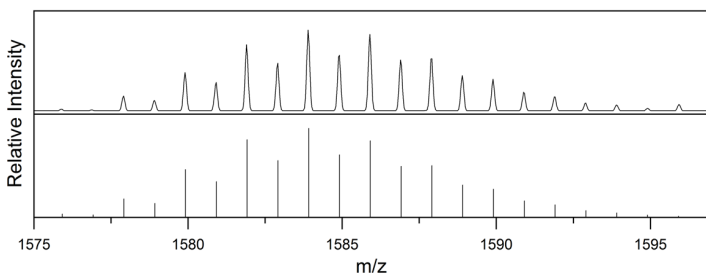
Supplementary Figure 25: Experimental pattern (top) and calculated pattern (bottom) for $[\text{Cu}_{10}\text{Zn}_2](\text{Cp}^*)_2(\text{Mes})_6$.



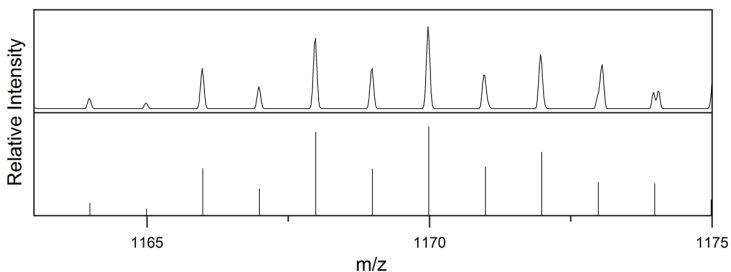
Supplementary Figure 26: Experimental pattern (top) and calculated pattern (bottom) for $[\text{Cu}_9\text{Zn}](\text{Cp}^*)_3(\text{Mes})_3$.



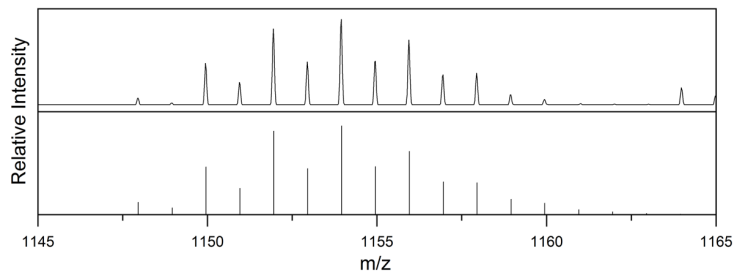
Supplementary Figure 27: Experimental pattern (top) and calculated pattern (bottom) for $[\text{Cu}_9\text{Zn}_3](\text{Cp}^*)_4(\text{Mes})_3$. Low intensity of the pattern gives this “truncated” aspect with peaks at the extremities of the pattern missing.



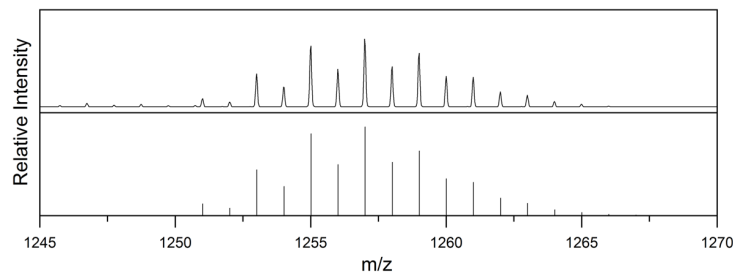
Supplementary Figure 28: Experimental pattern (top) and calculated pattern (bottom) for $[\text{Cu}_9\text{Zn}_2](\text{Cp}^*)_3(\text{Mes})_4$.



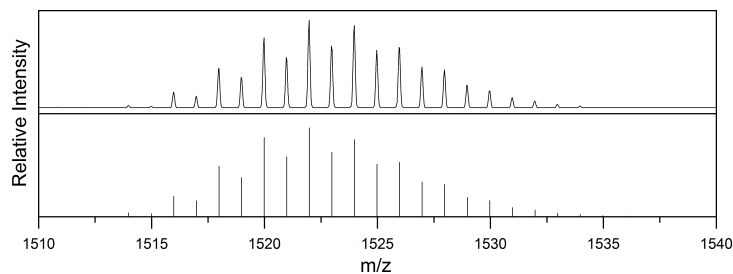
Supplementary Figure 29: Experimental pattern (top) and calculated pattern (bottom) for $[\text{Cu}_7\text{Zn}](\text{Cp}^*)_4(\text{Mes})$.



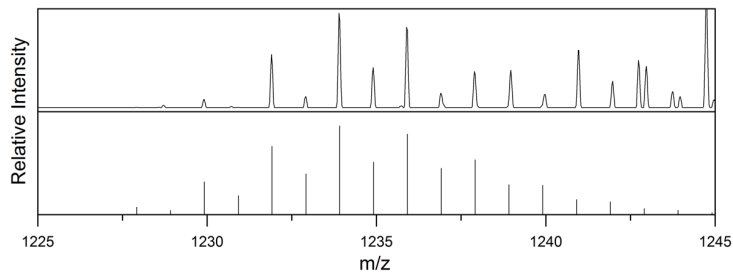
Supplementary Figure 30: Experimental pattern (top) and calculated pattern (bottom) for $[\text{Cu}_7\text{Zn}](\text{Cp}^*)_3(\text{Mes})_2$.



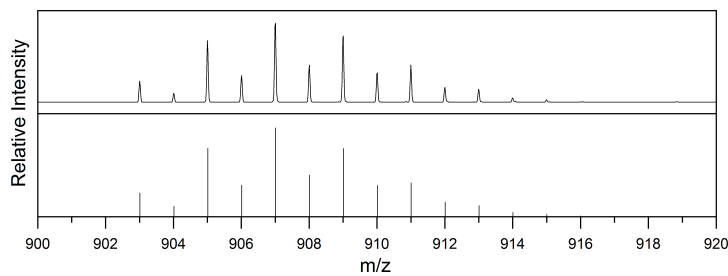
Supplementary Figure 31: Experimental pattern (top) and calculated pattern (bottom) for $[\text{Cu}_7\text{Zn}](\text{Cp}^*)_2(\text{Mes})_4$.



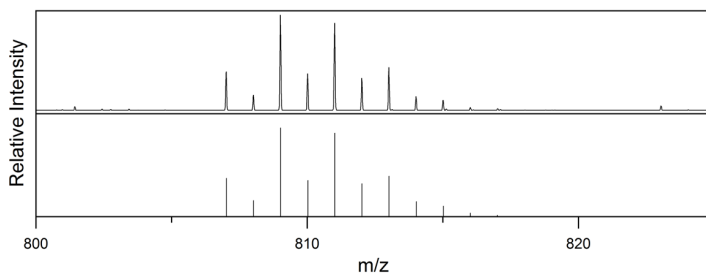
Supplementary Figure 32: Experimental pattern (top) and calculated pattern (bottom) for $[\text{Cu}_7\text{Zn}_3](\text{Cp}^*)_3(\text{Mes})_4$.



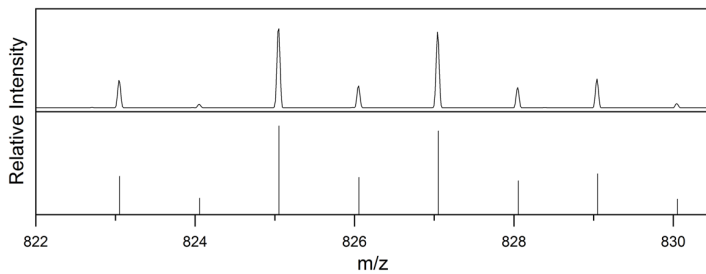
Supplementary Figure 33: Experimental pattern (top) and calculated pattern (bottom) for $[\text{Cu}_7\text{Zn}_2](\text{Cp}^*)_4(\text{Mes})$.



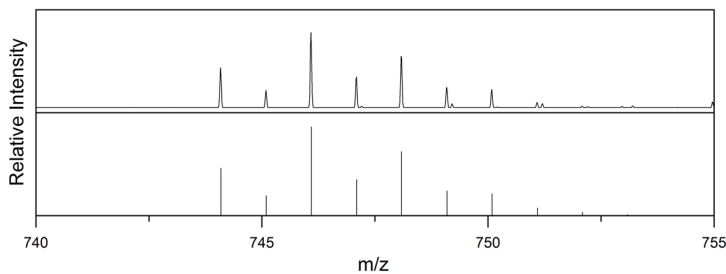
Supplementary Figure 34: Experimental pattern (top) and calculated pattern (bottom) for $[\text{Cu}_5\text{Zn}](\text{Cp}^*)_3(\text{Mes})$.



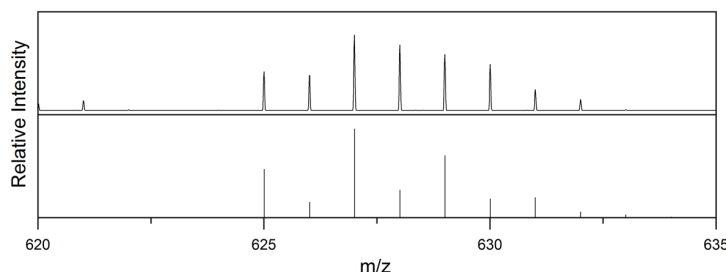
Supplementary Figure 35: Experimental pattern (top) and calculated pattern (bottom) for $[\text{Cu}_5](\text{Cp}^*)(\text{Mes})_3$.



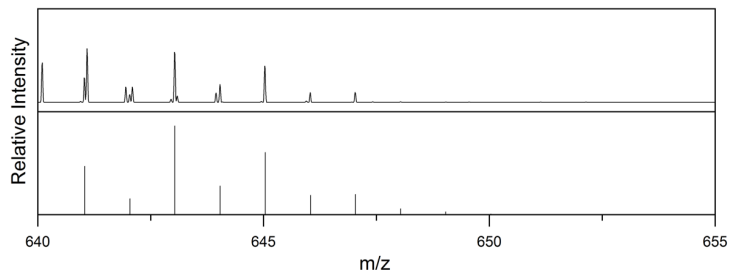
Supplementary Figure 36: Experimental pattern (top) and calculated pattern (bottom) for $[\text{Cu}_5](\text{Cp}^*)_2(\text{Mes})_2$.



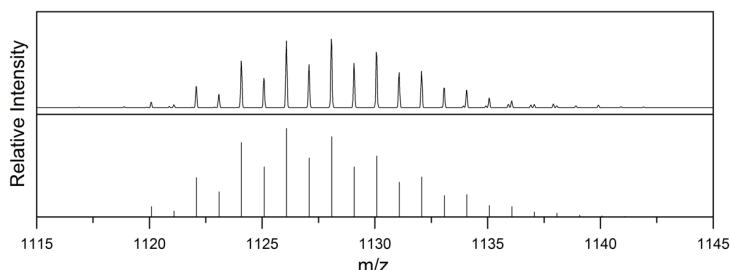
Supplementary Figure 37: Experimental pattern (top) and calculated pattern (bottom) for $[\text{Cu}_4](\text{Cp}^*)(\text{Mes})_3$.



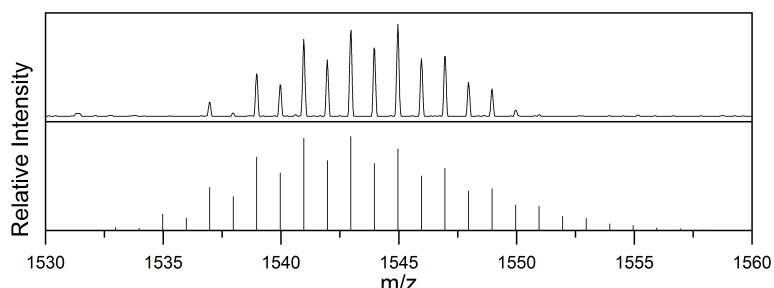
Supplementary Figure 38: Experimental pattern (top) and calculated pattern (bottom) for $[\text{Cu}_4](\text{Cp}^*)(\text{Mes})_2$.



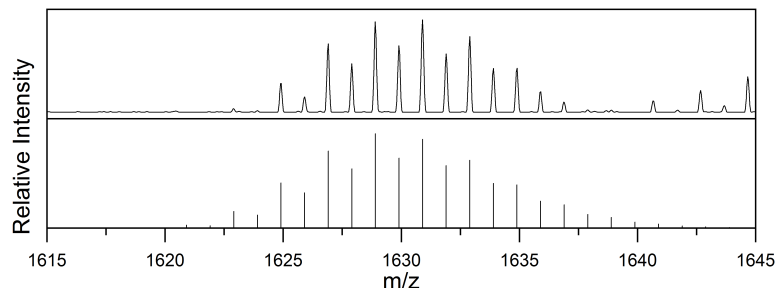
Supplementary Figure 39: Experimental pattern (top) and calculated pattern (bottom) for $[\text{Cu}_4](\text{Cp}^*)_2(\text{Mes})$.



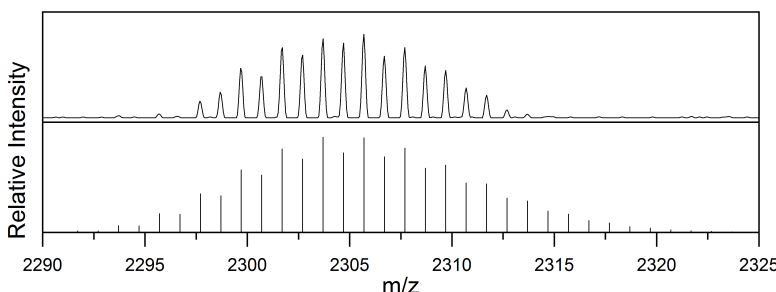
Supplementary Figure 40: Experimental pattern (top) and calculated pattern (bottom) for $[\text{Cu}_3\text{Zn}_4](\text{Cp}^*)_5(\mathbf{B})$.



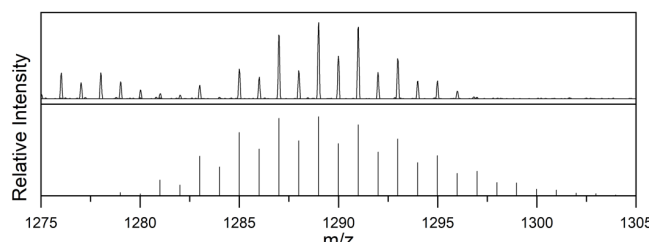
Supplementary Figure 41: Experimental pattern (top) and calculated pattern (bottom) for $[\text{Cu}_5\text{Zn}_5](\text{Cp}^*)_6(\text{CO}_2)_2(\mathbf{X})$.



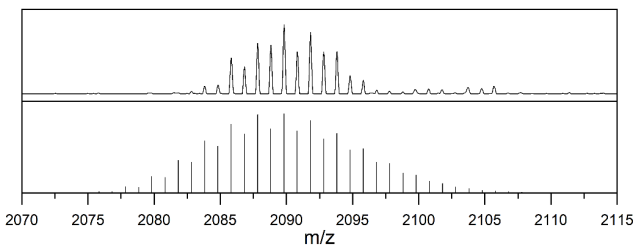
Supplementary Figure 42: Experimental pattern (top) and calculated pattern (bottom) for $[\text{Cu}_8\text{Zn}_3](\text{Cp}^*)_3(\text{Mes})_4(\text{CO}_2)$ (**Y**).



Supplementary Figure 43: Experimental pattern (top) and calculated pattern (bottom) for $[\text{Cu}_{11}\text{Zn}_6](\text{Cp}^*)_8(\text{CO}_2)_2(\text{HCO}_2)$ (**Z**).



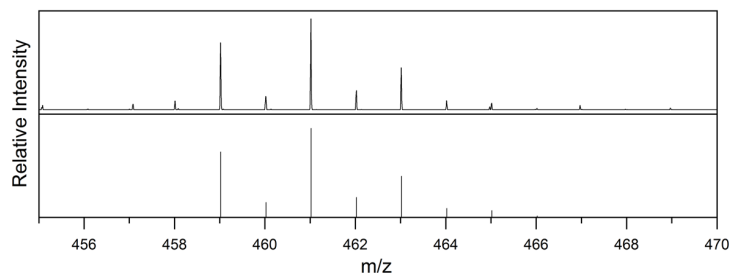
Supplementary Figure 44: Experimental pattern (top) and calculated pattern (bottom) for $[\text{Cu}_3\text{Zn}_6](\text{Cp}^*)_4(\text{Hex})_2\text{H}_2$.



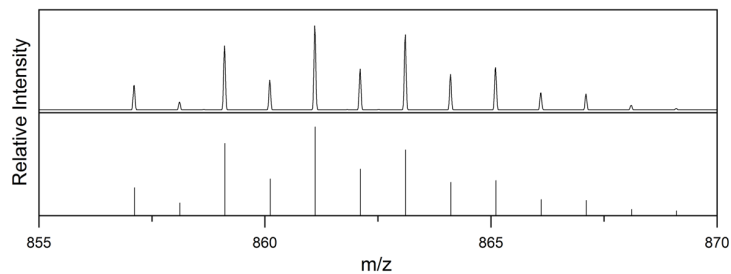
Supplementary Figure 45: Experimental pattern (top) and calculated pattern (bottom) for $[\text{Cu}_9\text{Zn}_7](\text{Cp}^*)_6(\text{Hex})_3\text{H}_3$ (**W**).

Fragments

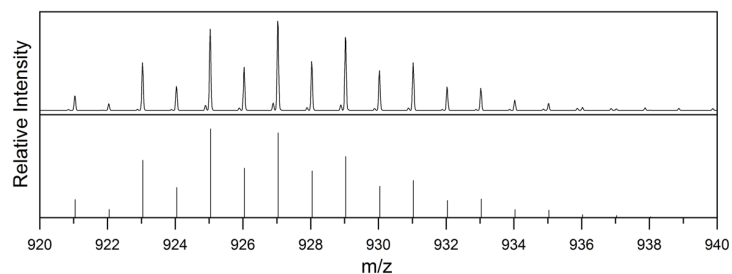
Below we list the data of the identified cluster fragment ions of clusters present in the libraries **{1}**-**{4}**: comparison of experimental and calculated peak patterns.



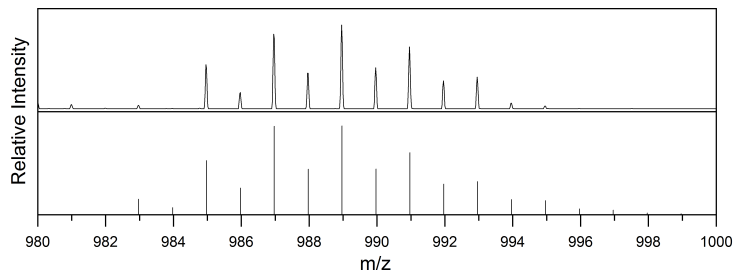
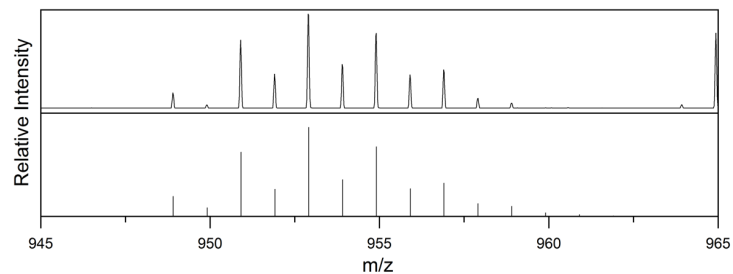
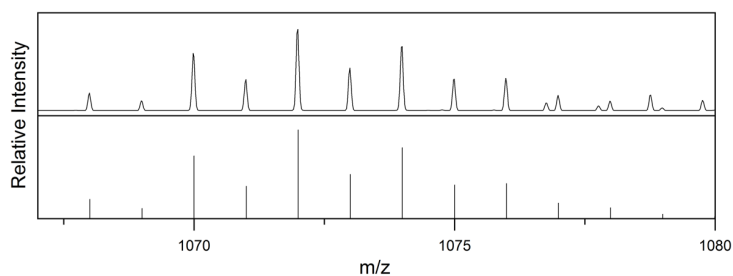
Supplementary Figure 46: Experimental pattern (top) and calculated pattern (bottom) for $[\text{Cu}_3](\text{Cp}^*)_2$.

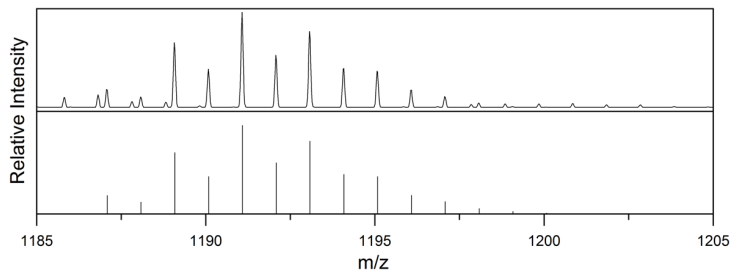


Supplementary Figure 47: Experimental pattern (top) and calculated pattern (bottom) for $[\text{Cu}_3\text{Zn}_2](\text{Cp}^*)_4$.

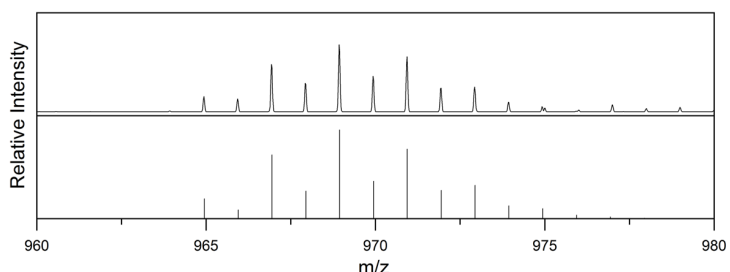


Supplementary Figure 48: Experimental pattern (top) and calculated pattern (bottom) for $[\text{Cu}_3\text{Zn}_3](\text{Cp}^*)_4$.

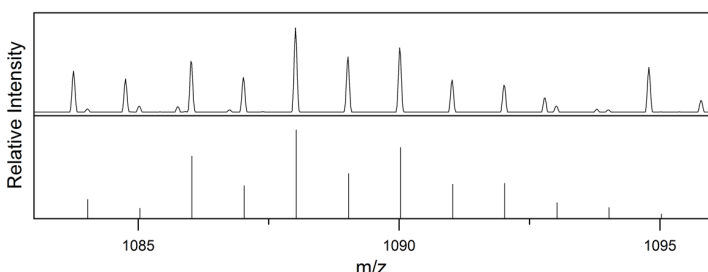
Supplementary Figure 49: Experimental pattern (top) and calculated pattern (bottom) for $[\text{Cu}_5\text{Zn}_2](\text{Cp}^*)_4$.Supplementary Figure 50: Experimental pattern (top) and calculated pattern (bottom) for $[\text{Cu}_7](\text{Cp}^*)_2(\text{Mes})_2$.Supplementary Figure 51: Experimental pattern (top) and calculated pattern (bottom) for $[\text{Cu}_7](\text{Cp}^*)_2(\text{Mes})_3$.



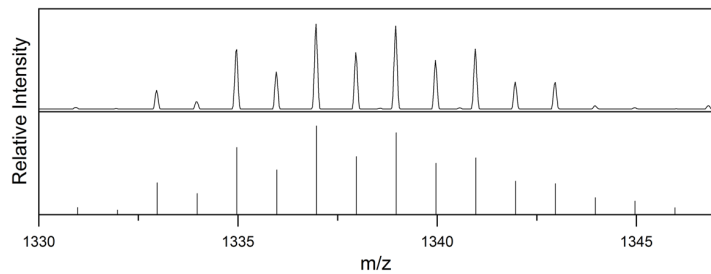
Supplementary Figure 52: Experimental pattern (top) and calculated pattern (bottom) for $[\text{Cu}_7](\text{Cp}^*)_2(\text{Mes})_4$.



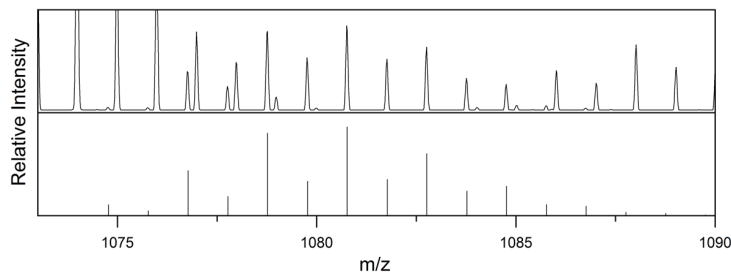
Supplementary Figure 53: Experimental pattern (top) and calculated pattern (bottom) for $[\text{Cu}_7](\text{Cp}^*)_3(\text{Mes})$.



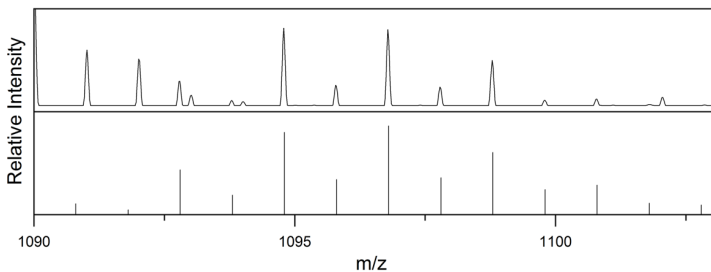
Supplementary Figure 54: Experimental pattern (top) and calculated pattern (bottom) for $[\text{Cu}_7](\text{Cp}^*)_3(\text{Mes})_2$.



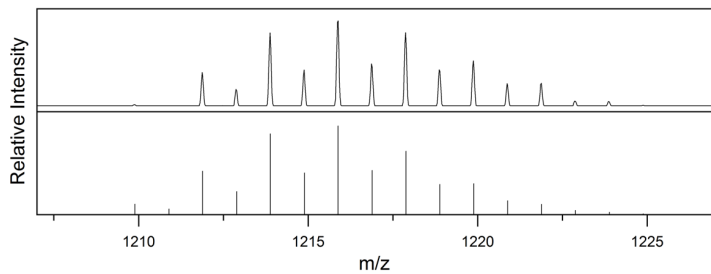
Supplementary Figure 55: Experimental pattern (top) and calculated pattern (bottom) for $[\text{Cu}_7\text{Zn}_2](\text{Cp}^*)_3(\text{Mes})_3$.



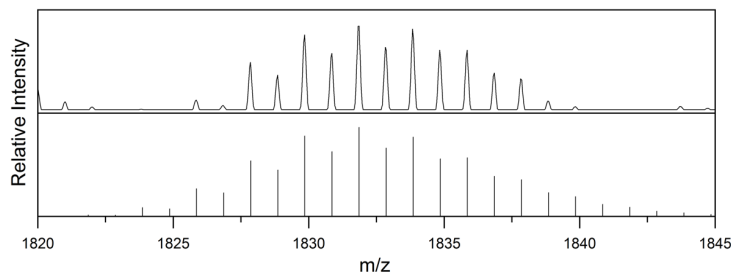
Supplementary Figure 56: Experimental pattern (top) and calculated pattern (bottom) for $[\text{Cu}_9](\text{Cp}^*)_2(\text{Mes})_2$. Low signal intensity and overlap with $[\text{Cu}_7](\text{Cp}^*)_2(\text{Mes})_3$ makes the pattern difficult to distinguish.



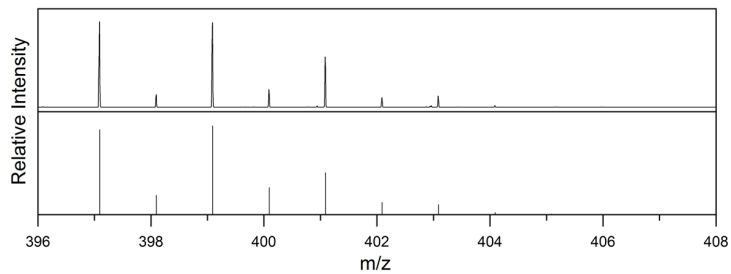
Supplementary Figure 57: Experimental pattern (top) and calculated pattern (bottom) for $[\text{Cu}_9](\text{Cp}^*)_3(\text{Mes})$. Low signal intensity makes the pattern difficult to distinguish.



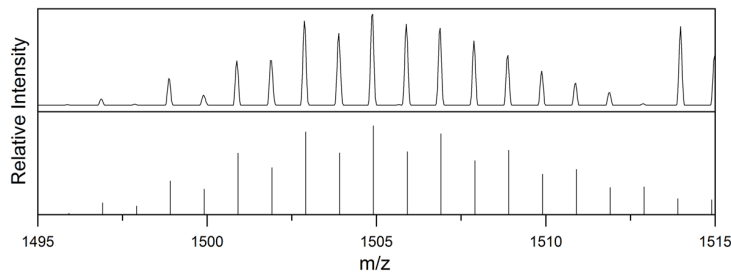
Supplementary Figure 58: Experimental pattern (top) and calculated pattern (bottom) for $[\text{Cu}_9](\text{Cp}^*)_3(\text{Mes})_2$.



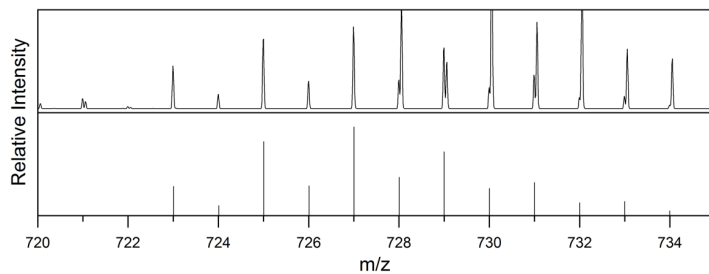
Supplementary Figure 59: Experimental pattern (top) and calculated pattern (bottom) for $[\text{Cu}_{10}\text{Zn}_3](\text{Cp}^*)_3(\text{Mes})_5$.



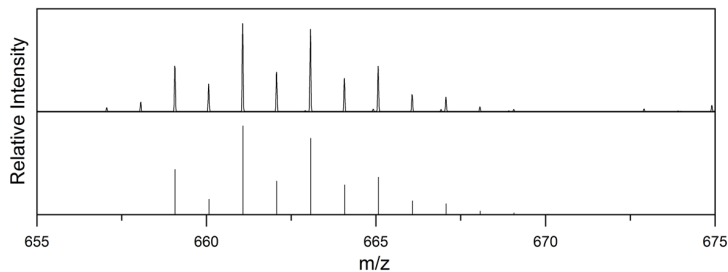
Supplementary Figure 60: Experimental pattern (top) and calculated pattern (bottom) for $[\text{CuZn}](\text{Cp}^*)_2$.



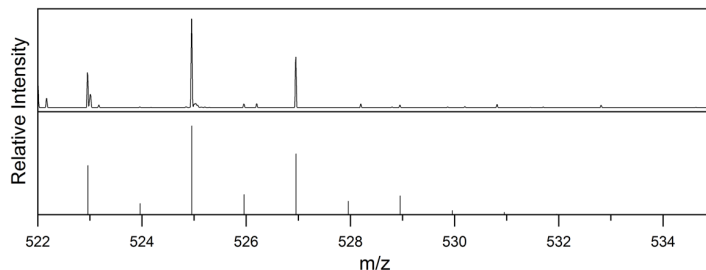
Supplementary Figure 61: Experimental pattern (top) and calculated pattern (bottom) for $[H_3Cu_6Zn_5(Cp^*)_5(Mes)]$ (**D**).



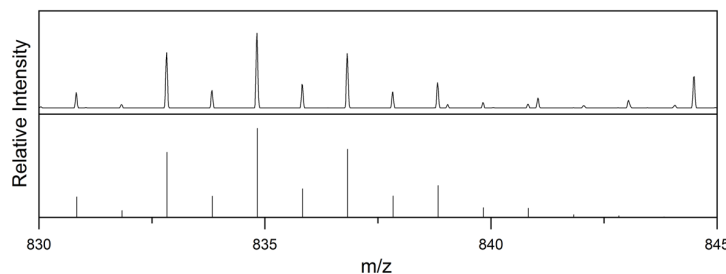
Supplementary Figure 62: Experimental pattern (top) and calculated pattern (bottom) for $[HCu_3Zn_2(Cp^*)_3]$. Low signal intensity and overlap with $[Cu_3Zn](Mes)_4$ makes the pattern difficult to distinguish.



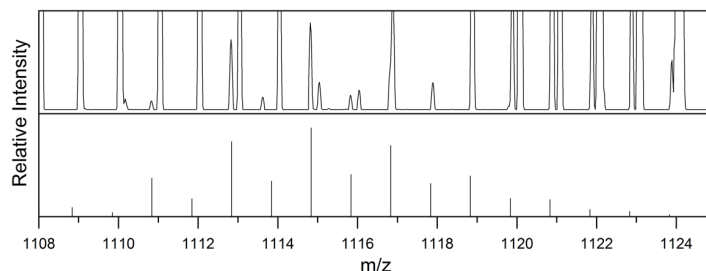
Supplementary Figure 63: Experimental pattern (top) and calculated pattern (bottom) for $[HCu_3Zn](Cp^*)_3$.



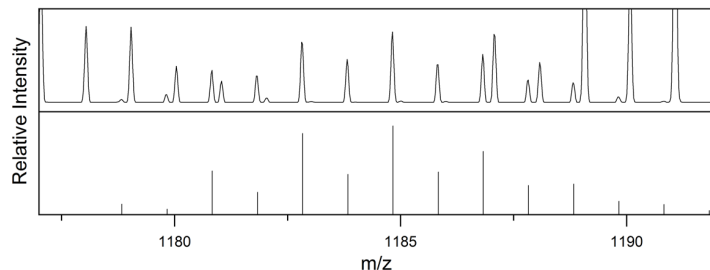
Supplementary Figure 64: Experimental pattern (top) and calculated pattern (bottom) for $[\text{HCu}_4](\text{Cp}^*)_2$. Low signal intensity makes the pattern difficult to distinguish.



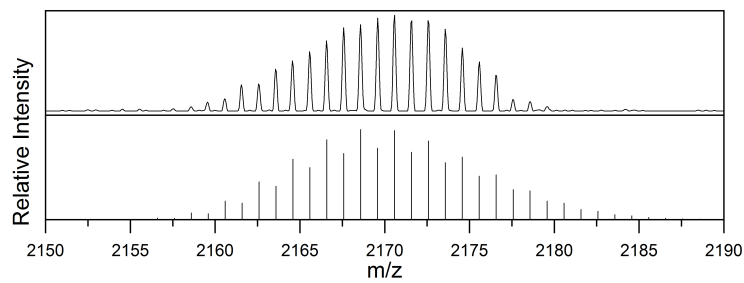
Supplementary Figure 65: Experimental pattern (top) and calculated pattern (bottom) for $[\text{HCu}_7](\text{Cp}^*)_2(\text{Mes})$.



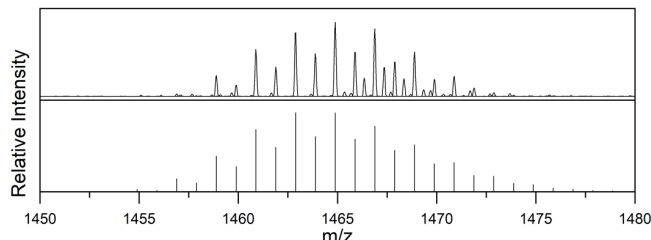
Supplementary Figure 66: Experimental pattern (top) and calculated pattern (bottom) for $[\text{HCu}_8\text{Zn}](\text{Cp}^*)_4$. Low signal intensity and overlap with $[\text{HCu}_8\text{Zn}_2](\text{Cp}^*)_4(\text{Mes})$ makes the pattern difficult to distinguish.



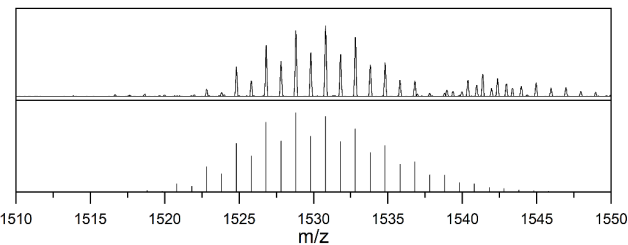
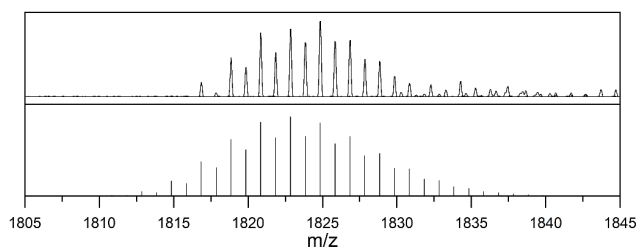
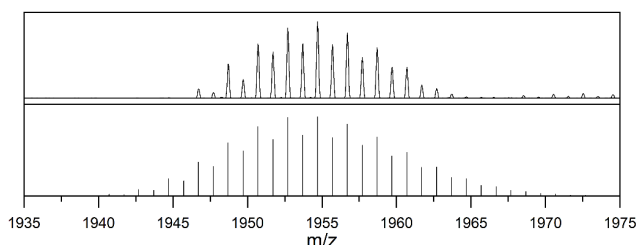
Supplementary Figure 67: Experimental pattern (top) and calculated pattern (bottom) for $[\text{HCu}_9](\text{Cp}^*)(\text{Mes})_4$. Low signal intensity and overlap with $[\text{Cu}_7](\text{Cp}^*)_2(\text{Mes})_4$ makes the pattern difficult to distinguish



Supplementary Figure 68: Experimental pattern (top) and calculated pattern (bottom) for $[\text{Cu}_{11}\text{Zn}_6](\text{Cp}^*)_7(\text{CO}_2)_2(\text{HCO}_2)$.



Supplementary Figure 69: Experimental pattern (top) and calculated pattern (bottom) for $[\text{Cu}_7\text{Zn}_4](\text{Cp}^*)_5(\text{Hex})\text{H}$.

Supplementary Figure 70: Experimental pattern (top) and calculated pattern (bottom) for $[\text{Cu}_7\text{Zn}_5](\text{Cp}^*)_5(\text{Hex})\text{H}$.Supplementary Figure 71: Experimental pattern (top) and calculated pattern (bottom) for $[\text{Cu}_9\text{Zn}_5](\text{Cp}^*)_5(\text{Hex})_3\text{H}_3$.Supplementary Figure 72: Experimental pattern (top) and calculated pattern (bottom) for $[\text{Cu}_9\text{Zn}_7](\text{Cp}^*)_5(\text{Hex})_3\text{H}_3$.

1.1.1.4. Fragmentation Analysis

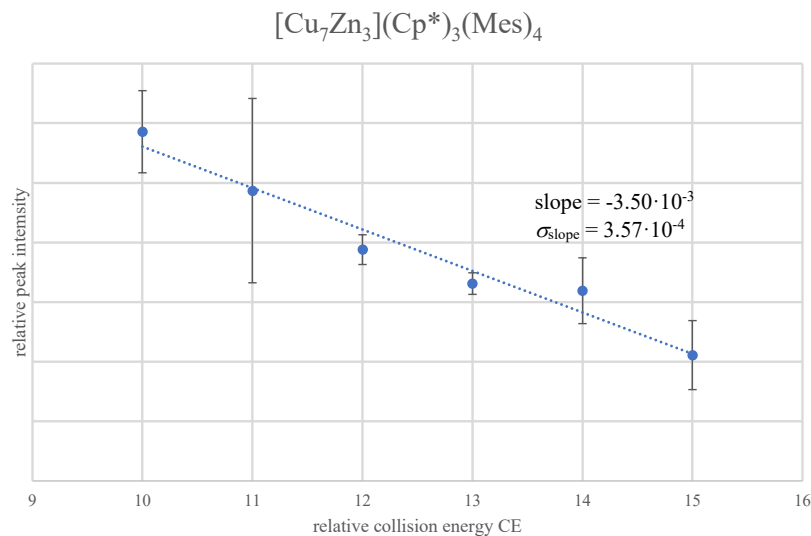
Fragmentation behavior was assessed based on an approach similar to energy dependent ESI-MS¹ and stepped collision energy in orbitrap systems known from peptide fragmentation².

Molecular ion peaks are associated with a continuous decrease of peak intensity for increasing collision energies. Species with such a fragmentation behavior may still be fragment formed during the ionization procedure however (e.g. due to thermal or discharge processes on the emitter). For fragment ions, an increase of peak intensity is expected for increasing collision energies due to their enhanced formation at higher collision energies. In some cases, no clear decision can be made either due to fluxional or continuous behavior of peak intensities at rising collision energies.

Spectra were recorded at normalized collision energies between 10 and 23. Note that 10 is the lowest possible collision energy using the given set-up and that use of normalized collision energies in arbitrary units is common for the given set-up.² For collision energies higher than 23, an overall decrease of peak intensities for all peaks in the spectrum was observed. Obviously, all the sensitive cluster species in the gas phase, be it fragments or molecular ions, are unstable under these experimental conditions.

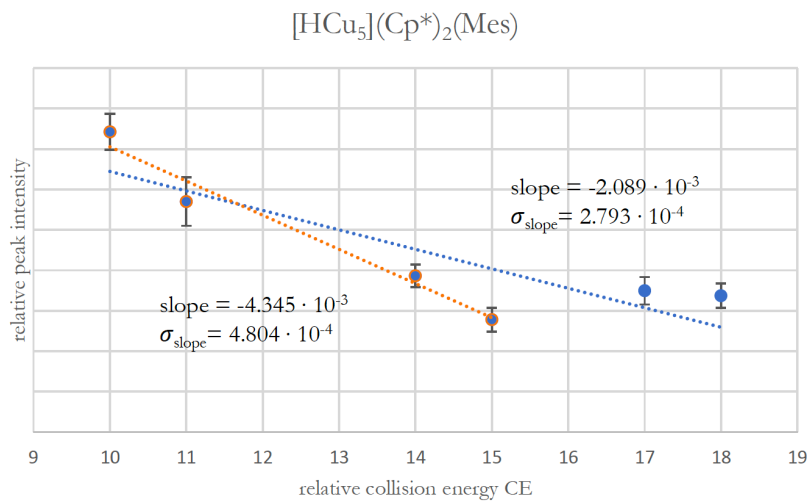
Peak intensities of interest (i.e. for the peaks unambiguously identified by labeling experiments) were determined by computerized integration relative to the overall integral of the spectrum. To determine the influence of statistic fluctuations of peak intensities, which are not correlated to the collision energy applied, each experiment was repeated five times. The average value of peak intensity I , as well as the corresponding coefficient of variation (CV) were calculated for every peak. Statistic fluctuations of peak intensities are supposed to occur during the ionization procedure. The analyte concentration on the LIFDI-emitter, which is hardly controllable during sample supply, chemical/physical modifications on the emitter's surface (e.g. metal deposition, geometric rearrangements) or thermal decomposition of part of the analyte during ionization might be possible reasons for these fluctuations. 60 mA/s was determined as the optimum heating rate with respect to a minimum variation coefficient of peak intensities under identical measurement conditions.

Data was thereafter analyzed as follows: average peak intensities at elevated collision energies were compared with the average peak intensity at standard conditions. Fragments are associated with an increase in peak intensity with respect to the average peak intensity at standard conditions. Contrary, parent ions are associated with a decrease in peak intensity. In detail, the development of peak intensities with rising collision energy was analyzed by linear regression analysis. A positive slope of the regression line is thereafter indicative of a fragment, a negative one indicative of a parent ion. Only in cases, in which the absolute value of the slope was higher than the standard deviation of the slope, the results can be considered as significant.



Supplementary Figure 73: CE vs. I plot of the ion $[\text{Cu}_7\text{Zn}_3](\text{Cp}^*)_3(\text{Mes})_4^+$. The species is clearly assigned as a molecular ion according to the CE vs. I plot. The regression was performed on the statistical means of five independent measurements under identical experimental conditions for each CE value. The error bars represent the standard deviations of these measurements.

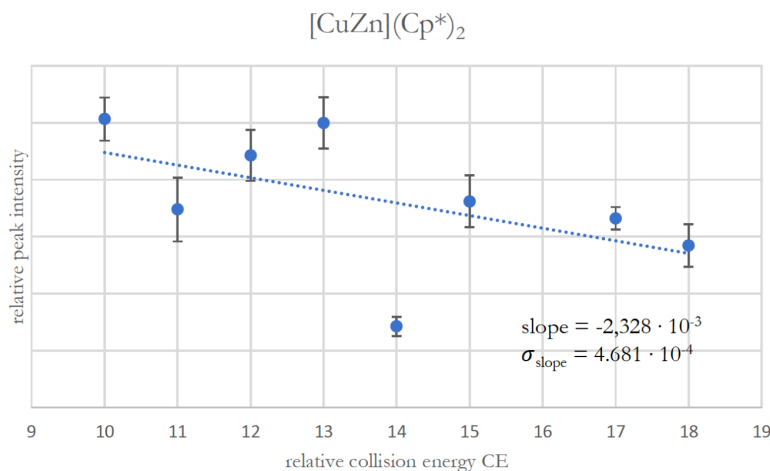
The resulting I vs. CE plots for every ion from the Cu/Zn library are shown below. Obviously and as expected, the onset of fragmentation processes, as well as the extent of fragmentation with respect to collision energy, are different for different ions. Whereas for the molecular ion $[\{\text{Cu}_7\text{Zn}_3](\text{Cp}^*)_3(\text{Mes})_4\}^+$ (Supplementary Figure 73) a continuous decrease in peak intensity is detected, the situation is more complicated for $\{\text{HCu}_5\}(\text{Cp}^*)_2(\text{Mes})\}^+$: deviation from linearity is observed at higher collision energies (17 and 18). The latter effect is explained by significant production of light fragments with $m/z < 200$, escaping the overall integral and distorting therefore the determined relative peak intensities (which are calculated with respect to the overall integral of all peaks in the spectrum). Similar effects were observed for several peaks. Due to the intrinsically different onset of fragmentation and due to the bias in the data at higher collision energies, the linear region in the CE vs. I plots is slightly different for different ions. Noteworthy, the analysis by linear regression does therefore only allow for qualitative analysis (fragment vs. parent ion) but not for a quantitative analysis of fragmentation processes.



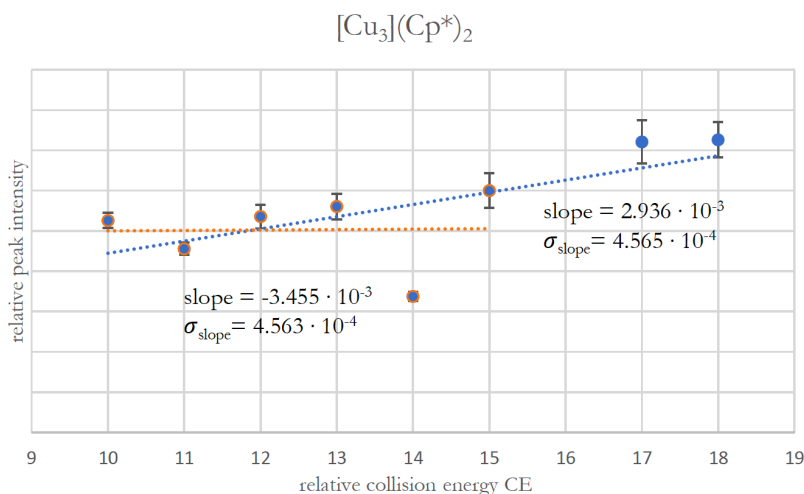
Supplementary Figure 74: CE vs. I plot of the ion $\{\text{HCu}_5\}(\text{Cp}^*)_2(\text{Mes})^+$. The species is clearly assigned as a molecular ion according to the CE vs. I plot. The slight increase in peak intensity at $\text{CE} > 15$ is supposed to be due to the bias in integration. The regression was performed on the statistical means of five independent measurements under identical experimental conditions for each CE value. The error bars represent the standard deviations of these measurements.

The resulting list of all molecular ion species and fragments obtained by careful analysis of all I vs. CE plots are given in Supplementary Tables 2 and 3. For some species, no significant variation in peak intensity was detected. Hence, no decision whether they are fragments or not is possible. They might either be rather robust molecular ions that do not undergo fragmentation or fragment ions prone to further fragmentation reactions. The latter situation would lead to a “steady state” situation, in which formation and decay of the species is in equilibrium and therefore independent on the collision energy applied. With the data and instrumentation at hand it is not possible to experimentally assign a fragment to a specific parent ion, which is due to the lack of an ion trap allowing for isolation of specific ions and study of their decay. However, the fragments can be tentatively assigned to a parent ion according to chemical considerations and according to fragmentation behavior observed for isolated species.

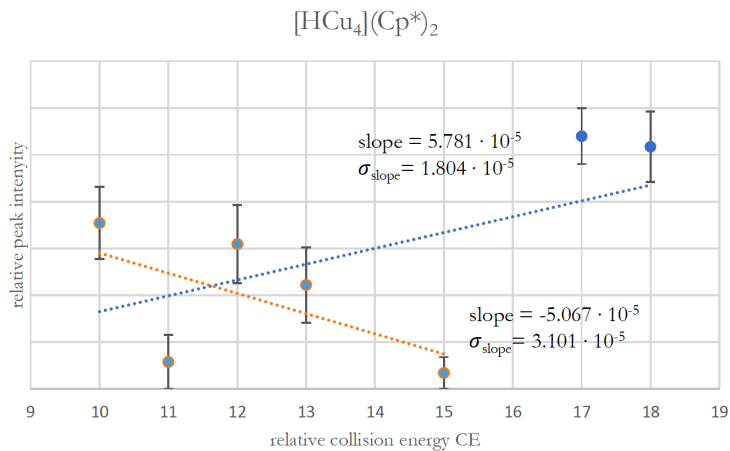
Note: Peak intensities were determined as relative integrals with respect to the overall integral of all peaks in the spectrum. This leads to a bias in integration at $\text{CE} > 15$ due to the enhanced formation of lighter fragments with $m/z < 200$, lying outside the measurement range. Actual peak intensities are therefore expected to be lower than detected at $\text{CE} > 15$. For the ions to which this situation applies, an additional fit is plotted for intensities until $\text{CE} = 15$ (in orange).



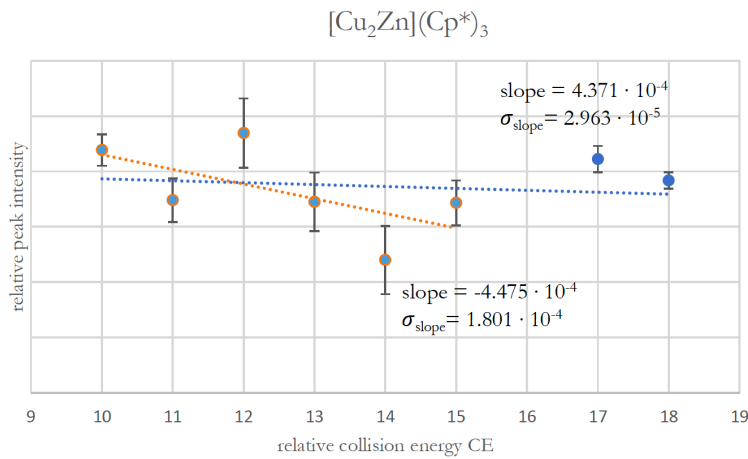
Supplementary Figure 75: CE vs. I plot of the ion $\{\text{[CuZn]}(\text{Cp}^*)_2\}^+$. The ion was identified in the LIFDI-MS spectrum of isolated A. The CE vs. I plot is indicative of a molecular ion. The species is supposed to be a fragment of A, which is formed (thermally) during the ionization process. Consequently, it shows a CE vs. I behavior like a molecular ion. The regression was performed on the statistical means of five independent measurements under identical experimental conditions for each CE value. The error bars represent the standard deviations of these measurements.



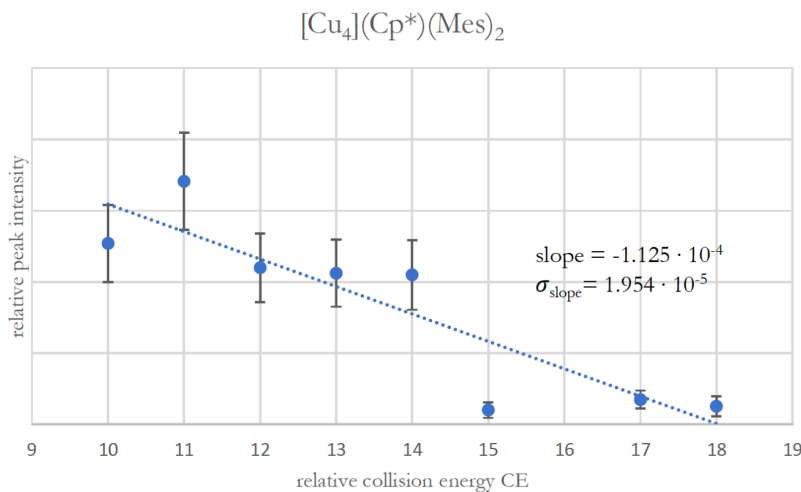
Supplementary Figure 76: CE vs. I plot of the ion $\{\text{[Cu}_3](\text{Cp}^*)_2\}^+$. The CE vs. I plot is indicative of a fragment ion. The species was observed in the LIFDI-MS spectrum of isolated A. The regression was performed on the statistical means of five independent measurements under identical experimental conditions for each CE value. The error bars represent the standard deviations of these measurements.



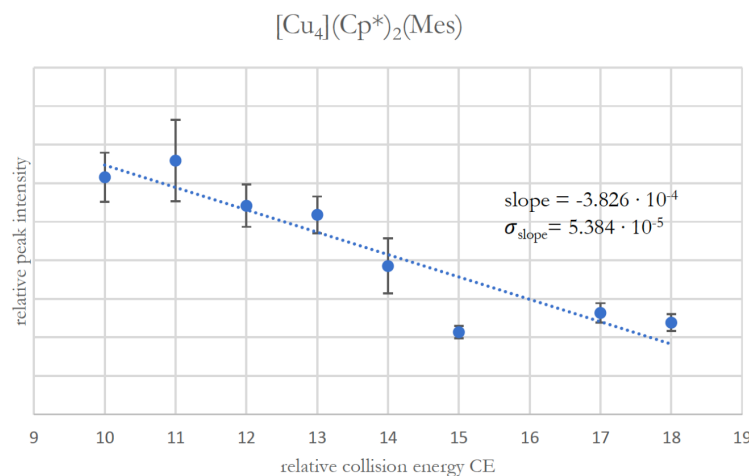
Supplementary Figure 77: CE vs. I plot of the ion $\{\text{HCu}_4\}(\text{Cp}^*)_2^+$. The species was identified in the LIFDI-MS spectrum of isolated A. The CE vs. I plot is indicative of a molecular ion if considering collision energies from 10-15. At higher collision energies, data interpretation is difficult due to the bias in integration. The species is supposed to be a fragment, which is formed (thermally) during the ionization process. Consequently, it shows a CE vs. I behavior like a molecular ion. The regression was performed on the statistical means of five independent measurements under identical experimental conditions for each CE value. The error bars represent the standard deviations of these measurements.



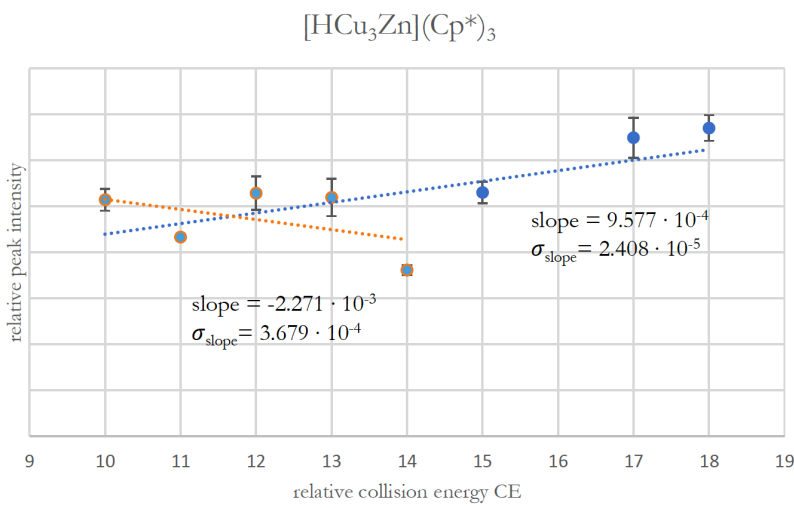
Supplementary Figure 78: CE vs. I plot of the ion $\{[\text{Cu}_2\text{Zn}](\text{Cp}^*)_3\}^+$. A clear assignment of the species is not possible. According to the slope in the CE = 10-15 region, the species might be a molecular ion. The regression was performed on the statistical means of five independent measurements under identical experimental conditions for each CE value. The error bars represent the standard deviations of these measurements.



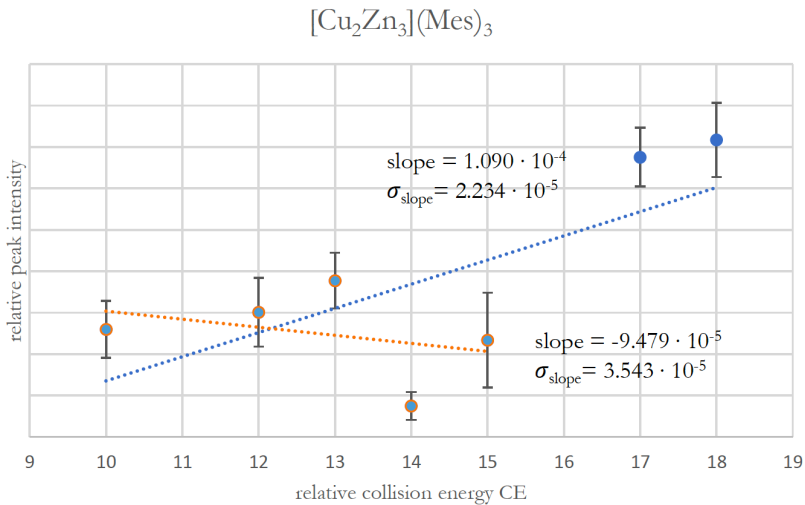
Supplementary Figure 79: CE vs. I plot of the ion $\{\text{[Cu}_4](\text{Cp}^*)(\text{Mes})_2\}^+$. The species is clearly assigned as a molecular ion according to the CE vs. I plot. However, it may also be a fragment formed during ionization. The regression was performed on the statistical means of five independent measurements under identical experimental conditions for each CE value. The error bars represent the standard deviations of these measurements.



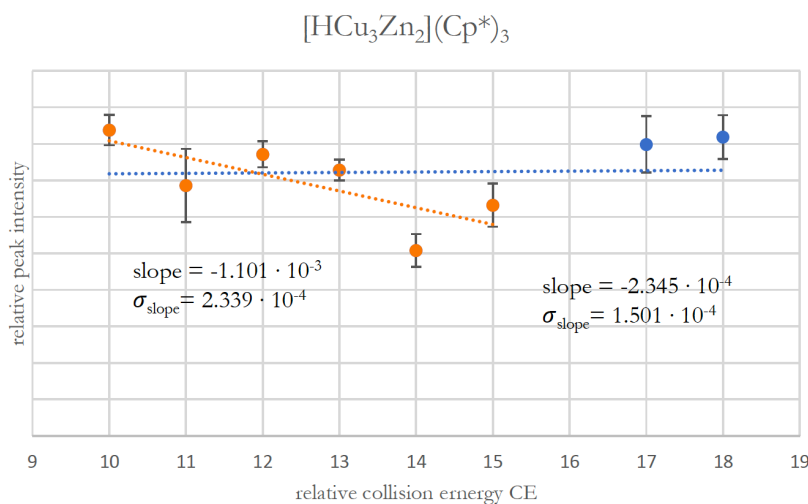
Supplementary Figure 80: CE vs. I plot of the ion $\{\text{[Cu}_4](\text{Cp}^*)_2(\text{Mes})\}^+$. The species is clearly assigned as a molecular ion according to the CE vs. I plot. However, it may also be a fragment formed during ionization. The regression was performed on the statistical means of five independent measurements under identical experimental conditions for each CE value. The error bars represent the standard deviations of these measurements.



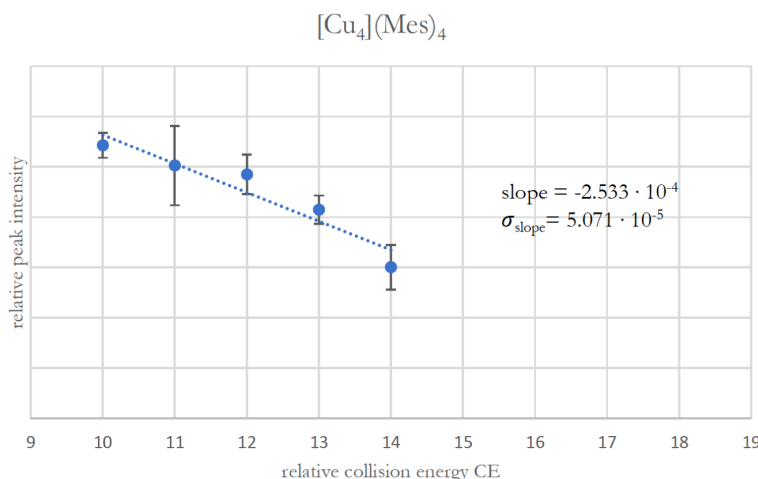
Supplementary Figure 81: CE vs. I plot of the ion $\{\text{HCu}_3\text{Zn}(\text{Cp}^*)\}^+$. A clear assignment of the species is not possible. However according to the CE = 10-14 region, it may be assigned as a molecular ion. The regression was performed on the statistical means of five independent measurements under identical experimental conditions for each CE value. The error bars represent the standard deviations of these measurements.



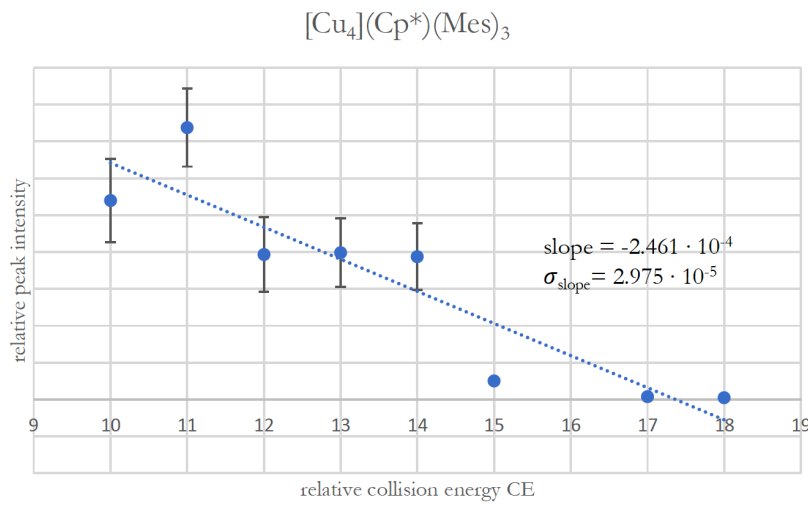
Supplementary Figure 82: CE vs. I plot of the ion $\{[\text{Cu}_2\text{Zn}_3](\text{Mes})_3\}^+$. A clear assignment of the species is not possible. However according to the CE = 10-14 region, it may be assigned as a molecular ion. The regression was performed on the statistical means of five independent measurements under identical experimental conditions for each CE value. The error bars represent the standard deviations of these measurements.



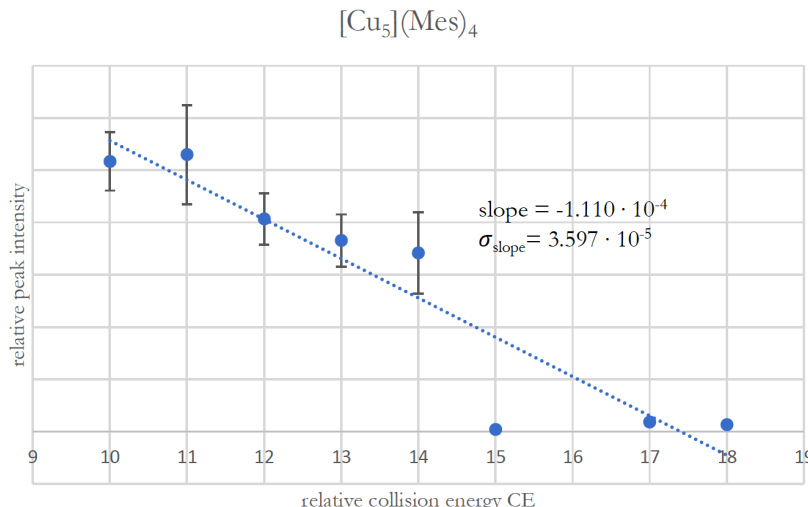
Supplementary Figure 83: CE vs. I plot of the ion $\{\text{HCu}_3\text{Zn}_2(\text{Cp}^*)_3\}^+$. The CE vs. I plot is indicative of a molecular ion if considering collision energies from 10–15. At higher collision energies, data interpretation is difficult due to the bias in integration. The species is supposed to be a fragment of A, which is formed (thermally) during the ionization process. Consequently, it shows a CE vs. I behavior like a molecular ion. The regression was performed on the statistical means of five independent measurements under identical experimental conditions for each CE value. The error bars represent the standard deviations of these measurements.



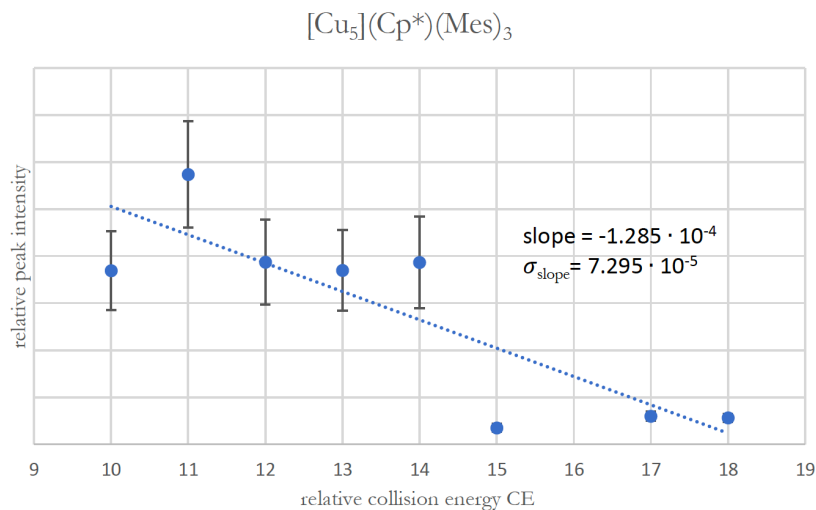
Supplementary Figure 84: CE vs. I plot of the ion $\{[\text{Cu}_4](\text{Mes})_4\}^+$. According to the CE vs. I plot, the species clearly is assigned as molecular ion. However, it is supposed that the species is formed out of $[\text{Cu}_5](\text{Mes})_5$ by loss of one CuMes unit during ionization. The regression was performed on the statistical means of five independent measurements under identical experimental conditions for each CE value. The error bars represent the standard deviations of these measurements.



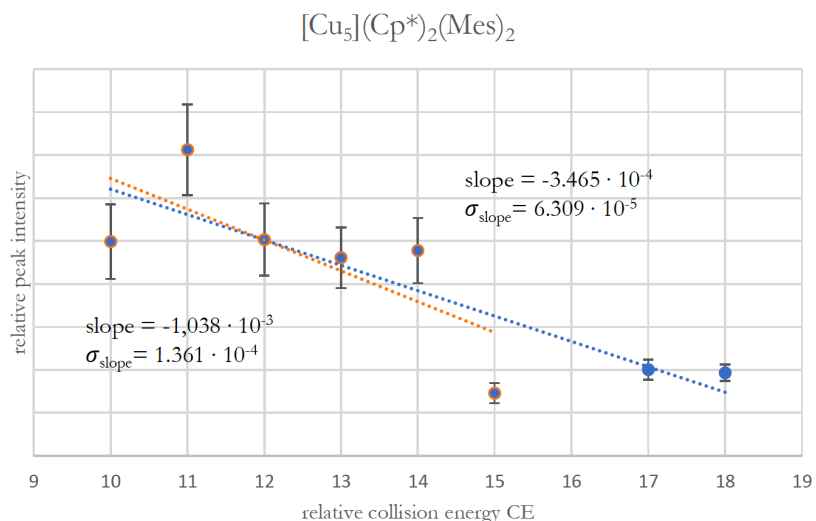
Supplementary Figure 85: CE vs. I plot of the ion $\{\text{[Cu}_4](\text{Cp}^*)(\text{Mes})_3\}^+$. The species is clearly assigned as a molecular ion according to the CE vs. I plot. However, it may also be a fragment formed during ionization. The regression was performed on the statistical means of five independent measurements under identical experimental conditions for each CE value. The error bars represent the standard deviations of these measurements.



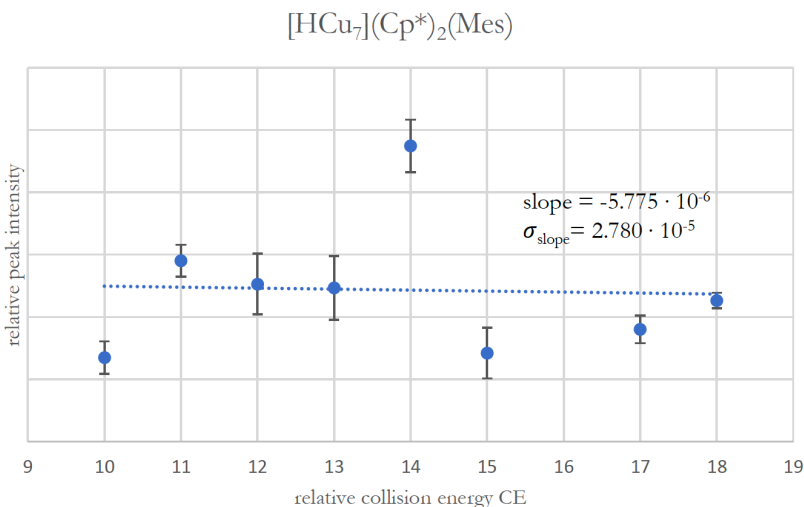
Supplementary Figure 86: CE vs. I plot of the ion $\{\text{[Cu}_5](\text{Mes})_4\}^+$. According to the CE vs. I plot, the species clearly is assigned as molecular ion. However, it is supposed that the species is formed out of $[\text{Cu}_5](\text{Mes})_5$ by loss of one Mes unit during ionization. The regression was performed on the statistical means of five independent measurements under identical experimental conditions for each CE value. The error bars represent the standard deviations of these measurements.



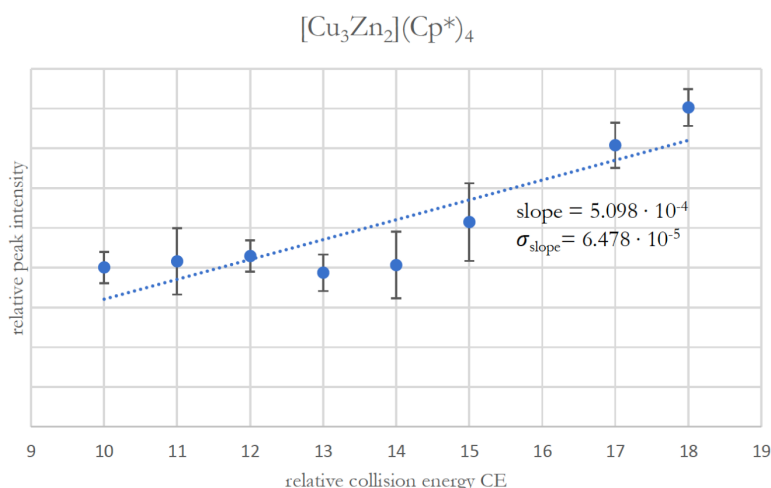
Supplementary Figure 87: CE vs. I plot of the ion $\{\text{[Cu}_5](\text{Cp}^*)(\text{Mes})_3\}^+$. The species is clearly assigned as a molecular ion according to the CE vs. I plot. However, it may also be a fragment formed during ionization. The regression was performed on the statistical means of five independent measurements under identical experimental conditions for each CE value. The error bars represent the standard deviations of these measurements.



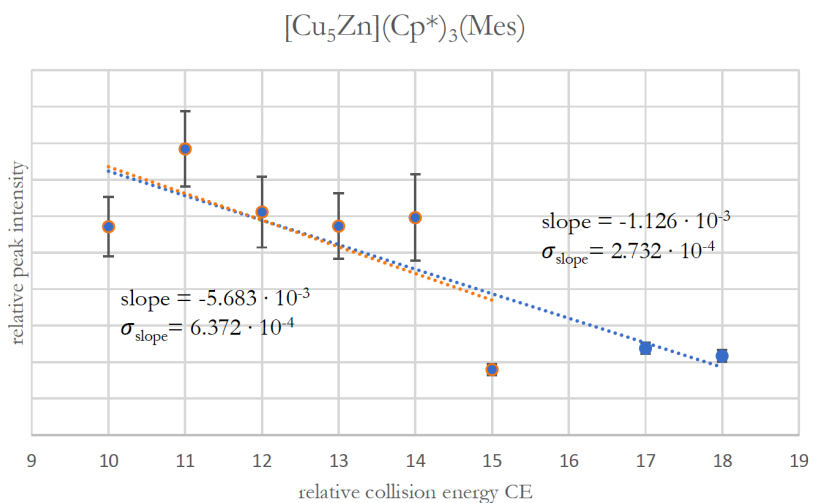
Supplementary Figure 88: CE vs. I plot of the ion $\{\text{[Cu}_5](\text{Cp}^*)_2(\text{Mes})_2\}^+$. The species is clearly assigned as a molecular ion according to the CE vs. I plot. However, it may also be a fragment formed during ionization. The regression was performed on the statistical means of five independent measurements under identical experimental conditions for each CE value. The error bars represent the standard deviations of these measurements.



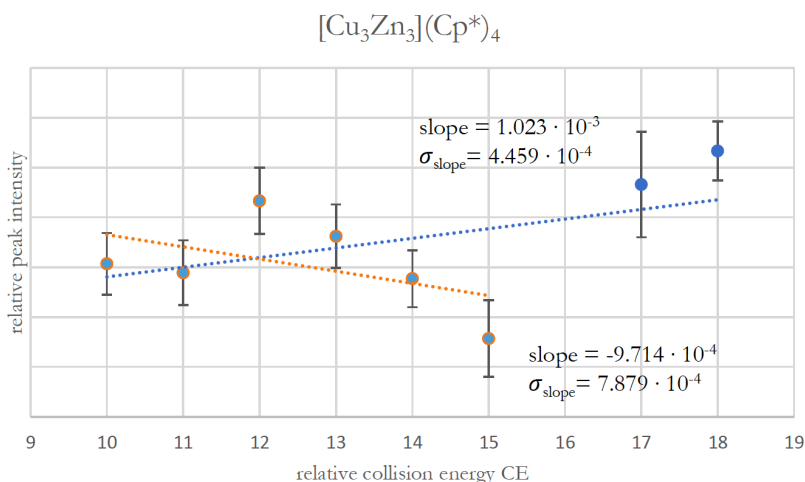
Supplementary Figure 89: CE vs. I plot of the ion $\{\text{HCu}_7](\text{Cp}^*)_2(\text{Mes})\}^+$. A clear assignment of the species is not possible. The regression was performed on the statistical means of five independent measurements under identical experimental conditions for each CE value. The error bars represent the standard deviations of these measurements.



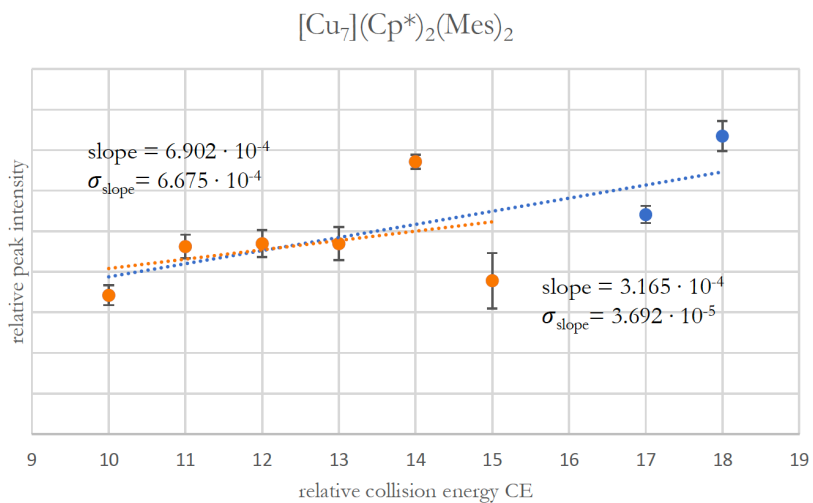
Supplementary Figure 90: CE vs. I plot of the ion $\{[\text{Cu}_3\text{Zn}_2](\text{Cp}^*)_4\}^+$. A clear assignment is difficult to make for this species, as the CE vs. I plot in the CE>15 region has to be regarded with care due to the bias in integration. However, an assignment as a fragment ion seems likely. The regression was performed on the statistical means of five independent measurements under identical experimental conditions for each CE value. The error bars represent the standard deviations of these measurements.



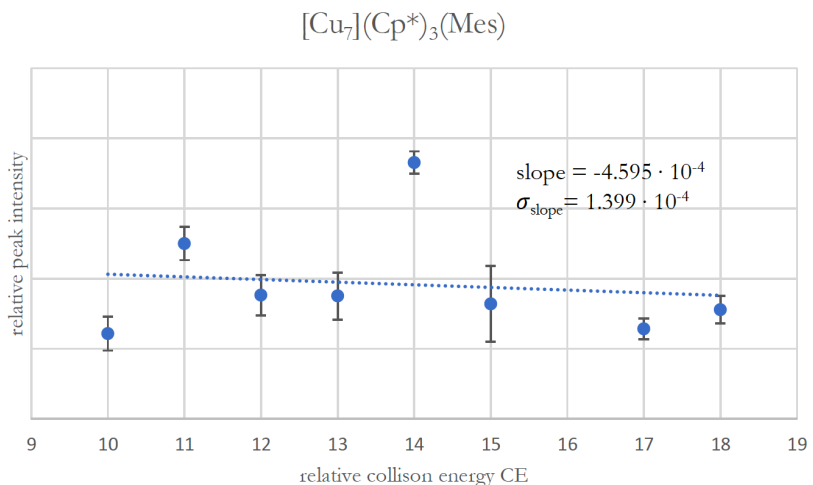
Supplementary Figure 91: CE vs. I plot of the ion $\{\text{[Cu}_5\text{Zn}](\text{Cp}^*)_3(\text{Mes})\}^+$. The species is clearly assigned as a molecular ion according to the CE vs. I plot. However, it may also be a fragment formed during ionization. The regression was performed on the statistical means of five independent measurements under identical experimental conditions for each CE value. The error bars represent the standard deviations of these measurements.



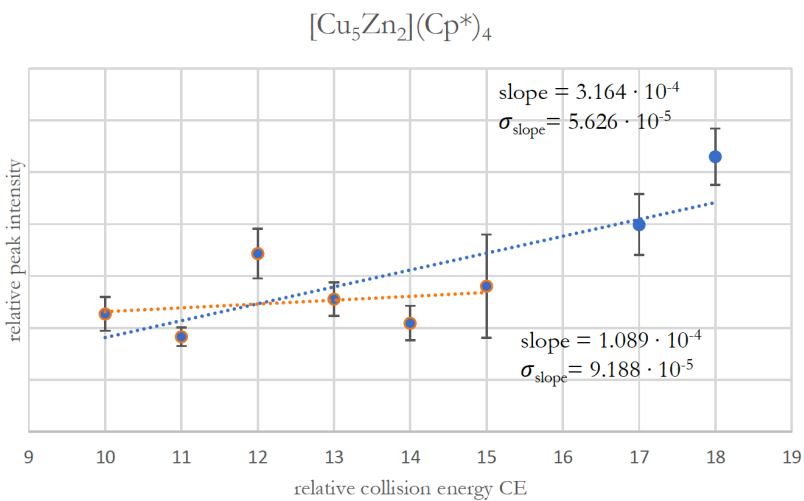
Supplementary Figure 92: CE vs. I plot of the ion $\{\text{[Cu}_3\text{Zn}_3](\text{Cp}^*)_4\}^+$. The data at CE > 15 has to be regarded with care due to bias in data integration. The regression was performed on the statistical means of five independent measurements under identical experimental conditions for each CE value. The error bars represent the standard deviations of these measurements.



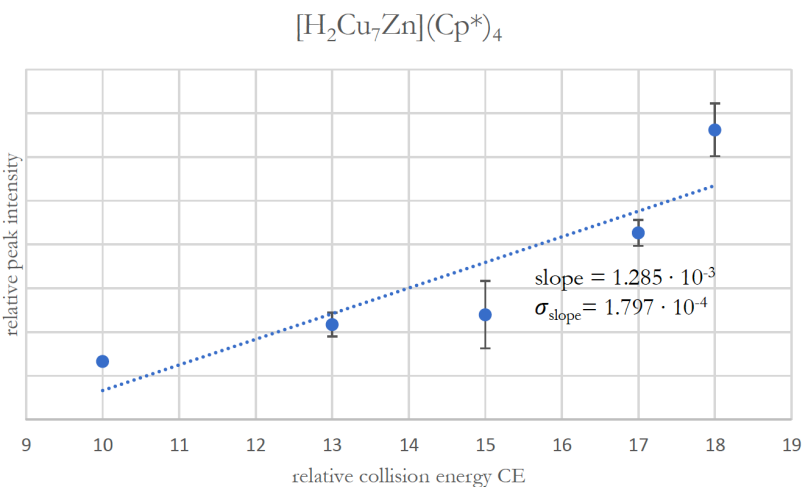
Supplementary Figure 93: CE vs. I plot of the ion $[\text{Cu}_7](\text{Cp}^*)_2(\text{Mes})_2^+$. Due to the bias in integration at $\text{CE} > 15$, a clear assignment is difficult for this species. However, it is likely to be a fragment ion (positive slope also in the $\text{CE} = 10 - 15$ region). The regression was performed on the statistical means of five independent measurements under identical experimental conditions for each CE value. The error bars represent the standard deviations of these measurements.



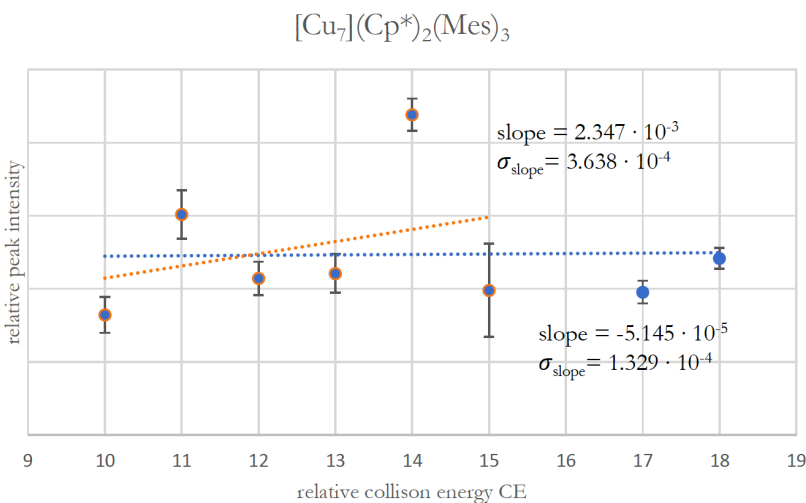
Supplementary Figure 94: CE vs. I plot of the ion $[\text{Cu}_7](\text{Cp}^*)_3(\text{Mes})^+$. Due to the steady-state behavior, a clear assignment is not possible for this species. The regression was performed on the statistical means of five independent measurements under identical experimental conditions for each CE value. The error bars represent the standard deviations of these measurements.



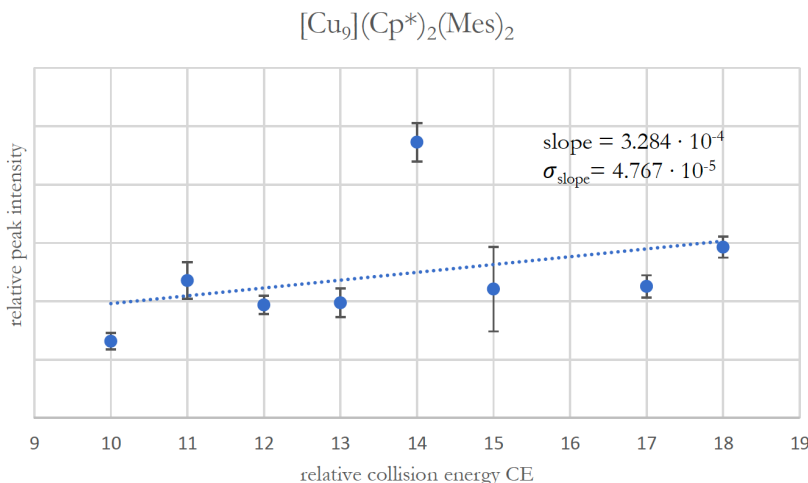
Supplementary Figure 95: CE vs. I plot of the ion $\{\text{Cu}_5\text{Zn}_2](\text{Cp}^*)_4\}^+$. A clear assignment for this species is difficult due to the bias in integration at $\text{CE} > 15$. However, it is supposed to be a fragment ion. The regression was performed on the statistical means of five independent measurements under identical experimental conditions for each CE value. The error bars represent the standard deviations of these measurements.



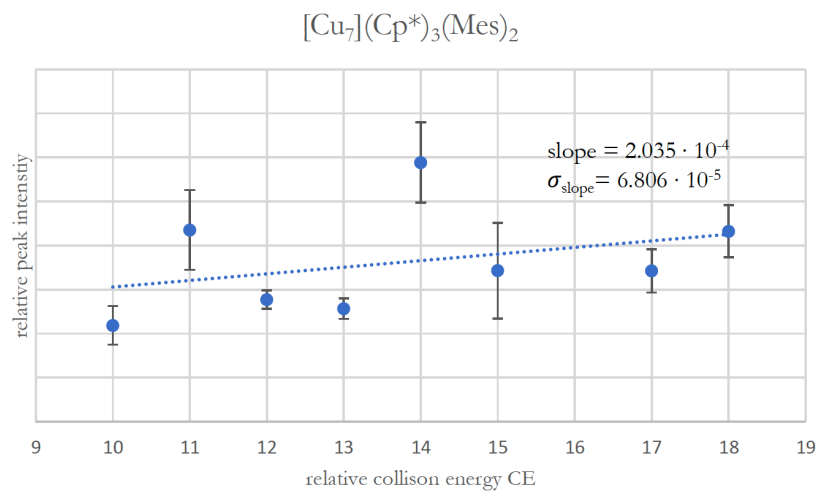
Supplementary Figure 96: CE vs. I plot of the ion $\{\text{H}_2\text{Cu}_7\text{Zn}](\text{Cp}^*)_4\}^+$. The species is identified as a fragment in isolated A. It shows also the behavior of a fragment ion in the CE vs. I plot. The regression was performed on the statistical means of five independent measurements under identical experimental conditions for each CE value. The error bars represent the standard deviations of these measurements.



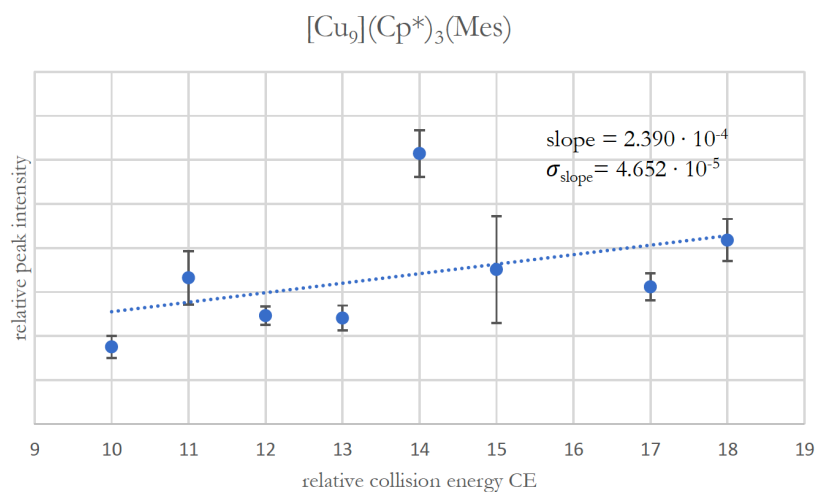
Supplementary Figure 97: CE vs. I plot of the ion $\{\text{[Cu}_7](\text{Cp}^*)_2(\text{Mes})_3\}^+$. A clear assignment is not possible for this species (no clear trend). The regression was performed on the statistical means of five independent measurements under identical experimental conditions for each CE value. The error bars represent the standard deviations of these measurements.



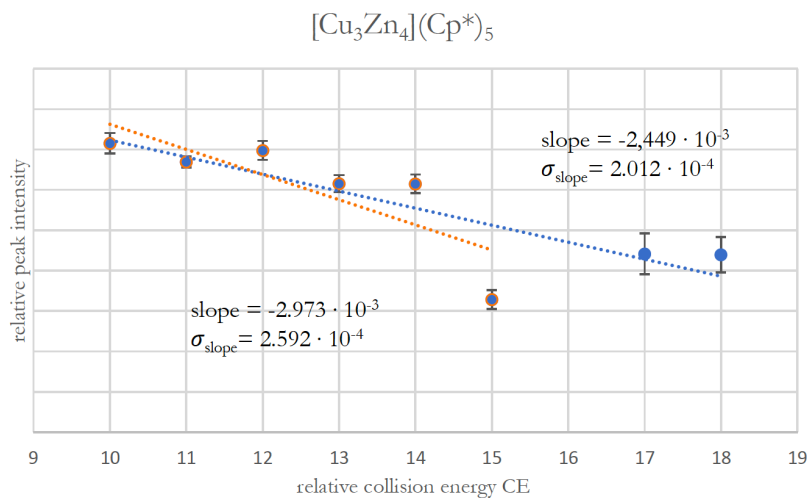
Supplementary Figure 98: CE vs. I plot of the ion $\{\text{[Cu}_9](\text{Cp}^*)_2(\text{Mes})_2\}^+$. A clear assignment is not possible for this species due to the bias in integration at $\text{CE} > 15$. The regression was performed on the statistical means of five independent measurements under identical experimental conditions for each CE value. The error bars represent the standard deviations of these measurements.



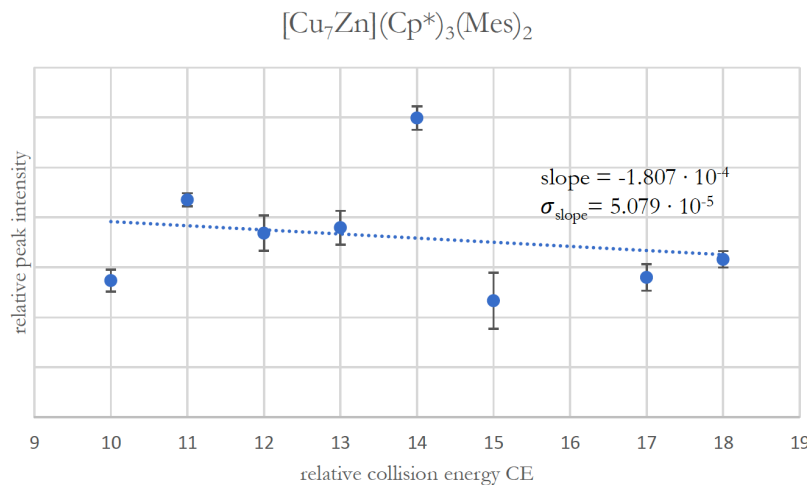
Supplementary Figure 99: CE vs. I plot of the ion $\{\text{Cu}_7](\text{Cp}^*)_3(\text{Mes})_2\}^+$. A clear assignment is not possible for this species due to the bias in integration at $\text{CE} > 15$. The regression was performed on the statistical means of five independent measurements under identical experimental conditions for each CE value. The error bars represent the standard deviations of these measurements.



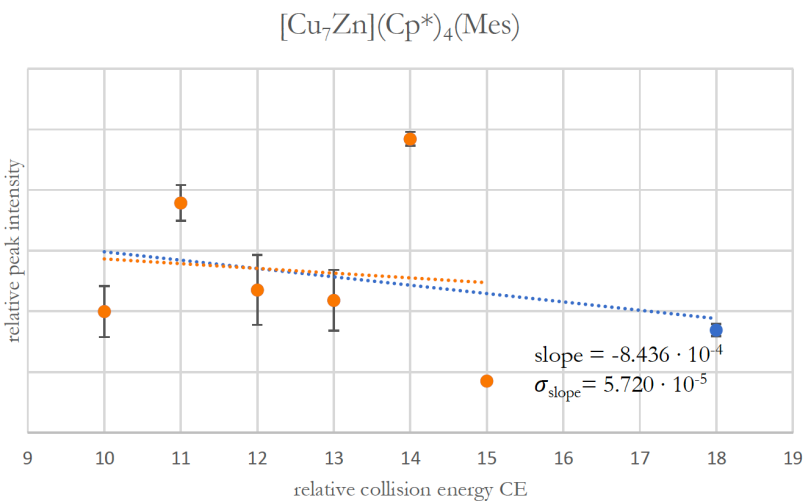
Supplementary Figure 100: CE vs. I plot of the ion $\{[\text{Cu}_9](\text{Cp}^*)_3(\text{Mes})\}^+$. A clear assignment is not possible for this species due to the bias in integration at $\text{CE} > 15$. The regression was performed on the statistical means of five independent measurements under identical experimental conditions for each CE value. The error bars represent the standard deviations of these measurements.



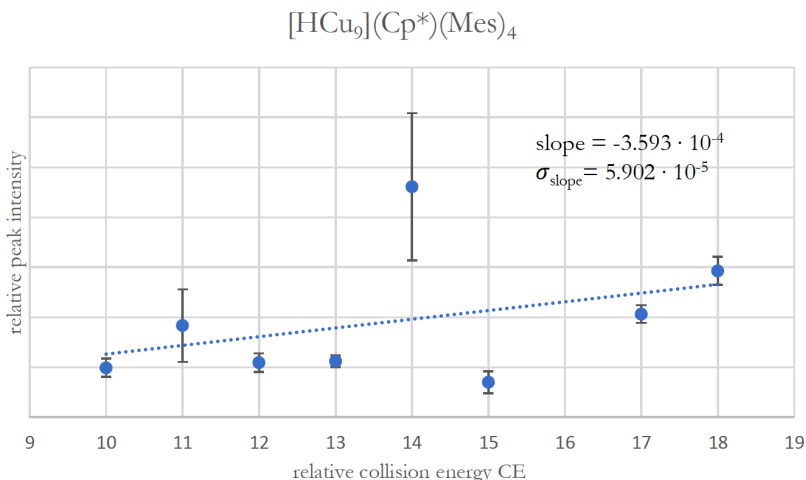
Supplementary Figure 101: CE vs. I plot of the ion $\{\text{Cu}_3\text{Zn}_4\}(\text{Cp}^*)_5^+$ (**B⁺**). The species is clearly assigned as a molecular ion and can also be isolated. The regression was performed on the statistical means of five independent measurements under identical experimental conditions for each CE value. The error bars represent the standard deviations of these measurements.



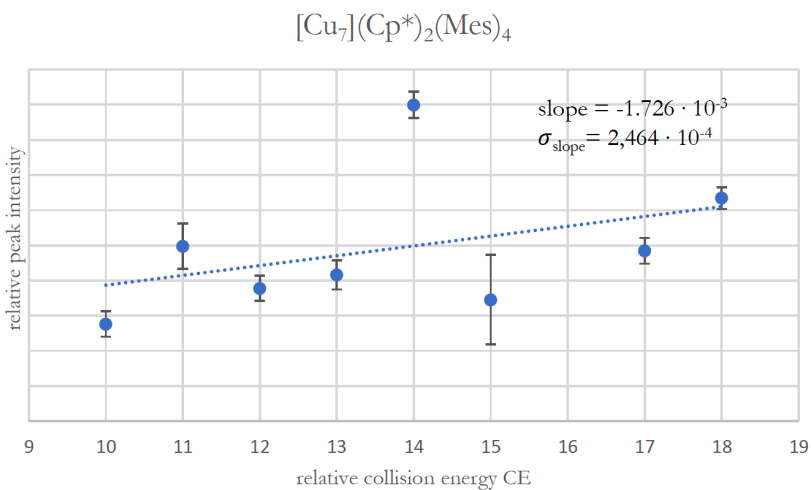
Supplementary Figure 102: CE vs. I plot of the ion $\{\text{Cu}_7\text{Zn}\}(\text{Cp}^*)_3(\text{Mes})_2^+$. A clear assignment is difficult for this species. However, it is likely to be a molecular ion, as the peak intensities at CE > 15 are expected to be even lower than detected. However, it may also be a fragment formed during ionization. The regression was performed on the statistical means of five independent measurements under identical experimental conditions for each CE value. The error bars represent the standard deviations of these measurements.



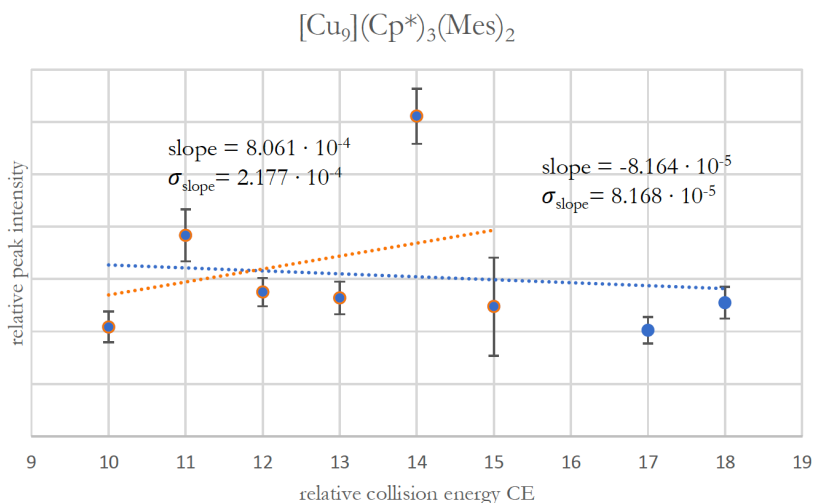
Supplementary Figure 103: CE vs. I plot of the ion $\{\text{[Cu}_7\text{Zn}](\text{Cp}^*)_4(\text{Mes})\}^+$. The species is clearly assigned as a molecular ion according to the CE vs. I plot. However, it may also be a fragment formed during ionization. The regression was performed on the statistical means of five independent measurements under identical experimental conditions for each CE value. The error bars represent the standard deviations of these measurements.



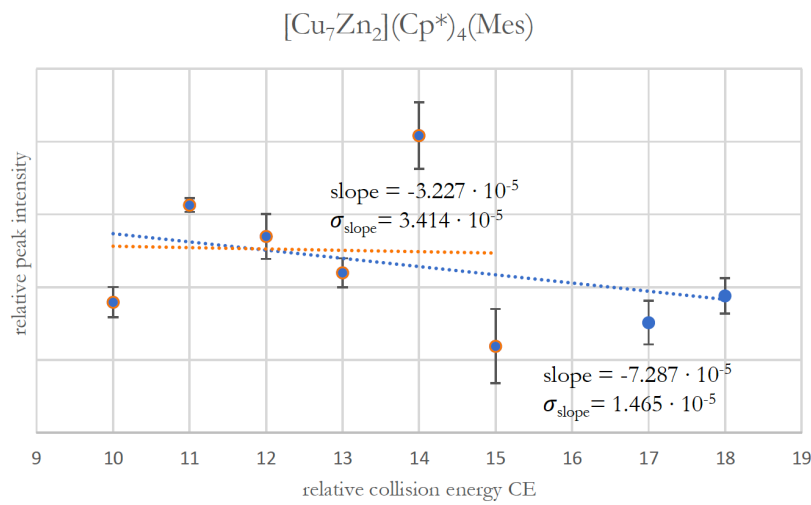
Supplementary Figure 104: CE vs. I plot of the ion $\{\text{[HCu}_9](\text{Cp}^*)(\text{Mes})_4\}^+$. A clear assignment is not possible for this species due to the bias in integration at $\text{CE} > 15$. The regression was performed on the statistical means of five independent measurements under identical experimental conditions for each CE value. The error bars represent the standard deviations of these measurements.



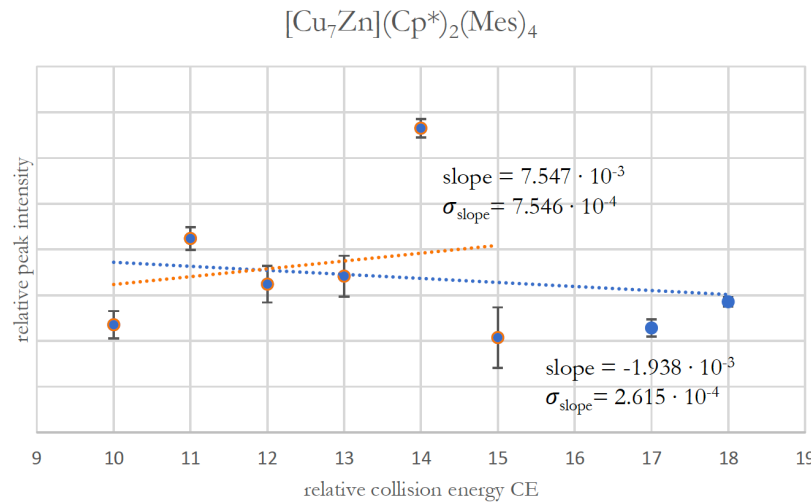
Supplementary Figure 105: CE vs. I plot of the ion $\{\text{[Cu}_7](\text{Cp}^*)_2(\text{Mes})_4\}^+$. A clear assignment is not possible for this species due to the bias in integration at $\text{CE} > 15$. The regression was performed on the statistical means of five independent measurements under identical experimental conditions for each CE value. The error bars represent the standard deviations of these measurements.



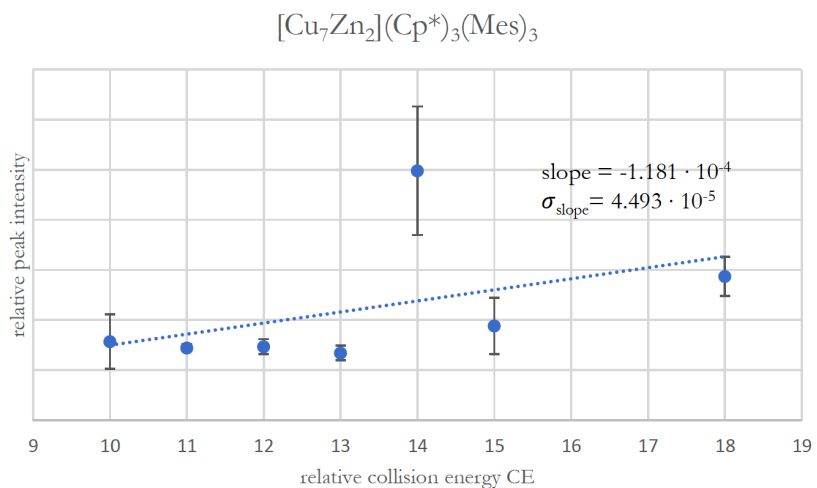
Supplementary Figure 106: CE vs. I plot of the ion $\{\text{[Cu}_9](\text{Cp}^*)_3(\text{Mes})_2\}^+$. A clear assignment is not possible for this species. The regression was performed on the statistical means of five independent measurements under identical experimental conditions for each CE value. The error bars represent the standard deviations of these measurements.



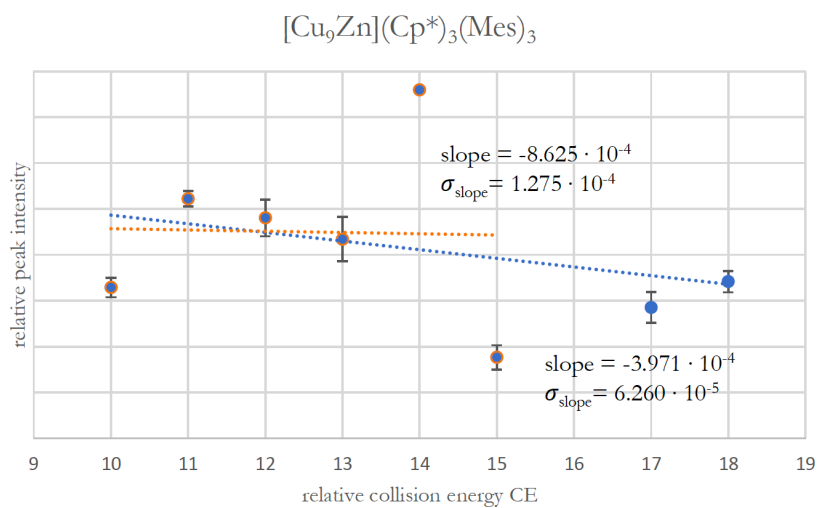
Supplementary Figure 107: CE vs. I plot of the ion $\{\text{[Cu}_7\text{Zn}_2](\text{Cp}^*)_4(\text{Mes})\}^+$. The species can be assigned as molecular ion if considering that a slight increase in peak intensity at $\text{CE} > 15$ is supposed to be caused by the bias in integration. It may however also be a fragment formed during ionization. The regression was performed on the statistical means of five independent measurements under identical experimental conditions for each CE value. The error bars represent the standard deviations of these measurements.



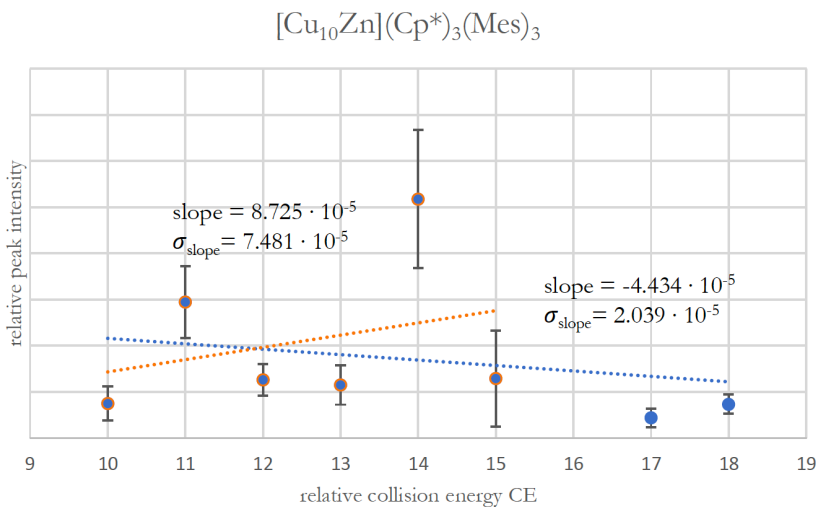
Supplementary Figure 108: CE vs. I plot of the ion $\{\text{[Cu}_7\text{Zn}](\text{Cp}^*)_2(\text{Mes})_4\}^+$. A clear assignment cannot be made for this species, however, it is likely to be molecular ion as the peak intensities at $\text{CE} > 15$ are expected to be even lower than detected. However, it may also be a fragment formed during ionization. The regression was performed on the statistical means of five independent measurements under identical experimental conditions for each CE value. The error bars represent the standard deviations of these measurements.



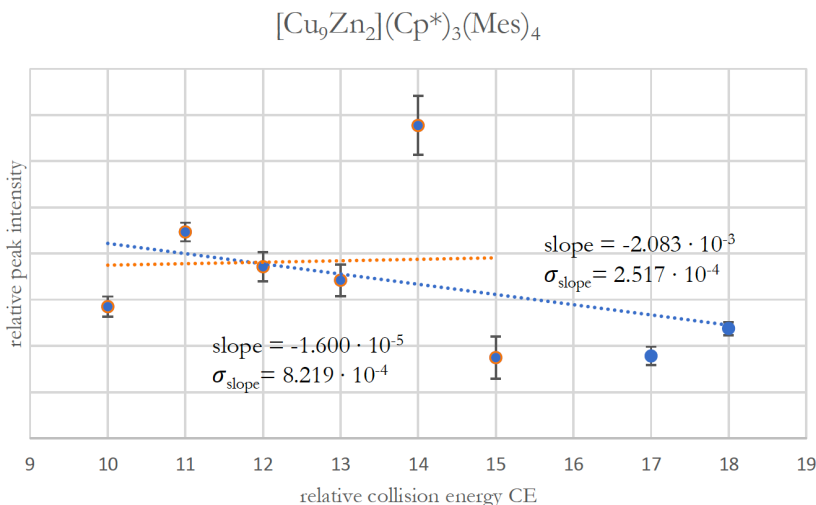
Supplementary Figure 109: CE vs. I plot of the ion $\{\text{[Cu}_7\text{Zn}_2](\text{Cp}^*)_3(\text{Mes})_3\}^+$. A clear assignment cannot be made for this species due to the bias in integration at $\text{CE} > 15$. The regression was performed on the statistical means of five independent measurements under identical experimental conditions for each CE value. The error bars represent the standard deviations of these measurements.



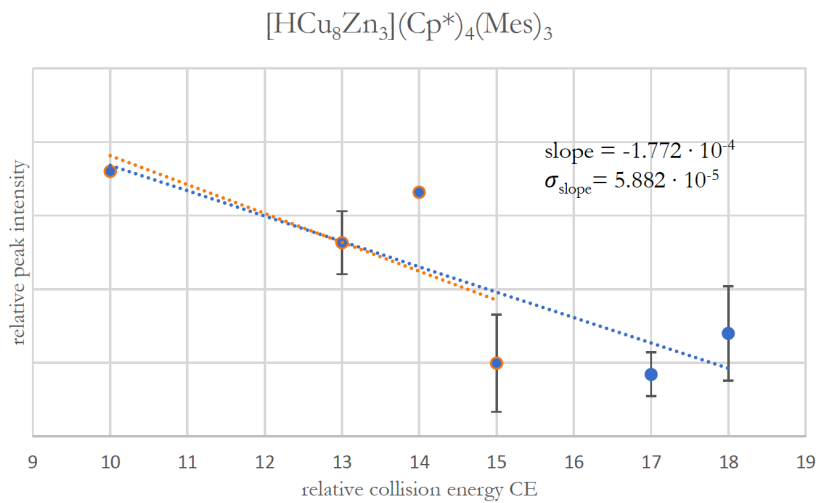
Supplementary Figure 110: CE vs. I plot of the ion $\{\text{[Cu}_9\text{Zn}](\text{Cp}^*)_3(\text{Mes})_3\}^+$. The species can be assigned as molecular ion if considering that a slight increase in peak intensity at $\text{CE} > 15$ is supposed to be caused by the bias in integration. The regression was performed on the statistical means of five independent measurements under identical experimental conditions for each CE value. The error bars represent the standard deviations of these measurements.



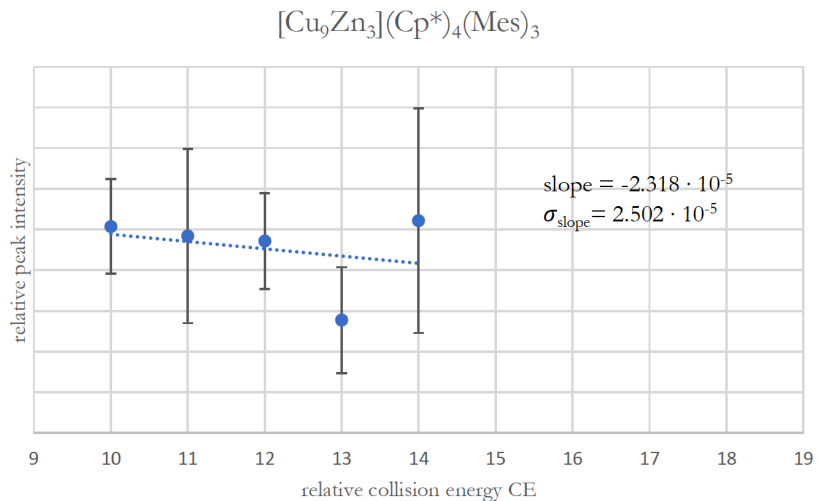
Supplementary Figure 111: CE vs. I plot of the ion $\{\text{[Cu}_{10}\text{Zn}](\text{Cp}^*)_3(\text{Mes})_3\}^+$. The species is assigned as molecular ion. Due to the bias in integration, the intensity values at CE = 17 and 18 are supposed to be actually even lower than detected. The regression was performed on the statistical means of five independent measurements under identical experimental conditions for each CE value. The error bars represent the standard deviations of these measurements.



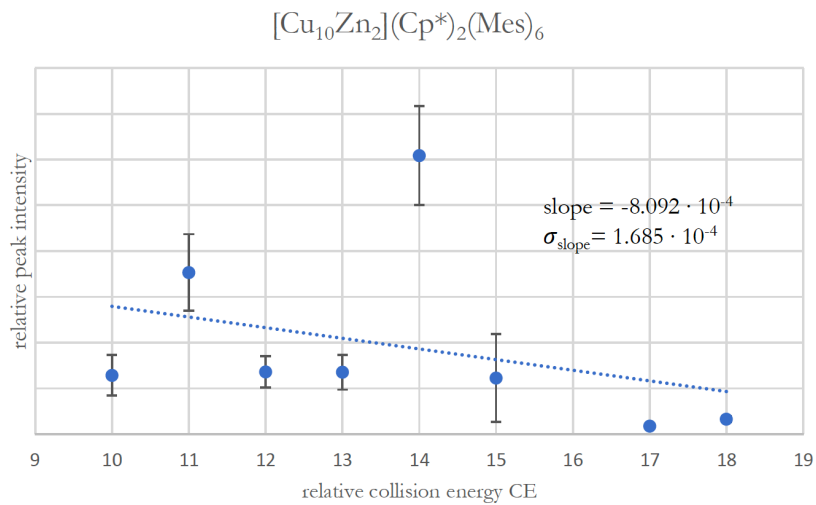
Supplementary Figure 112: CE vs. I plot of the ion $\{\text{[Cu}_9\text{Zn}_2](\text{Cp}^*)_3(\text{Mes})_4\}^+$. The species is assigned as molecular ion. Due to the bias in integration, the intensity values at CE = 17 and 18 are supposed to be even lower than detected. The regression was performed on the statistical means of five independent measurements under identical experimental conditions for each CE value. The error bars represent the standard deviations of these measurements.



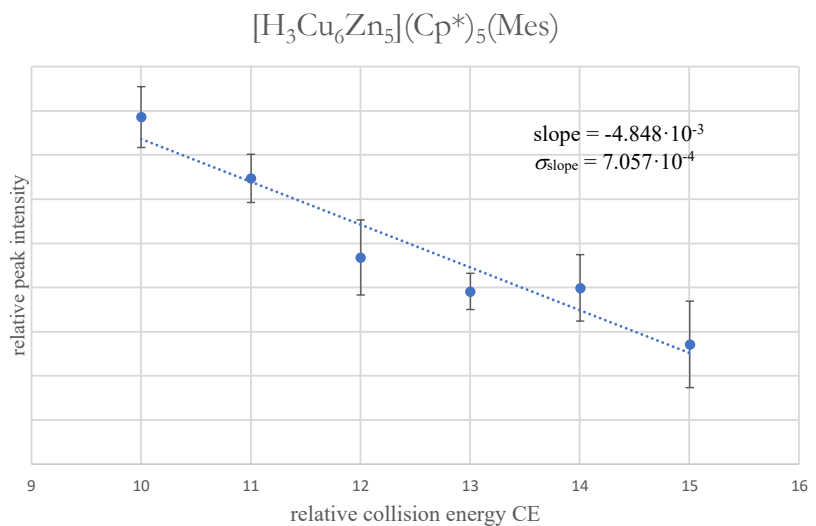
Supplementary Figure 113: CE vs. I plot of the ion $\{\text{HCu}_8\text{Zn}_3](\text{Cp}^*)_4(\text{Mes})_3\}^+(\text{E}^+)$. The species is assigned as molecular ion. Due to the bias in integration, the intensity values at CE = 17 and 18 are supposed to be actually even lower than detected. The regression was performed on the statistical means of five independent measurements under identical experimental conditions for each CE value. The error bars represent the standard deviations of these measurements.



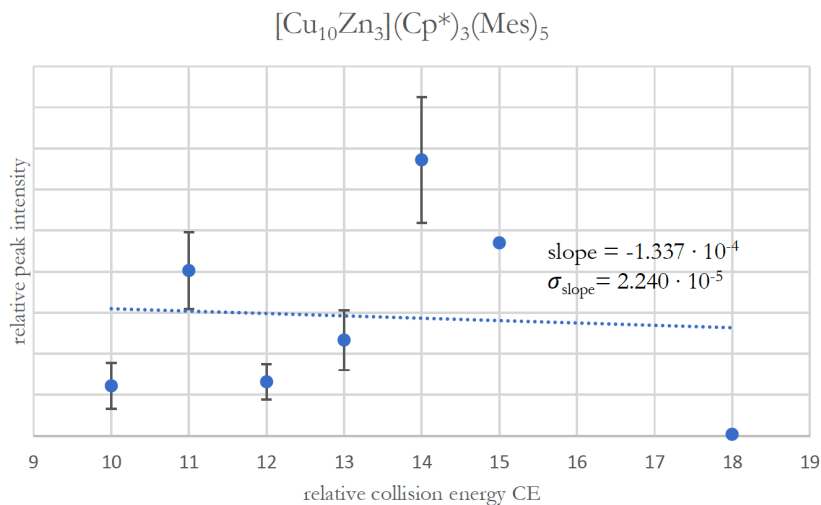
Supplementary Figure 114: CE vs. I plot of the ion $\{[\text{Cu}_9\text{Zn}_3](\text{Cp}^*)_4(\text{Mes})_3\}^+$. The species is assigned as a molecular ion. The regression was performed on the statistical means of five independent measurements under identical experimental conditions for each CE value. The error bars represent the standard deviations of these measurements.



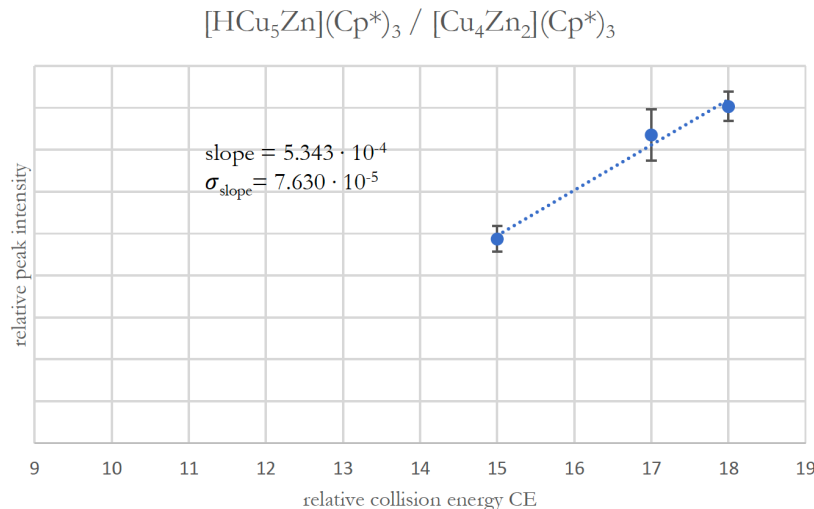
Supplementary Figure 115: CE vs. I plot of the ion $\{\text{[Cu}_{10}\text{Zn}_2](\text{Cp}^*)_2(\text{Mes})_6\}^+$. The species is assigned as molecular ion and can also be isolated. The regression was performed on the statistical means of five independent measurements under identical experimental conditions for each CE value. The error bars represent the standard deviations of these measurements.



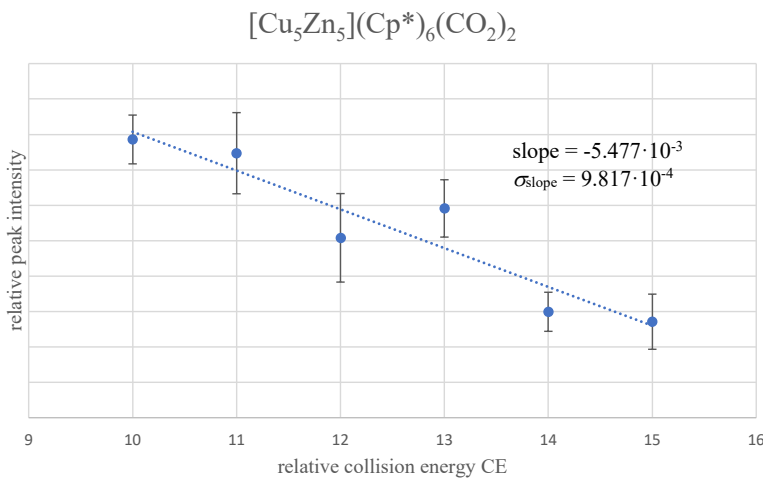
Supplementary Figure 116: CE vs. I plot of the ion $\{\text{[H}_3\text{Cu}_6\text{Zn}_5](\text{Cp}^*)_5(\text{Mes})\}^+(\text{D}^+)$. The species is assigned as molecular ion. The regression was performed on the statistical means of five independent measurements under identical experimental conditions for each CE value. The error bars represent the standard deviations of these measurements.



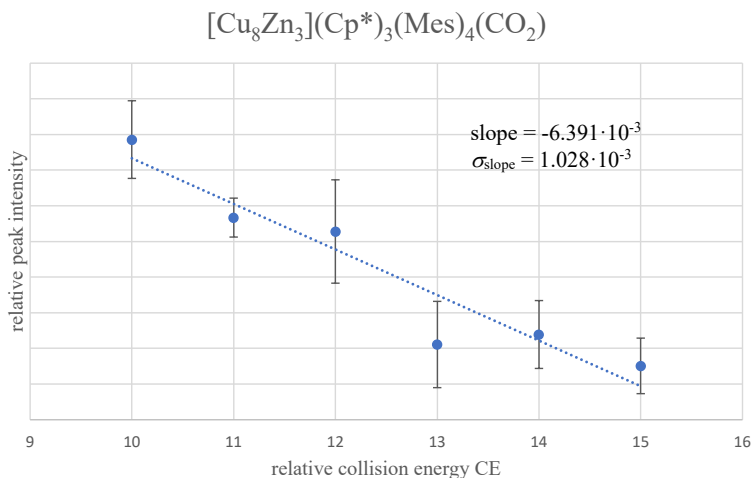
Supplementary Figure 117: CE vs. I plot of the ion $\{\text{[Cu}_{10}\text{Zn}_3](\text{Cp}^*)_3(\text{Mes})_5\}^+$. A clear assignment cannot be made for this species. The regression was performed on the statistical means of five independent measurements under identical experimental conditions for each CE value. The error bars represent the standard deviations of these measurements.



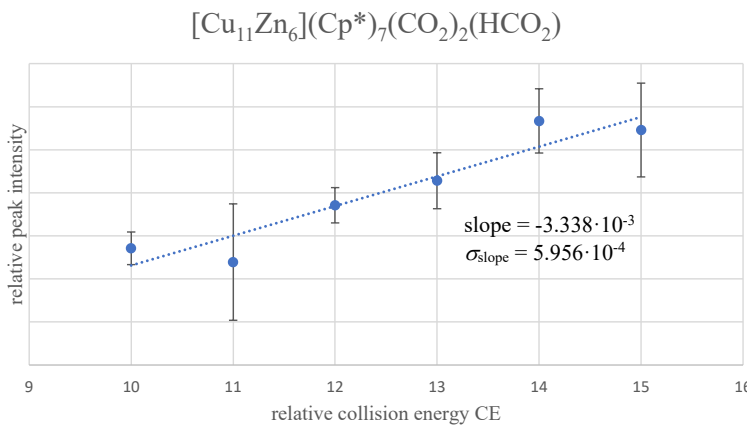
Supplementary Figure 118: CE vs. I plot of the ion $\{\text{[HCu}_5\text{Zn}](\text{Cp}^*)_3\}^+$ and $[\text{Cu}_4\text{Zn}_2](\text{Cp}^*)_3$. Both ions were identified by labeling experiments with ^{68}Zn . In the unlabeled spectra however, their peaks are overlapping. Both ions can be assigned as fragments according to the CE vs. I plots. The regression was performed on the statistical means of five independent measurements under identical experimental conditions for each CE value. The error bars represent the standard deviations of these measurements.



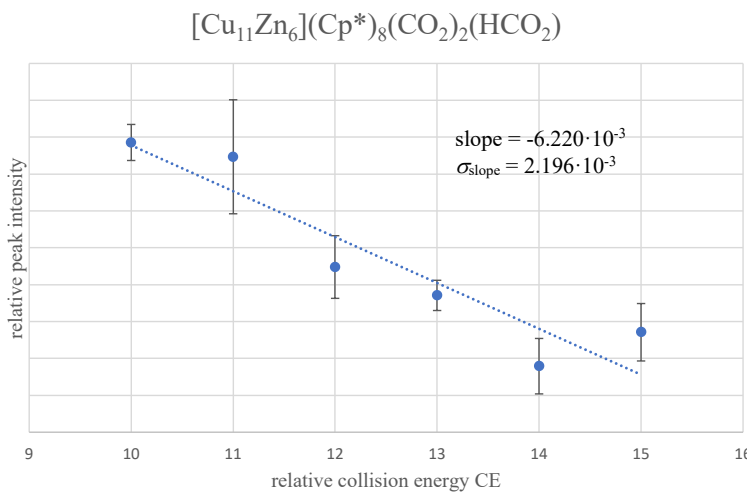
Supplementary Figure 119: CE vs. I plot of the ion $\{\text{[Cu}_5\text{Zn}_5](\text{Cp}^*)_6(\text{CO}_2)_2\}^+ (\mathbf{X}^+)$. The species is assigned as molecular ion. The regression was performed on the statistical means of five independent measurements under identical experimental conditions for each CE value. The error bars represent the standard deviations of these measurements.



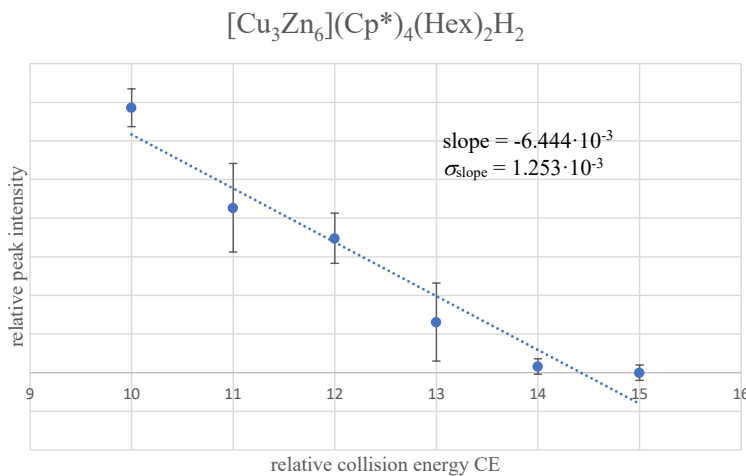
Supplementary Figure 120: CE vs. I plot of the ion $\{\text{[Cu}_8\text{Zn}_3](\text{Cp}^*)_3(\text{Mes})_4(\text{CO}_2)\}^+ (\mathbf{Y}^+)$. The species is assigned as molecular ion. The regression was performed on the statistical means of five independent measurements under identical experimental conditions for each CE value. The error bars represent the standard deviations of these measurements.



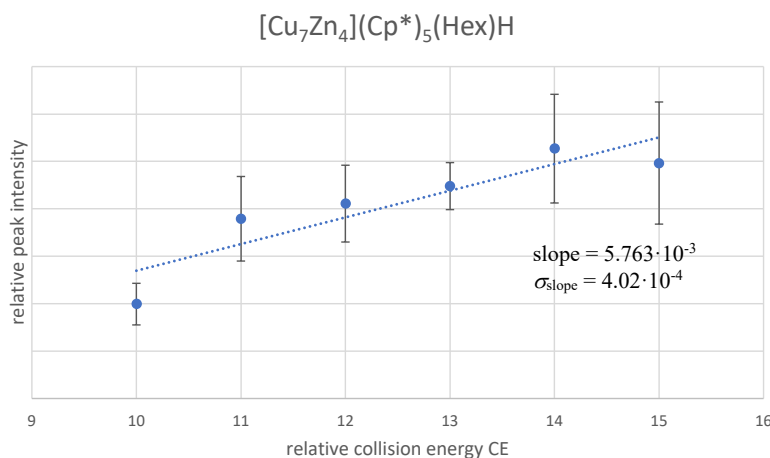
Supplementary Figure 121: CE vs. I plot of the ion $\{\text{[Cu}_{11}\text{Zn}_6](\text{Cp}^*)_7(\text{CO}_2)_2(\text{HCO}_2)\}^+$. The species is assigned as fragment ion. The regression was performed on the statistical means of five independent measurements under identical experimental conditions for each CE value. The error bars represent the standard deviations of these measurements.



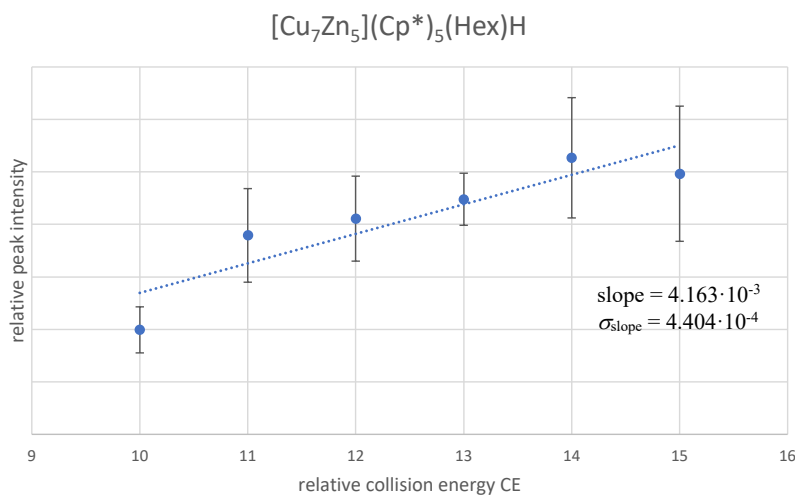
Supplementary Figure 122: CE vs. I plot of the ion $\{\text{[Cu}_{11}\text{Zn}_6](\text{Cp}^*)_8(\text{CO}_2)_2(\text{HCO}_2)\}^+ (\text{Z}^+)$. The species is assigned as molecular ion. The regression was performed on the statistical means of five independent measurements under identical experimental conditions for each CE value. The error bars represent the standard deviations of these measurements.



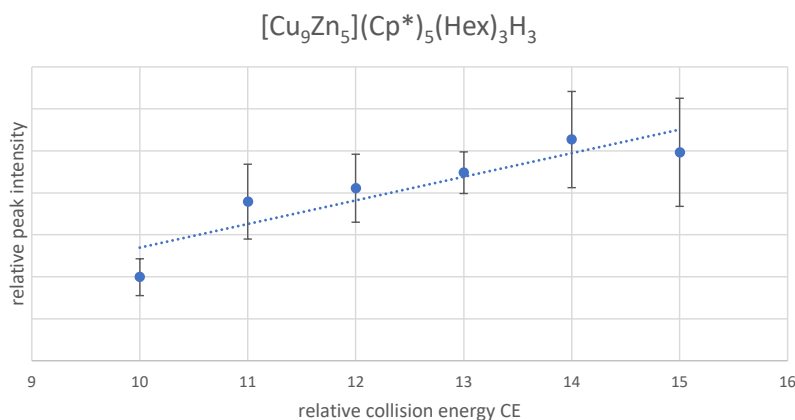
Supplementary Figure 123: CE vs. I plot of the ion $\{\text{[Cu}_3\text{Zn}_6](\text{Cp}^*)_4(\text{Hex})_2\text{H}_2\}^+$. The species is assigned as molecular ion. The regression was performed on the statistical means of five independent measurements under identical experimental conditions for each CE value. The error bars represent the standard deviations of these measurements.



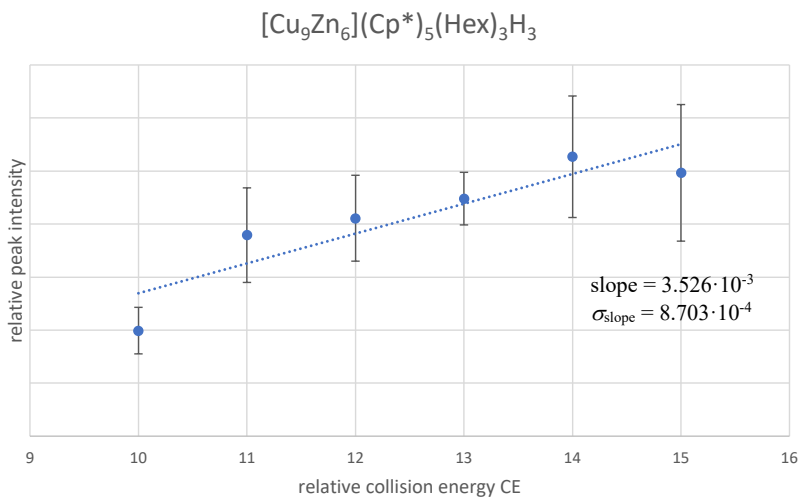
Supplementary Figure 124: CE vs. I plot of the ion $\{\text{[Cu}_7\text{Zn}_4](\text{Cp}^*)_5(\text{Hex})\text{H}\}^+$. The species is assigned as fragment ion. The regression was performed on the statistical means of five independent measurements under identical experimental conditions for each CE value. The error bars represent the standard deviations of these measurements.



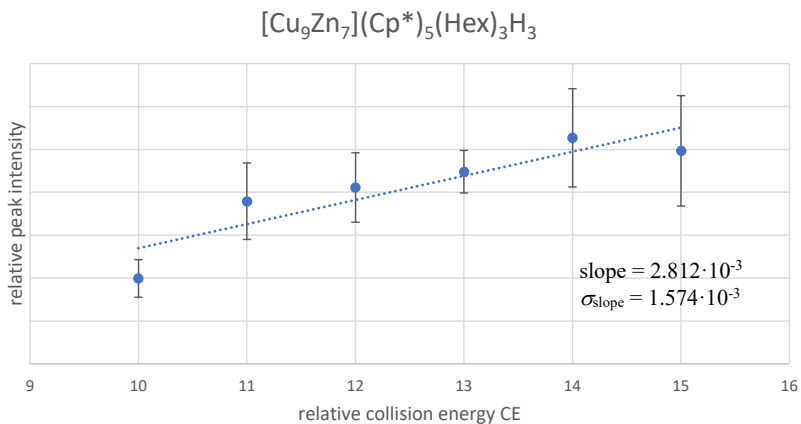
Supplementary Figure 125: CE vs. I plot of the ion $\{\text{[Cu}_7\text{Zn}_5](\text{Cp}^*)_5(\text{Hex})\text{H}\}^+$. The species is assigned as fragment ion. The regression was performed on the statistical means of five independent measurements under identical experimental conditions for each CE value. The error bars represent the standard deviations of these measurements.



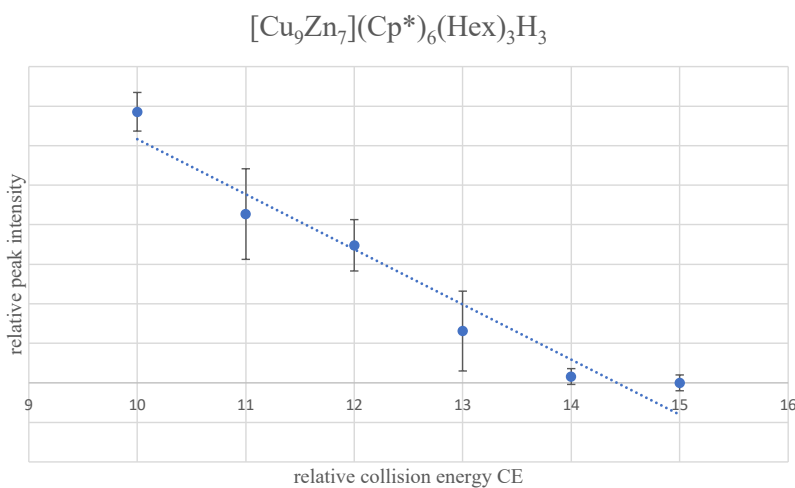
Supplementary Figure 126: CE vs. I plot of the ion $\{\text{[Cu}_9\text{Zn}_5](\text{Cp}^*)_5(\text{Hex})_3\text{H}_3\}^+$. The species is assigned as fragment ion, e.g. $[\text{W}^+ - \text{ZnZnCp}^*]$. The regression was performed on the statistical means of five independent measurements under identical experimental conditions for each CE value. The error bars represent the standard deviations of these measurements.



Supplementary Figure 127: CE vs. I plot of the ion $\{\text{[Cu}_9\text{Zn}_6](\text{Cp}^*)_5(\text{Hex})_3\text{H}_3\}^+$. The species is assigned as fragment ion, i.e. $[\text{W}^+ - \text{ZnCp}^*]$. The regression was performed on the statistical means of five independent measurements under identical experimental conditions for each CE value. The error bars represent the standard deviations of these measurements.

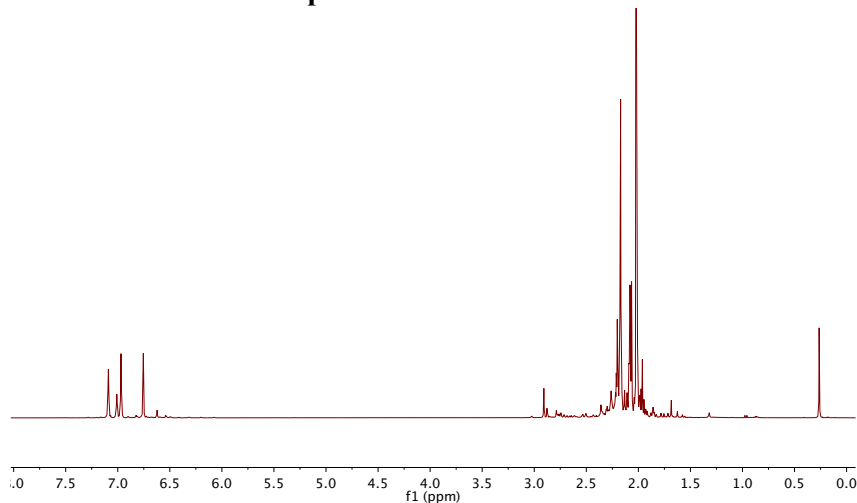


Supplementary Figure 128: CE vs. I plot of the ion $\{\text{[Cu}_9\text{Zn}_7](\text{Cp}^*)_5(\text{Hex})_3\text{H}_3\}^+$. The species is assigned as fragment ion, i.e. $[\text{W}^+ - \text{Cp}^*]$. The regression was performed on the statistical means of five independent measurements under identical experimental conditions for each CE value. The error bars represent the standard deviations of these measurements.

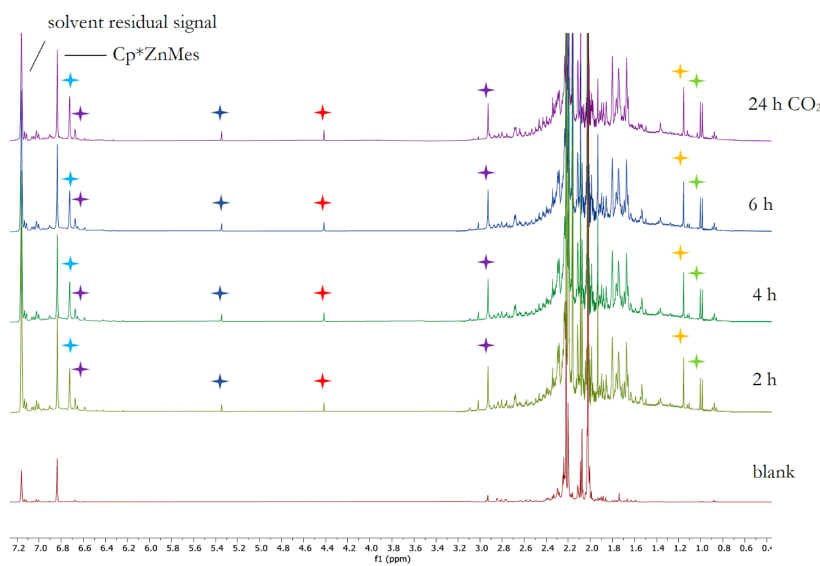


Supplementary Figure 129: CE vs. I plot of the ion $\{\text{[Cu}_9\text{Zn}_7](\text{Cp}^*)_6(\text{Hex})_3\text{H}_3\}^+$ (**W⁺**). The species is assigned as molecular ion. The regression was performed on the statistical means of five independent measurements under identical experimental conditions for each CE value. The error bars represent the standard deviations of these measurements.

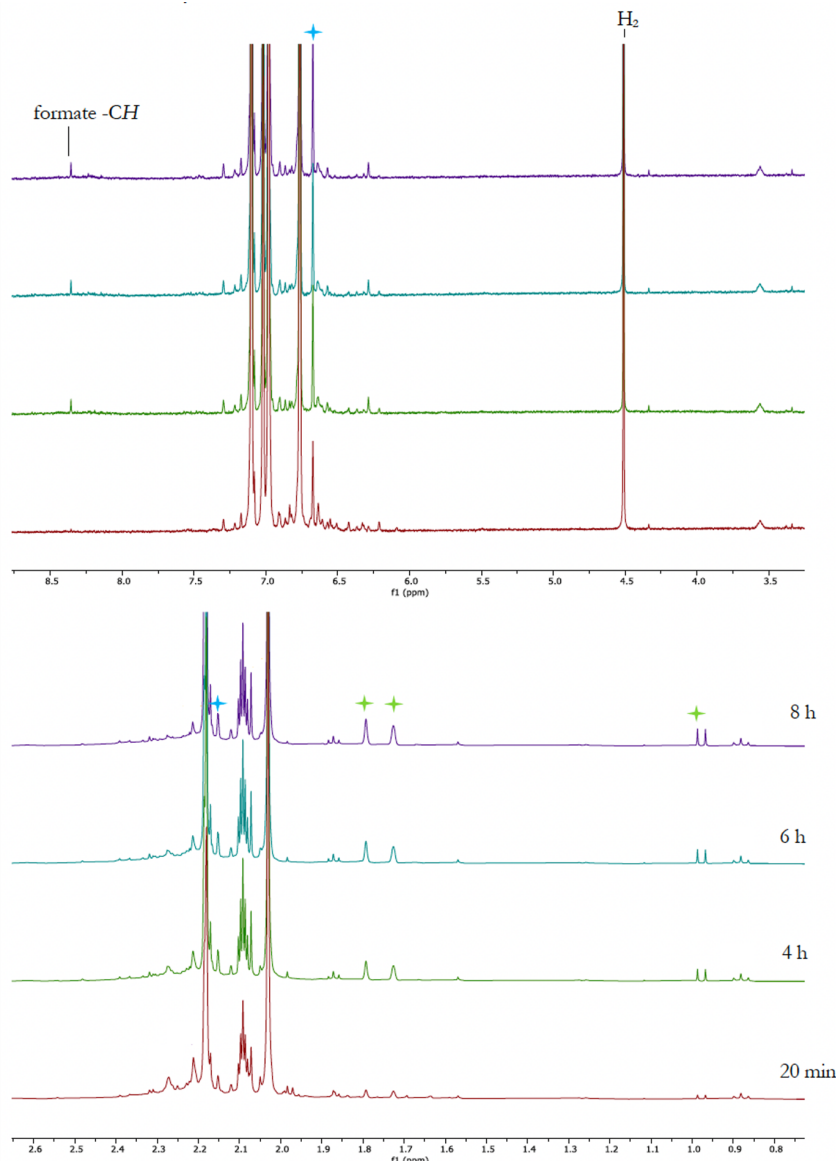
1.1.2. NMR Spectra



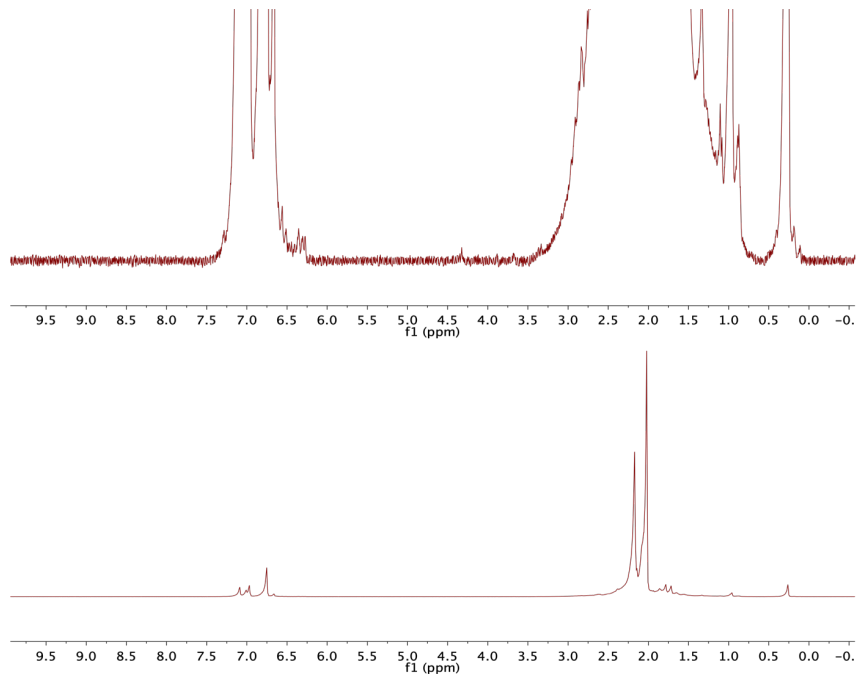
Supplementary Figure 130: ¹H NMR spectrum of the Cu/Zn library {1} (toluene-ds).



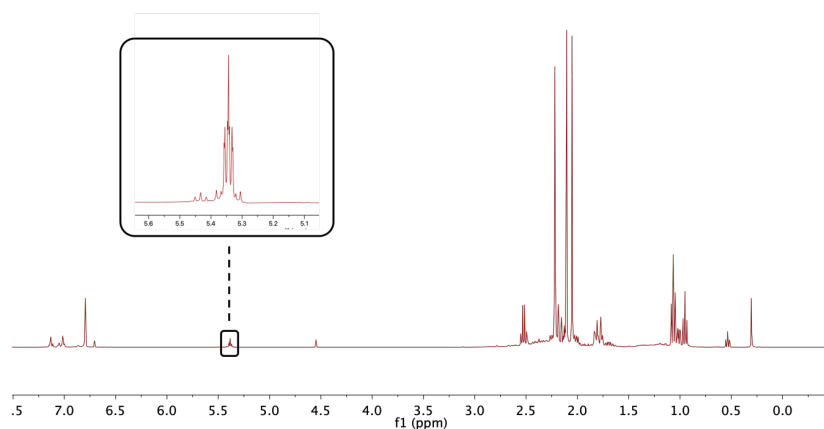
Supplementary Figure 131: Time dependent evolution in situ ¹H NMR of the reaction of the Cu/Zn library {1} with 1 bar CO₂ at room temperature (benzene-d₆) {2}. + Fulvene + Fulvalene + Cp*H + Mesitylene + Dihydrogen + [Cu₂]Mess.



Supplementary Figure 132: Time dependent evolution in situ ¹H NMR of the reaction of the Cu/Zn library {2} with 2 bar H₂ at room temperature after reaction with CO₂ (toluene-d₈) {3}. The formation of formate is observed after four hours already. + Mesitylene + Cp*H.

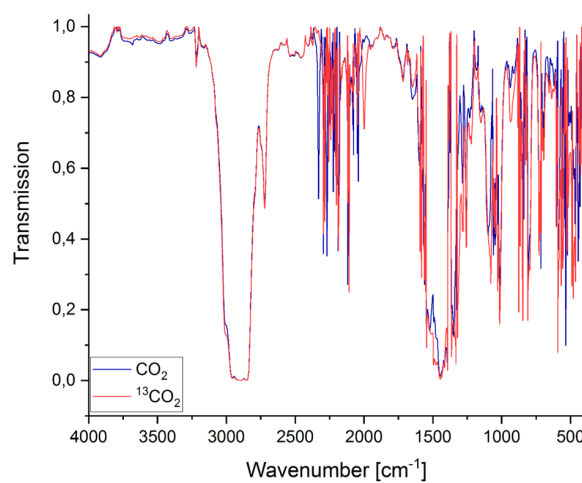


Supplementary Figure 133: Time dependent evolution in situ ^1H NMR of the reaction of the Cu/Zn library **{1}** with 2 bar D_2 at room temperature after reaction with CO_2 (toluene- d_8) **{3}**. No deuterated formate is observed, proving its formation from the dihydrogen gas applied to the library.

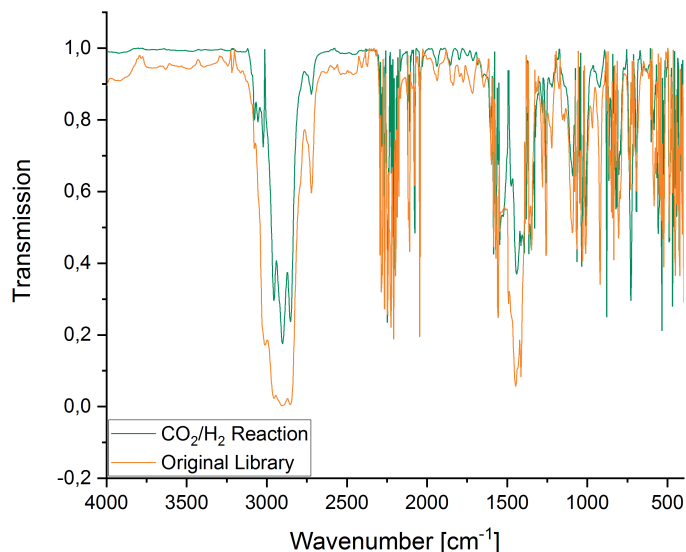


Supplementary Figure 134: ^1H NMR spectrum of the Cu/Zn library **{4}** (toluene- d_8) showing the formation of 3-hexene.

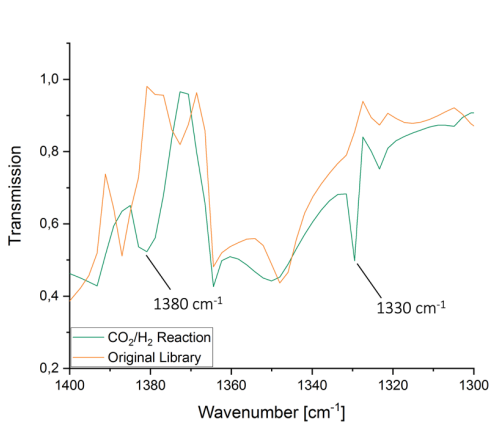
1.1.3. FT-IR Spectra



Supplementary Figure 135: Stacked FT-IR spectra of the Cu/Zn library {2} after reaction with 1 bar CO_2 at room temperature. No carbonyl vibration is observed, showing that the carbon dioxide is not split at the CO_2 bearing clusters.



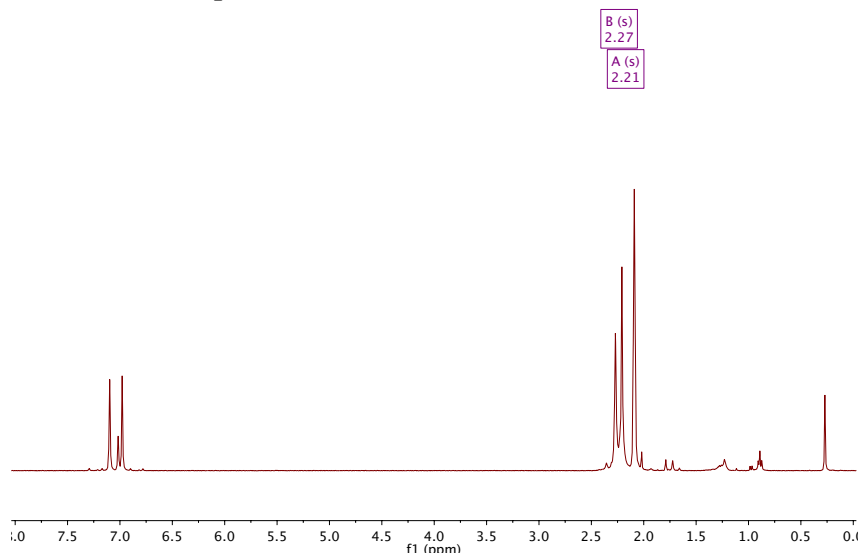
Supplementary Figure 136: Stacked FT-IR spectra of the original Cu/Zn library {1} (orange) and of the Cu/Zn library {3} after reaction with CO₂ and H₂ (green).



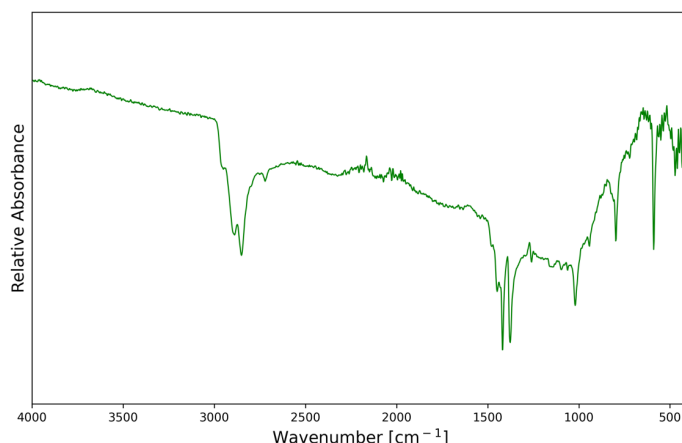
Supplementary Figure 137: Cut-out of the FT-IR spectra of the original Cu/Zn library {1} (orange) and of the Cu/Zn library {3} after reaction with CO₂ and H₂ (green). The absorption bands at 1330 and 1380 cm⁻¹ indicate the formation of copper-formate (C-H in plane bending / COO rocking and C-O symmetric stretching respectively).

1.2. $[\text{Cu}_4\text{Zn}_{10}]\text{Cp}^*_8(\text{F})$

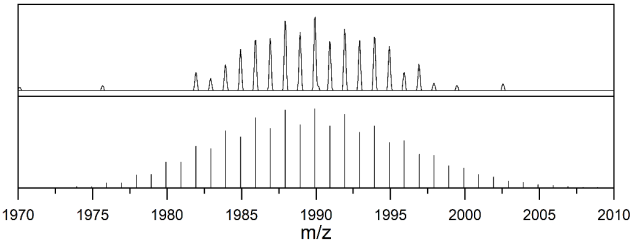
1.2.1. Experimental Characterization



Supplementary Figure 138: ${}^1\text{H}$ NMR spectrum of $[\text{Cu}_4\text{Zn}_{10}]\text{Cp}^*_8(\text{F})$ (toluene- d_6). δ [ppm] = 2.27 (s, 45H, Cp^*), 2.21 (s, 75H, Cp^*).



Supplementary Figure 139: ATR-IR spectrum of $[\text{Cu}_4\text{Zn}_{10}]\text{Cp}^*_8(\text{F})$. No hydride bands are observed. The C-H vibrations are observed between 2700 and 3000 cm^{-1} ; the aromatic C-C vibrations between 1300 and 1500 cm^{-1} .



Supplementary Figure 140: Experimental LIFDI-MS (top) and calculated (bottom) peak pattern for the molecular ion of $[\text{Cu}_4\text{Zn}_{10}]\text{Cp}^*_8$ (**F**).

1.2.1.1. Single-Crystal Crystallography

A black, plate-shaped crystal of **F**, $\text{C}_{80}\text{H}_{120}\text{Cu}_4\text{Zn}_{10}$, coated with perfluorinated ether and fixed on top of a Kapton micro sampler was used for X-ray crystallographic analysis. The X-ray intensity data were collected at 100(2) K on a Bruker D8 VENTURE three-angle diffractometer with a TXS rotating anode with MoK_α radiation ($\lambda=0.71073 \text{ \AA}$) using APEX4.³ The diffractometer was equipped with a Helios optic monochromator, a Bruker PHOTON-100 CMOS detector, and a low temperature device.

A matrix scan was used to determine the initial lattice parameters. All data were integrated with the Bruker SAINT V8.40B software package using a narrow-frame algorithm and the reflections were corrected for Lorentz and polarization effects, scan speed, and background. The integration of the data using a triclinic unit cell yielded a total of 203812 reflections within a 2 θ range [$^\circ$] of 4.01 to 50.05 (0.84 \AA), of which 16507 were independent. Data were corrected for absorption effects including odd and even ordered spherical harmonics by the multi-scan method (SADABS 2016/2).⁴ Space group assignment was based upon systematic absences, E statistics, and successful refinement of the structure.

The structure was solved by iterative methods using SHELXT and refined by full-matrix least-squares methods against F^2 by minimizing $\Sigma w(F_o^2 - F_c^2)^2$ using SHELXL in conjunction with SHELXL-E.⁵⁻⁷ All non-hydrogen atoms were refined with anisotropic displacement parameters. Hydrogen atoms were refined isotropically on calculated positions using a riding model with their U_{iso} values constrained to 1.5 times the U_{eq} of their pivot atoms for terminal sp^3 carbon atoms and a C–H distance of 0.98 \AA . Non-methyl hydrogen atoms were refined using a riding model with methylene, aromatic, and other C–H distances of 0.99 \AA , 0.95 \AA , and 1.00 \AA , respectively, and U_{iso} values constrained to 1.2 times the U_{eq} of their pivot atoms. Neutral atom scattering factors for all atoms and anomalous dispersion corrections for the non-hydrogen atoms were taken from International Tables for Crystallography.⁸ The unit cell of $\text{C}_{80}\text{H}_{120}\text{Cu}_4\text{Zn}_{10}$ contains 1.8 heavily disordered molecules of toluene which were treated as a diffuse contribution to the overall scattering without specific atom positions using the PLATON/SQUEEZE procedure.⁹

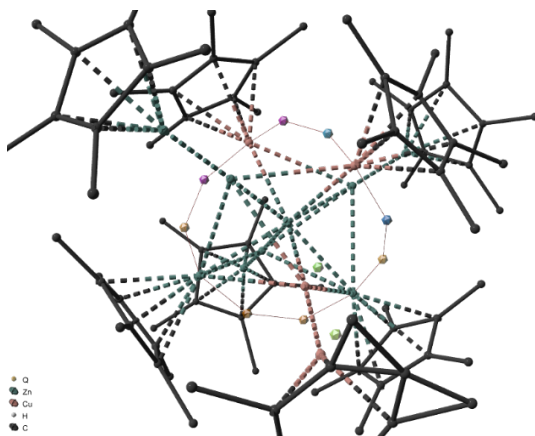
Crystallographic data for the structures reported in this paper have been deposited with the Cambridge Crystallographic Data Centre.¹⁰ Supplementary crystallographic data reported in this paper have been deposited with the Cambridge Crystallographic Data Centre (CCDC 2390361) and can be obtained free of charge from The Cambridge Crystallographic Data Centre via www.ccdc.cam.ac.uk/structures.¹⁰ This report and the CIF file were generated using FinalCif.¹¹

Supplementary Table 7: Crystal data and structure refinement for cluster F.

CCDC number	2390361
Empirical formula	C ₈₀ H ₁₂₀ Cu ₄ Zn ₁₀
Formula weight	1989.61
Temperature [K]	100(2)
Crystal system	triclinic
Space group (number)	P $\overline{1}$ (2)
<i>a</i> [\AA]	12.5626(9)
<i>b</i> [\AA]	16.6481(12)
<i>c</i> [\AA]	25.1386(19)
α [°]	99.320(3)
β [°]	99.634(3)
γ [°]	111.420(3)
Volume [\AA ³]	4680.7(6)
<i>Z</i>	2
ρ_{calc} [gcm ⁻³]	1.412
μ [mm ⁻¹]	3.432
<i>F</i> (000)	2032
Crystal size [mm ³]	0.076×0.149×0.280
Crystal colour	black
Crystal shape	plate
Radiation	MoK α ($\lambda=0.71073$ Å)
2 θ range [°]	4.01 to 50.05 (0.84 Å)
Index ranges	$-14 \leq h \leq 14$ $-19 \leq k \leq 19$ $-29 \leq l \leq 29$
Reflections collected	203812
Independent reflections	16507
	$R_{\text{int}} = 0.0458$
	$R_{\text{sigma}} = 0.0186$
Completeness to $\theta = 25.027^\circ$	99.9 %
Data / Restraints / Parameters	16507 / 949 / 1093
Goodness-of-fit on F^2	1.039
Final <i>R</i> indexes [$I \geq 2\sigma(I)$]	$R_1 = 0.0466$
Final <i>R</i> indexes [all data]	wR ₂ = 0.1232
Largest peak/hole [eÅ ⁻³]	$R_1 = 0.0524$
	wR ₂ = 0.1272
	1.95/-0.96

Refinement details:

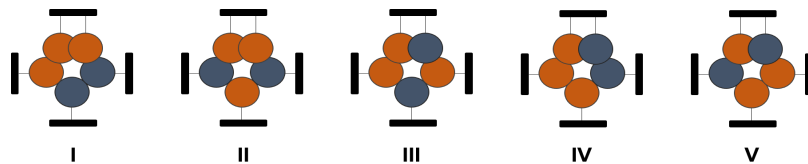
During refinement the structure of $[Cu_4Zn_{10}](Cp^*)_8$ has shown to be highly intricate. Overall, it comprises major disorder of metal atoms within the core. The issue is the fact that copper and zinc atoms cannot be distinguished from each other by using only crystallographic methods. Moreover, the first solution using SHELXT only showed 13 metal atoms instead of 14 and high residual electron density (up to 30 e⁻) around the inner cluster core (Supplementary Figure 141).



Supplementary Figure 141: First solution for $[Cu_4Zn_{10}](Cp^*)_8$ using SHELXT. The model only comprises 13 metal atoms and shows severe disorder of metal atoms around the inner cluster core.

Therefore, the 14th atom must be highly disordered in a circular fashion around the inner part of the cluster. Mass spectra acquired from isolated single crystals, however, unambiguously showed us that the sum formula $[Cu_4Zn_{10}](Cp^*)_8$ must be correct (Supplementary Figure 140). Note that there is no evidence for twinning for this structure (no split reflections, low symmetry, P-1).

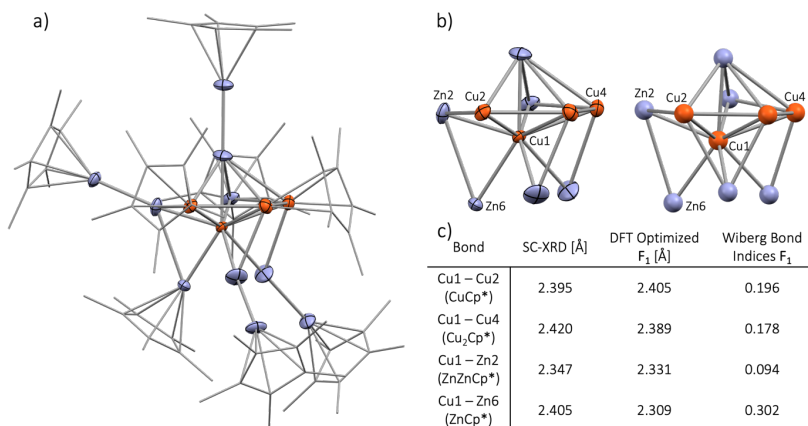
The only structural motif that can be directly assigned from the first solution are Cu1 as the innermost atom of the cluster as well as four Zn–Zn–Cp* units (named Zn1–Zn7, Zn2–Zn8, Zn3–Zn9 and Zn4–Zn10 in the final model). Only zinc is capable of forming such a structural motif to the best of our knowledge. We deduced thereof that disorder of metal atoms is limited to the inner core of $[Cu_4Zn_{10}](Cp^*)_8$. Hence, two zinc and three copper atoms (minus the four Zn–Zn–Cp* units and Cu1) must be “distributed” between four Cp* units. This results in three “capping” and one Cp* bridging two metal atoms. Consequently, only five principle isomers (neglecting enantiomers and diastereomers) may exist for the core of this compound (Supplementary Figure 142). DFT calculations (*vide infra*) showed us that isomer I with two bridging copper units is the one lowest in energy.

Supplementary Figure 142: Possible isomers for the core structure of $[Cu_4Zn_{10}](Cp^*)_8$.

Based on these data, we found in total four layers of disordered metal atoms during refinement. For that, the position and the atomic displacement parameters for atoms at the same positions were constrained to be equal using the commands EADP and EXYZ. All four layers were added up to 1 using SUMP. The over-all result of the DFG guided X-ray structural analysis of F is given in Supplementary Figure 143a.

1.2.2. DFT Bonding Analysis

The single crystal X-ray structure of F (Supplementary Figure 143a) suffers accuracy from its disordered nature and, owing to the close proximity of the Cu and Zn atomic numbers, some of the metal positions could not be clearly identified as M = Cu or Zn. This fairly unsymmetrical structure reveals a central Cu atom surrounded by eight moieties: four Zn-ZnCp*; three MCp* and a “bidentate” $M_2\{\mu-(\eta^2:\eta^2-Cp^*)\}$. This last coordination mode is expected to be highly fluctual. This results in a ninefold coordination of the central copper atom. Furthermore, some bonding interactions seems to exist between these nine metal atoms (Supplementary Figure 143a).

Supplementary Figure 143: a) Single-crystal X-Ray diffraction structure of F (ellipsoids drawn at 50% probability, Cp* as wireframe for clarity). b) Comparison of the experimental (left) and DFT optimized (right) $[Cu_4Zn_6]^{4+}$ core

of F. c) Selected representative bond lengths from the SC-XRD and DFT optimized structure as well as the associated Wiberg bond indices. Color code: copper = orange; zinc = blue, carbon = grey.

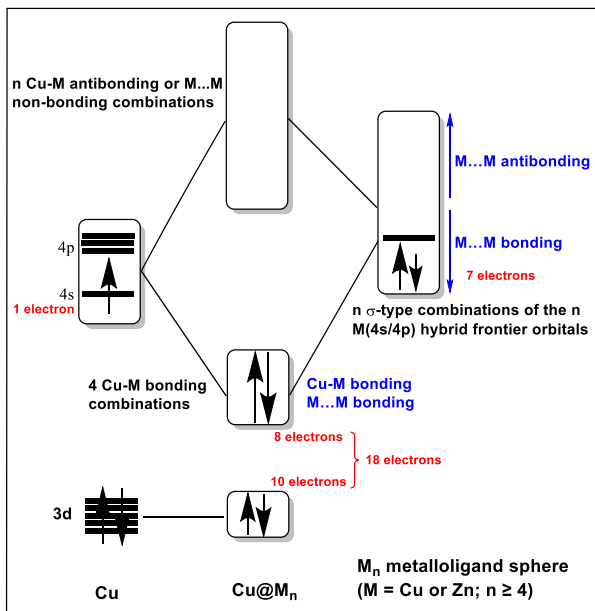
DFT calculations at the BP86/TZ2P/ D3(BJ) level (see details in the methods section of the main text) were carried out on F, in order to ascertain the Cu vs. Zn nature of the M positions and to provide a rationalization of its structure and stability. Calculations were performed from the X-ray structure of F as starting geometry and the optimizations of a series of isomers with various Cu vs. Zn distributions on the metal sites were performed. The ten most energetically favorable structures (Supplementary Table 8) exhibit significant structural differences between them. Nevertheless, the lowest energy isomer (**F₁**) is also the closest to the X-ray structure (Supplementary Figure 143b and Supplementary Table 9). From the electron counting point of view, the number of cluster metal valence electrons (discarding 3d electrons) of [Cu₄Zn₁₀](Cp*)₈ (**F**) is 4 + (10 x 2) – 8 = 16. Assuming that the Zn-Zn bonds in the four Zn-ZnCp* units are localized 2-electron/2-center bonds, the number of electrons associated with metal-metal bonding within the coordination sphere of the central Cu atom is 16 – (4 x 2) = 8. Together with the 10 non-bonding 3d(Cu) electrons, this results in a central Cu atom following the 18-electron rule, analogous to a regular ML_n organometallic complex (Supplementary Figure 144). However, regular organometallic complexes do not exhibit bonding between ligands, whereas in F several bonding contacts exist between the metalloligands surrounding the central Cu (Supplementary Figure 143). This is a result of the delocalization of the 8 cluster bonding electrons. This delocalization is caused by the number of metalloligands exceeding the number of available AOs for bonding to the central d¹⁰ copper center (four). This is further facilitated by the possibility of non-negligible overlap between the metalloligands, allowing the nine diffuse sp-type (4s/4p) frontier orbitals of the eight metalloligands (seven mono- and one bi-dentate) to interact between one another. This interaction causes a dispersion of the orbitals of the metalloligands sphere fragment, in turn allowing the bonding orbitals to interact preferentially with the 4s and 4p AOs of the central Cu, then conferring to the four MOs containing the 8 metal electrons with a substantial metalloligands···metalloligands bonding character, as exemplified by the corresponding Wiberg bond indices (Supplementary Table 8). This bonding situation, sketched in Supplementary Figure 144 was already put forward in the case of [CuZn₁₀](Cp*)₇.¹²

Supplementary Table 8: Relative total (ΔE) and free (ΔG) energies and HOMO-LUMO gaps (ΔE_{H-L}) of the computed isomers of [Cu₄Zn₁₀](Cp*)₈ (**F**) of lowest energy.

<i>Isomer</i>	<i>F₁</i>	<i>F₂</i>	<i>F₃</i>	<i>F₄</i>	<i>F₅</i>	<i>F₆</i>	<i>F₇</i>	<i>F₈</i>	<i>F₉</i>	<i>F₁₀</i>
ΔE (eV)	0.00	0.06	0.15	0.15	0.20	0.36	0.57	0.60	0.63	1.30
ΔG (eV)	0.00	0.12	0.11	0.22	0.20	0.42	0.56	0.54	0.64	1.17
ΔE_{H-L} (eV)	1.38	1.63	1.27	1.39	1.41	1.28	1.21	1.44	1.33	1.48

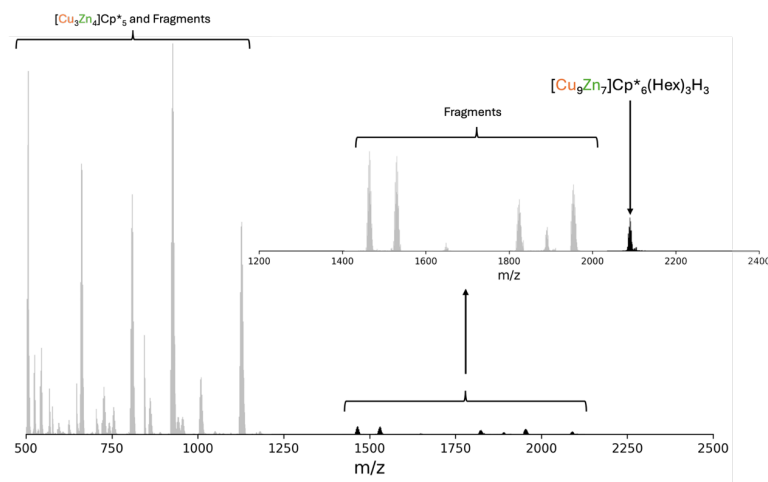
Supplementary Table 9: Selected computed data for F₁ (WBI = Wiberg bond index).

<i>Interatomic contact</i>	<i>Distance (Å)</i>	<i>WBI</i>	<i>Atom</i>	<i>Natural atomic charge</i>
Cu1-Cu2	2.405	0.196	Cu1	-0.72
Cu1-Cu3	2.493	0.120	Cu2	0.20
Cu1-Cu4	2.389	0.178	Cu3	0.34
Cu1-Zn1	2.407	0.056	Cu4	0.24
Cu1-Zn2	2.331	0.094	Zn1	0.56
Cu1-Zn3	2.328	0.084	Zn2	0.50
Cu1-Zn4	2.335	0.103	Zn3	0.55
Cu1-Zn5	2.321	0.238	Zn4	0.52
Cu1-Zn6	2.309	0.302	Zn5	0.82
Zn1-Zn7	2.318	0.517	Zn6	0.74
Zn2-Zn8	2.318	0.451	Zn7	0.70
Zn3-Zn9	2.309	0.502	Zn8	0.65
Zn4-Zn10	2.319	0.444	Zn9	0.71
Zn10			Zn10	0.66
Cu2-Cu3	2.415	0.165		
Cu3-Cu4	2.423	0.067		
Zn1-Cu2	2.538	0.090		
Zn1-Cu3	2.541	0.058		
Zn1-Cu4	2.723	0.033		
Zn1-Zn5	2.676	0.057		
Zn2-Cu2	2.692	0.064		
Zn3-Cu2	2.600	0.063		
Zn3-Cu3	2.502	0.088		
Zn4-Cu4	2.540	0.096		
Zn5-Cu4	2.513	0.123		
Zn4-Zn6	2.784	0.048		

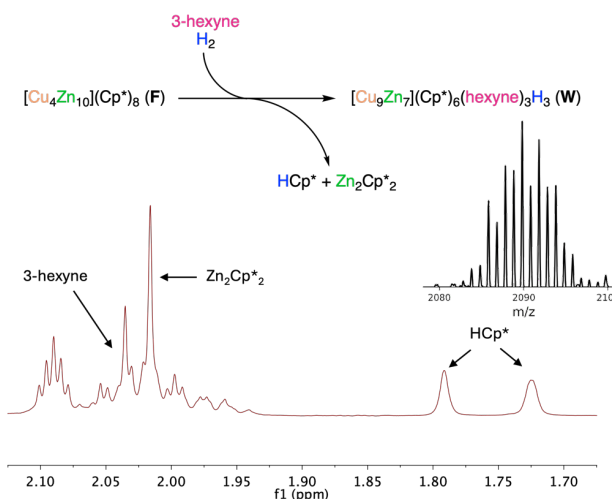


Supplementary Figure 144: Simplified MO interaction diagram for a stable cluster made of a central Cu atom surrounded by at least four metalloligands of the type CuCp^* , ZnCp^* , ZnZnCp^* ..., thus having (at least) one σ -type frontier orbital, and capable of allowing bonding interaction between them. In the case of F, the metalloligand sphere is composed of the following units: four 1-electron Zn-ZnCp^* , two 1-electron ZnCp^* , one 0-electron CuCp^* and a bidentate 1-electron $\text{Cu}_2\{\mu-(\eta^2:\eta^2-\text{Cp}^*)\}$.

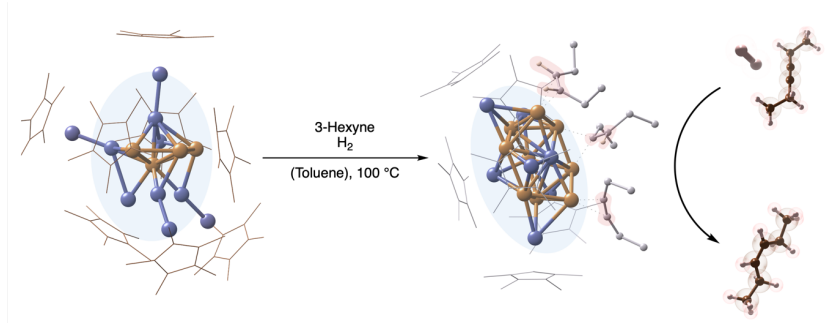
1.3. Catalytic Semi-Hydrogenation



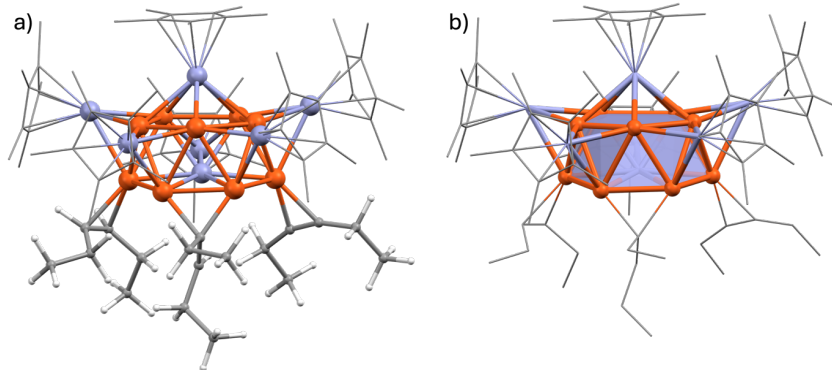
Supplementary Figure 145: In situ LIFDI-MS of the conversion of 3-hexyne with H_2 and 5.0 mol% $[\text{Cu}_4\text{Zn}_{10}]\text{Cp}^*\text{s}$ (**F**) at 100 °C showing the formation of $[\text{Cu}_9\text{Zn}_7](\text{Cp}^*)_6(\text{hex})_3\text{H}_3$ (**W**). $[\text{Cu}_3\text{Zn}_4]\text{Cp}^*\text{s}$ (**B**) is also observed as due to its facile ionization. It is detectable in the mass spectrum, as much lower quantities are sufficient as compared for $^1\text{H-NMR}$ observation.



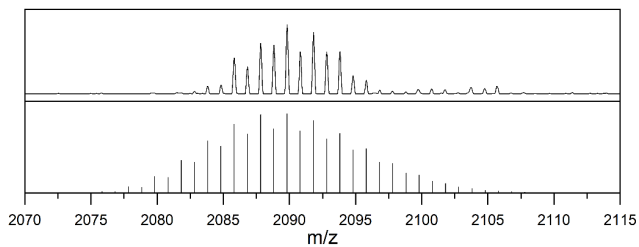
Supplementary Figure 146: Reaction scheme for the formation of species **W** from **F** upon conversion with 3-hexyne/ H_2 at 100 °C. The side products are identified by $^1\text{H-NMR}$ spectroscopy and the pattern of the molecular ion of **W** is shown.



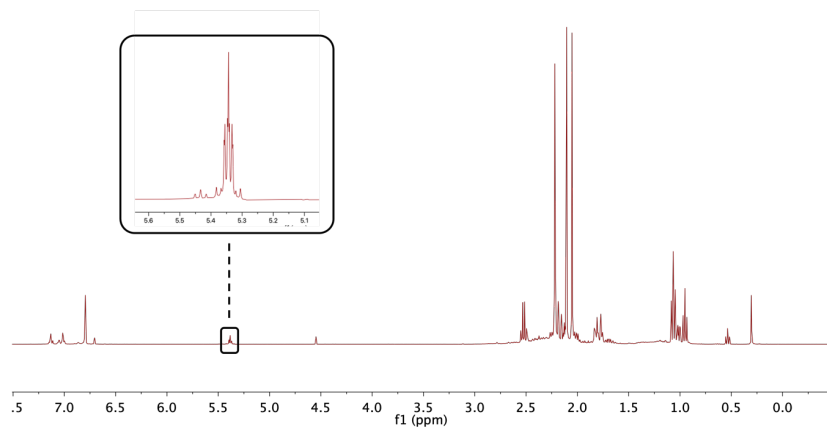
Supplementary Figure 147: Schematic representation for the formation of species **W** from **F** upon conversion with 3-hexyne/H₂ at 100 °C and subsequent semi-hydrogenation of 3-hexyne.



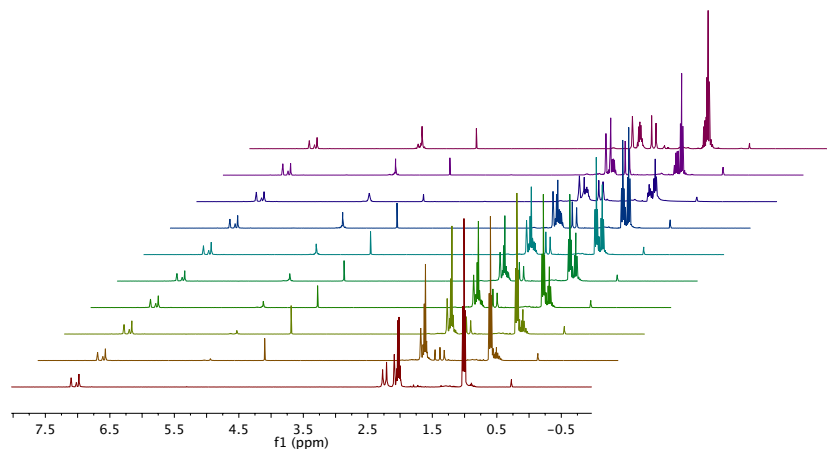
Supplementary Figure 148: Calculated structure of [Cu₉Zn₇](Cp*)₈(Hex)₃H₃ (**W**) showing species in a $\mu_1\eta^2$ -3-hexyne, $\mu_1\eta^2$ -cis-3-hexene and $\mu_2\eta^1$ -cis-3-hexenyl coordinated to cluster core as a result of hexyne insertion into cluster hydride species (alkyne semi-hydrogenation mechanism). a) Calculated structure of **W** (Cp* as wireframe for clarity) and b) Calculated structure of **W** with the surface of the Cu₉Zn pentagonal antiprism marked (ligands as wireframe for clarity). Color code: orange = copper, blue = zinc, grey = carbon and white = hydrogen.



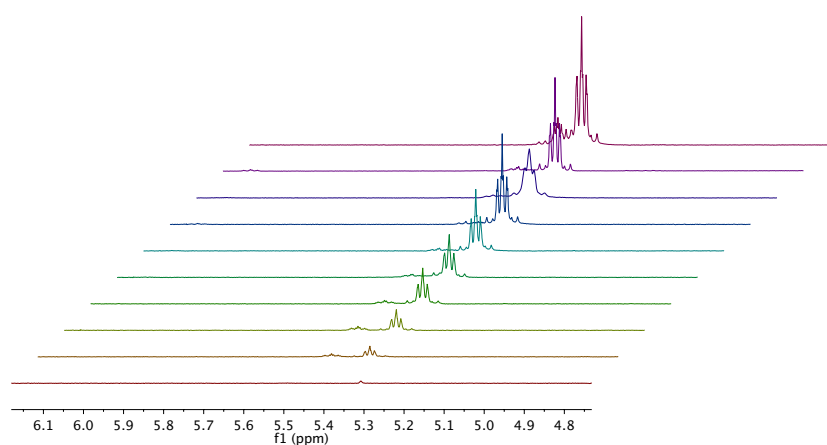
Supplementary Figure 149: Experimental pattern (top) and calculated pattern (bottom) for $[\text{Cu}_9\text{Zn}_7](\text{Cp}^*)_6(\text{Hex})_3\text{H}_3$ (**W**).



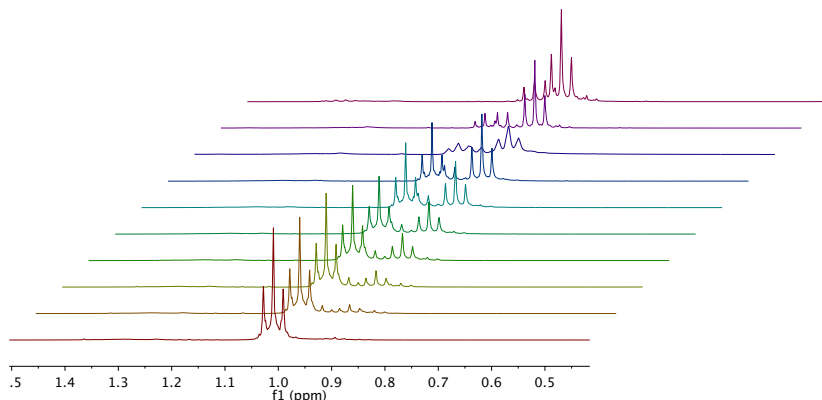
Supplementary Figure 150: ¹H NMR spectrum of the Cu/Zn library **{4}** (toluene-d₈) showing the catalytic formation of 3-hexene after 4 hours reaction time.



Supplementary Figure 151: ^1H NMR spectrum of the catalytic semi-hydrogenation of 3-hexyne with 5 mol% F (toluene-d₈). No n-hexane formation is observed.



Supplementary Figure 152: ^1H NMR spectrum of the catalytic semi-hydrogenation of 3-hexyne with 5 mol% F (toluene-d₈) focused on the CH₂ signals of the 3-hexens (cis and trans).



Supplementary Figure 153: ^1H NMR spectrum of the catalytic semi-hydrogenation of 3-hexyne with 5 mol% **F** (toluene- d_8) focused on the CH_3 signals of the 3-hexyne and 3-hexenes (*cis* and *trans*).

Calculation and Comparison of TOF data:

The TOF data were determined based on the conversion of 3-hexyne after four hours with both **F** and **{1}** as pre-catalyst and pre-catalytic system respectively. As the quantification of **F** in **{4}** is not possible due to an overlap of the different species of **{1}** in the ^1H NMR spectrum, the TOF is calculated based on the total molar amount of Cu in solution. In this regard, 5 mol% **F** $[\text{Cu}_4\text{Zn}_{10}](\text{Cp}^*)_8$ results in the presence of 20 mol% Cu with respect to the amount of 3-hexyne. For the catalytic semi-hydrogenation with **{1}** as pre-catalytic system (resulting in **{4}** during the catalysis), the conversion of 3-hexyne is performed with a total molar amount 27 mol% Cu (derived from the synthetic conditions of library **{1}**) with respect to the amount of 3-hexyne. Thus, we compare the obtained TOF values of the two experiments to the same level of mol% Cu present in the reaction solution. The conversion of 3-hexyne to *cis*- and *trans*-3-hexene and *n*-hexane was monitored via ^1H NMR. After four hours of reaction time, the conversion of 3-hexyne is observed to be 48% with the isolated **F** and 16% with **{4}**. This results in a TOF of $0.60 \text{ h}^{-1}\text{Cu}^{-1}$ when using isolated **F** as pre-catalyst (TOF = 2.4 h^{-1} based on **F**) and of $0.15 \text{ h}^{-1}\text{Cu}^{-1}$ with **{1}** as precatalytic system.

$$\begin{aligned} \text{TOF} &= \frac{\text{TON}}{t} = \frac{\frac{n_{\text{hexene}} \%}{n_{\text{cat}} \%}}{t} \\ \text{TOF}_F &= \frac{\frac{48 \text{ mol\%}}{20 \text{ mol\%}}}{4 \text{ h}} = 0.60 \text{ h}^{-1}\text{Cu}^{-1} \\ \text{TOF}_{\{4\}} &= \frac{\frac{16 \text{ mol\%}}{27 \text{ mol\%}}}{4 \text{ h}} = 0.15 \text{ h}^{-1}\text{Cu}^{-1} \end{aligned}$$

1.4. References

1. Dyson, P. J., Johnson, B. F., McIndoe, J. S. & Langridge-Smith, P. R. Energy-dependent electrospray ionisation mass spectrometry: applications in transition metal carbonyl chemistry. *Rapid Commun. Mass Spectrom.* **5**, 311-313 (2000)
2. Diedrich, J. K., Pinto, A. F. & Yates III, J. R. Energy dependence of HCD on peptide fragmentation: stepped collisional energy finds the sweet spot. *J. Am. Chem. Soc. Mass Spectrom.* **11**, 1690-1699 (2013)
3. APEX4 Suite of Crystallographic Software. Version 2021-10.0 ed: Bruker AXS Inc., Madison, Wisconsin, USA; 2021.
4. Krause, L., Herbst-Irmer, R., Sheldrick, G. M. & Stalke, D. 2015. *J. Appl. Cryst.* **48**, 3–10
5. Huebschle, C. B., Sheldrick, G. M. & Dittrich, B. *J. Appl. Cryst.* 1281–1284 (2011)
6. Sheldrick, G. M. *Acta Cryst.* **A71**, 3–8 (2015)
7. Sheldrick, G. M. *Acta Cryst.* 3–8 (2015)
8. *International Tables for Crystallography Volume C, Mathematical, Physical and Chemical Tables*. International Union of Crystallography: Chester, England, 2006.
9. Spek, A. *Acta Cryst.* 9-18 (2015)
10. Groom, C. R., Bruno, I. J., Lightfoot, M. P. & Ward, S. C. *Acta Cryst.* 171–179 (2016)
11. Kratzert, D. FinalCif, V106. [cited] Available from: <https://dkratzert.de/finalcif.html>.
12. Schütz, M., et al. Contrasting Structure and Bonding of a Copper-Rich and a Zinc-Rich Intermetalloid Cu/Zn Cluster. *Inorganic Chemistry* **13**, 9077-9085 (2020)

2 Computational Framework

The computational framework allows us to explore all different structural possibilities and compare the energies of the various possible structures of a given clusters to determine the most likely one. The energies of different structures can only be used relative to one another for a given sum formula.

2.1 Introduction to the Generation of Metal Complexes

The computational design of molecular structures can be achieved using global optimization algorithms such as Basi-Hopping Monte Carlo (BHMC),¹ where the Monte Carlo algorithm is combined with local optimization algorithms such as conjugated gradient, steepest descent, etc.² The investigation of phase space necessitates an extensive number of total energy minimization, which can be performed using either *ab initio* methods or force field theoretical frameworks.¹ Normally, those techniques, e.g., BHMC, have been applied for the study of a wide range of molecular systems, including particles (clusters and nanoclusters), in which the starting molecular configurations are atoms randomly distributed within a box space.¹

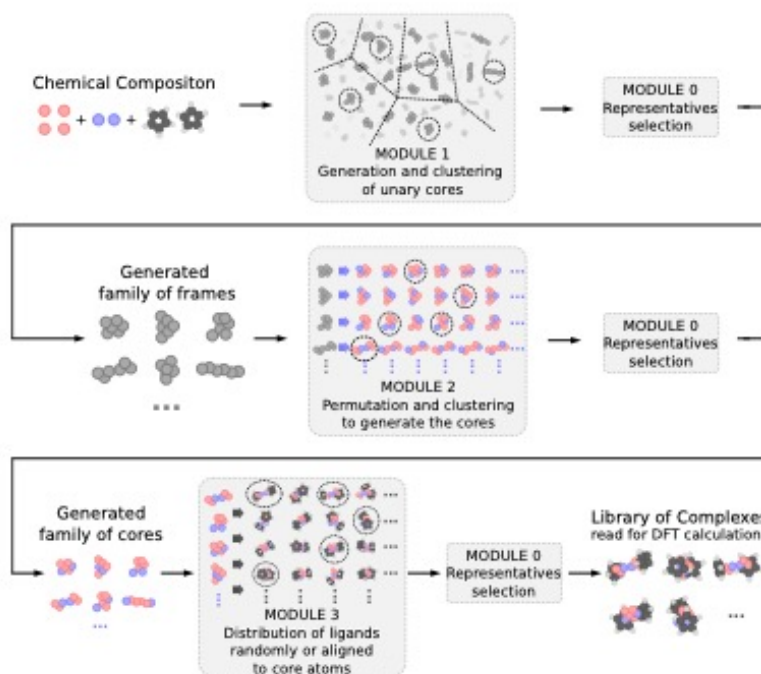
In general, metal complexes are composed of a metal core with a few atoms surrounded by ligand species. Thus, metal complexes can be visualized as molecular structures composed of two molecular fragments, namely (*i*) a core region composed of few atoms and (*ii*) chemical species connected to the core region (ligands).³ Therefore, the computational design of metal complexes can take advantage of this observation to accelerate the computational design of molecular trial configurations for evaluations by total energy methods.

Thus, our computational strategies take advantage of our computational global optimization techniques in the study of finite-size metal clusters,¹ density functional theory (DFT) calculations for finite-size systems,⁴ and machine learning-based algorithms.⁵ As expected in any development study, we considered and implemented several computational strategies (algorithms), such as different core generation procedures, various scripts for the distribution of ligands around the core region, different optimization routines, etc. Thus, in the end, the present document only summarizes the final and successful algorithm, which is summarized in

Figure 154. It contains several modules that work sequentially step by step to deliver a set of family structures for a selected metal complex.

As indicated in the flow chart, the present algorithm can be implemented using different levels of computational methodologies for the total energy evaluations at each step, namely *ab initio* calculations based on DFT or less accurate force field calculations. For example, for the DFT calculations, the following DFT implementations could be used: (i) Vienna *Ab initio* Simulation Package (VASP),^{6,7} Amsterdam Density Functional (ADF),⁸ GAMESS,⁹ GAUSSIAN,¹⁰ Fritz–Harber Institute - *Ab initio* Materials simulation package (FHI-aims),^{11,12} etc.

In this work, for the computational design of metal complexes, we selected the FHI-aims implementation, which provides great flexibility to control the computational cost of the DFT calculations by a proper selection of the basis-set; i.e., it contains different levels of the basis-set. In the following, we will discuss step by step all the computational details on the algorithms. Furthermore, we provided the procedure compiled in an automated Python language, namely `cluster_assembler`, which is available at <https://github.com/QTNano/Cluster-Assembler/>.



Supplementary Figure 154: Flowchart illustrating a general computational framework to design molecular structures for metal complexes.

2.2 Additional Computational Details on the Framework for the Generation of Metal Complexes

The proposed algorithm is general, however, to make the discussion easier, we selected the $[\text{Cu}_a\text{Zn}_b]$ system for our discussion, which will help to understand the proposed ideas and selected strategies to build up a family of metal complexes *ab initio* computational design, i.e., it does not include previous experimental knowledge on the metal complex structure.

2.2.1 Generation of Molecular Unary Frames

Given the desired chemical composition of the cores, e.g., $[\text{Cu}_a\text{Zn}_b]$, we start by generating a family of unary frames, e.g., $[\text{Cu}_{(a+b)}]$ and $[\text{Zn}_{(a+b)}]$. The process begins by defining the shape

of the box that will be used to construct the frame. Two types of boxes are considered: Sphere and Cube boxes. For example,

1. For the Sphere, the radius is determined by the following formula¹³:

$$\text{sphere_radius} = 2 \times d_0 \times \left(\text{factor} + \left(\frac{3 \times n_{\text{atoms}}}{4 \times \pi \times \sqrt{2}} \right)^{\frac{1}{3}} \right)$$

where d_0 is the covalent radius of the species, factor is a tolerance parameter, and n_{atoms} is the number of atoms in the frame.

2. For the Cube box, the edge length of the cube container is set to:

$$\text{cube_edge} = \text{sphere_radius} \times \left(\frac{4 \times \pi}{3} \right)^{\frac{1}{3}}$$

The atoms are iteratively added to the frame, with the constraint that each atom must be placed inside the defined box. Additionally, the distance to the nearest neighbor must respect the covalent radius of the species with a gamma tolerance. Specifically, the distance between the newly added atom and its closest neighbor must be within the range $d_0 - \gamma$ to $d_0 + \gamma$, where γ is a tolerance parameter that accounts for slight variations in the lengths of the bonds.

Finally, to guarantee that all frames are valid, we provide a Python function that checks the frame structure using a graph approach. For that, the frame structure is encoded as a graph, where nodes represent atoms, and edges represent the links between pairs of atoms whose distance is shorter than the covalent radius multiplied by a parameter greater than one, representing the tolerance for establishing the connection. If the resulting graph contains a single component, the frame is approved. Otherwise, it is rejected. At the end of this process, the generation of the frames is provided by Module 1, depicted in Supplementary Figure 154.

2.2.2 Clustering of Molecular Structures via Coulomb Matrix Representation

To manage the large number of trial configurations and identify unique structures, we apply the *k-means* clustering algorithm.¹⁴ First, we encode all structures into vectors using the eigenvalues of their Coulomb matrices,¹⁵ allowing us to group similar configurations effectively. The

Coulomb matrix is a representation of the molecular structure where each element M_{ij} is defined as:

$$M_{ij} = \begin{cases} 0.5Z_i^{2.4} & \text{if } i = j \\ \frac{Z_i Z_j}{\|\mathbf{R}_i - \mathbf{R}_j\|} & \text{if } i \neq j \end{cases}$$

in which, Z_i and Z_j are the atomic numbers of atoms i and j , respectively, and $\|\mathbf{R}_i - \mathbf{R}_j\|$ is the Euclidean distance between atoms i and j . The eigenvalues of the Coulomb matrix provide a compact, invariant descriptor of the molecular configuration that is used for clustering.

The *k-means* clustering algorithm is a partitioning method that divides n observations into k groups. Each observation belongs to the group with the nearest mean, or centroid. In our case, we select the configuration closest to the centroid as the representative of the group. Formally, given a set of observations (x_1, x_2, \dots, x_n) , where each observation is a d -dimensional real vector, *k-means* clustering aims to partition the n observations into k ($\leq n$) sets $S = \{S_1, S_2, \dots, S_k\}$ to minimize the within-group sum of squares (WCSS):

$$\arg \min_S \sum_{i=1}^k \sum_{x \in S_i} \|x - \mu_i\|^2$$

where μ_i is the mean of points in S_i (cluster centroid).

The number of groups, k , can be specified by the user or automatically determined. For automatic determination, we use silhouette analysis from multiple runs of the clustering algorithm.¹⁶ The silhouette score evaluates the similarity of an object to its own group compared to others. By running the clustering algorithm n times and evaluating the silhouette score for each run, we select the most frequent k (number of groups) which results in the highest silhouette score.

This method ensures that we efficiently and accurately identify unique configurations from the large set of trial structures, providing a robust way to analyze and filter the generated frames. It is worth noting that this module, named Module 0, might be invoked in the following modules as well, in order to reduce the number of chemical structures.

2.2.3 Generation of the Binary Core Structures

The next step in our methodology involves generating binary cores based on the frames provided by Module 1. Considering the same composition illustrated in Section 2.2.1, $[\text{Cu}_a\text{Zn}_b]$, we start by taking each frame, with the composition $[\text{Cu}_{(a+b)}]$ or $[\text{Zn}_{(a+b)}]$, and run all possible permutations by replacing the original atoms of the frame with a atoms of Zn and b atoms of Cu.

After generating all permutations, we apply the same connectivity filter used in Module 1 (see Section 2.2.1) to validate the cores produced by this step, which we refer to as Module 2. This filter ensures that the generated cores are chemically reasonable by checking that each atom is within a valid distance range from its nearest neighbors, adhering to the specified covalent-radius tolerance.

The permutation process can generate a large number of structures, especially when a and b are larger. Thus, to manage this potentially large number of structures and identify a small set of representative cores, we can also use the clustering method described in Section 2.2.2. This involves applying the *k-means* clustering method on data represented by the eigenvalues of the Coulomb matrix. This approach ensures that we maintain a diverse yet manageable set of binary core structures for further analysis and optimization. By combining the permutation of elemental compositions and clustering, Module 2 generates valid and representative binary cores based on the initial frames from Module 1.

2.2.4 Low-cost Geometric Optimizations for the Core

At the end of this step, we obtained a set of trial molecular configurations for the core; however, these fragments will be combined with the ligands in the following modules for final total energy optimizations. Therefore, in this step, it is not necessary to perform high-accurate geometry optimizations. Thus, it is recommended to use low-cost DFT calculations. In this step, we used lower-cost geometric optimizations based on smaller basis-set. Therefore, for the examples provided in the following sections, the family of binary cores was submitted at the PBE+TS-vdW optimization level with the *light-tier1* basis-set improvement and light convergence parameters of the FHI-aims¹¹ package. Additional information on the theoretical approach and computational details is provided in Section 2.2.9.

2.2.5 Generation of Sites on the Core Surface

We start by generating a set of n sites (points) uniformly distributed over a sphere that circumscribes the core (one of the fragments of the metal complex). For this purpose, two steps are considered:

- a) We use a Fibonacci approach, named the Fibonacci lattice, to distribute the sites.¹⁷ This method uses the Fibonacci sequence to distribute n points so that they are approximately equidistant from each other on the surface of the sphere;
- b) The sites defined in Step a) undergo a fine adjustment based on a coarse force field process. Each site is considered a charged particle that is loose over the surface of the sphere. Because the particles have the same charge, they repel each other until an equilibrium is reached. In equilibrium, the n points are almost equally spaced on the surface of the sphere.
- c) Furthermore, the defined sites can also be adjusted to the core surface (deformation), which can be activated by the user by selecting the deformation step.

Thus, our implementation provides great flexibility to the generation of the n points on the core region, which is a key part of the algorithm.

2.2.6 Addition of Ligands on the Core Surface

Given the sites, the method will begin to add the ligands selected by the user at a predetermined distance d . An arbitrary number of different ligands can be considered; for example, the user can choose to add m ligands A and n ligands B , e.g., Cp, Cp* for A and B , respectively. The ligands are added to the site using one of two distinct approaches, also selected by the user during the simulation:

- a) The ligands are randomly positioned. In this case, for each ligand, the molecule will be randomly rotated before addition;
- b) The ligands are positioned in an oriented manner. In this scenario, the user must provide a set of atoms from the ligand to orient the positioning.

2.2.7 Complexes Filtering

For large $[Cu_aZn_b]A_mB_n$ complexes with a large number of ligands, the generated structures may exhibit unrealistic configurations, such as closely spaced overlapping atoms, which can lead to issues in electronic structure calculations, i.e., those calculations cannot reach electronic convergence. To address this, we have implemented a filter to prevent atoms from overlapping. When applying this filter, we check if the following condition holds for all possible distances d between atoms a and b :

$$d \geq (r_a + r_b) \times 0.8, \quad (1)$$

where r_a and r_b represent the covalent radii of each pair of atoms a and b , respectively. If any distance between atoms violates this rule, the structure is discarded. The threshold of 0.8 can be adjusted to be more lenient or stricter, depending on the specific requirements.

2.2.8 Representative Complexes via Clustering Algorithm

Finally, since the number of complexes can be very large and with many redundancies (very similar structures), the clustering method depicted in Section 2.2.2 can also be activated to reduce the complexes to a smaller subset of representative molecular structures. Following this methodology, we ensure that the generated complexes are both chemically reasonable and diverse, providing a robust family of structures. Therefore, the combination of the *k-means* algorithm based on a Coulomb representation and the silhouette analysis from multiple runs¹⁶ plays a critical role in selecting the most successful molecular configurations for the evaluation of total energy by geometric optimizations.

2.2.9 Low-cost Geometric Optimization of Metal Complexes

At this step, the final family of $[Cu_aZn_b]R_n$ complexes is externally submitted to DFT calculations with low computational parameters for the self-consistent convergence of the electron density and optimization parameters. For the examples provided in the following sections, these complexes were optimized at the PBE+TS-vdW level with the *light-tier1* basis set and light convergence parameters using the FHI-aims software.¹¹ The optimized set provides

a $[\text{Cu}_a\text{Zn}_b]\text{R}_n$ family of local minimum configurations for each composition of interest, where we expect to find structures that closely resemble those obtained experimentally, as they exhibit lower relative energy. Although additional configurations, particularly those with a great variety of R_n ligands, can be manually designed, in which this final family of complexes can serve as inspiration. Moreover, additional physical-chemical properties observed experimentally for the complexes can guide this design process more efficiently towards new local minimum configurations.

2.2.10 Optimization with Tight Criteria

At this optional step, the selected representative structures via our clustering implementation can be externally submitted to DFT optimization with tight self-consistence parameters and optimization parameters, particularly to perform additional analysis, e.g., NBOs, AIMS, EDA-NOC, and others. Depending on the computational resources, this step can be done previously for a large number of configurations; however, it will increase the computational. From our computational tests, two-step geometric optimization plays an important role in reducing the computational cost.

2.3 Additional Details on the Theoretical Approach and Computational Details for the Optimization Calculations

All *ab initio* total energy calculations were based on spin-polarized DFT within the semi-local exchange-correlation energy functional proposed by Perdew–Burke–Ernzenhof (PBE).¹⁸ To improve the description of weak long-range interactions for all complexes, we used the Tkatchenko–Scheffler (TS) van der Waals (vdW) correction (vdW-TS).¹⁹ In this formalism, the attractive vdW energy correction is added to the plain DFT-PBE total energy.

The calculations were performed in the Fritz—Haber Institute - *Ab initio* Materials simulations (FHI-aims) package,¹¹ where the Kohn–Sham (KS) orbitals were expanded in numerical atom-centered orbitals (NAOs).¹² Specifically, we used the light-tier1 basis (adopting FHI-aims terminology), which are the first basis-set improvement from the free-atom orbitals

minimal basis.²⁰ The electrons were treated within the scalar-relativistic framework using the atomic zeroth-order relativistic approximation (atomic ZORA).²¹

The self-consistent electronic density (SCF) for the complexes was achieved by meeting the following convergence criteria, i.e. a total energy difference of less than 1.00×10^{-4} eV and atomic forces less than 1.00×10^{-2} eV Å⁻¹. Thus, to obtain the equilibrium geometries, we used an atomic force criterion of 1.00×10^{-1} eV Å⁻¹. Furthermore, to ensure the correct occupation of the electronic states, which is crucial for the complexes, we employed a Gaussian broadening parameter of 10 meV for all total energy calculations.

2.4 Cluster_Assembler - Documentation

The `cluster_assembler` package is the workflow implementation used in this work to design the metal complexes within the experimental living library, through DFT *ab initio* calculations combined with machine learning-based algorithms. The source code has been made available to the community under the Apache-2.0 license, accessible at <https://github.com/QTNano/Cluster-Assembler/>. In addition, detailed comments on its functionalities are also provided in the accompanying documentation, which is available at the same link.

1. **Description** – The code provides a general process, divided into four modules (0–3), to generate complexes (core + ligands), i.e., protected clusters. Further details about each step are provided in Section 1 of documentation file.
2. **Recommendations** – Before running the code, the user should check the following observations:
 - (a) If the main directory contains all mandatory files and folders: `main.py`, `mol.txt`, `/core`, `/ligands`, `/bin`, and properly prepared the `input parameters.json` file, which is fully-documented at our repository. Do not exclude the `*.py` files within these folders if you still pretend to run the code. Additional files as `job_pbs` and `environment.yml` are provided to run `cluster_assembler` on HPC facilities within specified Python-modules, respectively;

- (b) Check the installation of Python;
- (c) We strongly recommend installation Anaconda possibly via Anaconda.

3. **Installation** – Before running the code, the user has to mount all python-modules dependencies required for `cluster_assembler` toolbox run without any problem, by executing the following command:

```
$ conda env create -f environment.yml
```

4. **Running the Code** – The user has to set-up the `parameters.json` input file by specifying all the parameters according to the tasks that `cluster_assembler` will perform. Therefore, we recommend that inexperienced users keep advanced parameters set to their `default` values. However, all parameters can be adjusted as needed. Hence, after setting up the `parameters.json` file, the workflow can be started simply by running the following two commands:

```
$ conda activate py396  
$ python3 main.py parameters.json
```

Note that all folders are created in the same working directory where you called `python3 main.py`. Therefore, when the code or parameter file requires an address, e.g., `INPUT_FOLDER`, the user only needs to type the file's name. However, changing the folder directory requires you to provide the complete path for the address.

5. **Module 0 - Mod0** – *k-means* clustering tool to select the representatives unary cores, binary cores, and complexes. Thus, the original *k-means* clustering algorithm is available at https://github.com/quiles/Adsorption_Clus/blob/main/representative.py. However, a modified and enhanced version of *k-means* is internally implemented within `cluster_assembler` code.
6. **Module 1 - Mod1** – In this module, unary cores are generated, processed, analyzed, and clustered. Therefore, users can choose between combining external sources and internally

generating the unary cores using our implemented subroutine. Subsequently, the cores are checked according to the integrity filter and clustered by *k-means* if the RUN_MOD_ZERO flag is activated.

7. **Module 2 - Mod2** – From the unary cores, permutations — i.e., all possible or user-specified —are performed in each of the selected unary cores by an internal subroutine of `cluster_assembler`. Subsequently, the binary cores are checked according to the integrity filter and clustered by *k-means* if the RUN_MOD_ZERO flag is activated.

8. **Module 3 - Mod3** – Module responsible to distribute the ligands around the selected binary cores. Therefore, the ligands file (in *.xyz format) should be prepared beforehand in the `/ligands` folder, particularly when the ligand is oriented distributed. Thus, several ligands might be used in the process. However, their orientation regarding the complex core is controlled by the user, which can select a random or specific orientation (provided by a set of base atoms). An overlap filter iteratively excludes structures with overlapping atoms (integrity). The default threshold is set to $t = 1.25$, and can be manually tuned. The filtered complexes are again clustered by *k-means* if the RUN_MOD_ZERO flag is activated. Finally, the selected structures are the representatives within the living library family of structures, and can be externally optimized using methods such as DFT, Tight-Binding, etc.

9. **Additional Observations** to use the computational implementation:
 - (a) All submission job files for the `cluster_assembler` code at a personal computer (in `job.sh`) and HPC clusters (in `job.pbs`) are provided in the `/jobs` folder;
 - (b) Steps 2 and 3 must be done externally and can be automated using appropriate quantum chemistry software, e.g., FHI-aims, CREST, VASP, ADF;
 - (c) *k-means* needs the Pandas module needs to work properly. However, we strongly suggest the user install Anaconda since Pandas is already a part of Anaconda

distribution.

2.5 Computational Parameters to Generate the Family of Metal Complexes

Above in the Supplementary Table 10, we provide detailed input parameters for generating the $[A_aB_b](C)_c$ metal complexes' family reported herein. To enhance the unary frames set, we incorporated frames from our previous work,²² using DFT-optimized cores of $A_{(a+b)}$ and $B_{(b+a)}$ clusters for *INPUT_DATA*. A reduced final family of $[A_aB_b](C)_c$ complexes, containing the representative structures of the living libraries, was achieved by applying the Module 0 ($k = 15$), depicted on the following section. Based on the physico-chemical properties of this family, additional structures were added to the final set, ensuring a more complete representation of the configuration space by incorporating specific configurations with experimental physico-chemical features.

Supplementary Table 10: Selected input parameters for the `parameters.json` file used as input for the `Cluster_Assembler` code for the generation of the family of $[A_aB_b](C)_c$ metal complexes reported in this work. A reference guide explaining each input parameter can be found at <https://github.com/QTNano/Cluster-Assembler/>. All other parameters were set to their default values.

Complexes $[A_aB_b](C)_c$	Module 1			Module 2			Module 3			Final Family of Optimized $[A_aB_b](C)_c$ Complexes
	$A_{(a+b)}$ and $B_{(b+a)}$ frames	Trial $[A_aB_b]$ cores	Representative $[A_aB_b]$ cores	Optimized $[A_aB_b]$ cores	C Orientation	AB-C Distance (Å)	Trial $[A_aB_b](C)_c$ Complexes	Filtered $[A_aB_b](C)_c$ Complexes	Representative $[A_aB_b](C)_c$ Complexes	
$[\text{Cu}_2\text{Zn}_2](\text{Cp}^*)_3$	40	120	40	40	$\text{Cp}^*[0,1,2]$	2.25	400	*	20	18
$[\text{Cu}_2\text{Zn}_4](\text{Cp}^*)_5$	21	735	200	198	$\text{Cp}^*[0,1,2]$	2.25	1995840	*	300	289
$[\text{Cu}_5\text{Zn}_5](\text{Cp}^*)_6(\text{CO}_2)_2$	40	1080	200	179	$\text{Cp}^*[0,1,2]$ $\text{CO}_2[-1]$ $\text{Cp}^*[0,1,2]$	2.25	2160000	22314	300	208
$[\text{Cu}_6\text{Zn}_5](\text{Cp}^*)_5(\text{Mes})\text{H}_3$	54	7798	120	107	$\text{Mes}[1,1,12,13]$ $\text{H}[-1]$ $\text{Cp}^*[0,1,2]$	2.5	1979500	31873	300	218
$[\text{Cu}_8\text{Zn}_3](\text{Cp}^*)_3(\text{Mes})_4\text{CO}_2$	54	8910	300	278	$\text{Mes}[1,1,12,13]$ $\text{CO}_2[-1]$ $\text{Cp}^*[0,1,2]$	2.5	2085000	176285	300	209
$[\text{Cu}_8\text{Zn}_3](\text{Cp}^*)_4(\text{Mes})_3\text{H}$	54	8910	300	278	$\text{Mes}[1,1,12,13]$ $\text{H}[-1]$ $\text{Cp}^*[1,3,4]$	2.5	2085000	103278	300	159
$[\text{Cu}_9\text{Zn}_7](\text{Cp}^*)_6(\text{Hex})_3\text{H}_3$	200	*	300	291	$\text{Hex}[5,4,3]$ $\text{H}[-1]$ $\text{Cp}^*[0,1,2]$	2.5	2007900	11881	300	43
$[\text{Cu}_{11}\text{Zn}_6](\text{Cp}^*)_8(\text{CO}_2)_2(\text{HCO}_2)$	60	742560	300	290	$\text{CO}_2[-1]$ $\text{HCO}_2[-1]$ $\text{Cp}^*[0,1,2]$	2.5	2001000	3369	300	70
$[\text{Cu}_8\text{Al}_6](\text{Cp}^*)_6$	46	138138	200	197	$\text{Cp}^*[0,1,2]$	2.5	2019250	36176	300	213
$[\text{Ni}(\text{Gac})](\text{Cp}^*)_6$	61	104676	200	196	$\text{Cp}^*[0,1,2]$	2.5	2009000	20856	300	155

2.6 Additional Results for the A_aB_b Cores

Below, we will report all data obtained for the DFT calculations for the core fragments.

2.6.1 [CuZn₂]

Supplementary Table 11: Energetic and electronic properties for [CuZn₂] cores obtained with PBE/light-tier1 level and light SCF parameters: configuration number (i), relative total energy (ΔE_{tot}), total magnetic moment (m_{tot}), HOMO energy (ε_H), LUMO energy (ε_L), and LUMO-HOMO energy gap (E_g).

i	ΔE_{tot} (meV)	m_{tot} (μ_B)	ε_H (eV)	ε_L (eV)	E_g (eV)
39	465	1	-4.20	-3.55	0.66
27	461	1	-4.22	-3.55	0.66
8	453	1	-4.27	-3.58	0.69
9	453	1	-4.27	-3.59	0.68
34	435	1	-4.04	-3.41	0.63
5	433	1	-4.41	-3.73	0.68
31	430	1	-4.06	-3.41	0.65
32	418	1	-4.02	-3.40	0.62
16	417	1	-4.34	-3.65	0.69
14	410	1	-3.95	-3.34	0.62
24	382	1	-3.86	-3.27	0.59
19	356	1	-3.83	-3.24	0.59
2	343	1	-3.78	-3.20	0.59
36	176	1	-4.19	-3.59	0.60
10	174	1	-4.20	-3.60	0.60
12	172	1	-4.19	-3.60	0.60
21	158	1	-4.15	-3.55	0.60
20	143	1	-4.11	-3.52	0.59

Continued on next page

Supplementary Table 11: Energetic and electronic properties for [CuZn₂] cores obtained with PBE/light-tier1 level and light SCF parameters: configuration number (*i*), relative total energy (ΔE_{tot}), total magnetic moment (m_{tot}), HOMO energy (ε_H), LUMO energy (ε_L), and LUMO-HOMO energy gap (E_g).

<i>i</i>	ΔE_{tot}	m_{tot}	ε_H	ε_L	E_g
	(meV)	(μ_B)	(eV)	(eV)	(eV)
38	140	1	-4.09	-3.50	0.59
4	139	1	-4.09	-3.50	0.59
13	138	1	-4.08	-3.50	0.59
22	133	1	-4.06	-3.47	0.59
37	131	1	-4.03	-3.44	0.59
7	116	1	-4.00	-3.41	0.59
40	108	1	-3.94	-3.35	0.59
35	106	1	-3.98	-3.39	0.59
26	98	1	-3.93	-3.35	0.59
30	96	1	-3.94	-3.36	0.59
28	90	1	-3.88	-3.29	0.59
33	70	1	-3.86	-3.28	0.59
29	68	1	-3.84	-3.25	0.59
15	41	1	-3.78	-3.19	0.59
1	40	1	-3.81	-3.23	0.58
6	35	1	-3.76	-3.17	0.59
17	34	1	-3.78	-3.21	0.57
23	33	1	-3.73	-3.13	0.60
11	25	1	-3.75	-3.17	0.58
25	10	1	-3.71	-3.12	0.59
18	4	1	-3.71	-3.13	0.58
3	0	1	-3.69	-3.09	0.59

2.6.2 [Cu₃Zn₄]

The [Cu₃Zn₄] structures were used to design both [Cu₃Zn₄](Cp)₅ and [Cu₃Zn₄](Cp^{*})₅ complexes.

Supplementary Table 12: Energetic and electronic properties for [Cu₃Zn₄] cores obtained with PBE/light-tier1 level and light SCF parameters: configuration number (*i*), relative total energy (ΔE_{tot}), total magnetic moment (m_{tot}), HOMO energy (ε_H), LUMO energy (ε_L), and LUMO-HOMO energy gap (E_g).

<i>i</i>	ΔE_{tot} (meV)	m_{tot} (μ_B)	ε_H (eV)	ε_L (eV)	E_g (eV)
34	1485	3	-3.77	-3.62	0.16
32	1483	3	-3.83	-3.62	0.21
153	1418	3	-4.06	-3.75	0.31
117	1414	3	-4.04	-3.71	0.33
158	1409	3	-3.89	-3.75	0.14
43	1326	3	-3.92	-3.81	0.11
188	1277	1	-3.86	-3.73	0.12
189	1254	1	-4.09	-3.78	0.31
108	1222	3	-3.81	-3.66	0.15
148	1210	1	-3.93	-3.53	0.40
111	1205	1	-3.90	-3.51	0.39
186	1111	1	-3.95	-3.59	0.36
120	1061	1	-4.16	-3.77	0.39
151	1060	1	-4.15	-3.76	0.39
49	1059	3	-3.97	-3.77	0.20
55	1035	3	-4.04	-3.74	0.31
8	996	1	-3.74	-3.35	0.39
33	954	3	-3.89	-3.60	0.30
191	940	1	-4.04	-3.75	0.29

Continued on next page

Supplementary Table 12: Energetic and electronic properties for $[\text{Cu}_3\text{Zn}_4]$ cores obtained with PBE/light-tier1 level and light SCF parameters: configuration number (i), relative total energy (ΔE_{tot}), total magnetic moment (m_{tot}), HOMO energy (ε_H), LUMO energy (ε_L), and LUMO-HOMO energy gap (E_g).

i	ΔE_{tot} (meV)	m_{tot} (μ_B)	ε_H (eV)	ε_L (eV)	E_g (eV)
89	901	1	-4.15	-3.85	0.30
174	888	1	-3.73	-3.37	0.35
199	888	1	-4.38	-4.08	0.29
131	862	1	-3.97	-3.62	0.36
156	860	1	-3.81	-3.51	0.30
1	856	1	-3.92	-3.52	0.40
138	817	1	-4.02	-3.64	0.38
66	809	1	-3.86	-3.48	0.38
5	781	1	-3.94	-3.50	0.45
92	768	1	-3.97	-3.63	0.33
154	768	1	-3.92	-3.51	0.41
197	763	1	-3.66	-3.48	0.18
47	760	1	-3.90	-3.54	0.36
196	712	1	-4.56	-4.29	0.27
143	704	1	-3.84	-3.50	0.34
112	656	1	-4.06	-3.52	0.53
150	653	1	-4.05	-3.52	0.53
100	650	1	-3.88	-3.44	0.44
103	646	1	-3.88	-3.48	0.39
50	646	1	-4.25	-3.86	0.38
162	639	1	-3.54	-3.35	0.19
38	624	1	-3.81	-3.33	0.48

Continued on next page

Supplementary Table 12: Energetic and electronic properties for $[\text{Cu}_3\text{Zn}_4]$ cores obtained with PBE/light-tier1 level and light SCF parameters: configuration number (i), relative total energy (ΔE_{tot}), total magnetic moment (m_{tot}), HOMO energy (ε_H), LUMO energy (ε_L), and LUMO-HOMO energy gap (E_g).

i	ΔE_{tot} (meV)	m_{tot} (μ_B)	ε_H (eV)	ε_L (eV)	E_g (eV)
152	624	1	-3.96	-3.61	0.35
113	621	1	-3.96	-3.59	0.36
68	617	1	-3.84	-3.44	0.40
90	609	1	-3.80	-3.39	0.41
183	595	1	-3.88	-3.48	0.40
13	592	1	-3.77	-3.37	0.40
37	585	1	-3.84	-3.47	0.37
57	581	1	-3.79	-3.38	0.41
18	571	1	-3.61	-3.31	0.30
161	565	1	-3.92	-3.55	0.37
105	563	1	-4.41	-3.94	0.46
46	559	1	-3.94	-3.55	0.39
130	548	1	-4.09	-3.70	0.39
144	544	1	-3.92	-3.57	0.35
132	526	1	-4.06	-3.69	0.37
133	523	1	-3.87	-3.47	0.41
44	521	1	-3.63	-3.27	0.36
95	521	1	-4.11	-3.74	0.37
72	519	1	-4.16	-3.81	0.36
35	488	1	-4.06	-3.74	0.32
110	487	1	-3.94	-3.56	0.37
75	486	1	-3.97	-3.59	0.37

Continued on next page

Supplementary Table 12: Energetic and electronic properties for $[\text{Cu}_3\text{Zn}_4]$ cores obtained with PBE/light-tier1 level and light SCF parameters: configuration number (i), relative total energy (ΔE_{tot}), total magnetic moment (m_{tot}), HOMO energy (ε_H), LUMO energy (ε_L), and LUMO-HOMO energy gap (E_g).

i	ΔE_{tot} (meV)	m_{tot} (μ_B)	ε_H (eV)	ε_L (eV)	E_g (eV)
54	482	1	-3.87	-3.50	0.37
184	480	1	-4.10	-3.70	0.40
147	478	1	-3.92	-3.55	0.37
106	475	1	-4.17	-3.78	0.39
78	472	1	-3.90	-3.56	0.34
195	471	1	-3.78	-3.39	0.39
194	469	1	-4.00	-3.66	0.34
185	468	1	-4.03	-3.69	0.35
22	461	1	-4.06	-3.76	0.30
134	460	1	-3.87	-3.49	0.39
177	459	1	-4.14	-3.75	0.39
198	458	1	-4.14	-3.76	0.38
79	457	1	-3.88	-3.51	0.37
142	455	1	-3.96	-3.59	0.38
64	452	1	-4.06	-3.61	0.45
71	452	1	-3.94	-3.57	0.37
187	445	1	-3.88	-3.49	0.39
31	445	1	-3.89	-3.45	0.44
15	440	1	-3.89	-3.45	0.43
67	439	1	-3.89	-3.48	0.41
168	437	1	-3.98	-3.60	0.38
170	432	1	-3.91	-3.50	0.41

Continued on next page

Supplementary Table 12: Energetic and electronic properties for $[\text{Cu}_3\text{Zn}_4]$ cores obtained with PBE/light-tier1 level and light SCF parameters: configuration number (i), relative total energy (ΔE_{tot}), total magnetic moment (m_{tot}), HOMO energy (ε_H), LUMO energy (ε_L), and LUMO-HOMO energy gap (E_g).

i	ΔE_{tot} (meV)	m_{tot} (μ_B)	ε_H (eV)	ε_L (eV)	E_g (eV)
48	424	1	-3.90	-3.51	0.39
167	420	1	-3.89	-3.51	0.37
73	417	1	-3.73	-3.30	0.44
122	417	1	-3.80	-3.35	0.45
176	407	1	-4.30	-3.93	0.37
107	406	1	-3.71	-3.28	0.43
180	406	1	-3.69	-3.26	0.43
69	399	1	-4.06	-3.54	0.52
7	395	1	-3.91	-3.52	0.38
86	393	1	-4.15	-3.74	0.41
159	387	1	-3.53	-3.12	0.41
42	358	1	-3.93	-3.50	0.44
98	355	1	-4.14	-3.72	0.41
11	354	1	-3.91	-3.62	0.29
115	353	1	-3.96	-3.66	0.30
93	348	1	-3.75	-3.37	0.38
146	342	1	-4.12	-3.80	0.32
172	335	1	-3.81	-3.43	0.38
91	334	1	-4.12	-3.79	0.32
114	334	1	-4.03	-3.72	0.31
3	330	1	-3.90	-3.59	0.31
129	329	1	-3.83	-3.41	0.42

Continued on next page

Supplementary Table 12: Energetic and electronic properties for $[\text{Cu}_3\text{Zn}_4]$ cores obtained with PBE/light-tier1 level and light SCF parameters: configuration number (i), relative total energy (ΔE_{tot}), total magnetic moment (m_{tot}), HOMO energy (ε_H), LUMO energy (ε_L), and LUMO-HOMO energy gap (E_g).

i	ΔE_{tot} (meV)	m_{tot} (μ_B)	ε_H (eV)	ε_L (eV)	E_g (eV)
61	329	1	-3.82	-3.44	0.38
40	325	1	-3.60	-3.21	0.39
63	317	1	-4.02	-3.63	0.39
165	309	1	-3.76	-3.35	0.41
136	309	1	-3.65	-3.26	0.39
76	305	1	-3.87	-3.45	0.43
96	305	1	-4.01	-3.61	0.39
155	301	1	-3.64	-3.19	0.46
23	300	1	-4.02	-3.61	0.41
88	298	1	-4.08	-3.67	0.42
6	287	1	-4.02	-3.49	0.53
128	285	1	-3.86	-3.48	0.38
59	284	1	-3.76	-3.36	0.40
135	283	1	-3.85	-3.41	0.44
81	283	1	-3.82	-3.39	0.44
99	275	1	-3.73	-3.33	0.40
173	275	1	-3.58	-3.10	0.48
65	268	1	-3.76	-3.37	0.39
124	267	1	-3.87	-3.46	0.42
118	265	1	-3.83	-3.44	0.39
140	263	1	-3.46	-3.04	0.42
45	261	1	-3.67	-3.24	0.43

Continued on next page

Supplementary Table 12: Energetic and electronic properties for $[\text{Cu}_3\text{Zn}_4]$ cores obtained with PBE/light-tier1 level and light SCF parameters: configuration number (i), relative total energy (ΔE_{tot}), total magnetic moment (m_{tot}), HOMO energy (ε_H), LUMO energy (ε_L), and LUMO-HOMO energy gap (E_g).

i	ΔE_{tot} (meV)	m_{tot} (μ_B)	ε_H (eV)	ε_L (eV)	E_g (eV)
82	261	1	-3.81	-3.37	0.44
52	260	1	-3.73	-3.35	0.38
9	258	1	-3.86	-3.43	0.42
41	256	1	-3.68	-3.26	0.42
83	256	1	-3.71	-3.28	0.42
53	249	1	-3.70	-3.26	0.43
85	248	1	-3.76	-3.36	0.40
179	248	1	-3.78	-3.33	0.45
97	246	1	-3.84	-3.40	0.44
39	243	1	-3.76	-3.41	0.35
166	243	1	-3.59	-3.12	0.46
51	227	1	-3.87	-3.47	0.40
164	226	1	-3.73	-3.36	0.36
181	225	1	-3.71	-3.35	0.36
182	224	1	-3.61	-3.12	0.49
21	224	1	-3.94	-3.52	0.41
169	224	1	-3.73	-3.29	0.44
24	220	1	-3.89	-3.45	0.44
4	218	1	-3.94	-3.52	0.42
163	214	1	-3.91	-3.50	0.41
30	211	1	-3.83	-3.40	0.42
178	203	1	-3.90	-3.46	0.43

Continued on next page

Supplementary Table 12: Energetic and electronic properties for $[\text{Cu}_3\text{Zn}_4]$ cores obtained with PBE/light-tier1 level and light SCF parameters: configuration number (i), relative total energy (ΔE_{tot}), total magnetic moment (m_{tot}), HOMO energy (ε_H), LUMO energy (ε_L), and LUMO-HOMO energy gap (E_g).

i	ΔE_{tot} (meV)	m_{tot} (μ_B)	ε_H (eV)	ε_L (eV)	E_g (eV)
102	196	1	-3.89	-3.45	0.44
84	191	1	-3.83	-3.38	0.45
109	185	1	-3.83	-3.40	0.43
10	184	1	-3.83	-3.40	0.42
28	181	1	-3.83	-3.40	0.43
20	181	1	-3.86	-3.43	0.43
27	161	1	-3.93	-3.48	0.46
145	154	1	-3.81	-3.43	0.39
17	152	1	-4.05	-3.57	0.48
56	144	1	-3.72	-3.30	0.42
101	142	1	-3.69	-3.27	0.42
29	142	1	-3.85	-3.34	0.51
14	139	1	-4.07	-3.62	0.45
175	138	1	-3.69	-3.28	0.42
123	132	1	-3.84	-3.39	0.45
157	130	1	-3.76	-3.37	0.39
193	128	1	-3.76	-3.36	0.40
116	126	1	-3.78	-3.39	0.39
126	121	1	-3.76	-3.37	0.39
192	117	1	-3.76	-3.37	0.39
119	113	1	-3.74	-3.35	0.39
149	112	1	-3.75	-3.36	0.39

Continued on next page

Supplementary Table 12: Energetic and electronic properties for $[\text{Cu}_3\text{Zn}_4]$ cores obtained with PBE/light-tier1 level and light SCF parameters: configuration number (i), relative total energy (ΔE_{tot}), total magnetic moment (m_{tot}), HOMO energy (ε_H), LUMO energy (ε_L), and LUMO-HOMO energy gap (E_g).

i	ΔE_{tot} (meV)	m_{tot} (μ_B)	ε_H (eV)	ε_L (eV)	E_g (eV)
2	112	1	-3.93	-3.44	0.49
104	111	1	-3.81	-3.37	0.44
139	111	1	-4.04	-3.63	0.41
74	109	1	-3.81	-3.37	0.44
160	109	1	-3.84	-3.32	0.51
127	107	1	-3.81	-3.37	0.44
94	106	1	-4.02	-3.62	0.40
12	105	1	-3.80	-3.35	0.44
62	104	1	-3.80	-3.36	0.44
36	104	1	-3.80	-3.36	0.44
80	102	1	-3.92	-3.52	0.40
77	92	1	-3.97	-3.59	0.38
16	85	1	-3.73	-3.18	0.55
26	82	1	-3.74	-3.19	0.55
60	80	1	-3.99	-3.61	0.37
137	62	1	-3.96	-3.58	0.38
87	11	1	-3.82	-3.37	0.45
19	8	1	-3.79	-3.33	0.45
190	4	1	-3.80	-3.35	0.45
70	3	1	-3.78	-3.32	0.46
58	2	1	-3.80	-3.34	0.46
25	2	1	-3.78	-3.32	0.46

Continued on next page

Supplementary Table 12: Energetic and electronic properties for $[\text{Cu}_3\text{Zn}_4]$ cores obtained with PBE/light-tier1 level and light SCF parameters: configuration number (i), relative total energy (ΔE_{tot}), total magnetic moment (m_{tot}), HOMO energy (ε_H), LUMO energy (ε_L), and LUMO-HOMO energy gap (E_g).

i	ΔE_{tot}	m_{tot}	ε_H	ε_L	E_g
	(meV)	(μ_B)	(eV)	(eV)	(eV)
171	1	1	-3.80	-3.35	0.46
141	1	1	-3.79	-3.33	0.46
125	0	1	-3.78	-3.32	0.46

2.6.3 $[\text{Cu}_5\text{Zn}_5]$

Supplementary Table 13: Energetic and electronic properties for $[\text{Cu}_5\text{Zn}_5]$ cores obtained with PBE/light-tier1 level and light SCF parameters: configuration number (i), relative total energy (ΔE_{tot}), total magnetic moment (m_{tot}), HOMO energy (ε_H), LUMO energy (ε_L), and LUMO-HOMO energy gap (E_g).

i	ΔE_{tot}	m_{tot}	ε_H	ε_L	E_g
	(meV)	(μ_B)	(eV)	(eV)	(eV)
96	1803	3	-3.99	-3.88	0.11
97	1708	3	-4.02	-3.92	0.10
94	1588	3	-4.07	-3.87	0.20
178	1368	1	-3.85	-3.56	0.28
140	1319	3	-4.09	-3.78	0.31
12	1277	3	-4.09	-3.93	0.16
30	1203	3	-4.10	-3.99	0.12
177	1192	1	-3.74	-3.48	0.25
139	1075	1	-4.02	-3.74	0.28
176	1046	1	-3.76	-3.46	0.30
32	1016	1	-4.11	-4.04	0.07

Continued on next page

Supplementary Table 13: Energetic and electronic properties for $[\text{Cu}_5\text{Zn}_5]$ cores obtained with PBE/light-tier1 level and light SCF parameters: configuration number (i), relative total energy (ΔE_{tot}), total magnetic moment (m_{tot}), HOMO energy (ε_H), LUMO energy (ε_L), and LUMO-HOMO energy gap (E_g).

i	ΔE_{tot} (meV)	m_{tot} (μ_B)	ε_H (eV)	ε_L (eV)	E_g (eV)
68	1012	1	-3.95	-3.57	0.38
172	964	1	-3.96	-3.67	0.29
46	963	1	-4.04	-3.76	0.28
11	954	1	-4.15	-3.87	0.27
45	949	1	-3.92	-3.64	0.29
145	938	1	-3.91	-3.61	0.30
36	930	1	-3.75	-3.34	0.41
173	923	1	-4.22	-3.93	0.29
175	922	1	-3.95	-3.69	0.26
91	911	1	-4.21	-3.92	0.29
78	899	1	-3.98	-3.61	0.36
153	892	1	-3.88	-3.62	0.26
60	865	1	-4.12	-3.87	0.25
73	862	1	-3.83	-3.52	0.31
13	858	3	-4.21	-4.07	0.14
155	847	1	-3.77	-3.44	0.33
114	841	1	-3.91	-3.67	0.24
160	830	1	-4.25	-3.93	0.31
82	807	1	-4.30	-4.03	0.27
24	800	1	-4.18	-3.87	0.31
26	799	1	-4.13	-3.78	0.35
93	787	1	-4.04	-3.74	0.31

Continued on next page

Supplementary Table 13: Energetic and electronic properties for $[\text{Cu}_5\text{Zn}_5]$ cores obtained with PBE/light-tier1 level and light SCF parameters: configuration number (i), relative total energy (ΔE_{tot}), total magnetic moment (m_{tot}), HOMO energy (ε_H), LUMO energy (ε_L), and LUMO-HOMO energy gap (E_g).

i	ΔE_{tot} (meV)	m_{tot} (μ_B)	ε_H (eV)	ε_L (eV)	E_g (eV)
22	783	1	-4.03	-3.74	0.29
144	776	1	-3.90	-3.58	0.32
95	750	1	-3.89	-3.57	0.31
119	749	1	-4.13	-3.83	0.29
72	746	1	-4.04	-3.78	0.27
70	742	1	-3.94	-3.63	0.32
41	739	1	-3.85	-3.58	0.27
66	730	1	-4.07	-3.74	0.33
133	720	1	-4.20	-3.95	0.25
25	682	1	-4.10	-3.79	0.30
74	679	1	-4.11	-3.77	0.34
100	677	1	-4.02	-3.74	0.28
143	677	1	-4.14	-3.85	0.28
105	670	1	-3.66	-3.39	0.28
87	662	1	-4.14	-3.84	0.30
54	652	1	-4.14	-3.84	0.30
169	643	1	-3.74	-3.56	0.18
8	639	1	-4.30	-4.06	0.24
99	636	1	-4.18	-3.89	0.29
174	634	1	-4.05	-3.75	0.30
80	627	1	-4.18	-3.87	0.31
122	624	1	-3.89	-3.55	0.34

Continued on next page

Supplementary Table 13: Energetic and electronic properties for $[\text{Cu}_5\text{Zn}_5]$ cores obtained with PBE/light-tier1 level and light SCF parameters: configuration number (i), relative total energy (ΔE_{tot}), total magnetic moment (m_{tot}), HOMO energy (ε_H), LUMO energy (ε_L), and LUMO-HOMO energy gap (E_g).

i	ΔE_{tot} (meV)	m_{tot} (μ_B)	ε_H (eV)	ε_L (eV)	E_g (eV)
149	617	1	-3.74	-3.42	0.32
27	611	1	-4.14	-3.87	0.27
152	608	1	-4.02	-3.74	0.28
37	608	1	-3.88	-3.56	0.33
115	608	1	-4.03	-3.73	0.30
121	605	1	-4.13	-3.82	0.32
179	601	1	-3.78	-3.46	0.32
5	600	1	-4.01	-3.66	0.35
180	597	1	-3.89	-3.61	0.29
39	596	1	-3.97	-3.72	0.25
165	596	1	-3.88	-3.60	0.27
7	590	1	-4.22	-3.93	0.29
132	586	1	-4.16	-3.87	0.29
147	583	1	-3.74	-3.44	0.30
120	579	1	-4.08	-3.75	0.33
104	579	1	-4.09	-3.76	0.33
137	578	1	-3.90	-3.64	0.26
161	578	1	-4.28	-4.00	0.28
103	575	1	-3.81	-3.53	0.28
75	572	1	-4.06	-3.68	0.38
16	567	1	-3.89	-3.76	0.13
18	566	1	-4.23	-3.94	0.28

Continued on next page

Supplementary Table 13: Energetic and electronic properties for $[\text{Cu}_5\text{Zn}_5]$ cores obtained with PBE/light-tier1 level and light SCF parameters: configuration number (i), relative total energy (ΔE_{tot}), total magnetic moment (m_{tot}), HOMO energy (ε_H), LUMO energy (ε_L), and LUMO-HOMO energy gap (E_g).

i	ΔE_{tot} (meV)	m_{tot} (μ_B)	ε_H (eV)	ε_L (eV)	E_g (eV)
90	564	1	-4.09	-3.78	0.32
163	562	1	-3.83	-3.51	0.33
123	558	1	-4.07	-3.79	0.28
156	558	1	-3.83	-3.56	0.27
23	554	1	-4.08	-3.77	0.32
77	553	1	-4.04	-3.66	0.38
1	550	1	-4.06	-3.79	0.26
76	549	1	-4.03	-3.68	0.36
171	545	1	-3.90	-3.61	0.29
62	537	1	-3.99	-3.63	0.37
98	536	1	-3.90	-3.59	0.30
108	529	1	-4.00	-3.70	0.31
124	526	1	-3.80	-3.51	0.29
47	509	1	-4.37	-4.09	0.28
159	509	1	-4.10	-3.81	0.29
112	508	1	-3.78	-3.44	0.34
92	508	1	-4.01	-3.74	0.27
71	505	1	-4.12	-3.76	0.36
128	503	1	-4.39	-4.12	0.27
9	502	1	-3.88	-3.54	0.34
83	499	1	-4.13	-3.84	0.30
157	496	1	-3.83	-3.50	0.33

Continued on next page

Supplementary Table 13: Energetic and electronic properties for $[\text{Cu}_5\text{Zn}_5]$ cores obtained with PBE/light-tier1 level and light SCF parameters: configuration number (i), relative total energy (ΔE_{tot}), total magnetic moment (m_{tot}), HOMO energy (ε_H), LUMO energy (ε_L), and LUMO-HOMO energy gap (E_g).

i	ΔE_{tot} (meV)	m_{tot} (μ_B)	ε_H (eV)	ε_L (eV)	E_g (eV)
35	495	1	-4.03	-3.70	0.33
135	494	1	-4.14	-3.87	0.26
158	490	1	-4.05	-3.76	0.29
106	489	1	-4.15	-3.83	0.33
43	489	1	-3.81	-3.51	0.30
69	486	1	-4.03	-3.74	0.29
3	485	1	-4.02	-3.68	0.34
34	481	1	-3.73	-3.43	0.30
129	479	1	-4.25	-3.99	0.27
134	477	1	-4.24	-3.98	0.26
50	476	1	-4.23	-3.97	0.27
164	470	1	-3.88	-3.61	0.26
146	466	1	-3.83	-3.48	0.35
17	458	1	-4.04	-3.77	0.27
40	454	1	-3.88	-3.58	0.30
101	453	1	-3.76	-3.43	0.33
136	449	1	-4.01	-3.69	0.32
117	434	1	-3.89	-3.59	0.31
131	433	1	-3.97	-3.66	0.31
52	429	1	-3.97	-3.64	0.33
21	428	1	-4.13	-3.76	0.37
142	428	1	-3.89	-3.57	0.32

Continued on next page

Supplementary Table 13: Energetic and electronic properties for $[\text{Cu}_5\text{Zn}_5]$ cores obtained with PBE/light-tier1 level and light SCF parameters: configuration number (i), relative total energy (ΔE_{tot}), total magnetic moment (m_{tot}), HOMO energy (ε_H), LUMO energy (ε_L), and LUMO-HOMO energy gap (E_g).

i	ΔE_{tot} (meV)	m_{tot} (μ_B)	ε_H (eV)	ε_L (eV)	E_g (eV)
84	427	1	-4.21	-3.96	0.25
53	423	1	-4.14	-3.77	0.38
20	420	1	-3.79	-3.48	0.32
130	413	1	-4.22	-3.95	0.27
42	411	1	-4.04	-3.63	0.41
56	398	1	-3.93	-3.58	0.36
138	397	1	-3.98	-3.69	0.29
64	396	1	-3.97	-3.64	0.33
15	394	1	-3.90	-3.58	0.32
148	386	1	-3.85	-3.56	0.30
79	385	1	-3.93	-3.61	0.32
150	379	1	-3.98	-3.65	0.33
89	375	1	-3.80	-3.53	0.28
167	372	1	-3.89	-3.61	0.28
65	369	1	-3.76	-3.45	0.31
38	367	1	-4.17	-3.84	0.32
4	364	1	-3.86	-3.48	0.38
67	357	1	-4.16	-3.80	0.36
151	355	1	-4.16	-3.87	0.30
125	355	1	-4.03	-3.70	0.33
2	350	1	-3.94	-3.60	0.34
141	346	1	-3.89	-3.57	0.32

Continued on next page

Supplementary Table 13: Energetic and electronic properties for $[\text{Cu}_5\text{Zn}_5]$ cores obtained with PBE/light-tier1 level and light SCF parameters: configuration number (i), relative total energy (ΔE_{tot}), total magnetic moment (m_{tot}), HOMO energy (ε_H), LUMO energy (ε_L), and LUMO-HOMO energy gap (E_g).

i	ΔE_{tot} (meV)	m_{tot} (μ_B)	ε_H (eV)	ε_L (eV)	E_g (eV)
88	344	1	-3.95	-3.65	0.30
166	341	1	-3.78	-3.50	0.28
29	337	1	-3.89	-3.58	0.31
86	331	1	-4.05	-3.78	0.27
28	328	1	-3.91	-3.63	0.28
102	327	1	-4.13	-3.82	0.31
63	318	1	-3.95	-3.64	0.31
110	307	1	-4.13	-3.86	0.28
85	300	1	-4.10	-3.79	0.31
58	299	1	-3.88	-3.53	0.36
116	298	1	-4.05	-3.78	0.28
55	294	1	-4.02	-3.68	0.34
154	291	1	-3.98	-3.68	0.30
33	291	1	-4.11	-3.81	0.30
168	284	1	-3.76	-3.45	0.30
170	280	1	-3.79	-3.48	0.31
127	279	1	-4.01	-3.75	0.25
113	279	1	-3.77	-3.47	0.30
31	252	1	-3.90	-3.59	0.31
19	243	1	-4.02	-3.70	0.32
107	241	1	-3.85	-3.55	0.30
126	200	1	-3.89	-3.59	0.31

Continued on next page

Supplementary Table 13: Energetic and electronic properties for $[\text{Cu}_5\text{Zn}_5]$ cores obtained with PBE/light-tier1 level and light SCF parameters: configuration number (i), relative total energy (ΔE_{tot}), total magnetic moment (m_{tot}), HOMO energy (ε_H), LUMO energy (ε_L), and LUMO-HOMO energy gap (E_g).

i	ΔE_{tot} (meV)	m_{tot} (μ_B)	ε_H (eV)	ε_L (eV)	E_g (eV)
48	195	1	-4.05	-3.75	0.29
118	194	1	-3.82	-3.51	0.32
111	185	1	-3.84	-3.50	0.34
44	183	1	-4.06	-3.75	0.31
57	181	1	-3.81	-3.52	0.29
14	179	1	-3.90	-3.61	0.29
61	174	1	-3.68	-3.35	0.33
51	155	1	-4.18	-3.89	0.30
6	150	1	-3.96	-3.62	0.34
10	148	1	-3.83	-3.47	0.35
109	146	1	-3.97	-3.65	0.32
59	135	1	-3.69	-3.35	0.34
49	134	1	-4.10	-3.81	0.29
81	107	1	-3.86	-3.51	0.35
162	0	1	-3.88	-3.54	0.34

2.6.4 $[\text{Cu}_6\text{Zn}_5]$

Supplementary Table 14: Energetic and electronic properties for $[\text{Cu}_6\text{Zn}_5]$ cores obtained with PBE/light-tier1 level and light SCF parameters: configuration number (i), relative total energy (ΔE_{tot}), total magnetic moment (m_{tot}), HOMO energy (ε_H), LUMO energy (ε_L), and LUMO-HOMO energy gap (E_g).

i	ΔE_{tot} (meV)	m_{tot} (μ_B)	ε_H (eV)	ε_L (eV)	E_g (eV)
99	2580	2	-4.17	-4.00	0.17
52	1584	2	-3.98	-3.88	0.10
30	1549	2	-3.96	-3.67	0.29
47	1530	2	-3.73	-3.62	0.10
115	1503	0	-4.40	-3.13	1.27
100	1464	2	-3.84	-3.56	0.27
97	1455	2	-4.05	-3.83	0.21
28	1420	2	-3.81	-3.60	0.21
116	1397	0	-4.21	-3.10	1.11
33	1360	2	-4.12	-3.89	0.23
34	1349	0	-4.14	-4.03	0.11
96	1339	2	-4.04	-3.85	0.19
87	1338	2	-4.24	-4.06	0.18
11	1325	2	-3.92	-3.82	0.10
37	1290	0	-4.24	-3.89	0.35
36	1262	0	-4.26	-4.03	0.23
118	1246	2	-4.01	-3.76	0.25
117	1221	0	-4.22	-3.13	1.09
5	1200	2	-4.16	-3.80	0.36
75	1161	2	-3.80	-3.71	0.09
39	1158	0	-4.24	-3.62	0.62
114	1151	0	-4.29	-3.03	1.27

Continued on next page

Supplementary Table 14: Energetic and electronic properties for $[\text{Cu}_6\text{Zn}_5]$ cores obtained with PBE/light-tier1 level and light SCF parameters: configuration number (i), relative total energy (ΔE_{tot}), total magnetic moment (m_{tot}), HOMO energy (ε_H), LUMO energy (ε_L), and LUMO-HOMO energy gap (E_g).

i	ΔE_{tot} (meV)	m_{tot} (μ_B)	ε_H (eV)	ε_L (eV)	E_g (eV)
88	1144	0	-4.36	-3.86	0.50
32	1129	2	-4.07	-3.85	0.23
20	1125	2	-4.26	-4.12	0.14
35	1121	2	-4.26	-4.05	0.21
103	1107	2	-3.90	-3.75	0.15
66	1098	2	-4.06	-3.76	0.30
53	1098	0	-4.48	-3.70	0.78
23	1084	2	-4.00	-3.89	0.12
79	1083	0	-4.43	-3.50	0.93
106	1074	0	-4.45	-3.78	0.67
63	1011	0	-4.31	-3.29	1.02
78	996	2	-4.17	-3.98	0.20
60	968	0	-4.34	-3.86	0.48
86	955	0	-4.29	-3.94	0.35
8	955	0	-4.29	-3.60	0.69
68	951	2	-4.01	-3.89	0.12
51	937	0	-4.40	-3.63	0.77
29	936	0	-4.30	-3.25	1.06
69	933	2	-4.06	-3.82	0.25
9	924	0	-4.18	-3.66	0.53
77	923	0	-4.15	-3.31	0.84
62	910	0	-4.33	-3.35	0.98

Continued on next page

Supplementary Table 14: Energetic and electronic properties for $[\text{Cu}_6\text{Zn}_5]$ cores obtained with PBE/light-tier1 level and light SCF parameters: configuration number (i), relative total energy (ΔE_{tot}), total magnetic moment (m_{tot}), HOMO energy (ε_H), LUMO energy (ε_L), and LUMO-HOMO energy gap (E_g).

i	ΔE_{tot} (meV)	m_{tot} (μ_B)	ε_H (eV)	ε_L (eV)	E_g (eV)
55	858	2	-4.09	-3.80	0.29
119	853	0	-4.44	-3.59	0.85
45	853	2	-4.03	-3.92	0.12
17	850	0	-4.43	-3.33	1.11
43	838	0	-4.42	-3.88	0.55
73	836	0	-4.31	-3.30	1.01
21	834	0	-4.40	-3.55	0.85
104	831	0	-4.32	-3.31	1.00
26	829	2	-4.15	-4.06	0.09
90	825	0	-4.24	-3.04	1.20
85	810	0	-4.39	-3.81	0.58
95	810	2	-4.06	-3.86	0.20
89	809	2	-4.10	-3.97	0.12
80	804	0	-4.46	-3.65	0.81
15	803	0	-4.11	-3.48	0.62
16	802	0	-4.13	-3.49	0.64
102	778	0	-4.35	-3.14	1.21
4	754	0	-4.10	-3.17	0.93
93	751	0	-4.22	-3.11	1.12
50	742	0	-4.20	-3.71	0.49
101	730	0	-4.34	-3.10	1.24
111	718	0	-4.43	-3.25	1.18

Continued on next page

Supplementary Table 14: Energetic and electronic properties for $[\text{Cu}_6\text{Zn}_5]$ cores obtained with PBE/light-tier1 level and light SCF parameters: configuration number (i), relative total energy (ΔE_{tot}), total magnetic moment (m_{tot}), HOMO energy (ε_H), LUMO energy (ε_L), and LUMO-HOMO energy gap (E_g).

i	ΔE_{tot} (meV)	m_{tot} (μ_B)	ε_H (eV)	ε_L (eV)	E_g (eV)
72	716	0	-4.32	-3.36	0.96
6	706	0	-4.40	-3.15	1.25
18	693	0	-4.30	-3.47	0.84
3	688	0	-4.29	-3.75	0.55
48	678	0	-4.41	-3.25	1.16
61	675	0	-4.21	-3.20	1.01
64	663	0	-4.32	-3.75	0.57
76	658	0	-4.18	-3.26	0.92
98	652	0	-4.28	-3.71	0.57
105	631	0	-4.22	-3.13	1.10
1	628	0	-4.35	-3.78	0.57
56	617	0	-4.44	-3.36	1.08
31	606	0	-4.46	-3.47	0.99
41	594	2	-4.14	-3.87	0.27
57	590	0	-4.35	-3.41	0.94
12	588	0	-4.17	-3.87	0.31
25	571	0	-4.28	-3.63	0.65
59	548	0	-4.47	-3.64	0.84
91	542	0	-4.17	-3.58	0.59
40	540	2	-4.22	-4.09	0.13
42	533	0	-4.23	-3.72	0.51
82	497	0	-4.28	-3.71	0.57

Continued on next page

Supplementary Table 14: Energetic and electronic properties for $[\text{Cu}_6\text{Zn}_5]$ cores obtained with PBE/light-tier1 level and light SCF parameters: configuration number (i), relative total energy (ΔE_{tot}), total magnetic moment (m_{tot}), HOMO energy (ε_H), LUMO energy (ε_L), and LUMO-HOMO energy gap (E_g).

i	ΔE_{tot} (meV)	m_{tot} (μ_B)	ε_H (eV)	ε_L (eV)	E_g (eV)
38	494	0	-4.32	-3.39	0.93
19	449	0	-4.34	-3.23	1.11
22	449	0	-4.39	-3.55	0.84
109	445	0	-4.47	-3.04	1.43
10	438	0	-4.38	-3.28	1.11
112	397	0	-4.41	-3.33	1.07
70	388	2	-4.04	-3.77	0.27
107	382	0	-4.34	-3.68	0.66
92	367	0	-4.26	-3.15	1.11
65	332	0	-4.14	-3.84	0.30
67	285	0	-4.27	-3.69	0.59
71	277	0	-4.46	-3.40	1.06
24	259	0	-4.42	-3.78	0.64
44	171	0	-4.35	-3.77	0.58
94	160	0	-4.57	-3.81	0.76
108	105	0	-4.39	-2.92	1.47
2	83	0	-4.56	-3.83	0.73
13	66	0	-4.31	-3.80	0.52
14	26	0	-4.42	-3.84	0.58
7	0	0	-4.43	-3.73	0.70

2.6.5 [Cu₈Zn₃]

The [Cu₈Zn₃] structures were used to design both [Cu₈Zn₃](Cp^{*})₃(Mes)₄CO₂ and [Cu₈Zn₃](Cp^{*})₄(Mes)₃H complexes.

Supplementary Table 15: Energetic and electronic properties for [Cu₈Zn₃] cores obtained with PBE/light-tier1 level and light SCF parameters: configuration number (*i*), relative total energy (ΔE_{tot}), total magnetic moment (m_{tot}), HOMO energy (ε_H), LUMO energy (ε_L), and LUMO-HOMO energy gap (E_g).

<i>i</i>	ΔE_{tot} (meV)	m_{tot} (μ_B)	ε_H (eV)	ε_L (eV)	E_g (eV)
161	2299	4	-4.00	-3.94	0.06
109	2147	2	-4.15	-3.93	0.22
181	2134	4	-3.95	-3.80	0.14
165	1876	2	-3.98	-3.75	0.23
230	1867	2	-3.94	-3.66	0.28
106	1730	2	-4.25	-3.96	0.29
220	1726	4	-3.87	-3.67	0.20
87	1718	4	-4.11	-4.02	0.09
209	1711	4	-4.12	-4.01	0.11
239	1710	2	-4.15	-3.93	0.22
179	1693	2	-3.92	-3.69	0.23
160	1691	2	-3.94	-3.64	0.30
243	1666	2	-4.11	-3.93	0.18
216	1611	4	-3.88	-3.70	0.18
108	1597	0	-4.10	-3.85	0.25
86	1580	2	-4.13	-3.98	0.15
274	1575	2	-3.86	-3.66	0.20
279	1565	2	-4.03	-3.94	0.09
259	1565	2	-3.80	-3.53	0.27

Continued on next page

Supplementary Table 15: Energetic and electronic properties for $[\text{Cu}_8\text{Zn}_3]$ cores obtained with PBE/light-tier1 level and light SCF parameters: configuration number (i), relative total energy (ΔE_{tot}), total magnetic moment (m_{tot}), HOMO energy (ε_H), LUMO energy (ε_L), and LUMO-HOMO energy gap (E_g).

i	ΔE_{tot} (meV)	m_{tot} (μ_B)	ε_H (eV)	ε_L (eV)	E_g (eV)
215	1556	0	-4.19	-3.50	0.69
89	1555	2	-4.12	-3.99	0.13
159	1550	2	-3.85	-3.59	0.26
144	1544	2	-3.77	-3.68	0.10
81	1535	2	-4.06	-3.81	0.25
158	1498	2	-3.91	-3.67	0.25
253	1495	2	-3.77	-3.69	0.08
162	1491	2	-3.77	-3.70	0.07
227	1471	2	-3.97	-3.65	0.32
265	1446	0	-4.19	-3.56	0.63
57	1437	2	-4.04	-3.97	0.07
260	1433	2	-3.81	-3.74	0.07
282	1428	0	-4.06	-3.19	0.87
222	1417	2	-3.91	-3.75	0.16
110	1413	2	-4.05	-3.93	0.12
241	1399	2	-3.90	-3.77	0.12
180	1377	2	-4.06	-3.76	0.29
262	1373	2	-3.75	-3.61	0.15
84	1369	2	-4.11	-3.79	0.32
22	1369	2	-4.13	-3.82	0.31
248	1367	2	-3.66	-3.42	0.24
199	1366	2	-3.93	-3.67	0.26

Continued on next page

Supplementary Table 15: Energetic and electronic properties for $[\text{Cu}_8\text{Zn}_3]$ cores obtained with PBE/light-tier1 level and light SCF parameters: configuration number (i), relative total energy (ΔE_{tot}), total magnetic moment (m_{tot}), HOMO energy (ε_H), LUMO energy (ε_L), and LUMO-HOMO energy gap (E_g).

i	ΔE_{tot} (meV)	m_{tot} (μ_B)	ε_H (eV)	ε_L (eV)	E_g (eV)
212	1365	2	-4.12	-3.83	0.29
82	1361	2	-4.08	-3.84	0.24
252	1357	0	-4.38	-3.58	0.80
41	1355	2	-3.89	-3.76	0.13
261	1344	2	-3.84	-3.70	0.13
147	1317	2	-3.80	-3.71	0.10
278	1290	2	-3.90	-3.72	0.18
76	1274	2	-4.03	-3.95	0.08
39	1266	2	-3.96	-3.92	0.03
242	1264	2	-3.90	-3.80	0.10
290	1259	2	-3.83	-3.69	0.14
68	1251	2	-3.83	-3.72	0.11
130	1248	0	-4.12	-3.77	0.35
257	1222	0	-4.10	-3.28	0.83
271	1210	0	-4.18	-3.72	0.46
119	1193	2	-3.84	-3.70	0.14
145	1184	2	-3.83	-3.71	0.12
83	1179	0	-4.07	-3.58	0.49
213	1175	0	-4.08	-3.57	0.50
66	1170	0	-4.11	-3.60	0.52
131	1166	0	-4.18	-3.58	0.60
67	1151	2	-3.93	-3.82	0.11

Continued on next page

Supplementary Table 15: Energetic and electronic properties for $[\text{Cu}_8\text{Zn}_3]$ cores obtained with PBE/light-tier1 level and light SCF parameters: configuration number (i), relative total energy (ΔE_{tot}), total magnetic moment (m_{tot}), HOMO energy (ε_H), LUMO energy (ε_L), and LUMO-HOMO energy gap (E_g).

i	ΔE_{tot} (meV)	m_{tot} (μ_B)	ε_H (eV)	ε_L (eV)	E_g (eV)
75	1149	2	-4.07	-3.97	0.10
34	1127	2	-4.21	-4.08	0.14
263	1126	0	-4.17	-3.25	0.92
185	1114	0	-4.15	-3.34	0.80
122	1112	2	-3.91	-3.61	0.30
146	1109	2	-3.98	-3.72	0.26
56	1103	0	-4.15	-3.56	0.59
286	1098	0	-4.65	-3.30	1.35
121	1072	2	-3.87	-3.63	0.24
25	1052	2	-4.09	-3.98	0.11
28	1050	2	-4.12	-3.90	0.22
156	1048	2	-3.83	-3.77	0.06
143	1042	2	-3.83	-3.60	0.24
182	1040	0	-4.03	-3.41	0.62
35	1031	2	-4.14	-4.05	0.09
92	1029	2	-3.94	-3.80	0.13
74	1025	0	-4.29	-3.80	0.49
80	1021	0	-4.08	-3.66	0.43
136	1010	2	-3.95	-3.74	0.21
47	1006	2	-4.07	-3.85	0.22
247	999	0	-4.22	-3.28	0.93
50	992	0	-4.28	-3.68	0.60

Continued on next page

Supplementary Table 15: Energetic and electronic properties for $[\text{Cu}_8\text{Zn}_3]$ cores obtained with PBE/light-tier1 level and light SCF parameters: configuration number (i), relative total energy (ΔE_{tot}), total magnetic moment (m_{tot}), HOMO energy (ε_H), LUMO energy (ε_L), and LUMO-HOMO energy gap (E_g).

i	ΔE_{tot} (meV)	m_{tot} (μ_B)	ε_H (eV)	ε_L (eV)	E_g (eV)
12	988	2	-3.89	-3.72	0.17
43	983	2	-3.85	-3.75	0.10
258	980	0	-4.09	-3.34	0.75
27	979	2	-4.04	-3.93	0.11
284	975	0	-4.46	-3.26	1.19
235	972	0	-4.23	-3.87	0.37
5	970	2	-4.06	-3.84	0.22
8	969	2	-3.94	-3.77	0.16
210	961	0	-4.07	-3.53	0.54
19	960	2	-3.81	-3.66	0.14
69	955	2	-4.00	-3.74	0.26
183	954	0	-4.06	-3.30	0.76
153	952	0	-4.11	-3.64	0.47
206	948	2	-4.01	-3.76	0.25
238	945	0	-4.29	-3.98	0.31
52	943	2	-3.89	-3.80	0.09
276	942	0	-4.31	-3.44	0.87
102	930	0	-4.16	-3.72	0.44
224	919	2	-3.82	-3.65	0.17
117	917	0	-4.01	-3.38	0.63
78	914	0	-4.18	-3.64	0.54
285	911	0	-4.43	-3.25	1.18

Continued on next page

Supplementary Table 15: Energetic and electronic properties for $[\text{Cu}_8\text{Zn}_3]$ cores obtained with PBE/light-tier1 level and light SCF parameters: configuration number (i), relative total energy (ΔE_{tot}), total magnetic moment (m_{tot}), HOMO energy (ε_H), LUMO energy (ε_L), and LUMO-HOMO energy gap (E_g).

i	ΔE_{tot} (meV)	m_{tot} (μ_B)	ε_H (eV)	ε_L (eV)	E_g (eV)
138	909	2	-3.85	-3.72	0.13
155	906	0	-4.27	-3.67	0.60
283	906	0	-4.54	-3.11	1.43
140	899	2	-3.79	-3.51	0.28
281	895	0	-4.58	-3.36	1.21
93	885	2	-3.90	-3.71	0.20
101	869	2	-4.09	-4.03	0.06
267	868	0	-4.19	-3.47	0.72
275	863	0	-4.31	-3.30	1.01
133	857	2	-3.98	-3.85	0.14
139	855	2	-3.81	-3.65	0.16
115	851	2	-4.01	-3.89	0.12
264	846	0	-4.31	-3.24	1.07
149	842	0	-4.28	-3.55	0.73
137	833	2	-3.79	-3.52	0.28
33	832	0	-4.14	-3.75	0.39
118	830	0	-4.21	-3.39	0.82
225	829	0	-4.36	-3.27	1.09
18	827	2	-3.86	-3.67	0.19
17	824	2	-4.01	-3.81	0.20
120	818	0	-4.24	-3.51	0.73
85	817	0	-4.05	-3.61	0.44

Continued on next page

Supplementary Table 15: Energetic and electronic properties for $[\text{Cu}_8\text{Zn}_3]$ cores obtained with PBE/light-tier1 level and light SCF parameters: configuration number (i), relative total energy (ΔE_{tot}), total magnetic moment (m_{tot}), HOMO energy (ε_H), LUMO energy (ε_L), and LUMO-HOMO energy gap (E_g).

i	ΔE_{tot} (meV)	m_{tot} (μ_B)	ε_H (eV)	ε_L (eV)	E_g (eV)
13	813	2	-3.95	-3.74	0.22
88	811	2	-3.91	-3.80	0.11
29	810	2	-3.81	-3.64	0.17
96	792	2	-4.02	-3.78	0.24
112	792	2	-3.89	-3.72	0.16
114	788	2	-3.90	-3.88	0.03
30	781	2	-3.96	-3.93	0.03
3	779	2	-4.06	-3.91	0.15
214	764	2	-4.11	-4.03	0.08
277	760	0	-4.39	-3.34	1.06
90	756	0	-4.10	-3.57	0.54
240	751	0	-4.19	-3.41	0.78
232	744	0	-4.18	-3.69	0.49
36	744	0	-4.36	-3.79	0.57
37	741	0	-4.08	-3.39	0.68
198	739	0	-4.41	-3.44	0.97
26	739	0	-4.19	-3.60	0.58
48	737	0	-3.96	-3.56	0.40
172	733	0	-4.24	-3.10	1.13
233	732	0	-4.26	-3.75	0.51
46	727	0	-4.30	-3.56	0.75
125	724	0	-4.26	-3.29	0.96

Continued on next page

Supplementary Table 15: Energetic and electronic properties for $[\text{Cu}_8\text{Zn}_3]$ cores obtained with PBE/light-tier1 level and light SCF parameters: configuration number (i), relative total energy (ΔE_{tot}), total magnetic moment (m_{tot}), HOMO energy (ε_H), LUMO energy (ε_L), and LUMO-HOMO energy gap (E_g).

i	ΔE_{tot} (meV)	m_{tot} (μ_B)	ε_H (eV)	ε_L (eV)	E_g (eV)
91	715	0	-4.07	-3.46	0.61
134	706	0	-4.13	-3.56	0.57
38	695	0	-4.23	-3.65	0.58
59	692	0	-4.16	-3.46	0.71
229	690	0	-4.36	-3.44	0.92
127	683	0	-4.49	-3.67	0.82
184	682	0	-4.25	-3.40	0.84
16	681	0	-4.27	-3.47	0.81
268	677	0	-4.46	-3.55	0.91
211	674	2	-3.91	-3.75	0.16
49	659	0	-4.27	-3.47	0.80
178	657	0	-4.06	-3.57	0.49
251	655	0	-4.12	-3.43	0.70
65	650	0	-4.32	-3.28	1.04
70	645	0	-4.24	-3.27	0.97
197	644	0	-4.08	-3.42	0.66
128	626	0	-4.15	-3.60	0.55
9	626	0	-3.93	-3.43	0.50
23	622	2	-3.87	-3.76	0.11
132	622	0	-4.40	-3.60	0.80
204	611	0	-4.05	-3.58	0.48
53	610	0	-4.29	-3.33	0.96

Continued on next page

Supplementary Table 15: Energetic and electronic properties for $[\text{Cu}_8\text{Zn}_3]$ cores obtained with PBE/light-tier1 level and light SCF parameters: configuration number (i), relative total energy (ΔE_{tot}), total magnetic moment (m_{tot}), HOMO energy (ε_H), LUMO energy (ε_L), and LUMO-HOMO energy gap (E_g).

i	ΔE_{tot} (meV)	m_{tot} (μ_B)	ε_H (eV)	ε_L (eV)	E_g (eV)
40	608	0	-4.23	-3.86	0.37
221	606	0	-4.36	-3.16	1.21
154	604	0	-4.03	-3.70	0.34
126	603	0	-4.30	-3.56	0.74
244	599	0	-4.18	-3.51	0.67
270	595	0	-4.30	-3.55	0.75
7	592	2	-3.98	-3.68	0.30
124	592	0	-4.08	-3.44	0.64
62	591	0	-4.25	-3.52	0.73
150	590	0	-4.10	-3.41	0.68
195	589	0	-4.19	-3.40	0.79
280	585	0	-4.41	-3.04	1.37
151	583	0	-4.04	-3.62	0.41
237	576	0	-4.21	-3.75	0.46
187	575	0	-4.12	-3.61	0.51
272	565	0	-4.26	-3.53	0.73
6	551	0	-4.19	-3.57	0.62
77	549	0	-4.32	-3.17	1.15
171	542	0	-4.29	-3.53	0.77
107	533	0	-4.27	-3.62	0.65
202	532	0	-4.22	-3.68	0.53
44	516	0	-4.32	-3.41	0.91

Continued on next page

Supplementary Table 15: Energetic and electronic properties for $[\text{Cu}_8\text{Zn}_3]$ cores obtained with PBE/light-tier1 level and light SCF parameters: configuration number (i), relative total energy (ΔE_{tot}), total magnetic moment (m_{tot}), HOMO energy (ε_H), LUMO energy (ε_L), and LUMO-HOMO energy gap (E_g).

i	ΔE_{tot} (meV)	m_{tot} (μ_B)	ε_H (eV)	ε_L (eV)	E_g (eV)
200	512	0	-4.22	-3.44	0.78
63	511	0	-4.26	-3.25	1.01
10	500	0	-4.28	-3.48	0.80
218	499	0	-4.14	-3.49	0.66
226	498	0	-4.49	-3.43	1.06
287	497	0	-4.12	-3.13	0.99
188	491	0	-4.18	-3.50	0.67
236	486	0	-4.34	-3.84	0.49
72	485	0	-4.17	-3.36	0.80
97	484	0	-4.21	-3.45	0.76
4	480	0	-4.26	-3.51	0.75
167	479	0	-4.21	-3.64	0.57
100	478	0	-4.22	-3.74	0.48
103	477	0	-4.32	-3.66	0.67
203	476	0	-4.38	-3.36	1.02
148	473	0	-4.33	-3.60	0.72
168	466	0	-4.23	-3.67	0.56
104	466	0	-4.35	-3.64	0.71
234	460	0	-4.32	-3.61	0.71
207	456	0	-4.23	-3.57	0.66
192	456	0	-4.17	-3.56	0.61
152	452	0	-4.22	-3.54	0.68

Continued on next page

Supplementary Table 15: Energetic and electronic properties for $[\text{Cu}_8\text{Zn}_3]$ cores obtained with PBE/light-tier1 level and light SCF parameters: configuration number (i), relative total energy (ΔE_{tot}), total magnetic moment (m_{tot}), HOMO energy (ε_H), LUMO energy (ε_L), and LUMO-HOMO energy gap (E_g).

i	ΔE_{tot} (meV)	m_{tot} (μ_B)	ε_H (eV)	ε_L (eV)	E_g (eV)
289	451	0	-4.38	-3.39	0.98
61	448	0	-4.24	-3.23	1.01
113	443	0	-4.31	-3.54	0.78
45	441	0	-4.42	-3.32	1.11
256	440	0	-4.32	-3.16	1.16
273	438	0	-4.42	-3.66	0.75
11	436	0	-4.39	-3.69	0.70
94	426	0	-4.17	-3.49	0.68
129	417	0	-4.08	-3.27	0.81
201	404	0	-4.27	-3.38	0.89
245	391	0	-4.29	-3.18	1.10
174	391	0	-4.18	-3.39	0.80
14	382	0	-4.33	-3.51	0.82
111	379	0	-4.27	-3.56	0.71
173	373	0	-4.35	-3.58	0.76
176	362	0	-4.30	-3.62	0.68
166	359	0	-4.25	-3.52	0.72
191	358	0	-4.27	-3.37	0.90
98	355	0	-4.20	-3.46	0.74
141	354	0	-4.21	-3.47	0.74
60	351	0	-4.26	-3.27	0.99
20	345	0	-4.21	-3.42	0.79

Continued on next page

Supplementary Table 15: Energetic and electronic properties for $[\text{Cu}_8\text{Zn}_3]$ cores obtained with PBE/light-tier1 level and light SCF parameters: configuration number (i), relative total energy (ΔE_{tot}), total magnetic moment (m_{tot}), HOMO energy (ε_H), LUMO energy (ε_L), and LUMO-HOMO energy gap (E_g).

i	ΔE_{tot} (meV)	m_{tot} (μ_B)	ε_H (eV)	ε_L (eV)	E_g (eV)
219	342	0	-4.28	-3.62	0.66
269	338	0	-4.28	-3.40	0.88
73	336	0	-4.30	-3.22	1.08
54	327	0	-4.24	-3.43	0.81
194	320	0	-4.21	-3.46	0.76
31	316	0	-4.31	-3.28	1.02
142	307	0	-4.37	-3.22	1.16
163	301	0	-4.28	-3.40	0.88
177	299	0	-4.39	-3.13	1.26
175	290	0	-4.24	-3.31	0.92
249	287	0	-4.46	-3.29	1.16
217	276	0	-4.16	-3.42	0.74
288	275	0	-4.44	-3.32	1.12
170	273	0	-4.29	-3.38	0.91
58	256	0	-4.27	-3.51	0.76
123	253	0	-4.33	-3.22	1.11
169	250	0	-4.21	-3.57	0.64
51	243	0	-4.20	-3.25	0.95
55	240	0	-4.26	-3.32	0.95
223	226	0	-4.39	-3.60	0.80
1	220	0	-4.31	-3.62	0.70
266	218	0	-4.45	-3.43	1.03

Continued on next page

Supplementary Table 15: Energetic and electronic properties for $[\text{Cu}_8\text{Zn}_3]$ cores obtained with PBE/light-tier1 level and light SCF parameters: configuration number (i), relative total energy (ΔE_{tot}), total magnetic moment (m_{tot}), HOMO energy (ε_H), LUMO energy (ε_L), and LUMO-HOMO energy gap (E_g).

i	ΔE_{tot} (meV)	m_{tot} (μ_B)	ε_H (eV)	ε_L (eV)	E_g (eV)
164	217	0	-4.17	-3.42	0.75
193	209	0	-4.40	-3.23	1.17
228	194	0	-4.30	-3.31	0.99
190	180	0	-4.42	-3.30	1.12
196	175	0	-4.41	-3.31	1.11
189	168	0	-4.15	-3.31	0.83
71	150	0	-4.44	-3.11	1.33
246	138	0	-4.44	-3.42	1.03
208	135	0	-4.44	-3.14	1.30
231	129	0	-4.31	-3.31	0.99
157	117	0	-4.21	-3.50	0.70
24	112	0	-4.07	-3.36	0.71
64	107	0	-4.28	-3.20	1.07
186	105	0	-4.30	-3.22	1.07
254	98	0	-4.41	-3.32	1.09
32	67	0	-4.38	-3.47	0.91
250	18	0	-4.44	-3.24	1.19
105	0	0	-4.38	-3.21	1.17

2.6.6 $[\text{Cu}_4\text{Zn}_{10}]$

Supplementary Table 16: Energetic and electronic properties for [Cu₄Zn₁₀] cores obtained with PBE/light-tier1 level and light SCF parameters: configuration number (*i*), relative total energy (ΔE_{tot}), total magnetic moment (m_{tot}), HOMO energy (ε_H), LUMO energy (ε_L), and LUMO-HOMO energy gap (E_g).

<i>i</i>	ΔE_{tot}	m_{tot}	ε_H	ε_L	E_g
	(meV)	(μ_B)	(eV)	(eV)	(eV)
227	2334	2	-3.97	-3.80	0.17
168	1946	2	-4.05	-3.87	0.18
228	1896	2	-3.91	-3.75	0.16
26	1895	2	-3.84	-3.73	0.11
100	1794	2	-3.97	-3.89	0.09
152	1785	0	-4.32	-3.33	0.99
29	1675	2	-3.98	-3.75	0.23
154	1651	0	-4.20	-3.39	0.81
135	1599	2	-3.97	-3.83	0.14
61	1573	2	-3.77	-3.49	0.28
156	1550	0	-4.46	-3.14	1.32
163	1543	4	-4.03	-3.77	0.26
2	1531	2	-3.79	-3.60	0.19
4	1512	2	-4.04	-3.82	0.22
40	1486	2	-3.87	-3.79	0.09
120	1470	0	-4.06	-3.57	0.49
165	1451	2	-4.00	-3.72	0.28
198	1411	0	-4.27	-3.17	1.10
57	1401	0	-4.28	-3.39	0.89
208	1382	2	-3.82	-3.74	0.08
79	1376	2	-3.91	-3.80	0.12
112	1347	2	-4.00	-3.81	0.18

Continued on next page

Supplementary Table 16: Energetic and electronic properties for [Cu₄Zn₁₀] cores obtained with PBE/light-tier1 level and light SCF parameters: configuration number (*i*), relative total energy (ΔE_{tot}), total magnetic moment (m_{tot}), HOMO energy (ε_H), LUMO energy (ε_L), and LUMO-HOMO energy gap (E_g).

<i>i</i>	ΔE_{tot} (meV)	m_{tot} (μ_B)	ε_H (eV)	ε_L (eV)	E_g (eV)
162	1346	2	-3.86	-3.71	0.15
232	1343	2	-3.89	-3.79	0.10
81	1342	0	-4.09	-3.60	0.49
187	1331	0	-4.16	-3.15	1.01
99	1330	2	-3.97	-3.83	0.14
133	1330	2	-3.93	-3.79	0.14
222	1328	2	-3.92	-3.76	0.16
226	1324	0	-4.20	-3.35	0.86
8	1322	2	-3.87	-3.74	0.14
10	1311	2	-3.73	-3.63	0.11
189	1294	2	-3.90	-3.71	0.19
212	1289	2	-3.93	-3.71	0.22
213	1288	2	-4.02	-3.82	0.20
95	1283	0	-4.26	-3.59	0.67
176	1275	2	-3.92	-3.69	0.23
25	1271	0	-4.20	-3.51	0.69
202	1262	0	-4.32	-3.30	1.02
209	1256	2	-4.02	-3.77	0.25
234	1241	2	-3.86	-3.58	0.28
32	1234	2	-3.91	-3.81	0.10
206	1234	0	-4.03	-3.60	0.44
191	1234	2	-4.10	-3.89	0.21

Continued on next page

Supplementary Table 16: Energetic and electronic properties for [Cu₄Zn₁₀] cores obtained with PBE/light-tier1 level and light SCF parameters: configuration number (*i*), relative total energy (ΔE_{tot}), total magnetic moment (m_{tot}), HOMO energy (ε_H), LUMO energy (ε_L), and LUMO-HOMO energy gap (E_g).

<i>i</i>	ΔE_{tot} (meV)	m_{tot} (μ_B)	ε_H (eV)	ε_L (eV)	E_g (eV)
137	1233	2	-3.96	-3.72	0.25
94	1232	0	-4.28	-3.33	0.95
20	1229	2	-4.08	-3.81	0.27
53	1204	2	-3.97	-3.83	0.15
203	1187	2	-4.02	-3.81	0.21
171	1176	0	-4.04	-3.45	0.59
238	1175	0	-4.09	-3.46	0.63
1	1166	0	-4.42	-3.32	1.10
136	1157	2	-3.97	-3.85	0.12
180	1146	2	-3.90	-3.68	0.22
9	1145	0	-4.21	-3.54	0.66
128	1130	0	-4.26	-3.44	0.82
50	1127	0	-4.25	-3.24	1.01
45	1117	0	-4.32	-3.45	0.87
38	1097	0	-4.14	-3.47	0.67
106	1091	0	-4.21	-3.51	0.71
178	1076	2	-3.90	-3.74	0.17
204	1072	2	-3.90	-3.71	0.19
216	1069	0	-4.26	-3.45	0.80
12	1067	0	-4.19	-3.78	0.41
72	1055	0	-4.28	-3.45	0.83
219	1054	0	-4.42	-3.09	1.33

Continued on next page

Supplementary Table 16: Energetic and electronic properties for $[\text{Cu}_4\text{Zn}_{10}]$ cores obtained with PBE/light-tier1 level and light SCF parameters: configuration number (i), relative total energy (ΔE_{tot}), total magnetic moment (m_{tot}), HOMO energy (ε_H), LUMO energy (ε_L), and LUMO-HOMO energy gap (E_g).

i	ΔE_{tot} (meV)	m_{tot} (μ_B)	ε_H (eV)	ε_L (eV)	E_g (eV)
5	1040	2	-3.85	-3.61	0.24
215	1040	2	-4.04	-3.81	0.22
190	1035	0	-4.18	-3.58	0.59
205	1034	0	-4.14	-3.55	0.59
153	1032	0	-4.40	-2.99	1.41
197	1029	0	-4.12	-3.21	0.91
13	1023	2	-3.96	-3.81	0.14
115	1013	0	-4.12	-3.52	0.60
27	1008	0	-4.15	-3.53	0.62
105	997	0	-4.21	-3.36	0.85
122	982	0	-4.09	-3.34	0.76
169	977	0	-4.35	-3.47	0.88
183	976	0	-4.33	-3.30	1.02
161	967	0	-4.10	-3.51	0.59
65	962	0	-4.13	-3.35	0.78
233	957	2	-3.78	-3.70	0.08
126	936	0	-4.38	-3.34	1.05
200	935	2	-4.01	-3.78	0.24
103	932	0	-4.09	-3.35	0.74
80	929	0	-4.23	-3.50	0.73
196	927	0	-4.16	-3.07	1.09
89	924	0	-4.19	-3.25	0.94

Continued on next page

Supplementary Table 16: Energetic and electronic properties for [Cu₄Zn₁₀] cores obtained with PBE/light-tier1 level and light SCF parameters: configuration number (*i*), relative total energy (ΔE_{tot}), total magnetic moment (m_{tot}), HOMO energy (ε_H), LUMO energy (ε_L), and LUMO-HOMO energy gap (E_g).

<i>i</i>	ΔE_{tot} (meV)	m_{tot} (μ_B)	ε_H (eV)	ε_L (eV)	E_g (eV)
177	909	2	-3.74	-3.68	0.06
113	906	0	-4.30	-3.26	1.04
218	904	0	-4.20	-3.31	0.90
157	904	0	-4.34	-2.99	1.34
132	901	0	-4.51	-3.25	1.26
207	900	0	-4.06	-3.26	0.80
195	897	0	-4.28	-3.40	0.88
199	885	0	-4.00	-2.94	1.06
225	884	0	-4.31	-3.28	1.04
194	869	0	-4.12	-3.52	0.60
143	859	0	-4.36	-3.23	1.13
21	850	0	-4.37	-3.08	1.28
164	849	0	-4.30	-3.47	0.83
114	842	0	-4.23	-3.46	0.77
201	833	0	-4.30	-3.22	1.07
109	832	0	-4.14	-3.37	0.77
230	821	0	-4.32	-3.47	0.85
86	821	0	-4.05	-3.44	0.60
217	815	0	-4.28	-3.50	0.78
192	814	0	-4.29	-3.53	0.76
76	813	0	-4.17	-3.52	0.65
71	807	0	-4.15	-3.33	0.82

Continued on next page

Supplementary Table 16: Energetic and electronic properties for $[\text{Cu}_4\text{Zn}_{10}]$ cores obtained with PBE/light-tier1 level and light SCF parameters: configuration number (i), relative total energy (ΔE_{tot}), total magnetic moment (m_{tot}), HOMO energy (ε_H), LUMO energy (ε_L), and LUMO-HOMO energy gap (E_g).

i	ΔE_{tot} (meV)	m_{tot} (μ_B)	ε_H (eV)	ε_L (eV)	E_g (eV)
231	804	0	-4.10	-3.42	0.67
93	803	0	-4.24	-3.10	1.14
134	802	0	-4.15	-3.48	0.67
139	801	0	-4.18	-3.19	0.99
129	800	0	-4.12	-3.16	0.95
130	790	0	-4.28	-3.24	1.04
19	779	0	-4.30	-3.30	1.00
229	778	0	-4.41	-3.27	1.14
97	764	0	-4.23	-3.46	0.77
91	758	0	-4.15	-3.29	0.86
142	744	0	-4.36	-3.21	1.16
84	737	0	-4.22	-3.26	0.96
11	736	0	-4.31	-3.40	0.91
104	728	0	-4.18	-3.20	0.98
193	727	0	-4.07	-3.33	0.74
188	717	0	-4.28	-3.31	0.97
23	717	0	-4.19	-3.19	1.00
98	715	0	-4.01	-3.18	0.84
14	710	0	-4.29	-3.64	0.65
73	688	0	-4.29	-3.35	0.94
16	687	0	-4.21	-3.42	0.79
31	684	0	-4.40	-3.19	1.21

Continued on next page

Supplementary Table 16: Energetic and electronic properties for [Cu₄Zn₁₀] cores obtained with PBE/light-tier1 level and light SCF parameters: configuration number (*i*), relative total energy (ΔE_{tot}), total magnetic moment (m_{tot}), HOMO energy (ε_H), LUMO energy (ε_L), and LUMO-HOMO energy gap (E_g).

<i>i</i>	ΔE_{tot} (meV)	m_{tot} (μ_B)	ε_H (eV)	ε_L (eV)	E_g (eV)
159	682	0	-4.21	-3.37	0.84
125	680	0	-4.14	-3.27	0.88
167	676	0	-4.25	-3.58	0.67
185	670	0	-4.40	-3.01	1.39
140	662	0	-4.32	-3.22	1.10
237	662	0	-4.48	-2.93	1.55
108	660	0	-3.96	-3.36	0.60
42	660	0	-4.29	-3.13	1.15
240	657	0	-4.31	-3.03	1.27
15	653	0	-4.25	-3.34	0.91
110	645	0	-4.48	-3.12	1.36
116	645	0	-4.22	-3.12	1.10
181	644	0	-4.21	-3.26	0.95
155	639	0	-4.42	-3.08	1.35
166	628	0	-4.30	-3.25	1.05
214	627	0	-4.27	-3.16	1.11
22	622	0	-4.18	-3.33	0.85
107	602	0	-4.32	-3.32	1.00
90	602	0	-4.34	-3.19	1.15
96	599	0	-4.30	-3.23	1.07
37	597	0	-4.46	-3.20	1.25
28	587	0	-4.41	-3.13	1.28

Continued on next page

Supplementary Table 16: Energetic and electronic properties for [Cu₄Zn₁₀] cores obtained with PBE/light-tier1 level and light SCF parameters: configuration number (*i*), relative total energy (ΔE_{tot}), total magnetic moment (m_{tot}), HOMO energy (ε_H), LUMO energy (ε_L), and LUMO-HOMO energy gap (E_g).

<i>i</i>	ΔE_{tot} (meV)	m_{tot} (μ_B)	ε_H (eV)	ε_L (eV)	E_g (eV)
63	580	0	-4.28	-3.28	1.00
117	580	0	-4.12	-3.09	1.03
127	568	0	-4.11	-3.42	0.69
88	567	0	-4.32	-3.27	1.04
46	564	0	-4.28	-3.29	1.00
144	564	0	-4.16	-3.27	0.89
70	558	0	-4.02	-3.06	0.96
3	553	0	-4.14	-3.06	1.08
75	551	0	-4.15	-3.30	0.85
175	547	0	-4.33	-3.27	1.06
221	538	0	-4.22	-3.12	1.10
151	537	0	-4.37	-2.95	1.42
59	531	0	-4.31	-3.22	1.09
83	526	0	-4.10	-3.24	0.86
87	525	0	-4.35	-3.04	1.31
49	518	0	-4.32	-3.12	1.21
220	517	0	-4.16	-3.18	0.98
101	509	0	-4.44	-3.06	1.38
239	508	0	-4.33	-3.03	1.30
85	507	0	-4.41	-3.17	1.24
119	499	0	-4.28	-2.96	1.32
124	497	0	-4.18	-3.19	0.99

Continued on next page

Supplementary Table 16: Energetic and electronic properties for [Cu₄Zn₁₀] cores obtained with PBE/light-tier1 level and light SCF parameters: configuration number (*i*), relative total energy (ΔE_{tot}), total magnetic moment (m_{tot}), HOMO energy (ε_H), LUMO energy (ε_L), and LUMO-HOMO energy gap (E_g).

<i>i</i>	ΔE_{tot} (meV)	m_{tot} (μ_B)	ε_H (eV)	ε_L (eV)	E_g (eV)
147	486	0	-4.27	-3.13	1.14
145	474	0	-4.23	-3.31	0.92
179	461	0	-4.26	-3.33	0.93
141	460	0	-4.23	-2.88	1.35
211	459	0	-4.27	-3.16	1.11
224	456	0	-4.37	-3.03	1.33
123	455	0	-4.02	-3.00	1.02
77	453	0	-4.28	-3.50	0.79
39	448	0	-4.28	-2.96	1.32
92	444	0	-4.23	-3.14	1.09
55	443	0	-4.42	-3.21	1.20
64	434	0	-4.29	-2.97	1.32
67	432	0	-4.25	-3.13	1.12
18	423	0	-4.44	-3.44	1.00
34	418	0	-4.28	-3.02	1.26
235	405	0	-3.99	-3.14	0.85
102	390	0	-4.19	-2.99	1.19
74	385	0	-4.36	-3.39	0.98
69	380	0	-4.11	-3.38	0.73
184	377	0	-4.23	-3.27	0.96
44	368	0	-4.42	-3.21	1.21
186	365	0	-4.48	-3.30	1.19

Continued on next page

Supplementary Table 16: Energetic and electronic properties for [Cu₄Zn₁₀] cores obtained with PBE/light-tier1 level and light SCF parameters: configuration number (*i*), relative total energy (ΔE_{tot}), total magnetic moment (m_{tot}), HOMO energy (ε_H), LUMO energy (ε_L), and LUMO-HOMO energy gap (E_g).

<i>i</i>	ΔE_{tot} (meV)	m_{tot} (μ_B)	ε_H (eV)	ε_L (eV)	E_g (eV)
47	359	0	-4.27	-3.25	1.02
118	356	0	-4.17	-2.94	1.24
24	355	0	-4.35	-3.14	1.21
30	345	0	-4.30	-3.25	1.05
210	332	0	-4.50	-3.24	1.26
54	321	0	-4.34	-3.34	1.00
66	311	0	-4.37	-3.04	1.33
150	306	0	-4.28	-3.13	1.16
160	299	0	-4.46	-3.30	1.16
78	299	0	-4.49	-3.13	1.35
149	293	0	-4.38	-3.14	1.23
52	288	0	-4.22	-3.13	1.08
58	283	0	-4.32	-3.05	1.27
43	271	0	-4.09	-3.31	0.78
223	248	0	-4.43	-3.28	1.15
60	246	0	-4.37	-3.20	1.17
138	219	0	-4.25	-3.12	1.13
17	213	0	-4.27	-3.05	1.22
35	205	0	-4.24	-3.08	1.16
41	197	0	-4.43	-3.12	1.32
148	193	0	-4.05	-3.08	0.97
172	183	0	-4.36	-3.19	1.16

Continued on next page

Supplementary Table 16: Energetic and electronic properties for [Cu₄Zn₁₀] cores obtained with PBE/light-tier1 level and light SCF parameters: configuration number (*i*), relative total energy (ΔE_{tot}), total magnetic moment (m_{tot}), HOMO energy (ε_H), LUMO energy (ε_L), and LUMO-HOMO energy gap (E_g).

<i>i</i>	ΔE_{tot}	m_{tot}	ε_H	ε_L	E_g
	(meV)	(μ_B)	(eV)	(eV)	(eV)
236	174	0	-4.29	-3.05	1.24
62	174	0	-4.49	-3.27	1.22
111	163	0	-4.26	-2.94	1.32
33	145	0	-4.42	-3.24	1.18
56	99	0	-4.39	-3.12	1.27
146	97	0	-4.18	-3.09	1.09
182	77	0	-4.23	-3.21	1.03
7	61	0	-4.21	-3.05	1.16
173	42	0	-4.49	-2.94	1.55
68	39	0	-4.49	-3.05	1.43
131	8	0	-4.26	-3.04	1.22
6	0	0	-4.20	-3.20	0.99

2.6.7 [Cu₁₁Zn]

Supplementary Table 17: Energetic and electronic properties for [Cu₁₁Zn₆] cores obtained with PBE/light-tier1 level and light SCF parameters: configuration number (*i*), relative total energy (ΔE_{tot}), total magnetic moment (m_{tot}), HOMO energy (ε_H), LUMO energy (ε_L), and LUMO-HOMO energy gap (E_g).

<i>i</i>	ΔE_{tot}	m_{tot}	ε_H	ε_L	E_g
	(meV)	(μ_B)	(eV)	(eV)	(eV)
37	4780	1	-3.75	-3.56	0.20
35	4093	1	-3.87	-3.61	0.26

Continued on next page

Supplementary Table 17: Energetic and electronic properties for $[Cu_{11}Zn_6]$ cores obtained with PBE/light-tier1 level and light SCF parameters: configuration number (i), relative total energy (ΔE_{tot}), total magnetic moment (m_{tot}), HOMO energy (ε_H), LUMO energy (ε_L), and LUMO-HOMO energy gap (E_g).

i	ΔE_{tot} (meV)	m_{tot} (μ_B)	ε_H (eV)	ε_L (eV)	E_g (eV)
74	3982	1	-3.80	-3.61	0.19
94	3581	1	-3.98	-3.75	0.23
41	3505	1	-3.81	-3.62	0.18
48	3457	1	-3.91	-3.73	0.17
52	3102	1	-4.04	-3.87	0.17
97	3081	1	-3.90	-3.73	0.16
40	2892	1	-3.88	-3.70	0.18
175	2874	1	-3.79	-3.60	0.19
73	2841	1	-4.03	-3.86	0.17
75	2772	1	-4.01	-3.81	0.20
95	2674	1	-3.71	-3.51	0.19
179	2585	1	-3.89	-3.69	0.19
68	2507	1	-4.19	-4.00	0.19
38	2503	1	-3.92	-3.73	0.18
191	2461	1	-3.74	-3.54	0.21
155	2438	1	-3.94	-3.71	0.23
100	2436	1	-3.87	-3.65	0.21
135	2366	1	-4.23	-4.06	0.18
178	2336	1	-3.84	-3.66	0.18
43	2324	1	-3.85	-3.65	0.20
129	2309	1	-3.93	-3.73	0.20
23	2295	1	-3.84	-3.63	0.21

Continued on next page

Supplementary Table 17: Energetic and electronic properties for $[Cu_{11}Zn_6]$ cores obtained with PBE/light-tier1 level and light SCF parameters: configuration number (i), relative total energy (ΔE_{tot}), total magnetic moment (m_{tot}), HOMO energy (ε_H), LUMO energy (ε_L), and LUMO-HOMO energy gap (E_g).

i	ΔE_{tot} (meV)	m_{tot} (μ_B)	ε_H (eV)	ε_L (eV)	E_g (eV)
72	2228	1	-4.14	-3.97	0.17
120	2154	1	-4.00	-3.82	0.17
50	2150	1	-3.66	-3.41	0.25
205	2134	1	-3.81	-3.62	0.19
103	2106	1	-3.83	-3.63	0.20
219	2097	1	-3.83	-3.60	0.23
149	2095	1	-3.79	-3.61	0.18
12	2088	1	-3.93	-3.77	0.16
105	2062	1	-3.78	-3.56	0.22
67	2032	1	-3.94	-3.74	0.20
220	2031	1	-3.94	-3.73	0.21
46	2027	1	-4.01	-3.72	0.28
188	1991	1	-3.98	-3.80	0.18
186	1989	1	-3.90	-3.71	0.19
134	1964	1	-4.07	-3.82	0.25
127	1962	1	-3.93	-3.73	0.20
221	1957	1	-3.80	-3.55	0.25
133	1916	1	-3.96	-3.72	0.23
206	1914	1	-3.99	-3.81	0.19
64	1907	1	-3.94	-3.75	0.19
165	1834	1	-4.20	-3.98	0.22
130	1826	1	-3.91	-3.73	0.18

Continued on next page

Supplementary Table 17: Energetic and electronic properties for $[Cu_{11}Zn_6]$ cores obtained with PBE/light-tier1 level and light SCF parameters: configuration number (i), relative total energy (ΔE_{tot}), total magnetic moment (m_{tot}), HOMO energy (ε_H), LUMO energy (ε_L), and LUMO-HOMO energy gap (E_g).

i	ΔE_{tot} (meV)	m_{tot} (μ_B)	ε_H (eV)	ε_L (eV)	E_g (eV)
65	1823	1	-4.29	-4.11	0.17
146	1819	1	-4.00	-3.80	0.20
204	1815	1	-3.95	-3.77	0.18
5	1793	1	-3.86	-3.68	0.18
214	1779	1	-3.85	-3.64	0.21
124	1778	1	-3.99	-3.81	0.18
292	1775	1	-3.78	-3.54	0.24
90	1757	1	-3.96	-3.72	0.24
89	1747	1	-3.67	-3.51	0.16
196	1746	1	-4.05	-3.84	0.21
166	1720	1	-4.07	-3.90	0.17
159	1713	1	-3.71	-3.45	0.26
154	1708	1	-3.84	-3.68	0.16
101	1698	1	-4.16	-4.00	0.16
131	1691	1	-4.01	-3.76	0.25
79	1687	1	-4.11	-3.95	0.16
121	1674	1	-3.89	-3.70	0.18
11	1663	1	-4.04	-3.85	0.19
92	1646	1	-4.06	-3.90	0.16
29	1582	1	-3.91	-3.74	0.16
177	1577	1	-4.02	-3.85	0.17
115	1549	1	-4.26	-4.09	0.17

Continued on next page

Supplementary Table 17: Energetic and electronic properties for $[Cu_{11}Zn_6]$ cores obtained with PBE/light-tier1 level and light SCF parameters: configuration number (i), relative total energy (ΔE_{tot}), total magnetic moment (m_{tot}), HOMO energy (ε_H), LUMO energy (ε_L), and LUMO-HOMO energy gap (E_g).

i	ΔE_{tot} (meV)	m_{tot} (μ_B)	ε_H (eV)	ε_L (eV)	E_g (eV)
30	1541	1	-3.87	-3.71	0.16
69	1508	1	-3.64	-3.42	0.22
83	1502	1	-4.03	-3.87	0.17
108	1492	1	-4.02	-3.72	0.29
20	1482	1	-3.92	-3.73	0.19
4	1480	1	-4.08	-3.89	0.19
243	1480	1	-3.95	-3.75	0.20
167	1466	1	-3.78	-3.56	0.22
118	1461	1	-3.86	-3.67	0.19
71	1456	1	-3.69	-3.49	0.20
297	1451	1	-3.81	-3.55	0.26
7	1427	1	-4.00	-3.82	0.18
24	1411	1	-4.00	-3.83	0.16
213	1400	1	-3.76	-3.56	0.20
151	1398	1	-3.89	-3.71	0.18
99	1396	1	-4.26	-4.10	0.16
14	1392	1	-3.59	-3.37	0.22
91	1391	1	-4.18	-3.99	0.19
217	1390	1	-3.91	-3.72	0.19
194	1389	1	-3.85	-3.64	0.21
22	1386	1	-3.96	-3.78	0.19
126	1383	1	-3.97	-3.79	0.18

Continued on next page

Supplementary Table 17: Energetic and electronic properties for $[Cu_{11}Zn_6]$ cores obtained with PBE/light-tier1 level and light SCF parameters: configuration number (i), relative total energy (ΔE_{tot}), total magnetic moment (m_{tot}), HOMO energy (ε_H), LUMO energy (ε_L), and LUMO-HOMO energy gap (E_g).

i	ΔE_{tot} (meV)	m_{tot} (μ_B)	ε_H (eV)	ε_L (eV)	E_g (eV)
150	1380	1	-4.06	-3.85	0.21
9	1366	1	-3.69	-3.49	0.21
270	1364	1	-3.69	-3.47	0.22
202	1363	1	-3.95	-3.77	0.19
54	1360	1	-3.59	-3.37	0.22
10	1360	1	-3.94	-3.76	0.18
157	1358	1	-3.94	-3.75	0.20
210	1334	1	-4.06	-3.88	0.17
85	1334	1	-3.83	-3.66	0.17
51	1330	1	-3.97	-3.75	0.22
265	1314	1	-3.78	-3.55	0.23
266	1289	1	-3.85	-3.56	0.29
109	1272	1	-3.89	-3.71	0.18
25	1269	1	-4.19	-4.01	0.18
156	1265	1	-3.89	-3.70	0.20
152	1254	1	-4.05	-3.84	0.21
296	1244	1	-3.77	-3.57	0.20
244	1237	1	-3.97	-3.81	0.16
56	1219	1	-4.06	-3.87	0.19
269	1216	1	-4.02	-3.76	0.26
96	1209	1	-3.68	-3.47	0.21
111	1207	1	-3.95	-3.75	0.20

Continued on next page

Supplementary Table 17: Energetic and electronic properties for $[Cu_{11}Zn_6]$ cores obtained with PBE/light-tier1 level and light SCF parameters: configuration number (i), relative total energy (ΔE_{tot}), total magnetic moment (m_{tot}), HOMO energy (ε_H), LUMO energy (ε_L), and LUMO-HOMO energy gap (E_g).

i	ΔE_{tot}	m_{tot}	ε_H	ε_L	E_g
	(meV)	(μ_B)	(eV)	(eV)	(eV)
174	1204	1	-3.83	-3.61	0.22
281	1197	1	-3.80	-3.53	0.27
211	1197	1	-3.85	-3.64	0.20
132	1193	1	-3.85	-3.65	0.20
242	1176	1	-4.00	-3.80	0.21
114	1175	1	-3.81	-3.55	0.26
117	1170	1	-3.91	-3.73	0.17
279	1162	1	-3.89	-3.68	0.20
62	1153	1	-3.88	-3.68	0.20
45	1149	1	-3.64	-3.46	0.18
102	1148	1	-3.99	-3.79	0.20
288	1147	1	-3.77	-3.55	0.22
153	1147	1	-3.85	-3.61	0.24
18	1136	1	-4.01	-3.85	0.17
19	1133	1	-3.87	-3.71	0.17
268	1131	1	-3.64	-3.36	0.27
27	1126	1	-4.05	-3.85	0.20
216	1121	1	-3.92	-3.70	0.21
255	1111	1	-3.79	-3.57	0.21
143	1109	1	-4.16	-3.96	0.20
66	1105	1	-3.91	-3.73	0.18
247	1096	1	-4.08	-3.85	0.23

Continued on next page

Supplementary Table 17: Energetic and electronic properties for $[Cu_{11}Zn_6]$ cores obtained with PBE/light-tier1 level and light SCF parameters: configuration number (i), relative total energy (ΔE_{tot}), total magnetic moment (m_{tot}), HOMO energy (ε_H), LUMO energy (ε_L), and LUMO-HOMO energy gap (E_g).

i	ΔE_{tot} (meV)	m_{tot} (μ_B)	ε_H (eV)	ε_L (eV)	E_g (eV)
33	1095	1	-3.77	-3.55	0.21
190	1076	1	-4.12	-3.93	0.19
170	1072	1	-3.85	-3.62	0.23
274	1062	1	-3.81	-3.59	0.23
58	1059	1	-3.73	-3.54	0.19
32	1054	1	-3.78	-3.60	0.18
235	1054	1	-3.76	-3.49	0.27
53	1050	1	-3.96	-3.76	0.21
87	1048	1	-3.82	-3.61	0.21
261	1044	1	-3.75	-3.53	0.22
6	1036	1	-4.03	-3.85	0.18
187	1030	1	-4.01	-3.79	0.22
110	1026	1	-3.79	-3.57	0.22
180	1020	1	-3.89	-3.63	0.26
238	1019	1	-3.77	-3.58	0.19
280	1017	1	-3.90	-3.57	0.33
106	1014	1	-4.06	-3.89	0.17
236	1000	1	-3.85	-3.63	0.22
218	997	1	-3.59	-3.40	0.19
264	970	1	-3.85	-3.68	0.17
107	969	1	-4.14	-3.96	0.18
55	969	1	-3.97	-3.79	0.18

Continued on next page

Supplementary Table 17: Energetic and electronic properties for $[Cu_{11}Zn_6]$ cores obtained with PBE/light-tier1 level and light SCF parameters: configuration number (i), relative total energy (ΔE_{tot}), total magnetic moment (m_{tot}), HOMO energy (ε_H), LUMO energy (ε_L), and LUMO-HOMO energy gap (E_g).

i	ΔE_{tot} (meV)	m_{tot} (μ_B)	ε_H (eV)	ε_L (eV)	E_g (eV)
234	965	1	-3.96	-3.74	0.22
240	960	1	-3.82	-3.62	0.20
142	959	1	-3.90	-3.69	0.21
207	957	1	-3.97	-3.74	0.23
226	937	1	-3.78	-3.53	0.25
227	935	1	-3.91	-3.67	0.24
57	929	1	-3.71	-3.52	0.19
42	924	1	-4.08	-3.91	0.18
200	917	1	-3.89	-3.65	0.23
209	908	1	-3.68	-3.45	0.23
136	904	1	-3.85	-3.65	0.19
300	895	1	-4.03	-3.84	0.19
171	886	1	-3.88	-3.68	0.20
294	885	1	-3.63	-3.42	0.21
176	876	1	-3.76	-3.55	0.21
273	873	1	-4.08	-3.88	0.20
82	872	1	-3.90	-3.72	0.18
17	870	1	-3.72	-3.52	0.20
272	870	1	-3.79	-3.61	0.18
16	866	1	-3.89	-3.70	0.19
163	864	1	-3.91	-3.66	0.25
93	847	1	-3.86	-3.61	0.25

Continued on next page

Supplementary Table 17: Energetic and electronic properties for $[Cu_{11}Zn_6]$ cores obtained with PBE/light-tier1 level and light SCF parameters: configuration number (i), relative total energy (ΔE_{tot}), total magnetic moment (m_{tot}), HOMO energy (ε_H), LUMO energy (ε_L), and LUMO-HOMO energy gap (E_g).

i	ΔE_{tot} (meV)	m_{tot} (μ_B)	ε_H (eV)	ε_L (eV)	E_g (eV)
250	840	1	-4.11	-3.93	0.18
295	812	1	-3.89	-3.67	0.22
299	804	1	-3.66	-3.46	0.20
123	801	1	-3.98	-3.82	0.15
237	798	1	-4.09	-3.86	0.23
49	796	1	-4.07	-3.88	0.19
145	795	1	-3.99	-3.77	0.22
63	792	1	-3.73	-3.51	0.22
241	792	1	-3.78	-3.52	0.26
259	783	1	-3.76	-3.51	0.25
193	776	1	-3.92	-3.75	0.16
86	776	1	-4.19	-3.99	0.21
128	770	1	-3.93	-3.73	0.20
76	765	1	-3.97	-3.72	0.25
34	761	1	-3.95	-3.78	0.17
139	757	1	-4.29	-4.11	0.18
197	753	1	-4.01	-3.80	0.21
228	745	1	-3.72	-3.51	0.22
203	744	1	-3.74	-3.57	0.17
168	734	1	-3.82	-3.65	0.17
60	733	1	-4.10	-3.90	0.20
251	725	1	-3.80	-3.59	0.22

Continued on next page

Supplementary Table 17: Energetic and electronic properties for $[Cu_{11}Zn_6]$ cores obtained with PBE/light-tier1 level and light SCF parameters: configuration number (i), relative total energy (ΔE_{tot}), total magnetic moment (m_{tot}), HOMO energy (ε_H), LUMO energy (ε_L), and LUMO-HOMO energy gap (E_g).

i	ΔE_{tot} (meV)	m_{tot} (μ_B)	ε_H (eV)	ε_L (eV)	E_g (eV)
88	725	1	-4.18	-3.98	0.20
230	722	1	-3.82	-3.61	0.21
260	720	1	-3.96	-3.69	0.27
253	706	1	-4.02	-3.81	0.22
212	701	1	-3.94	-3.75	0.19
283	700	1	-4.17	-3.96	0.21
224	699	1	-4.00	-3.76	0.24
21	695	1	-3.91	-3.73	0.18
26	687	1	-3.77	-3.54	0.23
137	683	1	-3.95	-3.78	0.17
289	682	1	-3.82	-3.61	0.21
59	681	1	-3.98	-3.75	0.23
287	676	1	-3.85	-3.63	0.22
257	675	1	-3.70	-3.51	0.19
195	674	1	-4.09	-3.86	0.23
8	671	1	-3.98	-3.79	0.19
229	667	1	-3.77	-3.56	0.21
262	664	1	-4.02	-3.83	0.19
36	655	1	-3.90	-3.73	0.17
252	653	1	-3.83	-3.61	0.22
184	653	1	-4.01	-3.82	0.20
173	648	1	-3.78	-3.57	0.21

Continued on next page

Supplementary Table 17: Energetic and electronic properties for $[Cu_{11}Zn_6]$ cores obtained with PBE/light-tier1 level and light SCF parameters: configuration number (i), relative total energy (ΔE_{tot}), total magnetic moment (m_{tot}), HOMO energy (ε_H), LUMO energy (ε_L), and LUMO-HOMO energy gap (E_g).

i	ΔE_{tot}	m_{tot}	ε_H	ε_L	E_g
	(meV)	(μ_B)	(eV)	(eV)	(eV)
286	646	1	-3.88	-3.65	0.24
208	645	1	-4.09	-3.92	0.17
291	641	1	-3.72	-3.50	0.22
285	638	1	-3.90	-3.67	0.23
162	635	1	-3.77	-3.54	0.22
144	634	1	-4.14	-3.95	0.19
113	632	1	-3.95	-3.75	0.20
138	625	1	-4.19	-4.00	0.19
276	623	1	-4.20	-4.02	0.18
254	623	1	-3.91	-3.68	0.23
15	620	1	-3.99	-3.81	0.18
122	613	1	-3.96	-3.81	0.16
140	600	1	-3.88	-3.65	0.23
199	597	1	-3.94	-3.68	0.25
98	597	1	-4.02	-3.84	0.18
293	595	1	-4.03	-3.84	0.19
239	593	1	-3.71	-3.50	0.21
141	590	1	-3.90	-3.72	0.18
246	588	1	-3.93	-3.70	0.23
215	587	1	-3.90	-3.70	0.21
263	586	1	-3.83	-3.67	0.16
172	581	1	-3.95	-3.76	0.19

Continued on next page

Supplementary Table 17: Energetic and electronic properties for $[Cu_{11}Zn_6]$ cores obtained with PBE/light-tier1 level and light SCF parameters: configuration number (i), relative total energy (ΔE_{tot}), total magnetic moment (m_{tot}), HOMO energy (ε_H), LUMO energy (ε_L), and LUMO-HOMO energy gap (E_g).

i	ΔE_{tot} (meV)	m_{tot} (μ_B)	ε_H (eV)	ε_L (eV)	E_g (eV)
112	572	1	-4.11	-3.91	0.20
223	570	1	-3.99	-3.76	0.23
284	562	1	-3.98	-3.78	0.21
31	551	1	-3.82	-3.57	0.24
232	544	1	-3.99	-3.76	0.23
183	542	1	-4.21	-4.04	0.17
233	538	1	-3.72	-3.48	0.24
278	527	1	-3.84	-3.67	0.18
160	512	1	-3.83	-3.62	0.21
158	499	1	-3.87	-3.69	0.18
298	495	1	-3.94	-3.68	0.26
282	494	1	-3.83	-3.59	0.24
192	493	1	-3.86	-3.68	0.19
164	486	1	-4.00	-3.83	0.17
2	464	1	-4.03	-3.82	0.21
81	453	1	-3.81	-3.62	0.19
201	436	1	-3.98	-3.79	0.19
77	404	1	-4.11	-3.93	0.18
231	399	1	-3.98	-3.72	0.25
189	384	1	-3.96	-3.77	0.19
125	384	1	-3.86	-3.66	0.20
198	376	1	-3.81	-3.64	0.17

Continued on next page

Supplementary Table 17: Energetic and electronic properties for $[Cu_{11}Zn_6]$ cores obtained with PBE/light-tier1 level and light SCF parameters: configuration number (i), relative total energy (ΔE_{tot}), total magnetic moment (m_{tot}), HOMO energy (ε_H), LUMO energy (ε_L), and LUMO-HOMO energy gap (E_g).

i	ΔE_{tot} (meV)	m_{tot} (μ_B)	ε_H (eV)	ε_L (eV)	E_g (eV)
78	355	1	-4.06	-3.89	0.17
84	352	1	-4.10	-3.93	0.18
116	351	1	-3.97	-3.79	0.18
258	350	1	-4.12	-3.91	0.21
290	350	1	-4.03	-3.79	0.24
185	335	1	-3.77	-3.58	0.19
61	334	1	-3.96	-3.78	0.18
256	320	1	-3.85	-3.63	0.22
222	285	1	-4.00	-3.83	0.17
169	274	1	-4.19	-3.97	0.22
119	269	1	-3.85	-3.66	0.19
277	262	1	-4.04	-3.79	0.25
28	262	1	-4.01	-3.82	0.19
70	261	1	-3.85	-3.68	0.17
225	240	1	-3.92	-3.71	0.21
267	237	1	-4.08	-3.92	0.16
275	211	1	-4.13	-3.94	0.18
249	179	1	-3.95	-3.74	0.22
104	151	1	-3.86	-3.64	0.22
3	81	1	-3.94	-3.69	0.25
245	77	1	-3.84	-3.63	0.21
161	52	1	-3.85	-3.67	0.18

Continued on next page

Supplementary Table 17: Energetic and electronic properties for $[\text{Cu}_{11}\text{Zn}_6]$ cores obtained with PBE/light-tier1 level and light SCF parameters: configuration number (i), relative total energy (ΔE_{tot}), total magnetic moment (m_{tot}), HOMO energy (ε_H), LUMO energy (ε_L), and LUMO-HOMO energy gap (E_g).

i	ΔE_{tot}	m_{tot}	ε_H	ε_L	E_g
	(meV)	(μ_B)	(eV)	(eV)	(eV)
248	6	1	-4.05	-3.85	0.20
181	0	1	-3.94	-3.73	0.20

2.6.8 $[\text{Cu}_8\text{Al}_6]$

Supplementary Table 18: Energetic and electronic properties for $[\text{Cu}_8\text{Al}_6]$ cores obtained with PBE/light-tier1 level and light SCF parameters: configuration number (i), relative total energy (ΔE_{tot}), total magnetic moment (m_{tot}), HOMO energy (ε_H), LUMO energy (ε_L), and LUMO-HOMO energy gap (E_g).

i	ΔE_{tot}	m_{tot}	ε_H	ε_L	E_g
	(meV)	(μ_B)	(eV)	(eV)	(eV)
140	1860	2	-4.02	-3.78	0.24
55	1848	2	-4.08	-3.80	0.28
6	1784	4	-3.88	-3.64	0.24
185	1738	2	-4.30	-4.08	0.22
154	1680	0	-4.29	-3.72	0.57
162	1678	2	-4.07	-3.76	0.32
181	1663	4	-3.96	-3.85	0.11
178	1635	2	-3.93	-3.70	0.23
157	1609	2	-3.99	-3.83	0.17
194	1508	2	-4.20	-4.02	0.18
88	1483	2	-4.01	-3.89	0.12
10	1452	2	-4.13	-3.86	0.27

Continued on next page

Supplementary Table 18: Energetic and electronic properties for $[Cu_8Al_6]$ cores obtained with PBE/light-tier1 level and light SCF parameters: configuration number (i), relative total energy (ΔE_{tot}), total magnetic moment (m_{tot}), HOMO energy (ε_H), LUMO energy (ε_L), and LUMO-HOMO energy gap (E_g).

i	ΔE_{tot} (meV)	m_{tot} (μ_B)	ε_H (eV)	ε_L (eV)	E_g (eV)
43	1431	2	-3.87	-3.66	0.22
150	1417	2	-4.11	-3.96	0.15
149	1413	0	-4.23	-3.79	0.44
13	1403	2	-3.95	-3.73	0.22
176	1391	2	-4.02	-3.85	0.17
163	1388	2	-4.30	-4.06	0.24
184	1367	0	-4.27	-3.75	0.52
137	1362	0	-4.05	-3.76	0.29
145	1361	0	-4.08	-3.84	0.24
63	1344	2	-4.00	-3.96	0.03
95	1340	0	-4.04	-3.63	0.41
46	1318	2	-4.16	-3.93	0.24
75	1318	0	-4.18	-3.59	0.59
39	1311	2	-4.25	-3.96	0.29
34	1305	2	-3.99	-3.70	0.28
105	1297	2	-3.92	-3.79	0.12
32	1292	2	-4.00	-3.91	0.08
108	1284	2	-4.00	-3.74	0.26
122	1256	2	-4.01	-3.83	0.18
49	1254	0	-4.22	-3.80	0.42
47	1248	2	-4.09	-3.91	0.18
4	1247	0	-4.11	-3.72	0.39

Continued on next page

Supplementary Table 18: Energetic and electronic properties for $[Cu_8Al_6]$ cores obtained with PBE/light-tier1 level and light SCF parameters: configuration number (i), relative total energy (ΔE_{tot}), total magnetic moment (m_{tot}), HOMO energy (ε_H), LUMO energy (ε_L), and LUMO-HOMO energy gap (E_g).

i	ΔE_{tot} (meV)	m_{tot} (μ_B)	ε_H (eV)	ε_L (eV)	E_g (eV)
158	1240	2	-4.18	-3.98	0.21
83	1237	2	-4.22	-3.93	0.29
50	1232	2	-4.05	-3.87	0.18
116	1232	0	-4.26	-3.77	0.50
133	1231	0	-4.09	-3.64	0.45
124	1227	2	-3.93	-3.63	0.30
146	1226	2	-3.96	-3.90	0.06
155	1222	0	-4.38	-3.65	0.74
115	1221	2	-3.92	-3.63	0.29
74	1210	2	-4.11	-3.87	0.23
22	1203	2	-3.89	-3.72	0.17
132	1201	0	-4.21	-3.60	0.61
3	1191	2	-4.00	-3.63	0.37
175	1184	2	-3.97	-3.66	0.31
85	1178	2	-4.07	-3.91	0.17
78	1178	0	-4.20	-3.76	0.44
53	1178	2	-3.99	-3.83	0.15
18	1167	2	-4.15	-4.02	0.13
193	1166	2	-3.98	-3.90	0.07
106	1162	2	-3.75	-3.63	0.12
200	1155	2	-4.08	-3.84	0.24
71	1151	2	-4.20	-3.93	0.27

Continued on next page

Supplementary Table 18: Energetic and electronic properties for $[Cu_8Al_6]$ cores obtained with PBE/light-tier1 level and light SCF parameters: configuration number (i), relative total energy (ΔE_{tot}), total magnetic moment (m_{tot}), HOMO energy (ε_H), LUMO energy (ε_L), and LUMO-HOMO energy gap (E_g).

i	ΔE_{tot} (meV)	m_{tot} (μ_B)	ε_H (eV)	ε_L (eV)	E_g (eV)
89	1137	2	-4.21	-4.01	0.19
16	1117	2	-4.11	-3.90	0.21
135	1112	2	-4.10	-3.88	0.22
134	1109	2	-4.08	-4.03	0.05
69	1106	2	-4.17	-4.02	0.14
126	1106	2	-4.07	-3.89	0.18
66	1094	2	-3.99	-3.88	0.10
72	1093	2	-4.06	-3.90	0.17
97	1080	0	-4.33	-3.75	0.57
142	1078	0	-4.27	-3.88	0.39
187	1078	2	-3.99	-3.67	0.32
130	1066	2	-4.07	-3.80	0.26
52	1063	2	-3.96	-3.91	0.05
28	1057	2	-4.09	-3.92	0.17
197	1054	2	-4.05	-3.87	0.18
144	1047	0	-4.24	-3.87	0.37
114	1031	0	-4.24	-3.78	0.46
198	1028	2	-4.24	-4.00	0.24
110	1023	2	-3.99	-3.91	0.08
120	1022	0	-4.06	-3.70	0.36
125	1021	2	-3.96	-3.70	0.25
102	1016	2	-4.02	-3.86	0.16

Continued on next page

Supplementary Table 18: Energetic and electronic properties for $[Cu_8Al_6]$ cores obtained with PBE/light-tier1 level and light SCF parameters: configuration number (i), relative total energy (ΔE_{tot}), total magnetic moment (m_{tot}), HOMO energy (ε_H), LUMO energy (ε_L), and LUMO-HOMO energy gap (E_g).

i	ΔE_{tot} (meV)	m_{tot} (μ_B)	ε_H (eV)	ε_L (eV)	E_g (eV)
173	1001	2	-4.20	-4.02	0.18
54	997	2	-3.93	-3.70	0.23
42	993	0	-4.24	-3.66	0.58
107	993	2	-3.86	-3.78	0.08
136	990	0	-4.16	-3.55	0.60
186	987	0	-4.13	-3.60	0.53
31	987	2	-4.25	-4.05	0.20
113	980	0	-3.98	-3.53	0.45
183	978	2	-4.08	-3.72	0.36
33	975	2	-3.84	-3.79	0.05
19	966	0	-4.25	-3.81	0.44
30	956	2	-4.10	-3.97	0.13
188	955	2	-4.09	-3.83	0.26
160	952	2	-3.78	-3.74	0.05
192	946	0	-3.94	-3.74	0.20
77	943	2	-4.11	-4.05	0.06
1	938	2	-4.09	-3.76	0.33
15	937	2	-4.09	-3.85	0.24
36	936	2	-3.85	-3.66	0.19
80	930	2	-4.14	-3.94	0.21
7	928	2	-3.85	-3.66	0.19
70	927	2	-4.02	-3.97	0.06

Continued on next page

Supplementary Table 18: Energetic and electronic properties for $[Cu_8Al_6]$ cores obtained with PBE/light-tier1 level and light SCF parameters: configuration number (i), relative total energy (ΔE_{tot}), total magnetic moment (m_{tot}), HOMO energy (ε_H), LUMO energy (ε_L), and LUMO-HOMO energy gap (E_g).

i	ΔE_{tot} (meV)	m_{tot} (μ_B)	ε_H (eV)	ε_L (eV)	E_g (eV)
45	908	2	-4.08	-3.92	0.15
104	894	2	-3.79	-3.76	0.03
117	888	2	-4.14	-3.94	0.21
111	877	2	-3.86	-3.67	0.19
159	871	2	-4.24	-3.96	0.28
179	868	0	-3.97	-3.49	0.48
35	867	0	-4.23	-3.59	0.64
23	866	2	-3.89	-3.63	0.25
27	863	2	-4.25	-4.16	0.09
169	857	2	-4.03	-3.77	0.26
67	841	2	-3.89	-3.81	0.09
112	841	2	-3.83	-3.61	0.22
152	840	2	-3.92	-3.84	0.09
65	837	2	-4.13	-3.99	0.14
123	835	2	-3.95	-3.82	0.12
172	828	2	-3.94	-3.83	0.11
51	813	2	-3.96	-3.84	0.12
5	803	0	-4.03	-3.48	0.55
164	803	0	-4.14	-3.59	0.55
167	802	2	-4.11	-3.84	0.27
82	802	0	-4.20	-3.63	0.57
79	800	0	-4.15	-3.56	0.59

Continued on next page

Supplementary Table 18: Energetic and electronic properties for $[Cu_8Al_6]$ cores obtained with PBE/light-tier1 level and light SCF parameters: configuration number (i), relative total energy (ΔE_{tot}), total magnetic moment (m_{tot}), HOMO energy (ε_H), LUMO energy (ε_L), and LUMO-HOMO energy gap (E_g).

i	ΔE_{tot} (meV)	m_{tot} (μ_B)	ε_H (eV)	ε_L (eV)	E_g (eV)
147	798	0	-4.16	-3.70	0.46
41	767	0	-4.36	-3.71	0.66
40	761	0	-4.32	-3.68	0.64
156	759	0	-4.17	-3.59	0.58
81	758	2	-3.95	-3.81	0.14
98	742	0	-3.91	-3.60	0.31
161	725	0	-4.25	-3.61	0.64
84	712	0	-4.21	-3.63	0.58
86	710	0	-4.26	-3.61	0.64
24	700	0	-4.14	-3.59	0.55
99	699	2	-4.06	-3.89	0.17
8	699	2	-3.97	-3.80	0.17
93	689	2	-4.01	-3.84	0.17
182	689	2	-4.00	-3.86	0.14
129	683	2	-3.99	-3.77	0.22
12	676	2	-4.03	-3.74	0.28
139	676	0	-4.13	-3.69	0.44
119	675	0	-4.17	-3.86	0.32
189	662	0	-4.31	-3.77	0.55
59	656	2	-4.08	-3.99	0.09
48	650	0	-4.16	-3.64	0.52
166	645	2	-4.09	-3.84	0.25

Continued on next page

Supplementary Table 18: Energetic and electronic properties for $[Cu_8Al_6]$ cores obtained with PBE/light-tier1 level and light SCF parameters: configuration number (i), relative total energy (ΔE_{tot}), total magnetic moment (m_{tot}), HOMO energy (ε_H), LUMO energy (ε_L), and LUMO-HOMO energy gap (E_g).

i	ΔE_{tot} (meV)	m_{tot} (μ_B)	ε_H (eV)	ε_L (eV)	E_g (eV)
29	643	2	-4.14	-3.96	0.18
131	631	0	-4.32	-3.68	0.63
94	626	0	-4.33	-3.78	0.55
90	624	0	-4.07	-3.77	0.30
96	624	0	-4.30	-3.85	0.45
38	588	0	-4.29	-3.55	0.74
148	583	0	-4.28	-3.66	0.62
199	580	0	-4.45	-3.46	0.99
143	571	0	-4.26	-3.71	0.56
195	544	0	-4.10	-3.55	0.55
171	544	0	-4.21	-3.68	0.53
103	543	2	-4.07	-3.84	0.23
190	539	0	-4.30	-3.59	0.71
128	496	0	-4.22	-3.69	0.53
101	470	0	-4.06	-3.55	0.51
57	460	0	-4.18	-3.58	0.60
177	458	2	-4.02	-3.78	0.24
127	447	0	-4.27	-3.65	0.62
62	435	0	-4.08	-3.65	0.42
196	428	0	-4.25	-3.56	0.68
58	399	0	-4.33	-3.63	0.70
60	397	0	-4.23	-3.73	0.50

Continued on next page

Supplementary Table 18: Energetic and electronic properties for $[Cu_8Al_6]$ cores obtained with PBE/light-tier1 level and light SCF parameters: configuration number (i), relative total energy (ΔE_{tot}), total magnetic moment (m_{tot}), HOMO energy (ε_H), LUMO energy (ε_L), and LUMO-HOMO energy gap (E_g).

i	ΔE_{tot} (meV)	m_{tot} (μ_B)	ε_H (eV)	ε_L (eV)	E_g (eV)
121	397	0	-4.07	-3.79	0.27
109	381	0	-4.10	-3.54	0.56
44	376	0	-4.13	-3.70	0.43
153	371	0	-4.10	-3.63	0.47
91	353	0	-3.97	-3.63	0.34
92	351	0	-4.08	-3.79	0.30
56	343	0	-4.11	-3.37	0.74
180	335	0	-4.18	-3.54	0.64
2	328	0	-4.12	-3.79	0.33
61	325	0	-4.26	-3.89	0.38
11	323	0	-4.31	-3.46	0.85
17	320	0	-4.31	-3.52	0.79
9	307	0	-4.09	-3.48	0.60
174	298	0	-4.31	-3.42	0.88
100	296	0	-4.14	-3.57	0.57
64	281	0	-4.36	-3.64	0.72
138	248	2	-3.85	-3.72	0.13
26	239	0	-4.26	-3.57	0.69
37	237	0	-4.31	-3.78	0.53
165	222	0	-4.23	-3.51	0.72
73	181	0	-4.14	-3.46	0.69
14	159	0	-4.30	-3.52	0.78

Continued on next page

Supplementary Table 18: Energetic and electronic properties for $[\text{Cu}_8\text{Al}_6]$ cores obtained with PBE/light-tier1 level and light SCF parameters: configuration number (i), relative total energy (ΔE_{tot}), total magnetic moment (m_{tot}), HOMO energy (ε_H), LUMO energy (ε_L), and LUMO-HOMO energy gap (E_g).

i	ΔE_{tot} (meV)	m_{tot} (μ_B)	ε_H (eV)	ε_L (eV)	E_g (eV)
20	76	0	-4.13	-3.51	0.62
168	51	0	-4.24	-3.60	0.64
170	43	0	-4.15	-3.72	0.42
87	37	0	-4.38	-3.66	0.73
191	0	0	-4.32	-3.54	0.78

2.6.9 $[\text{Ni}_7\text{Ga}_6]$

Supplementary Table 19: Energetic and electronic properties for $[\text{Ni}_7\text{Ga}_6]$ cores obtained with PBE/light-tier1 level and light SCF parameters: configuration number (i), relative total energy (ΔE_{tot}), total magnetic moment (m_{tot}), HOMO energy (ε_H), LUMO energy (ε_L), and LUMO-HOMO energy gap (E_g).

i	ΔE_{tot} (meV)	m_{tot} (μ_B)	ε_H (eV)	ε_L (eV)	E_g (eV)
195	2478	4	-4.02	-3.89	0.13
75	2441	4	-3.88	-3.76	0.12
71	2106	4	-3.90	-3.77	0.13
153	2088	2	-3.90	-3.69	0.21
119	2080	4	-3.86	-3.81	0.05
16	2029	4	-3.99	-3.88	0.11
55	2009	4	-4.06	-3.84	0.22
38	2006	0	-3.92	-3.74	0.19
29	1987	2	-3.91	-3.66	0.25

Continued on next page

Supplementary Table 19: Energetic and electronic properties for $[Ni_7Ga_6]$ cores obtained with PBE/light-tier1 level and light SCF parameters: configuration number (i), relative total energy (ΔE_{tot}), total magnetic moment (m_{tot}), HOMO energy (ε_H), LUMO energy (ε_L), and LUMO-HOMO energy gap (E_g).

i	ΔE_{tot} (meV)	m_{tot} (μ_B)	ε_H (eV)	ε_L (eV)	E_g (eV)
133	1949	4	-3.89	-3.73	0.16
39	1884	2	-3.89	-3.67	0.22
33	1880	2	-3.92	-3.72	0.20
94	1834	4	-3.90	-3.80	0.10
26	1820	4	-4.00	-3.86	0.14
27	1814	2	-3.90	-3.73	0.18
126	1792	4	-3.94	-3.83	0.11
179	1782	2	-3.93	-3.75	0.18
15	1780	2	-3.89	-3.57	0.32
24	1744	4	-4.10	-3.87	0.23
134	1735	4	-3.94	-3.75	0.19
146	1722	2	-3.95	-3.76	0.19
43	1700	4	-3.89	-3.79	0.10
62	1681	2	-3.86	-3.68	0.18
199	1677	2	-3.94	-3.74	0.20
103	1663	2	-3.83	-3.62	0.21
92	1638	2	-3.99	-3.76	0.23
152	1635	4	-3.95	-3.77	0.18
22	1635	4	-4.06	-3.90	0.16
175	1634	2	-3.90	-3.68	0.22
69	1629	2	-3.88	-3.79	0.10
129	1618	2	-3.92	-3.73	0.19

Continued on next page

Supplementary Table 19: Energetic and electronic properties for [Ni₇Ga₆] cores obtained with PBE/light-tier1 level and light SCF parameters: configuration number (*i*), relative total energy (ΔE_{tot}), total magnetic moment (m_{tot}), HOMO energy (ε_H), LUMO energy (ε_L), and LUMO-HOMO energy gap (E_g).

<i>i</i>	ΔE_{tot} (meV)	m_{tot} (μ_B)	ε_H (eV)	ε_L (eV)	E_g (eV)
161	1591	2	-3.97	-3.81	0.16
148	1591	2	-3.93	-3.73	0.20
23	1589	4	-3.99	-3.83	0.15
123	1551	0	-3.96	-3.73	0.24
137	1545	2	-3.92	-3.68	0.24
127	1527	2	-3.96	-3.66	0.30
34	1522	2	-3.86	-3.71	0.15
57	1522	2	-3.91	-3.74	0.18
115	1516	2	-3.89	-3.82	0.07
66	1513	4	-3.90	-3.81	0.09
113	1500	2	-3.94	-3.74	0.20
67	1494	2	-4.08	-3.95	0.13
190	1487	4	-4.09	-3.91	0.17
32	1463	0	-3.88	-3.48	0.40
101	1451	2	-3.97	-3.75	0.22
74	1448	2	-3.90	-3.83	0.06
110	1429	2	-3.84	-3.71	0.14
130	1414	4	-3.98	-3.84	0.14
58	1385	2	-3.96	-3.78	0.18
131	1384	2	-3.97	-3.78	0.19
176	1373	2	-3.82	-3.56	0.27
187	1365	2	-3.91	-3.72	0.19

Continued on next page

Supplementary Table 19: Energetic and electronic properties for $[Ni_7Ga_6]$ cores obtained with PBE/light-tier1 level and light SCF parameters: configuration number (i), relative total energy (ΔE_{tot}), total magnetic moment (m_{tot}), HOMO energy (ε_H), LUMO energy (ε_L), and LUMO-HOMO energy gap (E_g).

i	ΔE_{tot} (meV)	m_{tot} (μ_B)	ε_H (eV)	ε_L (eV)	E_g (eV)
141	1364	0	-3.94	-3.65	0.28
128	1364	2	-3.95	-3.75	0.20
149	1358	2	-3.86	-3.69	0.17
186	1347	2	-3.86	-3.67	0.19
96	1327	4	-4.04	-3.90	0.14
147	1304	2	-3.90	-3.62	0.28
154	1300	2	-3.92	-3.72	0.21
160	1297	2	-3.90	-3.77	0.13
135	1236	2	-4.10	-3.93	0.18
136	1234	2	-3.81	-3.78	0.03
200	1225	2	-3.92	-3.78	0.14
65	1222	4	-4.00	-3.95	0.05
117	1210	2	-3.87	-3.67	0.20
139	1179	4	-4.02	-3.82	0.20
70	1177	2	-3.97	-3.68	0.30
95	1175	4	-4.06	-3.94	0.12
80	1175	2	-4.02	-3.83	0.19
158	1163	2	-3.88	-3.71	0.17
49	1160	2	-3.74	-3.60	0.14
105	1135	2	-3.86	-3.67	0.20
109	1121	2	-4.10	-3.94	0.16
40	1114	2	-3.90	-3.64	0.25

Continued on next page

Supplementary Table 19: Energetic and electronic properties for $[Ni_7Ga_6]$ cores obtained with PBE/light-tier1 level and light SCF parameters: configuration number (i), relative total energy (ΔE_{tot}), total magnetic moment (m_{tot}), HOMO energy (ε_H), LUMO energy (ε_L), and LUMO-HOMO energy gap (E_g).

i	ΔE_{tot} (meV)	m_{tot} (μ_B)	ε_H (eV)	ε_L (eV)	E_g (eV)
174	1113	2	-4.03	-3.77	0.26
50	1099	2	-3.99	-3.69	0.30
142	1098	2	-3.83	-3.63	0.21
102	1086	2	-3.95	-3.64	0.31
118	1070	4	-3.84	-3.76	0.08
37	1065	0	-3.86	-3.62	0.24
53	1062	2	-3.91	-3.79	0.12
185	1060	2	-3.89	-3.79	0.10
169	1055	2	-3.90	-3.80	0.10
145	1054	2	-3.94	-3.77	0.17
125	1050	2	-3.82	-3.76	0.06
25	1046	2	-3.99	-3.78	0.21
132	1033	2	-4.03	-3.82	0.21
138	1024	2	-4.01	-3.73	0.29
143	1013	2	-3.93	-3.75	0.19
60	1010	2	-3.99	-3.74	0.25
82	1005	0	-4.05	-3.82	0.23
20	998	2	-3.93	-3.64	0.29
193	993	2	-3.91	-3.82	0.10
116	991	2	-3.94	-3.79	0.14
151	991	2	-4.09	-3.80	0.30
97	991	2	-4.03	-3.73	0.29

Continued on next page

Supplementary Table 19: Energetic and electronic properties for $[Ni_7Ga_6]$ cores obtained with PBE/light-tier1 level and light SCF parameters: configuration number (i), relative total energy (ΔE_{tot}), total magnetic moment (m_{tot}), HOMO energy (ε_H), LUMO energy (ε_L), and LUMO-HOMO energy gap (E_g).

i	ΔE_{tot} (meV)	m_{tot} (μ_B)	ε_H (eV)	ε_L (eV)	E_g (eV)
81	989	4	-4.06	-3.94	0.12
48	986	2	-4.01	-3.80	0.21
83	983	2	-4.14	-4.02	0.12
156	978	2	-3.98	-3.82	0.16
72	966	2	-3.98	-3.74	0.24
61	948	4	-4.05	-3.89	0.17
1	938	2	-3.99	-3.82	0.17
178	935	2	-3.79	-3.64	0.16
167	927	2	-3.89	-3.69	0.19
191	924	2	-3.91	-3.72	0.19
171	920	2	-3.98	-3.80	0.18
90	918	2	-4.04	-3.88	0.16
111	914	0	-3.99	-3.73	0.26
17	908	2	-3.94	-3.78	0.17
64	907	2	-3.99	-3.88	0.11
56	891	2	-3.93	-3.72	0.20
31	891	2	-3.92	-3.72	0.20
150	887	2	-3.93	-3.82	0.11
35	880	2	-3.92	-3.71	0.21
121	873	2	-4.01	-3.83	0.17
164	860	2	-3.92	-3.70	0.21
183	855	2	-3.98	-3.80	0.18

Continued on next page

Supplementary Table 19: Energetic and electronic properties for $[Ni_7Ga_6]$ cores obtained with PBE/light-tier1 level and light SCF parameters: configuration number (i), relative total energy (ΔE_{tot}), total magnetic moment (m_{tot}), HOMO energy (ε_H), LUMO energy (ε_L), and LUMO-HOMO energy gap (E_g).

i	ΔE_{tot} (meV)	m_{tot} (μ_B)	ε_H (eV)	ε_L (eV)	E_g (eV)
107	846	2	-4.05	-3.88	0.17
47	844	2	-3.94	-3.77	0.17
112	842	2	-3.99	-3.86	0.13
45	831	2	-3.91	-3.77	0.14
194	810	2	-4.06	-3.82	0.24
19	806	2	-3.91	-3.65	0.25
79	805	2	-4.01	-3.86	0.16
120	803	2	-3.93	-3.68	0.26
104	792	4	-4.20	-3.95	0.24
59	784	2	-4.06	-3.83	0.22
21	783	0	-4.04	-3.67	0.36
162	774	2	-4.00	-3.82	0.18
30	768	2	-4.19	-3.88	0.31
28	763	2	-3.90	-3.67	0.22
18	748	2	-3.86	-3.60	0.26
98	732	2	-4.03	-3.89	0.14
192	728	2	-4.15	-3.89	0.26
196	715	4	-4.11	-4.01	0.10
51	705	2	-3.92	-3.81	0.11
68	701	2	-4.10	-3.88	0.22
198	689	2	-4.06	-3.82	0.25
188	685	2	-4.05	-3.90	0.14

Continued on next page

Supplementary Table 19: Energetic and electronic properties for $[Ni_7Ga_6]$ cores obtained with PBE/light-tier1 level and light SCF parameters: configuration number (i), relative total energy (ΔE_{tot}), total magnetic moment (m_{tot}), HOMO energy (ε_H), LUMO energy (ε_L), and LUMO-HOMO energy gap (E_g).

i	ΔE_{tot} (meV)	m_{tot} (μ_B)	ε_H (eV)	ε_L (eV)	E_g (eV)
197	679	0	-3.77	-3.53	0.24
166	673	0	-3.81	-3.44	0.37
189	666	2	-4.10	-3.82	0.28
44	665	2	-3.97	-3.72	0.25
89	663	0	-4.15	-3.95	0.19
106	662	2	-3.92	-3.77	0.15
63	657	2	-4.14	-3.92	0.22
52	649	2	-3.91	-3.72	0.19
155	643	2	-3.94	-3.79	0.14
124	637	2	-3.98	-3.76	0.21
122	622	2	-4.06	-3.73	0.32
114	618	2	-3.94	-3.84	0.10
11	612	4	-4.05	-3.85	0.19
144	601	2	-4.01	-3.79	0.23
41	584	2	-3.93	-3.61	0.31
2	573	2	-4.03	-3.86	0.18
93	562	2	-4.07	-3.81	0.27
77	537	2	-3.91	-3.65	0.26
184	521	2	-3.96	-3.65	0.31
88	513	2	-3.98	-3.84	0.15
4	510	2	-4.00	-3.82	0.18
76	498	2	-3.94	-3.69	0.25

Continued on next page

Supplementary Table 19: Energetic and electronic properties for $[Ni_7Ga_6]$ cores obtained with PBE/light-tier1 level and light SCF parameters: configuration number (i), relative total energy (ΔE_{tot}), total magnetic moment (m_{tot}), HOMO energy (ε_H), LUMO energy (ε_L), and LUMO-HOMO energy gap (E_g).

i	ΔE_{tot} (meV)	m_{tot} (μ_B)	ε_H (eV)	ε_L (eV)	E_g (eV)
170	471	2	-4.02	-3.86	0.17
3	470	2	-4.26	-4.08	0.18
14	463	2	-4.00	-3.86	0.14
36	461	2	-4.08	-3.89	0.19
13	458	0	-3.87	-3.62	0.25
91	457	2	-4.06	-3.94	0.12
78	405	0	-3.96	-3.76	0.20
140	404	2	-4.02	-3.77	0.25
157	402	2	-3.97	-3.82	0.15
73	393	2	-4.11	-3.78	0.33
86	386	2	-4.00	-3.87	0.13
163	358	4	-4.06	-4.00	0.06
173	337	0	-4.14	-3.90	0.24
108	326	2	-3.95	-3.82	0.13
172	319	2	-3.74	-3.60	0.14
42	284	2	-4.08	-3.84	0.24
46	283	2	-4.05	-3.84	0.22
180	281	0	-4.01	-3.83	0.18
9	269	2	-4.07	-3.69	0.38
85	262	2	-3.98	-3.76	0.22
181	260	0	-3.88	-3.60	0.28
159	251	2	-4.07	-3.88	0.20

Continued on next page

Supplementary Table 19: Energetic and electronic properties for $[Ni_7Ga_6]$ cores obtained with PBE/light-tier1 level and light SCF parameters: configuration number (i), relative total energy (ΔE_{tot}), total magnetic moment (m_{tot}), HOMO energy (ε_H), LUMO energy (ε_L), and LUMO-HOMO energy gap (E_g).

i	ΔE_{tot} (meV)	m_{tot} (μ_B)	ε_H (eV)	ε_L (eV)	E_g (eV)
99	158	2	-3.88	-3.72	0.16
8	96	2	-4.02	-3.83	0.19
10	83	2	-4.02	-3.83	0.19
84	71	2	-3.98	-3.77	0.21
182	58	2	-4.05	-3.88	0.17
177	35	2	-4.01	-3.83	0.18
5	5	2	-4.01	-3.69	0.33
6	0	2	-4.12	-3.90	0.22

2.7 Additional Results for Metal Complexes

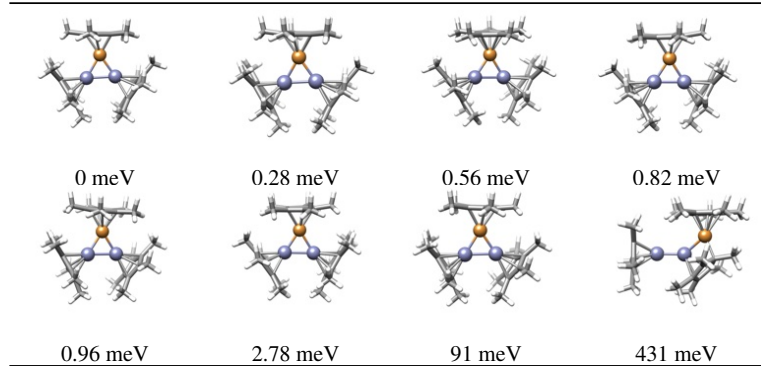
In the following subsections, we summarize a large number of results obtained for the computational design of molecular metal complexes. In particular, large part of the data is reported for the $[Cu_aZn_b]R_n$ complexes and also results for miscellaneous complexes using `cluster_assembler` protocol summarized above.

2.7.1 [CuZn₂](Cp^{*})₃ Complexes

Supplementary Table 20: Energetic and electronic properties for [CuZn₂](Cp^{*})₃ complexes obtained with PBE/light-tier1 level and light SCF parameters: configuration number (*i*), relative total energy (ΔE_{tot}), total magnetic moment (m_{tot}), HOMO energy (ε_H), LUMO energy (ε_L), and LUMO-HOMO energy gap (E_g).

<i>i</i>	ΔE_{tot} (meV)	m_{tot} (μ_B)	ε_H (eV)	ε_L (eV)	E_g (eV)
15	6626	0	-3.64	-3.53	0.11
20	4578	0	-4.30	-3.52	0.77
14	3572	0	-4.16	-3.70	0.46
19	3551	0	-4.15	-3.70	0.45
13	3549	0	-4.21	-3.76	0.44
10	3534	0	-4.20	-3.75	0.45
5	3489	0	-4.24	-3.80	0.44
8	3486	0	-4.25	-3.81	0.44
18	3449	0	-4.17	-3.72	0.44
6	2438	0	-4.32	-2.49	1.84
17	431	0	-3.87	-1.52	2.35
1	91	0	-3.97	-1.48	2.49
9	3	0	-3.97	-1.38	2.60
3	1	0	-3.97	-1.38	2.60
11	1	0	-3.97	-1.37	2.59
2	1	0	-3.97	-1.37	2.60
16	0	0	-3.96	-1.36	2.61
7	0	0	-3.97	-1.37	2.60

Supplementary Table 21: Optimized and filtered representative structures of $[\text{CuZn}_2](\text{Cp}^*)_3$ complexes obtained with PBE/light-tier1 level and light SCF parameters. The relative total energy (ΔE_{tot}) is depicted above each structure.



2.7.2 $[\text{Cu}_3\text{Zn}_4](\text{Cp}^*)_5$ Complexes

Supplementary Table 22: Energetic and electronic properties for $[\text{Cu}_3\text{Zn}_4](\text{Cp}^*)_5$ complexes obtained with PBE/light-tier1 level and light SCF parameters: configuration number (i), relative total energy (ΔE_{tot}), total magnetic moment (m_{tot}), HOMO energy (ε_H), LUMO energy (ε_L), and LUMO-HOMO energy gap (E_g).

i	ΔE_{tot} (meV)	m_{tot} (μ_B)	ε_H (eV)	ε_L (eV)	E_g (eV)
12	6403	0	-3.93	-3.51	0.42
124	6233	0	-3.68	-2.71	0.97
239	4815	0	-3.65	-2.87	0.78
233	4803	0	-3.83	-2.46	1.37
81	4676	0	-4.10	-2.82	1.28
2	4565	0	-3.68	-2.74	0.94
26	4469	0	-3.69	-3.47	0.22
8	4435	0	-4.03	-3.20	0.83
266	4305	0	-3.12	-2.95	0.17

Continued on next page

Supplementary Table 22: Energetic and electronic properties for $[\text{Cu}_3\text{Zn}_4](\text{Cp}^*)_5$ complexes obtained with PBE/light-tier1 level and light SCF parameters: configuration number (i), relative total energy (ΔE_{tot}), total magnetic moment (m_{tot}), HOMO energy (ε_H), LUMO energy (ε_L), and LUMO-HOMO energy gap (E_g).

i	ΔE_{tot} (meV)	m_{tot} (μ_B)	ε_H (eV)	ε_L (eV)	E_g (eV)
4	4284	0	-3.73	-2.91	0.82
19	4228	0	-3.78	-3.52	0.26
216	4056	0	-3.82	-2.44	1.38
205	3800	0	-3.77	-2.97	0.79
154	3671	0	-3.92	-2.99	0.92
97	3452	0	-3.62	-2.92	0.70
44	3448	0	-3.81	-2.68	1.14
160	3419	0	-4.03	-2.86	1.17
146	3389	0	-3.90	-2.66	1.24
168	3329	0	-3.68	-2.64	1.04
223	3293	0	-4.00	-3.13	0.87
167	3241	0	-3.74	-3.16	0.57
227	3214	0	-3.89	-2.97	0.92
131	3147	0	-3.58	-2.58	1.00
183	3138	0	-3.63	-2.56	1.06
299	3129	0	-3.79	-2.88	0.91
291	3128	0	-3.88	-3.10	0.77
70	3100	0	-4.24	-2.56	1.67
204	2941	0	-3.95	-2.42	1.53
138	2924	0	-3.76	-2.48	1.28
256	2892	0	-3.85	-2.58	1.27
133	2869	0	-3.70	-3.60	0.10

Continued on next page

Supplementary Table 22: Energetic and electronic properties for $[\text{Cu}_3\text{Zn}_4](\text{Cp}^*)_5$ complexes obtained with PBE/light-tier1 level and light SCF parameters: configuration number (i), relative total energy (ΔE_{tot}), total magnetic moment (m_{tot}), HOMO energy (ε_H), LUMO energy (ε_L), and LUMO-HOMO energy gap (E_g).

i	ΔE_{tot} (meV)	m_{tot} (μ_B)	ε_H (eV)	ε_L (eV)	E_g (eV)
33	2837	0	-4.13	-2.72	1.41
116	2758	0	-3.71	-2.61	1.10
232	2755	0	-3.82	-2.94	0.88
215	2704	0	-3.32	-2.99	0.33
217	2685	0	-3.44	-2.62	0.81
286	2671	0	-3.90	-2.54	1.36
293	2666	0	-3.62	-2.53	1.09
241	2663	0	-4.05	-2.90	1.15
78	2621	0	-3.59	-3.15	0.44
222	2512	0	-3.65	-2.70	0.94
31	2502	0	-3.95	-2.71	1.24
326	2445	0	-3.77	-2.59	1.18
150	2350	0	-3.74	-2.59	1.15
282	2338	0	-4.17	-2.99	1.18
255	2313	0	-4.00	-2.76	1.24
86	2294	0	-4.13	-3.03	1.10
55	2252	0	-4.31	-3.21	1.11
37	2209	0	-3.96	-2.93	1.02
111	2208	0	-3.51	-2.64	0.87
247	2204	0	-4.15	-3.35	0.80
56	2201	0	-4.21	-3.26	0.95
308	2176	0	-4.18	-2.58	1.60

Continued on next page

Supplementary Table 22: Energetic and electronic properties for $[\text{Cu}_3\text{Zn}_4](\text{Cp}^*)_5$ complexes obtained with PBE/light-tier1 level and light SCF parameters: configuration number (i), relative total energy (ΔE_{tot}), total magnetic moment (m_{tot}), HOMO energy (ε_H), LUMO energy (ε_L), and LUMO-HOMO energy gap (E_g).

i	ΔE_{tot} (meV)	m_{tot} (μ_B)	ε_H (eV)	ε_L (eV)	E_g (eV)
182	2133	0	-3.99	-3.29	0.69
115	2130	0	-3.82	-2.76	1.05
325	2123	0	-3.69	-2.74	0.95
54	2123	0	-4.24	-3.06	1.18
9	2114	0	-3.84	-2.77	1.07
93	2104	0	-4.19	-2.76	1.42
60	2085	0	-3.79	-2.73	1.05
149	2084	0	-3.92	-2.77	1.15
68	2069	0	-3.84	-2.25	1.60
109	2062	0	-3.52	-2.66	0.86
100	2062	0	-4.10	-3.02	1.08
288	2057	0	-4.14	-2.65	1.49
3	2055	0	-3.88	-2.77	1.11
158	2026	0	-4.26	-2.66	1.60
161	2025	0	-3.88	-2.87	1.01
218	2020	0	-3.71	-2.60	1.11
63	2009	0	-3.83	-2.59	1.23
113	2005	0	-3.96	-2.68	1.28
324	1988	0	-3.75	-2.59	1.16
297	1966	0	-4.00	-2.12	1.88
172	1962	0	-4.05	-3.54	0.52
274	1949	0	-3.80	-2.94	0.86

Continued on next page

Supplementary Table 22: Energetic and electronic properties for $[\text{Cu}_3\text{Zn}_4](\text{Cp}^*)_5$ complexes obtained with PBE/light-tier1 level and light SCF parameters: configuration number (i), relative total energy (ΔE_{tot}), total magnetic moment (m_{tot}), HOMO energy (ε_H), LUMO energy (ε_L), and LUMO-HOMO energy gap (E_g).

i	ΔE_{tot} (meV)	m_{tot} (μ_B)	ε_H (eV)	ε_L (eV)	E_g (eV)
84	1947	0	-3.99	-2.68	1.30
21	1946	0	-4.29	-2.93	1.35
173	1944	0	-3.84	-2.69	1.15
252	1940	0	-4.13	-2.46	1.67
300	1940	0	-3.98	-2.92	1.06
53	1937	0	-4.24	-3.17	1.08
126	1929	0	-4.25	-3.37	0.88
16	1924	0	-3.72	-2.72	1.00
235	1908	0	-4.00	-2.43	1.56
39	1894	0	-4.00	-2.46	1.54
226	1887	0	-3.74	-2.28	1.46
6	1882	0	-3.92	-2.45	1.47
157	1882	0	-3.87	-2.84	1.03
237	1881	0	-3.89	-2.41	1.49
238	1869	0	-4.05	-2.69	1.36
316	1868	0	-3.74	-2.57	1.17
87	1858	0	-3.67	-2.67	1.00
276	1853	0	-3.98	-2.37	1.61
127	1848	0	-4.41	-3.25	1.16
139	1839	0	-3.72	-2.58	1.15
275	1835	0	-3.80	-2.62	1.18
28	1827	0	-3.72	-2.73	1.00

Continued on next page

Supplementary Table 22: Energetic and electronic properties for $[\text{Cu}_3\text{Zn}_4](\text{Cp}^*)_5$ complexes obtained with PBE/light-tier1 level and light SCF parameters: configuration number (i), relative total energy (ΔE_{tot}), total magnetic moment (m_{tot}), HOMO energy (ε_H), LUMO energy (ε_L), and LUMO-HOMO energy gap (E_g).

i	ΔE_{tot} (meV)	m_{tot} (μ_B)	ε_H (eV)	ε_L (eV)	E_g (eV)
176	1802	0	-3.83	-2.66	1.17
195	1796	0	-4.08	-2.37	1.72
27	1795	0	-4.27	-2.65	1.62
49	1790	0	-4.10	-2.69	1.41
61	1788	0	-4.33	-2.96	1.38
210	1785	0	-4.12	-2.52	1.60
229	1767	0	-3.87	-2.65	1.23
136	1767	0	-3.94	-2.34	1.60
190	1766	0	-3.84	-2.58	1.26
98	1761	0	-4.12	-2.73	1.40
231	1753	0	-4.03	-2.40	1.63
67	1747	0	-4.05	-2.45	1.60
321	1739	0	-3.78	-2.54	1.24
162	1736	0	-3.68	-2.46	1.22
320	1736	0	-3.63	-2.50	1.13
181	1729	0	-4.04	-2.24	1.80
311	1726	0	-3.89	-2.40	1.49
92	1724	0	-4.09	-2.36	1.74
128	1724	0	-3.52	-2.63	0.89
121	1723	0	-4.05	-2.86	1.19
265	1720	0	-3.78	-2.67	1.11
262	1719	0	-3.92	-2.51	1.41

Continued on next page

Supplementary Table 22: Energetic and electronic properties for $[\text{Cu}_3\text{Zn}_4](\text{Cp}^*)_5$ complexes obtained with PBE/light-tier1 level and light SCF parameters: configuration number (i), relative total energy (ΔE_{tot}), total magnetic moment (m_{tot}), HOMO energy (ε_H), LUMO energy (ε_L), and LUMO-HOMO energy gap (E_g).

i	ΔE_{tot} (meV)	m_{tot} (μ_B)	ε_H (eV)	ε_L (eV)	E_g (eV)
187	1712	0	-3.93	-2.67	1.25
319	1710	0	-3.75	-2.06	1.69
110	1709	0	-3.98	-2.27	1.71
202	1702	0	-3.78	-2.28	1.50
108	1702	0	-3.89	-2.44	1.45
166	1696	0	-3.77	-2.56	1.21
250	1696	0	-3.86	-2.45	1.41
59	1694	0	-3.80	-2.28	1.51
203	1692	0	-4.08	-2.53	1.55
292	1679	0	-3.91	-2.48	1.43
212	1671	0	-4.20	-2.21	1.99
85	1666	0	-3.93	-2.62	1.31
290	1665	0	-4.01	-2.44	1.56
270	1664	0	-4.05	-2.59	1.45
244	1657	0	-3.90	-2.46	1.44
177	1655	0	-4.09	-2.59	1.50
82	1651	0	-3.64	-2.64	1.00
258	1648	0	-4.16	-2.73	1.43
101	1640	0	-3.72	-2.41	1.32
45	1638	0	-3.84	-2.62	1.21
137	1637	0	-3.59	-2.66	0.94
117	1636	0	-4.09	-2.54	1.56

Continued on next page

Supplementary Table 22: Energetic and electronic properties for $[\text{Cu}_3\text{Zn}_4](\text{Cp}^*)_5$ complexes obtained with PBE/light-tier1 level and light SCF parameters: configuration number (i), relative total energy (ΔE_{tot}), total magnetic moment (m_{tot}), HOMO energy (ε_H), LUMO energy (ε_L), and LUMO-HOMO energy gap (E_g).

i	ΔE_{tot} (meV)	m_{tot} (μ_B)	ε_H (eV)	ε_L (eV)	E_g (eV)
22	1633	0	-3.82	-2.68	1.15
119	1632	0	-4.25	-2.79	1.46
130	1628	0	-3.90	-2.49	1.41
47	1619	0	-3.71	-2.16	1.55
180	1603	0	-3.97	-2.74	1.23
197	1601	0	-4.03	-2.59	1.45
189	1599	0	-3.98	-2.58	1.40
112	1593	0	-3.62	-2.27	1.35
277	1591	0	-4.14	-2.63	1.51
155	1588	0	-3.56	-2.65	0.91
169	1587	0	-3.55	-2.69	0.86
186	1582	0	-3.49	-2.52	0.97
164	1575	0	-3.68	-2.68	1.00
322	1574	0	-3.90	-2.69	1.21
13	1573	0	-3.94	-2.53	1.40
99	1566	0	-4.07	-2.26	1.81
199	1561	0	-4.13	-2.54	1.59
107	1560	0	-4.00	-2.45	1.56
14	1557	0	-4.02	-2.58	1.44
32	1554	0	-3.49	-2.52	0.97
224	1551	0	-3.74	-2.02	1.72
51	1548	0	-4.07	-2.69	1.38

Continued on next page

Supplementary Table 22: Energetic and electronic properties for $[\text{Cu}_3\text{Zn}_4](\text{Cp}^*)_5$ complexes obtained with PBE/light-tier1 level and light SCF parameters: configuration number (i), relative total energy (ΔE_{tot}), total magnetic moment (m_{tot}), HOMO energy (ε_H), LUMO energy (ε_L), and LUMO-HOMO energy gap (E_g).

i	ΔE_{tot} (meV)	m_{tot} (μ_B)	ε_H (eV)	ε_L (eV)	E_g (eV)
135	1544	0	-3.91	-2.34	1.57
246	1542	0	-4.19	-2.87	1.32
185	1535	0	-3.86	-2.71	1.15
198	1531	0	-3.96	-2.50	1.46
36	1526	0	-3.83	-2.17	1.67
57	1524	0	-3.47	-2.52	0.95
174	1524	0	-4.01	-2.63	1.38
272	1518	0	-4.02	-2.52	1.50
71	1516	0	-4.04	-2.63	1.41
171	1514	0	-3.90	-2.43	1.47
15	1513	0	-4.05	-2.49	1.56
191	1508	0	-4.04	-2.39	1.65
65	1507	0	-4.04	-2.40	1.65
257	1507	0	-4.23	-2.55	1.68
122	1506	0	-3.89	-2.18	1.71
228	1504	0	-4.37	-2.58	1.80
46	1489	0	-3.60	-2.58	1.02
134	1477	0	-4.06	-2.62	1.43
208	1477	0	-3.80	-2.36	1.44
129	1472	0	-3.69	-2.64	1.05
118	1471	0	-4.12	-2.54	1.58
153	1461	0	-3.85	-2.48	1.37

Continued on next page

Supplementary Table 22: Energetic and electronic properties for $[\text{Cu}_3\text{Zn}_4](\text{Cp}^*)_5$ complexes obtained with PBE/light-tier1 level and light SCF parameters: configuration number (i), relative total energy (ΔE_{tot}), total magnetic moment (m_{tot}), HOMO energy (ε_H), LUMO energy (ε_L), and LUMO-HOMO energy gap (E_g).

i	ΔE_{tot} (meV)	m_{tot} (μ_B)	ε_H (eV)	ε_L (eV)	E_g (eV)
38	1458	0	-3.98	-2.06	1.91
25	1457	0	-3.97	-2.27	1.70
50	1454	0	-3.62	-2.57	1.05
243	1451	0	-3.71	-2.17	1.55
201	1451	0	-4.14	-2.35	1.79
152	1449	0	-4.15	-2.58	1.57
5	1445	0	-4.09	-2.33	1.77
89	1440	0	-4.15	-2.43	1.71
211	1433	0	-3.86	-2.44	1.42
142	1431	0	-4.18	-2.47	1.71
236	1430	0	-4.04	-2.68	1.36
140	1425	0	-4.02	-2.65	1.37
96	1423	0	-3.76	-2.40	1.36
289	1421	0	-3.97	-2.32	1.64
75	1416	0	-3.87	-2.02	1.85
80	1413	0	-4.02	-2.18	1.84
280	1405	0	-4.05	-2.62	1.43
294	1404	0	-4.03	-2.27	1.76
145	1398	0	-3.70	-2.41	1.29
295	1389	0	-3.92	-2.32	1.60
42	1389	0	-4.24	-2.56	1.68
52	1385	0	-4.11	-2.21	1.89

Continued on next page

Supplementary Table 22: Energetic and electronic properties for $[\text{Cu}_3\text{Zn}_4](\text{Cp}^*)_5$ complexes obtained with PBE/light-tier1 level and light SCF parameters: configuration number (i), relative total energy (ΔE_{tot}), total magnetic moment (m_{tot}), HOMO energy (ε_H), LUMO energy (ε_L), and LUMO-HOMO energy gap (E_g).

i	ΔE_{tot} (meV)	m_{tot} (μ_B)	ε_H (eV)	ε_L (eV)	E_g (eV)
317	1381	0	-4.43	-2.57	1.85
147	1380	0	-4.09	-2.76	1.32
90	1375	0	-4.09	-2.27	1.82
64	1373	0	-3.94	-2.45	1.49
285	1371	0	-3.80	-2.27	1.53
214	1368	0	-3.81	-2.37	1.44
151	1367	0	-3.74	-2.17	1.57
281	1367	0	-3.65	-2.24	1.41
58	1364	0	-3.94	-2.33	1.61
304	1360	0	-4.43	-2.70	1.73
296	1360	0	-3.97	-2.14	1.83
105	1353	0	-4.06	-2.22	1.85
248	1353	0	-4.30	-2.82	1.49
88	1347	0	-4.24	-1.86	2.37
125	1333	0	-4.12	-2.45	1.67
175	1331	0	-4.06	-2.43	1.63
264	1329	0	-3.95	-2.27	1.68
310	1329	0	-4.06	-2.31	1.75
23	1329	0	-4.06	-2.31	1.75
170	1328	0	-4.14	-2.50	1.64
77	1311	0	-3.94	-2.29	1.65
298	1309	0	-3.90	-2.32	1.58

Continued on next page

Supplementary Table 22: Energetic and electronic properties for $[\text{Cu}_3\text{Zn}_4](\text{Cp}^*)_5$ complexes obtained with PBE/light-tier1 level and light SCF parameters: configuration number (i), relative total energy (ΔE_{tot}), total magnetic moment (m_{tot}), HOMO energy (ε_H), LUMO energy (ε_L), and LUMO-HOMO energy gap (E_g).

i	ΔE_{tot} (meV)	m_{tot} (μ_B)	ε_H (eV)	ε_L (eV)	E_g (eV)
69	1308	0	-4.12	-2.41	1.71
103	1298	0	-4.02	-2.68	1.35
144	1295	0	-4.07	-2.24	1.83
79	1292	0	-4.03	-2.14	1.88
327	1285	0	-4.16	-2.58	1.58
305	1285	0	-4.16	-2.58	1.58
143	1283	0	-4.16	-2.72	1.43
200	1282	0	-4.00	-2.10	1.90
73	1282	0	-4.09	-2.61	1.47
72	1281	0	-4.06	-2.59	1.47
273	1279	0	-4.19	-2.46	1.73
17	1279	0	-3.87	-2.45	1.42
213	1276	0	-3.94	-2.30	1.64
40	1276	0	-4.21	-2.49	1.72
263	1260	0	-3.90	-2.48	1.42
132	1259	0	-4.02	-2.56	1.47
179	1257	0	-4.09	-2.60	1.50
104	1254	0	-3.89	-1.99	1.90
62	1248	0	-3.90	-2.45	1.45
278	1248	0	-4.08	-2.49	1.59
312	1247	0	-4.32	-2.67	1.65
287	1242	0	-3.92	-2.05	1.87

Continued on next page

Supplementary Table 22: Energetic and electronic properties for $[\text{Cu}_3\text{Zn}_4](\text{Cp}^*)_5$ complexes obtained with PBE/light-tier1 level and light SCF parameters: configuration number (i), relative total energy (ΔE_{tot}), total magnetic moment (m_{tot}), HOMO energy (ε_H), LUMO energy (ε_L), and LUMO-HOMO energy gap (E_g).

i	ΔE_{tot} (meV)	m_{tot} (μ_B)	ε_H (eV)	ε_L (eV)	E_g (eV)
219	1241	0	-3.78	-2.19	1.59
165	1238	0	-3.86	-2.59	1.27
268	1225	0	-4.25	-2.17	2.09
220	1225	0	-3.86	-2.40	1.45
83	1223	0	-4.01	-2.02	1.99
184	1216	0	-3.83	-2.41	1.42
43	1208	0	-4.17	-2.39	1.78
20	1207	0	-4.20	-2.29	1.91
35	1205	0	-3.96	-2.15	1.80
249	1194	0	-3.74	-2.61	1.13
234	1182	0	-4.08	-2.34	1.73
102	1182	0	-3.98	-2.36	1.63
209	1176	0	-4.00	-2.34	1.67
196	1166	0	-4.19	-2.89	1.30
30	1163	0	-4.03	-2.21	1.82
193	1157	0	-4.26	-2.90	1.37
7	1151	0	-4.09	-2.41	1.69
269	1151	0	-4.26	-2.13	2.12
34	1148	0	-4.07	-2.36	1.71
314	1144	0	-4.22	-1.95	2.27
221	1141	0	-4.27	-2.06	2.21
207	1133	0	-3.92	-2.28	1.64

Continued on next page

Supplementary Table 22: Energetic and electronic properties for $[\text{Cu}_3\text{Zn}_4](\text{Cp}^*)_5$ complexes obtained with PBE/light-tier1 level and light SCF parameters: configuration number (i), relative total energy (ΔE_{tot}), total magnetic moment (m_{tot}), HOMO energy (ε_H), LUMO energy (ε_L), and LUMO-HOMO energy gap (E_g).

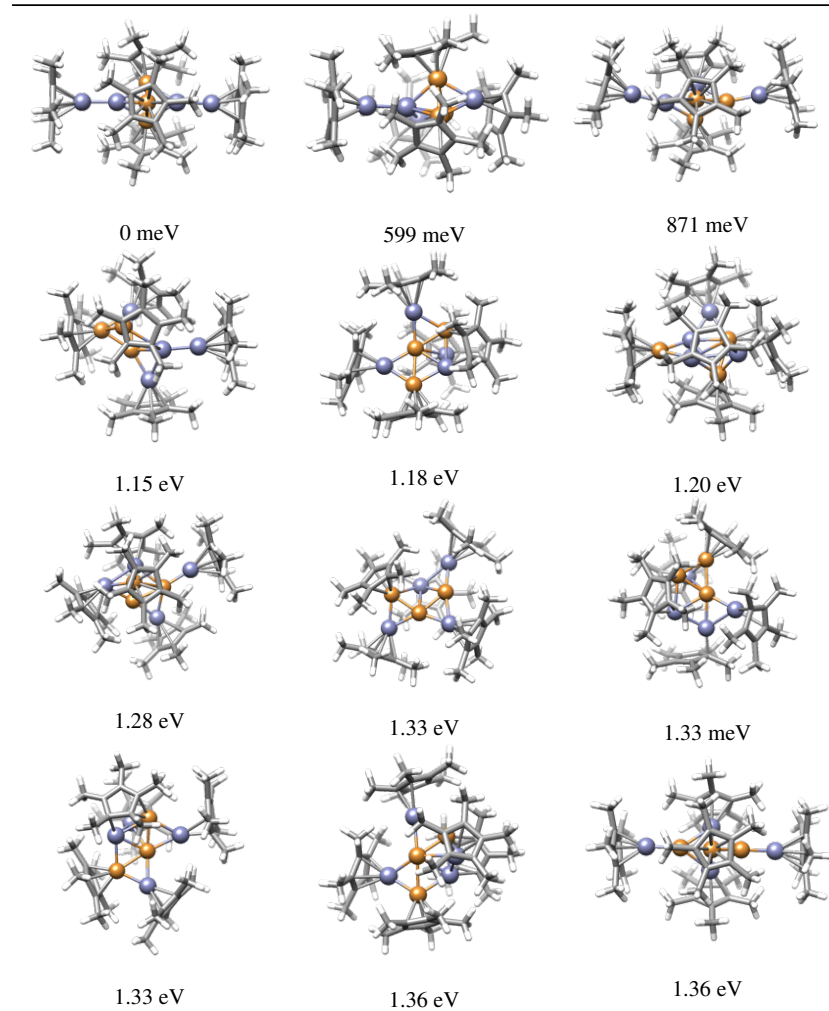
i	ΔE_{tot} (meV)	m_{tot} (μ_B)	ε_H (eV)	ε_L (eV)	E_g (eV)
1	1131	0	-4.16	-2.37	1.79
245	1123	0	-3.95	-2.10	1.85
267	1121	0	-4.22	-2.15	2.07
120	1118	0	-4.07	-1.94	2.13
283	1115	0	-4.08	-2.21	1.87
66	1114	0	-3.76	-2.67	1.08
76	1111	0	-4.06	-2.33	1.73
240	1110	0	-4.16	-2.40	1.76
260	1085	0	-3.97	-2.09	1.88
315	1078	0	-4.08	-1.97	2.11
284	1036	0	-4.16	-2.09	2.07
194	1019	0	-4.28	-2.05	2.23
192	1016	0	-3.95	-2.14	1.81
178	1013	0	-4.14	-2.19	1.95
148	1011	0	-3.62	-2.35	1.27
91	1007	0	-4.07	-2.37	1.69
279	999	0	-4.08	-2.23	1.86
41	997	0	-4.10	-2.29	1.81
309	991	0	-4.06	-2.27	1.79
94	985	0	-4.00	-2.17	1.83
259	976	0	-3.93	-1.91	2.02
141	971	0	-4.04	-1.94	2.10

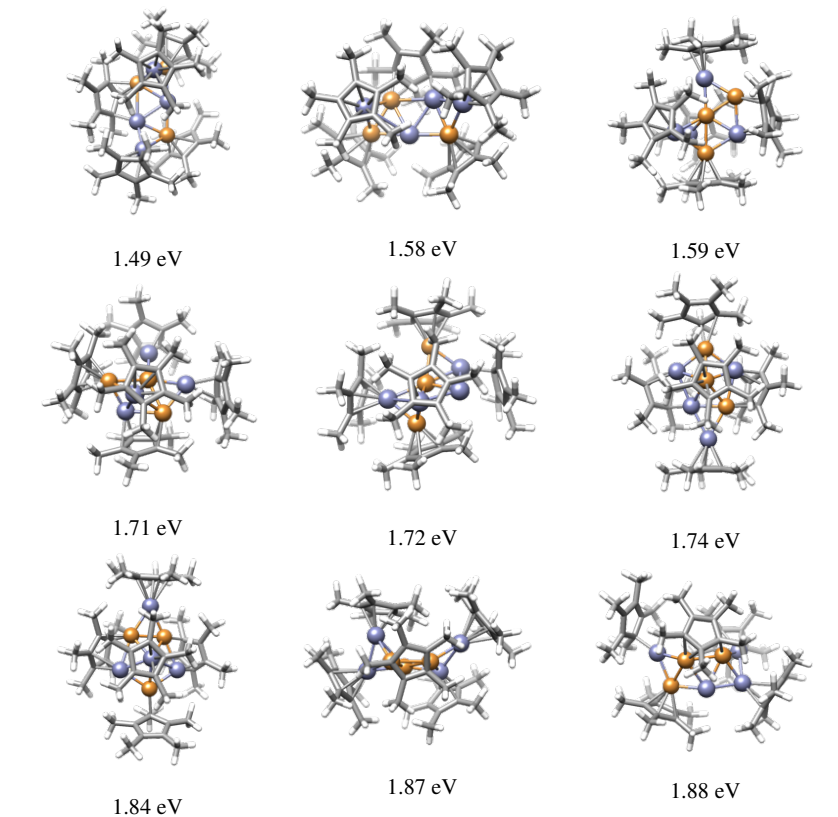
Continued on next page

Supplementary Table 22: Energetic and electronic properties for $[\text{Cu}_3\text{Zn}_4](\text{Cp}^*)_5$] complexes obtained with PBE/light-tier1 level and light SCF parameters: configuration number (i), relative total energy (ΔE_{tot}), total magnetic moment (m_{tot}), HOMO energy (ε_H), LUMO energy (ε_L), and LUMO-HOMO energy gap (E_g).

i	ΔE_{tot} (meV)	m_{tot} (μ_B)	ε_H (eV)	ε_L (eV)	E_g (eV)
188	970	0	-4.18	-2.36	1.82
261	959	0	-3.96	-1.93	2.03
251	949	0	-4.07	-2.02	2.05
163	935	0	-4.07	-2.13	1.93
230	927	0	-4.03	-2.02	2.01
225	920	0	-4.08	-2.19	1.89
18	888	0	-4.06	-2.19	1.87
48	871	0	-4.06	-2.23	1.83
74	811	0	-4.07	-2.12	1.95
114	772	0	-3.91	-2.27	1.64
254	739	0	-4.02	-2.62	1.40
11	678	0	-3.93	-2.36	1.57
271	635	0	-3.89	-2.33	1.57
253	599	0	-3.91	-2.26	1.64
307	0	0	-3.65	-1.79	1.86

Supplementary Table 23: Optimized and filtered representative structures of $[\text{Cu}_3\text{Zn}_4](\text{Cp}^*)_5$ complexes obtained with PBE+TS/light-tier1 level and light SCF parameters. The label and relative total energy (ΔE_{tot}) is depicted above each structure.





2.7.3 $[\text{Cu}_5\text{Zn}_5](\text{Cp}^*)_6(\text{CO}_2)_2$ Complexes

Supplementary Table 24: Energetic and electronic properties for $[\text{Cu}_5\text{Zn}_5](\text{Cp}^*)_6(\text{CO}_2)_2$ complexes obtained with PBE/light-tier1 level and light SCF parameters: configuration number (i), relative total energy (ΔE_{tot}), total magnetic moment (m_{tot}), HOMO energy (ε_H), LUMO energy (ε_L), and LUMO-HOMO energy gap (E_g).

i	ΔE_{tot} (meV)	m_{tot} (μ_B)	ε_H (eV)	ε_L (eV)	E_g (eV)
239	5875	1	-3.73	-3.56	0.17

Continued on next page

Supplementary Table 24: Energetic and electronic properties for $[\text{Cu}_5\text{Zn}_5](\text{Cp}^*)_6(\text{CO}_2)_2$ complexes obtained with PBE/light-tier1 level and light SCF parameters: configuration number (i), relative total energy (ΔE_{tot}), total magnetic moment (m_{tot}), HOMO energy (ε_H), LUMO energy (ε_L), and LUMO-HOMO energy gap (E_g).

i	ΔE_{tot} (meV)	m_{tot} (μ_B)	ε_H (eV)	ε_L (eV)	E_g (eV)
169	5758	1	-3.54	-3.37	0.17
197	5613	1	-3.62	-3.19	0.43
95	5559	1	-3.96	-3.71	0.26
62	5538	1	-3.81	-3.49	0.32
204	5022	1	-3.78	-2.83	0.94
245	4896	1	-3.30	-2.94	0.36
210	4893	1	-3.42	-3.19	0.23
49	4766	1	-3.64	-3.41	0.24
58	4713	1	-3.43	-3.26	0.18
83	4527	1	-3.24	-3.06	0.17
238	4411	1	-3.54	-3.38	0.15
167	4354	1	-3.18	-2.97	0.21
99	4333	1	-3.33	-2.95	0.38
143	4313	1	-3.84	-3.38	0.46
18	4247	1	-3.68	-3.53	0.15
94	4247	1	-3.46	-2.95	0.50
254	4194	1	-2.92	-2.62	0.30
205	4181	1	-3.22	-2.98	0.24
319	4045	1	-3.54	-3.36	0.18
76	3999	1	-3.79	-3.62	0.17
36	3960	1	-3.24	-2.94	0.30
221	3933	1	-3.22	-3.03	0.18

Continued on next page

Supplementary Table 24: Energetic and electronic properties for $[\text{Cu}_5\text{Zn}_5](\text{Cp}^*)_6(\text{CO}_2)_2$ complexes obtained with PBE/light-tier1 level and light SCF parameters: configuration number (i), relative total energy (ΔE_{tot}), total magnetic moment (m_{tot}), HOMO energy (ε_H), LUMO energy (ε_L), and LUMO-HOMO energy gap (E_g).

i	ΔE_{tot} (meV)	m_{tot} (μ_B)	ε_H (eV)	ε_L (eV)	E_g (eV)
158	3855	1	-3.98	-3.48	0.50
10	3816	1	-3.57	-2.76	0.81
257	3762	1	-3.55	-3.37	0.18
175	3733	1	-3.69	-3.51	0.19
288	3722	1	-3.90	-3.70	0.20
79	3671	1	-3.55	-3.31	0.24
53	3541	1	-3.68	-3.57	0.11
55	3540	1	-3.82	-3.59	0.23
136	3531	1	-3.53	-2.66	0.86
73	3528	1	-3.76	-2.69	1.07
181	3502	1	-3.44	-3.21	0.23
163	3492	1	-4.04	-3.58	0.46
17	3441	1	-3.90	-3.67	0.23
41	3428	1	-3.32	-3.08	0.24
35	3412	1	-3.68	-3.51	0.17
164	3406	1	-3.52	-3.34	0.19
77	3402	1	-3.78	-3.57	0.22
51	3371	1	-3.21	-2.86	0.35
86	3370	1	-3.61	-3.44	0.17
9	3289	1	-3.69	-3.52	0.18
328	3265	1	-3.77	-3.61	0.15
231	3249	1	-3.99	-3.77	0.22

Continued on next page

Supplementary Table 24: Energetic and electronic properties for $[\text{Cu}_5\text{Zn}_5](\text{Cp}^*)_6(\text{CO}_2)_2$ complexes obtained with PBE/light-tier1 level and light SCF parameters: configuration number (i), relative total energy (ΔE_{tot}), total magnetic moment (m_{tot}), HOMO energy (ε_H), LUMO energy (ε_L), and LUMO-HOMO energy gap (E_g).

i	ΔE_{tot} (meV)	m_{tot} (μ_B)	ε_H (eV)	ε_L (eV)	E_g (eV)
148	3233	1	-2.97	-2.64	0.33
139	3214	1	-3.87	-3.78	0.09
177	3208	1	-3.30	-3.09	0.21
179	3172	1	-3.60	-3.46	0.13
187	3165	1	-3.15	-2.89	0.26
19	3158	1	-3.92	-3.61	0.31
124	3156	1	-3.75	-3.57	0.19
183	3156	1	-3.32	-3.09	0.23
322	3149	1	-3.40	-3.00	0.41
91	3147	1	-3.19	-2.91	0.29
131	3123	1	-3.14	-2.95	0.20
105	3121	1	-3.43	-3.25	0.17
279	3100	1	-3.71	-3.47	0.24
5	3097	1	-3.16	-2.94	0.22
63	3078	1	-4.10	-3.44	0.66
286	3068	1	-3.88	-3.60	0.28
11	3048	1	-4.10	-3.32	0.78
60	3016	1	-3.85	-3.58	0.27
217	3012	1	-3.61	-3.44	0.18
13	3002	1	-4.11	-3.60	0.50
33	2975	1	-4.03	-3.70	0.33
118	2954	1	-3.30	-3.14	0.16

Continued on next page

Supplementary Table 24: Energetic and electronic properties for $[\text{Cu}_5\text{Zn}_5](\text{Cp}^*)_6(\text{CO}_2)_2$ complexes obtained with PBE/light-tier1 level and light SCF parameters: configuration number (i), relative total energy (ΔE_{tot}), total magnetic moment (m_{tot}), HOMO energy (ε_H), LUMO energy (ε_L), and LUMO-HOMO energy gap (E_g).

i	ΔE_{tot} (meV)	m_{tot} (μ_B)	ε_H (eV)	ε_L (eV)	E_g (eV)
107	2921	1	-3.84	-3.53	0.31
132	2906	1	-3.85	-3.42	0.43
285	2888	1	-3.91	-3.52	0.39
273	2886	1	-3.74	-3.63	0.11
23	2862	1	-4.03	-3.50	0.54
291	2860	1	-3.58	-3.41	0.17
228	2849	1	-3.67	-3.44	0.23
250	2843	1	-3.89	-3.52	0.37
39	2836	1	-3.88	-3.60	0.28
123	2830	1	-3.78	-3.49	0.29
216	2823	1	-3.46	-3.28	0.19
266	2786	1	-4.05	-3.53	0.52
274	2784	1	-3.77	-3.60	0.18
137	2773	1	-4.02	-3.65	0.37
247	2747	1	-3.99	-3.62	0.37
295	2746	1	-3.29	-3.12	0.17
185	2737	1	-3.74	-3.59	0.15
2	2736	1	-3.55	-3.30	0.25
71	2725	1	-4.06	-3.53	0.53
256	2724	1	-4.00	-3.57	0.43
81	2718	1	-3.88	-3.52	0.36
100	2705	1	-3.76	-3.62	0.14

Continued on next page

Supplementary Table 24: Energetic and electronic properties for $[\text{Cu}_5\text{Zn}_5](\text{Cp}^*)_6(\text{CO}_2)_2$ complexes obtained with PBE/light-tier1 level and light SCF parameters: configuration number (i), relative total energy (ΔE_{tot}), total magnetic moment (m_{tot}), HOMO energy (ε_H), LUMO energy (ε_L), and LUMO-HOMO energy gap (E_g).

i	ΔE_{tot} (meV)	m_{tot} (μ_B)	ε_H (eV)	ε_L (eV)	E_g (eV)
261	2687	1	-3.83	-3.50	0.33
130	2678	1	-3.95	-3.58	0.38
154	2672	1	-3.89	-3.66	0.23
26	2648	1	-4.09	-3.63	0.46
89	2640	1	-4.00	-3.80	0.20
37	2635	1	-3.58	-3.40	0.18
57	2621	1	-3.48	-3.22	0.26
156	2598	1	-3.96	-3.58	0.38
311	2594	1	-4.26	-3.93	0.32
193	2585	1	-3.74	-3.58	0.16
199	2572	1	-3.60	-3.44	0.16
68	2572	1	-3.80	-3.53	0.28
292	2563	1	-3.73	-3.49	0.24
173	2554	1	-3.35	-3.14	0.21
202	2526	1	-3.82	-3.63	0.19
32	2515	1	-3.82	-3.64	0.18
88	2512	1	-3.73	-3.61	0.12
186	2483	1	-3.90	-3.54	0.36
249	2426	1	-3.98	-3.67	0.31
108	2411	1	-3.89	-3.51	0.38
16	2395	1	-3.84	-3.60	0.24
182	2369	1	-3.89	-3.62	0.28

Continued on next page

Supplementary Table 24: Energetic and electronic properties for $[\text{Cu}_5\text{Zn}_5](\text{Cp}^*)_6(\text{CO}_2)_2$ complexes obtained with PBE/light-tier1 level and light SCF parameters: configuration number (i), relative total energy (ΔE_{tot}), total magnetic moment (m_{tot}), HOMO energy (ε_H), LUMO energy (ε_L), and LUMO-HOMO energy gap (E_g).

i	ΔE_{tot} (meV)	m_{tot} (μ_B)	ε_H (eV)	ε_L (eV)	E_g (eV)
7	2368	1	-3.80	-3.62	0.18
277	2363	1	-3.67	-3.53	0.14
224	2361	1	-3.91	-3.76	0.15
145	2343	1	-3.85	-3.52	0.34
3	2305	1	-3.72	-3.48	0.25
90	2302	1	-3.86	-3.52	0.34
308	2279	1	-3.99	-3.82	0.16
1	2275	1	-3.64	-3.42	0.22
114	2273	1	-3.90	-3.73	0.17
72	2273	1	-3.64	-3.48	0.16
78	2266	1	-3.46	-3.25	0.21
241	2198	1	-3.86	-3.67	0.19
125	2188	1	-3.42	-3.17	0.26
152	2183	1	-3.77	-3.61	0.17
248	2183	1	-3.92	-3.66	0.25
117	2175	1	-3.50	-3.34	0.16
44	2168	1	-3.78	-3.49	0.29
116	2152	1	-3.79	-3.71	0.08
43	2148	1	-3.71	-3.55	0.16
326	2142	1	-3.38	-3.16	0.22
268	2125	1	-3.88	-3.64	0.23
281	2124	1	-3.78	-3.34	0.44

Continued on next page

Supplementary Table 24: Energetic and electronic properties for $[\text{Cu}_5\text{Zn}_5](\text{Cp}^*)_6(\text{CO}_2)_2$ complexes obtained with PBE/light-tier1 level and light SCF parameters: configuration number (i), relative total energy (ΔE_{tot}), total magnetic moment (m_{tot}), HOMO energy (ε_H), LUMO energy (ε_L), and LUMO-HOMO energy gap (E_g).

i	ΔE_{tot} (meV)	m_{tot} (μ_B)	ε_H (eV)	ε_L (eV)	E_g (eV)
20	2105	1	-3.55	-3.36	0.19
174	2066	1	-3.57	-3.37	0.20
201	2063	1	-3.57	-3.43	0.14
42	2050	1	-3.53	-3.32	0.21
129	2035	1	-3.43	-3.25	0.18
155	2033	1	-3.99	-3.79	0.20
121	2025	1	-3.56	-3.39	0.17
142	2010	1	-4.07	-3.62	0.44
87	2010	1	-3.62	-3.49	0.13
127	2006	1	-3.56	-3.38	0.18
309	1999	1	-4.24	-4.08	0.16
258	1988	1	-3.68	-3.53	0.15
69	1981	1	-3.31	-3.12	0.19
162	1976	1	-3.49	-3.33	0.17
294	1973	1	-3.48	-3.33	0.16
212	1966	1	-3.19	-2.93	0.25
318	1965	1	-3.68	-3.47	0.21
312	1956	1	-4.29	-4.11	0.18
101	1937	1	-3.48	-3.29	0.18
209	1929	1	-3.85	-3.69	0.16
150	1907	1	-3.92	-3.70	0.22
240	1889	1	-3.37	-3.17	0.21

Continued on next page

Supplementary Table 24: Energetic and electronic properties for $[\text{Cu}_5\text{Zn}_5](\text{Cp}^*)_6(\text{CO}_2)_2$ complexes obtained with PBE/light-tier1 level and light SCF parameters: configuration number (i), relative total energy (ΔE_{tot}), total magnetic moment (m_{tot}), HOMO energy (ε_H), LUMO energy (ε_L), and LUMO-HOMO energy gap (E_g).

i	ΔE_{tot} (meV)	m_{tot} (μ_B)	ε_H (eV)	ε_L (eV)	E_g (eV)
15	1885	1	-3.26	-3.01	0.26
141	1855	1	-3.22	-3.03	0.19
298	1832	1	-3.21	-3.00	0.22
166	1828	1	-3.86	-3.69	0.17
161	1821	1	-3.48	-3.31	0.17
93	1804	1	-3.59	-3.42	0.16
138	1775	1	-3.86	-3.70	0.16
31	1763	1	-4.09	-3.84	0.25
134	1748	1	-3.62	-3.44	0.18
14	1737	1	-3.67	-3.54	0.13
56	1734	1	-3.49	-3.28	0.20
122	1727	1	-3.48	-3.31	0.17
96	1727	1	-3.20	-3.04	0.16
21	1707	1	-3.82	-3.67	0.15
195	1694	1	-3.49	-3.30	0.20
307	1691	1	-4.00	-3.74	0.26
284	1686	1	-3.60	-3.40	0.20
232	1685	1	-3.80	-3.61	0.19
74	1682	1	-3.31	-3.16	0.15
304	1674	1	-3.94	-3.58	0.36
84	1673	1	-3.56	-3.37	0.19
251	1668	1	-3.57	-3.42	0.16

Continued on next page

Supplementary Table 24: Energetic and electronic properties for $[\text{Cu}_5\text{Zn}_5](\text{Cp}^*)_6(\text{CO}_2)_2$ complexes obtained with PBE/light-tier1 level and light SCF parameters: configuration number (i), relative total energy (ΔE_{tot}), total magnetic moment (m_{tot}), HOMO energy (ε_H), LUMO energy (ε_L), and LUMO-HOMO energy gap (E_g).

i	ΔE_{tot} (meV)	m_{tot} (μ_B)	ε_H (eV)	ε_L (eV)	E_g (eV)
22	1667	1	-3.50	-3.25	0.25
176	1664	1	-3.73	-3.56	0.17
140	1662	1	-3.67	-3.52	0.15
223	1652	1	-3.56	-3.39	0.16
276	1644	1	-3.62	-3.44	0.19
252	1640	1	-3.70	-3.53	0.16
170	1637	1	-3.72	-3.58	0.14
52	1621	1	-3.35	-3.18	0.17
113	1620	1	-3.34	-3.19	0.16
267	1616	1	-3.68	-3.40	0.28
4	1616	1	-3.41	-3.25	0.17
115	1607	1	-3.54	-3.38	0.16
135	1596	1	-3.11	-2.92	0.19
208	1591	1	-3.58	-3.42	0.16
229	1588	1	-3.87	-3.65	0.23
236	1581	1	-3.32	-3.16	0.16
215	1577	1	-3.22	-3.05	0.18
259	1558	1	-3.61	-3.41	0.19
45	1515	1	-3.54	-3.38	0.16
70	1505	1	-3.48	-3.31	0.17
30	1494	1	-3.83	-3.48	0.35
317	1447	1	-4.07	-3.88	0.19

Continued on next page

Supplementary Table 24: Energetic and electronic properties for $[\text{Cu}_5\text{Zn}_5](\text{Cp}^*)_6(\text{CO}_2)_2$ complexes obtained with PBE/light-tier1 level and light SCF parameters: configuration number (i), relative total energy (ΔE_{tot}), total magnetic moment (m_{tot}), HOMO energy (ε_H), LUMO energy (ε_L), and LUMO-HOMO energy gap (E_g).

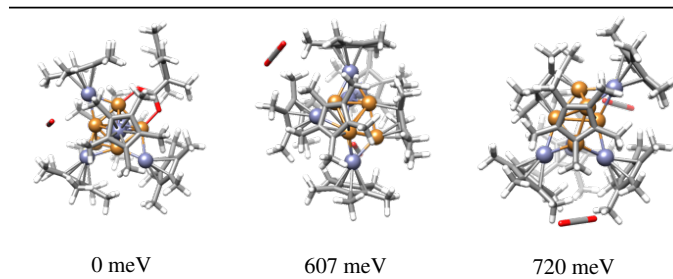
i	ΔE_{tot} (meV)	m_{tot} (μ_B)	ε_H (eV)	ε_L (eV)	E_g (eV)
6	1428	1	-3.43	-3.26	0.16
296	1423	1	-3.43	-3.27	0.16
144	1414	1	-3.37	-3.20	0.17
59	1411	1	-3.14	-2.95	0.19
153	1378	1	-3.39	-3.17	0.22
92	1370	1	-3.66	-3.48	0.19
85	1361	1	-3.33	-3.10	0.23
305	1316	1	-3.73	-3.48	0.25
168	1314	1	-3.51	-3.35	0.17
119	1296	1	-3.79	-3.63	0.17
66	1267	1	-3.41	-3.24	0.17
133	1254	1	-3.66	-3.42	0.24
29	1249	1	-3.31	-3.09	0.22
321	1225	1	-3.13	-2.76	0.37
235	1215	1	-3.39	-3.22	0.17
147	1187	1	-3.87	-3.69	0.18
171	1164	1	-3.10	-2.91	0.19
61	1147	1	-3.37	-3.19	0.18
47	1124	1	-3.15	-2.96	0.19
103	1084	1	-3.27	-3.11	0.16
316	1061	1	-3.98	-3.81	0.17
324	1025	1	-3.83	-3.46	0.37

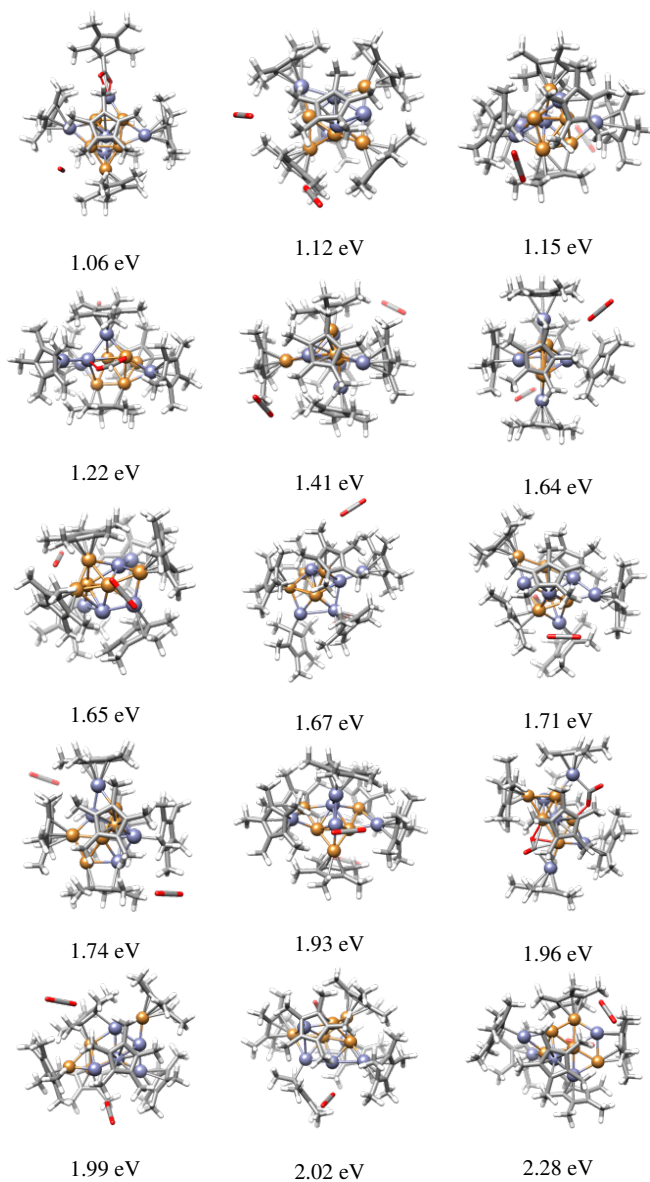
Continued on next page

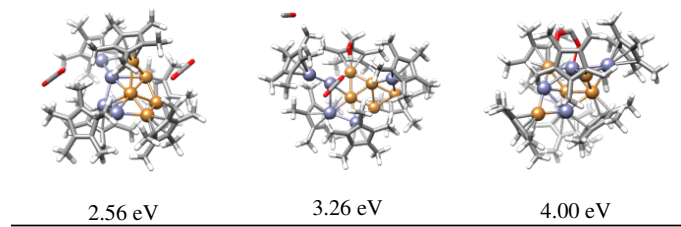
Supplementary Table 24: Energetic and electronic properties for $[\text{Cu}_5\text{Zn}_5](\text{Cp}^*)_6(\text{CO}_2)_2$ complexes obtained with PBE/light-tier1 level and light SCF parameters: configuration number (i), relative total energy (ΔE_{tot}), total magnetic moment (m_{tot}), HOMO energy (ε_H), LUMO energy (ε_L), and LUMO-HOMO energy gap (E_g).

i	ΔE_{tot} (meV)	m_{tot} (μ_B)	ε_H (eV)	ε_L (eV)	E_g (eV)
218	1018	1	-3.63	-3.44	0.19
314	984	1	-3.85	-3.69	0.16
271	944	1	-3.69	-3.43	0.26
38	914	1	-3.25	-3.03	0.22
315	914	1	-3.50	-3.33	0.17
310	778	1	-3.84	-3.67	0.17
102	720	1	-3.42	-3.25	0.17
323	607	1	-3.19	-3.03	0.16
320	575	1	-3.17	-3.01	0.16
325	0	1	-3.76	-3.58	0.18

Supplementary Table 25: Optimized and filtered representative structures of $[\text{Cu}_5\text{Zn}_5](\text{Cp}^*)_6(\text{CO}_2)_2$ complexes obtained with PBE+TS/light-tier1 level and light SCF parameters. The relative total energy (ΔE_{tot}) is depicted above each structure.







2.7.4 $[\text{Cu}_6\text{Zn}_5](\text{Cp}^*)_5(\text{Mes})\text{H}_3$ Complexes

Supplementary Table 26: Energetic and electronic properties for $[\text{Cu}_6\text{Zn}_5](\text{Cp}^*)_5(\text{Mes})\text{H}_3$ complexes obtained with PBE+TS/light-tier1 level and light SCF parameters: configuration number (i), relative total energy (ΔE_{tot}), total magnetic moment (m_{tot}), HOMO energy (ε_H), LUMO energy (ε_L), and LUMO-HOMO energy gap (E_g).

i	ΔE_{tot} (meV)	m_{tot} (μ_B)	ε_H (eV)	ε_L (eV)	E_g (eV)
173	6593	1	-4.03	-3.79	0.24
64	6272	1	-3.70	-2.67	1.03
197	5838	1	-3.84	-3.03	0.81
123	5128	1	-3.67	-3.48	0.19
28	5101	1	-3.76	-3.60	0.16
133	5032	1	-3.78	-3.43	0.35
273	4909	1	-3.76	-3.59	0.17
266	4796	1	-3.83	-2.84	0.99
70	4697	1	-3.82	-3.41	0.41
106	4642	1	-4.04	-3.61	0.43
94	4545	1	-4.04	-3.71	0.33
275	4406	1	-3.47	-3.25	0.22
57	4342	1	-3.75	-3.59	0.16
170	4316	1	-4.07	-3.30	0.78
323	4130	1	-3.79	-3.03	0.77

Continued on next page

Supplementary Table 26: Energetic and electronic properties for $[\text{Cu}_6\text{Zn}_5](\text{Cp}^*)_5(\text{Mes})\text{H}_3$ complexes obtained with PBE+TS/light-tier1 level and light SCF parameters: configuration number (i), relative total energy (ΔE_{tot}), total magnetic moment (m_{tot}), HOMO energy (ε_H), LUMO energy (ε_L), and LUMO-HOMO energy gap (E_g).

i	ΔE_{tot} (meV)	m_{tot} (μ_B)	ε_H (eV)	ε_L (eV)	E_g (eV)
185	4055	1	-3.78	-3.38	0.40
8	4006	1	-4.12	-3.73	0.39
37	3997	1	-3.80	-3.36	0.44
227	3959	1	-3.74	-3.55	0.19
224	3884	1	-4.06	-3.18	0.88
81	3798	1	-4.06	-3.20	0.86
233	3738	1	-3.18	-2.99	0.19
60	3733	1	-4.17	-3.51	0.66
240	3728	1	-3.70	-3.60	0.10
12	3688	1	-3.71	-2.74	0.97
255	3579	1	-4.02	-3.17	0.85
286	3542	1	-3.53	-3.35	0.18
281	3493	1	-3.19	-2.72	0.47
189	3447	1	-3.48	-3.26	0.22
53	3442	1	-3.63	-3.41	0.21
33	3420	1	-3.78	-3.30	0.48
54	3407	1	-3.50	-3.34	0.15
61	3357	1	-4.26	-3.52	0.74
102	3327	1	-3.66	-3.43	0.22
159	3304	1	-3.83	-3.67	0.16
195	3297	1	-4.11	-3.48	0.63
282	3288	1	-3.71	-2.93	0.78

Continued on next page

Supplementary Table 26: Energetic and electronic properties for $[\text{Cu}_6\text{Zn}_5](\text{Cp}^*)_5(\text{Mes})\text{H}_3$ complexes obtained with PBE+TS/light-tier1 level and light SCF parameters: configuration number (i), relative total energy (ΔE_{tot}), total magnetic moment (m_{tot}), HOMO energy (ε_H), LUMO energy (ε_L), and LUMO-HOMO energy gap (E_g).

i	ΔE_{tot} (meV)	m_{tot} (μ_B)	ε_H (eV)	ε_L (eV)	E_g (eV)
95	3256	1	-3.38	-3.22	0.16
174	3253	1	-3.60	-3.43	0.16
261	3247	1	-3.49	-3.25	0.24
10	3202	1	-4.12	-4.00	0.13
211	3202	1	-4.01	-2.95	1.06
288	3184	1	-3.74	-3.31	0.43
84	3159	1	-4.23	-3.68	0.55
268	3122	1	-3.47	-3.30	0.17
69	3115	1	-3.61	-3.41	0.20
30	3107	1	-3.65	-3.44	0.21
252	3096	1	-3.68	-3.46	0.22
46	3068	1	-3.55	-3.40	0.15
72	3063	1	-3.55	-3.33	0.22
11	3049	1	-3.79	-3.54	0.25
75	3038	1	-3.38	-3.14	0.23
14	3004	1	-4.32	-3.57	0.76
210	2997	1	-4.32	-4.23	0.09
278	2994	1	-3.21	-3.07	0.14
239	2978	1	-3.19	-2.57	0.62
76	2973	1	-3.71	-3.55	0.16
65	2949	1	-3.92	-3.47	0.45
142	2928	1	-4.08	-3.41	0.67

Continued on next page

Supplementary Table 26: Energetic and electronic properties for $[\text{Cu}_6\text{Zn}_5](\text{Cp}^*)_5(\text{Mes})\text{H}_3$ complexes obtained with PBE+TS/light-tier1 level and light SCF parameters: configuration number (i), relative total energy (ΔE_{tot}), total magnetic moment (m_{tot}), HOMO energy (ε_H), LUMO energy (ε_L), and LUMO-HOMO energy gap (E_g).

i	ΔE_{tot} (meV)	m_{tot} (μ_B)	ε_H (eV)	ε_L (eV)	E_g (eV)
35	2927	1	-4.24	-3.59	0.65
73	2921	1	-4.31	-3.59	0.72
263	2902	1	-3.38	-3.20	0.17
176	2901	1	-4.10	-3.69	0.40
232	2850	1	-3.57	-3.39	0.17
154	2847	1	-3.62	-3.43	0.19
265	2825	1	-3.54	-3.40	0.14
1	2790	1	-3.50	-3.25	0.26
34	2784	1	-4.01	-3.36	0.65
203	2782	1	-3.99	-3.85	0.14
101	2707	1	-3.46	-3.27	0.19
4	2678	1	-3.91	-3.70	0.21
161	2662	1	-4.21	-3.54	0.67
112	2655	1	-3.40	-3.18	0.22
115	2649	1	-4.09	-3.95	0.15
157	2620	1	-3.70	-3.53	0.18
49	2618	1	-4.20	-4.08	0.11
289	2612	1	-4.07	-3.30	0.77
55	2601	1	-3.93	-3.79	0.14
71	2585	1	-4.08	-3.62	0.47
196	2521	1	-4.02	-3.64	0.38
145	2517	1	-3.57	-3.41	0.16

Continued on next page

Supplementary Table 26: Energetic and electronic properties for $[\text{Cu}_6\text{Zn}_5](\text{Cp}^*)_5(\text{Mes})\text{H}_3$ complexes obtained with PBE+TS/light-tier1 level and light SCF parameters: configuration number (i), relative total energy (ΔE_{tot}), total magnetic moment (m_{tot}), HOMO energy (ε_H), LUMO energy (ε_L), and LUMO-HOMO energy gap (E_g).

i	ΔE_{tot} (meV)	m_{tot} (μ_B)	ε_H (eV)	ε_L (eV)	E_g (eV)
56	2508	1	-4.13	-3.72	0.42
132	2468	1	-3.51	-3.31	0.20
229	2444	1	-3.44	-3.28	0.16
241	2439	1	-3.99	-3.58	0.41
146	2437	1	-3.45	-3.24	0.22
87	2420	1	-3.99	-3.58	0.41
284	2419	1	-4.09	-3.38	0.71
13	2411	1	-3.94	-3.43	0.51
158	2375	1	-4.22	-3.56	0.66
235	2369	1	-3.58	-3.44	0.13
175	2350	1	-3.35	-3.18	0.17
96	2337	1	-3.42	-3.24	0.18
162	2331	1	-4.06	-3.69	0.37
315	2323	1	-4.12	-3.96	0.15
26	2320	1	-4.14	-3.36	0.77
82	2310	1	-3.08	-2.87	0.21
228	2305	1	-3.05	-2.83	0.21
164	2292	1	-3.94	-3.59	0.36
137	2288	1	-3.27	-3.07	0.21
198	2287	1	-3.80	-3.61	0.19
39	2272	1	-3.98	-3.52	0.45
110	2271	1	-4.18	-4.07	0.11

Continued on next page

Supplementary Table 26: Energetic and electronic properties for $[\text{Cu}_6\text{Zn}_5](\text{Cp}^*)_5(\text{Mes})\text{H}_3$ complexes obtained with PBE+TS/light-tier1 level and light SCF parameters: configuration number (i), relative total energy (ΔE_{tot}), total magnetic moment (m_{tot}), HOMO energy (ε_H), LUMO energy (ε_L), and LUMO-HOMO energy gap (E_g).

i	ΔE_{tot} (meV)	m_{tot} (μ_B)	ε_H (eV)	ε_L (eV)	E_g (eV)
251	2271	1	-3.84	-3.58	0.26
297	2271	1	-4.19	-3.49	0.70
194	2253	1	-4.09	-3.56	0.52
168	2246	1	-3.17	-2.93	0.24
287	2243	1	-4.10	-3.97	0.13
222	2230	1	-3.61	-3.47	0.14
7	2226	1	-3.79	-3.66	0.13
238	2211	1	-3.65	-3.36	0.29
23	2204	1	-3.78	-3.60	0.17
264	2198	1	-3.49	-3.33	0.17
83	2185	1	-3.52	-3.33	0.19
294	2180	1	-3.63	-3.22	0.41
165	2172	1	-3.59	-3.41	0.17
44	2129	1	-3.55	-3.36	0.19
277	2125	1	-3.33	-3.13	0.19
242	2107	1	-3.65	-3.46	0.19
256	2104	1	-3.84	-3.57	0.28
271	2096	1	-3.84	-3.69	0.16
249	2095	1	-3.67	-3.47	0.20
184	2094	1	-3.84	-3.64	0.20
121	2078	1	-4.10	-3.94	0.16
91	2069	1	-3.32	-2.89	0.43

Continued on next page

Supplementary Table 26: Energetic and electronic properties for $[\text{Cu}_6\text{Zn}_5](\text{Cp}^*)_5(\text{Mes})\text{H}_3$ complexes obtained with PBE+TS/light-tier1 level and light SCF parameters: configuration number (i), relative total energy (ΔE_{tot}), total magnetic moment (m_{tot}), HOMO energy (ε_H), LUMO energy (ε_L), and LUMO-HOMO energy gap (E_g).

i	ΔE_{tot}	m_{tot}	ε_H	ε_L	E_g
	(meV)	(μ_B)	(eV)	(eV)	(eV)
181	2064	1	-4.15	-3.73	0.42
150	2045	1	-3.60	-3.43	0.17
136	2032	1	-3.83	-3.69	0.14
190	2024	1	-4.09	-3.92	0.17
59	2006	1	-3.93	-3.51	0.42
45	2002	1	-4.09	-3.92	0.16
107	1981	1	-3.59	-3.37	0.21
308	1960	1	-3.70	-3.50	0.20
250	1955	1	-3.60	-3.47	0.13
85	1939	1	-4.02	-3.84	0.18
15	1927	1	-4.20	-4.02	0.18
2	1911	1	-3.41	-3.26	0.15
216	1910	1	-3.27	-3.04	0.24
24	1906	1	-3.93	-3.79	0.14
316	1905	1	-4.04	-3.80	0.24
40	1893	1	-3.58	-3.41	0.16
199	1886	1	-3.49	-3.32	0.17
32	1882	1	-3.83	-3.68	0.14
319	1873	1	-3.58	-3.40	0.18
306	1828	1	-3.95	-3.76	0.19
225	1824	1	-3.90	-3.74	0.16
126	1821	1	-3.69	-3.39	0.30

Continued on next page

Supplementary Table 26: Energetic and electronic properties for $[\text{Cu}_6\text{Zn}_5](\text{Cp}^*)_5(\text{Mes})\text{H}_3$ complexes obtained with PBE+TS/light-tier1 level and light SCF parameters: configuration number (i), relative total energy (ΔE_{tot}), total magnetic moment (m_{tot}), HOMO energy (ε_H), LUMO energy (ε_L), and LUMO-HOMO energy gap (E_g).

i	ΔE_{tot} (meV)	m_{tot} (μ_B)	ε_H (eV)	ε_L (eV)	E_g (eV)
52	1816	1	-3.72	-3.56	0.16
50	1793	1	-4.09	-3.71	0.37
214	1787	1	-4.04	-3.82	0.22
113	1785	1	-3.79	-3.62	0.17
248	1780	1	-3.62	-3.43	0.19
131	1776	1	-3.77	-3.59	0.17
98	1766	1	-3.96	-3.80	0.16
9	1763	1	-3.89	-3.49	0.40
322	1749	1	-3.60	-3.44	0.16
179	1738	1	-3.87	-3.70	0.17
231	1729	1	-3.87	-3.70	0.17
215	1721	1	-3.80	-3.62	0.18
269	1711	1	-3.92	-3.77	0.15
169	1705	1	-3.57	-3.39	0.18
144	1702	1	-3.91	-3.79	0.12
17	1682	1	-3.87	-3.68	0.19
314	1672	1	-4.09	-3.89	0.20
213	1650	1	-3.64	-3.41	0.22
149	1641	1	-3.72	-3.57	0.15
80	1630	1	-4.01	-3.86	0.15
20	1610	1	-3.50	-3.34	0.17
67	1603	1	-3.79	-3.62	0.17

Continued on next page

Supplementary Table 26: Energetic and electronic properties for $[\text{Cu}_6\text{Zn}_5](\text{Cp}^*)_5(\text{Mes})\text{H}_3$ complexes obtained with PBE+TS/light-tier1 level and light SCF parameters: configuration number (i), relative total energy (ΔE_{tot}), total magnetic moment (m_{tot}), HOMO energy (ε_H), LUMO energy (ε_L), and LUMO-HOMO energy gap (E_g).

i	ΔE_{tot} (meV)	m_{tot} (μ_B)	ε_H (eV)	ε_L (eV)	E_g (eV)
267	1600	1	-3.22	-2.84	0.38
312	1594	1	-3.81	-3.67	0.14
62	1578	1	-3.66	-3.48	0.18
118	1536	1	-4.02	-3.64	0.38
167	1535	1	-3.61	-3.45	0.16
212	1527	1	-3.75	-3.58	0.17
193	1524	1	-3.71	-3.57	0.14
29	1523	1	-3.50	-3.01	0.49
204	1520	1	-3.97	-3.82	0.15
105	1515	1	-3.97	-3.80	0.17
38	1506	1	-3.54	-3.33	0.21
172	1498	1	-3.54	-3.33	0.21
201	1492	1	-3.97	-3.67	0.30
279	1490	1	-3.74	-3.55	0.18
262	1481	1	-3.93	-3.71	0.22
237	1469	1	-3.55	-3.40	0.16
317	1459	1	-4.17	-4.01	0.16
254	1450	1	-3.74	-3.59	0.15
313	1449	1	-3.52	-3.34	0.18
78	1413	1	-3.56	-3.37	0.19
42	1409	1	-3.70	-3.53	0.17
48	1399	1	-3.63	-3.45	0.18

Continued on next page

Supplementary Table 26: Energetic and electronic properties for $[\text{Cu}_6\text{Zn}_5](\text{Cp}^*)_5(\text{Mes})\text{H}_3$ complexes obtained with PBE+TS/light-tier1 level and light SCF parameters: configuration number (i), relative total energy (ΔE_{tot}), total magnetic moment (m_{tot}), HOMO energy (ε_H), LUMO energy (ε_L), and LUMO-HOMO energy gap (E_g).

i	ΔE_{tot} (meV)	m_{tot} (μ_B)	ε_H (eV)	ε_L (eV)	E_g (eV)
299	1366	1	-3.69	-3.55	0.14
311	1315	1	-3.80	-3.62	0.17
200	1307	1	-3.85	-3.64	0.21
22	1272	1	-3.80	-3.65	0.16
134	1256	1	-3.55	-3.38	0.17
292	1249	1	-3.76	-3.63	0.13
274	1246	1	-3.59	-3.44	0.15
187	1237	1	-3.55	-3.39	0.16
74	1224	1	-3.69	-3.54	0.16
58	1223	1	-3.51	-3.30	0.20
3	1220	1	-3.93	-3.79	0.14
183	1204	1	-4.23	-4.13	0.10
298	1197	1	-3.13	-2.99	0.14
309	1160	1	-3.70	-3.53	0.17
206	1149	1	-3.38	-3.14	0.25
258	1122	1	-3.67	-3.52	0.15
109	1113	1	-3.66	-3.49	0.16
236	1096	1	-3.44	-3.23	0.21
93	1092	1	-3.76	-3.60	0.16
321	1089	1	-3.60	-3.44	0.17
6	1080	1	-3.71	-3.46	0.24
303	1059	1	-3.82	-3.68	0.14

Continued on next page

Supplementary Table 26: Energetic and electronic properties for $[\text{Cu}_6\text{Zn}_5](\text{Cp}^*)_5(\text{Mes})\text{H}_3$ complexes obtained with PBE+TS/light-tier1 level and light SCF parameters: configuration number (i), relative total energy (ΔE_{tot}), total magnetic moment (m_{tot}), HOMO energy (ε_H), LUMO energy (ε_L), and LUMO-HOMO energy gap (E_g).

i	ΔE_{tot} (meV)	m_{tot} (μ_B)	ε_H (eV)	ε_L (eV)	E_g (eV)
122	1049	1	-3.67	-3.39	0.28
205	1026	1	-3.58	-3.40	0.18
117	1018	1	-3.96	-3.78	0.18
166	1013	1	-3.65	-3.45	0.20
304	1000	1	-3.59	-3.43	0.15
310	997	1	-4.05	-3.88	0.16
31	993	1	-3.37	-3.14	0.23
182	986	1	-3.91	-3.75	0.16
86	981	1	-3.71	-3.48	0.23
259	979	1	-3.82	-3.69	0.13
305	972	1	-3.58	-3.45	0.13
51	940	1	-3.62	-3.47	0.15
178	928	1	-3.51	-3.34	0.17
141	919	1	-3.61	-3.44	0.18
253	900	1	-3.82	-3.60	0.22
18	889	1	-3.79	-3.62	0.16
147	855	1	-3.69	-3.48	0.21
226	845	1	-3.34	-3.18	0.16
36	824	1	-3.88	-3.72	0.16
302	812	1	-3.69	-3.55	0.14
324	803	1	-3.61	-3.44	0.18
207	793	1	-3.78	-3.56	0.21

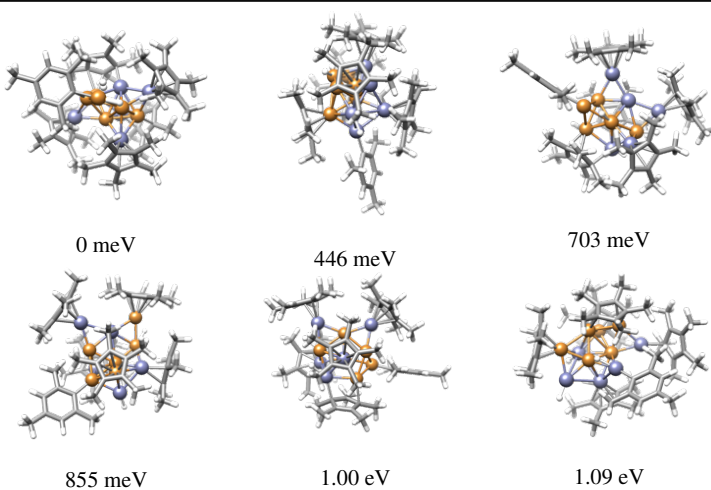
Continued on next page

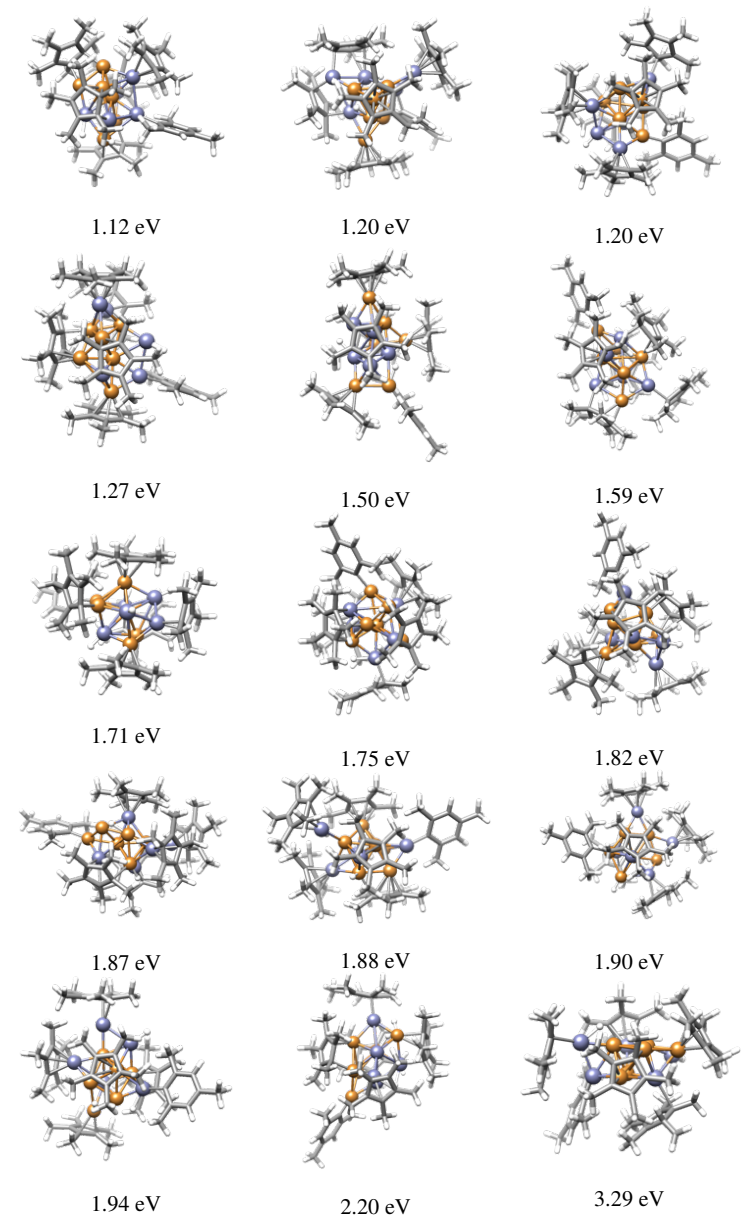
Supplementary Table 26: Energetic and electronic properties for $[\text{Cu}_6\text{Zn}_5](\text{Cp}^*)_5(\text{Mes})\text{H}_3$ complexes obtained with PBE+TS/light-tier1 level and light SCF parameters: configuration number (i), relative total energy (ΔE_{tot}), total magnetic moment (m_{tot}), HOMO energy (ε_H), LUMO energy (ε_L), and LUMO-HOMO energy gap (E_g).

i	ΔE_{tot}	m_{tot}	ε_H	ε_L	E_g
	(meV)	(μ_B)	(eV)	(eV)	(eV)
188	703	1	-3.64	-3.46	0.18
116	635	1	-3.70	-3.55	0.15
120	549	1	-3.36	-3.20	0.16
16	446	1	-3.64	-3.47	0.17
307	0	1	-3.50	-3.34	0.16

Continued on next page

Supplementary Table 27: Optimized and filtered representative structures of $[\text{Cu}_6\text{Zn}_5](\text{Cp}^*)_5(\text{Mes})(\text{H})_3$ complexes obtained with PBE+TS/light-tier1 level and light SCF parameters. The relative total energy (ΔE_{tot}) is depicted above each structure.





2.7.5 $[Cu_8Zn_3](Cp^*)_3(Mes)_4CO_2$ Complexes

Supplementary Table 28: Energetic and electronic properties for $[\text{Cu}_8\text{Zn}_3](\text{Cp}^*)_3(\text{Mes})_4\text{CO}_2$ complexes obtained with PBE+TS/light-tier1 level and light SCF parameters: configuration number (i), relative total energy (ΔE_{tot}), total magnetic moment (m_{tot}), HOMO energy (ε_H), LUMO energy (ε_L), and LUMO-HOMO energy gap (E_g).

i	ΔE_{tot} (meV)	m_{tot} (μ_B)	ε_H (eV)	ε_L (eV)	E_g (eV)
209	6783	1	-3.40	-3.21	0.19
78	6173	1	-4.43	-3.70	0.72
187	5880	1	-4.24	-3.71	0.53
102	5559	1	-3.80	-3.16	0.64
83	5516	1	-3.57	-3.39	0.18
282	5274	1	-4.21	-3.16	1.06
72	5188	1	-4.25	-3.47	0.78
212	4925	1	-4.01	-2.97	1.05
114	4911	1	-3.88	-3.08	0.80
111	4826	1	-3.70	-3.41	0.30
203	4824	1	-4.09	-3.37	0.73
37	4815	1	-4.30	-3.34	0.96
94	4743	1	-4.18	-3.07	1.11
267	4704	1	-3.52	-3.33	0.19
116	4680	1	-4.34	-3.44	0.90
298	4674	1	-3.78	-3.59	0.19
108	4529	1	-4.10	-3.89	0.20
86	4450	1	-4.22	-3.11	1.12
158	4432	1	-4.03	-3.21	0.81
123	4412	1	-4.21	-3.30	0.91
62	4399	1	-4.35	-3.62	0.73
23	4342	1	-4.06	-3.25	0.81

Continued on next page

Supplementary Table 28: Energetic and electronic properties for $[\text{Cu}_8\text{Zn}_3](\text{Cp}^*)_3(\text{Mes})_4\text{CO}_2$ complexes obtained with PBE+TS/light-tier1 level and light SCF parameters: configuration number (i), relative total energy (ΔE_{tot}), total magnetic moment (m_{tot}), HOMO energy (ε_H), LUMO energy (ε_L), and LUMO-HOMO energy gap (E_g).

i	ΔE_{tot} (meV)	m_{tot} (μ_B)	ε_H (eV)	ε_L (eV)	E_g (eV)
103	4284	1	-4.04	-3.26	0.78
112	4279	1	-3.68	-3.49	0.19
41	4251	1	-4.14	-3.81	0.33
265	4212	1	-4.04	-3.79	0.25
238	4166	1	-3.93	-2.84	1.09
285	4164	1	-4.12	-3.31	0.81
317	4069	1	-3.41	-2.75	0.66
223	4043	1	-3.88	-3.71	0.17
19	4038	1	-3.96	-2.97	0.99
142	4028	1	-3.48	-3.20	0.28
313	3997	1	-4.19	-3.99	0.20
293	3993	1	-4.31	-3.69	0.62
257	3976	1	-4.34	-3.65	0.70
180	3968	1	-3.84	-3.14	0.69
100	3964	1	-4.03	-3.25	0.78
30	3956	1	-3.85	-3.04	0.81
154	3907	1	-4.02	-3.88	0.14
300	3875	1	-3.26	-3.09	0.16
125	3846	1	-4.14	-3.62	0.52
10	3811	1	-4.08	-3.23	0.85
247	3790	1	-3.76	-3.53	0.23
181	3752	1	-3.63	-3.01	0.62

Continued on next page

Supplementary Table 28: Energetic and electronic properties for $[\text{Cu}_8\text{Zn}_3](\text{Cp}^*)_3(\text{Mes})_4\text{CO}_2$ complexes obtained with PBE+TS/light-tier1 level and light SCF parameters: configuration number (i), relative total energy (ΔE_{tot}), total magnetic moment (m_{tot}), HOMO energy (ε_H), LUMO energy (ε_L), and LUMO-HOMO energy gap (E_g).

i	ΔE_{tot} (meV)	m_{tot} (μ_B)	ε_H (eV)	ε_L (eV)	E_g (eV)
105	3738	1	-4.03	-3.22	0.81
35	3717	1	-4.07	-3.64	0.44
291	3717	1	-4.38	-3.60	0.78
61	3684	1	-4.15	-3.93	0.21
156	3681	1	-3.99	-3.12	0.87
202	3630	1	-3.31	-3.12	0.19
56	3620	1	-3.68	-3.51	0.18
214	3604	1	-4.32	-3.72	0.61
185	3589	1	-3.81	-2.99	0.82
107	3571	1	-4.05	-3.87	0.17
136	3554	1	-3.88	-3.71	0.18
13	3551	1	-3.97	-3.26	0.71
296	3519	1	-3.52	-2.96	0.56
345	3329	1	-4.14	-3.99	0.16
76	3257	1	-4.19	-4.05	0.14
64	3247	1	-3.57	-3.42	0.15
284	3237	1	-3.23	-3.06	0.17
126	3155	1	-3.61	-3.37	0.23
183	3127	1	-3.26	-2.98	0.29
8	3122	1	-3.86	-3.49	0.38
233	3086	1	-3.27	-3.08	0.19
256	3084	1	-4.21	-3.74	0.47

Continued on next page

Supplementary Table 28: Energetic and electronic properties for $[\text{Cu}_8\text{Zn}_3](\text{Cp}^*)_3(\text{Mes})_4\text{CO}_2$ complexes obtained with PBE+TS/light-tier1 level and light SCF parameters: configuration number (i), relative total energy (ΔE_{tot}), total magnetic moment (m_{tot}), HOMO energy (ε_H), LUMO energy (ε_L), and LUMO-HOMO energy gap (E_g).

i	ΔE_{tot} (meV)	m_{tot} (μ_B)	ε_H (eV)	ε_L (eV)	E_g (eV)
272	3070	1	-4.00	-3.47	0.53
297	3052	1	-3.24	-3.09	0.14
279	2991	1	-4.12	-3.98	0.14
47	2989	1	-3.73	-3.58	0.16
26	2985	1	-3.80	-3.57	0.23
171	2982	1	-3.37	-3.23	0.14
276	2979	1	-3.52	-3.30	0.21
163	2968	1	-4.12	-3.45	0.67
22	2957	1	-3.75	-3.57	0.18
221	2915	1	-4.00	-3.66	0.33
343	2896	1	-3.71	-3.49	0.22
9	2875	1	-3.53	-3.39	0.14
338	2862	1	-3.82	-3.58	0.24
110	2857	1	-3.78	-3.62	0.16
271	2838	1	-3.98	-3.82	0.16
179	2838	1	-4.08	-3.90	0.18
3	2811	1	-3.88	-3.74	0.15
14	2784	1	-3.60	-3.42	0.18
73	2783	1	-4.09	-3.93	0.16
194	2761	1	-3.62	-3.44	0.18
63	2760	1	-3.55	-3.22	0.33
269	2732	1	-4.16	-3.98	0.18

Continued on next page

Supplementary Table 28: Energetic and electronic properties for $[\text{Cu}_8\text{Zn}_3](\text{Cp}^*)_3(\text{Mes})_4\text{CO}_2$ complexes obtained with PBE+TS/light-tier1 level and light SCF parameters: configuration number (i), relative total energy (ΔE_{tot}), total magnetic moment (m_{tot}), HOMO energy (ε_H), LUMO energy (ε_L), and LUMO-HOMO energy gap (E_g).

i	ΔE_{tot} (meV)	m_{tot} (μ_B)	ε_H (eV)	ε_L (eV)	E_g (eV)
204	2716	1	-3.91	-3.73	0.17
259	2716	1	-3.75	-3.59	0.15
119	2683	1	-3.68	-3.51	0.17
208	2682	1	-3.62	-3.47	0.15
45	2648	1	-4.13	-3.98	0.16
231	2636	1	-4.07	-3.89	0.18
137	2607	1	-4.12	-3.91	0.21
250	2600	1	-3.41	-3.17	0.24
320	2583	1	-3.56	-3.37	0.19
168	2574	1	-3.23	-2.81	0.42
97	2565	1	-3.81	-3.64	0.17
346	2539	1	-3.46	-3.31	0.15
229	2523	1	-3.54	-3.38	0.16
248	2517	1	-3.58	-3.40	0.18
287	2495	1	-4.06	-3.86	0.20
20	2484	1	-3.82	-3.65	0.18
340	2477	1	-4.05	-3.87	0.19
243	2473	1	-3.95	-3.76	0.19
15	2472	1	-3.74	-3.55	0.19
16	2468	1	-3.89	-3.65	0.24
191	2449	1	-3.42	-3.21	0.22
252	2446	1	-3.78	-3.62	0.16

Continued on next page

Supplementary Table 28: Energetic and electronic properties for $[\text{Cu}_8\text{Zn}_3](\text{Cp}^*)_3(\text{Mes})_4\text{CO}_2$ complexes obtained with PBE+TS/light-tier1 level and light SCF parameters: configuration number (i), relative total energy (ΔE_{tot}), total magnetic moment (m_{tot}), HOMO energy (ε_H), LUMO energy (ε_L), and LUMO-HOMO energy gap (E_g).

i	ΔE_{tot} (meV)	m_{tot} (μ_B)	ε_H (eV)	ε_L (eV)	E_g (eV)
200	2445	1	-3.97	-3.78	0.19
341	2444	1	-4.09	-3.91	0.18
319	2425	1	-4.20	-4.04	0.15
166	2422	1	-3.70	-3.54	0.16
222	2416	1	-3.35	-3.13	0.23
93	2416	1	-3.66	-3.51	0.14
133	2410	1	-3.92	-3.72	0.20
292	2402	1	-3.83	-3.66	0.17
124	2402	1	-4.14	-3.97	0.17
68	2396	1	-3.66	-3.48	0.18
24	2396	1	-4.18	-4.01	0.17
232	2389	1	-3.73	-3.56	0.16
152	2382	1	-3.50	-3.32	0.18
175	2375	1	-3.86	-3.70	0.16
323	2366	1	-3.48	-3.30	0.18
335	2354	1	-3.53	-3.38	0.15
322	2345	1	-3.61	-3.40	0.21
98	2331	1	-3.61	-3.45	0.17
264	2329	1	-3.96	-3.81	0.15
92	2321	1	-3.64	-3.43	0.21
79	2316	1	-3.89	-3.76	0.13
153	2315	1	-3.92	-3.77	0.15

Continued on next page

Supplementary Table 28: Energetic and electronic properties for $[\text{Cu}_8\text{Zn}_3](\text{Cp}^*)_3(\text{Mes})_4\text{CO}_2$ complexes obtained with PBE+TS/light-tier1 level and light SCF parameters: configuration number (i), relative total energy (ΔE_{tot}), total magnetic moment (m_{tot}), HOMO energy (ε_H), LUMO energy (ε_L), and LUMO-HOMO energy gap (E_g).

i	ΔE_{tot} (meV)	m_{tot} (μ_B)	ε_H (eV)	ε_L (eV)	E_g (eV)
91	2309	1	-3.74	-3.57	0.16
186	2309	1	-3.51	-3.33	0.19
67	2305	1	-3.75	-3.59	0.16
281	2284	1	-3.88	-3.70	0.18
104	2256	1	-3.52	-3.37	0.15
99	2252	1	-3.96	-3.75	0.21
280	2250	1	-3.73	-3.59	0.15
197	2223	1	-3.66	-3.52	0.14
342	2221	1	-4.04	-3.85	0.19
178	2204	1	-3.74	-3.58	0.16
205	2199	1	-3.31	-3.09	0.22
289	2198	1	-3.99	-3.80	0.18
128	2191	1	-3.46	-3.30	0.16
173	2181	1	-3.82	-3.66	0.16
199	2180	1	-3.96	-3.80	0.16
329	2163	1	-3.95	-3.77	0.17
227	2146	1	-3.65	-3.38	0.26
330	2146	1	-3.96	-3.79	0.17
216	2145	1	-3.75	-3.59	0.16
315	2140	1	-3.75	-3.57	0.18
261	2139	1	-3.67	-3.53	0.14
33	2134	1	-3.82	-3.61	0.21

Continued on next page

Supplementary Table 28: Energetic and electronic properties for $[\text{Cu}_8\text{Zn}_3](\text{Cp}^*)_3(\text{Mes})_4\text{CO}_2$ complexes obtained with PBE+TS/light-tier1 level and light SCF parameters: configuration number (i), relative total energy (ΔE_{tot}), total magnetic moment (m_{tot}), HOMO energy (ε_H), LUMO energy (ε_L), and LUMO-HOMO energy gap (E_g).

i	ΔE_{tot} (meV)	m_{tot} (μ_B)	ε_H (eV)	ε_L (eV)	E_g (eV)
82	2132	1	-3.72	-3.54	0.18
167	2127	1	-3.63	-3.45	0.18
164	2119	1	-3.95	-3.80	0.15
288	2098	1	-3.66	-3.47	0.19
120	2096	1	-3.97	-3.79	0.18
134	2095	1	-3.41	-3.22	0.20
211	2090	1	-3.64	-3.45	0.19
235	2080	1	-3.90	-3.75	0.15
277	2075	1	-3.95	-3.73	0.21
213	2070	1	-3.74	-3.60	0.13
347	2069	1	-3.72	-3.55	0.17
2	2068	1	-3.79	-3.66	0.13
106	2064	1	-3.52	-3.37	0.15
7	2051	1	-3.89	-3.57	0.32
294	2050	1	-3.79	-3.62	0.17
305	2048	1	-3.91	-3.74	0.17
6	2041	1	-3.56	-3.38	0.18
198	2035	1	-3.89	-3.73	0.16
266	2034	1	-3.58	-3.37	0.22
336	2031	1	-3.64	-3.47	0.17
201	2027	1	-3.90	-3.74	0.16
328	2010	1	-3.75	-3.57	0.19

Continued on next page

Supplementary Table 28: Energetic and electronic properties for $[\text{Cu}_8\text{Zn}_3](\text{Cp}^*)_3(\text{Mes})_4\text{CO}_2$ complexes obtained with PBE+TS/light-tier1 level and light SCF parameters: configuration number (i), relative total energy (ΔE_{tot}), total magnetic moment (m_{tot}), HOMO energy (ε_H), LUMO energy (ε_L), and LUMO-HOMO energy gap (E_g).

i	ΔE_{tot}	m_{tot}	ε_H	ε_L	E_g
	(meV)	(μ_B)	(eV)	(eV)	(eV)
274	2009	1	-3.68	-3.52	0.16
210	1997	1	-3.97	-3.81	0.15
18	1978	1	-3.81	-3.64	0.17
65	1977	1	-3.57	-3.42	0.15
140	1968	1	-3.92	-3.75	0.17
334	1962	1	-3.76	-3.59	0.18
117	1956	1	-3.79	-3.59	0.20
31	1947	1	-3.74	-3.59	0.16
240	1938	1	-4.01	-3.86	0.14
192	1929	1	-3.50	-3.32	0.18
172	1923	1	-3.72	-3.51	0.21
32	1911	1	-3.81	-3.64	0.17
246	1908	1	-3.77	-3.61	0.16
333	1904	1	-3.65	-3.48	0.17
324	1902	1	-3.47	-3.29	0.18
25	1902	1	-3.94	-3.80	0.14
326	1900	1	-3.46	-3.30	0.16
66	1886	1	-3.79	-3.58	0.21
85	1885	1	-3.69	-3.52	0.17
50	1878	1	-3.94	-3.79	0.15
1	1875	1	-3.73	-3.56	0.17
331	1870	1	-3.69	-3.50	0.19

Continued on next page

Supplementary Table 28: Energetic and electronic properties for $[\text{Cu}_8\text{Zn}_3](\text{Cp}^*)_3(\text{Mes})_4\text{CO}_2$ complexes obtained with PBE+TS/light-tier1 level and light SCF parameters: configuration number (i), relative total energy (ΔE_{tot}), total magnetic moment (m_{tot}), HOMO energy (ε_H), LUMO energy (ε_L), and LUMO-HOMO energy gap (E_g).

i	ΔE_{tot} (meV)	m_{tot} (μ_B)	ε_H (eV)	ε_L (eV)	E_g (eV)
42	1865	1	-3.46	-3.29	0.17
176	1864	1	-3.59	-3.42	0.17
278	1860	1	-3.99	-3.81	0.18
225	1859	1	-3.75	-3.55	0.20
95	1854	1	-3.82	-3.68	0.13
132	1838	1	-3.72	-3.55	0.16
253	1830	1	-3.77	-3.61	0.16
327	1818	1	-3.99	-3.81	0.18
241	1815	1	-3.95	-3.54	0.40
4	1804	1	-3.81	-3.63	0.19
344	1801	1	-3.58	-3.38	0.20
224	1793	1	-3.64	-3.48	0.16
299	1772	1	-3.56	-3.39	0.18
283	1764	1	-3.40	-3.21	0.19
155	1737	1	-3.30	-3.15	0.15
273	1731	1	-3.45	-3.21	0.24
215	1726	1	-3.80	-3.64	0.17
193	1719	1	-3.48	-3.19	0.29
303	1711	1	-3.77	-3.61	0.16
255	1706	1	-3.42	-3.24	0.18
48	1702	1	-3.66	-3.51	0.15
177	1682	1	-3.66	-3.48	0.18

Continued on next page

Supplementary Table 28: Energetic and electronic properties for $[\text{Cu}_8\text{Zn}_3](\text{Cp}^*)_3(\text{Mes})_4\text{CO}_2$ complexes obtained with PBE+TS/light-tier1 level and light SCF parameters: configuration number (i), relative total energy (ΔE_{tot}), total magnetic moment (m_{tot}), HOMO energy (ε_H), LUMO energy (ε_L), and LUMO-HOMO energy gap (E_g).

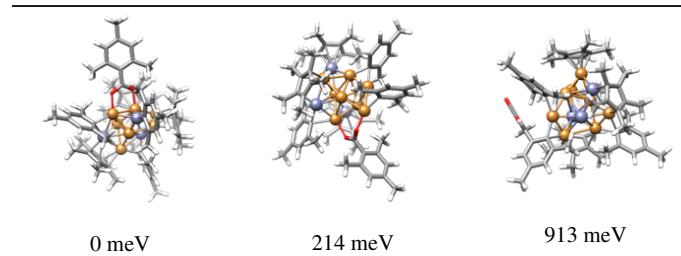
i	ΔE_{tot} (meV)	m_{tot} (μ_B)	ε_H (eV)	ε_L (eV)	E_g (eV)
44	1649	1	-3.59	-3.44	0.15
286	1643	1	-3.60	-3.45	0.15
318	1623	1	-3.67	-3.46	0.22
339	1606	1	-3.81	-3.65	0.16
182	1604	1	-3.78	-3.61	0.17
290	1554	1	-3.39	-3.24	0.15
53	1469	1	-3.49	-3.35	0.15
127	1466	1	-3.18	-3.03	0.15
115	1461	1	-3.18	-2.99	0.19
263	1455	1	-3.70	-3.52	0.18
162	1427	1	-3.57	-3.42	0.16
349	1398	1	-3.24	-3.05	0.20
302	1394	1	-3.48	-3.33	0.16
325	1385	1	-3.64	-3.48	0.16
188	1385	1	-3.79	-3.60	0.19
52	1384	1	-3.95	-3.82	0.13
157	1308	1	-3.76	-3.60	0.16
217	1276	1	-3.20	-3.02	0.18
135	1267	1	-3.59	-3.44	0.15
262	1151	1	-3.60	-3.45	0.15
332	1134	1	-3.74	-3.57	0.17
337	1122	1	-3.39	-3.24	0.15

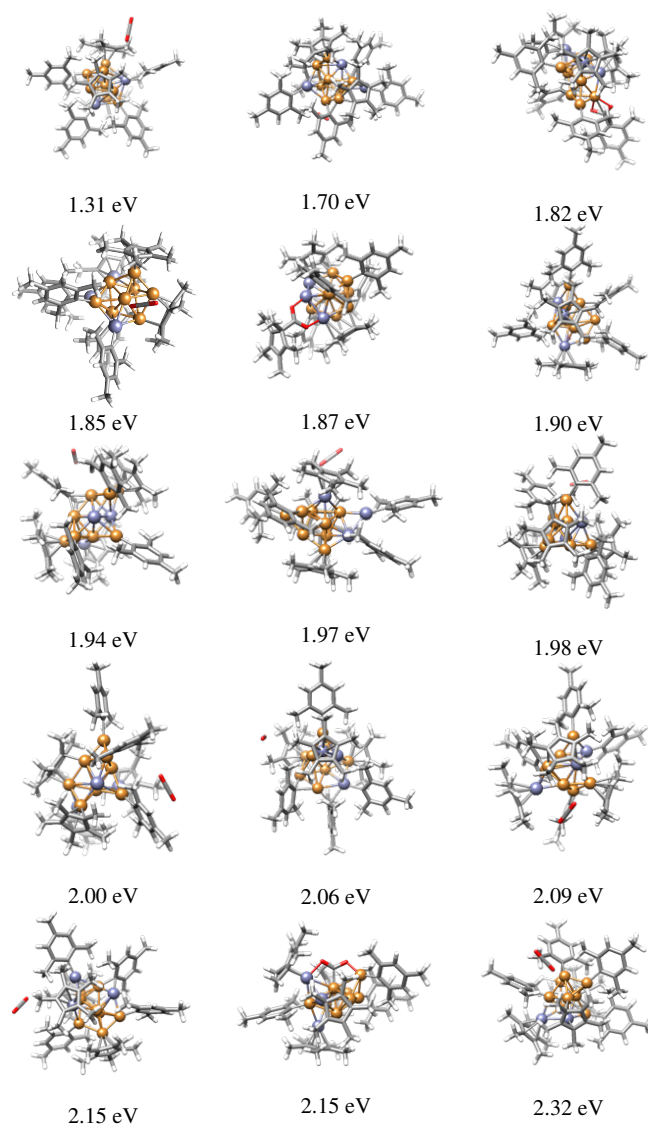
Continued on next page

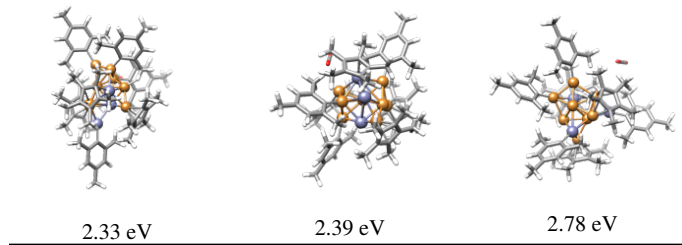
Supplementary Table 28: Energetic and electronic properties for $[\text{Cu}_8\text{Zn}_3](\text{Cp}^*)_3(\text{Mes})_4\text{CO}_2$ complexes obtained with PBE+TS/light-tier1 level and light SCF parameters: configuration number (i), relative total energy (ΔE_{tot}), total magnetic moment (m_{tot}), HOMO energy (ε_H), LUMO energy (ε_L), and LUMO-HOMO energy gap (E_g).

i	ΔE_{tot}	m_{tot}	ε_H	ε_L	E_g
	(meV)	(μ_B)	(eV)	(eV)	(eV)
237	1108	1	-3.64	-3.48	0.15
151	1099	1	-3.65	-3.47	0.17
75	1087	1	-3.56	-3.34	0.22
314	1066	1	-3.40	-3.23	0.17
306	1030	1	-3.83	-3.63	0.20
348	979	1	-3.14	-2.95	0.19
311	938	1	-3.12	-2.93	0.20
51	913	1	-3.19	-3.03	0.16
307	901	1	-3.85	-3.67	0.18
310	719	1	-3.67	-3.51	0.16
321	392	1	-3.41	-3.24	0.17
312	366	1	-3.06	-2.90	0.16
309	214	1	-3.07	-2.90	0.17
316	0	1	-3.08	-2.92	0.17

Supplementary Table 29: Optimized and filtered representative structures of $[\text{Cu}_8\text{Zn}_3](\text{Cp}^*)_3(\text{Mes})_4\text{CO}_2$ complexes obtained with PBE+TS/light-tier1 level and light SCF parameters. The relative total energy (ΔE_{tot}) is depicted above each structure.







2.7.6 $[\text{Cu}_8\text{Zn}_3](\text{Cp}^*)_4(\text{Mes})_3\text{H}$ Complexes

Supplementary Table 30: Energetic and electronic properties for $[\text{Cu}_8\text{Zn}_3](\text{Cp}^*)_4(\text{Mes})_3\text{H}$ complexes obtained with PBE+TS/light-tier1 level and light SCF parameters: configuration number (i), relative total energy (ΔE_{tot}), total magnetic moment (m_{tot}), HOMO energy (ε_H), LUMO energy (ε_L), and LUMO-HOMO energy gap (E_g).

i	ΔE_{tot} (meV)	m_{tot} (μ_B)	ε_H (eV)	ε_L (eV)	E_g (eV)
183	6846	2	-3.90	-3.59	0.31
191	6038	0	-3.99	-3.23	0.77
263	5476	0	-3.97	-3.82	0.15
134	5231	0	-3.70	-3.47	0.23
138	5082	0	-3.90	-3.70	0.20
71	4996	0	-3.70	-3.31	0.40
102	4673	0	-3.91	-3.03	0.87
88	4616	0	-3.85	-3.70	0.15
15	4429	0	-4.46	-3.42	1.04
256	4426	0	-3.82	-3.49	0.33
117	4395	0	-3.81	-3.60	0.21
32	4382	0	-4.12	-3.34	0.78
91	4339	0	-3.72	-3.55	0.17
19	4139	0	-4.06	-2.83	1.23

Continued on next page

Supplementary Table 30: Energetic and electronic properties for $[\text{Cu}_8\text{Zn}_3](\text{Cp}^*)_4(\text{Mes})_3\text{H}$ complexes obtained with PBE+TS/light-tier1 level and light SCF parameters: configuration number (i), relative total energy (ΔE_{tot}), total magnetic moment (m_{tot}), HOMO energy (ε_H), LUMO energy (ε_L), and LUMO-HOMO energy gap (E_g).

i	ΔE_{tot} (meV)	m_{tot} (μ_B)	ε_H (eV)	ε_L (eV)	E_g (eV)
295	4133	0	-3.42	-3.23	0.19
37	4051	0	-3.94	-3.78	0.15
42	4044	0	-4.03	-2.84	1.20
246	4028	0	-4.17	-3.19	0.98
153	3862	0	-3.96	-3.12	0.84
104	3808	0	-3.75	-3.05	0.70
202	3802	0	-3.79	-3.06	0.74
293	3752	0	-3.58	-3.42	0.17
103	3730	2	-3.44	-3.27	0.17
285	3675	0	-3.60	-3.41	0.19
196	3660	0	-4.36	-4.21	0.14
74	3581	0	-3.80	-3.61	0.18
10	3578	0	-4.03	-3.45	0.58
292	3576	0	-3.54	-3.42	0.13
150	3542	0	-3.65	-3.45	0.20
167	3518	0	-3.91	-3.74	0.17
259	3450	0	-3.67	-3.52	0.15
77	3421	0	-3.69	-3.09	0.60
14	3356	0	-3.47	-3.31	0.17
174	3248	0	-3.59	-3.44	0.15
243	3239	0	-3.35	-3.05	0.31
187	3195	0	-3.93	-3.77	0.16

Continued on next page

Supplementary Table 30: Energetic and electronic properties for $[\text{Cu}_8\text{Zn}_3](\text{Cp}^*)_4(\text{Mes})_3\text{H}$ complexes obtained with PBE+TS/light-tier1 level and light SCF parameters: configuration number (i), relative total energy (ΔE_{tot}), total magnetic moment (m_{tot}), HOMO energy (ε_H), LUMO energy (ε_L), and LUMO-HOMO energy gap (E_g).

i	ΔE_{tot} (meV)	m_{tot} (μ_B)	ε_H (eV)	ε_L (eV)	E_g (eV)
110	3191	0	-3.68	-3.25	0.44
296	3174	0	-3.94	-3.75	0.18
165	3168	0	-3.18	-3.04	0.14
120	3144	0	-3.81	-3.71	0.10
170	3137	0	-4.04	-3.38	0.67
137	3124	0	-3.78	-3.57	0.21
51	3102	0	-4.13	-3.95	0.18
203	3077	0	-3.22	-3.11	0.11
241	3075	0	-3.59	-3.42	0.17
255	3068	2	-3.98	-3.86	0.12
79	2958	0	-3.89	-3.20	0.69
298	2936	2	-3.50	-3.34	0.16
156	2930	0	-3.61	-3.48	0.13
242	2920	0	-3.54	-3.05	0.49
82	2843	0	-3.99	-3.38	0.61
215	2833	0	-4.11	-2.98	1.13
80	2798	0	-3.82	-3.62	0.20
101	2775	0	-3.80	-3.62	0.18
271	2702	0	-3.87	-3.05	0.83
121	2655	0	-3.72	-3.51	0.21
222	2639	0	-4.02	-2.77	1.25
189	2634	0	-4.01	-2.97	1.04

Continued on next page

Supplementary Table 30: Energetic and electronic properties for $[\text{Cu}_8\text{Zn}_3](\text{Cp}^*)_4(\text{Mes})_3\text{H}$ complexes obtained with PBE+TS/light-tier1 level and light SCF parameters: configuration number (i), relative total energy (ΔE_{tot}), total magnetic moment (m_{tot}), HOMO energy (ε_H), LUMO energy (ε_L), and LUMO-HOMO energy gap (E_g).

i	ΔE_{tot} (meV)	m_{tot} (μ_B)	ε_H (eV)	ε_L (eV)	E_g (eV)
221	2626	0	-3.99	-3.10	0.89
123	2624	0	-3.62	-3.01	0.61
126	2604	0	-4.10	-3.11	0.99
35	2591	0	-3.64	-2.72	0.92
276	2581	0	-3.93	-2.80	1.13
313	2431	0	-4.49	-3.57	0.92
25	2430	0	-3.48	-3.30	0.18
232	2424	0	-4.14	-3.64	0.50
319	2409	0	-4.16	-3.28	0.88
249	2323	0	-3.78	-2.73	1.05
317	2307	0	-4.29	-3.42	0.87
129	2303	0	-4.09	-3.22	0.87
192	2288	0	-4.07	-2.87	1.21
198	2272	0	-3.92	-3.74	0.18
125	2270	0	-4.06	-3.23	0.83
305	2243	0	-3.75	-3.13	0.62
154	2224	0	-4.04	-3.23	0.80
152	2213	0	-4.09	-3.01	1.08
274	2199	0	-4.05	-3.30	0.75
226	2196	0	-4.16	-3.07	1.09
267	2172	0	-4.14	-3.12	1.01
52	2152	0	-3.90	-3.20	0.70

Continued on next page

Supplementary Table 30: Energetic and electronic properties for $[\text{Cu}_8\text{Zn}_3](\text{Cp}^*)_4(\text{Mes})_3\text{H}$ complexes obtained with PBE+TS/light-tier1 level and light SCF parameters: configuration number (i), relative total energy (ΔE_{tot}), total magnetic moment (m_{tot}), HOMO energy (ε_H), LUMO energy (ε_L), and LUMO-HOMO energy gap (E_g).

i	ΔE_{tot} (meV)	m_{tot} (μ_B)	ε_H (eV)	ε_L (eV)	E_g (eV)
114	2147	0	-4.13	-3.37	0.76
320	2125	0	-4.11	-3.61	0.51
132	2124	0	-3.93	-3.51	0.42
147	2113	0	-3.59	-3.03	0.56
236	2100	0	-4.13	-3.10	1.03
244	2083	0	-4.20	-2.98	1.23
176	2063	0	-4.18	-3.30	0.88
149	2048	0	-4.12	-3.35	0.77
185	2024	0	-3.78	-2.73	1.05
195	2013	0	-4.04	-3.08	0.96
12	2008	0	-3.71	-3.58	0.14
97	1980	0	-4.11	-2.97	1.15
297	1965	0	-4.00	-2.59	1.40
53	1962	0	-4.29	-3.63	0.66
224	1944	0	-4.09	-3.21	0.88
252	1943	0	-4.05	-3.49	0.56
4	1900	0	-3.61	-3.32	0.29
34	1891	0	-3.89	-2.97	0.92
66	1833	0	-3.84	-2.95	0.89
155	1825	0	-4.05	-3.19	0.86
310	1821	0	-4.45	-3.45	1.00
8	1813	0	-3.83	-2.60	1.24

Continued on next page

Supplementary Table 30: Energetic and electronic properties for $[\text{Cu}_8\text{Zn}_3](\text{Cp}^*)_4(\text{Mes})_3\text{H}$ complexes obtained with PBE+TS/light-tier1 level and light SCF parameters: configuration number (i), relative total energy (ΔE_{tot}), total magnetic moment (m_{tot}), HOMO energy (ε_H), LUMO energy (ε_L), and LUMO-HOMO energy gap (E_g).

i	ΔE_{tot} (meV)	m_{tot} (μ_B)	ε_H (eV)	ε_L (eV)	E_g (eV)
46	1810	0	-3.80	-2.81	0.99
314	1807	0	-4.27	-3.08	1.19
268	1784	0	-4.22	-3.38	0.84
321	1774	0	-4.24	-2.99	1.24
261	1741	0	-3.94	-3.56	0.38
9	1731	0	-3.44	-3.32	0.12
127	1712	0	-3.94	-3.08	0.86
257	1689	0	-4.27	-3.04	1.24
143	1683	0	-4.10	-3.18	0.91
163	1676	0	-4.25	-3.13	1.12
61	1670	0	-4.16	-3.32	0.83
164	1665	0	-3.86	-3.34	0.52
288	1648	0	-3.78	-2.77	1.00
161	1644	0	-3.80	-3.08	0.72
300	1641	0	-4.16	-2.90	1.26
139	1625	0	-4.25	-3.01	1.24
287	1613	0	-3.98	-3.47	0.51
227	1604	0	-4.08	-3.26	0.82
124	1592	0	-4.20	-3.10	1.10
99	1586	0	-4.30	-2.66	1.64
159	1580	0	-3.90	-2.90	1.00
23	1570	0	-3.88	-2.97	0.91

Continued on next page

Supplementary Table 30: Energetic and electronic properties for $[\text{Cu}_8\text{Zn}_3](\text{Cp}^*)_4(\text{Mes})_3\text{H}$ complexes obtained with PBE+TS/light-tier1 level and light SCF parameters: configuration number (i), relative total energy (ΔE_{tot}), total magnetic moment (m_{tot}), HOMO energy (ε_H), LUMO energy (ε_L), and LUMO-HOMO energy gap (E_g).

i	ΔE_{tot} (meV)	m_{tot} (μ_B)	ε_H (eV)	ε_L (eV)	E_g (eV)
48	1547	0	-3.87	-2.75	1.12
190	1513	0	-4.02	-3.17	0.85
18	1508	0	-3.70	-3.22	0.47
316	1505	0	-4.31	-3.49	0.82
307	1505	0	-3.70	-2.94	0.76
225	1499	0	-4.04	-3.22	0.82
72	1496	0	-3.80	-3.02	0.78
245	1492	0	-4.23	-3.19	1.04
266	1456	0	-3.98	-2.97	1.01
131	1445	0	-4.13	-3.28	0.86
108	1408	0	-3.95	-2.88	1.07
118	1384	0	-3.80	-3.10	0.70
304	1358	0	-4.07	-3.16	0.91
5	1350	0	-4.09	-3.10	0.99
107	1336	0	-4.29	-3.30	0.99
201	1308	0	-4.31	-3.13	1.19
247	1286	0	-3.89	-3.07	0.82
27	1241	0	-3.81	-2.84	0.96
264	1210	0	-3.77	-2.74	1.04
223	1194	0	-3.77	-3.02	0.75
173	1193	0	-3.94	-3.28	0.66
39	1174	0	-4.01	-2.90	1.11

Continued on next page

Supplementary Table 30: Energetic and electronic properties for $[\text{Cu}_8\text{Zn}_3](\text{Cp}^*)_4(\text{Mes})_3\text{H}$ complexes obtained with PBE+TS/light-tier1 level and light SCF parameters: configuration number (i), relative total energy (ΔE_{tot}), total magnetic moment (m_{tot}), HOMO energy (ε_H), LUMO energy (ε_L), and LUMO-HOMO energy gap (E_g).

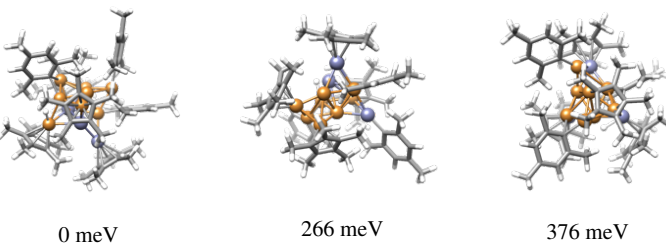
i	ΔE_{tot} (meV)	m_{tot} (μ_B)	ε_H (eV)	ε_L (eV)	E_g (eV)
81	1168	0	-3.94	-3.01	0.93
303	1150	0	-3.74	-3.11	0.63
177	1141	0	-4.38	-3.11	1.27
83	1111	0	-3.95	-3.06	0.89
148	1101	0	-4.08	-2.76	1.32
106	1100	0	-3.78	-2.97	0.81
168	1074	0	-3.99	-2.89	1.11
308	1073	0	-3.97	-3.07	0.89
70	1066	0	-4.03	-3.05	0.98
279	1006	0	-4.03	-3.05	0.98
50	963	0	-4.14	-2.96	1.18
318	939	0	-4.08	-2.91	1.18
265	935	0	-4.00	-3.38	0.61
181	897	0	-3.83	-2.58	1.25
199	890	0	-3.92	-2.95	0.98
49	885	0	-3.91	-3.57	0.34
92	871	0	-4.26	-2.83	1.43
128	866	0	-4.16	-2.97	1.20
228	817	0	-4.06	-2.73	1.33
93	794	0	-3.84	-3.01	0.83
95	757	0	-3.79	-2.96	0.83
45	727	0	-3.69	-2.95	0.74

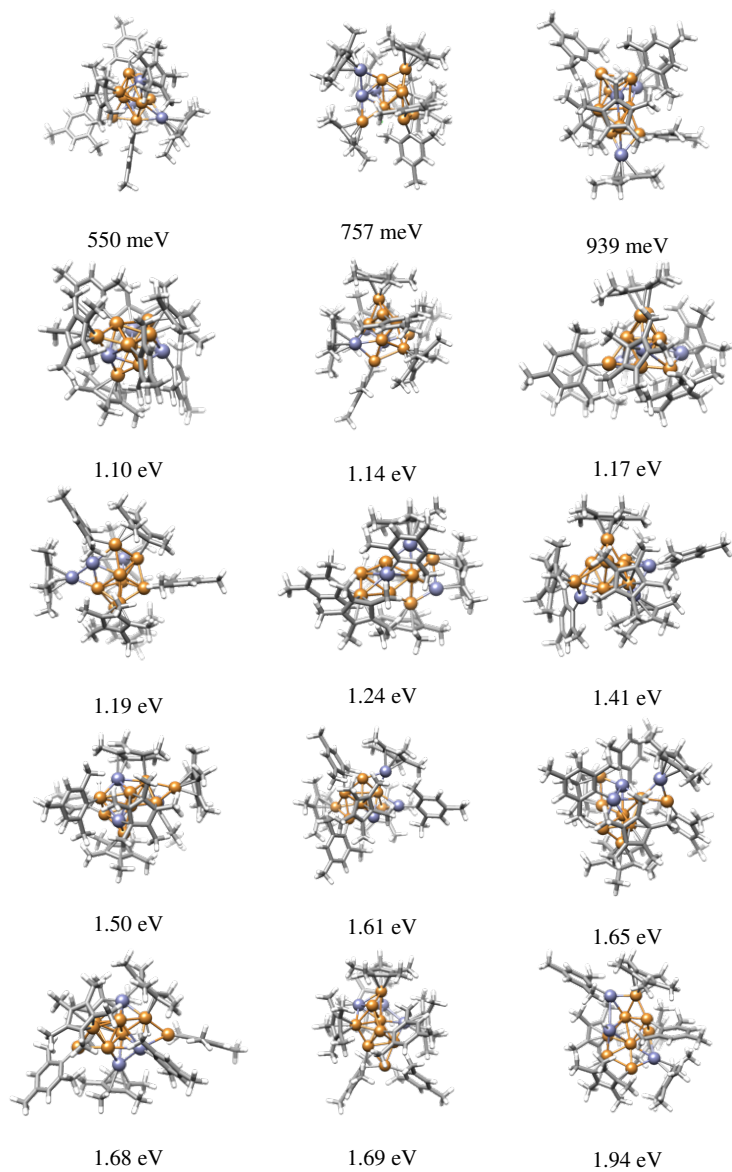
Continued on next page

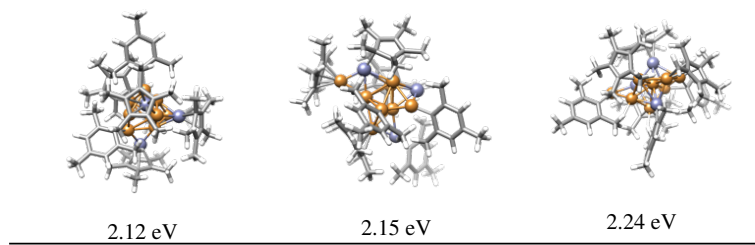
Supplementary Table 30: Energetic and electronic properties for $[\text{Cu}_8\text{Zn}_3](\text{Cp}^*)_4(\text{Mes})_3\text{H}$ complexes obtained with PBE+TS/light-tier1 level and light SCF parameters: configuration number (i), relative total energy (ΔE_{tot}), total magnetic moment (m_{tot}), HOMO energy (ε_H), LUMO energy (ε_L), and LUMO-HOMO energy gap (E_g).

i	ΔE_{tot} (meV)	m_{tot} (μ_B)	ε_H (eV)	ε_L (eV)	E_g (eV)
282	717	0	-4.13	-2.79	1.35
315	632	0	-4.42	-3.22	1.20
301	601	0	-4.30	-3.05	1.25
119	573	0	-3.97	-2.97	1.00
302	550	0	-4.28	-3.01	1.27
175	512	0	-4.02	-2.62	1.40
63	482	0	-3.81	-2.64	1.17
213	414	0	-3.74	-2.91	0.83
309	376	0	-4.04	-2.61	1.42
109	266	0	-3.76	-2.62	1.14
306	0	0	-3.92	-2.74	1.18

Supplementary Table 31: Optimized and filtered representative structures of $[\text{Cu}_8\text{Zn}_3](\text{Cp}^*)_4(\text{Mes})_3\text{H}$ complexes obtained with PBE+TS/light-tier1 level and light SCF parameters. The relative total energy (ΔE_{tot}) is depicted above each structure.







2.7.7 $[\text{Cu}_9\text{Zn}_7](\text{Cp}^*)_6(\text{Hex})_3\text{H}_3$ Complexes

Supplementary Table 32: Energetic and electronic properties for $[\text{Cu}_9\text{Zn}_7](\text{Cp}^*)_6(\text{Hex})_3\text{H}_3$ complexes obtained with PBE+TS/light-tier1 level and light SCF parameters: configuration number (i), relative total energy (ΔE_{tot}), total magnetic moment (m_{tot}), HOMO energy (ε_H), LUMO energy (ε_L), and LUMO-HOMO energy gap (E_g).

i	ΔE_{tot} (meV)	m_{tot} (μ_B)	ε_H (eV)	ε_L (eV)	E_g (eV)
105	9805	2	-3.65	-3.43	0.22
4	9804	2	-3.15	-2.95	0.21
193	9542	2	-3.82	-3.54	0.28
108	9494	2	-3.90	-3.76	0.14
241	9073	2	-3.35	-3.17	0.18
282	8981	0	-3.70	-3.12	0.57
253	8962	0	-3.48	-3.31	0.17
205	8937	0	-3.74	-3.54	0.20
43	8677	2	-3.67	-3.56	0.12
142	8576	2	-3.70	-3.46	0.24
281	8544	2	-3.83	-3.65	0.18
162	8405	0	-3.51	-3.35	0.17
273	8276	0	-3.64	-3.14	0.50
236	8268	2	-3.72	-3.58	0.14

Continued on next page

Supplementary Table 32: Energetic and electronic properties for $[\text{Cu}_9\text{Zn}_7](\text{Cp}^*)_6(\text{Hex})_3\text{H}_3$ complexes obtained with PBE+TS/light-tier1 level and light SCF parameters: configuration number (i), relative total energy (ΔE_{tot}), total magnetic moment (m_{tot}), HOMO energy (ε_H), LUMO energy (ε_L), and LUMO-HOMO energy gap (E_g).

i	ΔE_{tot} (meV)	m_{tot} (μ_B)	ε_H (eV)	ε_L (eV)	E_g (eV)
102	8259	2	-3.71	-3.47	0.23
221	8234	2	-3.51	-3.43	0.08
115	7416	2	-3.55	-3.38	0.17
52	7379	2	-3.35	-3.22	0.13
145	7355	2	-3.65	-3.51	0.13
144	7315	2	-3.81	-3.57	0.24
206	7247	0	-3.74	-3.23	0.51
53	7138	2	-3.77	-3.52	0.25
21	7116	0	-3.29	-2.87	0.42
242	7085	2	-3.65	-3.48	0.17
186	6973	2	-3.69	-3.68	0.02
101	6855	0	-3.42	-2.99	0.43
19	6571	0	-3.86	-2.99	0.87
201	6353	2	-3.48	-3.33	0.15
12	6293	0	-3.44	-3.07	0.37
55	6207	0	-3.73	-2.89	0.84
124	6136	0	-3.83	-3.33	0.50
294	6076	2	-3.66	-3.52	0.15
152	5919	0	-3.61	-2.81	0.80
313	5584	0	-3.85	-3.21	0.64
275	5509	0	-3.74	-2.85	0.89
2	5465	0	-3.79	-2.86	0.93

Continued on next page

Supplementary Table 32: Energetic and electronic properties for $[\text{Cu}_9\text{Zn}_7](\text{Cp}^*)_6(\text{Hex})_3\text{H}_3$ complexes obtained with PBE+TS/light-tier1 level and light SCF parameters: configuration number (i), relative total energy (ΔE_{tot}), total magnetic moment (m_{tot}), HOMO energy (ε_H), LUMO energy (ε_L), and LUMO-HOMO energy gap (E_g).

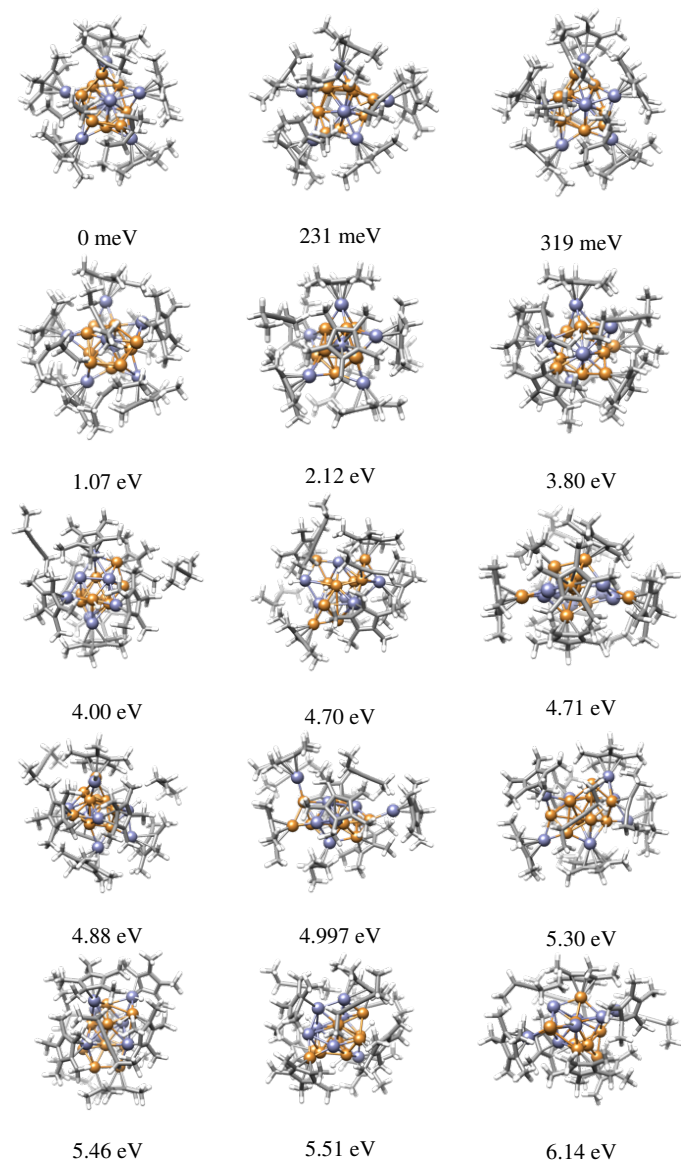
i	ΔE_{tot} (meV)	m_{tot} (μ_B)	ε_H (eV)	ε_L (eV)	E_g (eV)
214	5433	0	-3.59	-2.84	0.75
324	5402	0	-3.84	-3.01	0.83
320	5299	0	-3.90	-3.04	0.86
196	4993	0	-3.62	-2.77	0.85
284	4885	0	-3.71	-3.00	0.71
93	4707	0	-3.64	-2.93	0.71
31	4705	0	-3.74	-2.92	0.82
181	4303	0	-3.61	-2.79	0.82
312	4199	0	-3.63	-3.14	0.49
306	4092	0	-3.81	-2.82	0.99
311	4076	0	-3.98	-2.83	1.15
132	4009	0	-3.68	-2.85	0.83
310	3956	0	-3.85	-2.88	0.98
163	3831	0	-3.68	-3.01	0.68
315	3601	0	-3.82	-2.76	1.07
318	3557	0	-3.77	-2.93	0.83
319	3334	0	-3.58	-2.83	0.75
322	3274	0	-3.55	-2.65	0.90
302	3128	0	-3.91	-2.79	1.12
314	3110	0	-3.77	-2.95	0.82
309	3070	0	-3.82	-3.03	0.80
305	2953	0	-3.87	-2.84	1.03

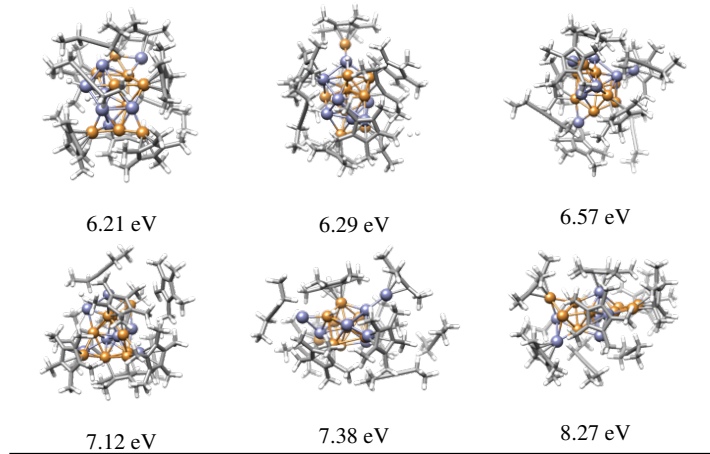
Continued on next page

Supplementary Table 32: Energetic and electronic properties for $[\text{Cu}_9\text{Zn}_7](\text{Cp}^*)_6(\text{Hex})_3\text{H}_3$ complexes obtained with PBE+TS/light-tier1 level and light SCF parameters: configuration number (i), relative total energy (ΔE_{tot}), total magnetic moment (m_{tot}), HOMO energy (ε_H), LUMO energy (ε_L), and LUMO-HOMO energy gap (E_g).

i	ΔE_{tot} (meV)	m_{tot} (μ_B)	ε_H (eV)	ε_L (eV)	E_g (eV)
307	2854	0	-3.76	-2.76	1.00
321	2732	0	-3.60	-2.78	0.82
323	2606	0	-3.43	-2.87	0.56
316	2174	0	-3.67	-2.87	0.80
317	2126	0	-3.80	-3.06	0.74
328	1338	0	-3.61	-2.59	1.02
326	1081	0	-3.51	-2.70	0.81
327	1069	0	-3.69	-2.53	1.16
329	1028	0	-3.51	-2.65	0.87
330	986	0	-3.45	-2.67	0.78
331	934	0	-3.37	-2.44	0.93
335	379	0	-3.46	-2.62	0.83
332	319	0	-3.35	-2.42	0.93
334	231	0	-3.34	-2.56	0.78
333	226	0	-3.36	-2.69	0.66
336	0	0	-3.29	-2.65	0.65

Supplementary Table 33: Optimized and filtered representative structures of $[\text{Cu}_9\text{Zn}_7](\text{Cp}^*)_6(\text{Hex})_3\text{H}_3$ complexes obtained with PBE/light-tier1 level and light SCF parameters. The relative total energy (ΔE_{tot}) is depicted above each structure.





2.7.8 $[\text{Cu}_{11}\text{Zn}_6](\text{Cp}^*)_8(\text{CO}_2)_2(\text{HCO}_2)$ Complexes

Supplementary Table 34: Energetic and electronic properties for $[\text{Cu}_{11}\text{Zn}_6](\text{Cp}^*)_8(\text{HCO}_2)(\text{CO}_2)_2$ complexes obtained with PBE+TS/light-tier1 level and light SCF parameters: configuration number (i), relative total energy (ΔE_{tot}), total magnetic moment (m_{tot}), HOMO energy (ε_H), LUMO energy (ε_L), and LUMO-HOMO energy gap (E_g).

i	ΔE_{tot} (meV)	m_{tot} (μ_B)	ε_H (eV)	ε_L (eV)	E_g (eV)
61	6360	1	-1.52	-1.51	0.01
195	6008	1	-1.76	-1.12	0.63
31	5989	1	-1.48	-1.44	0.04
204	5923	1	-1.50	-1.48	0.02
157	5842	1	-1.58	-1.57	0.02
214	5766	1	-1.02	-0.88	0.14
16	5583	1	-1.56	-1.52	0.04
252	5072	1	-1.52	-1.27	0.25
102	4859	1	-1.13	-1.00	0.13
184	4685	1	-1.17	-0.99	0.17

Continued on next page

Supplementary Table 34: Energetic and electronic properties for $[\text{Cu}_{11}\text{Zn}_6](\text{Cp}^*)_8(\text{HCO}_2)(\text{CO}_2)_2$ complexes obtained with PBE+TS/light-tier1 level and light SCF parameters: configuration number (i), relative total energy (ΔE_{tot}), total magnetic moment (m_{tot}), HOMO energy (ε_H), LUMO energy (ε_L), and LUMO-HOMO energy gap (E_g).

i	ΔE_{tot} (meV)	m_{tot} (μ_B)	ε_H (eV)	ε_L (eV)	E_g (eV)
41	4450	1	-1.81	-1.67	0.14
193	4353	1	-1.48	-1.13	0.35
283	4347	1	-1.95	-1.89	0.06
203	4344	1	-1.54	-1.37	0.17
25	4206	1	-1.29	-1.20	0.09
103	4182	1	-1.61	-1.59	0.02
162	4143	1	-1.50	-1.44	0.06
244	4049	1	-1.44	-1.37	0.07
29	4047	1	-1.85	-1.63	0.21
165	4032	1	-1.55	-1.53	0.02
262	3849	1	-1.70	-1.62	0.08
18	3842	1	-1.55	-1.53	0.02
153	3695	1	-1.84	-1.57	0.27
36	3629	1	-1.70	-1.68	0.02
20	3602	1	-1.41	-1.37	0.04
113	3594	1	-1.76	-1.70	0.06
93	3502	1	-1.15	-1.14	0.01
234	3455	1	-1.68	-1.65	0.03
28	3455	1	-1.35	-1.24	0.11
331	3429	1	-2.09	-1.99	0.11
206	3428	1	-1.62	-1.50	0.12
288	3407	3	-1.73	-1.58	0.14

Continued on next page

Supplementary Table 34: Energetic and electronic properties for $[\text{Cu}_{11}\text{Zn}_6](\text{Cp}^*)_8(\text{HCO}_2)(\text{CO}_2)_2$ complexes obtained with PBE+TS/light-tier1 level and light SCF parameters: configuration number (i), relative total energy (ΔE_{tot}), total magnetic moment (m_{tot}), HOMO energy (ε_H), LUMO energy (ε_L), and LUMO-HOMO energy gap (E_g).

i	ΔE_{tot} (meV)	m_{tot} (μ_B)	ε_H (eV)	ε_L (eV)	E_g (eV)
212	3387	1	-1.62	-1.44	0.18
211	3186	1	-1.55	-1.44	0.11
82	3177	1	-1.40	-1.30	0.10
174	3170	1	-1.90	-1.89	0.01
32	3060	1	-1.52	-1.48	0.04
143	3059	1	-1.82	-1.48	0.34
21	3055	1	-1.55	-1.46	0.09
43	2995	1	-1.63	-1.61	0.03
258	2981	1	-1.18	-1.17	0.01
285	2921	1	-1.75	-1.68	0.07
232	2910	1	-1.65	-1.63	0.02
161	2906	1	-1.60	-1.53	0.07
290	2878	1	-1.68	-1.60	0.08
224	2853	1	-1.97	-1.84	0.14
22	2835	1	-1.67	-1.65	0.02
154	2648	1	-1.67	-1.54	0.13
132	2599	1	-1.50	-1.48	0.02
268	2585	1	-1.62	-1.46	0.16
172	2578	1	-1.64	-1.53	0.11
282	2517	1	-1.13	-1.01	0.11
241	2491	1	-1.58	-1.37	0.21
295	2482	1	-1.46	-1.42	0.04

Continued on next page

Supplementary Table 34: Energetic and electronic properties for $[\text{Cu}_{11}\text{Zn}_6](\text{Cp}^*)_8(\text{HCO}_2)(\text{CO}_2)_2$ complexes obtained with PBE+TS/light-tier1 level and light SCF parameters: configuration number (i), relative total energy (ΔE_{tot}), total magnetic moment (m_{tot}), HOMO energy (ε_H), LUMO energy (ε_L), and LUMO-HOMO energy gap (E_g).

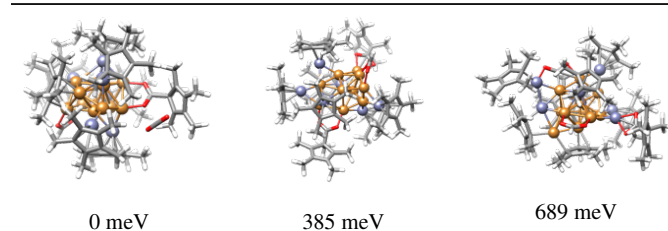
i	ΔE_{tot}	m_{tot}	ε_H	ε_L	E_g
	(meV)	(μ_B)	(eV)	(eV)	(eV)
306	2457	1	-1.74	-1.60	0.14
257	2428	1	-1.76	-1.66	0.10
259	2371	1	-1.61	-1.48	0.13
238	2367	1	-1.68	-1.66	0.02
191	2270	1	-1.65	-1.46	0.19
305	2183	1	-1.75	-1.60	0.15
13	2160	1	-1.34	-1.24	0.10
284	2150	1	-1.19	-1.06	0.13
37	2088	1	-1.73	-1.69	0.04
303	2013	1	-1.66	-1.55	0.11
319	1980	1	-1.41	-1.29	0.11
49	1877	1	-1.52	-1.41	0.11
26	1866	1	-1.76	-1.64	0.12
318	1840	1	-1.57	-1.45	0.12
221	1763	1	-1.51	-1.46	0.05
309	1717	1	-1.32	-1.20	0.11
46	1712	1	-1.65	-1.55	0.10
307	1674	1	-1.70	-1.59	0.11
225	1621	1	-1.53	-1.40	0.12
301	1597	1	-1.47	-1.38	0.10
121	1520	1	-1.26	-1.14	0.12
312	1459	1	-1.57	-1.45	0.11

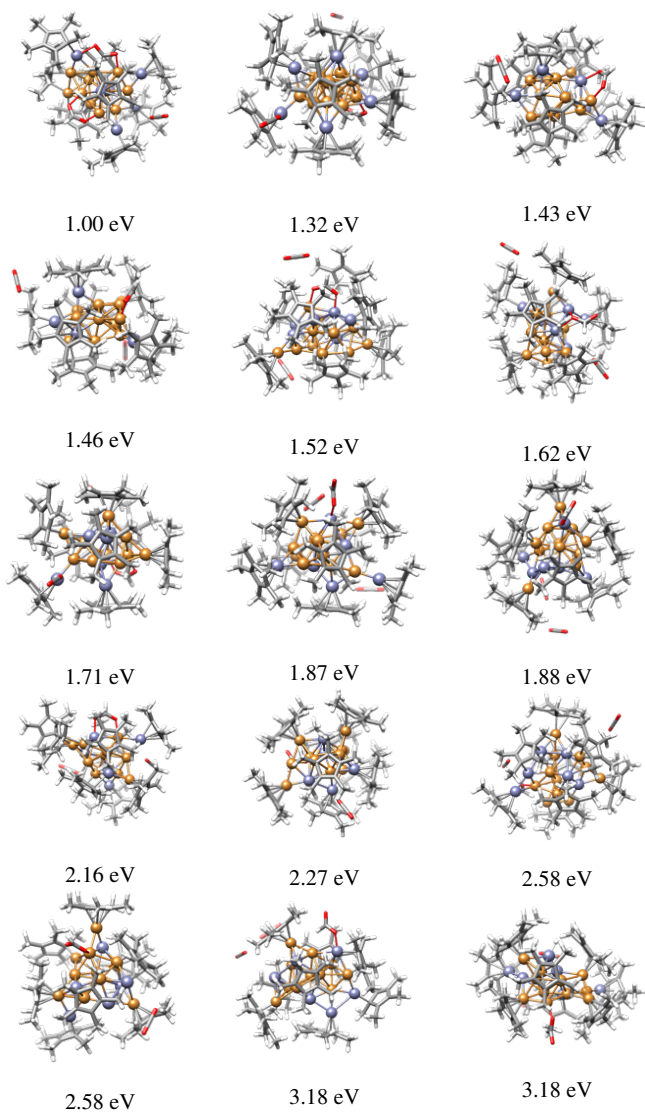
Continued on next page

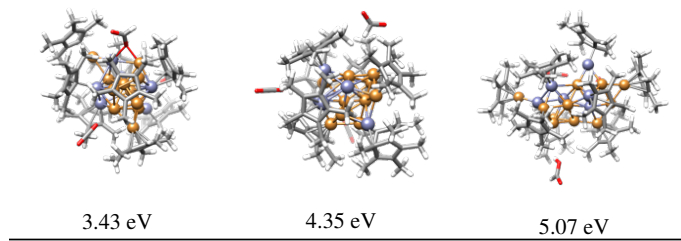
Supplementary Table 34: Energetic and electronic properties for $[Cu_{11}Zn_6](Cp^*)_8(HCO_2)(CO_2)_2$ complexes obtained with PBE+TS/light-tier1 level and light SCF parameters: configuration number (i), relative total energy (ΔE_{tot}), total magnetic moment (m_{tot}), HOMO energy (ε_H), LUMO energy (ε_L), and LUMO-HOMO energy gap (E_g).

i	ΔE_{tot}	m_{tot}	ε_H	ε_L	E_g
	(meV)	(μ_B)	(eV)	(eV)	(eV)
223	1426	1	-1.50	-1.39	0.12
327	1417	1	-1.53	-1.43	0.10
329	1324	1	-1.54	-1.42	0.12
325	1217	1	-1.57	-1.42	0.14
311	1211	1	-1.44	-1.33	0.11
315	1125	1	-1.45	-1.33	0.13
333	1096	1	-1.68	-1.57	0.11
308	1003	1	-1.39	-1.27	0.12
323	756	1	-1.42	-1.32	0.10
326	689	1	-1.46	-1.34	0.12
328	385	1	-1.33	-1.20	0.13
332	318	1	-1.57	-1.45	0.11
321	281	1	-1.54	-1.43	0.11
330	0	1	-1.27	-1.13	0.14

Supplementary Table 35: Optimized and filtered representative structures of $[Cu_{11}Zn_6](Cp^*)_8(CO_2)_2(HCO_2)$ complexes obtained with PBE/light-tier1 level and light SCF parameters. The relative total energy (ΔE_{tot}) is depicted above each structure.







2.7.9 $[\text{Cu}_8\text{Al}_6](\text{Cp}^*)_6$ Complexes

Supplementary Table 36: Energetic and electronic properties for $[\text{Cu}_8\text{Al}_6](\text{Cp}^*)_6$ complexes obtained with PBE+TS/light-tier1 level and light SCF parameters: configuration number (i), relative total energy (ΔE_{tot}), total magnetic moment (m_{tot}), HOMO energy (ε_H), LUMO energy (ε_L), and LUMO-HOMO energy gap (E_g).

i	ΔE_{tot} (meV)	m_{tot} (μ_B)	ε_H (eV)	ε_L (eV)	E_g (eV)
193	7749	0	-3.37	-3.05	0.33
55	6715	0	-3.26	-2.70	0.56
227	6615	0	-3.18	-2.53	0.64
188	6102	0	-3.12	-2.57	0.55
82	5917	0	-3.21	-2.98	0.23
13	5839	0	-3.05	-2.67	0.38
216	5673	0	-3.48	-3.04	0.44
36	5452	0	-3.34	-2.59	0.75
102	5417	0	-3.32	-2.58	0.73
262	5173	0	-3.05	-2.42	0.63
6	5164	0	-3.46	-2.82	0.64
75	5152	0	-3.39	-2.80	0.59
45	5125	0	-3.26	-2.72	0.54
105	5019	0	-3.10	-2.39	0.70

Continued on next page

Supplementary Table 36: Energetic and electronic properties for $[Cu_8Al_6](Cp^*)_6$ complexes obtained with PBE+TS/light-tier1 level and light SCF parameters: configuration number (i), relative total energy (ΔE_{tot}), total magnetic moment (m_{tot}), HOMO energy (ε_H), LUMO energy (ε_L), and LUMO-HOMO energy gap (E_g).

i	ΔE_{tot} (meV)	m_{tot} (μ_B)	ε_H (eV)	ε_L (eV)	E_g (eV)
276	4975	0	-3.21	-2.68	0.53
101	4902	0	-3.31	-2.97	0.34
134	4901	0	-3.19	-2.59	0.59
56	4887	0	-3.05	-2.47	0.58
278	4755	0	-3.50	-2.76	0.74
20	4717	0	-3.05	-2.65	0.40
61	4711	0	-3.44	-2.47	0.97
51	4600	0	-3.36	-2.77	0.59
180	4532	0	-3.19	-2.40	0.80
100	4506	0	-3.43	-2.77	0.66
57	4457	0	-3.24	-2.64	0.60
158	4415	0	-3.29	-2.57	0.72
201	4387	0	-3.19	-2.51	0.67
235	4358	0	-3.38	-2.98	0.40
202	4340	0	-3.23	-2.52	0.70
62	4262	0	-3.28	-2.43	0.85
171	4241	0	-3.33	-2.58	0.75
198	4238	0	-3.12	-2.68	0.44
14	4205	0	-3.54	-2.58	0.96
297	4203	0	-3.55	-2.89	0.66
311	4173	0	-2.94	-2.49	0.45
261	4157	0	-3.48	-2.67	0.81

Continued on next page

Supplementary Table 36: Energetic and electronic properties for $[Cu_8Al_6](Cp^*)_6$ complexes obtained with PBE+TS/light-tier1 level and light SCF parameters: configuration number (i), relative total energy (ΔE_{tot}), total magnetic moment (m_{tot}), HOMO energy (ε_H), LUMO energy (ε_L), and LUMO-HOMO energy gap (E_g).

i	ΔE_{tot} (meV)	m_{tot} (μ_B)	ε_H (eV)	ε_L (eV)	E_g (eV)
175	4066	0	-3.34	-2.62	0.71
48	4065	0	-3.26	-2.93	0.33
189	4021	0	-3.49	-2.62	0.87
190	4019	0	-2.93	-2.57	0.36
124	4004	0	-3.03	-2.64	0.39
108	4000	0	-3.31	-2.63	0.68
3	3966	0	-3.39	-2.36	1.03
248	3955	0	-3.18	-2.35	0.83
211	3927	0	-3.46	-2.93	0.53
196	3920	0	-3.26	-2.81	0.45
185	3914	0	-3.17	-2.92	0.26
296	3870	0	-3.24	-2.71	0.53
181	3862	0	-3.25	-2.61	0.64
68	3832	0	-3.39	-2.57	0.82
147	3794	0	-2.93	-2.62	0.31
139	3780	0	-3.23	-2.56	0.68
294	3765	0	-3.56	-2.98	0.58
83	3762	0	-3.04	-2.60	0.44
246	3745	0	-3.39	-2.29	1.10
179	3734	0	-3.59	-2.62	0.97
113	3729	0	-3.46	-2.70	0.75
312	3718	0	-2.94	-2.41	0.53

Continued on next page

Supplementary Table 36: Energetic and electronic properties for $[Cu_8Al_6](Cp^*)_6$ complexes obtained with PBE+TS/light-tier1 level and light SCF parameters: configuration number (i), relative total energy (ΔE_{tot}), total magnetic moment (m_{tot}), HOMO energy (ε_H), LUMO energy (ε_L), and LUMO-HOMO energy gap (E_g).

i	ΔE_{tot} (meV)	m_{tot} (μ_B)	ε_H (eV)	ε_L (eV)	E_g (eV)
95	3717	0	-3.52	-2.70	0.82
264	3702	0	-3.11	-2.47	0.64
149	3666	0	-3.32	-2.51	0.81
265	3625	0	-3.46	-2.78	0.68
131	3611	0	-3.48	-2.92	0.56
16	3534	0	-3.10	-2.38	0.72
126	3526	0	-3.28	-2.50	0.78
168	3513	0	-3.43	-2.89	0.53
274	3483	0	-3.29	-2.63	0.65
325	3472	0	-3.31	-2.98	0.33
266	3471	0	-3.61	-2.81	0.80
215	3465	0	-3.52	-2.65	0.87
281	3456	0	-3.32	-2.68	0.64
118	3448	0	-3.00	-2.42	0.58
191	3423	0	-3.37	-2.84	0.53
243	3417	0	-3.28	-2.46	0.82
161	3410	0	-3.35	-2.93	0.42
41	3399	0	-3.65	-2.68	0.97
44	3360	0	-3.57	-2.63	0.95
213	3347	0	-3.39	-2.71	0.68
169	3343	0	-3.50	-2.50	1.00
295	3340	0	-3.18	-2.63	0.55

Continued on next page

Supplementary Table 36: Energetic and electronic properties for $[\text{Cu}_8\text{Al}_6](\text{Cp}^*)_6$ complexes obtained with PBE+TS/light-tier1 level and light SCF parameters: configuration number (i), relative total energy (ΔE_{tot}), total magnetic moment (m_{tot}), HOMO energy (ε_H), LUMO energy (ε_L), and LUMO-HOMO energy gap (E_g).

i	ΔE_{tot} (meV)	m_{tot} (μ_B)	ε_H (eV)	ε_L (eV)	E_g (eV)
28	3310	0	-3.54	-2.81	0.72
289	3298	0	-3.55	-2.71	0.84
221	3291	0	-3.15	-2.64	0.51
199	3258	0	-3.01	-2.19	0.82
99	3255	0	-3.15	-2.62	0.52
129	3243	0	-3.49	-2.74	0.75
73	3223	0	-3.40	-2.69	0.71
222	3223	0	-3.01	-2.32	0.69
29	3209	0	-3.62	-2.58	1.04
220	3193	0	-2.91	-2.29	0.63
174	3155	0	-3.44	-2.77	0.67
208	3142	0	-3.39	-2.79	0.59
109	3139	0	-3.00	-2.39	0.61
77	3130	0	-3.52	-2.82	0.69
200	3129	0	-3.60	-2.82	0.78
292	3121	0	-3.10	-2.62	0.48
275	3119	0	-3.54	-2.99	0.56
42	3104	0	-3.11	-2.10	1.01
123	3102	0	-3.20	-2.38	0.82
89	3094	0	-3.40	-2.82	0.58
231	3092	0	-3.42	-2.68	0.74
97	3070	0	-3.04	-2.51	0.53

Continued on next page

Supplementary Table 36: Energetic and electronic properties for $[Cu_8Al_6](Cp^*)_6$ complexes obtained with PBE+TS/light-tier1 level and light SCF parameters: configuration number (i), relative total energy (ΔE_{tot}), total magnetic moment (m_{tot}), HOMO energy (ε_H), LUMO energy (ε_L), and LUMO-HOMO energy gap (E_g).

i	ΔE_{tot} (meV)	m_{tot} (μ_B)	ε_H (eV)	ε_L (eV)	E_g (eV)
273	3048	0	-3.33	-2.49	0.84
114	3047	0	-3.39	-2.65	0.74
250	3025	0	-3.29	-2.64	0.65
122	3018	0	-3.26	-2.75	0.51
67	3015	0	-3.17	-2.66	0.50
98	3013	0	-3.36	-2.29	1.07
271	2981	0	-3.41	-2.82	0.59
214	2977	0	-3.54	-2.47	1.06
219	2971	0	-3.25	-2.74	0.51
288	2960	0	-3.47	-2.47	1.01
186	2947	0	-3.52	-2.65	0.87
277	2944	0	-3.27	-2.62	0.65
52	2944	0	-3.54	-2.67	0.87
323	2910	0	-3.28	-2.59	0.69
163	2888	0	-3.24	-2.64	0.59
263	2876	0	-3.43	-2.61	0.82
120	2865	0	-3.26	-2.75	0.51
166	2843	0	-3.40	-2.47	0.92
115	2826	0	-3.48	-2.92	0.56
284	2744	0	-3.34	-2.50	0.84
91	2739	0	-3.31	-2.60	0.71
207	2735	0	-3.46	-2.63	0.83

Continued on next page

Supplementary Table 36: Energetic and electronic properties for $[Cu_8Al_6](Cp^*)_6$ complexes obtained with PBE+TS/light-tier1 level and light SCF parameters: configuration number (i), relative total energy (ΔE_{tot}), total magnetic moment (m_{tot}), HOMO energy (ε_H), LUMO energy (ε_L), and LUMO-HOMO energy gap (E_g).

i	ΔE_{tot} (meV)	m_{tot} (μ_B)	ε_H (eV)	ε_L (eV)	E_g (eV)
25	2711	0	-3.26	-2.41	0.86
140	2693	0	-3.36	-2.57	0.79
92	2654	0	-3.16	-2.62	0.54
252	2651	0	-3.60	-2.37	1.23
249	2625	0	-3.28	-2.31	0.97
197	2623	0	-3.27	-2.17	1.09
69	2595	0	-3.31	-2.53	0.78
245	2593	0	-3.54	-2.42	1.13
72	2576	0	-3.36	-2.56	0.79
244	2549	0	-3.31	-2.22	1.09
125	2542	0	-3.18	-2.60	0.58
217	2525	0	-3.26	-2.63	0.62
194	2500	0	-3.63	-2.69	0.94
241	2500	0	-3.35	-2.57	0.78
177	2496	0	-3.46	-2.89	0.57
43	2479	0	-3.39	-2.98	0.41
18	2474	0	-3.15	-2.60	0.55
286	2472	0	-3.46	-2.51	0.95
150	2455	0	-3.27	-2.23	1.04
327	2449	0	-3.15	-2.58	0.57
121	2443	0	-3.21	-2.56	0.65
256	2435	0	-3.27	-2.64	0.63

Continued on next page

Supplementary Table 36: Energetic and electronic properties for $[Cu_8Al_6](Cp^*)_6$ complexes obtained with PBE+TS/light-tier1 level and light SCF parameters: configuration number (i), relative total energy (ΔE_{tot}), total magnetic moment (m_{tot}), HOMO energy (ε_H), LUMO energy (ε_L), and LUMO-HOMO energy gap (E_g).

i	ΔE_{tot} (meV)	m_{tot} (μ_B)	ε_H (eV)	ε_L (eV)	E_g (eV)
2	2432	0	-3.71	-2.40	1.32
184	2427	0	-3.33	-2.64	0.69
155	2416	0	-3.51	-2.49	1.03
80	2408	0	-3.52	-2.32	1.20
63	2393	0	-3.26	-2.14	1.12
267	2387	0	-3.31	-2.48	0.83
310	2386	0	-3.21	-2.30	0.91
1	2385	0	-3.21	-2.35	0.86
225	2361	0	-3.10	-2.62	0.48
164	2335	0	-3.28	-2.37	0.91
151	2331	0	-3.53	-2.37	1.16
128	2330	0	-3.46	-2.39	1.07
26	2328	0	-3.41	-2.33	1.08
137	2323	0	-3.63	-2.29	1.33
71	2292	0	-3.42	-2.20	1.21
127	2285	0	-3.42	-2.54	0.88
272	2282	0	-3.31	-2.45	0.86
309	2259	0	-3.35	-2.24	1.11
54	2259	0	-3.48	-2.44	1.05
22	2258	0	-3.50	-2.40	1.10
142	2218	0	-3.40	-2.45	0.96
232	2205	0	-3.23	-2.11	1.12

Continued on next page

Supplementary Table 36: Energetic and electronic properties for $[\text{Cu}_8\text{Al}_6](\text{Cp}^*)_6$ complexes obtained with PBE+TS/light-tier1 level and light SCF parameters: configuration number (i), relative total energy (ΔE_{tot}), total magnetic moment (m_{tot}), HOMO energy (ε_H), LUMO energy (ε_L), and LUMO-HOMO energy gap (E_g).

i	ΔE_{tot} (meV)	m_{tot} (μ_B)	ε_H (eV)	ε_L (eV)	E_g (eV)
291	2184	0	-3.38	-2.55	0.84
182	2181	0	-3.57	-2.69	0.88
141	2179	0	-3.22	-2.18	1.04
233	2158	0	-3.28	-2.18	1.10
170	2154	0	-3.07	-2.14	0.93
298	2151	0	-3.56	-2.13	1.43
31	2143	0	-3.38	-2.20	1.18
10	2140	0	-3.35	-2.55	0.80
253	2129	0	-3.17	-2.51	0.65
117	2091	0	-3.30	-2.31	0.99
328	2078	0	-2.94	-2.15	0.80
226	2068	0	-3.39	-2.49	0.90
322	2064	0	-3.47	-2.47	1.00
47	2060	0	-2.87	-2.30	0.57
324	2023	0	-2.79	-2.42	0.37
5	1991	0	-3.52	-2.85	0.67
318	1945	0	-3.10	-1.82	1.28
315	1940	0	-3.18	-2.53	0.64
17	1916	0	-3.24	-2.34	0.90
283	1912	0	-3.35	-2.23	1.12
132	1900	0	-3.33	-2.12	1.22
280	1892	0	-3.38	-2.23	1.16

Continued on next page

Supplementary Table 36: Energetic and electronic properties for $[Cu_8Al_6](Cp^*)_6$ complexes obtained with PBE+TS/light-tier1 level and light SCF parameters: configuration number (i), relative total energy (ΔE_{tot}), total magnetic moment (m_{tot}), HOMO energy (ε_H), LUMO energy (ε_L), and LUMO-HOMO energy gap (E_g).

i	ΔE_{tot} (meV)	m_{tot} (μ_B)	ε_H (eV)	ε_L (eV)	E_g (eV)
64	1867	0	-3.44	-2.26	1.18
32	1866	0	-2.95	-2.17	0.78
160	1866	0	-3.19	-2.25	0.95
205	1866	0	-3.61	-2.48	1.13
228	1849	0	-3.21	-2.11	1.10
234	1848	0	-3.70	-2.23	1.47
173	1824	0	-3.54	-2.46	1.09
254	1807	0	-3.45	-2.48	0.97
165	1795	0	-3.54	-2.33	1.20
304	1744	0	-3.14	-2.36	0.78
34	1710	0	-3.40	-2.22	1.18
11	1697	0	-3.53	-2.31	1.21
53	1681	0	-3.29	-2.47	0.82
178	1678	0	-3.22	-2.26	0.96
136	1657	0	-3.26	-2.21	1.05
247	1604	0	-3.42	-2.35	1.07
316	1601	0	-3.25	-2.02	1.23
258	1581	0	-3.24	-2.39	0.86
112	1578	0	-3.35	-2.09	1.26
203	1573	0	-3.52	-2.51	1.01
293	1564	0	-3.35	-1.89	1.45
153	1536	0	-3.31	-2.24	1.07

Continued on next page

Supplementary Table 36: Energetic and electronic properties for $[Cu_8Al_6](Cp^*)_6$ complexes obtained with PBE+TS/light-tier1 level and light SCF parameters: configuration number (i), relative total energy (ΔE_{tot}), total magnetic moment (m_{tot}), HOMO energy (ε_H), LUMO energy (ε_L), and LUMO-HOMO energy gap (E_g).

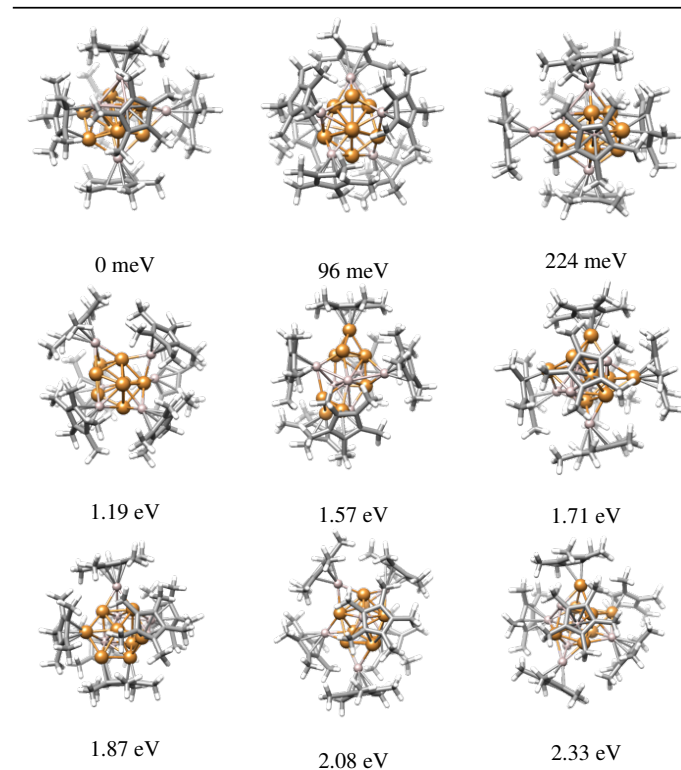
i	ΔE_{tot} (meV)	m_{tot} (μ_B)	ε_H (eV)	ε_L (eV)	E_g (eV)
183	1501	0	-3.38	-2.30	1.07
76	1487	0	-3.30	-2.52	0.78
135	1470	0	-3.50	-2.32	1.18
329	1469	0	-3.17	-2.42	0.75
148	1457	0	-3.17	-2.06	1.11
27	1441	0	-3.33	-2.26	1.07
326	1437	0	-3.03	-1.97	1.06
145	1383	0	-3.24	-2.11	1.13
172	1365	0	-3.47	-2.66	0.81
79	1357	0	-3.25	-2.02	1.23
224	1323	0	-3.42	-2.24	1.19
212	1202	0	-3.35	-2.00	1.35
317	1190	0	-3.15	-1.86	1.29
7	1185	0	-3.43	-2.27	1.16
218	939	0	-3.25	-2.12	1.13
242	885	0	-3.21	-2.42	0.79
60	713	0	-3.24	-1.96	1.28
96	466	0	-3.20	-2.24	0.96
308	461	0	-3.10	-1.86	1.24
162	224	0	-3.15	-1.94	1.22
306	197	0	-2.97	-1.97	1.00
301	184	0	-3.29	-1.72	1.57

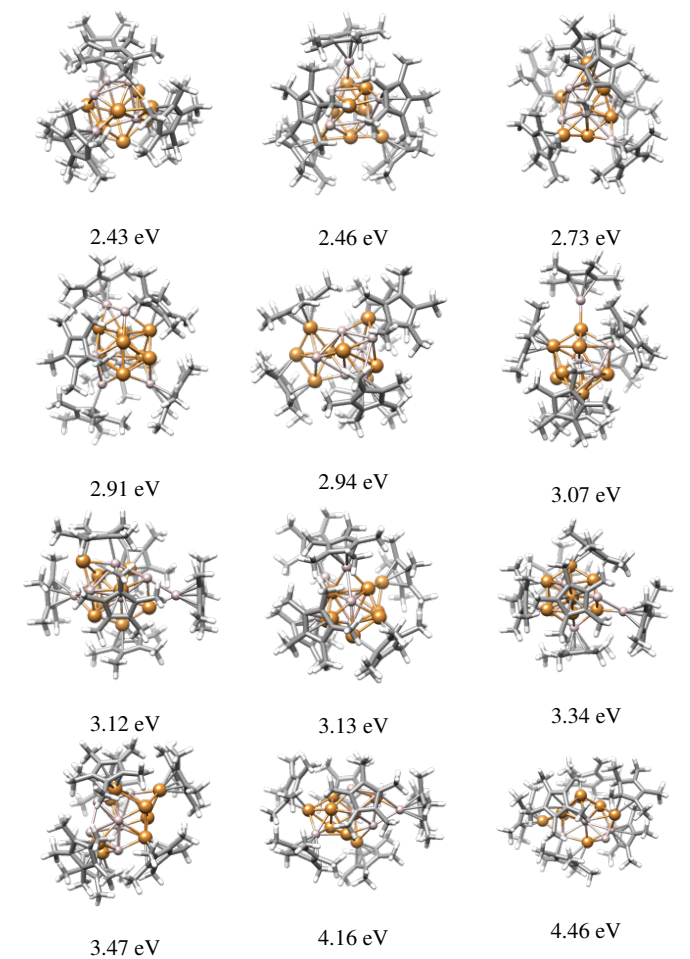
Continued on next page

Supplementary Table 36: Energetic and electronic properties for $[Cu_8Al_6](Cp^*)_6$ complexes obtained with PBE+TS/light-tier1 level and light SCF parameters: configuration number (i), relative total energy (ΔE_{tot}), total magnetic moment (m_{tot}), HOMO energy (ε_H), LUMO energy (ε_L), and LUMO-HOMO energy gap (E_g).

i	ΔE_{tot}	m_{tot}	ε_H	ε_L	E_g
	(meV)	(μ_B)	(eV)	(eV)	(eV)
330	96	0	-3.15	-1.92	1.24
303	0	0	-3.19	-1.76	1.43

Supplementary Table 37: Optimized and filtered representative structures of $[Cu_8Al_6](Cp^*)_6$ complexes obtained with PBE+TS/light-tier1 level and light SCF parameters. The relative total energy (ΔE_{tot}) is depicted above each structure.



**2.7.10 [Ni₇Ga₆](Cp^{*})₆ Complexes**

Supplementary Table 38: Energetic and electronic properties for $[Ni_7Ga_6](Cp^*)_6$ complexes obtained with PBE+TS/light-tier1 level and light SCF parameters: configuration number (i), relative total energy (ΔE_{tot}), total magnetic moment (m_{tot}), HOMO energy (ε_H), LUMO energy (ε_L), and LUMO-HOMO energy gap (E_g).

i	ΔE_{tot} (meV)	m_{tot} (μ_B)	ε_H (eV)	ε_L (eV)	E_g (eV)
261	9370	2	-3.29	-2.94	0.35
274	8736	2	-3.30	-3.12	0.18
137	8585	0	-3.29	-2.99	0.30
6	8283	2	-3.16	-2.97	0.19
111	8232	2	-3.47	-3.28	0.19
73	8175	2	-3.11	-2.88	0.23
62	8053	4	-3.30	-3.19	0.10
89	7997	2	-3.32	-3.15	0.17
233	7916	2	-3.40	-3.24	0.16
112	7711	0	-3.13	-2.65	0.48
257	7626	0	-3.31	-2.89	0.42
167	7577	2	-3.08	-2.95	0.13
146	7320	2	-3.29	-2.94	0.35
158	7061	2	-3.25	-3.01	0.24
267	6954	2	-3.17	-3.04	0.14
292	6905	0	-3.20	-2.64	0.57
156	6893	2	-3.29	-3.16	0.14
109	6862	2	-3.32	-3.06	0.26
229	6834	0	-3.43	-3.19	0.24
303	6813	0	-3.16	-2.98	0.18
171	6714	2	-3.28	-3.01	0.27
214	6661	0	-3.40	-2.89	0.51

Continued on next page

Supplementary Table 38: Energetic and electronic properties for $[Ni_7Ga_6](Cp^*)_6$ complexes obtained with PBE+TS/light-tier1 level and light SCF parameters: configuration number (i), relative total energy (ΔE_{tot}), total magnetic moment (m_{tot}), HOMO energy (ε_H), LUMO energy (ε_L), and LUMO-HOMO energy gap (E_g).

i	ΔE_{tot} (meV)	m_{tot} (μ_B)	ε_H (eV)	ε_L (eV)	E_g (eV)
66	6655	2	-3.24	-3.10	0.13
59	6608	2	-3.30	-3.19	0.11
52	6593	2	-3.15	-2.99	0.16
308	6524	2	-3.15	-2.97	0.18
23	6524	0	-3.28	-3.02	0.26
8	6519	0	-3.27	-3.12	0.15
3	6500	2	-3.28	-3.04	0.24
29	6484	0	-3.02	-2.62	0.40
311	6471	2	-3.06	-2.90	0.16
118	6454	0	-3.34	-2.92	0.42
187	6431	2	-3.31	-3.09	0.22
144	6399	2	-3.24	-2.96	0.28
150	6359	0	-3.33	-2.97	0.37
24	6293	2	-3.29	-3.06	0.23
175	6292	2	-3.39	-3.10	0.29
163	6266	2	-3.17	-3.00	0.17
305	6266	0	-3.14	-2.86	0.28
280	6223	2	-3.32	-3.15	0.17
128	6205	2	-3.15	-2.95	0.19
192	6182	0	-3.21	-2.89	0.33
139	6170	0	-3.33	-2.68	0.66
25	6127	0	-3.21	-2.76	0.45

Continued on next page

Supplementary Table 38: Energetic and electronic properties for $[Ni_7Ga_6](Cp^*)_6$ complexes obtained with PBE+TS/light-tier1 level and light SCF parameters: configuration number (i), relative total energy (ΔE_{tot}), total magnetic moment (m_{tot}), HOMO energy (ε_H), LUMO energy (ε_L), and LUMO-HOMO energy gap (E_g).

i	ΔE_{tot} (meV)	m_{tot} (μ_B)	ε_H (eV)	ε_L (eV)	E_g (eV)
301	6123	0	-3.10	-2.80	0.30
272	6119	2	-3.11	-2.86	0.26
234	6112	2	-3.27	-3.02	0.25
209	6095	2	-3.26	-3.02	0.24
18	6086	2	-3.23	-3.12	0.11
242	6070	0	-3.40	-2.70	0.71
159	6043	2	-3.19	-2.93	0.27
86	6002	0	-3.39	-3.11	0.27
186	5995	2	-2.92	-2.68	0.24
231	5961	0	-3.15	-2.79	0.36
165	5917	2	-3.23	-3.09	0.14
297	5898	0	-3.42	-2.98	0.44
122	5860	2	-3.33	-2.96	0.37
199	5780	2	-3.31	-3.15	0.16
41	5776	2	-3.09	-2.84	0.25
17	5760	2	-3.10	-2.88	0.22
85	5750	2	-3.39	-3.18	0.21
100	5744	0	-3.20	-2.68	0.52
153	5713	2	-3.20	-3.01	0.19
135	5710	0	-3.19	-2.73	0.46
241	5704	2	-3.01	-2.86	0.15
185	5704	2	-3.18	-2.92	0.27

Continued on next page

Supplementary Table 38: Energetic and electronic properties for $[Ni_7Ga_6](Cp^*)_6$ complexes obtained with PBE+TS/light-tier1 level and light SCF parameters: configuration number (i), relative total energy (ΔE_{tot}), total magnetic moment (m_{tot}), HOMO energy (ε_H), LUMO energy (ε_L), and LUMO-HOMO energy gap (E_g).

i	ΔE_{tot} (meV)	m_{tot} (μ_B)	ε_H (eV)	ε_L (eV)	E_g (eV)
244	5677	2	-3.23	-3.08	0.14
281	5654	2	-3.27	-3.07	0.20
61	5645	0	-3.36	-3.09	0.26
284	5625	0	-3.30	-2.75	0.56
309	5624	2	-3.25	-2.98	0.27
93	5608	2	-3.30	-3.16	0.14
253	5594	0	-3.22	-2.55	0.66
288	5591	0	-3.40	-2.72	0.68
271	5575	2	-3.21	-3.00	0.21
239	5566	2	-3.18	-2.86	0.32
42	5550	2	-3.17	-2.84	0.33
101	5532	0	-3.16	-2.87	0.29
63	5444	0	-3.02	-2.66	0.36
240	5442	0	-3.37	-3.07	0.30
38	5399	2	-3.25	-2.99	0.26
249	5305	4	-3.22	-3.07	0.15
169	5289	0	-3.32	-2.84	0.49
53	5273	0	-3.14	-2.72	0.42
102	5264	0	-3.24	-2.99	0.25
237	5255	2	-3.13	-2.95	0.18
12	5253	2	-3.27	-3.08	0.19
252	5250	0	-3.12	-2.86	0.27

Continued on next page

Supplementary Table 38: Energetic and electronic properties for $[Ni_7Ga_6](Cp^*)_6$ complexes obtained with PBE+TS/light-tier1 level and light SCF parameters: configuration number (i), relative total energy (ΔE_{tot}), total magnetic moment (m_{tot}), HOMO energy (ε_H), LUMO energy (ε_L), and LUMO-HOMO energy gap (E_g).

i	ΔE_{tot}	m_{tot}	ε_H	ε_L	E_g
	(meV)	(μ_B)	(eV)	(eV)	(eV)
226	5236	2	-3.07	-2.79	0.28
121	5211	2	-3.36	-3.18	0.18
217	5194	2	-3.17	-2.95	0.23
149	5189	2	-3.18	-3.07	0.11
204	5185	2	-3.30	-3.09	0.21
299	5183	2	-3.31	-3.16	0.15
183	5157	2	-3.42	-3.13	0.28
83	5150	2	-3.20	-3.02	0.17
191	5131	0	-3.29	-3.05	0.24
58	5128	2	-3.26	-2.97	0.29
134	5124	0	-3.33	-2.86	0.48
221	5101	0	-3.09	-2.68	0.42
224	5083	2	-3.22	-3.00	0.22
104	5077	0	-3.09	-2.86	0.23
76	5066	2	-3.10	-2.99	0.11
14	5065	2	-3.29	-3.03	0.25
65	5053	2	-3.22	-3.07	0.15
263	5048	2	-3.21	-3.02	0.19
219	5005	2	-3.26	-3.02	0.23
256	4963	2	-3.38	-3.19	0.19
72	4949	2	-3.16	-2.85	0.31
225	4937	2	-3.14	-2.92	0.21

Continued on next page

Supplementary Table 38: Energetic and electronic properties for $[Ni_7Ga_6](Cp^*)_6$ complexes obtained with PBE+TS/light-tier1 level and light SCF parameters: configuration number (i), relative total energy (ΔE_{tot}), total magnetic moment (m_{tot}), HOMO energy (ε_H), LUMO energy (ε_L), and LUMO-HOMO energy gap (E_g).

i	ΔE_{tot} (meV)	m_{tot} (μ_B)	ε_H (eV)	ε_L (eV)	E_g (eV)
194	4928	2	-3.12	-2.75	0.36
120	4919	2	-3.21	-2.95	0.26
33	4908	2	-3.01	-2.82	0.19
46	4848	2	-3.09	-2.98	0.12
57	4846	2	-2.97	-2.78	0.19
49	4821	0	-2.99	-2.66	0.33
114	4813	2	-3.08	-2.88	0.20
181	4807	0	-3.18	-2.65	0.54
290	4797	2	-3.22	-3.02	0.21
283	4795	0	-3.26	-2.70	0.56
166	4766	2	-3.11	-2.97	0.14
55	4748	2	-3.16	-2.89	0.28
238	4711	0	-3.02	-2.82	0.20
35	4690	0	-3.28	-2.72	0.55
202	4672	0	-3.31	-2.85	0.46
230	4651	2	-3.34	-3.14	0.20
7	4638	2	-3.10	-2.89	0.22
140	4553	0	-3.12	-2.99	0.13
235	4527	2	-3.37	-3.24	0.14
92	4513	0	-3.11	-2.78	0.33
232	4513	2	-3.24	-3.06	0.18
132	4506	2	-3.34	-3.08	0.26

Continued on next page

Supplementary Table 38: Energetic and electronic properties for $[Ni_7Ga_6](Cp^*)_6$ complexes obtained with PBE+TS/light-tier1 level and light SCF parameters: configuration number (i), relative total energy (ΔE_{tot}), total magnetic moment (m_{tot}), HOMO energy (ε_H), LUMO energy (ε_L), and LUMO-HOMO energy gap (E_g).

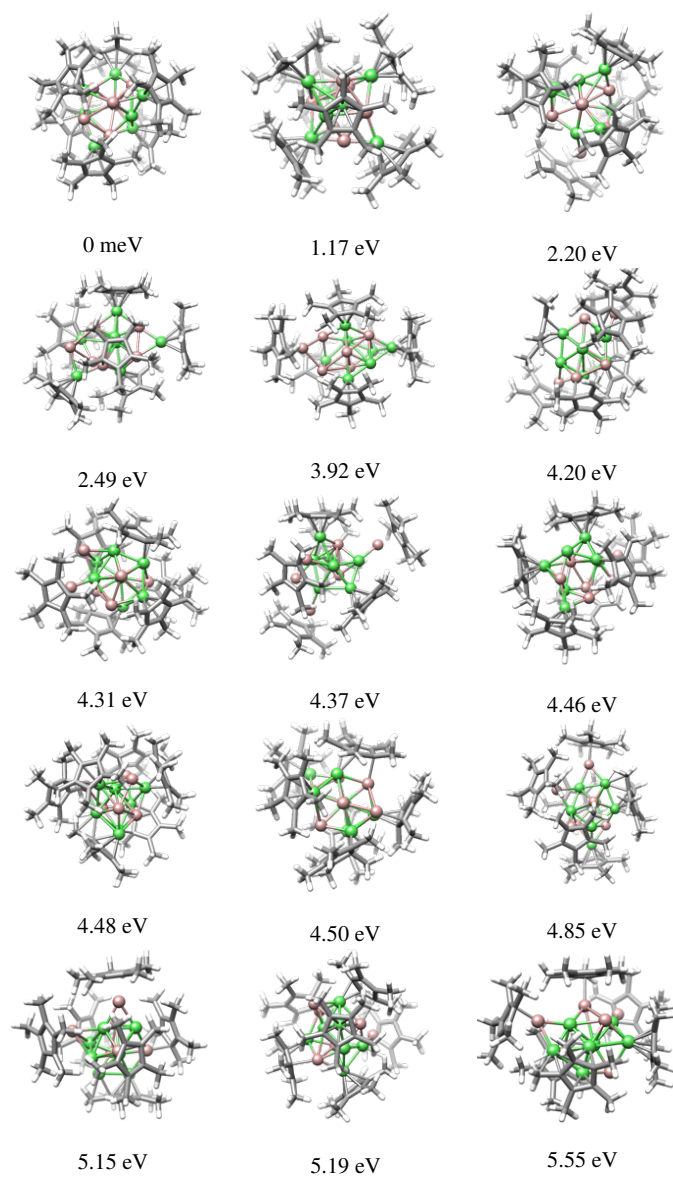
i	ΔE_{tot} (meV)	m_{tot} (μ_B)	ε_H (eV)	ε_L (eV)	E_g (eV)
172	4502	2	-3.15	-3.01	0.14
320	4500	0	-3.35	-2.97	0.38
1	4481	0	-3.28	-2.67	0.61
126	4465	0	-3.14	-2.64	0.50
177	4458	2	-3.09	-2.95	0.14
259	4375	2	-2.99	-2.81	0.18
21	4348	0	-3.28	-3.05	0.23
84	4314	0	-3.27	-2.59	0.68
173	4276	0	-3.29	-3.11	0.18
131	4255	2	-3.12	-2.97	0.15
220	4203	2	-3.29	-3.02	0.27
164	4197	2	-3.01	-2.93	0.08
60	4187	2	-3.33	-3.09	0.23
312	4176	2	-2.98	-2.76	0.21
228	4133	2	-3.13	-2.84	0.29
74	4034	0	-3.17	-2.77	0.40
266	3940	0	-3.02	-2.68	0.34
176	3933	0	-3.35	-2.88	0.47
15	3931	0	-3.22	-2.91	0.31
179	3926	2	-3.11	-2.99	0.12
313	3921	2	-3.21	-2.96	0.25
248	3905	2	-3.11	-2.83	0.29

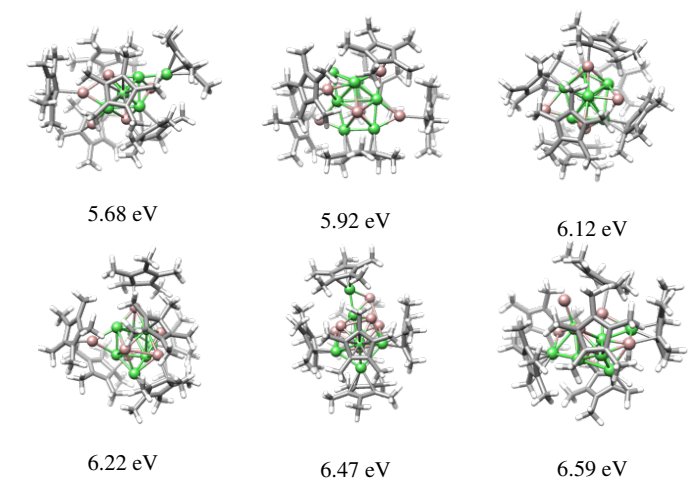
Continued on next page

Supplementary Table 38: Energetic and electronic properties for $[Ni_7Ga_6](Cp^*)_6$ complexes obtained with PBE+TS/light-tier1 level and light SCF parameters: configuration number (i), relative total energy (ΔE_{tot}), total magnetic moment (m_{tot}), HOMO energy (ε_H), LUMO energy (ε_L), and LUMO-HOMO energy gap (E_g).

i	ΔE_{tot} (meV)	m_{tot} (μ_B)	ε_H (eV)	ε_L (eV)	E_g (eV)
180	3852	2	-3.18	-3.04	0.14
141	3819	0	-3.28	-2.84	0.44
82	3778	2	-3.03	-2.95	0.09
282	3740	2	-3.13	-2.84	0.29
145	3596	0	-3.30	-2.72	0.58
254	3359	2	-2.98	-2.88	0.10
88	3079	0	-3.32	-2.69	0.63
316	2807	0	-3.22	-2.68	0.53
193	2727	0	-3.00	-2.70	0.30
315	2494	0	-3.34	-2.79	0.55
302	2394	0	-3.05	-2.82	0.23
307	2369	0	-3.13	-2.58	0.55
318	2196	2	-3.09	-2.79	0.30
306	2101	0	-3.11	-2.62	0.50
5	1173	0	-3.31	-2.68	0.63
304	0	0	-3.26	-2.62	0.64

Supplementary Table 39: Optimized and filtered representative structures of $[Ni_7Ga_6](Cp^*)_6$ complexes obtained with PBE+TS/light-tier1 level and light SCF parameters. The relative total energy (ΔE_{tot}) is depicted above each structure.





References

- 1 Rondina, G. G.; Da Silva, J. L. F. Revised Basin-Hopping Monte Carlo Algorithm for Structure Optimization of Clusters and Nanoparticles. *J. Chem. Inf. Model.* **2013**, *53*, 2282–2298, DOI: 10.1021/ci400224z.
- 2 Cha, S.-H. Comprehensive Survey on Distance/Similarity Measures Between Probability Density Functions. *Int. J. Math. Models Methods Appl. Sci.* **2007**, *1*, 300–307.
- 3 Weßing, J.; Ganeshamoorthy, C.; Kahlal, S.; Marchal, R.; Gemel, C.; Cador, O.; Da Silva, A. C. H.; Da Silva, J. L. F.; Saillard, J.-Y.; Fischer, R. A. The Mackay-type Cluster $[\text{Cu}_{43}\text{Al}_{12}](\text{Cp}^*)_{12}$: Open-shell 67-electron Superatom With Emerging Metal-like Electronic Structure. *Angew. Chem. Int. Ed.* **2018**, *57*, 14630–14634, DOI: 10.1002/anie.201806039.
- 4 Moraes, F. O.; Andriani, K. F.; Silva, J. L. F. D. Investigation of the Stability Mechanisms of Eight-Atom Binary Metal Clusters Using DFT Calculations and k-means Clustering Algorithm. *Makromol. Chem. Phys.* **2021**, *61*, 3411–3420, DOI: 10.1021/acs.jcim.1c00253.
- 5 de Mendonça, J. P. A.; Calderan, F. V.; Lourenço, T. C.; Quiles, M. G.; Da Silva, J.

L. F. Theoretical Framework Based on Molecular Dynamics and Data Mining Analyses for the Study of Potential Energy Surfaces of Finite-Size Particles. *Journal of Chemical Information and Modeling* **2022**, *62*, 5503–5512, DOI: 10.1021/acs.jcim.2c00957, PMID: 36302503.

6 Kresse, G.; Hafner, J. *Ab initio* Molecular Dynamics for Open-Shell Transition Metals. *Phys. Rev. B* **1993**, *48*, 13115–13118, DOI: 10.1103/physrevb.48.13115.

7 Kresse, G.; Furthmüller, J. Efficient Iterative Schemes For *Ab Initio* Total-Energy Calculations Using a Plane-Wave Basis set. *Phys. Rev. B* **1996**, *54*, 11169–11186, DOI: 10.1103/physrevb.54.11169.

8 te Velde, G.; Bickelhaupt, F. M.; Baerends, E. J.; Fonseca Guerra, C.; van Gisbergen, S. J. A.; Snijders, J. G.; Ziegler, T. Chemistry with ADF. *J. Comput. Chem.* **2001**, *22*, 931–967, DOI: 10.1002/jcc.1056.

9 Barca, G. M. J.; Bertoni, C.; Carrington, L.; Datta, D.; De Silva, N.; Deustua, J. E.; Fedorov, D. G.; Gour, J. R.; Gunina, A. O.; Guidez, E.; Harville, T.; Irle, S.; Ivanic, J.; Kowalski, K.; Leang, S. S.; Li, H.; Li, W.; Lutz, J. J.; Magoulas, I.; Mato, J.; Mironov, V.; Nakata, H.; Pham, B. Q.; Piecuch, P.; Poole, D.; Pruitt, S. R.; Rendell, A. P.; Roskop, L. B.; Ruedenberg, K.; Sattasathuchana, T.; Schmidt, M. W.; Shen, J.; Slipchenko, L.; Sosonkina, M.; Sundriyal, V.; Tiwari, A.; Galvez Vallejo, J. L.; Westheimer, B.; Wloch, M.; Xu, P.; Zahariev, F.; Gordon, M. S. Recent developments in the general atomic and molecular electronic structure system. *The Journal of Chemical Physics* **2020**, *152*, 154102, DOI: 10.1063/5.0005188.

10 Frisch, M. J.; Trucks, G. W.; Schlegel, H. B.; Scuseria, G. E.; Robb, M. A.; Cheeseman, J. R.; Scalmani, G.; Barone, V.; Petersson, G. A.; Nakatsuji, H.; Li, X.; Caricato, M.; Marenich, A. V.; Bloino, J.; Janesko, B. G.; Gomperts, R.; Mennucci, B.; Hratchian, H. P.; Ortiz, J. V.; Izmaylov, A. F.; Sonnenberg, J. L.; Williams-Young, D.; Ding, F.; Lipparini, F.; Egidi, F.; Goings, J.; Peng, B.; Petrone, A.; Henderson, T.; Ranasinghe, D.; Zakrzewski, V. G.; Gao, J.; Rega, N.; Zheng, G.; Liang, W.; Hada, M.; Ehara, M.; Toyota, K.;

- Fukuda, R.; Hasegawa, J.; Ishida, M.; Nakajima, T.; Honda, Y.; Kitao, O.; Nakai, H.; Vreven, T.; Throssell, K.; Montgomery, J. A., Jr.; Peralta, J. E.; Ogliaro, F.; Bearpark, M. J.; Heyd, J. J.; Brothers, E. N.; Kudin, K. N.; Staroverov, V. N.; Keith, T. A.; Kobayashi, R.; Normand, J.; Raghavachari, K.; Rendell, A. P.; Burant, J. C.; Iyengar, S. S.; Tomasi, J.; Cossi, M.; Millam, J. M.; Klene, M.; Adamo, C.; Cammi, R.; Ochterski, J. W.; Martin, R. L.; Morokuma, K.; Farkas, O.; Foresman, J. B.; Fox, D. J. Gaussian~16 Revision C.01. 2016; Gaussian Inc. Wallingford CT.
- 11 Blum, V.; Gehrke, R.; Hanke, F.; Havu, P.; Havu, V.; Ren, X.; Reuter, K.; Scheffler, M. *Ab initio Molecular Simulations With Numeric Atom-Centered Orbitals. Comput. Phys. Commun.* **2009**, *180*, 2175–2196, DOI: 10.1016/j.cpc.2009.06.022.
- 12 Havu, V.; Blum, V.; Havu, P.; Scheffler, M. Efficient Integration for all-Electron Electronic Structure Calculation Using Numeric Basis Functions. *J. Comput. Phys.* **2009**, *228*, 8367–8379, DOI: 10.1016/j.jcp.2009.08.008.
- 13 Cai, W.; Feng, Y.; Shao, X.; Pan, Z. Optimization of Lennard-Jones atomic clusters. *Journal of Molecular Structure: THEOCHEM* **2002**, *579*, 229–234, DOI: [https://doi.org/10.1016/S0166-1280\(01\)00730-8](https://doi.org/10.1016/S0166-1280(01)00730-8).
- 14 Jain, A. K.; Murty, M. N.; Flynn, P. J. Data Clustering: A Review. *ACM Comput. Surv.* **1999**, *31*, 264–323, DOI: 10.1145/331499.331504.
- 15 Rupp, M.; Tkatchenko, A.; Müller, K.-R.; von Lilienfeld, O. A. Fast and Accurate Modeling of Molecular Atomization Energies with Machine Learning. *Physical Review Letters* **2012**, *108*, 058301, DOI: 10.1103/PhysRevLett.108.058301.
- 16 Rousseeuw, P. J. Silhouettes: A graphical aid to the interpretation and validation of cluster analysis. *Journal of computational and applied mathematics* **1987**, *20*, 53–65.
- 17 Gonzalez, A. Measurement of Areas on a Sphere Using Fibonacci and Latitude-Longitude Lattices. *Mathematical Geosciences* **2010**, *42*, 49–64, DOI: 10.1007/s11004-009-9257-x.

- 18 Perdew, J. P.; Burke, K.; Ernzerhof, M. Generalized Gradient Approximation Made Simple. *Phys. Rev. Lett.* **1996**, *77*, 3865–3868, DOI: 10.1103/physrevlett.77.3865.
- 19 Tkatchenko, A.; Scheffler, M. Accurate Molecular Van Der Waals Interactions from Ground-State Electron Density and Free-Atom Reference Data. *Phys. Rev. Lett.* **2009**, *102*, 073005, DOI: 10.1103/physrevlett.102.073005.
- 20 Averill, F. W. An Efficient Numerical Multicenter Basis Set for Molecular Orbital Calculations: Application to FeCl₄. *J. Chem. Phys.* **1973**, *59*, 6412–6418, DOI: 10.1063/1.1680020.
- 21 van Lenthe, E.; Snijders, J. G.; Baerends, E. J. The Zero-Order Regular Approximation for Relativistic Effects: The Effect of Spin–Orbit Coupling in Closed Shell Molecules. *J. of Chem. Phys.* **1996**, *105*, 6505–6516, DOI: 10.1063/1.472460.
- 22 Chaves, A. S.; Piotrowski, M. J.; Da Silva, J. L. F. Evolution of the Structural, Energetic, and Electronic properties of the 3d, 4d, and 5d Transition-Metal Clusters (30 TM_n Systems for n = 2 – 15): A Density Functional Theory Investigation. *Phys. Chem. Chem. Phys.* **2017**, *19*, 15484–15502, DOI: 10.1039/c7cp02240a.

7.5 Supporting Information for Study V

SUPPORTING INFORMATION

Cuprophilic Interactions in Polymeric $[\text{Cu}_{10}\text{O}_2(\text{Mes})_6]_n$

Raphael Bühler,^{a,b} Robert M. Wolf,^{a,b} Christian Gemel,^{a,b} Johannes Stephan,^{a,b} Simon N. Deger,^{a,b} Samia Kahla,^c Roland A. Fischer^{*a,b} and Jean-Yves Saillard^{*c}

*Email: jean-yves.saillard@univ-rennes1.fr

*Email: roland.fischer@tum.de

- a) Technical University of Munich, TUM School of Natural Sciences, Department of Chemistry,
Chair of Inorganic and Metal-Organic Chemistry, Lichtenbergstraße 4, 85748 Garching,
Germany
- b) Catalysis Research Centre, Technical University of Munich, Ernst-Otto-Fischer Straße 1, 85748
Garching, Germany
- c) Univ Rennes, CNRS, ISCR-UMR 6226, 35000 Rennes, France

Table of Content

Analytical Methods.....	3
NMR.....	4
ATR-IR.....	5
UV/Vis.....	5
Powder XRD.....	6
LIFDI-MS	7
Luminescence.....	11
Single Crystal X-Ray Diffraction	12
DFT	14
References.....	15

Analytical Methods

NMR spectra were recorded on a *Bruker AVIII 400 US* spectrometer (¹H, 400 MHz) in benzene-d₆ or toluene-d₈. Chemical shifts (in δ) are described in ppm relative to tetramethylsilane (TMS) and referenced to the solvent resonances as internal standards. Solid-state magic angle spinning (MAS) NMR spectroscopic measurements were performed at room temperature in 4 mm ZrO₂ rotors (rotational frequency 11 kHz) on a *Bruker Avance 300* spectrometer whereat spectra were referenced using the external standard adamantane (¹H: 2.00 ppm, ¹³C: 29.47 ppm)

Liquid Injection Field Desorption Ionization Mass Spectrometry (LIFDI-MS) was measured directly from an inert atmosphere glovebox with a *Thermo Fisher Scientific Exactive Plus Orbitrap* (mass accuracy 3 ppm; external calibration) equipped with an ion source from *Linden CMS* and evaluated using the *FreeStyle 1.3* program from *ThermoFisher Scientific*.

The FT-IR spectra were taken on an *ALPHA-T FT-IR* spectrometer from *Bruker* with an ATR setup operated in a glovebox under argon atmosphere with 128 scans per measurement and a resolution of 4 cm⁻¹. The spectra were evaluated using the software *OPUS*.

Solution UV/Vis spectra were measured in toluene under an inert atmosphere in quartz cuvettes with an *Agilent Carry 60* spectrometer. The solid-state UV-Vis spectra were taken on a *Shimadzu UV-VIS-NIR UV-3600i Plus* spectrophotometer with an Integrating-Sphere unit. The samples were placed between two quartz slides and the reflection was measured.

Solid-state fluorescence measurements were performed with the sample placed between two quartz slides on a *Edinburgh Instruments F55* spectrofluorometer equipped with a xenon lamp. Quantum yields were measured on a *Hamamatsu Quantaurus-QY* spectrometer.

PXRD measurements of pestled samples were performed using the transmission geometry of a *STOE STADI P* diffractometer equipped with a Ge(111) monochromator and a *MYTHEN2R 1K* detector (*DECTRIS*). X-ray Mo K α radiation ($\lambda=0.7093\text{ \AA}$) operated at 50 kV (voltage) and 40 mA (intensity) was used for the measurements. All checks were carried out utilizing a flatbed sample carrier and a measurement range from 2.0° to 39.5° (2θ). For this purpose, the sample, was fixed between two adhesive strips (*Scotch® Magic™ Tape 810, 3M*) and placed in the centre of the carrier.

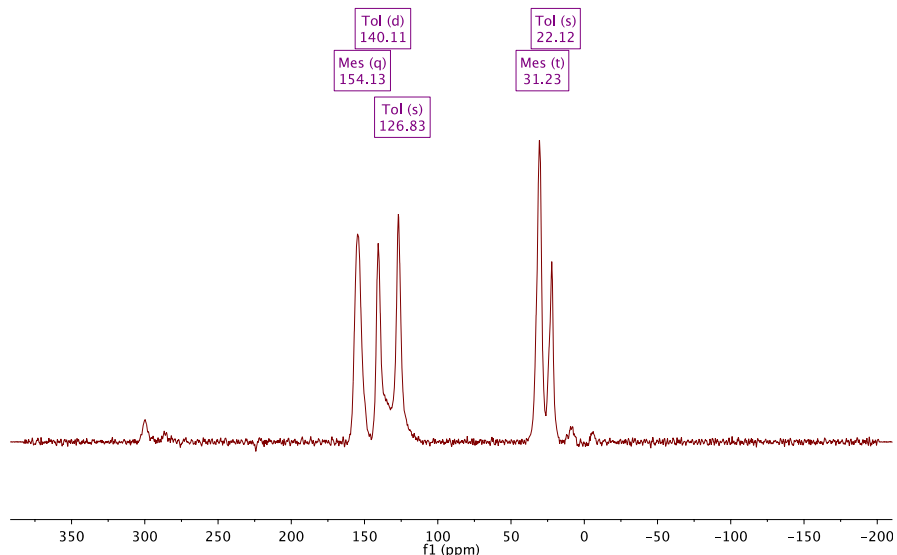
NMR

Figure S1: ¹³C MAS NMR spectrum of **1** at room temperature.

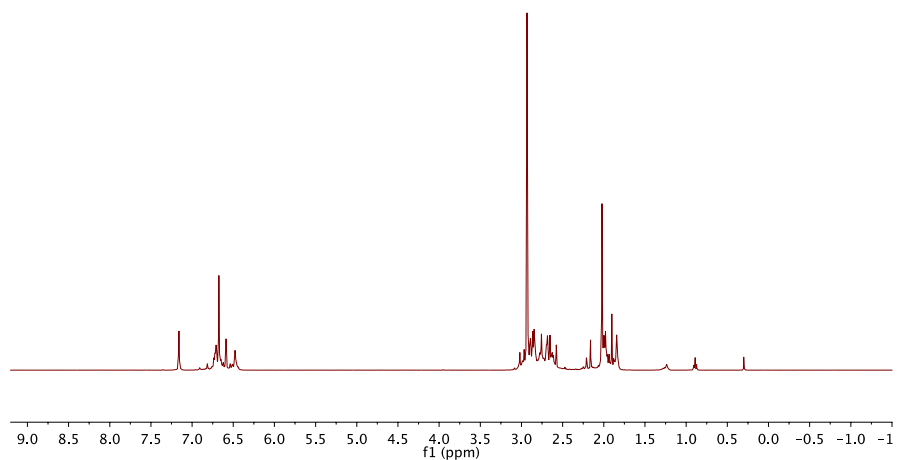


Figure S2: ¹H NMR spectrum of **1** in benzene-*d*₆ at room temperature.

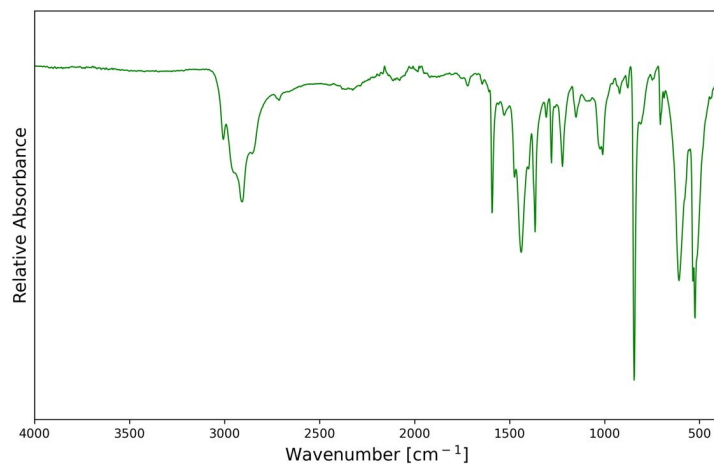
ATR-IR

Figure S3: ATR-IR spectrum of **1**.

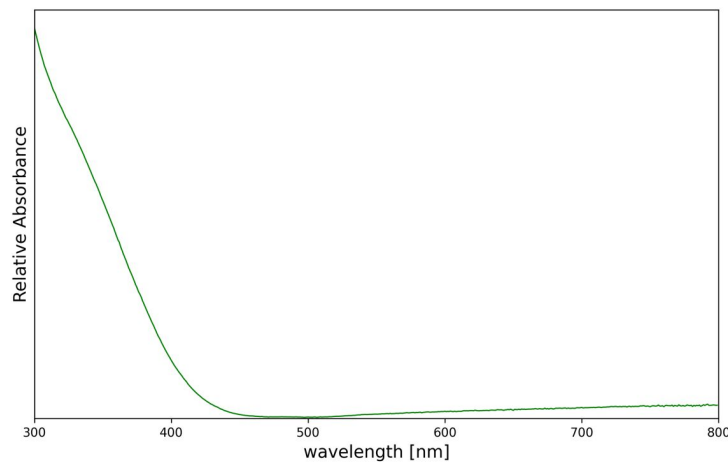
UV/Vis

Figure 4: UV/Vis spectrum of **1** as solution in toluene.

Powder XRD

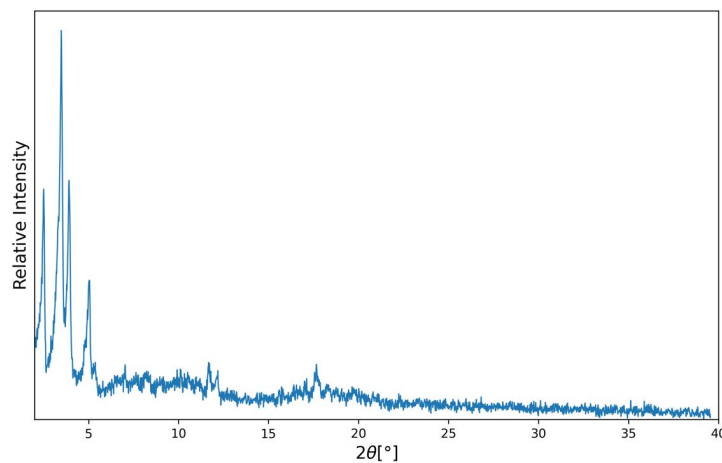


Figure S5: Powder XRD of **1**.

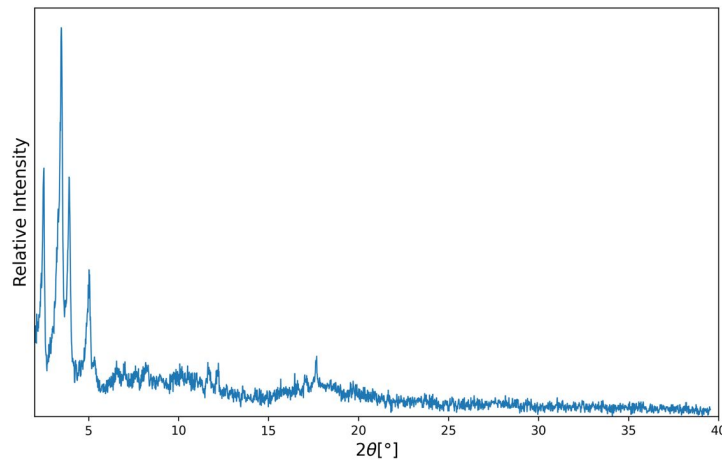


Figure S6: Powder XRD of **1** after recrystallisation.

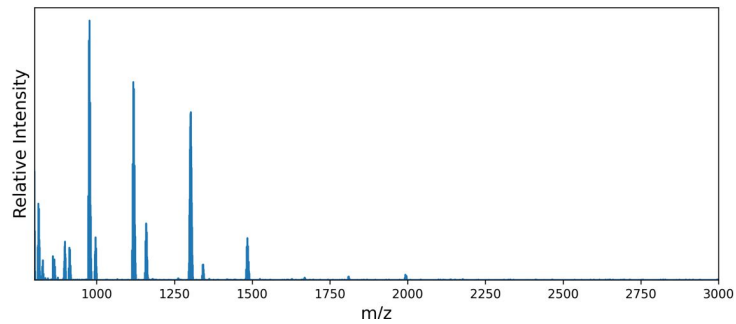
LIFDI-MS

Figure S7: LIFDI mass spectrum of **1** at CE = 10.

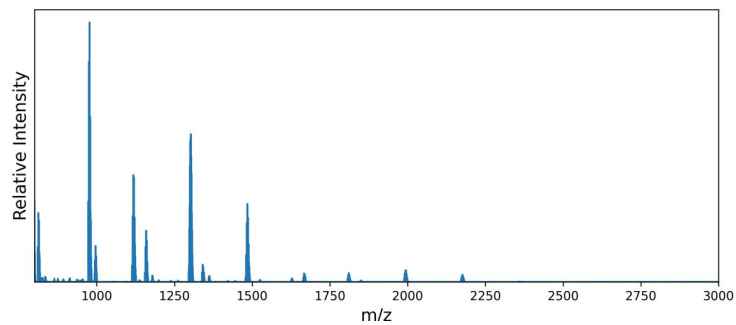


Figure S8: LIFDI mass spectrum of **1** at CE = 20.

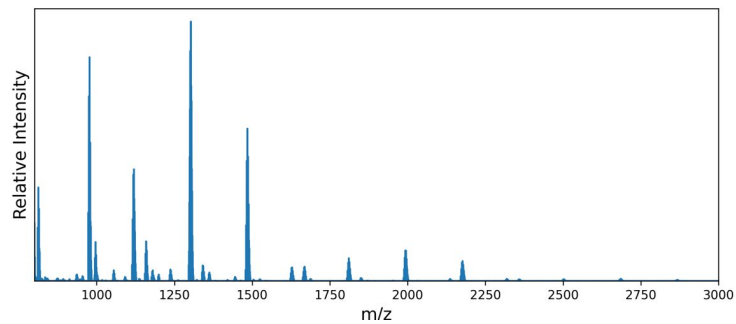


Figure S9: LIFDI mass spectrum of **1** at CE = 40.

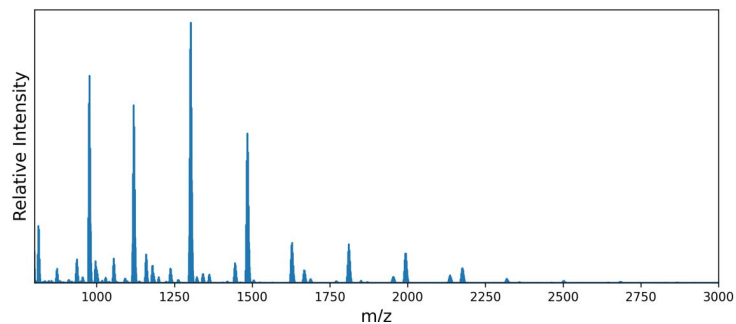


Figure S10: LIFDI mass spectrum of **1** at CE = 80.

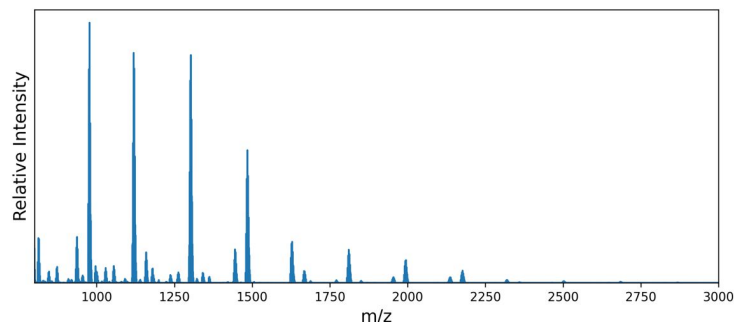


Figure S11: LIFDI mass spectrum of **1** at CE = 120.

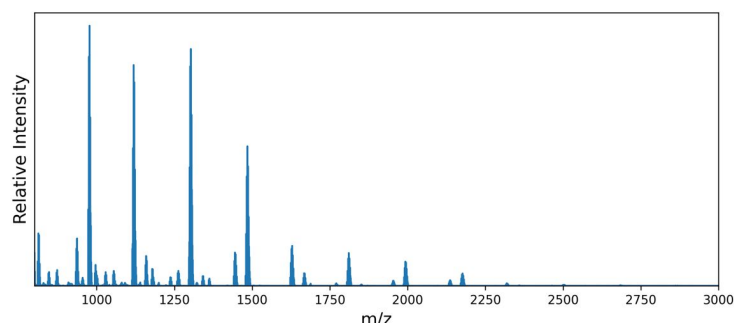


Figure S12: LIFDI mass spectrum of **1** at CE = 160.

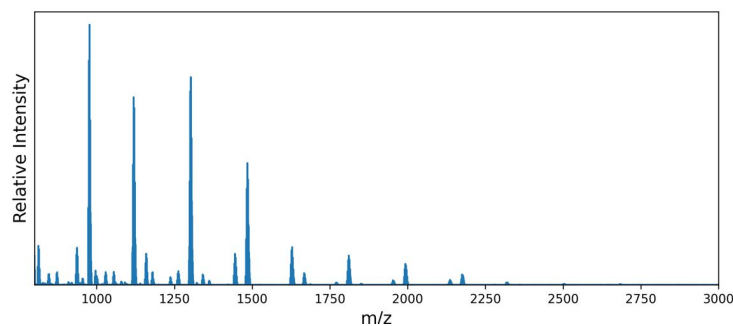


Figure S13: LIFDI mass spectrum of **1** at CE = 200.

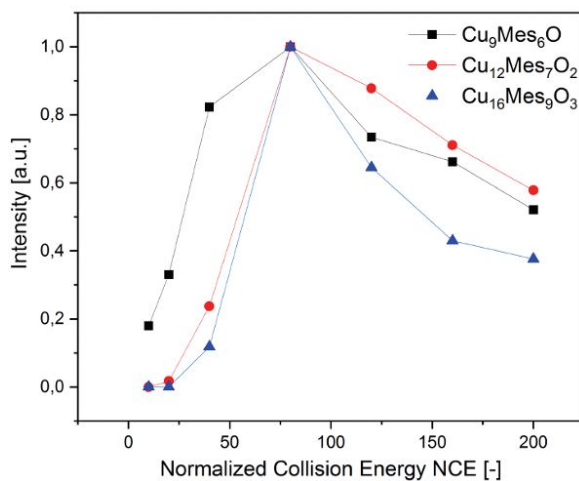


Figure S14: Relative intensities at different collision energies for selected ions identified from the LIFDI mass spectra of **1**.

Table S1: List of the main signal patterns in the LIFDI-MS of $[Cu_{10}O_2Mes_6]_n$. The most dominant signal pattern of each n is colorized.

$Cu_xMes_{x-(2n+1)}O_n$	Composition	m/z
$n = 0$	Cu_5Mes_4	792.99
	Cu_6Mes_5	977.00
	Cu_7Mes_6	1159.02
	Cu_8Mes_7	1341.04
	Cu_9Mes_8	1525.05
	$Cu_8Mes_5O(-H)$	1117.85
$n = 1$	$Cu_9Mes_6O(-H)$	1301.87
	$Cu_{10}Mes_7O$	1484.88
	$Cu_{11}Mes_8O$	1668.92
	$Cu_{11}Mes_6O_2$	1445.74
$n = 2$	$Cu_{12}Mes_7O_2$	1628.72
	$Cu_{13}Mes_8O_2$	1810.77
	$Cu_{14}Mes_9O_2$	1992.80
	$Cu_{15}Mes_{10}O_2$	2176.77
	$Cu_{16}Mes_{11}O_2$	2358.78
	$Cu_{15}Mes_8O_3$	1954.60
$n = 3$	$Cu_{16}Mes_9O_3$	2136.61
	$Cu_{17}Mes_{10}O_3$	2318.62
	$Cu_{18}Mes_{11}O_3$	2502.63
	$Cu_{19}Mes_{12}O_3$	2684.66
	$Cu_{20}Mes_{13}O_3$	2864.67

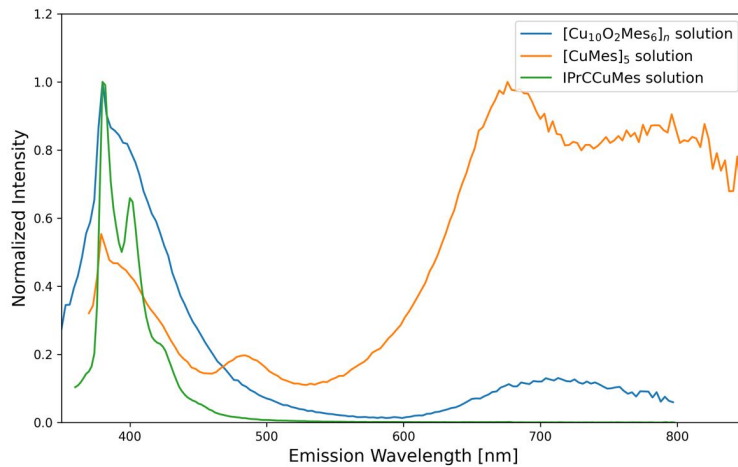
Luminescence

Figure S15: Emission spectra of solutions of **1**, $[\text{CuMes}]_5$ and IPrCuMes.

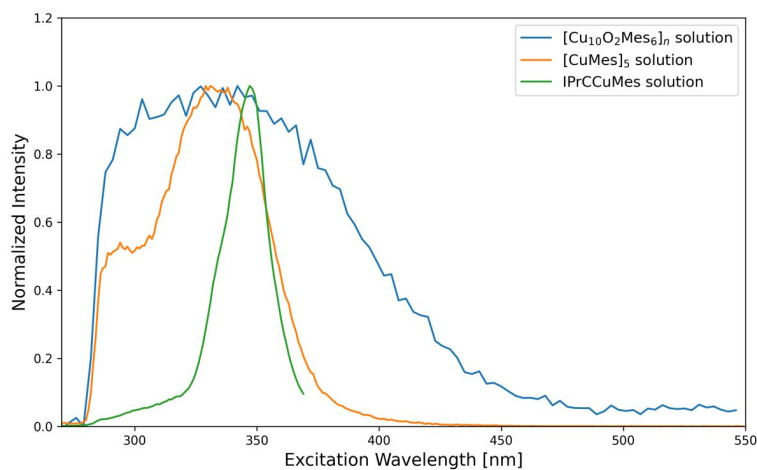


Figure S16: Excitation spectra of solutions of **1**, $[\text{CuMes}]_5$ and IPrCuMes.

Single Crystal X-Ray Diffraction

SC-XRD data were collected on a Bruker D8-Venture single crystal x-ray diffractometer equipped with a TXS rotating anode with MoK_α radiation ($\lambda = 0.71073 \text{ \AA}$), a Bruker Photon CMOS detector and a Helios, using the Bruker APEX4 software package.^[C1] Single crystals were coated with perfluorinated ether, fixed on top of a micro sampler and frozen under a stream of cold nitrogen. A matrix scan was used to determine the initial lattice parameters. All data were integrated with the Bruker SAINT V8.40B software package using a narrow-frame algorithm and the reflections were corrected for Lorentz and polarisation effects, scan speed, and background.^[C2] Data were corrected for absorption effects including odd and even ordered spherical harmonics by the multi-scan method (SADABS 2016/2).^[C3] Space group assignment was based upon systematic absences, E statistics, and successful refinement of the structure.

The structures were solved by direct methods using SHELXT and refined by full-matrix least-squares methods against F^2 by minimizing $\Sigma w(F_o^2 - F_c^2)^2$ using SHELXL in conjunction with SHELXLE.^[C4-C6] All non-hydrogen atoms were refined with anisotropic displacement parameters. Hydrogen atoms were refined isotropically on calculated positions using a riding model with their U_{iso} values constrained to 1.5 times the U_{eq} of their pivot atoms for terminal sp³ carbon atoms and a C–H distance of 0.98 Å. Non-methyl hydrogen atoms were refined using a riding model with methylene, aromatic, and other C–H distances of 0.99 Å, 0.95 Å, and 1.00 Å, respectively, and U_{iso} values constrained to 1.2 times the U_{eq} of their pivot atoms. A split layer refinement was used for disordered groups and additional restraints on distances, angles and anisotropic displacement parameters were employed to ensure convergence within chemically reasonable limits, if necessary. Disordered mesityl ligands were treated using the DSR plugin within SHELXLE.^[C7] The unit cell contains 0.7 disordered molecules of toluene which were treated as a diffuse contribution to the overall scattering without specific atom positions using the PLATON/SQUEEZE procedure.^[C8]

Neutral atom scattering factors for all atoms and anomalous dispersion corrections for the non-hydrogen atoms were taken from International Tables for Crystallography.^[C9] Crystallographic data for the structures reported in this paper have been deposited with the Cambridge Crystallographic Data Centre.^[C10] Supplementary crystallographic data reported in this paper have been deposited with the Cambridge Crystallographic Data Centre (CCDC 2360768) and can be obtained free of charge from The Cambridge Crystallographic Data Centre via www.ccdc.cam.ac.uk/structures. Images of the crystal structures were generated with *Mercury* and *Povray*.^[C11]

Table S2: Crystallographic and structure refinement data for $[Cu_{10}O_2Mes_6]_n$.

Deposition number (CCDC)	2360768
Chemical formula	$C_{54}H_{66}Cu_{10}O_2$
Formula weight	1382.46
Temperature	100(2) K
Wavelength	0.71073 Å
Crystal size	0.028 x 0.093 x 0.162 mm
Crystal system	monoclinic
Space group	C 1 2/c 1
Unit cell dimensions	a = 16.451(5) Å b = 33.723(10) Å c = 12.890(4) Å
Volume	5803.(3) Å ³
Z	4
Density (calculated)	1.582 g/cm ³
Absorption coefficient	3.620 mm ⁻¹
F(000)	2784
Diffractometer	Bruker D8 Venture
Radiation source	TXS rotating anode, Mo
Theta range for data collection	2.29 to 26.37°
Index ranges	-20<=h<=20, -42<=k<=42, -16<=l<=16
Reflections collected	121416
Independent reflections	5938 [R(int) = 0.0565]
Coverage of independent reflections	99.9%
Absorption correction	Multi-Scan
Max. and min. transmission	0.7450 and 0.6370
Structure solution technique	direct methods
Structure solution program	XT, VERSION 2018/2
Refinement method	Full-matrix least-squares on F ²
Refinement program	SHELXL-2019/1 (Sheldrick, 2019)
Function minimized	$\Sigma w(F_o^2 - F_c^2)^2$
Data / restraints / parameters	5938 / 798 / 479
Goodness-of-fit on F ²	1.048
Δ/σ_{\max}	0.003
Final R indices	5012 data; $I > 2\sigma(I)$ all data
Weighting scheme	$W = 1/[\Sigma^2(F_o^2) + (0.0409P)^2 + 8.7151P]$ where P = $(F_o^2 + 2F_c^2)/3$
Largest diff. peak and hole	0.637 and -0.319 eÅ ⁻³
R.M.S. deviation from mean	0.072 eÅ ⁻³
	$R_1 = 0.0258,$ $wR_2 = 0.0674$ $R_1 = 0.0355,$ $wR_2 = 0.0725$

DFT

Table S3. DFT-optimized Cu...Cu distances and corresponding Wiberg bond indices in the $Cu_n(\mu\text{-Mes})_n$ ($n = 4, 5$) and $Cu_n(\mu\text{-H})_n$ ($n = 2\text{-}5$) models.

	Cu...Cu optimized distance (av.)	Corresponding Wiberg bond index (av.)
$Cu_4(\mu\text{-Mes})_4$	2.404	0.085
$Cu_5(\mu\text{-Mes})_5$	2.436	0.093
$Cu_2(\mu\text{-H})_2$	2.157	0.171
$Cu_3(\mu\text{-H})_3$	2.357	0.083
$Cu_4(\mu\text{-H})_4$	2.392	0.114
$Cu_5(\mu\text{-H})_5$	2.438	0.108

Table S4. Copper NAO and QTAIM charge distribution in the $Cu_n(\mu\text{-Mes})_n$ ($n = 4, 5$) and $Cu_n(\mu\text{-H})_n$ ($n = 2\text{-}5$) models.

	NAO charge	NAO configuration	QTAIM charge
$Cu_4(\mu\text{-Mes})_4$	0.62	$4s^{0.53}3d^{9.83}4p^{0.01}$	0.37
$Cu_5(\mu\text{-Mes})_5$	0.63	$4s^{0.54}3d^{9.82}4p^{0.01}$	0.37
$Cu_2(\mu\text{-H})_2$	0.67	$4s^{0.35}3d^{9.96}4p^{0.02}$	0.40
$Cu_3(\mu\text{-H})_3$	0.53	$4s^{0.52}3d^{9.93}4p^{0.02}$	0.37
$Cu_4(\mu\text{-H})_4$	0.48	$4s^{0.59}3d^{9.91}4p^{0.01}$	0.37
$Cu_5(\mu\text{-H})_5$	0.47	$4s^{0.62}3d^{9.90}4p^{0.01}$	0.35

References

- [C1] *APEX4 Suite of Crystallographic Software, Version 2021-10.0*, Bruker AXS Inc., Madison, Wisconsin, USA, **2021**.
- [C2] Bruker, *SINT, V8.40B*, Bruker AXS Inc., Madison, Wisconsin, USA.
- [C3] L. Krause, R. Herbst-Irmer, G. M. Sheldrick, D. Stalke, *J. Appl. Cryst.* **2015**, *48*, 3–10.
- [C4] G. M. Sheldrick, *Acta Cryst.* **2015**, *A71*, 3–8.
- [C5] G. M. Sheldrick, *Acta Cryst.* **2015**, *C71*, 3–8.
- [C6] C. B. Huebschle, G. M. Sheldrick, B. Dittrich, *J. Appl. Cryst.* **2011**, *44*, 1281–1284.
- [C7] D. Kratzert, J. J. Holstein, I. Krossing, *J. Appl. Cryst.*, **2015**, *48*, 933–938.
- [C8] Ed. E. Prince, *International Tables for Crystallography Volume C, Mathematical, Physical and Chemical Tables*, International Union of Crystallography, Chester, England, **2006**, 500–502; 219–222; 193–199.
- [C9] C. R. Groom, I. J. Bruno, M. P. Lightfoot, S. C. Ward, *Acta Cryst.* **2016**, *B72*, 171–179.
- [C10] A. L. Spek, *Acta Cryst.* **2015**, *C71*, 9–18.
- [C11] C. F. Macrae, I. J. Bruno, J.A. Chisholm et al., *J. Appl. Cryst.*, **2008**, *41* (2), 466–470.

8 Appendix

8.1 Complete List of Publications

8.1.1 First Author Publications

Peer Reviewed Journal Publications:

- (1) C–H and Si–H Activation Reactions at Ru/Ga Complexes: A Combined Experimental and Theoretical Case Study on the Ru–Ga Bond
M. Muhr[‡], R. Bühler[‡], H. Liang, J. Gilch, C. Jandl, S., Kahlal, J.-Y. Saillard, C. Gemel, R. A. Fischer, *Chem. Eur. J.* **2022**, 28, e202200887.
- (2) Photochemically Generated Reactive Sites at Ruthenium/Gallium Complexes: Catalysis vs. Cluster Growth
R. Bühler[‡], M. Muhr[‡], J. Stephan, R. M. Wolf, M. Schütz, C. Gemel , R. A. Fischer, *Dalton Trans.* **2023**, 52, 10905-10910.
- (3) Homoleptic Hexa- and Penta-Coordinated Gallium(I) Amide Complexes of Ruthenium and Molybdenum
R. Bühler[‡], R. J. J. Weininger[‡], J. Stephan, M. Muhr, B. M.-T. Bock, C. Gemel, R. A. Fischer, *Dalton Trans.* **2024**, 53, 17162-17168.
- (4) Cuprophilic Interaction in Polymeric $[Cu_{10}O_2(Mes)_6]_n$
R. Bühler, R. M. Wolf, C. Gemel, J. Stephan, S. N. Deger, S. Kahlal, R. A. Fischer, J.-Y. Saillard, *Inorg. Chem.* **2024**, 63, 17617-17625.
- (5) A living library concept to capture the dynamics and reactivity of mixed-metal clusters for catalysis
R. Bühler[‡], M. Schütz[‡], K. F. Andriani, J.-P. A. de Mendonça, V. K. Ocampo-Restrepo, C. Gemel, J. L. F. Da Silva, R. A. Fischer, *Nat. Chem.*, accepted.

[‡] Equal contribution

8.1.2 Contributions to other Publications

Peer Reviewed Journal Publications:

- (1) Enabling LIFDI-MS measurements of highly air sensitive organometallic compounds: a combined MS/glovebox technique
M. Muhr, P. Heiß, M. Schütz, R. Bühler, C. Gemel, M.H. Linden, H.B. Linden, R.A. Fischer, *Dalton Trans.* **2021**, 50, 9031-9036.
- (2) Stereo-controlled cyclopropanation catalysis within the confined pores of porphyrin MOFs
K. Hemmer, R. Bühler, M. Elsner, M. Cokoja, R. A. Fischer, *Catal. Sci. Technol.* **2023**, 13, 3304-3312.
- (3) Catalytic Alkyne Semihydrogenation with Polyhydride Ni/Ga Clusters
M. Muhr, H. Liang, L. Allmendinger, R. Bühler, F. E. Napoli, D. Ukaj, M. Cokoja, C. Jandl, S. Kahlal, J.-Y. Saillard, C. Gemel, R. A. Fischer, *Angew. Chem. Int. Ed.* **2023**, 62, e202308790.
- (4) Benzene-1,4-Di(dithiocarboxylate) Linker-Based Coordination Polymers of Mn²⁺, Zn²⁺, and Mixed-Valence Fe^{2+/3+}
M. Aust, M.I. Schönherr, D.P. Halter, L. Schröck, T. Pickl, S.N. Deger, M.Z. Hussain, A. Jentys, R. Bühler, Z. Zhang, K. Meyer, M. Kuhl, J. Eichhorn, D.D. Medina, A. Pöthig, R.A. Fischer, *Inorg. Chem.* **2024**, 63, 1, 129-140.
- (5) All-Hydrocarbon Ligated Superatomic Gold/Aluminium Clusters
I. Antsiburov, M. Schütz, R. Bühler, M. Muhr, J. Stephan, C. Gemel, W. Klein, S. Kahlal, J.-Y. Saillard, R. A. Fischer, *Inorg. Chem.* **2024**, 63, 8, 3749-3756

8.1.3 Conference Contributions

- (1) **Leopoldina Conference: Exploratory Photochemistry: Light Creates Structure**
Poster Presentation: Photochemically Induced Reactive Sites at Intermetalloid Clusters: Catalysis vs. Cluster Growth – *October 2021*
- (2) **44th International Conference on Coordination Chemistry**
Oral Presentation: Living Libraries of Metal Clusters: a Combined Experimental and Theoretical Methodology – *September 2022*
- (3) **55th Annual Conference of the DGMS**
Workshop Co-Organization: Field Ionization, Field Desorption and Liquid Injection Field Desorption Ionization: Fundamentals, Techniques, Applications and Prospects – *March 2024*
- (4) **55th Annual Conference of the DGMS**
Poster Presentation: Living Libraries of Metal Clusters: Exploring Chemical Complexity via LIFDI-MS – *March 2024*
- (5) **45th International Conference on Coordination Chemistry**
Poster Presentation: Living Libraries of Metal Clusters – *July 2024*

8.2 Reprint Permissions

Friday, August 23, 2024 at 14:30:20 Central European Summer Time

Betreff: RE: THESIS/DISSERTATION USE – SCIENCE FIGURE – STUDT ET AL 2008 DOI: 10.1126/science.1156660
Datum: Mittwoch, 21. August 2024 um 21:03:38 Mitteleuropäische Sommerzeit
Von: Dana James
An: Raphael Bühler
CC: permissions
Anlagen: image001.png

AAAS MATERIAL:

Figure 4 from Studt et al., *SCIENCE*, 6 Jun 2008
Vol 320, Issue 5881, pp. 1320-1322, DOI: 10.1126/science.1156660

YOUR RE-USE: THESIS/DISSERTATION

Title: Metal-Substrate Interactions at Ligated Heterometallic Complexes and Clusters
Publication date: November 2024

Dear Raphael:

Thank you very much for your interest in the AAAS material identified in your request.

We are pleased to have you include this material in your thesis or dissertation subject to the following guidelines. These guidelines also appear on our website:

<https://www.science.org/content/page/reprints-and-permissions> under the heading ‘Using AAAS material in a thesis or dissertation’.

REPRODUCING AAAS MATERIAL IN YOUR THESIS OR DISSERTATION

AAAS permits the use of content published in its journals but only provided the following criteria are met:

1. If you are using figures/tables, permission is granted for use in print and electronic versions of your dissertation or thesis.
2. A full-text article may be used only in print versions of a dissertation or thesis. AAAS does not permit the reproduction of full-text articles in electronic versions of theses or dissertations.
3. The following credit line must be printed along with the AAAS material: “From [Insert Full Reference Citation]/ Reprinted with permission from AAAS”.
4. All required credit lines and notices must be visible any time a user accesses any part of the AAAS material and must appear on any printed copies that an authorized user might make.
5. The AAAS material may not be modified or altered except that figures and tables may be modified with permission from the author. Author permission for any such changes must be secured prior to your use.
6. AAAS must publish the full paper prior to your use of any of its text or figures.
7. If the AAAS material covered by this permission was published in *Science* during the years 1974-1994, you must also obtain permission from the author, who may grant or withhold permission, and who may or may not charge a fee if permission is granted. See original article for author’s address. This condition does not apply to the news articles published in *Science*.
8. Permission covers the distribution of your dissertation or thesis on demand by a third-party distributor (e.g. ProQuest/UMI), provided the AAAS material covered by this permission remains in situ and is not distributed by that third party outside of the context of your thesis/dissertation.
9. Permission does not apply to figures/photos/artwork or any other content or material included in your work that are credited to non-AAAS sources. If the requested material is sourced to or

1 of 3

references non-AAAS sources, you must obtain authorization from that source as well before using that material. You agree to hold harmless and indemnify AAAS against any claims arising from your use of any content in your work that is credited to non-AAAS sources.

10. By using the AAAS Material identified in your request, you agree to abide by all the terms & conditions herein.

11. AAAS makes no representations or warranties as to the accuracy of any information contained in the AAAS material covered by this permission, including any warranties of merchantability or fitness for a particular purpose.

If how you wish to use the content falls outside of these guidelines or if you have any questions, please let me know.

Kind regards,

Dana



Dana James (she/her)

Rights and Licensing Coordinator, Office of Publishing

American Association for the Advancement of Science

1200 New York Avenue, NW | Washington, DC 20005

| djames@aaas.org | www.aaas.org | www.science.org


RB ? Q

Mechanistic Insights into an Unprecedented C–C Bond Activation on a Rh/Ga Bimetallic Complex: A Combined Experimental/Computational Approach



Most Trusted. Most Cited. Most Read.

Author: Thomas Cadenbach, Christian Gemel, Rochus Schmid, et al

Publication: Journal of the American Chemical Society

Publisher: American Chemical Society

Date: Dec 1, 2005

Copyright © 2005, American Chemical Society

PERMISSION/LICENSE IS GRANTED FOR YOUR ORDER AT NO CHARGE

This type of permission/license, instead of the standard Terms and Conditions, is sent to you because no fee is being charged for your order. Please note the following:

- Permission is granted for your request in both print and electronic formats, and translations.
- If figures and/or tables were requested, they may be adapted or used in part.
- Please print this page for your records and send a copy of it to your publisher/graduate school.
- Appropriate credit for the requested material should be given as follows: "Reprinted (adapted) with permission from {COMPLETE REFERENCE CITATION}. Copyright {YEAR} American Chemical Society." Insert appropriate information in place of the capitalized words.
- One-time permission is granted only for the use specified in your RightsLink request. No additional uses are granted (such as derivative works or other editions). For any uses, please submit a new request.

If credit is given to another source for the material you requested from RightsLink, permission must be obtained from that source.

BACK

CLOSE WINDOW





RightsLink

**Dehydrogenative Double C–H Bond Activation in a Germylene-Rhodium Complex******Author:** Jesús Campos, Joaquín López-Serrano, María M. Alcaide, et al**Publication:** Chemistry - A European Journal**Publisher:** John Wiley and Sons**Date:** Oct 27, 2021

© 2021 The Authors. Chemistry - A European Journal published by Wiley-VCH GmbH

Open Access Article

This is an open access article distributed under the terms of the [Creative Commons CC BY](#) license, which permits unrestricted use, distribution, and reproduction in any medium, provided the original work is properly cited.

You are not required to obtain permission to reuse this article.

For an understanding of what is meant by the terms of the Creative Commons License, please refer to [Wiley's Open Access Terms and Conditions](#).

Permission is not required for this type of reuse.

Wiley offers a professional reprint service for high quality reproduction of articles from over 1400 scientific and medical journals. Wiley's reprint service offers:

- Peer reviewed research or reviews
- Tailored collections of articles
- A professional high quality finish
- Glossy journal style color covers
- Company or brand customisation
- Language translations
- Prompt turnaround times and delivery directly to your office, warehouse or congress.

Please contact our Reprints department for a quotation. Email corporatesaleseurope@wiley.com or corporatesalesusa@wiley.com or corporatesalesDE@wiley.com.



RightsLink



A Bimetallic Nickel–Gallium Complex Catalyzes CO₂ Hydrogenation via the Intermediacy of an Anionic d¹⁰ Nickel Hydride



Most Trusted. Most Cited. Most Read.

Author: Ryan C. Cammarota, Matthew V. Vollmer, Jing Xie, et al

Publication: Journal of the American Chemical Society

Publisher: American Chemical Society

Date: Oct 1, 2017

Copyright © 2017, American Chemical Society

PERMISSION/LICENSE IS GRANTED FOR YOUR ORDER AT NO CHARGE

This type of permission/license, instead of the standard Terms and Conditions, is sent to you because no fee is being charged for your order. Please note the following:

- Permission is granted for your request in both print and electronic formats, and translations.
- If figures and/or tables were requested, they may be adapted or used in part.
- Please print this page for your records and send a copy of it to your publisher/graduate school.
- Appropriate credit for the requested material should be given as follows: "Reprinted (adapted) with permission from {COMPLETE REFERENCE CITATION}. Copyright {YEAR} American Chemical Society." Insert appropriate information in place of the capitalized words.
- One-time permission is granted only for the use specified in your RightsLink request. No additional uses are granted (such as derivative works or other editions). For any uses, please submit a new request.

If credit is given to another source for the material you requested from RightsLink, permission must be obtained from that source.

BACK

CLOSE WINDOW



Rightslink® by Copyright Clearance Center

20.08.24, 12:37

CCC
RightsLink

SPRINGER NATURE

Advances in Catalysts and Processes for Methanol Synthesis from CO₂
Author: G. Centi, S. Perathoner
Publication: Springer eBook
Publisher: Springer Nature
Date: Jan 1, 2013
Copyright © 2013, Springer-Verlag London

Order Completed

Thank you for your order.

This Agreement between Raphael Bühler ("You") and Springer Nature ("Springer Nature") consists of your license details and the terms and conditions provided by Springer Nature and Copyright Clearance Center.

Your confirmation email will contain your order number for future reference.

License Number	5853010705428	Printable Details	
License date	Aug 20, 2024		
Licensed Content		Order Details	
Licensed Content Publisher	Springer Nature	Type of Use	Thesis/Dissertation
Licensed Content Publication	Springer eBook	Requestor type	academic/university or research institute
Licensed Content Title	Advances in Catalysts and Processes for Methanol Synthesis from CO ₂	Format	print and electronic
Licensed Content Author	G. Centi, S. Perathoner	Portion	figures/tables/illustrations
Licensed Content Date	Jan 1, 2013	Number of figures/tables/illustrations	1
		Will you be translating?	no
		Circulation/distribution	1 - 29
		Author of this Springer Nature content	no
About Your Work		Additional Data	
Title of new work	Metal-Substrate Interactions at Ligated Heterometallic Complexes and Clusters	Portions	Reprint figure 3 of the original work in order to underline the state of the art
Institution name	Technical University of Munich	The Requesting Person / Organization to Appear on the License	Raphael Bühler
Expected presentation date	Nov 2024		

<https://s100.copyright.com/AppDispatchServlet>

Seite 1 von 2

Rightslink® by Copyright Clearance Center

20.08.24, 12:37

Requestor Location		Tax Details
Mr. Raphael Bühler Occamstr. 4		
Requestor Location	München, Bayern 80802 Germany Attn: Mr. Raphael Bühler	
Billing Information		
Billing Type	Invoice Mr. Raphael Bühler Occamstr. 4	
Billing address	München, Germany 80802 Attn: Mr. Raphael Bühler	
Total: 0.00 EUR		
CLOSE WINDOW		ORDER MORE

© 2024 Copyright - All Rights Reserved | [Copyright Clearance Center, Inc.](#) | [Privacy statement](#) | [Data Security and Privacy](#)
| [For California Residents](#) | [Terms and Conditions](#)Comments? We would like to hear from you. E-mail us at
customercare@copyright.com



Friday, August 23, 2024 at 14:33:55 Central European Summer Time

Betreff: RE: THESIS/DISSERTATION USE – SCIENCE FIGURE – BEHRENS ET AL 2012 DOI: 10.1126/science.1219831
Datum: Donnerstag, 22. August 2024 um 02:32:04 Mitteleuropäische Sommerzeit
Von: Dana James
An: Raphael Bühler
CC: permissions
Anlagen: image002.png

AAAS MATERIAL:

Figure 2 from Behrens et al., *SCIENCE*, 19 Apr 2012
Vol 336, Issue 6083, pp. 893-897, DOI: 10.1126/science.1219831

YOUR RE-USE: THESIS/DISSERTATION

Title: Metal-Substrate Interactions at Ligated Heterometallic Complexes and Clusters
Publication date: November 2024

Dear Raphael:

Thank you very much for your interest in the AAAS material identified in your request.

We are pleased to have you include this material in your thesis or dissertation subject to the following guidelines. These guidelines also appear on our website:

<https://www.science.org/content/page/reprints-and-permissions> under the heading ‘Using AAAS material in a thesis or dissertation’.

REPRODUCING AAAS MATERIAL IN YOUR THESIS OR DISSERTATION

AAAS permits the use of content published in its journals but only provided the following criteria are met:

1. If you are using figures/tables, permission is granted for use in print and electronic versions of your dissertation or thesis.
2. A full text article may be used only in print versions of a dissertation or thesis. AAAS does not permit the reproduction of full text articles in electronic versions of theses or dissertations.
3. The following credit line must be printed along with the AAAS material: “From [Insert Full Reference Citation]/ Reprinted with permission from AAAS”.
4. All required credit lines and notices must be visible any time a user accesses any part of the AAAS material and must appear on any printed copies that an authorized user might make.
5. The AAAS material may not be modified or altered except that figures and tables may be modified with permission from the author. Author permission for any such changes must be secured prior to your use.
6. AAAS must publish the full paper prior to your use of any of its text or figures.
7. If the AAAS material covered by this permission was published in *Science* during the years 1974-1994, you must also obtain permission from the author, who may grant or withhold permission, and who may or may not charge a fee if permission is granted. See original article for author’s address. This condition does not apply to the news articles published in *Science*.
8. Permission covers the distribution of your dissertation or thesis on demand by a third party distributor (e.g. ProQuest/UMI), provided the AAAS material covered by this permission remains in situ and is not distributed by that third party outside of the context of your thesis/dissertation.
9. Permission does not apply to figures/photos/artwork or any other content or material included in your work that are credited to non-AAAS sources. If the requested material is sourced to or

references non-AAAS sources, you must obtain authorization from that source as well before using that material. You agree to hold harmless and indemnify AAAS against any claims arising from your use of any content in your work that is credited to non-AAAS sources.

10. By using the AAAS Material identified in your request, you agree to abide by all the terms & conditions herein.

11. AAAS makes no representations or warranties as to the accuracy of any information contained in the AAAS material covered by this permission, including any warranties of merchantability or fitness for a particular purpose.

If how you wish to use the content falls outside of these guidelines or if you have any questions, please let me know.

Kind regards,

Dana



Dana James (she/her)

Rights and Licensing Coordinator, Office of Publishing

American Association for the Advancement of Science

1200 New York Avenue, NW | Washington, DC 20005

| djames@aaas.org | www.aaas.org | www.science.org



RightsLink

[Sign in/Register](#)


Magic Number Pt13 and Misshapen Pt12 Clusters: Which One is the Better Catalyst?



Most Trusted. Most Cited. Most Read.

Author: Takane Imaoka, Hirokazu Kitazawa, Wang-Jae Chun, et al

Publication: Journal of the American Chemical Society

Publisher: American Chemical Society

Date: Sep 1, 2013

Copyright © 2013, American Chemical Society

PERMISSION/LICENSE IS GRANTED FOR YOUR ORDER AT NO CHARGE

This type of permission/license, instead of the standard Terms and Conditions, is sent to you because no fee is being charged for your order. Please note the following:

- Permission is granted for your request in both print and electronic formats, and translations.
- If figures and/or tables were requested, they may be adapted or used in part.
- Please print this page for your records and send a copy of it to your publisher/graduate school.
- Appropriate credit for the requested material should be given as follows: "Reprinted (adapted) with permission from {COMPLETE REFERENCE CITATION}. Copyright {YEAR} American Chemical Society." Insert appropriate information in place of the capitalized words.
- One-time permission is granted only for the use specified in your RightsLink request. No additional uses are granted (such as derivative works or other editions). For any uses, please submit a new request.

If credit is given to another source for the material you requested from RightsLink, permission must be obtained from that source.

[BACK](#)[CLOSE WINDOW](#)

Rightslink® by Copyright Clearance Center

20.08.24, 13:12



RightsLink

The Mackay-Type Cluster [Cu₄₃Al₁₂](Cp*)₁₂: Open-Shell 67-Electron Superatom with Emerging Metal-Like Electronic Structure



Author: Roland A. Fischer, Jean-Yves Saillard, Juarez L. F. Da Silva, et al
 Publication: Angewandte Chemie International Edition
 Publisher: John Wiley and Sons
 Date: Jul 24, 2018

© 2018 Wiley-VCH Verlag GmbH & Co. KGaA, Weinheim

Order Completed

Thank you for your order.

This Agreement between Raphael Bühler ("You") and John Wiley and Sons ("John Wiley and Sons") consists of your license details and the terms and conditions provided by John Wiley and Sons and Copyright Clearance Center.

Your confirmation email will contain your order number for future reference.

License Number 5853021295388

[Printable Details](#)

License date Aug 20, 2024

Licensed Content

Licensed Content	John Wiley and Sons
Publisher	
Licensed Content	Angewandte Chemie International Edition
Publication	
Licensed Content	The Mackay-Type Cluster [Cu ₄₃ Al ₁₂](Cp*) ₁₂ : Open-Shell 67-Electron Superatom with Emerging Metal-Like Electronic Structure
Title	
Licensed Content	Roland A. Fischer, Jean-Yves Saillard, Juarez L. F. Da Silva, et al
Author	
Licensed Content	Jul 24, 2018
Date	
Licensed Content	57
Volume	
Licensed Content	44
Issue	
Licensed Content	5
Pages	

Order Details

Type of use	Dissertation/Thesis
Requestor type	University/Academic
Format	Print and electronic
Portion	Figure/table
Number of figures/tables	1
Will you be translating?	No

About Your Work

Title of new work	Metal-Substrate Interactions at Ligated Heterometallic Complexes and Clusters
Institution name	Technical University of Munich
Expected presentation date	Nov 2024

Additional Data

Portions	Reprint figure 2 of the original work in order to underline the state of the art
The Requesting Person / Organization to Appear on the License	Raphael Bühler

Rightslink® by Copyright Clearance Center

20.08.24, 13:12

Requestor Location	Tax Details
Mr. Raphael Bühler Occamstr. 4	Publisher Tax ID EU826007151
Requestor Location München, Bayern 80802 Germany Attn: Mr. Raphael Bühler	

Would you like to purchase the full text of this article? If so, please continue on to the content ordering system located here: [Purchase PDF](#)
If you click on the buttons below or close this window, you will not be able to return to the content ordering system.

Total: 0.00 EUR

CLOSE WINDOW ORDER MORE

© 2024 Copyright - All Rights Reserved | [Copyright Clearance Center, Inc.](#) | [Privacy statement](#) | [Data Security and Privacy](#)
| [For California Residents](#) | [Terms and Conditions](#)Comments? We would like to hear from you. E-mail us at
customercare@copyright.com



Rightslink® by Copyright Clearance Center

20.08.24, 13:19

CCC
RightsLink

SPRINGER NATURE

Modern cluster design based on experiment and theory

Author: Takamasa Tsukamoto et al
Publication: Nature Reviews Chemistry
Publisher: Springer Nature
Date: Mar 24, 2021

Copyright © 2021, Springer Nature Limited

Order Completed

Thank you for your order.

This Agreement between Raphael Bühler ("You") and Springer Nature ("Springer Nature") consists of your license details and the terms and conditions provided by Springer Nature and Copyright Clearance Center.

Your confirmation email will contain your order number for future reference.

License Number	5853030182592	Printable Details
License date	Aug 20, 2024	
Licensed Content		Order Details
Licensed Content Publisher	Springer Nature	Type of Use Thesis/Dissertation
Licensed Content Publication	Nature Reviews Chemistry	Requestor type academic/university or research institute
Licensed Content Title	Modern cluster design based on experiment and theory	Format print and electronic
Licensed Content Author	Takamasa Tsukamoto et al	Portion figures/tables/illustrations
Licensed Content Date	Mar 24, 2021	Number of figures/tables/illustrations 1
		Would you like a high resolution image with your order? no
		Will you be translating? no
		Circulation/distribution 1 - 29
		Author of this Springer Nature content no
About Your Work		Additional Data
Title of new work	Metal-Substrate Interactions at Ligated Heterometallic Complexes and Clusters	Portions Reprint figure 3 of the original work in order to underline the state of the art
Institution name	Technical University of Munich	The Requesting Person / Organization to Appear on the License Raphael Bühler
Expected presentation date	Nov 2024	

<https://s100.copyright.com/AppDispatchServlet>

Seite 1 von 2

Rightslink® by Copyright Clearance Center

20.08.24, 13:19

Requestor Location		Tax Details
Mr. Raphael Bühler Occamstr. 4		
Requestor Location	München, Bayern 80802 Germany Attn: Mr. Raphael Bühler	
Billing Information		
Billing Type	Invoice Mr. Raphael Bühler Occamstr. 4	
Billing address	München, Germany 80802 Attn: Mr. Raphael Bühler	
Total: 0.00 EUR		
CLOSE WINDOW		ORDER MORE

© 2024 Copyright - All Rights Reserved | [Copyright Clearance Center, Inc.](#) | [Privacy statement](#) | [Data Security and Privacy](#)
| [For California Residents](#) | [Terms and Conditions](#)Comments? We would like to hear from you. E-mail us at
customercare@copyright.com



Rightslink® by Copyright Clearance Center

20.08.24, 13:21

CCC
RightsLink

The Al₅₀Cp*₁₂ Cluster – A 138-Electron Closed Shell (L = 6) Superatom

Author: Hannu Häkkinen, Henrik Grönbeck, Robert L. Whetten, et al
Publication: European Journal of Inorganic Chemistry
Publisher: John Wiley and Sons
Date: May 13, 2011

Copyright © 2011 WILEY-VCH Verlag GmbH & Co. KGaA, Weinheim

Order Completed

Thank you for your order.

This Agreement between Raphael Bühler ("You") and John Wiley and Sons ("John Wiley and Sons") consists of your license details and the terms and conditions provided by John Wiley and Sons and Copyright Clearance Center.

Your confirmation email will contain your order number for future reference.

License Number	5853030341923 <th> Printable Details</th>	Printable Details
License date	Aug 20, 2024	
Licensed Content		Order Details
Licensed Content Publisher	John Wiley and Sons	Type of use Dissertation/Thesis
Licensed Content Publication	European Journal of Inorganic Chemistry	Requestor type University/Academic
Licensed Content Title	The Al ₅₀ Cp* ₁₂ Cluster – A 138-Electron Closed Shell (L = 6) Superatom	Format Print and electronic
Licensed Content Author	Hannu Häkkinen, Henrik Grönbeck, Robert L. Whetten, et al	Portion Figure/table
Licensed Content Date	May 13, 2011	Number of figures/tables 1
Licensed Content Volume	2011	Will you be translating? No
Licensed Content Issue	17	
Licensed Content Pages	4	
About Your Work		Additional Data
Title of new work	Metal-Substrate Interactions at Ligated Heterometallic Complexes and Clusters	Portions Reprint figure 2 of the original work in order to underline the state of the art
Institution name	Technical University of Munich	The Requesting Person / Organization to Appear on the License Raphael Bühler
Expected presentation date	Nov 2024	

<https://s100.copyright.com/AppDispatchServlet>

Seite 1 von 2

Rightslink® by Copyright Clearance Center

20.08.24, 13:21

Requestor Location	Tax Details
Mr. Raphael Bühler Occamstr. 4	Publisher Tax ID EU826007151
Requestor Location München, Bayern 80802 Germany Attn: Mr. Raphael Bühler	

Would you like to purchase the full text of this article? If so, please continue on to the content ordering system located here: [Purchase PDF](#)
If you click on the buttons below or close this window, you will not be able to return to the content ordering system.

Total: 0.00 EUR

CLOSE WINDOW ORDER MORE

© 2024 Copyright - All Rights Reserved | [Copyright Clearance Center, Inc.](#) | [Privacy statement](#) | [Data Security and Privacy](#)
| [For California Residents](#) | [Terms and Conditions](#) Comments? We would like to hear from you. E-mail us at
customercare@copyright.com

<https://s100.copyright.com/AppDispatchServlet>

Seite 2 von 2



Rightslink® by Copyright Clearance Center

20.08.24, 13:23

CCC
RightsLink

CO₂ and H₂ Activation on Zinc-Doped Copper Clusters

Author: Bárbara Zamora, László Nyulászi, Tibor Höltzl
 Publication: ChemPhysChem
 Publisher: John Wiley and Sons
 Date: Dec 6, 2023

© 2023 The Authors. *ChemPhysChem* published by Wiley-VCH GmbH

Order Completed

Thank you for your order.

This Agreement between Raphael Bühler ("You") and John Wiley and Sons ("John Wiley and Sons") consists of your license details and the terms and conditions provided by John Wiley and Sons and Copyright Clearance Center.

Your confirmation email will contain your order number for future reference.

License Number	5853030469583 <th> Printable Details</th>	Printable Details	
License date	Aug 20, 2024		
Licensed Content		Order Details	
Licensed Content Publisher	John Wiley and Sons	Type of use	Dissertation/Thesis
Licensed Content Publication	ChemPhysChem	Requestor type	University/Academic
Licensed Content Title	CO ₂ and H ₂ Activation on Zinc-Doped Copper Clusters	Format	Print and electronic
Licensed Content Author	Bárbara Zamora, László Nyulászi, Tibor Höltzl	Portion	Figure/table
Licensed Content Date	Dec 6, 2023	Number of figures/tables	1
Licensed Content Volume	25	Will you be translating?	No
Licensed Content Issue	1		
Licensed Content Pages	14		
About Your Work		Additional Data	
Title of new work	Metal-Substrate Interactions at Ligated Heterometallic Complexes and Clusters	Portions	Reprint figure 7 of the original work in order to underline the state of the art
Institution name	Technical University of Munich	The Requesting Person / Organization to Appear on the License	Raphael Bühler
Expected presentation date	Nov 2024		

<https://s100.copyright.com/AppDispatchServlet>

Seite 1 von 2

Rightslink® by Copyright Clearance Center

20.08.24, 13:23

Requestor Location	Tax Details
Mr. Raphael Bühler Occamstr. 4	Publisher Tax ID EU826007151
Requestor Location München, Bayern 80802 Germany Attn: Mr. Raphael Bühler	

Would you like to purchase the full text of this article? If so, please continue on to the content ordering system located here: [Purchase PDF](#)
If you click on the buttons below or close this window, you will not be able to return to the content ordering system.

Total: 0.00 EUR

CLOSE WINDOW ORDER MORE

© 2024 Copyright - All Rights Reserved | [Copyright Clearance Center, Inc.](#) | [Privacy statement](#) | [Data Security and Privacy](#)
| [For California Residents](#) | [Terms and Conditions](#) Comments? We would like to hear from you. E-mail us at
customercare@copyright.com



Rightslink® by Copyright Clearance Center

20.08.24, 13:26



The Intermetalloid Cluster [(Cp*AlCu)6H4], Embedding a Cu6 Core Inside an Octahedral Al6 Shell: Molecular Models of Hume-Rothery Nanophases

Author: Roland A. Fischer, Christian Gemel, Rüdiger W. Seidel, et al
Publication: Angewandte Chemie International Edition
Publisher: John Wiley and Sons
Date: Jun 24, 2014

© 2014 WILEY-VCH Verlag GmbH & Co. KGaA, Weinheim

Order Completed

Thank you for your order.

This Agreement between Raphael Bühler ("You") and John Wiley and Sons ("John Wiley and Sons") consists of your license details and the terms and conditions provided by John Wiley and Sons and Copyright Clearance Center.

Your confirmation email will contain your order number for future reference.

License Number 5853030661896

[Printable Details](#)

License date Aug 20, 2024

Licensed Content

Licensed Content Publisher	John Wiley and Sons
Licensed Content Publication	Angewandte Chemie International Edition
Licensed Content Title	The Intermetalloid Cluster [(Cp*AlCu)6H4], Embedding a Cu6 Core Inside an Octahedral Al6 Shell: Molecular Models of Hume-Rothery Nanophases
Licensed Content Author	Roland A. Fischer, Christian Gemel, Rüdiger W. Seidel, et al
Licensed Content Date	Jun 24, 2014
Licensed Content Volume	53
Licensed Content Issue	30
Licensed Content Pages	5

Order Details

Type of use	Dissertation/Thesis
Requestor type	University/Academic
Format	Print and electronic
Portion	Figure/table
Number of figures/tables	1
Will you be translating?	No

About Your Work

Title of new work	Metal-Substrate Interactions at Ligated Heterometallic Complexes and Clusters
Institution name	Technical University of Munich
Expected presentation date	Nov 2024

Additional Data

Portions	Reprint figure 1 of the original work in order to underline the state of the art
The Requesting Person / Organization to Appear on the License	Raphael Bühler

Rightslink® by Copyright Clearance Center

20.08.24, 13:26

Requestor Location	Tax Details
Mr. Raphael Bühler Occamstr. 4	Publisher Tax ID EU826007151
Requestor Location München, Bayern 80802 Germany Attn: Mr. Raphael Bühler	

Would you like to purchase the full text of this article? If so, please continue on to the content ordering system located here: [Purchase PDF](#)
If you click on the buttons below or close this window, you will not be able to return to the content ordering system.

Total: 0.00 EUR

CLOSE WINDOW ORDER MORE

© 2024 Copyright - All Rights Reserved | [Copyright Clearance Center, Inc.](#) | [Privacy statement](#) | [Data Security and Privacy](#)
| [For California Residents](#) | [Terms and Conditions](#) Comments? We would like to hear from you. E-mail us at
customercare@copyright.com



Rightslink® by Copyright Clearance Center

20.08.24, 13:29

CCC
RightsLink

Catalytic Alkyne Semihydrogenation with Polyhydride Ni/Ga Clusters
Author: Roland A. Fischer, Christian Gemel, Jean-Yves Saillard, et al
Publication: Angewandte Chemie International Edition
Publisher: John Wiley and Sons
Date: Jul 28, 2023

© 2023 The Authors. *Angewandte Chemie International Edition* published by Wiley-VCH GmbH

Order Completed

Thank you for your order.

This Agreement between Raphael Bühler ("You") and John Wiley and Sons ("John Wiley and Sons") consists of your license details and the terms and conditions provided by John Wiley and Sons and Copyright Clearance Center.

Your confirmation email will contain your order number for future reference.

License Number	5853030816737	Printable Details
License date	Aug 20, 2024	
Licensed Content		Order Details
Licensed Content Publisher	John Wiley and Sons	Type of use Dissertation/Thesis
Licensed Content Publication	Angewandte Chemie International Edition	Requestor type Author of this Wiley article
Licensed Content Title	Catalytic Alkyne Semihydrogenation with Polyhydride Ni/Ga Clusters	Format Print and electronic
Licensed Content Author	Roland A. Fischer, Christian Gemel, Jean-Yves Saillard, et al	Portion Figure/table
Licensed Content Date	Jul 28, 2023	Number of figures/tables 2
Licensed Content Volume	62	Will you be translating? No
Licensed Content Issue	36	
Licensed Content Pages	6	
About Your Work		Additional Data
Title of new work	Metal-Substrate Interactions at Ligated Heterometallic Complexes and Clusters	Portions Reprint figure 2 and 5 of the original work in order to underline the state of the art
Institution name	Technical University of Munich	The Requesting Person / Organization to Appear on the License Raphael Bühler
Expected presentation date	Nov 2024	

<https://s100.copyright.com/AppDispatchServlet>

Seite 1 von 2

Rightslink® by Copyright Clearance Center

20.08.24, 13:29

Requestor Location	Tax Details
Mr. Raphael Bühler Occamstr. 4	Publisher Tax ID EU826007151
Requestor Location München, Bayern 80802 Germany Attn: Mr. Raphael Bühler	

Would you like to purchase the full text of this article? If so, please continue on to the content ordering system located here: [Purchase PDF](#)
If you click on the buttons below or close this window, you will not be able to return to the content ordering system.

Total: 0.00 EUR

CLOSE WINDOW ORDER MORE

© 2024 Copyright - All Rights Reserved | [Copyright Clearance Center, Inc.](#) | [Privacy statement](#) | [Data Security and Privacy](#)
| [For California Residents](#) | [Terms and Conditions](#) Comments? We would like to hear from you. E-mail us at
customercare@copyright.com



Rightslink® by Copyright Clearance Center

20.08.24, 13:31



RightsLink



Assignment of individual structures from intermetallic nickel gallium cluster ensembles

SPRINGER NATURE

Author: Maximilian Muhr et al
Publication: Communications Chemistry
Publisher: Springer Nature
Date: Feb 13, 2024

Copyright © 2024, The Author(s)

Creative Commons

This is an open access article distributed under the terms of the [Creative Commons CC BY license](#), which permits unrestricted use, distribution, and reproduction in any medium, provided the original work is properly cited.

You are not required to obtain permission to reuse this article.

To request permission for a type of use not listed, please contact [Springer Nature](#)

© 2024 Copyright - All Rights Reserved | [Copyright Clearance Center, Inc.](#) | [Privacy statement](#) | [Data Security and Privacy](#)
| [For California Residents](#) | [Terms and Conditions](#)Comments? We would like to hear from you. E-mail us at customercare@copyright.com

20.08.24, 14:04



CUSTOMER INFORMATION

Billing Address	Customer Location
Mr. Raphael Bühler Occamstr. 4 München, Bayern 80802 Germany +49 15780789044 raphael.buehler@tum.de	Mr. Raphael Bühler Occamstr. 4 München, Bayern 80802 Germany
PO Number (optional)	Payment options
N/A	Invoice

ORDER REVIEW

1. Chemical Society reviews		0,00 EUR	
Article: Intermetallic phases meet intermetalloid clusters			
ISSN	0306-0012	Publisher	ROYAL SOCIETY OF CHEMISTRY, ETC.]
Type of Use	Republish in a thesis/dissertation on	Portion	Chart/graph/table/figure
LICENSED CONTENT			
Publication Title	Chemical Society reviews	Rightsholder	Royal Society of Chemistry
Article Title	Intermetallic phases meet intermetalloid clusters	Publication Type	Journal
Author / Editor	CHEMICAL SOCIETY (GREAT BRITAIN)	Start Page	8496
Date	01/01/1972	End Page	8510
Language	English	Issue	15
Country	United Kingdom of Great Britain and Northern Ireland	Volume	50
REQUEST DETAILS			
Portion Type	Chart/graph/table/figure	Distribution	Worldwide
Number of Charts / Graphs / Tables / Figures Requested	1	Translation	Original language of publication
		Copies for the Disabled?	No

<https://marketplace.copyright.com/rs-ui-web/mp/checkout/review-details>

Seite 1 von 2

20.08.24, 14:04

Format (select all that apply)	Print, Electronic	Minor Editing Privileges?	No
Who Will Republish the Content?	Academic institution	Incidental Promotional Use?	No
Duration of Use	Life of current edition	Currency	EUR
Lifetime Unit Quantity	Up to 499		
Rights Requested	Main product		

NEW WORK DETAILS

Title	Metal-Substrate Interactions at Ligated Heterometallic Complexes and Clusters	Institution Name	Technical University of Munich
Instructor Name	Roland A. Fischer	Expected Presentation Date	2024-11-01
ADDITIONAL DETAILS			

Order Reference Number	N/A	The Requesting Person / Organization to Appear on the License	Raphael Bühler
------------------------	-----	---	----------------

REQUESTED CONTENT DETAILS

Title, Description or Numeric Reference of the Portion(s)	Reprint figure 6 of the original work in order to underline the state of the art	Title of the Article / Chapter the Portion Is From	Intermetallic phases meet intermetalloid clusters
Editor of Portion(s)	Schütz, Max; Gemel, Christian; Klein, Wilhelm; Fischer, Roland A.; Fässler, Thomas F.	Author of Portion(s)	Schütz, Max; Gemel, Christian; Klein, Wilhelm; Fischer, Roland A.; Fässler, Thomas F.
Volume / Edition	50	Issue, if Republishing an Article From a Serial	15
Page or Page Range of Portion	8496-8510	Publication Date of Portion	2021-08-02

Total Items: 1**Total Due: 0,00 EUR**

I have read and accept the Marketplace Permissions General Terms and Conditions and any applicable Publisher Terms and Conditions

Back

Rightslink® by Copyright Clearance Center

20.08.24, 14:06



Cooperative Bond Activation and Facile Intramolecular Aryl Transfer of Nickel-Aluminum Pincer-type Complexes

Author: Connie C. Lu, Matthew V. Vollmer, Brendan J. Graziano

Publication: Angewandte Chemie

Publisher: John Wiley and Sons

Date: Jun 1, 2021

© 2021 Wiley-VCH GmbH

Order Completed

Thank you for your order.

This Agreement between Raphael Bühler ("You") and John Wiley and Sons ("John Wiley and Sons") consists of your license details and the terms and conditions provided by John Wiley and Sons and Copyright Clearance Center.

Your confirmation email will contain your order number for future reference.

License Number 5853050017489

[Printable Details](#)

License date Aug 20, 2024

Licensed Content

Licensed Content Publisher	John Wiley and Sons
Licensed Content Publication	Angewandte Chemie
Licensed Content Title	Cooperative Bond Activation and Facile Intramolecular Aryl Transfer of Nickel-Aluminum Pincer-type Complexes
Licensed Content Author	Connie C. Lu, Matthew V. Vollmer, Brendan J. Graziano
Licensed Content Date	Jun 1, 2021
Licensed Content Volume	133
Licensed Content Issue	27
Licensed Content Pages	8

Order Details

Type of use	Dissertation/Thesis
Requestor type	University/Academic
Format	Print and electronic
Portion	Figure/table
Number of figures/tables	1
Will you be translating?	No

About Your Work

Title of new work	Metal-Substrate Interactions at Ligated Heterometallic Complexes and Clusters
Institution name	Technical University of Munich
Expected presentation date	Nov 2024

Additional Data

Portions	Reprint Scheme 1 of the original work in order to underline the state of the art
The Requesting Person / Organization to Appear on the License	Raphael Bühler

Rightslink® by Copyright Clearance Center

20.08.24, 14:06

Requestor Location		Tax Details	
Mr. Raphael Bühler Occamstr. 4		Publisher Tax ID	EU826007151
Requestor Location	München, Bayern 80802 Germany Attn: Mr. Raphael Bühler		
<p>Would you like to purchase the full text of this article? If so, please continue on to the content ordering system located here: Purchase PDF If you click on the buttons below or close this window, you will not be able to return to the content ordering system.</p>			
Total: 0.00 EUR			
CLOSE WINDOW		ORDER MORE	

© 2024 Copyright - All Rights Reserved | [Copyright Clearance Center, Inc.](#) | [Privacy statement](#) | [Data Security and Privacy](#)
| [For California Residents](#) | [Terms and Conditions](#) Comments? We would like to hear from you. E-mail us at
customercare@copyright.com

Rightslink® by Copyright Clearance Center

20.08.24, 14:10



RightsLink

AlCp* as a Directing Ligand: C₆H and Si₂H Bond Activation at the Reactive Intermediate [Ni(AlCp*)₃]


Author: Roland A. Fischer, Manuela Winter, Mirza Cokoja, et al
Publication: Angewandte Chemie International Edition
Publisher: John Wiley and Sons
Date: Apr 16, 2004

Copyright © 2004 WILEY-VCH Verlag GmbH & Co. KGaA, Weinheim

Order Completed

Thank you for your order.

This Agreement between Raphael Bühler ("You") and John Wiley and Sons ("John Wiley and Sons") consists of your license details and the terms and conditions provided by John Wiley and Sons and Copyright Clearance Center.

Your confirmation email will contain your order number for future reference.

License Number 5853050235585

[Printable Details](#)

License date Aug 20, 2024

 Licensed Content

Licensed Content	John Wiley and Sons
Publisher	
Licensed Content	Angewandte Chemie
Publication	International Edition
Licensed Content	AlCp* as a Directing Ligand:
Title	C ₆ H and Si ₂ H Bond
	Activation at the Reactive
	Intermediate [Ni(AlCp*) ₃]
Licensed Content	Roland A. Fischer, Manuela
Author	Winter, Mirza Cokoja, et al
Licensed Content	Apr 16, 2004
Date	
Licensed Content	43
Volume	
Licensed Content	17
Issue	
Licensed Content	4
Pages	

 Order Details

Type of use	Dissertation/Thesis
Requestor type	University/Academic
Format	Print and electronic
Portion	Figure/table
Number of figures/tables	1
Will you be translating?	No

 About Your Work

Title of new work	Metal-Substrate Interactions at Ligated Heterometallic Complexes and Clusters
Institution name	Technical University of Munich
Expected presentation date	Nov 2024

 Additional Data

Portions	Reprint Scheme 1 of the original work in order to underline the state of the art
The Requesting Person / Organization to Appear on the License	Raphael Bühler

Rightslink® by Copyright Clearance Center

20.08.24, 14:10

Requestor Location	Tax Details
Mr. Raphael Bühler Occamstr. 4	Publisher Tax ID EU826007151
Requestor Location München, Bayern 80802 Germany Attn: Mr. Raphael Bühler	

Would you like to purchase the full text of this article? If so, please continue on to the content ordering system located here: [Purchase PDF](#)
If you click on the buttons below or close this window, you will not be able to return to the content ordering system.

Total: 0.00 EUR

CLOSE WINDOW ORDER MORE

© 2024 Copyright - All Rights Reserved | [Copyright Clearance Center, Inc.](#) | [Privacy statement](#) | [Data Security and Privacy](#)
| [For California Residents](#) | [Terms and Conditions](#) Comments? We would like to hear from you. E-mail us at
customercare@copyright.com

<https://s100.copyright.com/AppDispatchServlet>

Seite 2 von 2





RightsLink



C–H and Si–H Activation Reactions at Ru/Ga Complexes: A Combined Experimental and Theoretical Case Study on the Ru–Ga Bond

Author: Maximilian Muhr, Raphael Bübler, Hao Liang, et al

Publication: Chemistry - A European Journal

Publisher: John Wiley and Sons

Date: Aug 3, 2022

© 2022 The Authors. Chemistry - A European Journal published by Wiley-VCH GmbH

Order Completed

Thank you for your order.

This Agreement between Raphael Bübler ("You") and John Wiley and Sons ("John Wiley and Sons") consists of your license details and the terms and conditions provided by John Wiley and Sons and Copyright Clearance Center.

Your confirmation email will contain your order number for future reference.

License Number 5883711052778

[Printable Details](#)

License date Oct 07, 2024

Licensed Content

Licensed Content Publisher	John Wiley and Sons
Licensed Content Publication	Chemistry - A European Journal
Licensed Content Title	C–H and Si–H Activation Reactions at Ru/Ga Complexes: A Combined Experimental and Theoretical Case Study on the Ru–Ga Bond
Licensed Content Author	Maximilian Muhr, Raphael Bübler, Hao Liang, et al
Licensed Content Date	Aug 3, 2022
Licensed Content Volume	28
Licensed Content Issue	54
Licensed Content Pages	6

Order Details

Type of use	Dissertation/Thesis
Requestor type	Author of this Wiley article
Format	Print and electronic
Portion	Full article
Will you be translating?	No

About Your Work

Title of new work	Metal-Substrate Interactions at Ligated Heterometallic Complexes and Clusters
Institution name	Technical University of Munich
Expected presentation date	Nov 2024

Additional Data

The Requesting Person / Organization to Appear on the License	Raphael Bübler
---	----------------

Requestor Location

Mr. Raphael Bühler
Occamstr. 4

Tax Details

Publisher Tax ID EU826007151

Requestor Location

München, Bayern 80802
Germany
Attn: Mr. Raphael Bühler

Would you like to purchase the full text of this article? If so, please continue on to the content ordering system located here: [Purchase PDF](#)
If you click on the buttons below or close this window, you will not be able to return to the content ordering system.

Total: 0.00 EUR

CLOSE WINDOW

ORDER MORE

© 2024 Copyright - All Rights Reserved | [Copyright Clearance Center, Inc.](#) | [Privacy statement](#) | [Data Security and Privacy](#)
| [For California Residents](#) | [Terms and Conditions](#)Comments? We would like to hear from you. E-mail us at
customercare@copyright.com





RightsLink

**Cuprophilic Interactions in Polymeric [Cu10O2(Mes)6]n**

Author: Raphael Bühler, Robert M. Wolf, Christian Gemel, et al

Publication: Inorganic Chemistry

Publisher: American Chemical Society

Date: Sep 1, 2024

Copyright © 2024, American Chemical Society

PERMISSION/LICENSE IS GRANTED FOR YOUR ORDER AT NO CHARGE

This type of permission/license, instead of the standard Terms and Conditions, is sent to you because no fee is being charged for your order. Please note the following:

- Permission is granted for your request in both print and electronic formats, and translations.
- If figures and/or tables were requested, they may be adapted or used in part.
- Please print this page for your records and send a copy of it to your publisher/graduate school.
- Appropriate credit for the requested material should be given as follows: "Reprinted (adapted) with permission from {COMPLETE REFERENCE CITATION}. Copyright {YEAR} American Chemical Society." Insert appropriate information in place of the capitalized words.
- One-time permission is granted only for the use specified in your RightsLink request. No additional uses are granted (such as derivative works or other editions). For any uses, please submit a new request.

If credit is given to another source for the material you requested from RightsLink, permission must be obtained from that source.

BACK

CLOSE WINDOW

© 2024 Copyright - All Rights Reserved | [Copyright Clearance Center, Inc.](#) | [Privacy statement](#) | [Data Security and Privacy](#)
 | [For California Residents](#) | [Terms and Conditions](#) Comments? We would like to hear from you. E-mail us at
customercare@copyright.com



9 Eidestattliche Erklärung



Eidesstattliche Erklärung

Ich, Raphael Bühler, (Vor- und Nachname) erkläre an Eides statt, dass ich die bei der promotionsführenden Einrichtung

TUM School of Natural Sciences, Department für Chemie, Lehrstuhl für Anorganische und Metallorganische Chemie

der TUM zur Promotionsprüfung vorgelegte Arbeit mit dem Titel:

Metal-Substrate Interactions at Heterometallic Complexes and Clusters

unter der Anleitung und Betreuung durch: Prof. Dr. Dr. h. c. Roland A. Fischer

ohne sonstige Hilfe erstellt und bei der Abfassung nur die gemäß § 7 Abs. 6 und 7 angegebenen Hilfsmittel benutzt habe.

Ich habe keine Organisation eingeschaltet, die gegen Entgelt Betreuer*innen für die Anfertigung von Dissertationen sucht, oder die mir obliegenden Pflichten hinsichtlich der Prüfungsleistungen für mich ganz oder teilweise erledigt.

Ich habe die Dissertation in dieser oder ähnlicher Form in keinem anderen Prüfungsverfahren als Prüfungsleistung vorgelegt.

Teile der Dissertation wurden in *Chem. Eur. J.*, *Dalton Trans.*, *Inorg. Chem.*, *Nat. Chem.* veröffentlicht.

Ich habe den angestrebten Doktorgrad noch nicht erworben und bin nicht in einem früheren Promotionsverfahren für den angestrebten Doktorgrad endgültig gescheitert.

Ich habe bereits am _____ bei der promotionsführenden Einrichtung
_____ der Hochschule _____ unter Vorlage einer Dissertation mit dem Thema

die Zulassung zur Promotion beantragt mit dem Ergebnis:

Ich habe keine Kenntnis über ein strafrechtliches Ermittlungsverfahren in Bezug auf wissenschaftsbezogene Straftaten gegen mich oder eine rechtskräftige strafrechtliche Verurteilung mit Wissenschaftsbezug.

Die öffentlich zugängliche Promotionsordnung sowie die Richtlinien zur Sicherung guter wissenschaftlicher Praxis und für den Umgang mit wissenschaftlichem Fehlverhalten der TUM sind mir bekannt, insbesondere habe ich die Bedeutung von § 27 PromO (Nichtigkeit der Promotion) und § 28 PromO (Entzug des Doktorgrades) zur Kenntnis genommen. Ich bin mir der Konsequenzen einer falschen Eidestattlichen Erklärung bewusst.

Mit der Aufnahme meiner personenbezogenen Daten in die Alumni-Datei bei der TUM bin ich

einverstanden, nicht einverstanden.

München, den 04.09.2024

Ort, Datum, Unterschrift